



ALMA MATER STUDIORUM
UNIVERSITÀ DI BOLOGNA
SCUOLA DI MEDICINA E CHIRURGIA

3 - 5 September 2014
Bologna (Italy)

XIX

International Conference on
Mechanics in Medicine and Biology

Book of abstracts

ISBN: 978-88-901675-1-5

*Edited by Romano Zannoli,
Ivan Corazza and Rita Stagni*

www.icmmb19.org

Congress Chair: Romano Zannoli

Scientific Secretary: Ivan Corazza

Local Scientific Committee (University of Bologna):

Gastone Castellani

Ivan Corazza

Luca Cristofolini

Francesco Grigioni

Nicola Lopomo

Pasqualino Maietta Latessa

Emanuela Marcelli

Rita Stagni

Carlo Ventura

Romano Zannoli

International Scientific Committee:

Yos S. Morsi, PhD (Swinburne University of Technology, Australia)

Sakin Goyal, PhD (University of California)

Fong-Chin Su, PhD (National Cheng Kung University, Taiwan)

Shuichi Takayama, PhD (University of Michigan, USA)

Kheng-Lim Goh, PhD (University of Newcastle)

Miguel Cerrolaza Rivas, PhD (Central University of Venezuela)

Zhang Ming, PhD (The Hong Kong Polytechnic University)

Ming-Shaung Ju, PhD (National Cheng Kung University, Taiwan)

Liz G. Nallim, PhD (National University of Salta, Argentina)

Keith W. K. Ng, PhD (Macquarie University, Australia)

Zong-Ming Li, PhD (Cleveland Clinic, USA)

Felix Bljakhman, PhD PhD (Ural State University, The Russian Federation)

Zhong Liang, PhD (National Heart Centre, Singapore)

Eddie Yin-Kwee Ng, PhD, PGDipTHE (Nanyang Technological University, Singapore)

Dieter Liepsch, Dr.-Ing. habil. (Institut für Biotechnik e.V., Germany)

Tin-Kan Hung, PhD (University of Pittsburgh)

Feng Xu, PhD (Xi'an Jiaotong University, China)

Dhanjoo N. Ghista, PhD (Missouri State University, USA)

Bernardo Innocenti, PhD (École Polytechnique de Bruxelles, Belgium)

3 September

Bioengineering Elements of Tissue Engineering – An Optimum Thereby for
Cardiovascular Heart Diseases (YOS MORSI)

S1M: Cardiovascular - Implantable devices

Chairs: Yos Morsi, Emanuela Marcelli

EFFECTS OF ANTIBACTERIAL NANOSTRUCTURED COMPOSITE FILMS ON VASCULAR STENTS
HAN-YI CHENG

OPTIMIZATION AND DEGRADATION SIMULATIONS OF MAGNESIUM ALLOY STENT
FRANCESCO MIGLIAVACCA

DESIGN OF A NEW POLYMERIC HEART VALVE PROSTHESIS
PAOLA BAGNOLI

INTEGRATED APPROACH TO THE MANAGEMENT LVAD PATIENTS: A
CASE REPORT ABOUT THE USEFULNESS OF COOPERATION BETWEEN
MARCO MASETTI

BIOLOGICAL SAFETY ASSESSMENT OF A CARDIOVASCULAR IMPLANTABLE DEVICE: A
MANDATORY UPHILL WALK TOWARDS CLINICAL APPLICATION
PIERO TRABUCCO

Yos Morsi

Tissue Engineering and Biomaterials

The concept of Cardiac Tissue Engineering

Tissue engineering can be used to create a viable cellular environment that is supportive for integration, vascularization and attachment between implanted biomaterials and native tissue. Recently cardiovascular tissue engineering has introduced various new strategies for arteries and heart valves with degree of clinical success. However, myocardial tissue engineering is recognised as one of the most promising treatment for heart failure, but still in very early experimental stages and there are a number of real challenges to overcome. Nevertheless, there is some progress reported in literature. For example using three-dimensional (3-D) biodegradable scaffolds various kinds of 3-D myocardial tissues have been successfully regenerated by seeding for example cardiomyocytes into poly(glycolic acid), gelatin, alginate or collagen scaffolds. However, insufficient cell proliferation and attachment into the scaffolds and the occurrence of the inflammatory response make the generation of myocardial tissues is far from satisfactory. What is clear however, generated layered cell myocardial tissues sheets have enormous potential for clinical applications.

In this theme, the bioengineering strategies to create a viable tissue engineering substrates or devices for the heart and its components

Future research will also be discussed

EFFECTS OF ANTIBACTERIAL NANOSTRUCTURED COMPOSITE FILMS ON VASCULAR STENTS

HAN-YI CHENG

*Institute of Biomedical Materials and Tissue Engineering, College of Oral Medicine, Taipei Medical University, Taipei 110, Taiwan
Research Center for Biomedical Devices and Prototyping Production, Taipei Medical University, Taipei 110, Taiwan
Research Center for Biomedical Implants and Microsurgery Devices, Taipei Medical University, Taipei 110, Taiwan
E-mail: chytmu@gmail.com*

CHEN-HAN LEE

*School of Dental Technology, College of Oral Medicine, Taipei Medical University, Taipei, Taiwan
E-mail: leech@gmail.com*

LONG-SHENG LU

*Department of Radiation Oncology, Taipei Medical University Hospital, Taipei Taiwan
E-mail: 123007@h.tmu.edu.tw*

LIANG-YO YANG

*Department of Physiology, School of Medicine, College of Medicine, Taipei Medical University, 250 Wu Hsing Street, Taipei 110, Taiwan
Research Center for Biomedical Devices and Prototyping Production, Taipei Medical University, Taipei 110, Taiwan
E-mail: yanghy@tmu.edu.tw*

KENG-LIANG OU

*Institute of Biomedical Materials and Tissue Engineering, College of Oral Medicine, Taipei Medical University, Taipei 110, Taiwan
Research Center for Biomedical Devices and Prototyping Production, Taipei Medical University, Taipei 110, Taiwan
Research Center for Biomedical Implants and Microsurgery Devices, Taipei Medical University, Taipei 110, Taiwan
E-mail: klou@tmu.edu.tw*

The purpose of this research was to investigate stresses resulting from different thicknesses and compositions of hydrogenated Cu-incorporated diamond-like carbon (a-C:H/Cu) films at the interface between vascular stent and the artery using three-dimensional reversed finite element models (FEM). Blood flow velocity variation in vessels with plaques was examined by angiography, and the a-C:H/Cu films were characterized by transmission electron microscopy (TEM) to analyze surface morphology. FEM models were constructed using a computer-aided reverse design system, and the effects of antibacterial nanostructured composite films in the stress field were investigated. The maximum stress in the vascular stent occurred at the intersections of net-like structures. Data analysis indicated that the stress decreased by 15% in vascular stents with antibacterial nanostructured composite films compared to the control group, and the stress decreased with increasing film thickness. The present results confirmed that antibacterial nanostructured composite films improve the biomechanical properties of vascular stents and release abnormal stress to prevent restenosis. The results of the present study offer the clinical benefit of inducing superior biomechanical behavior in vascular stents.

Keywords: 3D-reversed model, biomechanics, finite element analysis, surface treatment, vascular stent

1. Introduction

Angioplasty is accepted as a safe technique for treating myocardial infarction, coronary artery heart disease, and thrombus. The clinical effects of stenting are influenced by various factors such as inadequate balloon expansion, artery injury, stent recoil, and restenosis, which is the most critical problem. In the 1980s, neointimal hyperplasia and elastic recoil were investigated extensively, and many cardiologists researched methods to eliminate these problems[1, 2]. Previously, neointimal hyperplasia occurred approximately in 40% of patients within 3–6 months after stenting. Subsequently, a repeat of the procedure was usually performed for restenosis[3, 4]. Coated-surface technology is widely used in medical devices because of their outstanding biocompatibility properties. Diamond-like carbon (DLC) has been proposed for use in blood-contacting devices[5-7] such as electrosurgical devices, artificial hearts, mechanical heart valves, and artery stents[8, 9]. Various reports have shown that the anticoagulation property of DLC is related to the bonding structure, hydrophobicity, and smooth surface[10, 11]. Restenosis is a common problem after stenting because of vessel overloading, and platelet adhesion and activation. However, a DLC film is suitable to prevent blood clotting[12, 13].

Finite element analysis (FEA) is a useful tool that could be applied to quantify the biomechanical behavior in the vascular stent and surrounding arteries. FEA has been used to study the biomechanical behavior of various medical applications, including temporomandibular joint replacement, dental implants, and vascular stents under a number of loading conditions[14, 15]. Hydrogenated Cu-incorporated a-C:H/Cu films were prepared in the present study using a radiofrequency plasma magnetron sputtering system at various CH₄/Ar gas ratios. The use of a-C:H/Cu films as promising anticoagulation and antibacterial coatings for biomedical applications was examined. The mechanical behavior at the stent-artery interface is an important factor for the clinical success of stenting; however, investigations of this behavior through experimental and theoretical analyses have thus far been scarce. To examine the biomechanical behavior of film-coated stents, the magnitude and location of the maximum stresses must be determined. Therefore, the aim of the present study was to examine the use of 3D finite element models (FEM) to quantify the maximum stresses in vascular stents with nanostructured composite films.

2. Materials and methods

2.1. Angiography test

Angiography is a biomedical imaging technique that is used to visualize blood vessels in the human body, such as arteries, veins, and heart chambers can be observed using contrast media. The arm vessels of six patients were selected because the vascular image of the arm is more stable than that of other parts. A special gray scale range for blood was adopted to show the regions of blood flow, and noise points could be erased. Variation of the gray scale at each moment could be used to determine changes in blood flow.

2.2. Preparation and evaluation of the a-C:H/Cu film

A deposition process that combined radio-frequency (RF) plasma and a magnetron sputtering system was used to deposit the a-C:H/Cu film on a glass substratum (diameter, 1 cm; thickness, 2 mm). Various gas mixture ratios of CH₄/Ar were fed into the chamber to deposit onto the films after the cleaning process[16]. For deposition of the a-C:H/Cu films, nano-Cu particles were generated by sputtering a copper target (99.99% purity), which was fixed at 60 mm directly above the substratum. The microstructures of the deposited films were examined with a high-resolution transmission electron microscope (HR-TEM, PHILIPS F-20) operated at 250 kV.

2.3. 3D-reversed model analysis

The 3D image models were built using the ANSYS Workbench 12.1 (ANSYS, Inc) finite element program. The vascular stents and arteries were regarded as continuous integers. The vascular stent in this study was standard type (Biosensors International Group, Ltd.; outer diameter: 3.0 mm, thickness: 0.1 mm). Clinical MRI showed that the artery had an outer diameter of 4.5 mm and a thickness of 0.5 mm, with plaques extending 5 mm and showing a central thickness of 0.5 mm. According to hyperelastic material laws, unloading follows the initial response of the stress-strain relationship, which is the rule for soft tissues in biomechanics. The balloon (diameter: 2.8 mm) was modeled in a cylindrical shape. The balloon simulated procedure was divided into two phases. The two important processes involved were converging and reinforcing of the mesh, which allow the model to approximate the actual object more accurately. Because of the deformation requirement, three types of elements were used in the present models: a 20-node solid element (Solid186) was used for the vascular stent. A 4-node shell element (Shell181) was used for the balloon, and an 8-node hyperelastic element (Hyper58) was adopted in the artery. The numbers of nodes and elements were 19,852-20,412 and 12,699-13,462, respectively. The vascular stent is characterized by the properties of the 316 L stainless steel. The biomechanical properties of the a-C:H/Cu film, and tissue have been described in previous studies[17, 18].

In the present study, the parameters were categorized into two groups on the basis of the thickness of the coated film and the percentage of the metallic Cu element. The thicknesses of these coated films varied from 0 (control group) to 500 μ m, and all models simulated with different percentages of metallic Cu element varied from 0% to 80%, for comparison. The von Mises stresses of the vascular stent and the artery were investigated in this study.

3. Results

Figure1 shows the blood flow velocity variation in vessels with plaques. The blood flow decreased through the narrow parts of vessels. The pixel of blood suddenly stopped increasing, and it indicated the blood was jammed because of plaques. Blood velocity decreased by >20% of the initial value. The present of plaques blocked blood flow and decreased the blood velocity, resulting in an increase in stress.

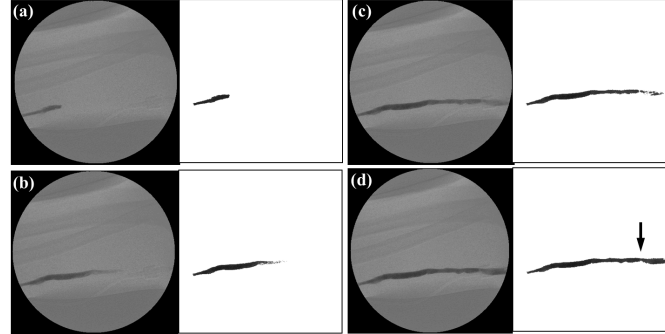


Fig. 1 Angiography test of artery with plaques (arrow) (a) $t = 0.015$ s, (b) $t = 0.020$ s, (c) $t = 0.025$ s, (d) $t = 0.030$ s (Lift: clinical image, Right: pixel image).

To better understand the effect of Cu doping on the microstructural variation of the a-C:H film, the samples were subjected to TEM. Cu doping resulted in the embedding of sphere-like nanoparticles became embedded in the film. Moreover, the SAEDP consisting of ring spots revealed the presence of nano-polycrystalline structures in the film. The size and number of nano-Cu particles were proportional to the Cu content. Therefore, the production of a-C:H/Cu films varied with the CH₄/Ar ratio, and transformation of the amorphous-like phase into a nano-polycrystalline phase was induced by Cu doping/ion bombardment and radical reactions. Figure 4(b) shows a TEM cross-section image showing Cu particles embedded in the DLC film, and crystallized within molecular system.

The highest stresses occurred at the intersections of the net-like structure in the vascular stent models. Figure 2 shows the von Mises stress distribution in the vascular stent with a 500 nm a-C:H/Cu film with 80% metallic Cu element (a-C:H/Cu-500:80) and without a-C:H/Cu film (control group). The highest stress in the vascular stent of the control group was 719.22 MPa, and that in the nanostructured film group varied between 597.62 and 715.40 MPa.

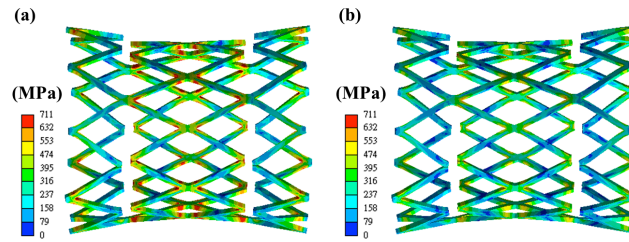


Fig. 2 Von Mises stress distributions of vascular stent in the (a) control group and (b) a-C:H/Cu-500/80 group.

On the other hand, the stress distribution was more uniform among the group of thicker-coated films. Remarkably, the maximum von Mises stress was reduced by 16.91% in the a-C:H/Cu-500:80 group, relative to the control group. The stress distribution showed significant stress in the untreated group. Surface treatments were shown to have the potential to decrease the abnormal stress concentration in the vascular stent. In the artery, the maximum stresses were observed at the intersections of the net-like structure of stents as shown in Fig. 3.

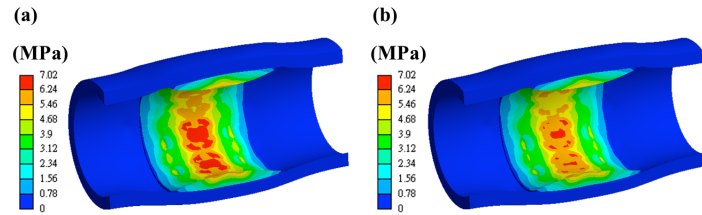


Fig. 3 Von Mises stress distributions of artery in the (a) control group and (b) a-C:H/Cu-500/80 group.

The highest stress for the artery was >10% lower in the a-C:H/Cu-500:80 group than in the control group. Coated layers decreased the stresses at the interface between the vascular stent and the artery. Although no significant differences in the maximum stresses were detected between the groups with different percentages of the metallic Cu element, the maximum von Mises stress in the vascular stent and artery was slightly smaller in the groups with a metallic Cu element than in those without. As described above, data analysis indicated deduced stresses in vascular stents and arteries resulting from the a-C:H/Cu film, although the maximum stresses did not differ significantly between the films with and without a metallic Cu element. In our study, the maximum stress was observed at intersections of the net-like structure. Applied stress is considered one of the most important factors determining the effectiveness of vascular stents.

4. Conclusion

Although previous studies have used FEA to examine vascular stents, few models have built stents with antibacterial nanostructured composite film. In the present study, this factor was considered important because evidence had indicated that the coated film is a critical factor for stress, and that overloading may induce a greater response to injury on the vessel wall, ultimately resulting in restenosis. Therefore, the interaction stress between the vascular stent and the artery is considered as an important factor. The aim of the present study was to understand the interface stress distribution in stenting operations. Our results indicate that vascular stents with a-C:H/Cu films may decrease overloading stress and release abnormal stress concentration to prevent restenosis. The present data suggest the clinical benefit of inducing a superior biomechanical behavior of the vascular stent.

Acknowledgements

The authors would like to thank the Department of Health, Executive Yuan, Taiwan for financially supporting this research under contract No. MOHW103-TDU-N-211-133001. The authors

would also like to thank the International Congress of Oral Implantologists under contract No. A-101-057 for financially supporting this research.

References

1. Jia, H., et al., *A novel polymer-free paclitaxel-eluting stent with a nanoporous surface for rapid endothelialization and inhibition of intimal hyperplasia: Comparison with a polymer-based sirolimus-eluting stent and bare metal stent in a porcine model*. Journal of Biomedical Materials Research Part A, 2011. **98A**(4): p. 629-637.
2. Yin, T.-Y., et al., *Endothelialization and in-stent restenosis on the surface of glycoprotein IIIa monoclonal antibody eluting stent*. Journal of Biomedical Materials Research Part A, 2012. **100A**(6): p. 1398-1406.
3. Stewart, H.J.S., et al., *Substrate-induced phenotypical change of monocytes/macrophages into myofibroblast-like cells: A new insight into the mechanism of in-stent restenosis*. Journal of Biomedical Materials Research Part A, 2009. **90A**(2): p. 465-471.
4. Indolfi, L., et al., *Microsphere-integrated drug-eluting stents: PLGA microsphere integration in hydrogel coating for local and prolonged delivery of hydrophilic antirestenosis agents*. Journal of Biomedical Materials Research Part A, 2011. **97A**(2): p. 201-211.
5. Hauert, R., *A review of modified DLC coatings for biological applications*. Diamond and Related Materials, 2003. **12**(3-7): p. 583-589.
6. Fedel, M., et al., *Surface properties and blood compatibility of commercially available diamond-like carbon coatings for cardiovascular devices*. Journal of Biomedical Materials Research Part B: Applied Biomaterials, 2009. **90B**(1): p. 338-349.
7. Krishnan, L.K., et al., *Quantitation of platelet adhesion to Ti and DLC-coated Ti in vitro using 125I-labeled platelets*. Biomolecular Engineering, 2002. **19**(2-6): p. 251-253.
8. Lee, B., et al., *Surface grafting of blood compatible zwitterionic poly(ethylene glycol) on diamond-like carbon-coated stent*. Journal of Materials Science: Materials in Medicine, 2011. **22**(3): p. 507-514.
9. Kim, J.H., et al., *Comparison of diamond-like carbon-coated nitinol stents with or without polyethylene glycol grafting and uncoated nitinol stents in a canine iliac artery model*. British Journal of Radiology, 2011. **84**(999): p. 210-215.
10. McLaughlin, J.A., et al., *Properties of diamond like carbon thin film coatings on stainless steel medical guidewires*. Diamond and Related Materials, 1996. **5**(3-5): p. 486-491.
11. Roy, R.K. and K.R. Lee, *Biomedical applications of diamond-like carbon coatings: A review*. Journal of Biomedical Materials Research Part B: Applied Biomaterials, 2007. **83**(1): p. 72-84.
12. Yang, P., et al., *Activation of platelets adhered on amorphous hydrogenated carbon (a-C:H) films synthesized by plasma immersion ion implantation-deposition (PIII-D)*. Biomaterials, 2003. **24**(17): p. 2821-2829.
13. Snyder, T.A., et al., *Preclinical biocompatibility assessment of the EVAHEART ventricular assist device: Coating comparison and platelet activation*. Journal of Biomedical Materials Research Part A, 2007. **81A**(1): p. 85-92.
14. Cheng, H.-Y., et al., *Stress effect on bone remodeling and osseointegration on dental implant with novel nano/microporous surface functionalization*. Journal of Biomedical Materials Research Part A, 2013. **101A**(4): p. 1158-1164.
15. Chu, K.-T., et al., *Enhancement of biomechanical behavior on osseointegration of implant with SLAffinity*. Journal of Biomedical Materials Research Part A, 2013. **101A**(4): p. 1195-1200.
16. Lee, F.-P., et al., *Antibacterial nanostructured composite films for biomedical applications: microstructural characteristics, biocompatibility, and antibacterial mechanisms*. Biofouling, 2013. **29**(3): p. 295-305.
17. Chung, J.-W., et al., *Biaxial elastic modulus of very thin diamond-like carbon (DLC) films*. Diamond and Related Materials, 2001. **10**(11): p. 2069-2074.

18. Heckmann, O., et al., *Crystallographic structure of cobalt films on Cu(001): elastic deformation to a tetragonal structure*. Surface Science, 1994. **312**(1–2): p. 62-72.

OPTIMIZATION AND DEGRADATION SIMULATIONS OF MAGNESIUM ALLOY STENT

FRANCESCO MIGLIAVACCA, WEI WU, DARIO GASTALDI

*Laboratory of Biological Structure Mechanics, Department of Chemistry, Materials and Chemical Engineering 'Giulio Natta',
Politecnico di Milano, Milan, 20133, Italy
francesco.migliavacca@polimi.it*

LORENZA PETRINI

*Department of Civil and Environmental Engineering, Politecnico di Milano
Milan, 20133, Italy
lorenza.petrini@polimi.it*

Introduction

Biodegradable magnesium (Mg) alloy stents (MAS) constitute a promising candidate which might present improved long-term clinical performances over commercial bare metal or drug eluting stents. MAS are expected to provide a temporary opening to a narrowed artery until it remodels and to disappear progressively. It would be particularly useful in treatment of congenital heart disease in growing babies. However, MAS were found to show limited mechanical support for diseased vessels due to fast degradation¹. Moreover, magnesium has a lower strength and elongation capability with respect to stainless steel 316L (SS316L) which is the standard reference for stent applications. In this paper we propose an approach based on finite element analysis (FEA) to improve MAS properties. The numerical results are also validated by experimental tests.

Material and Methods

As a first step, new design concept of MAS was proposed and a shape optimization process with FEA was applied on two dimensional (2D) stent models. Different magnesium alloys were considered, however the final choice fell onto AZ31 alloy. The main difficulty in this process was related to the fact that a MAS has two additional and controversial demands in mechanical properties compared to conventional SS316L stents. First, SS316L stents undergo large local strain (about 0.4-0.5) during stent expansion², while most magnesium alloys have much lower fracture elongation (usually below 0.2)³; this means that the deformation of MAS needs to be well controlled. Second, the elastic modulus of magnesium alloys is about 25% of SS316L; hence, a MAS needs more material (e.g. widening stent strut) to get enough scaffolding. However, more material may increase the strain demand during expansion. Moreover, the degradation time, which is mainly controlled by both uniform and stress corrosion processes⁴, requires at the same time to increase mass and to reduce maximum stress. An optimization algorithm based on the adaptive response surface method (ARSM)⁶ was applied to control the shape evolution. The minimization of the maximum principal strain was selected as objective function. A morphing procedure was used to facilitate the optimization involving iterations between a parametric CAD, a FEA code and an optimization code. Among the solutions having the maximum principal strains below a selected limit (0.118), the design with maximum normalized mass was chosen as the optimized (OPT) design.

As a second step, a biodegradable material model was proposed to study the behavior of the optimized stent in terms of corrosion under loadings resembling those *in vivo*. The numerical model is based on the continuum damage approach to scale linearly with the scalar damage parameter (D) for both the elastic and plastic properties of the undamaged material. Two corrosion mechanisms are considered in a cooperating way. The former is the uniform corrosion damage (D_U), which has phenomenological correspondence to the micro galvanic mechanism experimentally observed in Mg alloys that results in corrosive attack uniformly distributed on the surface exposed to the aggressive environment. The latter is the stress corrosion damage (D_{SC}), describing the damage related to stress corrosion process, namely the localization of the corrosion attack in the areas of the material where the maximum principal stress is more concentrated and the corrosive phenomenon evolves mediated by the stress field⁵. The corrosion damage variable D responsible for the global degradation is considered as a linear superposition of the two mechanisms under the isotropic damage assumption. When D equals 0, it means the element of the FEA stent model is intact; while when D equals 0.9, it means that the element is completely damaged and will be deleted in the model during simulation. The developed numerical model was used to compare the degradation process of the 3D optimized geometry and of a conventional design concept (called CON hereinafter) designed by the Institute of Metal Research, CAS, Shenyang, China (Fig. 1).

Finally, an experimental validation for the developed FEA procedure (optimization plus degradation modeling) was carried out thus proving its practical applicability for designing MAS. Twelve stent samples of AZ31 were manufactured according to the two MAS designs OPT and CON (Fig. 1), and each design had six samples. All samples were balloon expanded and subsequently immersed in D-Hanks' solution for a degradation test lasting 14 days. After 1, 3, 7 and 14 days of degradation, one, one, one and three samples of each stent design were removed from the solution, respectively (named CON-1 to CON-6; OPT-1 to OPT-6), cleaned in distilled water and then dried in air at room temperature. The breaking points and the surface morphology of these removed samples were observed using a stereo microscope and a scanning electronic microscope.

Results and Conclusions

The optimization history of responses of maximum principle strain and normalized mass (left) is plotted in figure 2. The results with the maximum principle strain below the selected-limit (80% tensile limit) were shaded for distinction and the model of iteration 20 (indicted by arrows) was chosen as the optimized design.. The main dimensions of the optimized design are indicated. The results of the simulation of the degradation process for CON and OPT design are plotted in figure 3. The normalized time unit t^* was set as 1 according to the ring break of the OPT model because the OPT model preserved its structural integrity longer than the CON model. Red circles indicate those locations on rings that were expected to be rapidly attacked and broken by stress corrosion.

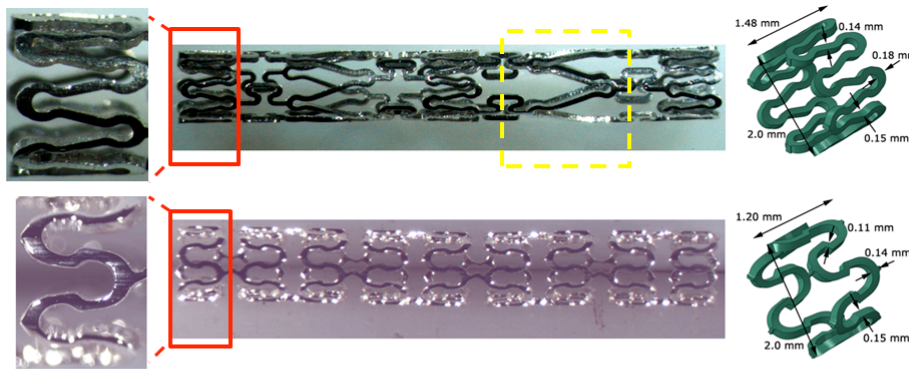


Fig. 1. CON sample (top) and OPT sample (bottom) used for experimental validation. The CON sample has two kinds of rings: short (indicated by solid red box) and long (indicated by dash yellow box). CON and OPT models for degradation process simulation are also plotted on the left. Note that the CON model only considered the short ring of the CON design.

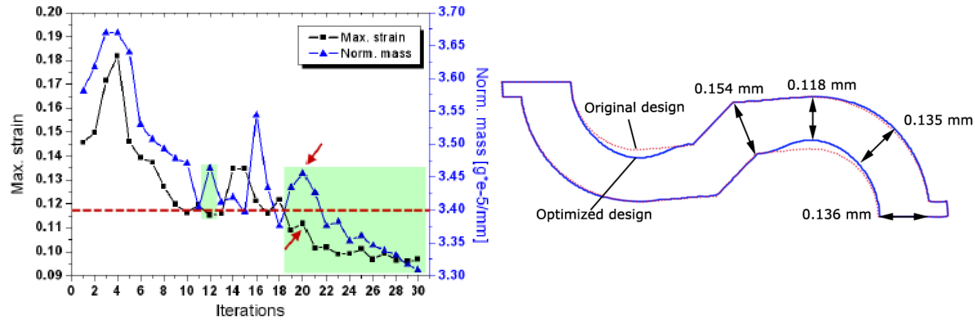


Fig. 2. Left: Optimization history and selected design (indicted by arrows). Right: Layout comparison of the original and optimized design.

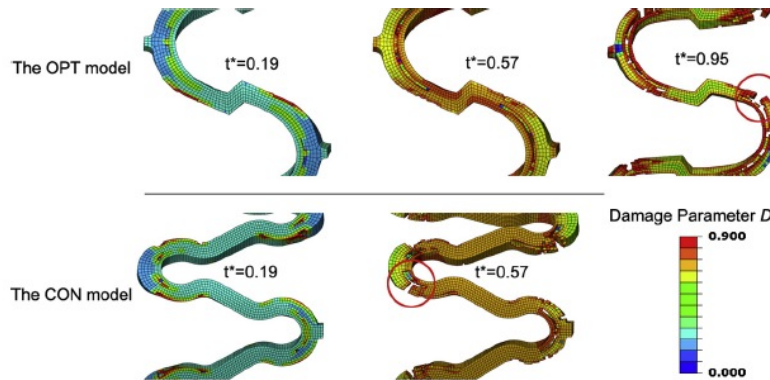
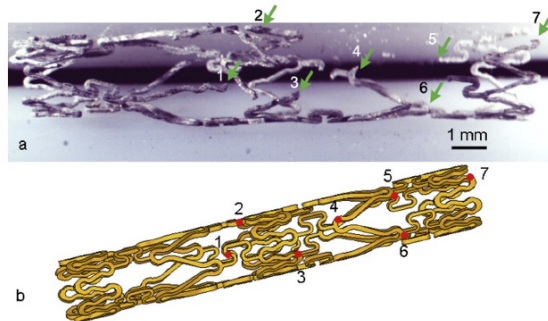


Fig. 3. Results of the simulation of the degradation process for OPT (upper part) and CON (lower part) design in terms of damage parameter D .

The experimental results showed that the samples of the optimized design had better corrosion resistance than that of the conventional design. CON-2 sample after 3 days of immersion is shown in figures 4a and 4b: it has seven break points caused by degradation. The locations on the short rings (points 3 and 7) were compatible with the location predicted in the simulation. OPT-2 had only 1 fracture after 3 days, and 7 days were necessary to have five locations broken by degradation in OPT-3 (Figure 4c and Figure 4d). Also in this case four locations (points 10, 20, 40 and 50) were compatible with those simulated. With the good match between the simulation and the experimental results, the work shows that the FEA numerical modeling constitutes an effective tool for design and thus the improvement of novel biodegradable MAS.



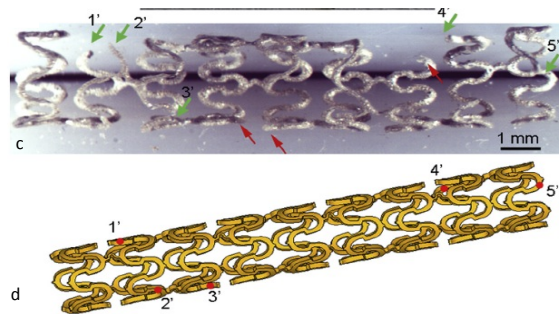


Fig. 4. Configuration of CON-2 after 3 days and OPT-3 after 7 days of degradation. The fracture locations due to corrosion are indicated by green arrows on the stent and by red points on the model.

References

1. Slottow TLP, Pakala R, Waksman R, Serial imaging and histology illustrating the degradation of a bioabsorbable magnesium stent in a porcine coronary artery, *Eur Heart J.* **29**:314, 2008.
2. McGarry JP, O'Donnell BP, McHugh PE, et al, Analysis of the mechanical performance of a cardiovascular stent design based on micromechanical modeling, *Comp Mater Sci* **31**:421-438, 2004.
3. Dalla Torre FH, Hanzi AC, Uggowitzer PJ, Microstructure and mechanical properties of microalloyed and equal channel angular extruded Mg alloys, *Scripta Mater* **59**:207-210, 2008.]
4. Winzer N, Atrens A, Dietzel W, Song G, Kainer KU, Stress corrosion cracking in magnesium alloys: Characterization and prevention. *Jom* **59**:49-53, 2007.
5. Winzer N, Atrens A, Song GL, et al, A critical review of the stress corrosion cracking (SCC) of magnesium alloys, *Adv Eng Mat*, **7**:659-693, 2005.
6. Wang GG, Dong ZM, Aitchison P. Adaptive response surface method—a global optimization scheme for approximation-based design problems. *Eng Optimiz* **33**:707–733, 2001.

DESIGN OF A NEW POLYMERIC HEART VALVE PROSTHESIS

FRANCESCO DE GAETANO, PAOLA BAGNOLI, ADRIANO ZAFFORA

*Department of Chemistry, Materials and Chemical Engineering "Giulio Natta", Politecnico di Milano,
Piazza Leonardo da Vinci 32, 20133 Milan, Italy*

francesco.degaetano@polimi.it

www.labsmech.polimi.it

MARTA SERRANI, J. BRUBERT, JOANNA STASIAK, GEOFF D. MOGGRIDGE

*Department of Chemical Engineering & Biotechnology, University of Cambridge,
Pembroke Street, Cambridge, CB23RA, UK*

ms2214@cam.ac.uk

MARIA LAURA COSTANTINO

*Department of Chemistry, Materials and Chemical Engineering "Giulio Natta", Politecnico di Milano,
Piazza Leonardo da Vinci 32, 20133 Milan, Italy*

marialaura.costantino@polimi.it

The potential of Polymeric Heart Valves (PHV) is to combine the good haemodynamic performances of biological valves with the durability of mechanical valves. The aim of this work is to design and develop a new supra-annular tri-leaflet prosthetic heart valve made from styrenic block co-polymers. A computational finite element model was implemented to optimize the thickness of the leaflets and the orientation of the polymer microstructures, to improve PHV mechanical and hydrodynamic performance. Based on the model outcomes, a prototype valve was developed, and 8 valves were developed and tested *in vitro* under continuous and pulsatile flow conditions, as prescribed by ISO5840 Standard. A specially designed pulse duplicator allowed testing of the PHVs at different flow rates and frequency conditions. All the PHVs met the requirements specified in ISO5840, in terms of both regurgitation and Effective Orifice Area (EOA), demonstrating their potential as heart valve prostheses.

Keywords: Heart Valve Prosthesis; Finite Element Model; pulse duplicator; styrenic block co-polymer.

1. Introduction

Two categories of Heart Valve (HV) prostheses are currently available: mechanical HV, fabricated from synthetic hard materials, or biological HV, made from xenograft tissues¹. The former demonstrated high durability, on the other hand they promote turbulent flow and require daily anticoagulant treatment. The latter have preferable fluid dynamics and hemocompatibility performances, but do not display high durability and present significant risk of failure due to tissue degradation¹. Despite current improvement in manufacturing of valve prostheses, clinical applications claim for new generation of HVs, able to meet long term reliability and effectiveness requirements². Recently, emerging material technologies allowed the development of novel polymers with improved and tunable properties: styrenic block co-polymer elastomers have a suitable micro-morphology which may mimic the structure and function of anisotropic collagen in the native valve³. The arrangement of these micro-domains can be optimized to enhance valve durability. The aim of this work was to design and develop PHV prototypes, on the basis of the outcomes of an ad-hoc implemented computational Finite Element Model and to test their performance by *in vitro* trials under continuous and pulsatile conditions.

2. Material and Methods

2.1 Finite element model (FEM)

CAD modeling was used to draw the PHV leaflet shape (Fig. 1-a) to fit into the host anatomy and guarantee appropriate coaptation of the leaflets in closed position avoiding backward flow. A single leaflet of a trileaflet HV (120° periodicity) was considered. FEM modeling (ABAQUS, Inc., Providence, RI) was used to analyze the mechanical behavior of the valve as a function of the leaflet thickness ($t_{24}=0.24$ mm, $t_{35}=0.35$ mm and $t_{60}=0.60$ mm) and material properties. Each 3D solid model was discretized with hexahedral elements (Fig. 1-c).

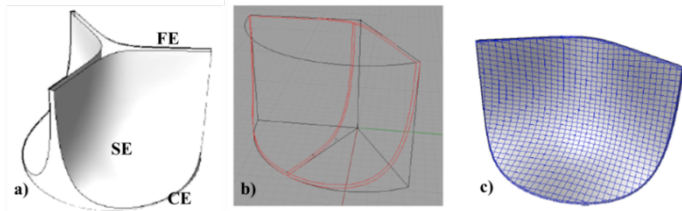


Fig. 1. PHV CAD model: (a) Sketch of a trileaflet heart valve (FE=Free Edge, CE=Commissure Edge, SE=belly Shape Edge); (b) automatic drawing procedure to model the edges; c) 3D solid model of the leaflet.

The mechanical effect of omitted leaflets was accounted by means of kinematic constraints. Uniform static pressure (24 kPa) was applied over the convex face of the leaflet to simulate the maximum transvalvular pressure gradient (diastolic load). The polymer mechanical behavior was modeled by a newly formulated hyperelastic anisotropic constitutive law; the model parameters were optimized on experimental data. An iterative reorientation procedure of the polymer chains was identified to optimize material response according to the hypothesis that the fibers shall align with the maximum principal stress directions.

2.2 Prototype in vitro testing

Based on the CAD design and FEM outcomes, 8 PHV prototypes (Fig. 2) were manufactured by compression moulding from poly(styrene-isoprene/butadiene-styrene), with 19% polystyrene weight fraction.

In-vitro tests were performed under both continuous and pulsatile flow on a test bench (Fig. 2) as recommended by ISO5840 Standard, using distilled water at 25°C.

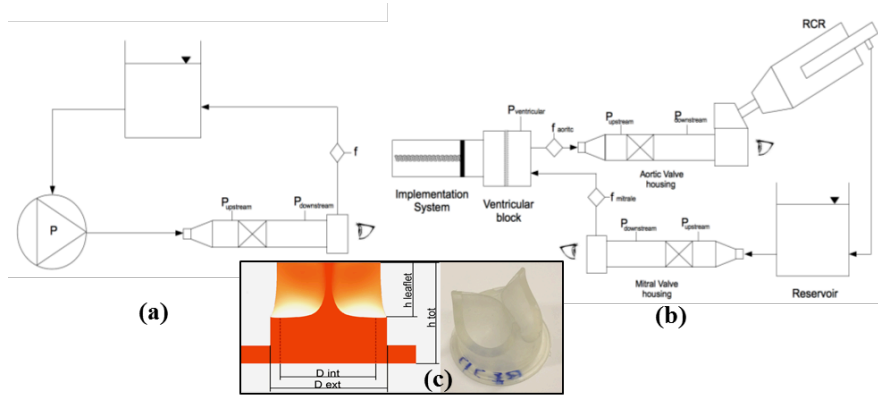


Fig. 2. Outline of the experimental set up for continuous (a) and pulsatile (b) flow tests. In the detail (c): sketch (left) and picture (right) of a PHV: $h_{\text{leaflet}} = 10.8 \text{ mm}$; $h_{\text{tot}} = 21 \text{ mm}$; $D_{\text{int}} = 22 \text{ mm}$; $D_{\text{ext}} = 28 \text{ mm}$.

Steady tests were performed at flow rates from 0 to 10 l/min (step 0.5 l/min). Regurgitation tests were run applying a backpressure in the range of 28 mmHg to 128 mmHg (steps 5 mmHg). A pulse duplicator was specifically designed to perform pulsatile flow tests (Fig.2-b) replicating the peripheral compliance and the resistances of the cardiovascular system by a Resistance-Compliance-Resistance (RCR) analogue.

Each PHV was tested under 3 different frequencies (45 bpm, 70 bpm, 120 bpm), 3 backpressures (80 mmHg, 120 mmHg, 160 mmHg) and 4 mean flow rates (2 l/min, 3.5 l/min, 5 l/min and 7 l/min) for at least 15 consecutive cycles.

3. Results and Discussion

3.1 Finite element model results

Finite element analysis for t24, t35 and t60 models calculated the stress distribution within the leaflet (Fig. 3).

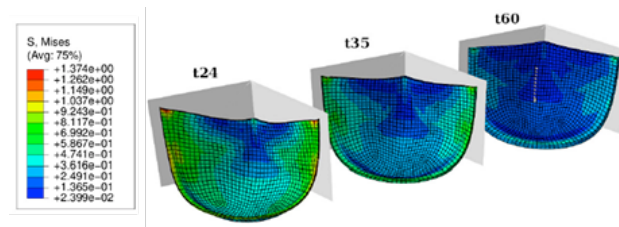


Fig. 3. Von Mises Stress map at different leaflet thickness.

Under the diastolic load, all the leaflet geometries assure appropriate coaptation of the leaflets but t24 displays significant stress increase near the junction between free-edge and commissural regions. Model t60 presents no significant stress peaks but a reduced coaptation area; moreover, the high thickness of the

leaflet may limit opening and closing of the PHV. Model t35 shows to be the best compromise among the analyzed geometries.

Five iterations of the reorientation procedure were required to optimize the leaflet obtaining an almost radial orientation, from the belly SE zone to the commissures. The optimized leaflet withstand more uniform stress state: 60% of the elements show maximum principal stress lower than 0.4 MPa.

3.2 In vitro tests results

PHV mean transvalvular pressure drop (8.36 ± 1.33 mmHg) and mean regurgitation (175.3 ± 19 ml/min) were recorded during continuous flow tests. Figure 4 (a-b) shows minimal leakage area formed during the closing phase of the valve.

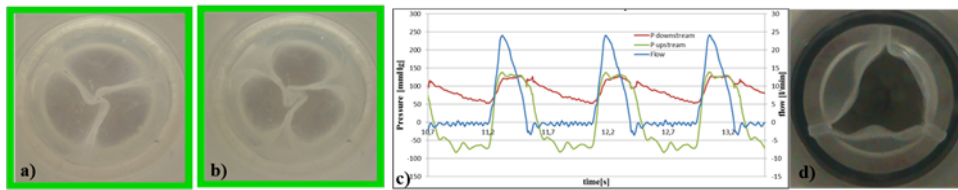


Fig.4. In vitro tests results: a-b) PHVs during static regurgitation tests at backpressure 28 mmHg (a) and 128 mmHg (b); c) Pressure and flow courses of the PHV during pulsatile tests; d) maximum opening of the PHV.

During pulsatile flow tests mean (12.20 ± 1.41 mmHg) and maximum (30.09 ± 4.7 mmHg) systolic pressure differences were recorded. Regurgitation ($7.13\% \pm 1.33$) and Effective Orifice Area EOA (1.445 ± 0.08 cm²) of all the PHVs meet the requirements provided by ISO5840 Standard (i.e. regurgitation <10% of the stroke volume and EOA >1 cm²).

The performances of PHVs under pulsatile tests are comparable with those of some bi-leaflet mechanical prostheses currently on the market⁴, having a comparable tissue annulus diameter.

4. Conclusions

The computational model may be used as a tool for the optimization of the design of new PHV: an automatic parametric CAD procedure allows the investigation of a large class of leaflet design and a standardized FEM procedure gives information about the mechanical response of the device before prototyping. The leaflet took advantages from reorientation process: the reduction of the vertical sliding of the leaflet at constant contact area remarks the stabilization of the closure of the valve.

The experimental hydrodynamic evaluation of PHVs prototypes showed that all 8 PHVs met the minimum requirements specified by ISO5840 Standard, in terms of both regurgitation and EOA, demonstrating their effectiveness.

References

1. Edmunds, L.H. et al., Directions for improvement of substitute heart valves: National Heart, Lung, and Blood Institute's Working Group report on heart valves, *J Biomed Mater Res*, **38**: 263-266, 1997.
2. Ghanbari, H. et al., Polymeric heart valves: new materials, emerging hopes, *Trends in Biotechnology*, **27**(6): 359-367, 2009.
3. Stasiak, J. et al., Effect of Stretching on the Structure of Cylinder- and Sphere-Forming Styrene-Isoprene-Styrene Block Copolymers, *Macromolecules*, **42**: 5256–5265, 2009.
4. Bottio T., et al., Small aortic annulus: the hydrodynamic performance of 5 commercially available bileaflet mechanical valves, *The Journal of Thoracic and Cardiovascular Surgery*, **128**(3): 457-462, 2011.

INTEGRATED APPROACH TO THE MANAGEMENT LVAD PATIENTS: A CASE REPORT ABOUT THE USEFULNESS OF COOPERATION BETWEEN ENGINEERS AND CLINICIANS

MARCO MASETTI¹, MARCUS GRANEGGER^{2,3}, HEINRICH SCHIMA^{2,3}, DANIEL ZIMPFER⁴,
FRANCESCO MOSCATO^{2,3}

¹ Cardiology, DIMES Department, University of Bologna, Bologna, Italy. ²Ludwig-Boltzmann-Cluster for Cardiovascular Research, Vienna, ³Center for Medical Physics and Biomedical Engineering, Medical University of Vienna, ⁴Dept. of Cardiac Surgery, Medical University of Vienna, Vienna, Austria

Left ventricular assist devices (LVAD) can support the failing left ventricle (LV) in patients waiting for heart transplantation or even for lifetime. In this context, understanding the interaction between the pump and the heart is crucial. However, the utility of a combined evaluation of information derived from the pump curves analysis and from transthoracic echocardiography (TTE) is still poorly explored, especially with the HeartWare HVAD, one of the newer pumps.

We report the experience of collaboration between engineers and clinicians at Medical University of Vienna during 2013, in which this combined approach lead to pump adjustments useful in clinical practice in two patients.

In one patient affected by dilated cardiomyopathy (DCMP), interrogation of pump controller revealed a pattern of suction because of excessive LV unloading by the LVAD. Pump power was 3.8 Watts, speed 2700/min, pump estimated flow 4 l/min. TTE showed interventricular septum shifted to the left chamber and small LV end-diastolic (EDD) and end-systolic (ESD) diameters (35 mm and 21 mm); aortic valve was closed in all beats, and right ventricle dilated. Pump speed was decreased to 2640/min, fluid intake was increased. After one month, pump power remained stable, estimated pump flow increased to 4.6 l/min, TTE showed a more central septum position, and larger LV (EDD/ESD: 51/43 mm); aortic valve was still closed, indicating a poor residual left ventricular function. Another patient with a recovering heart was identified, characterized by a normal right and left heart function at baseline speed of 2400 rpm (left ventricular EDV: 69ml, estimated EF 43%). In this patient, even when the speed was increased until suction occurred, the AV opened substantially. The shape of the systolic portion of the pump flow signal also reflected a prolonged opening time of the AV as observed in M-mode US. This patient was successfully weaned from the LVAD.

An integrated technical and clinical approach is useful for the management of patients with LVAD and early detection of potentially life-threatening events in an ambulatory setting

Keywords: LVAD; pump signal; echocardiography

BIOLOGICAL SAFETY ASSESSMENT OF A CARDIOVASCULAR IMPLANTABLE DEVICE: AN UPHILL WALK TOWARDS CLINICAL APPLICATION

PIERO TRABUCCO

Product Verification and Process Validation, Sorin Group Italy, Saluggia, Italy

A medical device or material that comes in contact with the patient's body is expected to perform its intended function without resulting in any adverse effect to a patient. Cardiovascular devices may lead to potentially serious adverse effects ranging from short-term (acute) to long-term (chronic) phenomena, especially when permanently implanted and in contact with blood. Worldwide, national and federal regulatory agencies require an overall safety assessment of a medical device to grant its use for clinical application, and biocompatibility is an important part of such assessment. For this reason, cardiovascular devices are subject to *in vitro* and *in vivo* biological testing to assess the interaction between device and tissue, cells or body fluids of the patient. No device is completely risk-free and the goal of device designers is to minimize risk while maximizing benefit to patients. Biocompatibility plays a key role in the development of cardiovascular devices and is an important input requirement for their design. The purpose of this lecture is to outline the main aspects related to the safe and effective use of medical devices with respect to biocompatibility and to provide a framework for determining the appropriate steps to plan a successful biological evaluation of a cardiovascular implantable device.

S1P: Biomaterials - Cells and tissues

Chairs: Carlo Ventura, Valeria Panzetta

A NEW NON-ENZYMATIC METHOD AND DEVICE TO OBTAIN A FAT TISSUE DERIVATIVE BY
MILD MECHANICAL FORCES FROM HUMAN LIPOASPIRATES

FRANCESCA BIANCHI

HIERARCHICAL MECHANICS OF SOFT CONNECTIVE TISSUES

KHENG LIM GOH

EFFECTS OF RADIO ELECTRIC CONVEYED FIELD ON DIFFERENT CELLS TYPE

RICCARDO TASSINARI

THE EFFECT OF DROP SPREADING AREA ON THE FORMATION OF B CELL AGGREGATES BY
THE MODIFIED HANGING-DROP METHOD

FENG XU

CONTROL OF CELL ADHESION BY A CHANGE IN THE REDOX STATE OF PEDOT:PSS
SUBSTRATES

MARCO MARZOCCHI

A NEW NON-ENZYMATIC METHOD AND DEVICE TO OBTAIN A FAT TISSUE DERIVATIVE BY MILD MECHANICAL FORCES FROM HUMAN LIPOASPIRATES

BIANCHI FRANCESCA, OLIVI ELENA, GHERMANDI SARA

*Laboratory of Molecular Biology and Stem Cell Engineering – National Institute of Biostructures and Biosystems - DIMES, S.
Orsola – Malpighi Hospital, University of Bologna, Italy
francibi@alice.it*

PASQUINELLI GIANANDREA, VALENTE SABRINA

Surgical Pathology Unit, Department of Hematology, Oncology and Clinical Pathology, University of Bologna, Italy

TREMOLADA CARLO

Istituto Image, Milano Italy (DRI Federation)

VENTURA CARLO

*Laboratory of Molecular Biology and Stem Cell Engineering – National Institute of Biostructures and Biosystems - DIMES, S.
Orsola – Malpighi Hospital, University of Bologna, Italy
carlo.ventura@unibo.it*

In the past decade human adipose tissue has been identified as a source of multipotent stem cells, called adipose-derived stem cells (ASCs), that share phenotypic and functional characteristics with mesenchymal stem cells (MSCs). The possibility to use these cells in clinical practice is subjected to in vitro expansion and to the regulatory restrictions imposed by cGMP Guidelines, that delay their applications in humans. The conventional method of isolation of ASCs involves enzymatic digestion, which is a costly and time-consuming process.

Here, we present an innovative system, named Lipogems, providing a non-expanded, ready-to-use fat product. The system uses mild mechanical forces in a completely closed system, avoiding enzymes, additives and other manipulations. This product can be transplanted immediately in vivo, or it can be cultured in vitro giving rise to a highly homogeneous population of MSCs.

Differently from unprocessed lipoaspirate, the non-expanded Lipogems product can be cryopreserved, and it encompasses a remarkably preserved vascular stroma, that is comprised with a significantly higher percentage of pericytes and hMSCs, and lower amount of hematopoietic elements. Moreover, the transcription of vasculogenic genes in Lipogems-derived MSCs was enhanced at a significantly greater extent by pro-vasculogenic molecules, when compared to MSCs isolated from enzymatically-digested lipoaspirates.

HIERARCHICAL MECHANICS OF SOFT CONNECTIVE TISSUES

KHENG LIM GOH^{1,2}

¹ *School of Mechanical and Systems Engineering, Newcastle University, Newcastle, UK*

² *NUInternational Singapore Pte Ltd. (NUI), Singapore*

Email: kheng-lim.goh@ncl.ac.uk

Extracellular matrix (ECM) of soft connective tissues such as ligaments and tendons is an example of fibre-reinforced composite with a hierarchical architecture [1,2]. Of late, interest in the mechanics of the hierarchy of soft connective tissues is concerned with establishing a comprehensive structure-function relationship at the respective levels (i.e. from tropocollagen (TC) molecule to tissue) of the hierarchical architecture [3]. This is a challenging area of work, involving a multidisciplinary approach that invokes the principles of classical mechanics and quantum mechanics for biochemistry, biophysics and molecular biology to name a few. The intent of this lecture is to review the key findings on the mechanical response of ECM at the respective levels of the hierarchical architecture, identified by key structural units of ECM, namely TC molecule (the lowest level), microfibril, collagen fibril, collagen fibre and fascicle, to provide insights that may lend support to establishing a comprehensive structure-function relationship of ECM. To wrap up this lecture, we introduce a framework for ECM mechanics that supports the goal for establishing the structure-function relationship (see Figure 1, [3]). The framework describes the integration of the mechanisms of reinforcement by the structural units at the respective levels of the hierarchical architecture in a consistent manner, both to allow comparison of these mechanisms and to make prediction of the interconnection of these mechanisms that can also assist in the identification of effective mechanical pathways. For design considerations, this framework is a step in the direction towards the development of effective strategies for engineering materials to replace or repair damaged tissues.

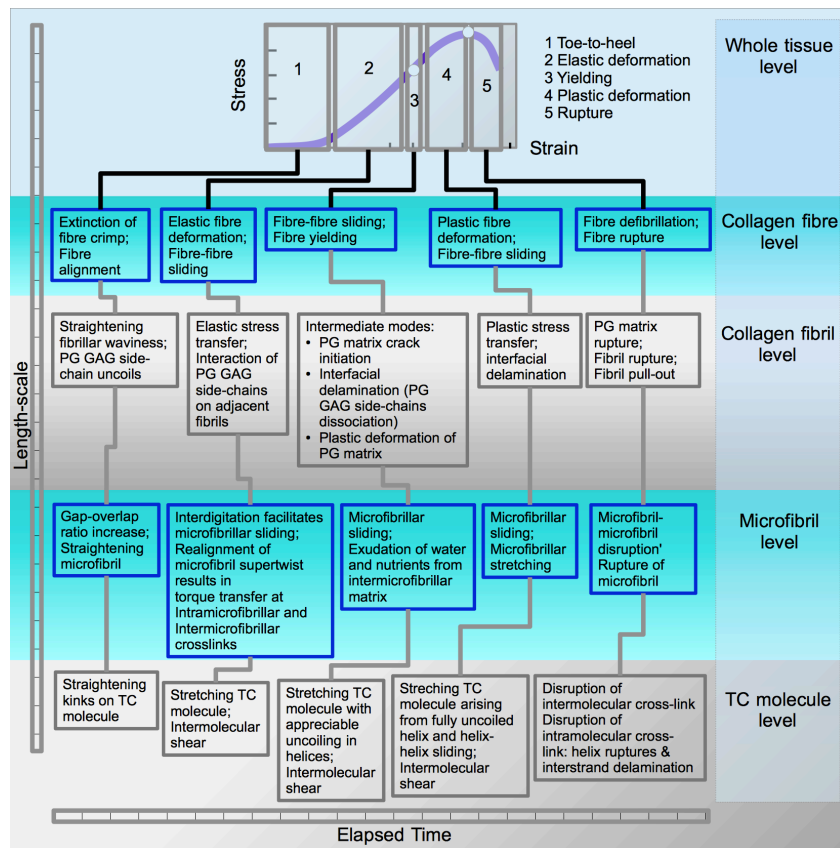


Figure 1. A framework for the mechanics of extracellular matrix (ECM) in soft connective tissue [3]. The framework integrates the findings from low-dimensional to macroscopic studies, to describe the mechanisms of stress uptake in ECM structural units at the respective levels of the hierarchical architecture. The aim of the framework is both to allow for comparison and to make prediction of the interconnection (mechanical pathway, highlighted by thick gray lines) of the mechanisms that can also assist in the identification of new mechanical pathways. PG, proteoglycan; GAG, glycosaminoglycan; TC, tropo-collagen

References

1. Goh KL, Meakin JR, Aspden RM, Hukins DWL, Influence of fibril taper on the function of collagen to reinforce extracellular matrix. *Proceedings of the Royal Society of London Biological Science*, 272, 1979 (2005)
2. Goh KL, Meakin JR, Aspden RM, Hukins DWL, Stress transfer in collagen fibrils reinforcing connective tissues: Effects of collagen fibril slenderness and relative stiffness. *Journal of Theoretical Biological*, 245, 305 (2007).
3. Goh KL, Listrat A, Béchet D, Hierarchical Mechanics of Connective Tissues: Integrating Insights from Nano to Macroscopic Studies, *Journal of Biomedical Nanotechnology* (*In Press*)

EFFECTS OF RADIO ELECTRIC CONVEYED FIELD ON DIFFERENT CELLS TYPE

TASSINARI RICCARDO, CAVALLINI CLAUDIA
*DIMES, University of Bologna, via Massarenti 9
Bologna, 40139, Italy
rikta@libero.it*

RINALDI SALVATORE, FONTANI VANIA
*Department of Regenerative Medicine,
Rinaldi Fontani Institute, Viale Belfiore 43,
Firenze, 50144, Italy*

TAGLIOLI VALENTINA, VENTURA CARLO
*DIMES, University of Bologna, via Massarenti 9
Bologna, 40139, Italy
carlo.ventura@unibo.it*

Abstract:

The wide spread of equipment using radio frequency (RF) has focused the interest of scientists on the effects of electromagnetic fields (EMF) on humans. EMF interact and modify the behavior of cells and subcellular components, even changing DNA conformation and cytoskeletal array, opening the possibility to develop a fine tuning of the cellular fate .

In particular, we are interested on determining the biological effects of EMF in the field of regenerative medicine. We are testing REAC (Radio Electric Asymmetric Conveyer) technology: ultra-high frequencies (UHF, 2.4 GHz) at low intensity ($400 \mu\text{Watt} \cdot \text{m}^2$) “permeate” cells, while culture medium plunged electrodes transmit micro-currents to the cells induced by the same EMF conveyed by REAC. Previous studies demonstrated the biological effects generated by REAC on embryonic stem cells and human fibroblasts. Now we are examining the possibility that REAC may affect also differentiated cells, interrupting pathological processes after myocardial infarction, on the basis of evidence obtained by the in vivo use of REAC. For this reason, we have analyzed the effects on cell death and recovery from a induced ischemia-reperfusion process. Data obtained show the ability of REAC to improve the survival outcome of cell subject to damage .

Keywords: Electromagnetic Fields, Cell Death

THE EFFECT OF DROP SPREADING AREA ON THE FORMATION OF B CELL AGGREGATES BY THE MODIFIED HANGING-DROP METHOD

BIN GAO^{A,B,C}, XIAOHUI ZHANG^{A,B#}, LUYUAN YANG^{A,B}, FENG XU^{A,B#}

^a Key Laboratory of Biomedical Information Engineering of Ministry of Education, School of Life Science and Technology, Xi'an Jiaotong University, Xi'an 710049, P.R. China

^b Biomedical Engineering and Biomechanics Center, Xi'an Jiaotong University, Xi'an 710049, P.R. China

^c Department of Endocrinology and Metabolism, Xijing Hospital, Fourth Military Medical University, Xi'an, 710054, P.R. China

[#] xiaohuizhang@mail.xjtu.edu.cn, fengxu@mail.xjtu.edu.cn

Hanging-drop method is one of the most widely used approaches to fabricate three-dimensional (3D) islet models for diabetes research. Recently, we have found that drops with the same volume may give different spread areas during hanging process, which may affect the cell aggregation behavior. However, this has been ignored nobody in previous studies. In this study, we investigated the variation in droplet geometries using a 30- μ l drop with different spreading areas, and their effects on the formation of INS-1 cell aggregates. The results indicate that the larger the spreading area the larger the maximum volume and radius of curvature, the smaller the contact angle. The INS-1 cell aggregates reached the maximum diameter on day 4 during the 7-day cell culture. INS-1 cell aggregates with better morphology were observed when using hanging-drops with spreading areas of 5 mm or 6 mm in diameter. This platform enables the precise manipulation of hanging-drop geometry, and the better control over the formation of 3D islet aggregates.

Keywords: Hanging drop; 3D islet model; spreading area.

1. Introduction

Diabetes is currently one of the major risk factors for cardiovascular diseases, where the incidence of type 1 diabetes is 1 in 300 with a steadily increase worldwide (3% per year)^[1]. Traditionally, *in vitro* diabetes research is conducted by culturing cells on a two-dimensional (2D) flat, rigid plastic substrates, which cannot recapitulate the native cell microenvironment. In contrast, three-dimensional (3D) cell culture models enable the establishment of cell-cell and cell-ECM interactions that closely mimic the biochemistry and mechanics of the native cell microenvironment. Numerous studies have demonstrated that increases in cell viability, insulin secretion and cell connection were observed in 3D islet models

compared to 2D cultures ^[2-4]. Therefore, it is important to fabricate *in vitro* 3D model of islets for physiological and pathological studies, diabetes drug efficiency tests, as well as for islet transplanted *in vivo* to treat diabetes.

Hanging-drop method is one of the most commonly used approaches to fabricate 3D islet models among all the tissue engineering methods. The traditional hanging-drop procedure employs the medium containing the islet cells drop on a plate (*e.g.* glass slide), after the plate turnover the drop hanging on the plate. The cells in the hanging-drops of culture media descend due to the gravity and assemble to a cell spheroid, free of contact with any support matrices or surfaces. By using this method, the islet aggregates formed *in vitro* showed viability and functions^[5]. However, most of the studies mainly focused on the applications of the hanging-drop method, but ignored the variations during the fabrication process such as drop spreading area. As we known, materials with different hydrophobicity ^[6] (*i.e.* glass, plastic and PMMA) result in different spreading areas when using a same volume of drops. So far nobody has looked into the effect of drop spreading area on the formation of islet aggregates by using the hanging-drop method. The aim of this work is to identify the optimal spreading area for generating islet aggregates using the hanging-drop method to obtain 3D islet models with good viability and functionality.

2. Materials and Methods

2.1 Design and fabrication of hanging-drop plates

Poly(methyl methacrylate) (PMMA) of 1.5 mm thickness was used to create hanging-drop plates (Fig. 1a) that are compatible to the standard 6-well cell culture plates. Each plate consists of 6 surface tension-mediate units created by using a laser cutter. For each unit, two concentric circles were created. The inner circle (control line) was designed to control the spreading area of the hanging-drops, while the second one was designed to fit for the 6-well culture plates. In this study, the diameter of the first circle ranges from 4 mm to 9 mm (*i.e.*, spreading diameter).

2.2 Preparation of islet hanging-drops

The INS-1 cells were used to form islet aggregates using the hanging-drop methods. The INS cells were cultured in RPMI-1640 medium supplemented with 10% fetal bovine serum, 11.1 mmol/l D-glucose, 100 U/ml penicillin, 100 µg/ml streptomycin, 10 mmol/l HEPES, 2 mmol/l L-glutamine, 1 mmol/l sodium pyruvate, and 50 µmol/l-mercaptoethanol as previously described ^[7]. 30-µl cell suspension at a density of 4×10^6 cells/ml was pipetted on the plate, which was then turnover and put on top of the 6-well plate. PBS is pre-added to the wells to prevent evaporation during cell culture.

2.3 Evaluation of islet aggregate formation

The morphology of the hanging-drops including curve radius and contact angle (α angle) was observed using microscope, and the images were processed using ImagePlus Pro. The drop diameters with different spreading areas were also recorded and compared. Values were averaged and expressed as means \pm SEM. Statistical differences were determined by Student's *t* test, one-way ANOVA (SPSS). Differences were considered statistically significant at $p < 0.05$.

The viability of the INS-1 cells within the islet aggregates were examined by live/dead assay (Invitrogen). Briefly, islet aggregates were incubated in 10 mM Calcein AM and 10 mM EthD-1 in PBS for 20 min at 37°C, then imaged using fluorescent microscopy at excitation of 515 nm and emission of 635 nm.

3. Results and discussion

To assess the effect of spreading area on the shape of drop morphology, we hanged drops with fixed spreading diameters of 4-9 mm (**Fig. 1**). We observed that the maximum volume of the hanging-drop increased from $35.01 \pm 0.67 \mu\text{l}$ to $134.60 \pm 0.94 \mu\text{l}$ with increasing drop spreading diameter. There was significant difference for the maximum volume of drops with different spreading areas ($p < 0.05$). In addition, the radius of curvature also increased with increasing drop spreading area. For instance, the radius of curvature was 0.21 ± 0.01 mm when the drop diameter is 4 mm, whereas the radius of curvature was 0.69 ± 0.10 mm when the drop diameter increased to 9 mm. There was significant difference in the radii of curvature of the drops among drops with different spreading areas ($p < 0.05$), while the contact angle presented the opposite tendency. With increasing spreading area, the contact angle decreased from 89.70 ± 10.44 to 22.33 ± 5.95 ($p < 0.05$). We also found that hanging-drops with spreading diameter of 4 mm was not stable, thus spreading areas with diameters from 5 mm to 9 mm were used for our experiments.

To assess the effect of drop spreading area on cell aggregate formation, we cultured INS-1 cells in 30 μl drops with spread areas of 5, 7, 9 mm (**Fig. 2**). The aggregations of INS-1 cells were observed daily for 7 days. We observed that INS-1 cells formed aggregates in all drops. However, aggregates formed in 5 mm spreading hanging drops exhibited better morphology with a spheroid-like micro-tissue, while aggregates formed in 7 mm and 9 mm hanging drops gave pie-shaped morphology. This may be due to the fact that when the drop spreading area is bigger, it is more like a 2D culture and thus more difficult for cells to form spheroid. These were further confirmed with the live/dead staining results. We further

quantified the change of aggregate size with culture time. We observed that the size of aggregate formed in 5 mm spreading drops significantly decreased with culture time, with significant difference as compared to day 1 ($p < 0.05$). In the case of 7 mm and 9 mm spreading drops, the aggregate diameter increased to maximum at day 4. At day 4, the diameter of cell aggregates increased with increasing spreading area ($p < 0.05$). In addition, we also checked the viability of formed cell aggregates and observed good viability for all spreading areas (**Fig. 2d**). However, more cell death as observed for these pie-like aggregates, maybe due to the limitation in oxygen and nutrient transport.

We for the first time proved that even though drops with same volume was used for the hanging-drop method, the islet cell aggregates with different sizes may form if the spreading areas are different. In this work, we only studied the effects of drop spreading area on the cell viability. We will further evaluate their effects on the insulin secretion, which is the most important function of islets in the continuous study. In brief, as a common method for the fabrication of islet models, the standardization of the operation procedures of hanging-drop methods is recommended to avoid the unexpected variations in the generation of cell aggregates between experiments.

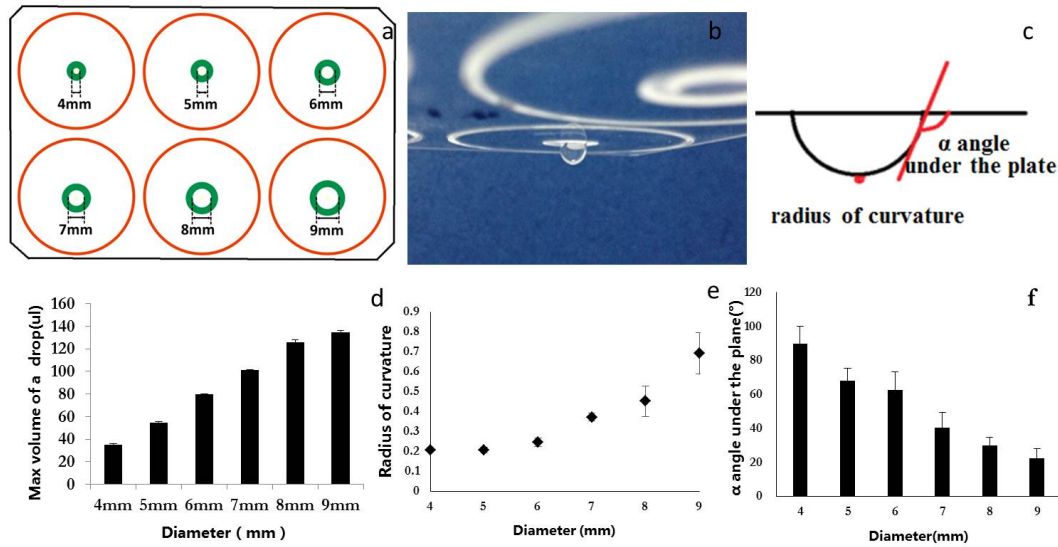


Figure 1. Schematics of hanging-drop plate design and drop evaluation. (a) The structure of hanging drop plate; (b) The shape of a drop on the plate; (c) Schematics of the drop geometry; (d) Max volume of a drop with gradient diameter; (e) Radius of curve of a drop with gradient diameter; (f) α angle of a drop with gradient diameter.

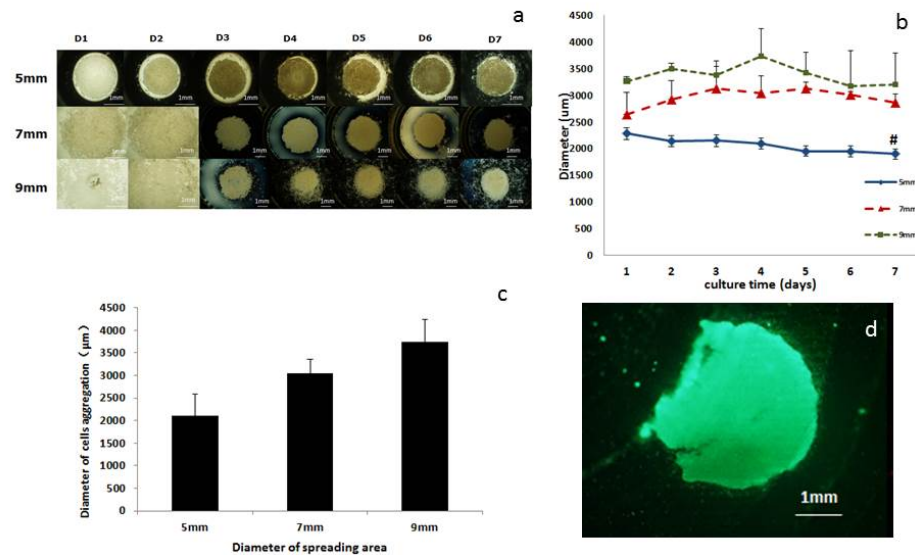


Figure 2. Geometry of cell aggregates in hanging-drops. (a) Different islet aggregates from day 1 to day 7 (4×); (b) Diameter of cell aggregates from day 1 to day 7 ($p < 0.05$); (c) Diameter of islet aggregates with different spreading areas at day 4; (d) Live/Dead image of INS-1 cell aggregates formed with spreading area of 5 mm in diameter cultured for 4 days (4×).

Reference

1. Gan, M.J., A. Albanese-O'Neill, and M.J. Haller, *Type 1 diabetes: current concepts in epidemiology, pathophysiology, clinical care, and research*. Current problems in pediatric and adolescent health care, 2012. **42**(10): p. 269-291.
2. Cavallari, G., et al. *Rat pancreatic islet size standardization by the "hanging drop" technique*. in *Transplantation proceedings*. 2007. Elsevier.
3. Pethig, R., et al., *Dielectrophoretic assembly of insulinoma cells and fluorescent nanosensors into three-dimensional pseudo-islet constructs*. Nanobiotechnology, IET, 2008. **2**(2): p. 31-38.
4. Hauge-Evans, A., et al., *Pancreatic beta-cell-to-beta-cell interactions are required for integrated responses to nutrient stimuli: enhanced Ca^{2+} and insulin secretory responses of MIN6 pseudoislets*. Diabetes, 1999.

48(7): p. 1402-1408.

5. Tung, Y.-C., et al., *High-throughput 3D spheroid culture and drug testing using a 384 hanging drop array*. Analyst, 2011. **136**(3): p. 473-478.
6. Yoshimitsu, Z., et al., *Effects of surface structure on the hydrophobicity and sliding behavior of water droplets*. Langmuir, 2002. **18**(15): p. 5818-5822.
7. Asfari, M., et al., *Establishment of 2-mercaptoethanol-dependent differentiated insulin-secreting cell lines*. Endocrinology, 1992. **130**(1): p. 167-178.

CONTROL OF CELL ADHESION BY A CHANGE IN THE REDOX STATE OF PEDOT:PSS SUBSTRATES

MARCO MARZOCCHI^{*,‡}, ISACCO GUALANDI^{*}, ERIKA SCAVETTA[†], MARIA CALIENNI^{*}, ISABELLA ZIRONI^{*},
GASTONE CASTELLANI^{*} and BEATRICE FRABONI^{*}

^{*} *Department of Physics and Astronomy, University of Bologna, Italy*

[†] *Department of Industrial Chemistry, University of Bologna, Italy*

[‡] *marco.marzocchi4@unibo.it*

The use of conducting polymers as materials for bioelectronics is a rapidly-growing research field. Their mechanical and electrical properties, together with their excellent biocompatibility, make them more suitable for being used as an interface between electronics and cell tissues than “traditional” inorganic semiconductors. Moreover, the fact that the electronic properties of conducting polymers can be modified in response to electrical stimuli creates the opportunity to use these materials as active substrates for cell growth[1-3]. We employed two different techniques, spin-coating and electro-polymerization, to deposit thin films of a bio-compatible conducting polymer widely used in organic electronics, poly(3,4-ethylene dioxythiophene) doped with poly(styrenesulfonate) (PEDOT:PSS). These techniques impart quite different physical and chemical properties to the films, namely surface roughness, electrical conductivity, and redox-state properties. Furthermore, the oxidation state of this polymer can be reversibly changed through an electrochemical reaction. We characterized the effects of a change in the oxidation state of PEDOT:PSS thin films, deposited using different deposition methods, by atomic force microscopy, optical absorption, electrical and electrochemical analyses. Finally, we studied the effects of cell adhesion and proliferation on these films by growing primary human dermal fibroblasts (hDF) and human glioblastoma (T98G) cell cultures.

Keywords: Bioelectronics; conjugated polymers ;PEDOT:PSS; redox reactions; cell growth; cell adhesion.

References

1. Wan AMD, Schur RM, Ober CK, Fischbach C, Gourdon D, Malliaras GG, Electrical Control of Protein Conformation, *Adv Mat* **24**:2501-2505, 2012.
2. Gumus A, Califano JP, Wan AMD, Huynh J, Reinhart-King CA, Malliaras GG, Control of cell migration using a conducting polymer device, *Soft Matter*, **6**:5138-5142, 2010.
3. Saltó C, Saindon E, Bolin N, Kanciurzevska A, Fahlman M, Jager EWH, Tengvall P, Arenas E, Berggren M, Control of Neural Stem Cell Adhesion and Density by an Electronic Polymer Surface Switch, *Langmuir*, **24**:14133-14138, 2008.

S2M: X-ray imaging

Chairs: Nico Lanconelli, Pier Luca Rossi

AUTOMATED CARBON DIOXIDE DIGITAL ANGIOGRAPHY FOR LOWER LIMB ARTERIAL
DISEASE EVALUATION: SAFETY ASSESSMENT AND COMPARISON WITH STANDARD
IODINATED CONTRAST MEDIA ANGIOGRAPHY

FILIPPO SCALISE

RADIOLOGICAL OPTIMIZATION OF BUBBLE DYNAMICS IN CARBON DIOXIDE ANGIOGRAPHY

DAVID BIANCHINI

TEXTURE ANALYSIS FEATURES: PHANTOM STUDIES FOR RELIABILITY ASSESSMENT IN PET
AND CT IMAGING TECHNIQUES

GIACOMO FELICIANI

FEASIBILITY STUDY FOR THE DEVELOPMENT OF A NEW CT SCANNER DEVOTED TO HUMAN
INNER EAR

MARIA PIA MORIGI

"SHARE & MEET" PROJECT: AN INNOVATIVE REMOTIZATION SOLUTION FOR DIGITAL
IMAGING AND RADIOTHERAPY TREATMENT PLANNING

MATTEO BOTTEGHI

AUTOMATED CARBON DIOXIDE DIGITAL ANGIOGRAPHY FOR LOWER LIMB ARTERIAL DISEASE EVALUATION: SAFETY ASSESSMENT AND COMPARISON WITH STANDARD IODINATED CONTRAST MEDIA ANGIOGRAPHY.

FILIPPO SCALISE
Policlinico di Monza, Monza, Italy
filippo.scalise@policlinicodimonza.it

Abstract

Introduction: Carbon dioxide (CO₂) has been validated as contrast agent in a large series of studies. Particular advantages of CO₂ over iodinated contrast medium (ICM) are the absence of nephrotoxicity and allergic reactions. One of the limitations of CO₂ angiography was the difficulty of CO₂ manual injection due to its compressibility. The manual gas injection does not permit an optimal control of the gas output. Development of an automated CO₂ injector has overcome these problems.

Aim: it was to compare the feasibility, safety, and diagnostic accuracy of automated CO₂ digital subtraction angiography (DSA) in comparison with ICM DSA in the evaluation of critical limb ischemic (CLI) patients.

Methods: DSA with both CO₂ and ICM, to directly compare the two techniques, was performed on 40 consecutive CLI patients. Sixteen females and 24 males participated in the study (mean age 71.7 years). We assessed the diagnostic accuracy of CO₂ in identifying arterial stenosis in the lower limb with the ICM DSA used as the gold standard.

Results: The overall diagnostic accuracy of CO₂ DSA was 96.9% (sensitivity 99.0%; specificity 96.1%; PPV 91.1%; NPV 99.6%). Tolerable minor symptoms occurred in 3 patients. No allergic reactions and no significant decline in renal function were observed in patients receiving the CO₂ injection.

Conclusions: Automated Carbon Dioxide DSA is a technology that is conceptually different from ICM angiography. This modality should be considered as the standard choice for CLI patients undergoing angiographic evaluation, who are known to have renal insufficiency or contrast allergy. To obtain high quality images it is necessary to optimize both the operational and radiological protocols. The automated Carbon Dioxide DSA is a valuable and safe alternative to traditional ICM DSA for evaluating CLI patients.

RADIOLOGICAL OPTIMIZATION OF BUBBLE DYNAMICS IN CARBON DIOXIDE ANGIOGRAPHY

DAVID BIANCHINI⁽¹⁾, IVAN CORAZZA⁽¹⁾ AND ROMANO ZANNOLI⁽¹⁾

(1) *Dipartimento di Medicina Specialistica Diagnostica e Sperimentale, Università di Bologna, ITALY*

The using of carbon dioxide as contrast medium (CM) is increasing in the diagnosis of vascular diseases such as peripheral stenosis and fistulae. This radiological technique produces images through a digital subtraction (DS) of the images obtained with CM injected and a series of masks images.

The two phase system (blood, CO₂) remain separate by a surface until the gas is been dissolved. The radiological contrast of the x-ray image is given by integral dose on the pixels under the bubble respect to the pixel's dose in the surround. Since the bubble is moving in the vessel, the fluoroscopy pulse time and the frame frequency change the contrast to noise ratio (CNR) of the contrast medium. This create moving artifacts that reduce the diagnostic outcome of the exam. To evaluate the best operational procedure we started with a laboratory model of the dynamical system. In this study has been realized a phantom made of 15cm of water with inside different glass vessels of various diameters. The images are taken with a PAXSCAN 4030 FP irradiated with RQR5 and RQR7 (IEC61267) x-ray field in different frame rate and integration time configuration. Moreover an algorithm to find the best radiological parameters has been developed to maximize the image quality indexes with no changing in entrance dose. The image quality improvement is evaluated in term of increment of the figure of merit of the image (CNR²/Dose). The results shows the limits of the common used stacking technique and find out how long integration time protocols are less efficient than high frame rate protocols even in condition of high frame rate.

References

- [1] Cho, Kyung, and Irvin F. Hawkins, eds. *Carbon dioxide angiography: principles, techniques, and practices*. CRC Press, 2013.
- [2]Corazza, Ivan, et al. "Mechanical aspects of CO₂ angiography." *Physica Medica* 29.1 (2013): 33-38.
- [3]Kariya, S., et al. CO₂ microbubble contrast enhancement in x-ray angiography." *Clinical radiology* 68.4 (2013): 346-351.]

TEXTURE ANALYSIS FEATURES: PHANTOM STUDIES FOR RELIABILITY ASSESSMENT IN PET AND CT IMAGING TECHNIQUES

GIACOMO FELICIANI,

*Post-graduate school in medical physics, University of Bologna, via massarenti 9,
40138 Bologna, Italy.
giacomo.feliciani@studio.unibo.it*

FEDERICA FIORONI

*Medical physics department, IRCCS - Arcispedale Santa Maria Nuova, viale risorgimento 80,
42123 Reggio Emilia. Italy
federica.fioroni@asmn.re.it*

MAURO IORI

*Medical physics department, IRCCS - Arcispedale Santa Maria Nuova, viale risorgimento 80,
42123 Reggio Emilia. Italy
mauro.iori@asmn.re.it*

1. Introduction

Increasing interest is found in textural features for tumor characterization in PET and CT imaging techniques. In general there is no universally agreed definition for texture analysis but in this work it will be referred to the analysis of the spatial variation of pixels intensities. Despite standard analysis methods which relies just on pixel intensities (SUV or HU mean, maximum, skewness, kurtosis etc.) textural features keep trace of their spatial arrangements¹. For this reason these methods are well suited for image segmentation to establish boundaries and to discriminate different regions. Even if recent publication employ texture indices there is still a lack of comprehension in what they represent and how they relate to conventional analysis methods. The aim of this study is to investigate features behavior varying well-known phantom properties to assess their reliability in structure discrimination and to find relationships between standard analysis and feature indices.

2. Methods

2.1. PET image acquisition:

Data from NEMA IEC Body Phantom SetTM (Data Spectrum Corporation, Hillsborough, NC) shown in Fig.1 were acquired on a PET/CT GE Discovery STE scanner. Spheres of different radius were equally filled with 12 KBq/ml activity concentration of ¹⁸F-FDG and scanned for different timings. PET images were reconstructed on a 256×256 image matrix using 3-D VUE Point HD algorithm varying reconstruction steps and Gaussian post-filter width. Spheres contour segmentation was performed on a GE Advantage Workstation 4.4, using a 40% SUV_{MAX} threshold algorithm. Textural analysis on contoured volumes was conducted employing the Chang Gung Image texture analysis toolbox².

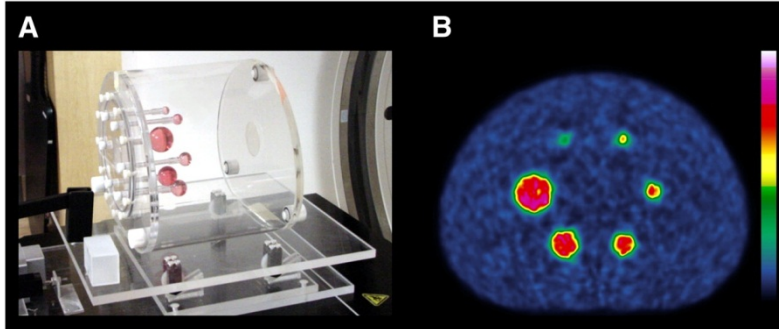


Fig. 1. Image of an NEMA IEC Body Phantom (A) and relative PET acquisition(B)

2.2. CT image acquisition

Images of a Catphan600 CT phantom Fig.2A were acquired with a Philips Brilliance 64 CT scanner varying kV and mA in the scanning protocol. Subsequently different filters (from scanner options) were applied to data to evaluate textural features response. Fig.2B and 2C show 2 modules analyzed with the software cited in section 1.1. The first one contains cylinders of different radius and width whereas in the second one cylinders' materials are varying.

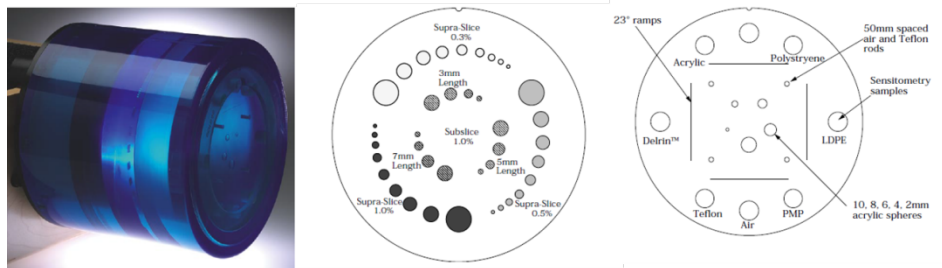


Fig. 2. Strain gauges in measurement position (left) and strain gauge support detail on forearm (right)

The relationship between standard and textural indices were studied as well as their robustness with respect to the nature of the test involved (Stability with volume variation, sensitivity to different materials etc.).

3. Results:

Many of the 74 textural features analyzed regardless the type of test were strictly correlated to standard indices thus providing no additional information. Features detected in this way were discarded and not discussed anymore along this work. Indices less sensible to partial volume effect and discriminating more among different materials (for CT acquisition) were considered the most reliable ones for image segmentation and tumor characterization.

4. Conclusions:

We analyzed a large range of textural indices for the most common phantoms and acquisition modalities employed in quality assurance practices. We proved that it is extremely important to acquire knowledge of textural features in detail for tumor characterization and image segmentation in order to avoid misunderstanding in clinical studies. Finally we point out that this study is just a starting point for further analysis as we didn't provide wide range information among different scanner brands.

References

1. Nailon WH. Texture Analysis Methods for Medical Image Characterisation. *www.intechopen.com*. 2004.
2. Cheng N-M, Fang Y-HD, Chang JT-C, et al. Textural features of pretreatment 18F-FDG PET/CT images: prognostic significance in patients with advanced T-stage oropharyngeal squamous cell carcinoma. *J Nucl Med*. 2013;54(10):1703–9. doi:10.2967/jnumed.112.119289.

FEASIBILITY STUDY FOR THE DEVELOPMENT OF A NEW CT SCANNER DEVOTED TO HUMAN INNER EAR

M.P. MORIGI, R. BRANCACCIO, M. BETTUZZI, F. CASALI

*Department of Physics and Astronomy, University of Bologna
Viale Berti Pichat 6/2, 40127 - Bologna, Italy
mariapia.morigi@unibo.it*

A. BRAVIN, T. BROCHARD, P. TAFFOREAU, J.C. LABICHE

European Synchrotron Radiation Facility, Grenoble, France

Inner ear diseases include not only hearing loss but also equilibrium disorders. In these cases the normal life is seriously affected and simple actions like walking and moving are seriously impaired by the appearing of symptoms like dizziness, nausea, vomit. Imaging the inner ear is a very interesting radiological challenge, in fact present medical CT scanners do not have the spatial resolution necessary to image the fine structures of the inner ear. As a consequence, when inner ear diseases are treated surgically, the physician has to proceed to the operation without any trustable image guidance. In addition, without good imaging, it is not possible to follow up the therapeutical effects of medications. Therefore a dedicated and performing CT system for inner ear imaging would be extremely useful also to avoid unnecessary surgeries. In the framework of a research project funded by the Italian National Institute of Nuclear Physics we studied this issue and performed an experiment at the European Synchrotron Radiation Facility to determine whether, under ideal conditions (parallel and monochromatic X-ray beam, high resolution detector), it was possible to obtain tomographic images of the inner ear with satisfactory resolution and contrast. This experiment can be considered as a "reference benchmark" for the CT imaging of the human ear, a target which a new CT scanner devoted to middle and inner ear should approach.

Keywords: inner ear; computed tomography; high resolution

1. Introduction

The human ear has a very complex structure which, beyond sounds perception, is also responsible for sensing motion, gravity and linear acceleration. It is normally divided in outer, middle and inner ear. The last one is composed by the cochlea, the semicircular channels and the vestibula system which contains the otolith organs for sensing gravity and linear acceleration. Inner ear diseases include not only hearing loss but also equilibrium disorders. In these cases the normal life is seriously affected and simple actions like walking and moving are seriously impaired by the appearing of symptoms like dizziness, nausea, vomit. CT is commonly used as a standard method to diagnose disease and to plan surgery. However, present medical CT scanners are able to give images with a minimum voxel size of about 0.3 mm, thus some anatomical details like the semicircular channels and the otoliths are not clearly observable (Figure 1).

Given the fact that inner ear diseases are often treated surgically, the physician has to proceed to the operation without any trustable image guidance. In addition, without good imaging, it is not possible to follow up the therapeutical effects of medications.

Worldwide, preclinical developments of high resolution inner ear CT imaging have been done on small animals (i.e. mice).^{1,2} In human beings, the accurate detection of anatomical details like the semicircular channels and the otoliths is made particularly difficult because they are relatively small and contoured by the skull and the petromastoid bone which are very radio-opaque to X-rays. For this reason imaging the inner ear is a very interesting radiological challenge that has been faced by our research group in the

framework of the research project RITOR (Research for Inner Ear CT), funded by the Italian National Institute for Nuclear Physics.

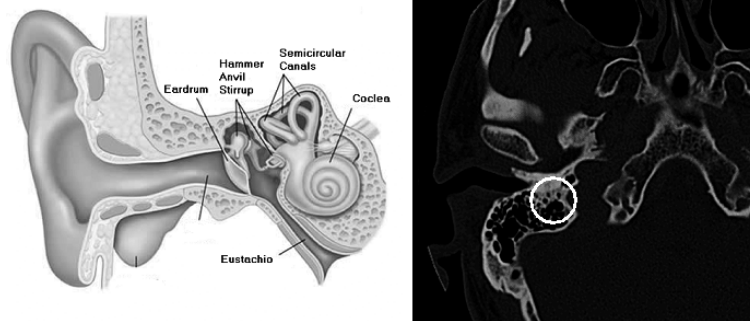


Fig. 1. Scheme of ear anatomy (left) and tomographic image (right) of the inner ear (inside the circle) obtained by means of a standard medical CT scanner: the contrast is good, but the anatomy of the labyrinth and other parts of the inner ear is poorly defined.

A specific X-ray scanner for human inner ear should satisfy the following requests:

- good spatial resolution (around $50\ \mu\text{m}$);
- high dynamic range;
- short scanning time and fast reconstruction;
- low dose.

Obviously it is really difficult to achieve all these features in a single instrument because some of them are contradictory and mutually exclusive; for this reason our research was focused on the study of the CT system components to find the best balance between the different demands, but first we wanted to obtain a "reference benchmark" of human ear CT imaging, a target which a dedicated and high-performing CT system should approach. Therefore we decided to perform several experimental tests both with a standard X-ray source and with synchrotron radiation. We carried out a lot of tests in our laboratory at the Department of Physics and Astronomy of Bologna University with two different cone-beam CT systems and a human head phantom containing a real human skull embedded in a plastic material. We obtained very clear images of the inner ear (see Ref. 3), but the scanning time was very long and not adequate for a clinical application. Then we decided to test another kind of detector; for this purpose we carried out an experiment at the ID17-ESRF beamline (Grenoble, France) with a dedicated high resolution linear detector to determine whether, under ideal conditions (parallel and monochromatic X-ray beam), it was possible to obtain tomographic images of the inner ear with satisfactory resolution and contrast.

2. Materials and Methods

The tomographic tests at ESRF were performed with an innovative linear detector, composed by an APOGEE CCD camera model ALTA-U9000, with 3056×3056 pixels of $12\ \mu\text{m}$, coupled with a GOS scintillator by means of a fiber optical fan, 50 cm wide, which can be intended as a "geometry transducer" (Figure 2). In fact, it transforms the CCD matrix 3056×3056 in an equivalent one, about 30000×300 , that is 300 slices of 30000 pixels, with a minimum pixel size of $16\ \mu\text{m}$.⁴ The image collected by the camera is composed of displaced frames with respect to the real image. This has to be

taken into account within the reconstruction software. However, this method allows the pixels of the CCD to virtually expand horizontally, giving a very high image definition along this direction.

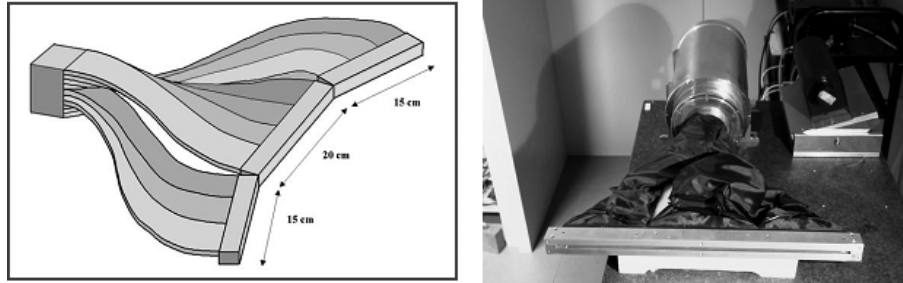


Fig. 2. The Fiber Optical fan, made of coherent FO bundles, that works as a “geometry transducer”.

The tomographic tests were performed at an energy of 55 keV using a plexiglass head phantom made by the company Finceramica (Faenza, Italy). One slice of this phantom has been modified to include an hydroxyapatite insert in order to simulate the skull and the petromastoid part of the temporal bone (Figure 3). The design is based on the head phantom model by Günter Lauritsch and Herbert Bruder.⁵ Some artificial holes, with diameters ranging from 1 to 3 mm, have been drilled in the hydroxyapatite to simulate the semicircular channels of the inner ear. Moreover the porous structure of the hydroxyapatite allows to insert small wires and aluminium particles of size comparable to the otoliths.



Fig. 3. Pictures of the plexiglass head phantom and of the modified slice with enclosed a geometric hydroxyapatite insert to simulate the skull and the petromastoid part of the temporal bone.

3. Results and discussion

Several acquisitions using different voxel sizes from 69 to 46 μm have been performed. Figure 4 shows a 3D rendering of the hydroxyapatite insert and a detail of the iron wire positioned inside a hole in the plexiglass phantom (voxel size of 69 μm). The CT analysis carried out at higher resolution was performed in "local tomography" modality. The voxel size for this acquisition was 46 μm . Figure 5 shows a detail of the hydroxyapatite used to simulate the petrous bone: the porous structure of the

hydroxyapatite is clearly reproduced. The four holes have diameters ranging from 1.5 to 2 mm and represent the semicircular channels of the ear. A bright spot inside one hole, corresponding to a copper wire of 200 μm , is also clearly visible.

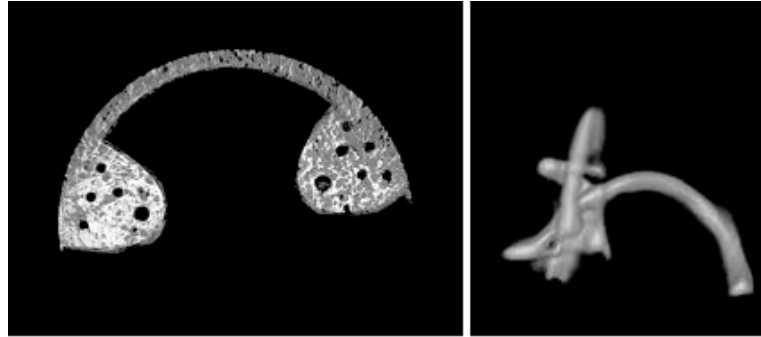


Fig. 4. 3D tomographic reconstruction of the hydroxyapatite insert (left) and detail of the iron wire (right) positioned inside a hole in the plexiglass.

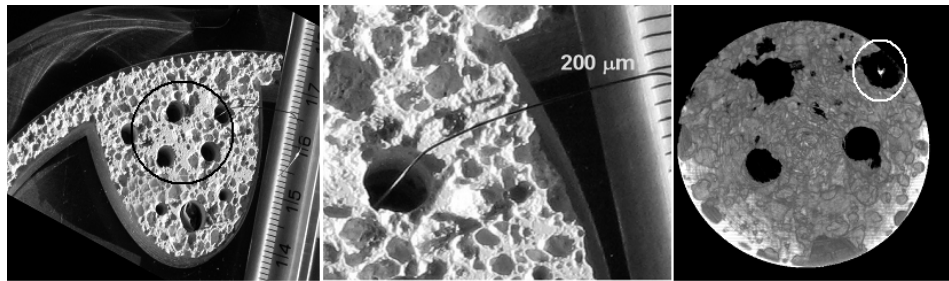


Fig. 5. Pictures of the region of interest analyzed at higher resolution (black circle, left); detail of the hole where a copper wire of 200 μm is placed (centre); tomographic reconstruction of the region of interest (right).

4. Conclusions

The experimental tests carried out at ESRF and in our laboratory at the Department of Physics and Astronomy of Bologna University indicate that it is possible to obtain tomographic images of the inner ear with satisfactory resolution and contrast. These results can be considered as a "reference benchmark" for the future development of a new CT system for in vivo imaging of the inner ear.

References

1. Van Spaendonck MP, Cryns K, Van De Heyning PH, Scheuermann DW, Van Camp G, Timmermans JP, High resolution imaging of the mouse inner ear by microtomography: A new tool in inner ear research, *Anat. Rec.* **259**(2): 229–236, 2000.
2. Ritman EL, Micro-computed tomography – current status and developments, *Annu. Rev. Biomed. Eng.* **6**, 185–208, 2004.

3. Bettuzzi M, Brancaccio R, Morigi MP, Gallo A, Strolin S, Casali F, Lamanna E, Ariù M, CT Imaging of the Internal Human Ear: Test of a High Resolution Scanner, *Nucl. Instrum. Meth. A.* **648**(1), S60-S64, 2011.
4. Bettuzzi M, Brancaccio R, Berdondini A, Morigi MP, Casali F, Flisch A, Miceli A, High resolution computed tomography for industrial applications based on coherent fiber optics ribbons, *Proc. 5th World Congress on Industrial Process Tomography*, Bergen, Norway, pp. 958 - 964, 2007.
5. Lauritsch G, Bruder H, Head Phantom, *Phantom database*, <http://www.imp.uni-erlangen.de>, 1999.

"SHARE & MEET" PROJECT: AN INNOVATIVE REMOTIZATION SOLUTION FOR DIGITAL IMAGING AND RADIOTHERAPY TREATMENT PLANNING

MATTEO BOTTEGHI

Department of Clinical and Molecular Sciences
Marche University, Ancona, Italy
m.botteghi@univpm.it

ETIN-OSA O. OSA, MD

Department of Radiation Oncology
New York University School of Medicine, New York, NY
Etin-Osa.Osa@nyumc.org

EUGENIO LUCIANI

Softmed Srl, Falciano, San Marino

ISMAEL KHANGANE

IT Department
Catholic University of Health and Allied Sciences, Mwanza, Tanzania

NESTORY MASALU, MD

Department of Oncology
Bugando Medical Centre, Mwanza, Tanzania

on behalf of AFRICOG (African Italian Cooperative Oncology Group)

Abstract:

The incidence of pathologies like tumors and infections is a significant public health burden in developing countries. Although telemedicine implementation largely remains a privilege of developed countries with more economic resources, it could be of great utility and efficacy in developing countries lacking appropriate health care facilities by allowing for the performance of good level health care practices. "Share and Meet" project includes a novel intercontinental telematic platform oriented to oncology and its related branches. The project goals are: to provide telecommunication (TLC) services between health care facilities in developed and developing countries including conference calling, second opinion, and distant learning; to share radiology and microscopy images and patient medical records for diagnostic purposes; and to carry out Good Clinical Practice (GCP) clinical trials through data collection, monitoring, and evaluation. There is currently a longstanding partnership between several Italian institutions and the Bugando Medical Centre Department of Oncology in Mwanza, Tanzania (BMC-Tanzania) with cooperative programs including training of BMC medical staff in Italy through e-learning programs, support in establishing a Radiation Oncology Department in BMC, public health screening programs for the Tanzanian population, and shared clinical and basic science research programs. The telematic platform, developed by Softmed, is strengthening this remote cooperation and partnership. Services currently available include the sharing of workflows and international GCPs, teleconsulting between the specialists of the hospitals, clinical data remote entry, and monitoring of patients enrolled in research trials. The pilot implementation confirmed the project feasibility. "Share and Meet" is characterized by a high level of innovation based on cost-effective solutions which increase efficiency and efficacy of health practices, allow interdisciplinary and synergistic cooperation, and can boost the use of telemedicine in low income countries.

Keywords: telemedicine, digital imaging, remote radiotherapy, telepathology, digital divide

Rationale:

Pathologies like tumors and infections are a significant public health concern in developing countries.

Many international institutions aim to promote cultural and scientific actions both in developed and developing countries on human solidarity issues, with a special focus on sanitary related health and social care. One of their main goals is to develop tools and procedures focused on prevention, diagnosis, and treatment.

Vittorio Tison Association (Tison), IRST Cancer Research Hospital, Softmed, and Patologi Oltre Frontiera Association (POF) cooperate in the sanitary mission founded in BMC, a hospital located in the city of Mwanza, in the northern region of Tanzania. BMC serves the Victoria Lake Zone, an area with over 14 million inhabitants. The Oncology Operative Unit supervised by Tison in BMC represents the core of the first Tanzanian National Cancer Institute and a model of sanitary management in Sub Saharan African countries' public institutions.

The complex path of oncologic care requires the support of anatomopathology laboratories to perform diagnostic exams like cytology and immunohistochemistry, and diagnostic imaging.

In addition, radiotherapy (RT) is a critical component of oncologic curative treatment and palliation. However, developing countries currently lack many of these resources and services.

Where distance is a critical factor, telemedicine is one tool used by health care professionals using Information and Communication Technologies (ICTs) to deliver health care services, to exchange information necessary for disease prevention, diagnosis, treatment, evaluation, research and training of health professionals. The implementation of telemedicine could be of great help and efficacy in developing countries that lack the necessary resources to provide high level health care practices. Collaborations especially in digital imaging and radiotherapy treatment planning between developed and developing countries separated by significant physical distance can be enhanced using the "Share and Meet" intercontinental telematics platform.

Objectives:

The "Share & Meet" project utilizes a novel worldwide telematic platform oriented to several sanitary branches with a special focus in oncology. The main project goals are:

- to provide TLC services between healthcare facilities in developed and developing countries, allowing for conference calling, second opinion, and distant learning
- to share radiology and microscopy images and patients medical records for diagnostic purposes
- to design a radiotherapy remotization model to facilitate and enhance radiotherapy treatment planning in developing countries
- to allow the remote control of medical instrumentation
- to carry out GCP clinical trials through data collection, monitoring, and evaluation
- to encourage and support scientific research

Material and methods:

Softmed integrates the core technology solutions and network layouts which the "Share & Meet" project is based on.

"Share & Meet" creates intranet links between worldwide operating sites and implements several optimization and redundancy strategies in the transmission layer including: IP Load Balance and links aggregation to group the bandwidth available on the connections to the Internet and to other wide area networks, provided over heterogeneous media; Double Path VPN tunnels to allow High Availability of the international links which can operate in Active/Active redundancy compensating for the latency and variance in packets transmission and overcoming inevitable problems arising from the shortage of

connectivity solutions from developing countries' Internet Service Providers (ISPs); duplication of voice and data packets to reduce the impact of packet loss on single Internet connections; IP packet overhead reduction to maximize the effectiveness of the transmission.

Due to specific Quality of Service (QoS) protocols, "Share & Meet" can support simultaneous real time and asynchronous data transfer and can optimize the usage of different connections according to the type of data, the priority of services, the commitment of the network, and in case of failure of a connection.

The privacy for sensitive patient data is assured by the support for the main data encryption protocols and VPN technology.

We performed the first survey of the BMC building in May 2011. This was followed by a general assessment of the internet connection services available in Tanzania delivered on landlines and GSM technologies, the ICT facilities existing in BMC, the needs and lacks in local working procedures, the development plans released by the charities and NGOs operating in BMC involving the Tanzanian public health authorities.

In 2012, a new building dedicated to the Radiotherapy department was completed in a compound adjacent to the BMC main building. This RT clinic includes an IT room where the "Share & Meet" IT core devices are hosted.

Four landlines connections were delivered to the IT room: 3 ADSL2+ copper lines and 1 optical fibre.

The digital link between IRST and BMC has been realized during the early pilot phase.

Some services already available on-site at BMC include: voice over IP telecounselling with international workgroups, secure access to medical records software remotely hosted in IRST datacenter, sharing of workflows and international GCPs, e-learning programs implemented through web conference and remote dashboard tools, and remote entry and monitoring of patients enrolled in research trials.

Development is ongoing for two high innovation facilities: a new approach to telepathology, and a remotization model for RT treatment planning.

Pathologic anatomy laboratory investigation is the foundation of the diagnostic process. Mainly for the reading of microscopic slides resulting from cytological and histological sampling, accurate interpretation relies on both appropriate sample preparation and competence of the pathologist making the diagnosis through visual image inspection and interpretation. In developing countries, there is limited availability of expert medical pathologists, in the range of 1 to 10 pathologists per 10 million people. In developed countries the availability of medical pathologists is in the order of some hundreds per 10 million people. Telepathology is often the main method used to share diagnostic images allowing the double-blind check operated by remote pathologists to reach an accurate diagnosis.

Diagnostic specimen slides are digitized with microscopic scanners, most commonly using magnification rates of 5x, 20x, and 40x. The resulting image file's dimension range between 500 MB and 2 GB.

Since the '90s, POF projects have implemented a model of telepathology based on satellite internet connection to transfer the diagnostic images. Some limitations of this approach include low bandwidth, high cost, and limited service continuity. Frequently, the only available connection is shared with several users so the file transfers must be performed during night hours. All these factors decrease the effectiveness of the telepathology facility.

Based on the experience collected by POF operators on their operative sites, on average, it is possible to upload about 1 digitalized slide per night or a few slides per week. This transfer rate value could be adequate to support basic cytology activity, but is considered inadequate for the workload of a formal diagnostic histologic lab.

“Share & Meet” can provide higher speed and availability for the ICT services. On the operative site of BMC, experimental sessions are underway with the digital microscope Menarini D-SIGHT rev. 05; a following session will be performed with the Aperio ScanScope scanner which is able to automatically scan slides in unattended mode.

The digital images are codified with JPEG2000 compression.

At its first step, our procedure begins with the digital acquisition of all the slides at a medium rate of 5x, followed by the file upload on a remote server using an encryption protected channel. Next, the first level of double-blind visual investigation is provided by the international pathologist team to highlight the most relevant slides’ areas, then a second step of digital acquisition of these areas at a high rate of 20-40x and the file upload of the updated images is performed, and lastly, the second visual investigation to reach a final diagnosis is performed.

A Radiotherapy department requires a large sanitary staff including medical doctors, physicists, and nurses. The devices used for RT planning and treatments need to be serviced and maintained frequently. The full implementation of an RT department in developing countries remains a significant challenge. Nevertheless, RT is one of the main and critical components of curative and palliative treatments for oncologic patients.

Tison is in the process of setting up an RT unit in BMC. An Elekta Linear Accelerator was already been allocated from Ravenna Hospital to be moved to Mwanza and commissioned in the local RT building in BMC. Subsequently, IAEA will provide a Cobalt therapy machine.

IRST RT and IT staff are in the process of coordinating the commissioning of new RT machinery in Ravenna Hospital RT department, which will be connected to the existing IRST RT department to share the activity between the two sites. The RT devices installed in both sites are Accuray Tomotherapy unit and Elekta Linear Accelerator.

Images and data are codified in DICOM format.

We have begun to outline a remotization model for the RT treatment planning between the twin IRST and Ravenna RT departments, with the further aim of applying this design to the interconnection between IRST and BMC RT departments allowing the Italian staff to support the BMC working procedures.

Results:

Regarding the application of “Share & Meet” in the telepathology field, the preliminary extrapolation and first experimental data indicate an improvement of a factor between 10 and 100 in the overall images transmission rate in comparison to the previous models. To enlarge the data set, a subsequent more detailed experimental session will take place in Mwanza in October 2014.

Our survey suggests the feasibility of a collaboration between remote RT departments to perform diagnostic imaging on a patient at the first site, transfer the data set to a different site where a different staff will design the treatment plan, share the treatment plan with the first site, and ultimately provide the final RT therapy plan to the patient.

Further work is ongoing in understanding the most involved parameters and sizing of the remote RT model.

The early experimental stages revealed some needs. For instance, in the file transfer layer, a specific solution to compensate transfer session disconnections with an incremental strategy, and the multiple file contemporary transmission over the same aggregate multichannel are required.

The most immediate extension of the model concerns the remotization of radiologic imaging, to integrate and complete the diagnostic path.

The remote RT model provides additional challenges regarding the reproducibility of the working set on the remote sites, the exact tuning of devices, a strong quality control procedure, and harmony between therapeutic approach and good clinical practices.

Share & Meet is being implemented in other developing world scenarios, with different availability of basic resources and local infrastructures. This suggests the implementation of a benchmarking procedure to characterize the environmental parameters.

Where only satellite coverage is available, to provide a network connection, the use of data transmission over HF radio carriers between the remote operative site and a concentrator site better served by the ISPs are being evaluated.

The first level project's goal is to ensure the working continuity for the departments located in the developing countries with a small local staff. Subsequently, training programs will be provided to medical and paramedical local staff focusing the working processes towards the achievement of autonomy in the operations. Remote counselling should assume the role of supervising the processes and performing independent quality control.

The long term cooperation experience with BMC is showing the relevance of scientific research in low income countries in helping to better understand the specific pathologies of these populations and mutually enrich the knowledge base.

Conclusions:

Practical collaborations between health care sites in developed and developing countries utilizing the "Share and Meet" program, a novel intercontinental telematics platform oriented to oncology and its related branches, are feasible.

"Share & Meet" is characterized by a high level of innovation based on cost-effective solutions which increase the efficiency and efficacy of health practices, allow interdisciplinary and synergistic cooperation, could boost the use of telemedicine in underdeveloped countries, and reduce the knowledge gaps inherent to the digital divide, in a scenario of virtuous globalization.

S2P: Biomaterials and nanotechnology

Chairs: Kheng Lim Goh, Michele Bianchi

WETTING ABILITY OF BIOLOGICAL LIQUIDS IN PRESENCE OF METALLIC NANOPARTICLES
CRISTINA SCOLARO

THE VOLUME DYNAMICS OF GEL ACTUATOR IN THE COURSE OF PERIODIC BENDING IN DC
ELECTRIC FIELD
FELIKS BLYAKHMAN

MULTIFUNCTIONAL TITANIUM SURFACES FOR ORTHOPEDIC IMPLANTS
SARA FERRARIS

WETTING ABILITY OF BIOLOGICAL LIQUIDS IN PRESENCE OF METALLIC NANOPARTICLES

C. SCOLARO, L. TORRISI

*Dottorato di Ricerca in Fisica, Università di Messina
V.le F. S. D'Alcontres 31, 98166 S. Agata, Messina, Italy,
cscolaro@unime.it*

The wetting ability of biological liquids is measured at room temperature and at 37°C on different materials including biocompatible surfaces and biological tissues. Measurements as a function of the surface treatments, roughness and surface tension are presented, demonstrating that surfaces can be hydrophobic and hydrophilic and that the treatments change their functionality. The inclusion in the liquid drop of metallic nanoparticles, at different concentrations and different species, modify significantly the contact angle, often improving the wet ability of many surfaces and enhancing the adhesion forces at the solid-liquid interface.

Keywords: Wetting ability, nanoparticles, surface roughness.

1. Introduction

Nanoparticles (NP) with dimensions ranging between tens and hundreds of nanometers, play important role at the surface of solids, controlling the physical and chemistry properties of the solid-liquid interfaces. In nanotechnology has been demonstrated that nanoscale materials may have remarkably different properties compared to the bulk. For example Au-NP have interesting catalytic properties, not presented by the bulk gold [1]. When a liquid is placed into contact with a solid, the liquid's spread onto the solid surface as a function of the solid surface energy. The resulting shape of the liquid drop depends on the forces at the three interfaces: the liquid-solid, the liquid-air and the air-solid, according to the Young's equation [2]:

$$\sigma_{SV} = \sigma_{SL} + \sigma_{LV} (\cos\theta) \quad (1)$$

where σ_{SV} , σ_{SL} and σ_{LV} represent the energy per unit area at the solid-vapor, solid-liquid, and liquid-vapor interfaces, respectively, while θ is the contact angle of the liquid on the solid. When the surface energy at the solid-liquid interface is high or the solution's surface tension is low, the contact angle is small and the drop spreads out over the surface; it is the case of hydrophilic surface. When the surface energy is low, the drop maintains the spherical shape on the surface; it is the case of hydrophobic surface. Between these, at around 90 degrees, the surface has intermediate properties. These forces depends on many properties of the solid surface, such as the roughness and morphology, chemical reactivity, elemental composition, electrical properties etc.. Also the liquid properties control the wetting ability, in terms of liquid composition, surface tension, properties of solution, etc.. In particular solutions containing NP modify significantly the wetting ability of the solvent with the solid surface, due to adhesion forces, electrochemical properties, roughness, nature of the liquid-solid interface, dimensions and shape of the nanoparticles, etc.. From this point of view the NP may control the adhesion of interface between solids and liquids determining the best coupling for optimal hydrophilic surfaces or the bad coupling for

hydrophobic surfaces. Bio-medicine, microelectronics and metallurgy are strongly interested to these aspects concerning the coupling of biomaterial and prosthesis with biological tissues and the transport of drugs using NP, the growth of superconductor layers on monocrystals and their doping and the use of NP to enhance the wetting during material welding [3].

2. Experimental set-up

Nanoparticles of different metals (Ti, Cu, Ag and Au) have been prepared using laser ablation in water. Nd:Yag laser at 1064 nm wavelength, 3 ns pulse duration and 200 mJ pulse energy was employed at 10 Hz repetition rate focalizing the laser light on the metal surface with 1 mm² spot size. The metal was placed in a little container in which was added 10 ml water. Irradiation for 10 minutes produces ablation of the order of 1-10 mg thus a solution with a concentration of 1-10 mg/10 ml solvent, depending on the nature of the ablated metal, was obtained. NP are produced with dimensions of the order of 10-100 nm in dimension and with a spherical shape. NP coalescence effects are observed as a function of the NP permanence time in water. The method used to measure the wetting angles is the *sessile drop* that involves the measurement of profile of a liquid droplet resting on a solid surface [4]. Basically consists in the measurement of the contact angle between the tangent to a profile drop, deposited on the sample surface and the surface itself. The drop is generated depositing 1 ml liquid on the surface with a microsyringe. A CCD camera connected to the eyepiece of an aligned optical microscope records the images of the drops and of the substrate cross-section. A software permits to calculate the contact angle and for each material 6 measures were carried out, of which it is calculated the average. The sample is moved horizontally to allow a new deposition in a different part of the pattern. Roughness measurements were made using a surface profilometer Tencor P-10. This device allows analysis of surfaces of solid materials (polymers, metals, plastics) measuring the horizontal and the vertical roughness. The analysis is done using a diamond point that sweeps the surface of the specimen to follow the profile. A transducer converts the movement of the tip in value relative height. All information are transmitted to a computer, connected to the instrument, which show the surface of the sample itself.

The tip can be used with a force between 1-50 mg and has a range, in horizontal and vertical position, between 0-300 µm with a depth resolution of 1 nm. SEM analysis and X-ray fluorescence analysis were employed to observe the NP deposited on different substrates using high resolution microscopy.

3. Results and discussion

Fig. 1 shows typical examples of surface profiler for the PMMA surface (a) and Ti surface (b) used in this investigation. The average roughness is of about 30 nm for PMMA and 4.5 µm for Ti. The roughness influence strongly the wetting ability decreasing the contact angle with the increment of the surface roughness [4].

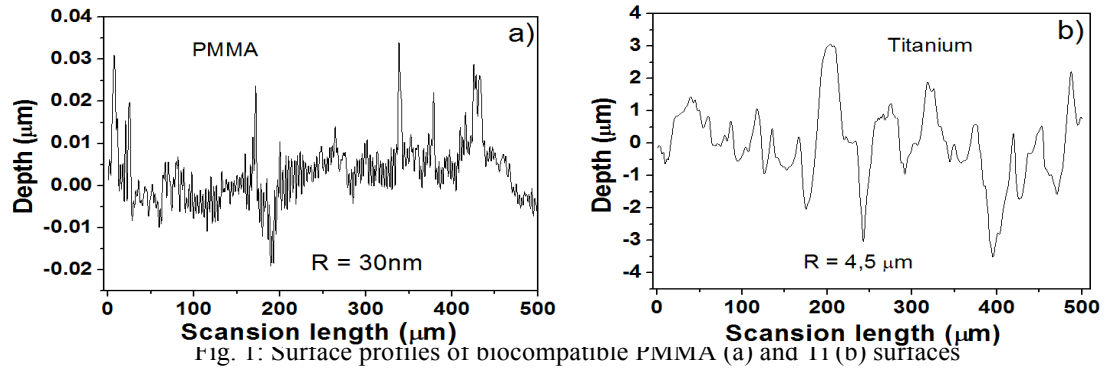


Fig. 2 shows, as an example, a comparison of drops images on biocompatible Ti substrate using a pure physiological liquid without (a) and with the Ti NP (b) at a concentration of 5 mg/10 ml, and drops of pure physiological liquid on PMMA surface without (c) and with (d)) Ti NP at the same concentration. Such measuring were performed using different solutions (water, physiological liquids and blood), different substrates (Al, Cu, Ti, Ag, Al₂O₃, polyethylene and polymethylmethacrylate), different nanoparticles (Ti, Cu, Ag, Au) and different temperatures (20°C and 37°C). The temperature increment decreases the contact angle measured at room temperature.

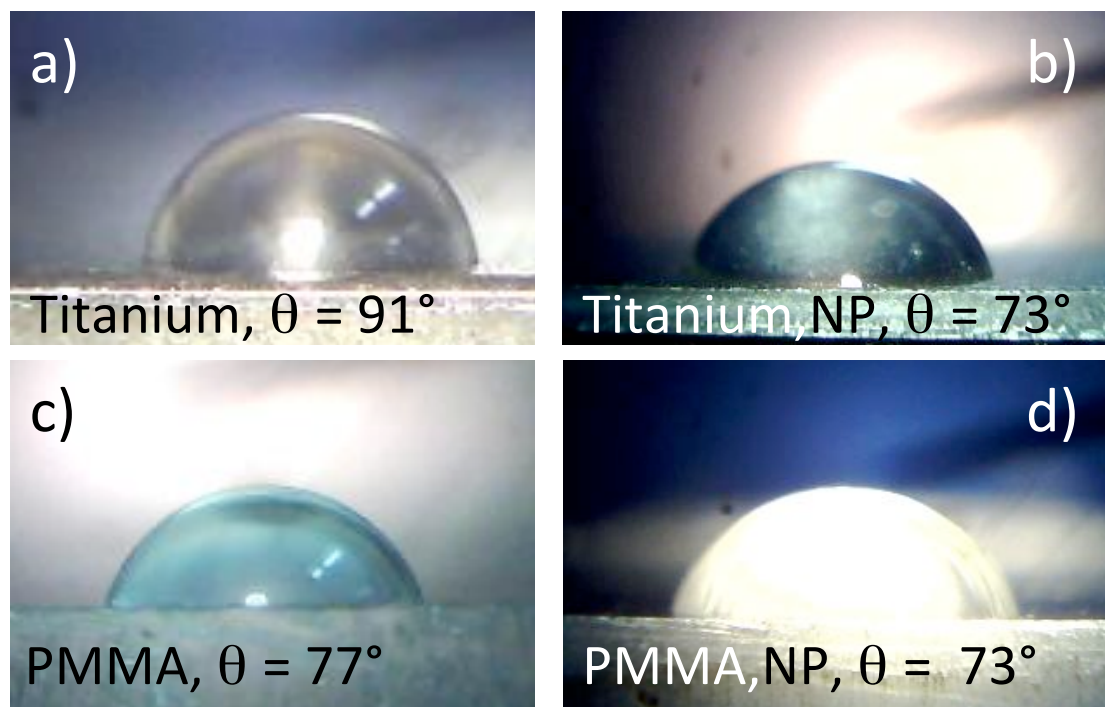


Fig. 2; Contact angle for water on Ti (a) and on PMMA (c) and for water containing Ti NP on Ti (b) and on PMMA (d).

The water contact angle decreases going from aluminium to polyethylene, titanium, polymethylmetacrylate, silicon and glass, where it was evaluated of 96° , 94° , 91° , 77° , 67° and 40° , respectively. Generally the use of NP decreases the contact angle enhancing the wetting ability of the surface. A lot of results are summarized in Fig. 3 for water solutions without and with Ag NP (a) and without and with Au NP (b). In both cases NPs induce contact angle decrement improving the adhesion with the solid surface that means increasing the adhesion forces of adherence between the liquid and the substrate.

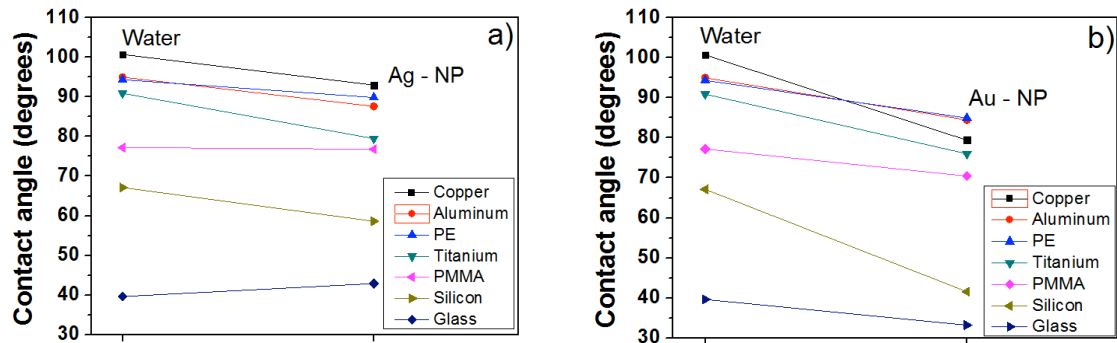


Fig. 3: Contact angle measurements for water and for water containing Ag NP (a) and Au NP (b) as a function of different surfaces.

Fig. 4 shows a SEM image of Ti NP deposited on Al substrate reporting an average dimension of 100 nm for the NP. (a). The same figure shows the dependence of the water wetting angle on the roughness of the aluminum solid surface (b). Generally mirror polished surfaces are hydrophobic while high roughness surfaces, obtainable with peculiar treatments using lasers, chemical attack and sandblasting, show high hydrophilicity [5]. Surface treatments of the same surfaces may decrease the contact angles up to about 10% with respect to the maximum value for mirror conditions. The use of NP in solution may decrease the contact angle up to about 50% with respect to the solution without NP. For special surface NP doesn't decrease the wetting angle or may increase it, such as for Ag NP in water deposited as a drop on glass surfaces.

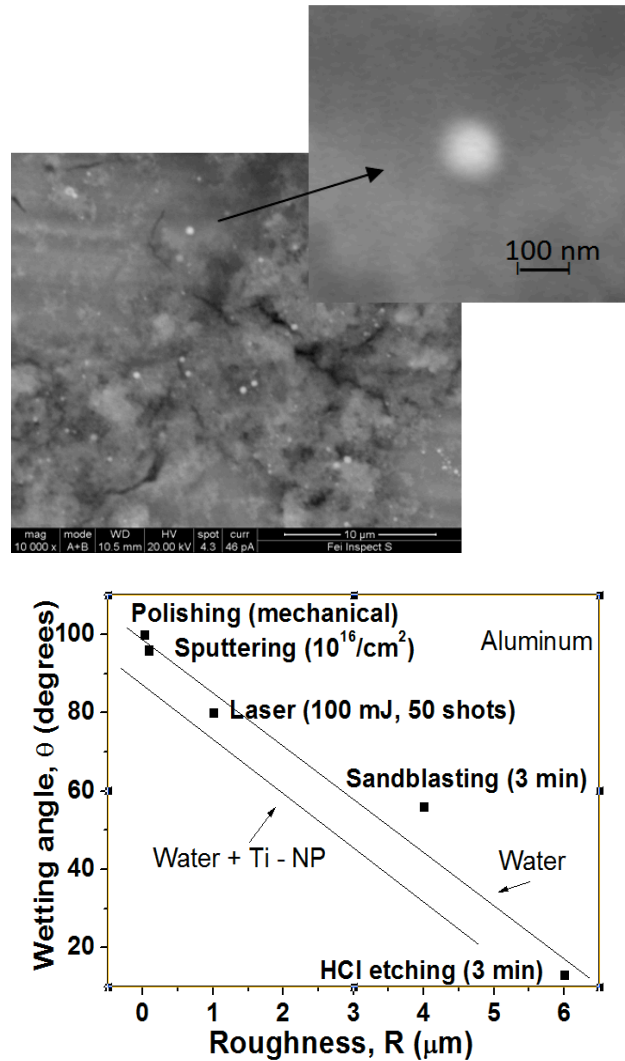


Fig. 4: SEM image of Ti NP on Al surface (a) and contact angle of water deposited on aluminum surface vs. roughness (b).

4. Conclusions

The wetting ability of biological solutions with biocompatible surfaces, based on different materials (metals, ceramics and polymers), plays an important role for the implantation of prosthesis in the body for the attachment of cells and tissues to biomaterials and for the formation of optimal adhesion between different media [6]. Particularly interesting appears the use of nanoparticles that may improve the wetting

ability enhancing significantly the contact adherence and consequently the adhesion forces between different materials. This new field of interest involves the sub-microscopic study of the solid-liquid interfaces, taking into account many important parameters such as the surface roughness, which enhances the adhesion, such as the body temperature, the nature of the solutions and of the surface, and the liquid tension surface that decrease it. All these aspects are very important in different actual fields of interest, from biomaterials preparation to biomedicine research, and from microelectronics to new nanotechnology applications.

References

1. Heddle J.G., Gold Nanoparticle-Biological Molecule Interactions and Catalysis, *Catalysts* 2013, 683-708
2. Frost D. W., Study of adsorption of biological and nanoparticle solutions at the solid-liquid interface, B.S., University of Arkansas, Internal Report, Manhattan, Kansas, 2007
3. Langer R. Biomaterials in drug delivery and tissue engineering: one laboratory's experience. *Acc. Chem Res* 2000; 33: 94-101
4. Scolaro C., Torrisi L., Italiano A. and Cutroneo M., Ruolo della bagnabilità e rugosità in superfici di materiali biocompatibili, *Proc. XI Convegno Nazionale Bioingegneria "Aspetti Clinico-Fisici ed Ingegneristici Applicati"*, Messina, Facoltà di Ingegneria, ISBN 978-88-96398-07-4, 5 Luglio 2013
5. Torrisi L., Scolaro C. and Foti G., Techniques of treatment of aluminum to modify the surface wetting properties, Submitted to *Appl. Surf. Sci.* 2014
6. Scolaro C., Torrisi L., Cutroneo M., Velardi L., Wetting ability modifications in biocompatible polymers induced by pulsed lasers, *Proc. VI Conf. Int. PPLA 2013*, pg. 52, Lecce, Università del Salento, 2-4 ottobre 2013

THE VOLUME DYNAMICS OF GEL ACTUATOR IN THE COURSE OF PERIODIC BENDING IN DC ELECTRIC FIELD

BLYAKHMAN F.A.^{#,+}

[#]Biomedical Physics Dept., Ural State Medical University,
Yekaterinburg, 620028, Russian Federation

⁺Physics Dept., Ural Federal University named after the first President of Russia B.N.Yeltsyn
Yekaterinburg 620028, Russian Federation
feliks.blyakhman@urfu.ru

SAFRONOV A.P.^{*}

^{*}Chemical Dept., Ural Federal University named after the first President of Russia B.N.Yeltsyn
Yekaterinburg 620083, Russian Federation
alexander.safronov@usu.ru

FILIPOVICH M.A.⁺

⁺Physics Dept., Ural Federal University named after the first President of Russia B.N.Yeltsyn
Yekaterinburg 620083, Russian Federation
fab2@uw.edu

SHKLYAR T.F.^{#,+}

[#]Biomedical Physics Dept., Ural State Medical University,
Yekaterinburg 620028, Russian Federation

⁺Physics Dept., Ural Federal University named after the first President of Russia B.N.Yeltsyn
Yekaterinburg, 620083, Russian Federation
t.f.shklyar@urfu.ru

The periodic bending in the DC electrical field (1 V/mm) was studied on sodium polyacrylate gels with different network density immersed in 0.8 mM CaCl₂ solution. The gel stripes 2x2 mm in the cross section and 10 -15 mm in length were affixed by one end perpendicular to the electric field. The other end of the stripe remained free. Up to four consequent bending displacements of the free end of the stripe in opposite directions were observed while the electrical field was kept constant. The angle of inclination from the vertical position and the area of the planar projection of the stripe were monitored by means of digital optical recording. It was found that the gel stripe substantially contracted during its bending in the DC field. The dynamics of the gel contraction was well fitted by the combination of the Gaussian and exponential decay functions. The underlying mechanism of the gel actuator periodic bending based on the dynamics of gel volume change in DC electric field was proposed.

Keywords: polyelectrolyte gels; actuator; DC electric field; mechanical behavior.

Introduction

The polyelectrolyte gels are the electroactive smart materials which resemble some cell's structures¹ and which are promising for the different applications in the area of biomedical engineering.² Recently, we have reported for the first time that the rodlike polyelectrolyte gel samples placed in the DC electric field across the field lines apart from the electrodes produced the periodic bending.³

In our latest publication, we demonstrated that in the course of the actuator's bending, the gel shrinks much as a whole.⁴ Therefore, the gel volume change at different solutions as a function of time may contribute to the mechanical behavior of gel actuators.

In this paper, we provide experimental data on the gel volume change in the course of gel actuator bending in DC electric field. The aim of the study is to determine the qualitative description of actuator contraction dynamics due to DC electric field application.

Methods

Polyacrylic acid gels with sodium counterions (20% of ionization) were synthesized by the free-radical polymerization in 2.7M aqueous solution with N,N'-methylene-diacrylamide as a cross-linker. In order to make gels with varying network density, cross-linker to monomer ratio was set at 1:25 and 1:100. Polymerization was carried out in the PE probe tubes 10 mm in diameter. Then, the gel samples were washed in distilled water and cut by a razor blade to elongated rectangular actuators 10 mm in length and 2x2 mm in cross-section.

Actuators were placed into the experimental cell made of a Teflon ring 5 mm in height and 20 mm in the inner diameter mounted upon a glass plaque. Two 5x5 mm platinum foil electrodes were placed at the opposite walls of the cell. All experiments were performed under the constant voltage 27 V. The distance between electrodes was set at 27 mm so the electric-field intensity was equal to 1.0 V/mm.

The gel actuator was positioned in the center of the cell between the electrodes with its longer axis across the electrical field lines. One end of the sample was affixed in a gap in the wall of the cell, while the other end was left free to move in the applied field. During the experiments, the cell was filled with 16 ml of 0.8 mM CaCl_2 to cover on the electrodes and the gel sample. Computerized optical system of laboratory design was used for the video recording of the gel sample bending in the applied DC field.

Figure 1A presents the layout of the geometrical parameters of the planar projection of the gel stripe, which were monitored during its bending. They were: the angle (θ) of the free end displacement (inclination) from the vertical (initial) position and the apparent area (S) of the projective image of the gel stripe. The contours of actuator were outlined by hand, and the area of delineated figure was calculated with the use of the original software. The evolution of the geometrical parameters under the applied direct current was analyzed at the 10 sec ramp.

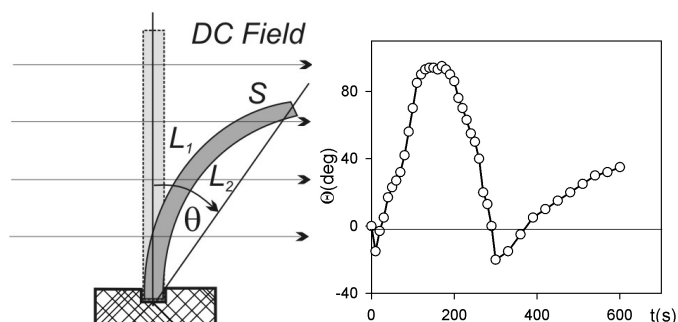


Fig. 1. Layout of the parameters monitored under the applied DC current (A), and typical plot of the evolution of the angle of inclination with time for the gel with network density 1:100 (B).

The statistic software packages “Statistica 6.0” and “SigmaPlot” 12.0 were used for the statistical analysis. Mean value (M) and standard deviation (SD) were calculated. The best fit of the data approximation was tested as well.

Results

The most obvious demonstration of the mechanical oscillatory bending of the gel stripe in the DC field are the changes in the angle of the inclination to the vertical position, which can readily be observed by the naked eye. Figure 1B (see above) presents the typical plot of the angle of inclination (θ) against time. Positive values of θ correspond to the anodal displacement of the gel with regard to the initial (vertical) position, while negative values indicate the gel bending to the cathode. In first 20 sec the gel noticeably bends to the cathode with the maximal inclination of 20 degrees.

The anodal bending follows this relatively short step, and it is substantially longer and more pronounced. At its maximal anodal bending, the gel stripe is aligned almost parallel to the electric field. The anodal bending is followed by the reversal cathodal displacement, which results in the straightening of the gel stripe in the initial position across the DC field. The third step of bending ends in the moderate inclination of the stripe toward the cathode, which is comparable to the inclination during the first step. The fourth bending took place only for the weakly cross-linked gels with the network density lower than 1:100. For example, Table 1 presents the mean values and SD ($n=5$) of the duration and the maximal inclination of the consequent three steps for the gels with different network density.

Network density	1 st step (cathodal)		2 nd step (anodal)		3 rd step (cathodal)	
	Duration (s)	θ max (deg)	Duration (s)	θ max (deg)	Duration (s)	θ max (deg)
1:25	28 \pm 5	6 \pm 2	390 \pm 102	76 \pm 6	1400 \pm 250	1 \pm 6

1:100	16±5	9±3	198±132	82±5	1010±88	30±11
-------	------	-----	---------	------	---------	-------

Table 1. Duration and maximal inclination of the steps of gel bending.

Although the average values are much dispersed, the general trend is quite clear: the decrease in the network density of the gel makes the consequent steps of the bending less durable and the maximal inclination in these steps more substantial.

Figure 2 presents the time plot of the area of the gel stripe projection (S) for the gels with 1:25 and 1:100 network densities. The mean values and SD ($n=5$) are displayed.

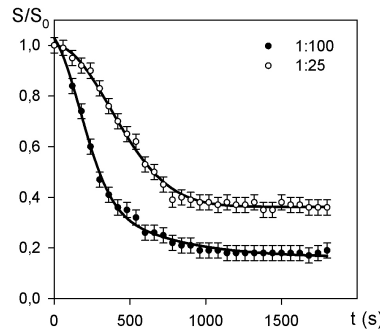


Fig. 2. Time dependence of the area of the gel stripe in the planar projection. Network densities 1:25, 1:100.

Assuming the isotropic volume changes of the gel, the relative degree of gel swelling is given by the equation: $\alpha / \alpha_0 = (S / S_0)^{3/2}$. The plots in Figure 2 indicate that the degree of swelling of the gel stripes does not remain constant in the applied experimental conditions. The dynamics of the gel contraction was well fitted by the combination of the Gaussian and exponential decay functions. The fitting parameters are listed in Table 2.

$$y(t) = y_0 + a \exp\left(-\frac{1}{2}\left(\frac{t}{\tau_1}\right)^2\right) + b \exp\left(-\frac{t}{\tau_2}\right) \quad (1)$$

Gel	y_0	a	τ_1	b	τ_2	R^2
1:25	0.36	0.63	373	0	0	0.996
1:100	0.16	0.47	187	0.40	453	0.995

Table 2. Parameters of Equation (1) for time evolution of the apparent area of the gel stripe.

With the decrease in the network density the maximal contraction of the gel (y_0) increases and the characteristic time of the Gaussian decay (τ_1) diminishes.

Discussion

If the elongated stripe or filament of sodium polyacrylate gel is placed in the DC electrical field across the field lines with one end affixed, it undergoes several periodic inclinations in the opposite directions starting from bending to cathode. According to the general theoretical consideration, the gel bending is based on the redistribution of ions inside and outside the polyelectrolyte gel.⁵ When DC electric field is applied, free ions, which are present in the gel and in the surrounding solution, begin moving to the oppositely charged electrode.

The gel contains Na^+ counterions, which compensate the negative electrical charge of the carboxylate residues attached to the chains of the macromolecular network. The swelling of the polyelectrolyte gel is affected by the several factors, among which the osmotic pressure of counterions is one of the most strong. In the experimental setup, the gel stripes were placed in the 0.8 mM solution of CaCl_2 , which contained divalent Ca^{2+} cations. Due to the diffusion Ca^{2+} cations enter the gel interior while Na^+ ions leave it for the surrounding solution.

According to the electroneutrality condition, the $\text{Ca}^{2+}/\text{Na}^+$ ionic exchange should result in the two-fold diminishing of the counterions concentration in the gel network as Ca^{2+} is divalent, and it can compensate the charge of the two carboxylate residues. Therefore, the osmotic pressure, which is proportional to the concentration of the counterions inside the gel, will also decrease. One can see from Figure 2 that the relative contraction of the dense gel with the network density 1:25 is lower than that of the weak gel with 1:100 networking. These results are in a good agreement with the data obtained for other polyelectrolyte gels.⁶

Meanwhile, the contraction of the NaPAA gel in CaCl_2 solution as a whole cannot provide by itself the periodic bending of the gel stripe in the DC electrical field. From the general point of view, it is clear that the bending of the gel stripe is tightly linked to the local swelling of its opposed sides marked as L_1 and L_2 in Figure 1A (see above). If the cathodal side swells more than anodal side, the stripe bends to the anode, and vice versa. The same happens if the cathodal side shrinks less than the anodal side. It makes the analysis of the local swelling of the stripe crucially important for the understanding of the underlying reasons for the periodic bending, and it is the subject of our future investigation.

Acknowledgments

The study is supported by the Russian Foundation for Basic Research (grants ##13-08-01050a and 13-03-96068r-a).

References

1. Shklyar T, Dinislamova O, Safronov A, Blyakhman F, Effect of cytoskeletal elastic properties on the mechanoelectrical transduction in excitable cells, *Journal of Biomechanics* **45**:1444–1449, 2012.
2. Shahinpoor M, Kim K, Ionic polymer–metal composites: III. Modeling and simulation as biomimetic sensors, actuators, transducers, and artificial muscles, *Smart Mater Struct* **13**:1362–1388, 2004.
3. Safronov A, Shakhnovich M, Kalganov A, et al, DC electric fields produce periodic bending of polyelectrolyte gels, *Polymer* **52**:2430-2436, 2011.
4. Filipovich MA, Shklyar TF, Safronov AP, et al, Effect of the polyelectrolyte hydrogel actuator network density on its mechanical behavior in the DC electric field, *IFMBE Proc. 15th Int. Conf. Biomedical Engineering*, Singapore, pp. 247-250, 2014.
5. Doi M, Matsumoto M, Hirose Y, Deformation of ionic polymeric gels by electric fields, *Macromolecules* **25**:5504–5511, 1992.
6. Osada Y, Gong P, Electrical behaviors and mechanical responses of polyelectrolyte gels, *Polymer Gels and Networks*, Marcel Dekker, New York, Basel, pp. 177-217, 2002.

MULTIFUNCTIONAL TITANIUM SURFACES FOR ORTHOPEDIC IMPLANTS

SARA FERRARIS, SILVIA SPRIANO

*Department of Applied Science and Technology, Institute of Materials Physics and Engineering
Corso Duca degli Abruzzi 24, 10129, Torino, Italy
sara.ferraris@polito.it; silvia.spriano@polito.it*

Fast and physiological bone integration coupled with reduced bacterial contamination and even active antibacterial behavior are nowadays the main challenges for orthopedic implants. An innovative and patented surface treatment able to produce nanotextured bioactive and even antibacterial titanium based surfaces is the topic of the present research. The treatment foresees a first acid etching in diluted hydrofluoric acid, followed by a controlled oxidation in hydrogen peroxide. The result is a multi-scale surface topography (micro and nano textures) and an high density of surface hydroxyl groups. These features impart to titanium surfaces inorganic bioactivity (ability to induce hydroxyapatite precipitation in simulated body fluid), high wettability and protein absorption ability, high osteoblast adhesion, proliferation and differentiation. A further biological functionalization (biomolecular grafting) or introduction of an antibacterial agent can improve surface properties adding biological bioactivity or antibacterial action respectively.

Keywords: titanium, bone integration, surface modification

1. Introduction

Ti6Al4V is one of the most widely used materials for the realization of orthopedic prostheses, due to its good mechanical properties and biocompatibility. The improvement of bone integration ability and reduction of bacterial contamination are the main challenges of the research on materials for orthopedic applications.

Several strategies have been proposed in the scientific literature, in patents and in clinical applications in order to improve the bone bonding ability of titanium surfaces. Modification of surface topography, bioactive coatings and chemical/electrochemical treatments aimed to obtain bioactive oxide layers can be cited as the most important ones [1, 2, 3]. These strategies are based on the consolidated knowledge that surface roughness, chemical composition and charge are the main factors affecting biological interactions. An increasing interest on biological functionalization (surface grafting of specific biological molecules) has also been registered in the last years, in order to improve the bone-implant interaction [4].

The problem of prosthetic infections and the concomitant development of increasing bacterial resistance to common antibiotics are at the basis of a growing attention to antibacterial surfaces for medical implants [5,6]. The rationale of these surfaces includes both anti-adhesive materials (able to reduce bacterial adhesion to their surface) and active antibacterial materials (which are able to exert a bactericidal activity).

In the last years the attention of scientists has been focused on nano-features of surfaces both for improving their cell stimulating ability, also to reduce bacterial colonization and even to exert an antibacterial action (e.g. silver nanoparticles) [7,8].

The present papers summarizes recent results on innovative multifunctional titanium surfaces, developed and patented by the authors, characterized by nanotextured topography, in vitro bioactivity, tunable antibacterial activity and bone stimulating ability.

2. Materials and Methods

Ti6Al4V alloy (ASTM B348, Gr5, Titanium Consulting and Trading) disks were obtained by automatic cutting. Samples were polished by SiC abrasive papers up to 4000 grit and washed in acetone and water in an ultrasonic bath in order to obtain homogeneous and clean surfaces.

The surface modification process foresees a first acid etching in diluted hydrofluoric acid (HF) aimed to remove the native oxide layer and a subsequent controlled oxidation in hydrogen peroxide for obtaining a micro- and nano-textured oxide layer [9,10]. The whole process requires less than 4 hours to be completed. The control of process parameters allowed to couple the micro and nano-texture to various surface topographies (e.g. pre-existing micro or macro roughness from blasting, etching, sintering).

The possibility to add antibacterial activity to the modified surface was explored by the addition of the precursor of an inorganic antibacterial agent (e.g. silver) in the hydrogen peroxide solution [11,12].

On the other hand the opportunity to functionalize the modified surface with a biomolecule was performed by organic chloride activation followed by enzyme grafting (alkaline phosphatase for instance) [9,13].

Surface topography was analyzed by means of Scanning Electron Microscopy (SEM), Field Emission Scanning Electron Microscopy (FESEM) and Atomic Force Microscopy (AFM). Surface chemistry was investigated through Energy Dispersive Spectroscopy (EDS), Infrared Spectroscopy (FTIR) and X-Ray photoelectron Spectroscopy (XPS). Surface wettability was determined by contact angle measurements and protein absorption by BCA analyses. In vitro bioactivity was investigated by immersion in Simulated Body Fluid (SBF) and SEM observation of hydroxyapatite precipitation.

The activity of the grafted biomolecule (ALP) was verified by enzymatic activity test for biologically functionalized samples [13].

Silver release was quantified by spectrophotometric measurement for Ag-enriched surfaces and their antibacterial activity by means of inhibition halo tests against *S aureus* [12].

In vitro biological behavior of modified surfaces was investigated by osteoblast cell culture [1, 12,14].

3. Results and discussion

A micro-roughness (Fig 1a, due to acid etching) and nanotexture (Fig. 1d, due to controlled oxidation in hydrogen peroxide) can be obtained on Ti6Al4V surfaces by the proposed treatment (Fig. 1). A proper optimization of process parameters allows to superimpose the described nanotexture to various pre-existing topographies (e.g. blasted surfaces, Fig. 1b or electron beam melted ones, Fig. 1c).

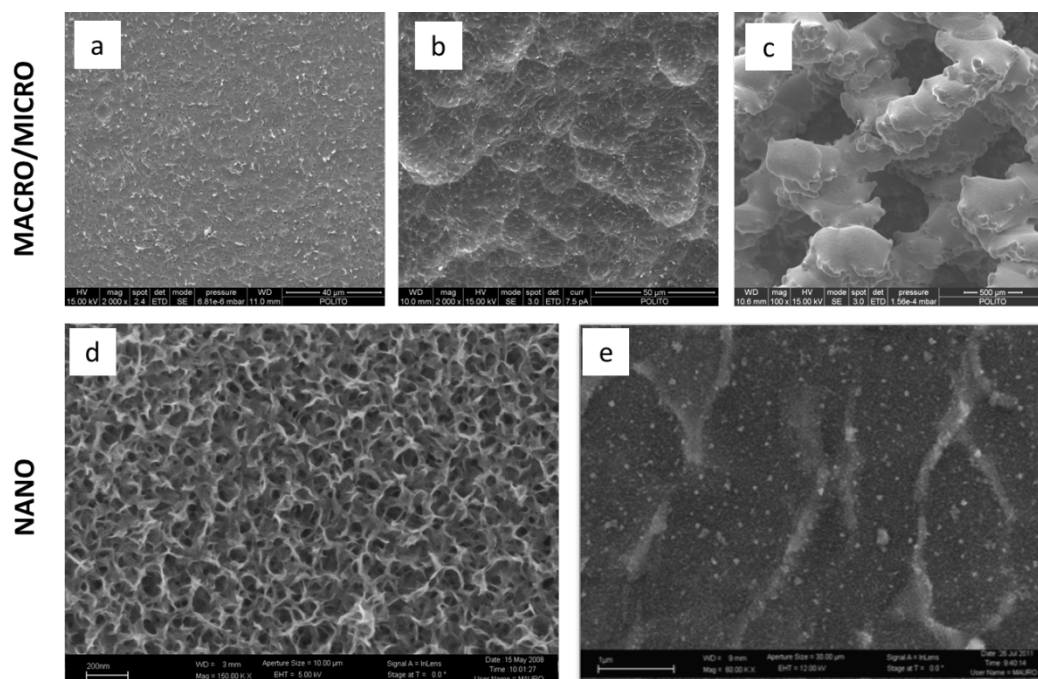


Figure 1: SEM/FESEM images of polished and treated surface (a), blasted and treated surface (b), 3D surface from electron beam melting and treated (c), nanotexture on treated surfaces (d), nanotexture enriched with silver nanoparticles (e)

Modified surfaces are rich in hydroxyls group, as demonstrated by XPS detailed analysis of oxygen region (Fig. 2a) and FTIR analyses (Fig. 2b). The presence of OH groups is an important feature, in fact it is correlated to surface wettability and bioactivity and it is useful for a further grafting of selected biomolecules.

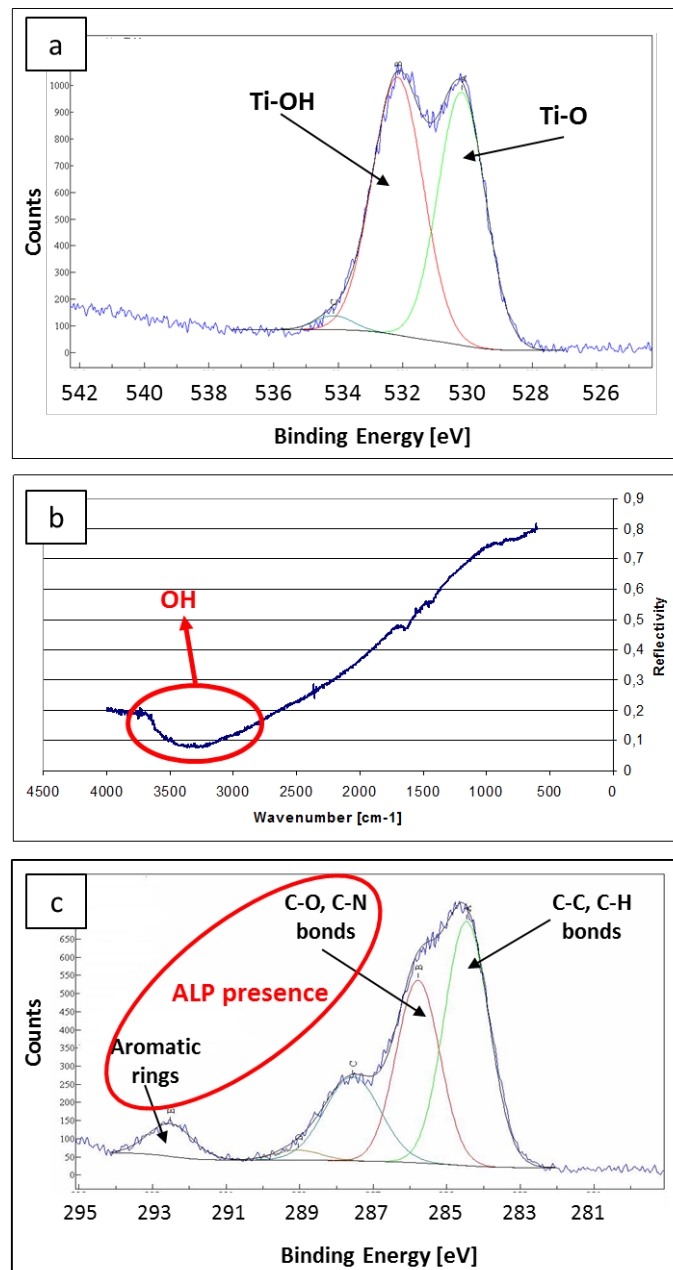


Figure2: XPS detailed analysis of oxygen region for a modified Ti6Al4V surface (a), FTIR spectrum of the same surface (b), XPS detailed analysis of an ALP grafted Ti6Al4V surface.

A significant improvement of surface wettability has been observed after the treatment (halving of the water contact angle compared to bare surfaces), together with a significant increase in the protein absorption ability. The inorganic bioactivity of modified surfaces has been evaluated in SBF, hydroxyapatite precipitation has been observed after 2 weeks soaking.

Alkaline phosphatase grafting to surface hydroxyl groups has been performed via trisyl chloride activation, as described in [13]. ALP presence has been verified by specific signal in the detailed XPS analysis of carbon region (Fig. 2c) and by enzymatic activity tests. It has been observed that the enzyme maintains its activity after grafting and is also able to improve the surface inorganic bioactivity [13].

The addition of AgNO_3 in the hydrogen peroxide solution allows the deposition of silver nanoparticles within the nanotextured surface layer, as reported in Fig. 1e. The presence of silver confers antibacterial properties to the modified surfaces, in fact a significant inhibition halo has been observed on silver containing Ti6Al4V samples against *S aureus* [12]. Silver containing surfaces release silver ions up to 2 weeks and they maintain an in vitro bioactive behavior.

A good biocompatibility for osteoblasts cells has been observed for all the modified surfaces. Moreover, it has been evidenced that the combination of micro and nano textures promotes at the same time osteoblast adhesion, proliferation and differentiation.

Conclusion

An innovative surface treatment for Ti6Al4V alloy has been developed and patented by the authors. Modified surfaces present a multiscale surface topography characterized by a peculiar nanotexture, high density of hydroxyls groups, in vitro bioactivity, high wettability and protein absorption ability and they improve osteoblasts adhesion, proliferation and differentiation. The grafting of a biomolecule (alkaline phosphatase) and introduction of silver nanoparticles have been performed on the same surfaces, in order to respectively improve their biological properties or confer antibacterial activity.

Acknowledgments

C. Cassinelli, CL Bianchi, A. Venturello, L. Rimondini, M. Miola are kindly acknowledged for their help in materials characterizations.

References

- [1] Spriano S.; Ferraris S; Bianchi C.L; Cassinelli C; Torricelli P; Fini M; Rimondini L; Giardino R, Bioactive titanium surfaces, In: Titanium alloys : preparation, properties, and applications, Nova Science Publishers, 2010
- [2] Lausmaa J, Mechanical, thermal, chemical and electrochemical surface treatment of titanium, In Springer, Titanium in Medicine – Chapter 8, Springer; 2001; 231-266
- [3] de Jonge LT, Leeuwenburgh, Wolke JGC, Jansen JA, Organic-Inorganic surface modifications for titanium implant surfaces, *Pharmaceutical Research* 25: 2357-2369, 2008
- [4] Bhola R, Su F, Krull CE, Functionalization of titanium based metallic biomaterials for implant applications, *J Mater sci Mater ed* 22: 1147-1159, 2011
- [5] Zhao L, Chu PK, Zhang Y, Wu Z, Antibacterial coatings on titanium implants, *J Biomed Mater res B* 91: 470-480, 2009

- [6] Simchi A, Tamjid E, Pishbin F, Boccaccini AR, Recent progress in inorganic and composite coatings with bactericidal capability for orthopedic applications, *Nanomedicine: Nanotechnology, Biology and Medicine* 7:22-39, 2011
- [7] F Variola, J Brunski, G Orsini, P Tambasco de Oliveira, R Wazen, A nanci, Nanoscale surface modifications of medically-relevant metals: state of the art and perspectives, *Nanoscale* 3 (2011): 335-353
- [8] Rai M, Yadav A, Gade A, Silver nanoparticles as a new generation of antimicrobials, *Biotechnology Advances* 27: 76-83, 2009
- [9] Spriano S., Vernè E., Ferraris S., Multifunctional Titanium Surfaces for Bone Integration, European Patent 2214732
- [10] Ferraris S., Spriano S., Pan G., Venturello A., Bianchi CL, Chiesa R., Faga MG, Maina G., Vernè E., Surface modification of Ti-6Al-4V alloy for biomineralization and specific biological response: Part I, inorganic modification, *J mater Sci Mater Med* 22: 533-545, 2011
- [11] Spriano S., Vernè E., Ferraris S., Procedimento per la produzione di superfici di titanio multifunzionali per riduzione del rischio di infezione e incrementata osteointegrazione e prodotto realizzato mediante tale procedimento, Patent TO2011A000716
- [12] Ferraris S., Venturello A., Miola M., Cochis A., Rimondini L, Spriano S., Antibacterial and bioactive nanostructured titanium surfaces for bone integration, submitted to *Applied Surface Science*
- [13] Ferraris S., Spriano S., Bianchi CL, Cassinelli C., Vernè E., Surface modification of Ti-6Al-4V alloy for biomineralization and specific biological response: Part II, Alkaline phosphatase grafting, *J Mater Sci Mater Med* 22: 1835-1842, 2008
- [14] Spriano S.; Ferraris S.; Pan G.; Cassinelli C.; Vernè E., Osteoblast behavior on bioactive and ALP grafted Ti6Al4V alloy, submitted to *Surface and Coatings Technology*

4 September

S3M: Biomechanical clinical applications - Gait and feet

Chairs: Bernardo Innocenti, Francesca Colle

EFFICACY OF A SLOW RECOVERY INSOLE IN REDUCING PLANTAR PRESSURE DURING
WALKING GAIT

ROOZBEH NAEMI

EVALUATION OF MOTOR STABILITY IN ELDERLY SUBJECTS THROUGH INSTRUMENTAL
STABILITY MEASURES AND CLINICAL RATING SCALES

PAOLA TAMBURINI

RELATIONSHIP BETWEEN CLINICAL RATING SCALES AND INSTRUMENTAL GAIT STABILITY
MEASURES

PAOLA TAMBURINI

DESIGN WITH FINITE ELEMENT METHOD (FEM) OF A MODULAR SMALL DIMENSIONS
FORCE PLATFORM FOR GAIT ANALYSIS

PAOLA TAMBURINI

SENSITIVITY ANALYSIS OF SIMULATED ANKLE JOINT MOTION TO THE VARIATION OF THE
PIVOT-POINT POSITION

FABRIZIO NARDINI

RECONCILING BAREFOOT AND SHOD CONDITIONS IN THE OXFORD FOOT MODEL FOR
PLANTAR PRESSURE MEASUREMENT

ABIGAIL JAITMAN

THE MECHANICS OF THE FOOT-TO-GROUND INTERACTION DURING GAIT: CORRELATION
BETWEEN JOINTS MOBILITY AND PLANTAR PRESSURE IN THE HEALTHY FOOT

PAOLO CARAVAGGI

FINITE ELEMENT MODELING AND CLUSTER ANALYSIS: A COMBINED APPROACH FOR
IDENTIFICATION OF DIABETIC FOOT PATIENTS AT RISK OF PLANTAR ULCERS

ANNAMARIA GUIOTTO

EFFICACY OF A SLOW RECOVERY INSOLE IN REDUCING PLANTAR PRESSURE DURING WALKING GAIT

ROOZBEH NAEMI^{*†}, KIMBERLEY LINYARD-TOUGH*, AOIFE HEALY*, NACHIAPPAN CHOCKALINGAM*

**Centre for Sport, Health and Exercise Research
Faculty of Health Science, Staffordshire University,
Science Centre, Leek Road, Stoke on Trent, UK*

*[†]r.naemi@staffs.ac.uk
<https://www.staffs.ac.uk/staff/profiles/rn7.jsp>*

Plantar pressure assessment is recognised as an effective tool to assess the efficacy of insoles in reducing the risk factors associated with plantar soft tissue injuries during walking. The slow rebound Poron (SR) insole was claimed to result in a custom fit during each use and believed to be more effective in increasing the contact area and consequently reducing the contact pressure and peak contact pressure compared to a normal Poron (NP) insole. The aim of the study was to compare the effectiveness of SR or NP in increasing the Contact Area (CA), and reducing the Contact Pressure (CP) at different regions of the foot during walking when compared to a control insole made of EVA (EV). Plantar pressure data during walking was collected from nine healthy individuals using in-shoe plantar pressure sensors. The results indicated that only the NP insole increased the CA and decreased the CP on the entire foot compared to the EV insole. The expected decrease in CP as a result of increase in CA was not observed at any region of the foot in any of the tested insoles. CP showed a positive significant correlation with CA in heel, hallux and heel centre in all three insoles.

Keywords: Plantar pressure; insole material; slow rebound; foot regions; contact area.

1. Introduction:

Plantar pressure assessment has been used to assess the efficacy of insole in reducing the risk factors associated with soft tissue injuries during weight bearing activities of daily living. Conformity has been used as a strategy to decrease plantar pressure and has been shown to work through increasing the contact area between the foot and the insole, and subsequently leading to a decreased contact pressure for an equal applied force. While the conformity can be increased by using customised insoles that closely fit to the shape of the foot¹, it has also been shown that the plantar pressure parameters can also be altered when a flat insole made of a different material is used^{2,3}.

Poron® (Rogers Corporation) has been recognised as an effective material in reducing plantar pressure in patients with diabetes and peripheral neuropathy^{4,5}. A variety of Poron including a normal (Poron 4708), and a slow rebound variation (Proron 96) are available and are commonly used in clinical practice. The slow rebound Poron was claimed to result in a custom fit during each use and believed to be more effective in increasing the contact area and consequently reducing the contact pressure during use when compared to a normal Poron.

A previous study⁶ found no significant difference between the peak plantar pressure for the forefoot area among five different participants when they compared a slow rebound Poron insole against a normal Poron. However there is a paucity of studies in which the differences in contact area and contract pressure were considered between the two variations of Poron insole across the entire foot region.

While investigating the contact area and its correlation with contact pressure could shed more light on the efficacy of slow rebound Poron compared to a normal Poron, such correlation has never been investigated across different foot regions.

2. Aim:

The aim of the study was to compare the effectiveness of the normal or slow rebound Poron insole on increasing the Contact Area (CA), and reducing the Contact Pressure (CP) at different regions of the foot during walking.

3. Method:

Nine healthy individuals with body mass (76.8 ± 24.4 kg) and shoe UK size (8 ± 1) participated in this study after appropriate ethical approval was granted from the Faculty's Ethics Committee.

Flat insoles were cut from sheets of 6.35 mm thickness slow rebound and normal Poron material sheets with the same hardness (Shore O hardness = 18) (Figure 1). A 6 mm flat insole was cut from a low density EVA sheet (Shore A hardness = 25 / shore O hardness = 35) and was used to represent the control condition (Figure 1). All insoles were tested in a Plimsoll (Figure 1).

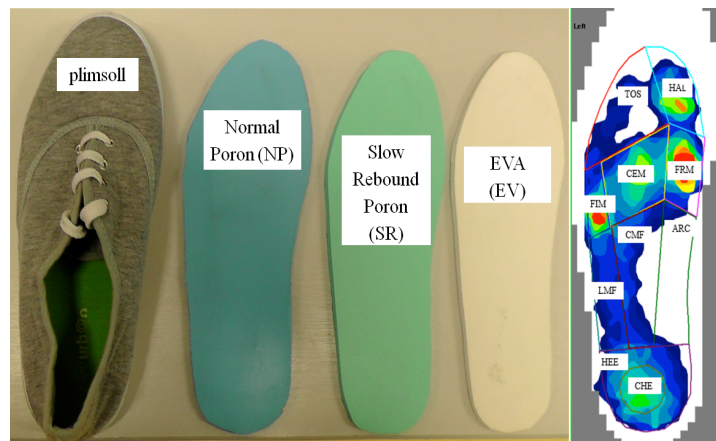


Fig.1. From left to right: Plimsoll, Normal Poron insole, Slow rebound insole, EVA insole and the plantar pressure profile together with the template created to assess the plantar pressure parameters at 10 different plantar regions of the foot.

F-scan (Tekscan Inc., USA) in-shoe pressure measurement system was used to measure the pressure between the insole and the foot, while the participant walked across a ten m walkway at their preferred speed (1.3 ± 0.2 m/s). Plantar pressure data was recorded from each foot over five consecutive stance phases during each trial. Five trials were collected for each insole condition: the EVA (control), slow Rebound Poron (SR) and the Normal Poron (NP). A template was designed to divide the foot into ten

different regions, including underneath the arch (ARC), Centre of the Midfoot (CMF), Centre of Foot (CHE), Hallux (HAL), Heel (HEE), First Metatarsophalangeal joint (FRM), Central Metatarsophalangeal joints (CEM), Fifth Metatarsophalangeal joint (FIM), and Lateral Midfoot (LMF) and Toes (TOS) (Figure 1). CA and CP were averaged across 25 trials for the left and right foot separately for each participant. A repeated measure ANOVA was performed to identify significant differences in CA and CP between the three different insole conditions (SR), (NP) and (EV) across the ten foot regions.

4. Results:

4.1. Significant differences ($P < 0.05$):

CA (SR vs NP): There was a significant increase in the CA at the ARC ($\eta^2=0.409$, $p=0.020$) and CMF ($\eta^2=0.719$, $p=0.021$) in SR compared to NP condition (Figure 2).

CA (SR vs EV): There was a significant increase in the CA at the ARC ($\eta^2=0.409$, $p=0.010$), CMF ($\eta^2=0.719$, $p=0.000$) and LMF ($\eta^2=0.592$, $p=0.000$) in NP compared to EV (Figure 2).

CA (NP vs EV): The results showed that there was a significant increase ($\eta^2=0.557$, $p=0.001$) in the CA for the entire foot in NP ($77.10 \pm 12.98 \text{ cm}^2$) compared to EV ($70.19 \pm 11.97 \text{ cm}^2$), while CMF ($\eta^2=0.719$, $p=0.000$) and LMF ($\eta^2=0.592$, $p=0.012$) had significantly higher CA in the NP compared to EV condition (Figure 2).

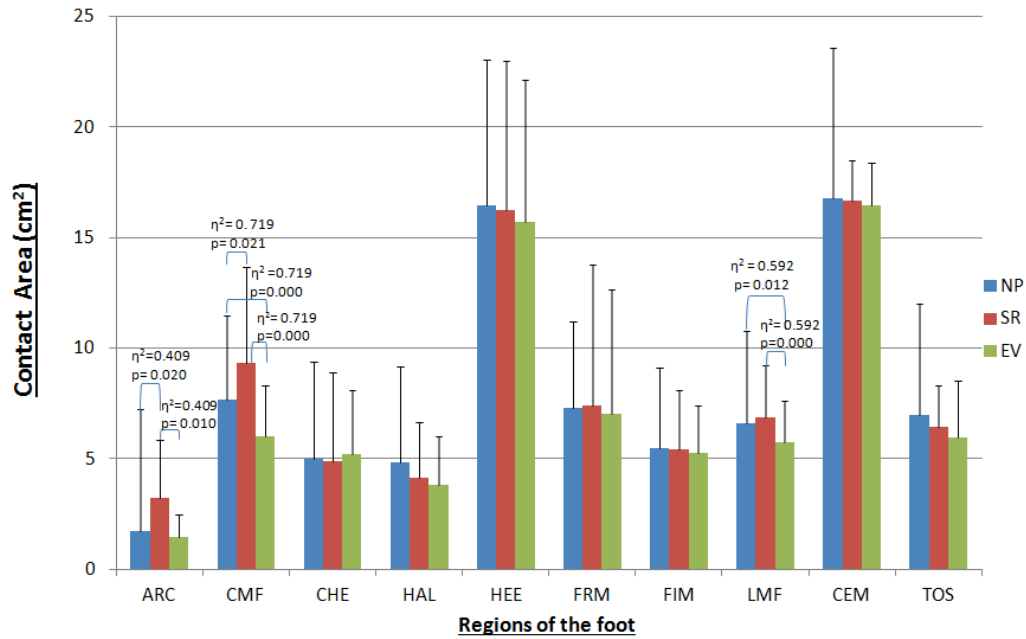


Fig.2. CA across different regions of the foot for SR, NP, and EV. Significant differences are shown with the bracket.

CP (SR vs NP): There was a significant ($\eta^2 = 0.494$, $P = 0.010$) increase in the CP at ARC region in SR compared to the NP condition (Figure 3).

CP (SR vs EV): There was a significant increase in the CP in the ARC ($\eta^2 = 0.494$, $p = 0.004$), CMF ($\eta^2 = 0.318$, $P = 0.042$) and LMF ($\eta^2 = 0.296$, $P = 0.049$) regions in SR as compared to EV condition (Figure 3).

CP (NP vs EV): There was a significant decrease ($\eta^2 = 0.386$, $p = 0.015$) in CP for the entire foot in NP (65.01 ± 27.16 kPa) compared to EV (101.16 ± 28.35 kPa) (Figure 3).

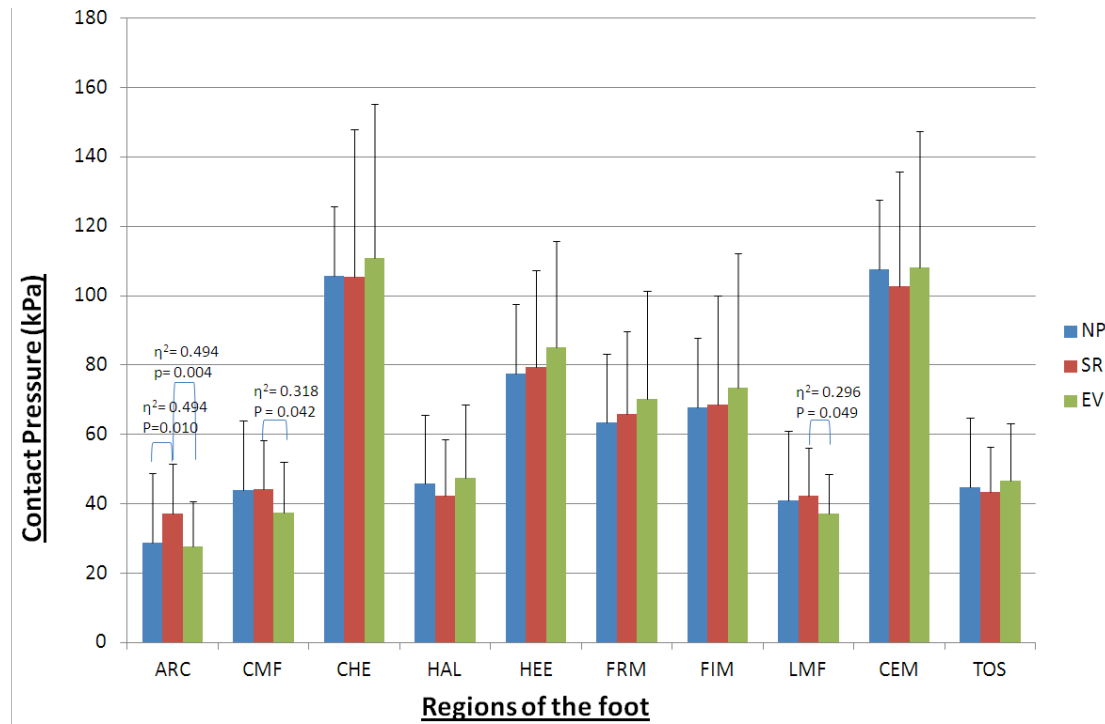


Fig.3. CP across different regions of the foot for SR, NP, and EV. Significant differences are shown with the bracket.

4.2. Significant relationships ($p < 0.05$)

NP: CA and CP were significantly correlated in NP condition at CHE ($r = 0.701$, $p = 0.001$), HAL ($r = 0.597$, $p = 0.009$), HEE ($r = 0.477$, $p = 0.045$), and FRM ($r = 0.544$, $p = 0.020$).

SR: CA and CP were significantly correlated in SR condition at CHE ($r = 0.734$, $p = 0.001$), HAL ($r = 0.623$, $p = 0.006$), HEE ($r = 0.500$, $p = 0.035$) and FIM ($r = 0.652$, $p = 0.003$).

EV: CA and CP were significantly correlated in EV condition at CHE ($r = 0.734$, $p = 0.001$), HAL ($r = 0.663$, $p = 0.006$), HEE ($r = 0.592$, $p = 0.010$) FRM ($r = 0.589$, $p = 0.010$), FIM ($r = 0.507$, $p = 0.032$) and CEM ($r = 0.469$, $p = 0.50$)

5. Discussion

Both SR and NP significantly increased CA at CMF and LMF. While SR showed significantly higher CA in CMF compared to NP and significantly higher CA at ARC compared to both NP and EV, NP showed to significantly increase CA over the entire foot compared to the EV insole condition. SR showed a significant increase in the CP in ARC area compared to both EV and NP conditions. This may have implications in cases where increasing pressure underneath the arch is not desirable. In fact NP was the only insole that increased the CA and decreased the CP on the entire foot. Tests of correlation showed significant and positive correlations between CA and both CP in the HEE, HAL, CHE region in all tested

insoles. While in NP condition there was a significant positive correlation between CO and CA at FRM, similar correlation was observed in FIM in SR condition. Also positive significant correlations were observed at FRM, FIM and CEM in EV condition. The lack of any negative correlation contradicted the expected decrease in CP as a result of the increase in CA. In fact, no negative correlation was observed between the CA and CP at different regions of the foot for any of the tested insoles. This may be attributed to the thickness of the insoles that were tested and more studies are needed in future to investigate the effect of insole thickness on the reported parameters in this study.

6. Conclusion:

The results of this study indicated that only NP insole increased the CA and decreased the CP on the entire foot compared to the EV insole. SR showed to significantly increase CA in ARC and CMF compared to NP. The expected decrease in the CP as a result of increase in CA was not observed for any region of the foot and instead CP was in positive significant correlation with CA in HEE, HAL and CHE regions in all tested insoles.

Acknowledgement:

Funding from DiabSmart project is acknowledged. DiabSmart project was funded by the European Commission, Grant Agreement Number 285985, under Industry Academia partnerships and Pathways (FP7-PEOPLE-2011-IAPP). This project has a focus on development of a new generation of Diabetic footwear using an integrated approach and Smart materials.

References:

- 1- Bus S, Ulbrecht J, Cavanagh P, Pressure relief and load redistribution by custom-made insoles in diabetic patients with neuropathy and foot deformity, *Clin. Biomech.* **19**: 629-638, 2004.
- 2- Tsung B Y S, Zhang M, Mak A F T, Wong M W N W, Effectiveness of insoles on plantar pressure redistribution, *J. Rehabil. Res. Dev.* **41**: 767-768, 2004.
- 3- Healy A, Dunning D, Chocklingam N. Effects of insole material on lowerlimb kinematics and plantar pressure during treadmill walking, *Prosthet. Orthot. Int.* **36**: 53-62, 2011.
- 4- Birke J A, Foto J G, Pfiefer L A, Effect of orthosis material hardness on walking pressure in high-risk diabetes patients, *J. Prosthet. Orthot.* **11**: 43-46, 1999.
- 5- Burns J, Begg L, Vicaretti M, Comparison of orthotic materials on foot pain, comfort and plantar pressure in the neuroischemic diabetic foot: a case report, *J. Am. Podiatr. Med. Assoc.* **98**:143-148, 2008.
- 6- Tong J W, Ng E Y, Preliminary investigation on the reduction of plantar loading pressure with different insole materials, *The Foot* **20**:1-6. 2010.

EVALUATION OF MOTOR STABILITY IN ELDERLY SUBJECTS THROUGH INSTRUMENTAL STABILITY MEASURES AND CLINICAL RATING SCALES

FEDERICO RIVA, PAOLA TAMBURINI, ALICE CONI

*Department of Electrical, Electronic and Information Engineering "Guglielmo Marconi", University of Bologna, Via Risorgimento
2,*

Bologna, 40136, Italy

f.riva@unibo.it

RITA STAGNI

*Department of Electrical, Electronic and Information Engineering "Guglielmo Marconi",
University of Bologna, Italy*

*Health Sciences and Technologies, Interdepartmental Center for Industrial Research (HST-ICIR),
Ozzano dell'Emilia, Italy*

rita.stagni@unibo.it

The understanding of locomotor stability is a critical issue in the assessment of fall risk in elderly subjects. Clinical assessment of fall risk is typically based on clinical rating scales; however, this approach heavily relies on the clinician's subjective judgment. Instrumental measures of gait variability and stability can represent a promising solution for the objective quantification of locomotor function and fall risk. The integration of the two approaches could lead to a more objective assessment of fall risk in elderly subjects, and can improve the understanding of the physiological correlate of gait stability measures. The aim of the present study was to assess the relationship between instrumental variability and stability measures based on trunk acceleration during gait and clinical rating scales in a large sample of elderly subjects.

Keywords: Gait stability; clinical scales; old adults.

1. Introduction

Falls in the elderly represent a major community and public health problem, with large clinical and economic consequences¹. The understanding of locomotor stability is a critical issue in clinical assessment procedures. Clinicians and physical therapists typically use clinical rating scales and questionnaires for fall risk assessment in the elderly population purposes. However, this approach highly relies on the clinician's subjective judgment². More reliable and objective tools for the quantification of motor function and gait stability are needed. Instrumental measurements have been shown to represent a valid and objective complement to clinical rating scales in balance, gait and metabolic consumption assessment of both healthy and pathologic subjects³⁻⁶. In particular, instrumental variability and stability measurements of stride time and trunk accelerations during gait recently resulted promising in the assessment of gait stability and fall risk in healthy elderly subjects⁷. For an effective exploitation in clinical practice, the association between stability measures and clinical scales has to be assessed, in order to understand the relationship between the two approaches. Moreover, the administration of both clinical scales and instrumental measurements can

help better define the physiological correlate of stability measures, which is generally still not known. Instrumental measurements could hence lead to a more rapid and reliable quantification of the features quantified by clinical scales, avoiding inter-operator differences. The aim of the present study is the assessment of the relationship between instrumental variability and stability measures based on trunk accelerations during gait and some of widely used clinical rating scales.

2. Materials & Methods

Seventy community dwelling old adults (35 males and 35 females, 76 ± 7 years, 76 ± 13 kg, 168 ± 9 cm) participated in the study. Subjects' recruitment was conducted in collaboration with Cesena Municipality, involving five old adults community centres. Four clinical rating scales were administered to subjects, in order to obtain a description of their motor function and independence in daily living. Barthel Index (BI), Cumulative Illness Rating Scale (CIRS, composed of Severity Index, SI, and Co-morbidity Index, CI) and Mini-BESTest (MBT) were administered to subjects by the same operators, avoiding possible bias introduced by inter-operator differences. Due to time/location constraints, MBT was only administered to 39 subjects (19 males and 20 females, 76 ± 6 years, 77 ± 12 kg, 168 ± 8 cm). Subjects also performed an instrumented overground gait task (on a 100 m long road) wearing an IMU (Opal, APDM, USA) located on the trunk, at the height of the fifth lumbar vertebra. Eleven gait variability and stability measures, namely Standard Deviation (SD), Coefficient of Variation (CV), Non-stationary index (NI), Inconsistency of Variance (IV), Poincaré Plots (PSD1/PSD2), Maximum Floquet Multipliers (maxFM), short/long-term Lyapunov exponents (sLE/lLE), Harmonic Ratio (HR), Index of Harmonicity (IH), Multiscale Entropy (MSE) and Recurrence Quantification Analysis (RQA), were calculated on stride time and trunk acceleration data during gait. The two latter measures produce 6 and 5 sub-measures respectively, based on the time scale in MSE or based on the feature of the recurrence plot that are analyzed in RQA, namely recurrence rate (rr), determinism (det), average length of diagonal lines (avg), maximum length of diagonal lines (max), divergence (div). Each measure was calculated for anterior-posterior (AP), medio-lateral (ML) and vertical (V) acceleration directions. In order to assess the correlation between clinical parameters and stability measures, log transformed measures were used as inputs for linear regression models (SPSS Statistics 20.0, IBM, Armonk, NY, USA).

3. Results

Variability measures (SD, CV, PSD1 and PSD2) showed negative correlation with BI and MBT. The only stability measure that correlated (positively) with MBT and BI was IH in the ML direction. CIRS (SI and CI) correlated with MSE (ML and V directions), RQA (V direction), maxFM and lLE. NI, IV, HR and sLE showed no significant correlation with clinical rating scale outcomes. Correlation results are shown in Table 1. For the sake of brevity, only significant correlation values are shown.

Table 1 Correlation results (p-value < 0.05) between variability/stability measures and clinical rating scales

	<i>BI</i>	<i>MBT</i>	<i>SI</i>	<i>CI</i>
SD	0,014	0,034		
CV	0,014			
PSD1	0,018	0,036		
PSD2	0,010	0,030		
MSE ML $\tau = 3$			0,026	
MSE ML $\tau = 4$			0,020	
MSE ML $\tau = 5$			0,019	
MSE ML $\tau = 6$			0,010	
MSE V $\tau = 1$			0,047	
MSE V $\tau = 2$			0,046	
MSE V $\tau = 4$				0,047
MSE V $\tau = 5$				0,044
MSE V $\tau = 6$				0,025
RQA V rr			0,023	0,011
RQA V max				0,026
iHML	0,039	0,014		
maxFM tot			0,006	0,015
maxFM AP			0,002	0,023
maxFM ML			0,027	0,007
maxFM V			0,005	
ILE tot			0,021	
ILE ML			0,019	
ILE V			0,008	

4. Discussion

BI and MBT negatively correlated with stride time variability measures, meaning that a relationship exists between the deterioration of the overall motor functionality and the increase in stride time variability. BI and MBT were also found to be linked to the harmonicity of acceleration signal in the ML direction, confirming the importance of ML trunk oscillations during gait for functionality assessment. CIRS correlated with stability measures, in particular with MSE in ML and V directions, suggesting a link between cumulative illness and gait stability in elderly subjects. Moreover, MSE was previously found to be linked to fall history in elderly subjects, and should hence to be taken into consideration for gait stability assessment.

In conclusion, gait variability and stability measures showed promising correlation with clinical rating scales in the elderly population, and could be considered for complementing the standard clinical scores in the assessment of fall risk. A more reliable quantification of locomotor features could be obtained from instrumental measurements, allowing to avoid inter-operator differences.

References

1. Fuller GF, Falls in the elderly, *Am Fam Physician* 61(7), 2159–2168, 2173–2174, 2000.
2. Hamacher D, Singh N et al., Kinematic measures for assessing gait stability in elderly individuals: a systematic review, *J R Soc Interface* 8(65), 1682-1698, 2011.
3. Sawacha Z, Carraro E et al., Relationship between clinical and instrumental balance assessments in chronic post-stroke hemiparesis subjects, *J Neuroeng Rehabil* 10:95, 2013.
4. O’Sullivan JD, Said CM et al. Gait analysis in patients with Parkinson's disease and motor fluctuations: Influence of levodopa and comparison with other measures of motor function, *Mov Disord* 13(6):900-906, 1998.
5. Gillain S, Warzee E et al. The value of instrumental gait analysis in elderly healthy, MCI or Alzheimer's disease subjects and a comparison with other clinical tests used in single and dual-task conditions *Ann Phys Rehabil Med* 52(6):453-474, 2009.
6. Frazzitta G, Maestri R et al., Rehabilitation in Parkinson's disease: assessing the outcome using objective metabolic measurements, *Mov Disord* 25(5):609-614, 2010.
7. Riva F, Toebes M et al., Estimating fall risk with inertial sensors using gait stability measures that do not require step detection, *Gait Posture* 38(2), 170-174, 2013.

EVALUATION OF MOTOR STABILITY IN ELDERLY SUBJECTS THROUGH INSTRUMENTAL STABILITY MEASURES AND CLINICAL RATING SCALES

FEDERICO RIVA, PAOLA TAMBURINI, ALICE CONI

*Department of Electrical, Electronic and Information Engineering "Guglielmo Marconi", University of Bologna, Via Risorgimento
2,*

Bologna, 40136, Italy

f.riva@unibo.it

RITA STAGNI

*Department of Electrical, Electronic and Information Engineering "Guglielmo Marconi",
University of Bologna, Italy*

*Health Sciences and Technologies, Interdepartmental Center for Industrial Research (HST-ICIR),
Ozzano dell'Emilia, Italy*

rita.stagni@unibo.it

The understanding of locomotor stability is a critical issue in the assessment of fall risk in elderly subjects. Clinical assessment of fall risk is typically based on clinical rating scales; however, this approach heavily relies on the clinician's subjective judgment. Instrumental measures of gait variability and stability can represent a promising solution for the objective quantification of locomotor function and fall risk. The integration of the two approaches could lead to a more objective assessment of fall risk in elderly subjects, and can improve the understanding of the physiological correlate of gait stability measures. The aim of the present study was to assess the relationship between instrumental variability and stability measures based on trunk acceleration during gait and clinical rating scales in a large sample of elderly subjects.

Keywords: Gait stability; clinical scales; old adults.

1. Introduction

Falls in the elderly represent a major community and public health problem, with large clinical and economic consequences¹. The understanding of locomotor stability is a critical issue in clinical assessment procedures. Clinicians and physical therapists typically use clinical rating scales and questionnaires for fall risk assessment in the elderly population purposes. However, this approach highly relies on the clinician's subjective judgment². More reliable and objective tools for the quantification of motor function and gait stability are needed. Instrumental measurements have been shown to represent a valid and objective complement to clinical rating scales in balance, gait and metabolic consumption assessment of both healthy and pathologic subjects³⁻⁶. In particular, instrumental variability and stability measurements of stride time and trunk accelerations during gait recently resulted promising in the assessment of gait stability and fall risk in healthy elderly subjects⁷. For an effective exploitation in clinical practice, the association between stability measures and clinical scales has to be assessed, in order to understand the relationship between the two approaches. Moreover, the administration of both clinical scales and instrumental measurements can

help better define the physiological correlate of stability measures, which is generally still not known. Instrumental measurements could hence lead to a more rapid and reliable quantification of the features quantified by clinical scales, avoiding inter-operator differences. The aim of the present study is the assessment of the relationship between instrumental variability and stability measures based on trunk accelerations during gait and some of widely used clinical rating scales.

2. Materials & Methods

Seventy community dwelling old adults (35 males and 35 females, 76 ± 7 years, 76 ± 13 kg, 168 ± 9 cm) participated in the study. Subjects' recruitment was conducted in collaboration with Cesena Municipality, involving five old adults community centres. Four clinical rating scales were administered to subjects, in order to obtain a description of their motor function and independence in daily living. Barthel Index (BI), Cumulative Illness Rating Scale (CIRS, composed of Severity Index, SI, and Co-morbidity Index, CI) and Mini-BESTest (MBT) were administered to subjects by the same operators, avoiding possible bias introduced by inter-operator differences. Due to time/location constraints, MBT was only administered to 39 subjects (19 males and 20 females, 76 ± 6 years, 77 ± 12 kg, 168 ± 8 cm). Subjects also performed an instrumented overground gait task (on a 100 m long road) wearing an IMU (Opal, APDM, USA) located on the trunk, at the height of the fifth lumbar vertebra. Eleven gait variability and stability measures, namely Standard Deviation (SD), Coefficient of Variation (CV), Non-stationary index (NI), Inconsistency of Variance (IV), Poincaré Plots (PSD1/PSD2), Maximum Floquet Multipliers (maxFM), short/long-term Lyapunov exponents (sLE/lLE), Harmonic Ratio (HR), Index of Harmonicity (IH), Multiscale Entropy (MSE) and Recurrence Quantification Analysis (RQA), were calculated on stride time and trunk acceleration data during gait. The two latter measures produce 6 and 5 sub-measures respectively, based on the time scale in MSE or based on the feature of the recurrence plot that are analyzed in RQA, namely recurrence rate (rr), determinism (det), average length of diagonal lines (avg), maximum length of diagonal lines (max), divergence (div). Each measure was calculated for anterior-posterior (AP), medio-lateral (ML) and vertical (V) acceleration directions. In order to assess the correlation between clinical parameters and stability measures, log transformed measures were used as inputs for linear regression models (SPSS Statistics 20.0, IBM, Armonk, NY, USA).

3. Results

Variability measures (SD, CV, PSD1 and PSD2) showed negative correlation with BI and MBT. The only stability measure that correlated (positively) with MBT and BI was IH in the ML direction. CIRS (SI and CI) correlated with MSE (ML and V directions), RQA (V direction), maxFM and lLE. NI, IV, HR and sLE showed no significant correlation with clinical rating scale outcomes. Correlation results are shown in Table 1. For the sake of brevity, only significant correlation values are shown.

Table 1 Correlation results (p-value < 0.05) between variability/stability measures and clinical rating scales

	<i>BI</i>	<i>MBT</i>	<i>SI</i>	<i>CI</i>
SD	0,014	0,034		
CV	0,014			
PSD1	0,018	0,036		
PSD2	0,010	0,030		
MSE ML $\tau = 3$			0,026	
MSE ML $\tau = 4$			0,020	
MSE ML $\tau = 5$			0,019	
MSE ML $\tau = 6$			0,010	
MSE V $\tau = 1$			0,047	
MSE V $\tau = 2$			0,046	
MSE V $\tau = 4$				0,047
MSE V $\tau = 5$				0,044
MSE V $\tau = 6$				0,025
RQA V rr			0,023	0,011
RQA V max				0,026
iHML	0,039	0,014		
maxFM tot			0,006	0,015
maxFM AP			0,002	0,023
maxFM ML			0,027	0,007
maxFM V			0,005	
ILE tot			0,021	
ILE ML			0,019	
ILE V			0,008	

4. Discussion

BI and MBT negatively correlated with stride time variability measures, meaning that a relationship exists between the deterioration of the overall motor functionality and the increase in stride time variability. BI and MBT were also found to be linked to the harmonicity of acceleration signal in the ML direction, confirming the importance of ML trunk oscillations during gait for functionality assessment. CIRS correlated with stability measures, in particular with MSE in ML and V directions, suggesting a link between cumulative illness and gait stability in elderly subjects. Moreover, MSE was previously found to be linked to fall history in elderly subjects, and should hence to be taken into consideration for gait stability assessment.

In conclusion, gait variability and stability measures showed promising correlation with clinical rating scales in the elderly population, and could be considered for complementing the standard clinical scores in the assessment of fall risk. A more reliable quantification of locomotor features could be obtained from instrumental measurements, allowing to avoid inter-operator differences.

References

1. Fuller GF, Falls in the elderly, *Am Fam Physician* 61(7), 2159–2168, 2173–2174, 2000.
2. Hamacher D, Singh N et al., Kinematic measures for assessing gait stability in elderly individuals: a systematic review, *J R Soc Interface* 8(65), 1682-1698, 2011.
3. Sawacha Z, Carraro E et al., Relationship between clinical and instrumental balance assessments in chronic post-stroke hemiparesis subjects, *J Neuroeng Rehabil* 10:95, 2013.
4. O’Sullivan JD, Said CM et al. Gait analysis in patients with Parkinson's disease and motor fluctuations: Influence of levodopa and comparison with other measures of motor function, *Mov Disord* 13(6):900-906, 1998.
5. Gillain S, Warzee E et al. The value of instrumental gait analysis in elderly healthy, MCI or Alzheimer's disease subjects and a comparison with other clinical tests used in single and dual-task conditions *Ann Phys Rehabil Med* 52(6):453-474, 2009.
6. Frazzitta G, Maestri R et al., Rehabilitation in Parkinson's disease: assessing the outcome using objective metabolic measurements, *Mov Disord* 25(5):609-614, 2010.
7. Riva F, Toebes M et al., Estimating fall risk with inertial sensors using gait stability measures that do not require step detection, *Gait Posture* 38(2), 170-174, 2013.

DESIGN WITH FINITE ELEMENT METHOD (FEM) OF A MODULAR SMALL DIMENSIONS FORCE PLATFORM FOR GAIT ANALYSIS

PAOLA TAMBURINI

*Department of Electrical, Electronic and Information Engineering "Guglielmo Marconi", University of Bologna,
Italy
paola.tamburini3@unibo.it*

RITA STAGNI

*Department of Electrical, Electronic and Information Engineering "Guglielmo Marconi", University of Bologna, Italy
Health Sciences and Technologies, Interdepartmental Center for Industrial Research (HST-ICIR),
Ozzano dell'Emilia, Italy
rita.stagni@unibo.it*

ANGELO CAPPELLO

*Department of Electrical, Electronic and Information Engineering "Guglielmo Marconi", University of Bologna,
Italy
Angelo.cappello@unibo.it*

The gait analysis of subjects with short and non-uniform gait is difficult using the common commercial force platforms. The present work consists in the design, based on finite element method (FEM) analysis, of a force platform of small dimensions (0.40x0.40 m) considering static and dynamic simulation of its behaviour. The aim of this project is to improve, with a simple and low cost structure, the instrumentation available for the gait analysis of children and neurologic patients. The applicability of gait analysis to children and neurologic patients, improved the flexibility of force platforms without losing the performance provided by traditional force platforms (e.g. for postural analysis)

Keywords: gait analysis, force plate, dynamometry, FEM analysis

1. Introduction

Gait analysis of subjects with short and non-uniform gait, typical children, children with cerebral palsy, elderly and stroke patients, can result critical in terms of ground reaction force (GRF) quantification with traditional force platforms.

The standard *de facto* of commercial force platforms dimension (0.60x0.40 m) can determine problems resulting from the double contact of the foot on the same platform that does not allow the identification of the GRF under each foot. The current proposal of the companies is the use of standard force platforms arranged so as to achieve a sensitive corridor. This solution allows the acquisition of several steps, but maintaining the size of the force platform does not solve the problem of double contact.

The aim of this work is the design, by finite element method (FEM), of a small modular force platform (0.40x0.40 m) to solve the problem of double contact, maintaining the reference performance of commercial larger platforms. The small dimensions require the use of large number of platforms in order to

instrument a corridor. However, the simplicity of the design and materials used allows the use of multiple force platforms at low cost. Electronics dedicated to the acquisition of the output signal is not required because a commercial evaluation board can be exploited, that is able to independently manage the output of the strain gauges. This solution simplifies the realization of instrumented corridors.

2. Materials & Methods

The design of the proposed small modular force platform [1] was performed aiming to obtaining a performance comparable to that of commercial force platforms.

For modularity purpose and to allow the differentiate short steps, the total dimension of the force platform is: 0.40x0.40x0.105 m.

- 1 aluminium top 0.40x0.40x0.02 m
- 4 aluminium hollow cylindrical posts with inner radius 0.013 m and outer radius 0.011 m and height 0.07 m
- 1 steel base 0.40x0.40x0.015 m.

The minimum number of mono-axial strain gauges is used for deformation sensing: six for each post, longitudinally arranged. The total number of strain gauges used is twenty-four per platform.

The output of each strain gauge is directly provided as input to a commercial evaluation board (e.g. Texas Instruments DDC264 DDC1128). This removes the need for *ad hoc* electronics for signal acquisition. In addition, the commercial evaluation board manages current signals, solving the problem of signal attenuation introduced by the cable length that is present when using voltage signals.

COMSOL Multiphysics was used for implementing the FEM.

For a six component force platform, the output vector provides the three components of the force (F_x , F_y , F_z) applied to the force platform and the three components of the moment (M_x , M_y , M_z) of the force in the orthogonal directions of space (x and y on, and z orthogonal to the force plate plane). The coordinates of the point of application of the force on the platform (x_p , y_p , z_p) results from the output components according to the equations:

$$\begin{aligned} M_x &= F_z y_p \\ M_y &= -F_z x_p \\ M_z &= F_y x_p - F_x y_p + M_T \approx F_y x_p - F_x y_p \end{aligned}$$

The free torque M_T is neglected because the Young modulus of the aluminium and the foot soft tissue are very different.

Static analysis was perform to estimate the platform calibration matrix based on least square fitting. A uniformly distributed load was applied to a surface of radius $R_{Area} = 0.05$ m and 576 simulations were implemented considering applied forces varying between -200 N and 200 N for F_x and F_y and between -2000 N and -200 N for F_z , in 9 different points of application. The coordinates (x_{cop} , y_{cop}) of centre of pressure (COP) of distributed load were all possible combination of $x_{cop} = [0.05, 0.20, 0.35]$ m, and $y_{cop} =$

[0.05, 0.20, 0.35] m; which were used in order to cover most of the surface of the platform. The large number of testing conditions used for the estimation of the calibration matrix was chosen in order to cover the largest number of possible operative conditions.

Eighty-four additional simulations were performed to test the calibration matrix and quantify the error that the system commits in the estimation of applied loads and moments. For these testing simulations, loads and corresponding application points were chosen in order to test the calibration matrix with settings not exploited in the estimation of the calibration matrix.

Dynamic analysis was implemented with the default COMSOL eigenfrequencies solver, allowing the estimation of the resonance frequency of the force platform.

3. Results

The median error made in the determination of the forces is between -0.0378% and 0.0041%. The maximum error made in the determination of the forces ranges from a minimum of 0.0325% to a maximum of 0.8075 %. These results are valid regardless of the value of the applied load. The median error made in the determination of the moments is between 0.0028 % and 0.0372 %. The maximum error made in the determination of the moments is in M_x 0.1112 % at -45 Nm, in M_y 0.2401 % at 15 Nm and in M_z 3.435 % at 10 Nm. Choosing a reference value exciding 20 Nm, the maximum error committed in the determination of M_x does not change. For M_y is 0.1540 % and for M_z is 0.6090 %.

The median and the maximum error in the determination of the forces and moments, based on the calculated calibration matrix, resulting from the 84 additional simulations are illustrated in Tables 1 and 2.

The resonance frequency resulting from the dynamic analysis was 350 Hz.

Table 1 Median and Maximum error in the determination of the Forces

<i>Component of the Force</i>	<i>Median Error %</i>	<i>Maximum Error %</i>
F_x	-0.0378	0.8075
F_y	-0.0022	0.2137
F_z	0.0041	0.0325

Table 2 Median and Meximun error in the determination of the Moments

<i>Component of the Moment</i>	<i>Median Error %</i>	<i>Maximum Error % Reference Value (Nm)</i>
M_x	0.0070	0.112 - 45
M_y	0.0028	0.2401 15
M_z	0.0372	3.435 10

4. Discussion

The gait analysis of subjects with short and non-uniform gait is difficult using the common commercial force platforms. The present work consists in the design of a force platform of small dimensions to improve, with a simple and low cost structure, the instrumentation available for the gait analysis of children and neurologic patients.

The range of the forces used, and the resonance frequency are comparable to those of commercial platforms [2].

In order to obtain a proper functioning of the device, once built, it will be necessary to calibrate *in situ*. This will help to compensate for the error introduced by non-alignment in the positioning of the strain gauges, mechanical crosstalk and more [3 4].

The low cost of mechanical structure and the use of commercial evaluation board encourages the creation of multiple platforms. An *ad hoc* support base is provided in such a way as to allow the isolation of the structure and then a proper measure. In addition, the support base allows solving many of the critical issues related to the installation.

The starter kit, which consists of two platforms, allows the standard balance analysis achieved with commercial platforms. Furthermore it allows us to distinguish the GRF of each foot and through integration techniques we are able to estimate a global GRF.

References

1. Schmiedmayer H-B, Kastner J, Parameters influencing the accuracy of the point of force application determined with piezoelectric force plates, JBIOMECH 32:1237-1242, 1999. Sawacha Z, Carraro E et al., Relationship between clinical and instrumental balance assessments in chronic post-stroke hemiparesis subjects, *J Neuroeng Rehabil* 10:95, 2013.
2. www.bertec.com.
3. Cedraro, A. Cappello, L. Chiari, A portable system for in-situ re-calibration of force platforms: experimental validation, GAIT&POSTURE, 29(3):449-453, 2009.,
4. Cappello A, Bagalà F, Cedraro A, Chiari L, Non-linear re-calibration of force platforms GAIT&POSTURE 33(4):724-726, 2011.

SENSITIVITY ANALYSIS OF SIMULATED ANKLE JOINT MOTION TO THE VARIATION OF THE PIVOT-POINT POSITION

NICOLA SANCISI, FABRIZIO NARDINI

*DIN-Department of Industrial Engineering, University of Bologna, Viale del Risorgimento 2, 40136
Bologna, Italy
nicola.sancisi@unibo.it, fabrizio.nardini2@unibo.it*

VINCENZO PARENTI CASTELLI

*DIN-Department of Industrial Engineering, University of Bologna, Italy
CIRI Health Sciences & Technologies, Ozzano dell'Emilia, Bologna, Italy
vincenzo.parenti@unibo.it*

CLAUDIO BELVEDERE, ALBERTO LEARDINI

*Movement Analysis Laboratory, Istituto Ortopedico Rizzoli, Bologna, Italy
claudio.belvedere@ior.it, leardini@ior.it*

Recent studies proved that the ankle joint motion is nearly spherical and can be accurately modeled by a single degree of freedom spatial spherical mechanism. In this study, the global optimal pivot-point position, i.e. the center of this spherical motion, is obtained for two specimens, and the relevant sensitivity of the ankle motion to the pivot-point position is analyzed.

Keywords: Ankle joint; Passive motion; Spatial spherical mechanism; Pivot point; Sensitivity.

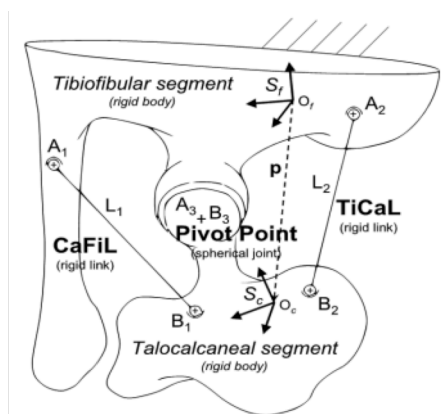
1. Introduction

In virtually unloaded conditions, the tibiotalar (ankle) joint behaves as a single degree-of-freedom (1DoF) system.^{1,2} In these conditions, throughout the joint flexion arc, fibers within the ligaments remain nearly isometric and articular surfaces are nearly rigid. Relevant theoretical models have shown that the ligaments and the articular surfaces act together as mechanisms to control the passive joint kinematics.³⁻⁷ In particular, isometric fibers were identified within the calcaneal-fibular and tibio-calcaneal ligaments, rigid contacts were associated to the articular surfaces between the tibio-fibular mortise and the talus.⁶

Further kinematic measurements also revealed that a nearly-spherical motion is experienced by this joint: a point of the joint (i.e. the pivot point) was identified where the relative motion between the tibia and talus was almost null over the full flexion arc.⁷ Based on this experimental evidence, a Spherical Parallel Mechanisms (SPM) was defined: the two isometric ligaments were modeled as binary links of constant length, and the tibia and talus were also connected by a spherical pair centered at the pivot point, in order to approximate the nearly spherical motion observed for the ankle joint (Figure 1).^{4,5,7} The model is therefore a 1DoF-SPM, assumed kinematically equivalent to the original joint.

In this most recent study (Ref. 7), the SPM model geometry was identified for 9 different ankle specimens, proving a high accuracy for the passive motion modelling in each of these. These results confirmed also that the ankle joint passive motion is actually spherical-like, and the coordinates of the pivot point were obtained for each specimen. This pivot-point position, in particular, is important both for the design of new ankle joint devices and for the improvement of current full lower limb models,⁸ where the ankle is often approximated by a spherical joint. However, due to the scopes of the previous study (Ref. 7), the optimal pivot-point position was determined by limiting the search domain to be within a preliminary estimate based on experimental data. Moreover, no analyses were performed on the sensitivity of the simulated ankle motion to the variation of the pivot-point position.

2. Methods



An iterative procedure⁹ is used to optimize the geometry of the 1DoF-SPM model. Sixteen parameters define the model: the coordinates of A_j and B_j , $j = 1, 2, 3$, in the tibiofibular (S_f) and talocalcaneal (S_c) reference systems⁷ respectively (14 parameters), and the length of the isometric fibers of the ligaments (2 parameters). The procedure starts from a first guess geometry gathered from the experimental sessions.

where the ankle passive motion and articular geometry (including the ligament attachment areas) were measured. These parameters are then optimized via an optimization strategy,⁷ by reducing to a minimum the differences between the experimental and model motion. In order to determine the global optimal pivot-point position for the specimens, no constraints are imposed on the final position of A_3 and B_3 , whereas the distance between the experimental and the final position of the points A_j and B_j , $j = 1, 2$ is constrained to be smaller than 4 mm.

The sensitivity analysis is then performed starting from the obtained geometry of the 1DoF-SPM for the two specimens. A cubic volume with a side of 6 mm centered at the determined optimal pivot point is explored, by creating a grid of points with one millimeter steps from one point to another in all directions. A similar optimization procedure is then carried out for every point of the grid, by imposing the pivot-point position in $S_f(A_3)$. Therefore only the remaining 13 model parameters out of the 16 were optimized.

3. Results and discussions

The position of the global optimal pivot point for the two specimens is reported in Table 1 together with the position of the constrained pivot point previously obtained⁷ and the difference between the two. The x, y coordinates are almost the same, while z, the medio/lateral position, changed significantly.

The results from the sensitivity analysis are shown in Fig. 2, where the contour lines of the error on parallel sagittal planes -3, 0, +3 mm respectively distant from the global optimal pivot point along the medio/lateral axis are represented. The present analysis shows a low sensitivity of the joint motion when moving the pivot point along the medio/lateral axis. On each sagittal plane, the error shows an ellipse-like trend, with a higher sensitivity along the distal/proximal direction. This information can be useful for pre-surgical planning, prosthetic design and multi-body modelling of the lower limb.

Table 1. For the two specimens, the global pivot point (PP_glb), the constrained pivot point (PP_const) and the difference between the two (PP_diff). The x, y, z axes are the posterior(-)/anterior(+), the distal(-)/proximal(+) and the medio(-)/lateral(+) axes respectively, the origin is in the mid-point between the malleoli.

Specimens	#2			#5		
	x (mm)	y (mm)	z (mm)	x (mm)	y (mm)	z (mm)
PP_glb	3.75	2.02	-9.5	3.15	-2.72	-9.24
PP_const	3.35	2.82	-13.33	4.21	-4.13	1.88
PP_diff	0.39	-0.79	3.83	-0.96	1.41	11.12

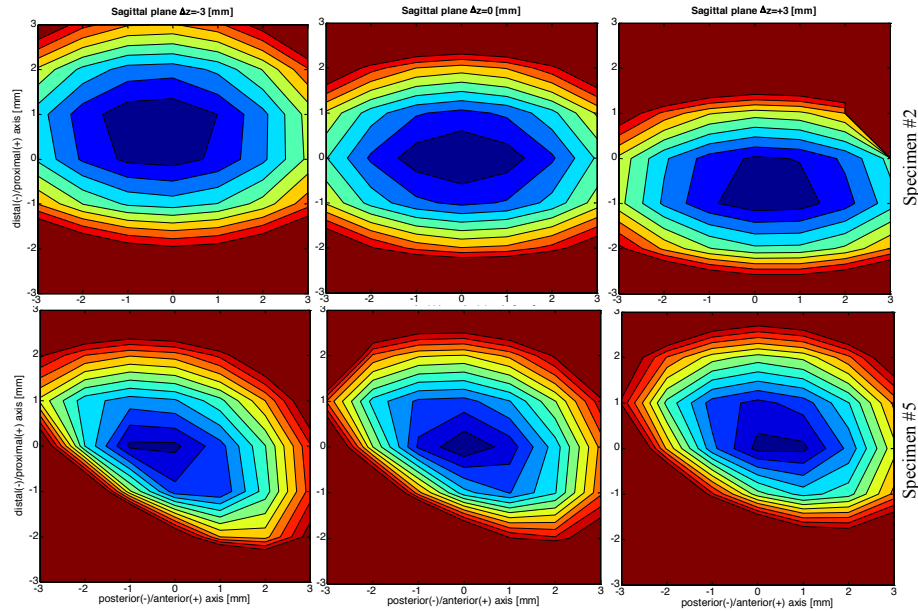


Figure 1. Motion errors on three parallel sagittal planes for Specimen #2 (top row) and #5 (bottom row). Coordinates are measured from the global optimal pivot point in S_F . Dark red represents errors greater than the double of the dark blue.

References

1. O'Connor JJ, Lu TW, Wilson DR, Feikes J, Leardini A, Review: Diarthrodial joints - Kinematic pairs, mechanisms or flexible structures?, *Comput Methods Biomed Engin.* 1(2): 123-150, 1998.
2. Leardini A, O'Connor JJ, Catani F, Giannini S, Kinematics of the human ankle complex in passive flexion: a single degree of freedom system, *J Biomech* 32(2):111-118, 1999.
3. Leardini A, O'Connor JJ, Catani F, Giannini S, A geometric model of the human ankle joint, *J Biomech* 32(6):585-591, 1999.
4. Di Gregorio R, Parenti-Castelli V, O'Connor JJ, Leardini A, Mathematical models of passive motion at the human ankle joint by equivalent spatial parallel mechanisms, *Med. Biol. Eng. Comput.* 45(3):305-313, 2007.
5. Franci R, Parenti-Castelli V, A one-degree-of-freedom spherical wrist for the modelling of passive motion of the human ankle joint. In: *Kecskemethy A(Ed) Proceedings of IAK 2008, Conference on interdisciplinary applications of kinematics*, Lima, Peru, pp. 1-13, 2008.
6. Franci R, Parenti-Castelli V, Belvedere C, Leardini A, A new one-DOF fully parallel mechanism for modelling passive motion at the human tibiotalar joint, *J Biomech* 42(10): 1403-1408, 2009.
7. Sancisi N, Baldisserri B, Parenti-Castelli V, Belvedere C, Leardini A, One-degree-of-freedom spherical model for the passive motion of the human ankle joint, *Med Biol Eng Comput* 52:363-373, 2014.
8. Dumas R, Moissenet F, Gasparutto X, Chèze L, Influence of joint models on lower-limb musculo-tendon forces and three-dimensional joint reaction forces during gait, *Proc Inst Mech Eng Part H* 226(2):146-160, 2012.
9. Sancisi N, Parenti-Castelli V, A1-dof parallel spherical wrist for the modelling of the knee passive motion, *Mech Mach Theory* 45(4):658-665, 2010.

RECONCILING BAREFOOT AND SHOD CONDITIONS IN THE OXFORD FOOT MODEL FOR PLANTAR PRESSURE MEASUREMENT

A. D. JAITMAN, M. CHAPPELL, N. EVANS
School of Engineering, University of Warwick
Coventry, CV4 7AL, UK
A.D.Jaitman@warwick.ac.uk

The foot plays an important role as it is the only connection that the human body has with the floor when walking, running, etc. The two main techniques commonly used to study the lower limb in biomechanics are Gait Analysis and Plantar Pressure measurements. However, they require different settings: one requires barefoot experimentation and the other one requires subject to be shod. The method proposed in this paper solves this problem by designing shoes that can mimic both conditions. This allows the analysis of both approaches simultaneously and therefore provides valuable inputs for a well validated model of the foot.

1. Introduction

The difficulties arising in foot modelling are inherent in the complex composition of the foot, which is commonly divided into three different segments according to their function: rear-, mid- and forefoot¹. Most foot models developed during recent years simplify the foot geometry, structure and materials². Two well validated techniques for analysing foot biomechanics are Gait Analysis and Plantar Pressure measurement.

Many previous experiments on foot modelling could not be truly validated due to their lack of precision in terms of marker placement during gait analysis and their inability to replicate the experiment under the exact same conditions^{3,4}. All of the studies referred to the motion within the foot and its kinematics, but none of them are conclusive regarding the dynamics. These problems are mainly due to the fact that not all of the available methodologies can be used simultaneously. Given that the two studied methodologies require different conditions, it is fundamental to find a way to perform both experiments at the same time, obtaining accurate and reliable outputs. In this paper a way to reconcile both methods and compare their results in the framework of the Oxford Foot Model⁵ is explored.

In terms of the techniques employed, Gait is defined as the manner of walking⁶ and its study allows analysis of movement patterns, kinematics and kinetics, as well as the forces that are produced by movements and reactions with a force plate commonly used in such experiments⁷. This analysis has been employed in order to study the lower limb, through the implementation of a multi-segment foot model: the Oxford Foot Model.

Foot Plantar Pressure is the pressure acting between the foot and the support surface during these activities. A force plate in the Gait Laboratory permits calculation of the total force applied by the foot to the ground and a Tekscan plantar pressure insole system allows the measurement of the force distribution over the subject's foot.

Not only are we interested in the forces between the foot and the ground, but also in the internal forces involving soft tissue and joints. The response to a force will be determined by the plantar

pressure. Therefore, plantar pressure is a critical issue when examining the foot.

2. Methods

2.1. Methodology

The paper reports results on the reliability of the Oxford Foot Model under barefoot and shod conditions, as well as repeatability intra-person and inter-session. The method proposed introduces the use of specially designed shoes to enable simultaneous gait and plantar pressure analysis.

Experimental analysis was carried out in the School of Engineering's Gait Laboratory and surroundings. The laboratory consists of 12 infrared (IR) cameras, 1 force plate and 2 video cameras (digital). The cluster of IR cameras is able to capture the movement of reflective markers attached to a subject, as long as they are seen by at least three cameras. After the input of certain physical subject specific parameters to the system, a total of 43 markers are placed on the subject's lower limb in line with the Oxford Foot Model guidelines. The plantar pressure system, on the other hand, requires only a step calibration.

A repeatability analysis was first performed in order to understand which sensitivity to consider for the rest of the experiments. The same subject was marked up across four successive days and performed a dynamic trial. Results of the assessments were compared to study the median and the standard deviation for the angles studied.

The experiment consisted of three sessions of 30 trials each. One third of these were in a barefoot condition, another third in a shod condition and the last 30 trials wearing the designed shoes. The last two sets of trials included analysis of the plantar pressure using Tekscan insoles.

Static and dynamic trials were conducted. First a static trial was performed and used to scale the model for the participating subject. The participants were asked to stand on the force plate and remain still for a few seconds. Afterwards, the subjects were asked to walk at their own pace, stepping first with the right foot on the force plate, and then with the left foot. Each session consisted of a total of 15 trials for each leg. All the acquired information was processed using Vicon Nexus to gain a deeper knowledge about different joint angles. The evaluated angles were:

- FF/HFA: Forefoot with respect to hind foot.
- FF/TBA: Forefoot with respect to tibia.
- Hallux with respect to forefoot.

The analysis was performed over two gait cycle events: Foot Strike and Toe Off (first and fifth events in figure 1).

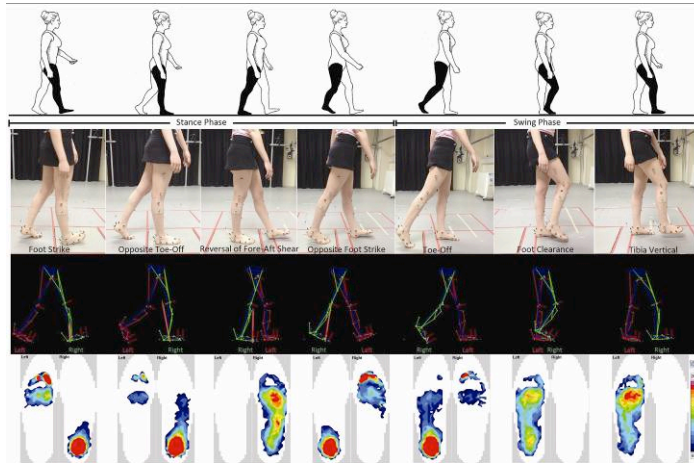


Fig. 1. Complete Gait Cycle analysed simultaneously with Motion Capture System (Vicon Nexus 1.7.1) and Plantar Pressure Insoles (Tekscan).

2.2. Subjects

The number of subjects participating was 15; this number yielded enough statistical power to obtain significant results. The number of subjects lies within the upper bound of previous studies which normally included 7-15 participants. The age of the participants was between 22 and 34. The only eligibility requirement for the participants was that they were capable of walking around the Gait Laboratory for up to 15 minutes. Males and females were asked to participate, though no analysis was performed by gender due to the small sample sizes. Experiments complied with all data protection requirements as stated in the BSREC ethical approval^a obtained.

3. Results

While the results for the same person, under barefoot and shod conditions, showed a significant difference; the gait designed shoes proved to be reliable as the error introduced was smaller than for the repeatability analysis, as shown in figure 2.

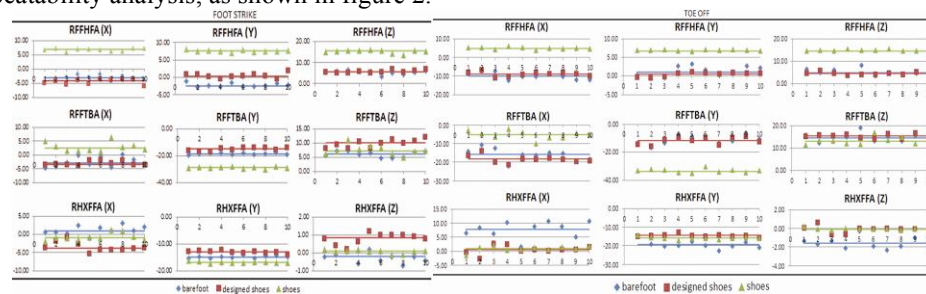


Fig. 2. Results for one person (three studied angles), foot strike and toe off for the three conditions.

4. Discussion

The designed shoes proved to be reliable in terms of marker placement and plantar pressure (figure 3). The utilisation of a plantar pressure mat is under consideration as it would overcome the mentioned constraints; however it would only allow the analysis of one stance at a time.

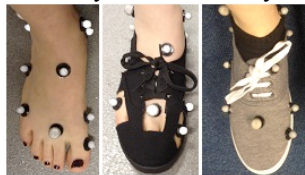


Fig 3. Oxford Foot Model marker placement: barefoot, designed shoes and shoes.

5. Conclusion

The proposed method can be used to reconcile barefoot and shod conditions in the Oxford Foot Model as it can mimic both conditions to study gait and plantar pressure at the same time. It is a promising method for conducting further research on foot modelling in order to obtain valuable information at the same time by triggering both systems simultaneously.

Parameterized state space models are under development to simulate the foot, using experimental analysis to parameterize and validate the models. Foot is also being analysed from a structural numerical perspective, initially trialling a two-part model of the foot which consists of nine spring-damper systems and was introduced by Gilchrist et al⁸.

References

1. Wu G., Siegler S., Allard P., Kirtley C., Leardini A., Rosenbaum D., Whittle M., D'Lima D.D., Cristofolini L., Witte H., Schmid O., Stokes I.; Standardization and Terminology Committee of the International Society of Biomechanics (2002): ISB recommendation on definitions of joint coordinate system of various joints for the reporting of human joint motion--part I: ankle, hip, and spine. International Society of Biomechanics. *Journal of Biomechanics* 35(4):543-8
2. Qiu T.X., Teo E.C., Yan Y.B., Lei W. (2011) Finite element modeling of a 3D coupled foot-boot model. *Medical Engineering & Physics* 33(10):1228-33.
3. Deschamps, K., Staes F., Roosen P., Nobels F., Desloovere K., Bruyninckx H., Matricali G.A. (2011): Body of evidence supporting the clinical use of 3D multisegment foot models: a systematic review. *Gait Posture* 33(3):338-49.
4. Bishop, C., Paul G., Thewlis D.(2012): Recommendations for the reporting of foot and ankle models. *Journal of Biomechanics*, 2012. 45(13):2185-94.
5. Carson M.C., Harrington M.E., Thompson N., O'Connor J.J., Theologis T.N. (2001): Kinematic analysis of a multi-segment foot model for research and clinical applications: a repeatability analysis. *Journal of Biomechanics* 34(10):1299-307.
6. Whittle, M.W., Chapter 2 - Normal gait, in *Gait Analysis (Fourth Edition)*. 2007, Butterworth-Heinemann: Edinburgh. p. 47-100.

7. Switaj T.L., O'Connor F.G. (2008): The sports medicine resource manual – Chapter 43: Gait Analysis. Elsevier Pages 536-542.
8. Gilchrist, L.A. and D.A. Winter, *A two-part, viscoelastic foot model for use in gait simulations*. J Biomech, 1996. **29**(6): p. 795-8.

THE MECHANICS OF THE FOOT-TO-GROUND INTERACTION DURING GAIT: CORRELATION BETWEEN JOINTS MOBILITY AND PLANTAR PRESSURE IN THE HEALTHY FOOT

PAOLO CARAVAGGI, ALBERTO LEARDINI

*Movement Analysis Laboratory, Istituto Ortopedico Rizzoli, via di Barbiano 1/10
Bologna, 40136, Italy*

paolo.caravaggi@ior.it, leardini@ior.it

CLAUDIA GIACOMOZZI

*Department of technology and health, Istituto Superiore della Sanità, via Regina Elena 299
Roma, 00161, Italy*

c_giacomozzi@yahoo.com

Baropodometry and multi-segmental foot kinematics are frequently employed to get better insight into the mechanics of the foot-ground interaction in both biomedical research and clinical settings. Only a few studies have thus far addressed the association between intersegmental kinematics and the plantar loading of foot regions. The authors aimed here at better understanding the relationships between foot joint mobility and plantar loading by focusing on the correlation analysis between kinematic and kinetic global measures.

An integrated pressure-force-kinematics system has been used to measure plantar pressure and rotations between foot segments during the stance phase of walking in 10 healthy subjects. An anatomically-based masking was applied to each footprint to obtain six regions according to the position of reflecting markers tracked by a stereophotogrammetric system; hence each kinematic segment could be paired with a corresponding loaded area of the plantar surface on an anatomical basis. Possible relationships between segmental motion and relevant baropodometric data were explored by means of correlation analysis.

Weak-to-moderate negative correlations ($r^2 < 0.5$) were found between mean and peak pressure and inter-segmental range of motion across all foot joints. In general, larger motion in the foot joints during walking was associated with lower pressure and pressure-time integral at rearfoot and forefoot and with larger pressure at midfoot.

The study helps to improve our understanding of the relationships between joint mobility and plantar loading in the healthy foot and represents a fundamental preliminary analysis before addressing a number of possible clinical applications.

keywords: kinematics, baropodometry, plantar pressure, foot joints, mobility

1. Introduction

The foot is generally regarded as a flexible structure which can adjust its flexibility in response to various external conditions and variable dynamic states, i.e. gait phases, within the motor tasks of daily living. In gait, both joint kinematics and plantar pressure have shown to be affected by functional and structural factors^{1 2}. In fact, pressure distribution can be seen as the effectiveness of the musculoskeletal system in absorbing the ground reaction forces and managing propulsion via the foot and its joints. Excessive repetitive load may develop into calluses, which become sites of peak pressure and pain. The relationship

between foot joints mobility and plantar pressure has not been thoroughly investigated. Aim of this study was to combine a multi-segment kinematic model ³ with advanced baropodometric analysis based on anatomical masking ⁴, to investigate correlations between intersegmental kinematics and regional baropodometric parameters in the normal-arched healthy foot.

2. Methods

Ten able-bodied subjects (26.8 ± 6.9 years; 67.5 ± 12.6 Kg; BMI 22.0 ± 2.7) with normal-arched feet volunteered in the study. An eight-camera motion system (Vicon, UK) was used to track foot segments during the stance phase of level walking, according to an established protocol ³. This implies tracking fourteen 10mm reflective spherical markers in correspondence of relevant anatomical landmarks of the shank and foot (Fig. 1, left). Simultaneously, a pressure plate (Novel GmbH, Germany) recorded foot plantar pressure over three repetitions. An anatomical-based selection was employed to divide the pressure footprints in six subareas ⁴ (Fig. 1, bottom right). Maximum of mean and peak pressure, of vertical force, contact-area and -time, and pressure- and force- time integrals, were determined for each subarea. The relationship between range of motion (ROM) in each anatomical plane of each foot joint and of the medial longitudinal arch (Fig.1, top right) to baropodometric parameters in each subarea was investigated using Pearson's and Spearman's coefficients.

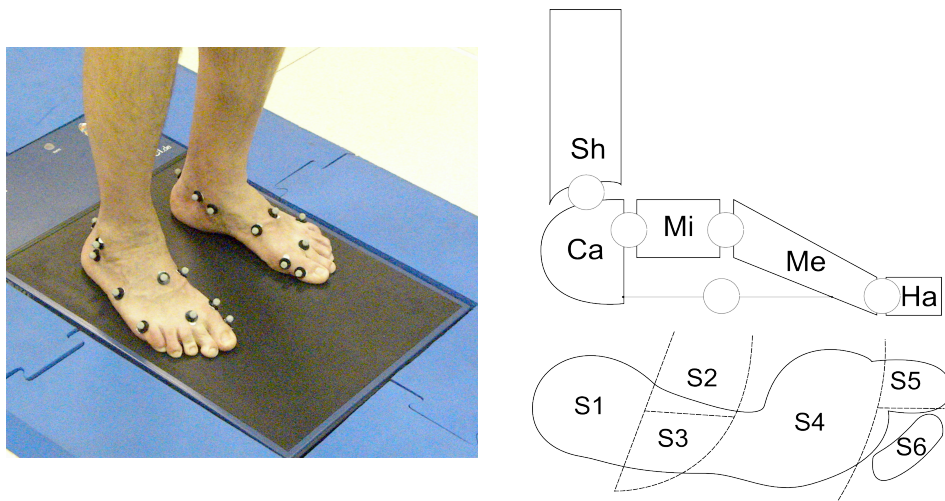


Fig. 1. Left, feet of one of the subjects who volunteered in the study fitted with skin markers for kinematic analysis. Top right, multisegment model of the foot, where: SH is the shank; CA is the calcaneus; MI is the midfoot; ME is the metatarsus, and HA is the hallux. The circles represent the articulations included in the kinematic model. Bottom right, the six foot sub-regions according to the location of the reflecting markers placed on the foot.

3. Results

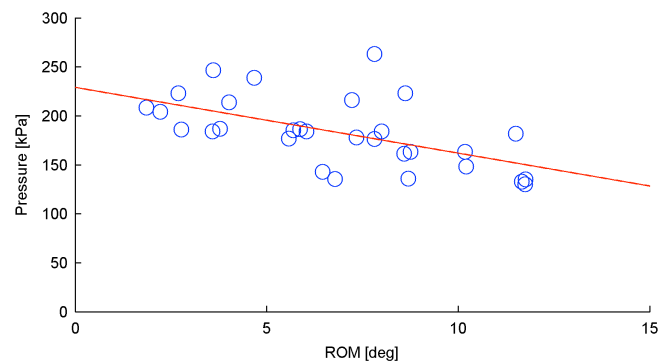


Fig. 2. A Pearson's $r = -0.57$ ($r^2=0.32$, $p=0.001$) was found between peak pressure (kPa) at the forefoot and frontal-plane ROM (deg) at the ankle joint. The linear regression line (red) is superimposed to the data points.

Most of the statistically significant correlations ($p<0.05$) between foot joints ROM and baropodometric parameters were moderate (Pearson's $|r| = 0.36 - 0.67$). In general, motion at the foot joints was negatively correlated with pressure and pressure-time integral at rearfoot and forefoot (Fig. 2) and positively correlated at midfoot. Strong correlation was found between ROM of the medial longitudinal arch angle and pressure-time-integral at the forefoot (Spearman Rho = - 0.93, $p<0.05$).

4. Conclusions

The association between limited joint mobility and increased plantar pressure has been previously shown in the diabetic foot^{5 6 7}. According to the sample of normal feet analyzed in this study, those feet presenting smaller joint mobility are associated with larger pressure at the rear- and fore-foot. A trend for decreased pressure at the midfoot was also detected in those feet presenting a stiffer medial longitudinal arch. A more flexible foot may allow better distribution of pressure at the plantar foot surface during gait thus limiting the contribution to plantar tissue damage especially in at-risk groups such as the diabetic feet⁸.

References

1. Morag, E.; Cavanagh, P. R., Structural and functional predictors of regional peak pressures under the foot during walking. *Journal of biomechanics* **1999**, 32 (4), 359-370.
2. Teyhen, D. S.; Stoltenberg, B. E.; Collinsworth, K. M.; Giesel, C. L.; Williams, D. G.; Kardouni, C. H.; Molloy, J. M.; Goffar, S. L.; Christie, D. S.; McPoil, T., Dynamic plantar pressure parameters associated with static arch height index during gait. *Clinical biomechanics* **2009**, 24 (4), 391-396.
3. Leardini, A.; Benedetti, M. G.; Berti, L.; Bettinelli, D.; Natio, R.; Giannini, S., Rear-foot, mid-foot and fore-foot motion during the stance phase of gait. *Gait & posture* **2007**, 25 (3), 453-62.
4. Giacomozzi, C.; Leardini, A.; Caravaggi, P., Correlates between Kinematics and Baropodometric Measurements for an Integrated In-Vivo Assessment of the Segmental Foot Function in Gait. *Journal of biomechanics* **2014**, in press.

5. Fernando, D. J.; Masson, E. A.; Veves, A.; Boulton, A. J., Relationship of Limited Joint Mobility to Abnormal Foot Pressures and Diabetic Foot Ulceration. *Diabetes care* **1991**, *14* (1), 8-11.
6. Viswanathan, V.; Snehalatha, C.; Sivagami, M.; Seena, R.; Ramachandran, A., Association of limited joint mobility and high plantar pressure in diabetic foot ulceration in Asian Indians. *Diabetes research and clinical practice* **2003**, *60* (1), 57-61.
7. Rao, S.; Saltzman, C. L.; Yack, H. J., Relationships between segmental foot mobility and plantar loading in individuals with and without diabetes and neuropathy. *Gait & posture* **2010**, *31* (2), 251-255.
8. Giacomozzi, C.; D'Ambrogio, E.; Cesinaro, S.; Macellari, V.; Uccioli, L., Muscle performance and ankle joint mobility in long-term patients with diabetes. *BMC musculoskeletal disorders* **2008**, *9*, 99.

FINITE ELEMENT MODELING AND CLUSTER ANALYSIS: A COMBINED APPROACH FOR IDENTIFICATION OF DIABETIC FOOT PATIENTS AT RISK OF PLANTAR ULCERS

ANNAMARIA GUIOTTO* ⁽¹⁾, ZIMI SAWACHA* ⁽¹⁾, ALESSANDRA SCARTON ⁽¹⁾, GABRIELLA GUARNERI ⁽²⁾, ANGELO AVOGARO ⁽²⁾, CLAUDIO COBELLI ⁽¹⁾

⁽¹⁾ *Department of Information Engineering, University of Padova, Via Gradenigo 6B
Padova, Italy * Equal contributors*

⁽²⁾ *Department of Clinical Medicine & Metabolic Disease, University Polyclinic, Via Giustiniani 2
Padova, Italy*

Diabetic foot is an invalidating complication that can lead to foot ulcers. 3D finite element (FE) models (FEM) allow characterizing the loads developed in the different structures of the foot. A cluster analysis is a multivariate statistical technique used to group objects based on their characteristics. The aim of this study was to apply cluster analysis to FE-simulated plantar pressures and internal stresses of a group of diabetic neuropathic subjects in order to identify those at risk of plantar ulcers. Sixteen subjects underwent routine gait analysis in the 5 years preceding the study and experimental kinematics, kinetics and plantar pressure were acquired. 5 years clinical follow up was performed and afterward 6 subjects ulcerated. 3D FE analysis was ran by applying subjects specific boundary conditions to a 3D FEM developed segmenting bones, cartilage and skin from one neuropathic subject's MRI. The FE-simulated plantar stresses, von Mises, normal stresses in the soft tissues were used to run cluster analysis; three clusters were defined: 5 ulcerated subjects were grouped in one cluster with 3 non-ulcerated subjects. A longer follow up and a larger dataset is needed. This combined approach may infer useful informations on the risk of ulceration prior to wounds evolution.

Keywords: Diabetic foot; Gait analysis; Finite element analysis; Three-dimensional; Multidisciplinary biomechanics approach; Cluster analysis.

1. Introduction

The prevalence of foot ulceration (FU) among patients with diabetes mellitus ranges from 1.3% to 4.8% in the community ¹. The pathophysiology of diabetic FU is multifactorial, but diabetic peripheral neuropathy (DPN) is thought to be responsible for most cases. Diabetes' complications cause alterations in foot structure and function, subsequently leading to increased plantar pressure (PP), which is a predictive risk factor for the development of diabetic FU ¹⁻². Recently others indicated that mechanical stress concentrations in deep tissues of the plantar pad of the DPN subjects' (DPNS) play a dominant role in the mechanism of foot injuries and may lead to FU ³⁻⁵. Some experimental and numerical techniques have been explored to study this mechanical interaction between external and internal stresses and strains. While experimental analyses are limited solely to measurements of interfacial variables, a reliable numerical model (as FEM) can provide both the interfacial pressures and insight into internal stresses and strains tolerated by the plantar tissue ³⁻⁵. Moreover FEMs allow taking into account the critical aspects of the diabetic foot: the movement, the morphology, the tissue properties and the loads. Several recent models have used the FEMs to predict the loading of the foot's components during standing and gait ³⁻⁵, in particular applied to diabetic foot pathology. However it should be considered that state of art foot FEMs have been developed under simplified assumptions such as foot sub-segments, material properties, and generic boundary conditions. The authors recently developed a foot FEM based on a neuropathic subject MRI ⁵. A cluster analysis (CA) is a multivariate statistical technique used to group objects based

on their characteristics ⁶. This technique has provided an objective method of classifying different subjects based on their biomechanics characteristics and has recently been applied to gait analysis data ⁶. The aim of this study was to combined the two different methodologies (FEM and CA) in order to identify DPNS at risk of FU. With this purpose, a FE analysis was ran with the data of 16 DPNS and FE-simulated contact pressures and internal stresses were calculated. The latters were used as input to k-means CA and hierarchical CA.

2. Methods

2.1 Experimental set up

Groups	non US	SD	US	SD
Subjects [#]	10		6	
Sex [# of males]	6 (60%)		4 (66.6%)	
BMI mean[kg/m ²]	24.3	2.9	26.3	2.0
Age mean [years]	63.2	6.4	62.3	4.1
Peripheral neuropathy [#]	10 (100%)	-	6 (100%)	
Diabetic retinopathy [#]	6 (60%)	-	5 (83.3%)	
Microalbuminury [#]	2 (20%)	-	1 (16.6%)	
Vasculopathy [#]	3 (30%)	-	1 (16.6%)	
Type of diabetes [#]	type1: 6	type2: 4	type1: 2,	type2: 4
HbA1c mean	7.97	1.28	8.7	1.04
Years of disease mean	28.1	12.5	20.8	20.2
Cavus foot [#]	9 (90%)		6 (100%)	
Valgus Hindfoot [#]	4 (40%)		2 (33.3%)	
Varus Hindfoot [#]	1 (10%)		1 (16.6%)	
Hallux valgus [#]	4 (40%)		3 (50%)	
Foot deformities [#]	5 (50%)		3 (50%)	
Plantar callosity [#]	4 (50%)		3 (50%)	

Table 1. Demographic and clinical data the DPNS. # = number of subject, SD = standard deviation.

Sixteen DPNS (Table 1) underwent gait analysis in the 5 years preceding the study and kinematics, kinetics and plantar pressure were experimentally measured by means of 4 segments 3D foot kinematic model ²: 6 cameras stereophotogrammetric system (60Hz, BTS S.r.l, Padova), 2 force plates (FP4060-10, Bertec Corporation, USA), 2 PP systems (0.64 cm² resolution, 150 Hz, Imagortesi, Piacenza). The signals coming from all systems were synchronized as ². A static trial and at least 3 gait cycles of each limb were collected. Neurological evaluation, Michigan Neuropathy Screening Instrument questionnaire and physical examination as in ² were performed on every DPNS. The protocol was approved by the local Ethic Committee of the University Clinic of Padova and written informed consent obtained. 5 years clinical follow up was performed and afterword 6 subjects developed FU (ulcerated subjects (US)) under metatarsals heads.

2.2 Finite element models

Of the 16 subjects, one (age 61 years, BMI 25.8 kg/m²) was used to develop a foot FEM as in ⁵. His foot MRI in a completely unload condition was acquired with 1.5 T device

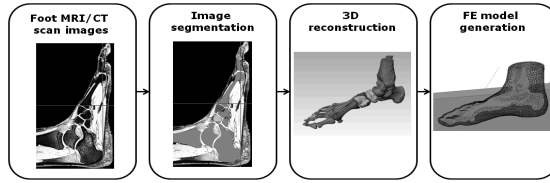


Figure 1: Workflow of the development of the FE model of the foot.

(Siemens Avanto, spacing between slides: 0.7mm, slice thickness: 1.5mm, multi-fast-field-echo sequence). The gray-scale-images were segmented with Simpleware-ScanIP software (v.5.0) into 30 bones, cartilages between them, and the foot skin as contour of the homogenous mass of foot soft-tissues (Figure 1). The mesh was generated with the Simpleware-ScanFE (7 mm edges - 84386 elements ³⁻⁵) and imported into Abaqus-CAE FEA software (Simulia, v.6.12), where a 3D horizontal plate was drawn and meshed with hexahedral elements (8 mm edges) to simulate the ground support. Material properties of different tissues were obtained from the literature (Table 2). For the plantar soft-tissues isotropic, nearly incompressible, hyperelastic second-order polynomial formulation was used as in ⁵ (increased stiffness by a factor 2 ⁷).

Component	E [MPa]						ν	
Plate ¹⁷ - linear elastic isotropic	68900						0.3	
Bones ⁹ - linear elastic isotropic	7300						0.3	
Cartilage ⁶ - linear elastic isotropic	1.01						0.4	
Plantar fascia ^{6,7} - linear elastic isotropic	350						-	
Tendons/ ligaments ^{6,7} - linear elastic isotropic	250						-	
Soft tissues coefficients ⁶	C_{10}	C_{01}	C_{20}	C_{11}	C_{02}	D_1	D_2	
	[N/mm ²]	[N/mm ²]	[N/mm ²]	[N/mm ²]	[N/mm ²]	[mm ² /N]	[mm ² /N]	
DPNS model ⁷	0.17113	-0.1168	0.078	-0.0464	0.01702	1.82636	0	

Table 2. Homogeneous, isotropic, linear elastic and hyperelastic 2nd order polynomial soft tissue materials.

FE analysis was ran by applying each DPNS's experimental vertical load and angular positions during loading response, midstance and push-off phases of gait (when critical loads occur in the foot of the DPNS). Gastrocnemius-soleus muscle force acting through the Achilles tendon was applied (50% of the ground load ³⁻⁵). The superior surfaces of the tibia, fibula and soft-tissues were fixed to simulate the effects of constraints from superior-lying tissues. A coefficient of friction of 0.6 ⁴ was used in the contact surface between the deformable plantar soft tissues and the rigid plate. After the simulations, the PP at foot-supporting interface and both von Mises and normal stresses in the soft tissues were considered for the K-means and hierarchical CA.

3. Results

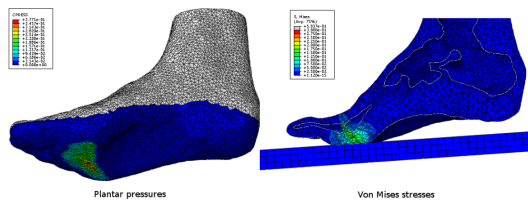


Figure 2 Results of a1 US's FEM simulation: Plantar pressures (left) and Von Mises internal stresses (right).

DPNS FEM's validity was assessed through comparison between the FE-simulated stress distribution and the experimentally measured one. The DPNS FEM loaded with their subject-specific static standing vertical forces underestimated the experimental peak PP of 6.3% (difference between the simulated and the experimental peak PP in percentage of the experimental ones). The comparison between the experimental and simulated data within the different sub-phases of the stance phase of gait showed that there was a good agreement in the overall patterns of predicted and measured although every FE simulations overestimated both contact pressures and contact area under the lateral mid foot. Peak stress level calculated from the internal plantar soft-tissues was expressed in terms of von Mises and normal stresses (Figure 2). The hierarchical CA (Ward's linkage) gave the best results and led to the definition of 3 well defined clusters (Table 3): 5 US

were included in one cluster with only 3 non US and this was the cluster characterized by the larger presence of diabetes complications.

Cluster	N° subjects US/ non US	Push-off			Mid-stance		
		Peak PP	Mean PP	Von Mises	Peak PP	Mean PP	Von Mises
1	0 / 3	0.423	0.108	0.000381	0.323	0.080	0.000251
		0.052	0.023	0.000174	0.020	0.010	0.000044
2	1 / 4	0.371	0.097	0.000348	0.275	0.060	0.000245
		0.041	0.019	0.000050	0.017	0.007	0.000024
3	5 / 3	0.390	0.104	0.000378	0.277	0.062	0.000228
		0.035	0.007	0.000042	0.028	0.004	0.000021

Table 3. Results of the hierarchical CA: 3 clusters (values in % of the subject's weight).

4. Discussion

In this study, a 3D DPNS model was developed, based on MRI data. Gait analysis driven FE analyses were ran with the data of 16 DPNS and results used for performing CA. Innovations consist in the integration of FEM, gait analysis and CA for providing insight in diabetic foot prevention. In term of FEM validity, results demonstrated a good agreement between the simulated and experimental peak PP values. CA results showed that 5 out of 6 subjects were correctly identified and developed FU. Correspondence was found between FE-simulated and clinical examinations at follow up. Limitations of the current study can be found that should not be neglected: only one subject specific MRI based model was developed and the other FE analysis were run by applying DPNS subject specific boundary conditions; material properties were taken from literature⁴⁻⁹; a longer follow up is needed in order to verify whether the 3 DNS included in cluster 2 and the 3 DNS in cluster 3 will develop FU; a larger dataset is needed to validate this methodology. Despite limitations, the method may have significant impact in providing a useful tool for diabetic foot prevention.

References

1. Boulton AJ, Vileikyte L, Ragnarson-Tennvall G, Apelqvist J. The global burden of diabetic foot disease. *The Lancet*. 2005;366(9498):1719-1724.
2. Sawacha Z, Guarneri G, Cristofori G, Guiotto A, Avogaro A, Cobelli C. Integrated kinematics-kinetics-plantar pressure data analysis: A useful tool for characterizing diabetic foot biomechanics. *Gait & Posture*. 2012;36(1):20-26.

3. Cheung JT-M, Zhang M, Leung AK-L, Fan Y-B. Three-dimensional finite element analysis of the foot during standing--a material sensitivity study. *J Biomech.* 2005;38(5):1045-1054.
4. Gefen A, Megido-Ravid M, Itzhak Y, Arcan M. Biomechanical analysis of the three-dimensional foot structure during gait: a basic tool for clinical applications. *J Biomech Eng.* 2000;122(6):630-639.
5. Guiotto A, Sawacha Z, Scarton A, Guarneri G, Avogaro A, Cobelli C. 3D finite element model of the diabetic neuropathic foot: a gait analysis driven approach. *Proceedings ISB 2013, Natal, Brasil.*
6. Sawacha Z, Guarneri G, Avogaro A, Cobelli C. A New Classification of Diabetic Gait Pattern Based on Cluster Analysis of Biomechanical Data. *J Diabetes Sci Technol.* 2010;4(5):1127-1138.

S3P: Radiobiology - radiation therapy

Chairs: Maria Pia Morigi, Pier Luca Rossi

3D MODELING OF HIP PROSTHESES FOR USE IN EXTERNAL BEAMS RADIOTHERAPY

PLANNINGS

FEDERICO ZAGNI

EFFECT OF X-IRRADIATION ON CELL MORPHOLOGY, CYTOSKELETON NETWORK AND

ADHESION

VALERIA PANZETTA

DEFORMABLE REGISTRATION OF PET IN HEAD AND NECK CANCER TOMOTHERAPY

TREATMENT: IS TEXTURE ANALYSIS A GOOD PREDICTOR?

GABRIELE GUIDI

SCRIPTING AUTOMATION AND BIOMECHANICAL MODELING FOR ADAPTIVE RADIATION

THERAPY

CLAUDIO VECCHI

AN ARTIFICIAL NEURAL NETWORK TO PREDICT TIME OF REPLANNING FOR TOMOTHERAPY

TREATMENTS

NICOLA MAFFEI

REAL-TIME MODEL FOR ADAPTIVE RADIATION THERAPY: A BIOMECHANICAL APPROACH

USING A LEGO MINDSTORMS

GABRIELE GUIDI

TOWARD AN OPTIMIZATION OF RADIOTHERAPY TREATMENT IN HUMANS GLIOBLASTOMA

BASED ON A CANCER STEM CELLS KINETIC MODEL

ANDREA CORAZZA

ADVANCED MRI TECHNIQUES USED TO EVALUATE PARAMETERS FOR A GLIOBLASTOMA

GROWTH KINETIC MODEL IN HUMAN

LUIGI MANCO

3D MODELING OF HIP PROSTHESES FOR USE IN EXTERNAL BEAMS RADIOTHERAPY PLANNINGS

ZAGNI F¹, BARUFFALDI F², BORDINI B², STEA S², VANINI R¹, ROMANI F¹, MARENGO M¹

¹Medical Physics Department, University Hospital "S. Orsola-Malpighi", Bologna, Italy; ²Laboratorio di Tecnologia Medica, Istituto Ortopedico Rizzoli, Bologna, Italy.

1. Introduction

Radiotherapy treatment planning for patients with metallic hip prosthesis, for pelvic or abdomen malignancies, is often challenging. A very detailed knowledge of the prosthesis position and dimensions, necessary in the organ contouring process, is needed to achieve accurate dose distribution estimations in the surroundings of the hip. However, CT (Computed Tomography), the base methodology used to acquire data as regards patient's centering and distribution of density of tissues in the treated volume, is not designed for such high-Z materials, as, in fact, typical diagnostic XR beams are heavily attenuated by metal objects. For this reason, in such cases, CT imaging of this regions is often degraded and inaccurate, resulting in difficult and approximate contouring of the prosthesis.

The aim of this work was to establish a methodology to model known components of prosthesis implants, to be used in the phase of contouring during the treatment planning, in order to provide to physicians more geometrical information on the prosthesis implant, in addition to the CT imaging.

2. Materials and Methods

Since diagnostic CT is not able to accurately reconstruct 3D voxel matrices (in DICOM format, the standard in a treatment planning system, TPS) of thick metal objects, such as the majority of prosthesis implants, we researched for an alternative approach. It has to be noted that many manufacturers of prosthesis components will usually not release detailed 3D mesh models of their products. For this reason, we had to develop a method to create our own mesh model from scratch, using the physical prosthetic component, and afterwards to convert it to DICOM format, being the standard for storing, processing and transmission of medical imaging such as CT scans and radiotherapy planning.

In this work we developed and validated the model of an APTA[®] stem (Adler Ortho s.r.l., Milano, Italy), the femoral component of a hip prosthesis, made of a titanium alloy, currently adopted and implanted to patients in many relevant Institutions, like the Rizzoli Orthopaedic Institute in Bologna.

2.1 Acquisition of the 3D model

In order to acquire a digitized 3D model of the prosthesis component, a photogrammetry approach was followed. This technique allows for the creation of a 3D mesh model from still images of the object of interest. Several pictures from different point of views are taken, in order to acquire the corresponding outline profiles, and as much details of the object surface as possible. More precisely, the software used in this work (3D Software Object Modeler, *3DSOM* [1]), requires a calibration map visible in every picture,

in a fixed position with respect to the investigated object. The map contains dots patterns which act as a reference, in order for the software to evaluate the camera position and distance from the object, for each picture. It also contains a calibration unit for the size, which allows the generation of correctly scaled (in mm) models. The acquisition setup of the pictures used in this work is presented in figure 1. The uniform contrasting background was helpful to isolate the object, so that a semi-automatic masking procedure could be used to identify the surface outlines from every angles. In the subsequent step the software performs the reconstruction of the 3D mesh model of the surface, based on the camera shot locations and on the masked outlines from all the acquired point of views. Fine tuning parameters, such as the number of used polygons, were adjusted in order to improve accuracy of the model. The final mesh model resulted in a polygon mesh, which could be saved in VRML (*Virtual Reality Modeling Language*) or STL (*STereoLithography*) file format. It has to be pointed out that even this acquisition system is adequate to allow for a description of the object sufficiently accurate as regards radiation treatment planning, by no way it can be considered as a reverse engineering attempt to model the real prosthetic component.

In this work we took 30 pictures, 20 of which from a single orbit at half height of the stem (see figure 1), while the reminder from different positions to better reveal shape details contrasting to the background.

2.2 Conversion to DICOM

In order to retrieve the geometrical properties of the 3D model of the stem inside a radiotherapy TPS, the obtained mesh had to be converted to DICOM. This operation was not straightforward, since a 3D mesh is a collection of vertices and faces describing the surface of an object, while DICOM is essentially a map of a physical property inside a volumetric region, sampled in a defined number of voxels, plus a descriptive header. The conversion was divided in two steps, the *rasterisation* and the actual generation of the DICOM file.

In the first step, the polygon mesh of the stem, which was generated as a closed surface, was mapped to a volumetric region with dimensions equal to the maximum extension of the surface along the three spatial axis. To this aim *binvox* [2] was used. This software implements an algorithm based on the work of Nooruddin, 2003 [3], and generates a binary raw image in which each voxel, if assigned to the inside of the surface, is set to one, otherwise is set to zero. Voxel size was derived from the 3D mesh, which was previously calibrated, so to preserve dimensional information. At first, the image was generated at higher resolution, in order to perform a more precise evaluation in the validation process (paragraph 2.3).

In the second step, in order to generate a DICOM set which could be imported in a TPS system, a number of requirements must be met. For example, the structure of the DICOM header should be the same of that used by the TPS. For this reason, a full header of a routine centering CT image was exported and customized to match the properties of the new image being generated. This was accomplished using *dcmTk* [4] software, a set of tools to manipulate and generate DICOM images. With *ImageJ* [5], the raw data of the volume image were converted to 16-bit format, down-sampled to match the voxel size of routine CT images (1.0x1.0x3.0 mm) and voxel values rescaled to obtain realistic CT numbers.

2.3 Validation

We assessed how accurately the modeled prosthetic stem, stored in the DICOM image, preserved shape

and size of the original one. With *ImageJ*, length measurements (performed through line profiles) of different cross sections along the stem (figure 2) were compared to measurements performed with a caliber. Moreover, using the original mesh model of the stem provided by the factory, another model in DICOM format was generated following the same procedure described in paragraph 2.2 and the same cross sections were measured with *ImageJ*.

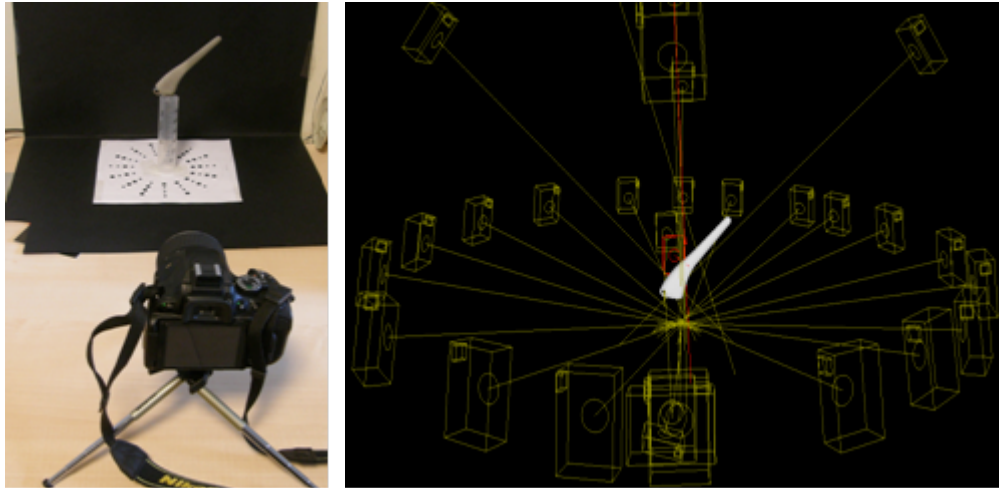
2.4 Preliminary tests in a research radiation therapy software

To test the feasibility of importing and contouring the patient stem implantation with the modeled one, we used a research platform for radiotherapy planning, CERR [6], under Matlab environment, and an anonymized treatment plan of a patient with a hip prosthesis. CERR allowed for the automatic generation of the contour of the stem, using a thresholding algorithm. The contour was then merged to the patient plan and, through translation and rotation algorithms suitably implemented, it could be aligned to the patient physical prosthesis by exploiting the most visible parts in the CT image, corresponding to the thinnest section of the stem

3. Results

The obtained model in DICOM format, as shown with the 3D viewer of ImageJ, was reported in figure 2. Shape and size comparison, as indicated in figure, were reported in Table 1. Slight deviations were observed, 5% on average in the comparison with the model provided by the factory, and 2% in the comparison with measurements with the caliber. Anyway differences were, in all cases but one, less than 1 mm, equal to the pixel size of CT images used in this work. It was observed that the obtained model was inclined to overestimate the lesser of the stem geometrical axis, being anyway a minor issue which may depend on the optimization parameters used in 3DSOM. Also, the hole size at the top of the stem was slightly underestimated.

As an example, in figure 3 was reported a centering CT in which is visible the contouring performed by the physician without any help and the structure derived from the model developed in this work.



(a) (b)
 Figure 1. Still images acquisition setup (a) and camera shot positions as evaluated in 3DSOM during the mesh model reconstruction (b).

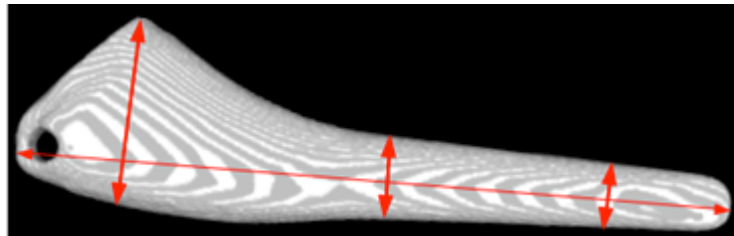


Figure 2. 3D mesh model converted to DICOM of the femoral prosthetic stem obtained in this work. Measurements sections reported in Table 1 are indicated with arrows.

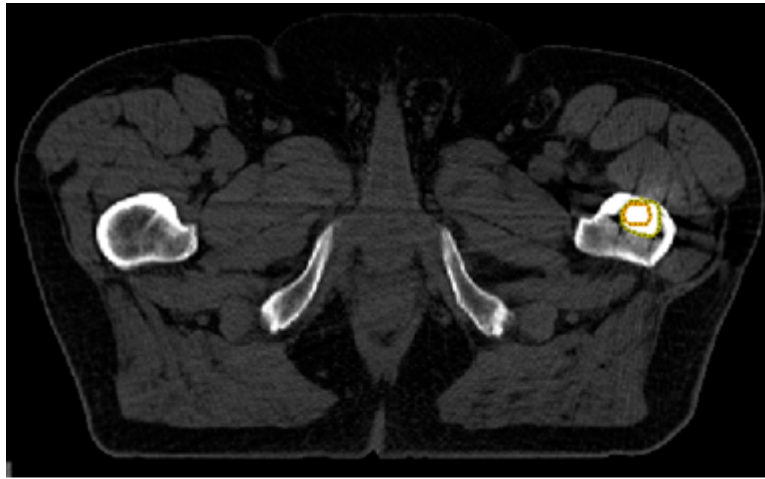


Figure 3. CT slice of a patient in which two contours of the prosthetic stem are compared. The smaller one, in orange, is derived from the 3D model, while the other is the contouring

4. Conclusion

This work shows that accurate modeling of highly asymmetric objects, such as prosthesis components, using the photogrammetry technique may be achieved. The methodology proposed for the conversion of the mesh model to DICOM format showed good performance and may be further automatized. The preliminary tests conducted in a research environment showed that, given proper alignment tools, the model of a prosthesis may be usefully exploited in a TPS, in order to better characterize it in cases of poor CT imaging.

Acknowledgements

Authors wish to thanks Adler Ortho S.r.l., Milano, Italy, for providing the original mesh of the prosthetic model. This study has been partially funded by Italian Health Ministry, project GR2010-2308995 "Manufacturing information of orthopedic articular prosthesis. Analysis of specific safety issues for radiotherapy, magnetic resonance, orthopedic surgery and identification of a traceability model".

References

1. Baumberg A, Lyons A, Taylor R, *3D SOM-A commercial software solution to 3D scanning*. Graphical Models vol. 67(6) 476–495, 2005
2. Patrick Min's *binvox* reference website: <http://www.cs.princeton.edu/~min/binvox/>
3. Nooruddin S and Turk G, *Simplification and Repair of Polygonal Models Using Volumetric Techniques*. IEEE Trans. on Visualization and Computer Graphics, vol. 9, n. 2, 191-205, April 2003
4. Eichelberg M, et al. *Ten years of medical imaging standardization and prototypical implementation: the DICOM standard and the OFFIS DICOM toolkit (DCMTK)*. Proc. SPIE 5371, Medical Imaging 2004: PACS and Imaging Informatics, 57, 2004
5. Schneider CA, Rasband WS, Eliceiri KW. *NIH Image to ImageJ: 25 years of image analysis*. Nature Methods 9, 671-675, 2012
6. Deasy J, Blanco I, Clark V. *CERR: A computational environment for radiotherapy research*. Medical Physics vol. 30, 979, 2003

EFFECT OF X-IRRADIATION ON CELL MORPHOLOGY, CYTOSKELETON NETWORK AND ADHESION

VALERIA PANZETTA¹, MARTA DE MENNA², DEBORA BUCCI², VITTORIA GIOVANNINI², MARIAGABRIELLA PUGLIESE³, MARIA QUARTO³, SABATO FUSCO¹, PAOLO NETTI^{1,2,4}
valeria.panzetta@it.it, marta.demenna@me.com, vi.giovannini@studenti.unina.it, de.bucci@studenti.unina.it, pugliese@na.infn.it,
quarto@na.infn.it, sabato.fusco@iit.it, nettipa@unina.it

1. Introduction

It's well known the ability of X-irradiation to produce chromosomal damage inducing a decrease of reproductive ability among cell population [1-2]. Nevertheless, cells, in which a single ionization is not sufficient for death induction, but affect reproductive functions, have many physiological activities that continue. In this paper we investigated the effects of 2 different doses of X-irradiation (1 and 2 Gy) on some of these activities (*i. e.* spreading, proliferation, migration) focusing the attention on the cytoskeleton (CSK) structure on two cell lines, BALB/c 3T3 and Simian virus 40-transformed BALB/c 3T3 (SVT2) cells. Indeed, CSK is involved in virtually all cellular processes and abnormalities in its function can result in many diseases, such as cancer [3-4]. Our studies showed that the alteration in the cytoskeletal architecture during malignant transformation is correlated with a less spread morphology, small adhesion plaques (the structures that form a physical link between the extracellular and the intracellular domain of the plasma membrane), an increased motility and an increased deformability. Finally, we investigated how X-irradiation alter cytoskeleton dynamics in both cell lines, assessing cell proliferation, spreading areas and migration ability.

2. Materials and Methods

2.1 Cell Cultures

Experiments were performed on BALB/c 3T3 and Sv40-transformed BALB/c 3T3 cells (SVT2). Cell lines were cultured at 37°C in 5% CO₂ in Dulbecco's modified Eagle's medium (Euroclone Ltd., UK) supplemented with 10% fetal bovine serum (FBS, BioWhittaker, MD), 2 mM L-glutamine (Sigma, St. Louis, MO), 1000 U/L penicillin (Sigma, St. Louis, MO), and 100 mg/L streptomycin (Sigma, St. Louis,

¹ Center for Advanced Biomaterials for health Care@CRIB, Istituto Italiano di Tecnologia, Largo Barsanti e Matteucci, 53, 80125 Napoli, Italy

² Interdisciplinary Research Centre on Biomaterials, Federico II University of Naples, Piazzale Tecchio, 80, 80126, Napoli, Italy

³ Dipartimento di Fisica, Università Federico II, and INFN-Sezione di Napoli, Monte S. Angelo, Via Cintia, 80126 Napoli, Italy

⁴ Dipartimento di Ingegneria dei Materiali e della Produzione, Università di Napoli Federico II, Piazzale Tecchio 80, 80126, Napoli, Italy

MO). For proliferation curve, BALB/c 3T3 and SVT2 were cultured at a final concentration of 200 cells/cm², while for migration experiments and spreading evaluation at a concentration of (inserire dati), respectively.

2.2 Cell X-rays irradiation

Cell lines were exposed to X-rays produced by a Thomson tube (TR 300F, 250 kVp, 0.8 Gy/min, Stabilipan, Siemens) and filtered by 1-mm-thick copper foil. Irradiation was performed using the facility installed at the Department of Physics of University of Naples Federico II. Before each irradiation a physical dosimetry was performed, using an ionization chamber (Victoreen, Mödling, Austria).

2.3 Cell viability and Proliferation assay

Trypan Blue exclusion was used to evaluate the effects of X-rays on cell viability. Cell aliquots were collected at different time intervals (0, 1, 3, 6 days) and stained for 5 minutes with Trypan Blue. Cell proliferation was measured by counting cells in Neubauer hemocytometer.

2.4 Cell migration

Cell migration experiments were performed by time-lapse microscopy (Olympus IX81 inverted microscope with 10x objective). Phase contrast images were collected at 5-min intervals for 12 hours. Manual cell tracking was carried out using ImageJ and the Manual Tracking plugin (<http://rsweb.nih.gov/ij/>). Speed was calculated by analyzing the acquired data with Chemotaxis and Migration Tool plugin (http://www.ibidi.de/applications/ap_chemo.html).

2.5 Cell spreading analysis

To assess the capacity of the two cell lines to spread before and after irradiation, images of Phalloidin-Alexa-488 were captured, imported into ImageJ software for postprocessing and analysis of ventral area of cells.

3. Results and Discussion

The first important finding of this study is that X-rays doses of 1-2 Gy depressed substantially the proliferative activity in SVT2, but not in BALBc/3T3 cells one day after irradiation. We observed an approximately constant 30-35% decrease in the proliferating SVT2 cells when irradiated with lower dose. While the number of proliferating transformed cells decreased rapidly 2.4 fold after 1-3 days up to 4-5 fold 6 days post treatment with high dose. On the other hand, BALBc/3T3 cells had a reduced proliferation compared to SVT2 cells and seemed to be not very sensitive to low dose. In the case of high dose treatment there was a decrease in proliferating cells up to 40% after 6 days from irradiation. The effects could be ascribed to the combination of two different effects, cell death and proliferation arrest (Fig. 1).

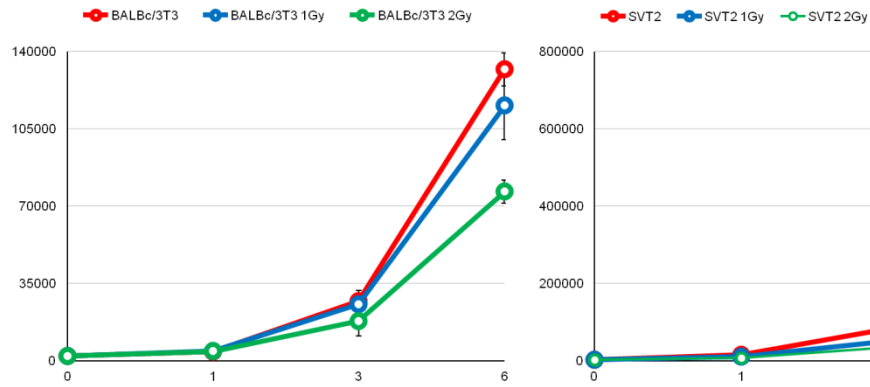


Fig. 1. The proliferative capacity of SVT2 cells surviving after irradiation was profoundly affected already 24 h after irradiation in a dose-dependent way. BALBc/3T3 seemed to be sensitive to the high dose only at long time (3-6 days), while they were not very responsive to the low X-ray dose.

Further, we analyzed the morphology and cytoskeletal organization of the cells in both control conditions and after treatment with two doses of X-rays using fluorescent microscopy. The morphology and cytoskeleton in BALBc/3T3 and SVT2 cells are compared in Fig. 2. BALBc/3T3 cells showed in control condition a high spreading (Fig. 2 A-B), well organized actin cytoskeleton and bigger vinculin adhesion plaques (data not shown) compared to transformed cells (Fig. 2 G-H). 24 hours after irradiation, both BALBc/3T3 and SVT2 resulted to be more spread compared to control cells when irradiated with higher dose and to have a more actin-rich cytoskeleton (Fig. 2 K-L), while there were no effect in spreading area and cytoskeletal organization when cells were treated with a dose of 1 Gy (Fig. 2 I-J).

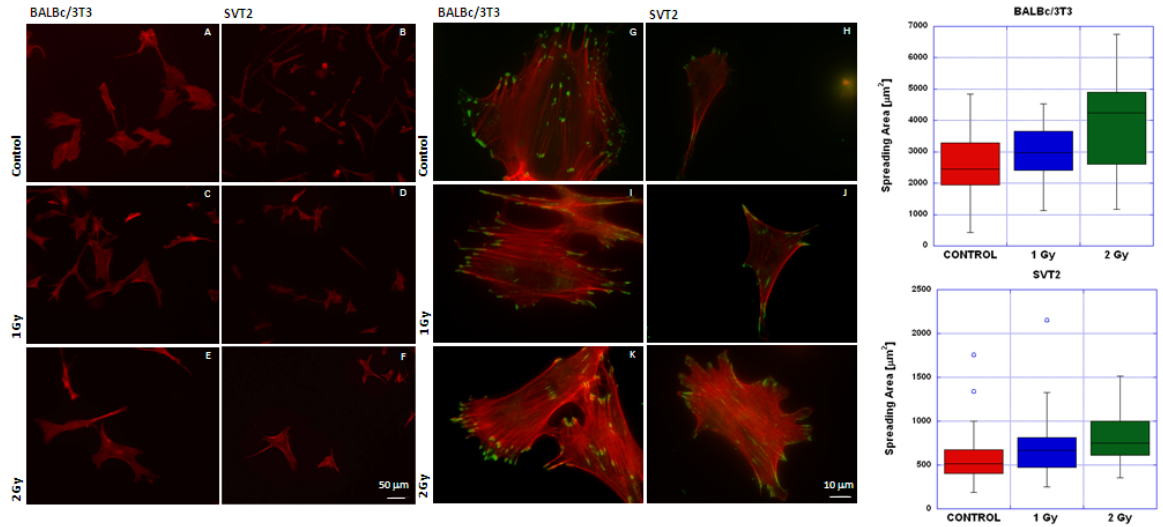


Fig 2. X-rays with dose of 2 Gy seemed to induce an increase in spreading and structuring of cytoskeleton at 24 h after irradiation. The increase in mean spreading area we measured when the two cell lines were irradiated with lower dose was not resulted significantly different.

Quantitative time-lapse video microscopic analysis revealed random motility speeds of BALBc/3T3 were significantly decreased ($0.27 \pm 0.15 \mu\text{m}/\text{min}$) compared to speeds of transformed cells ($0.77 \pm 0.32 \mu\text{m}/\text{min}$) when the cell lines were not irradiated. Cell migration analysis showed that BALBc/3T3 cells responded rapidly to 2 Gy irradiation, by reducing their motility speed already at 6 h ($0.20 \pm 0.11 \mu\text{m}/\text{min}$) and also at 72 h after irradiation ($0.21 \pm 0.12 \mu\text{m}/\text{min}$), while no variation in velocity was observed for lower dose. SVT2 cells seemed to be less responsive to X-rays in terms of migration ability at short time, while their motility rate resulted reduced in a significant way ($p < 0.05$) at longer time both at low dose ($0.67 \pm 0.26 \mu\text{m}/\text{min}$) and high dose ($0.65 \pm 0.29 \mu\text{m}/\text{min}$). These results could be explained considering the modified dynamics of assembly/disassembly of cytoskeletal network and focal adhesion plaques, as demonstrated by the increase in spreading and the presence of a more structured cytoskeleton in treated cells.

We hypothesize that the observed increase in spreading and reduced velocity in treated SVT2 cells could ensure the shape stability of the cells and ultimately a mechanically integrity to the cytoskeleton structure.

4. Conclusions

The intrinsic migratory ability of malignant cancer cells is the way they utilize to invade adjacent tissues and the vasculature and, then, to form metastasis.

Morphological and functional variations we observed in SVT2 cells, when they were irradiated with a dose of 1 Gy, suggested a more structured and stiff cytoskeletal network.

We suppose that the stiffening of the cytoskeleton can be associated to a reduction in the invasive and metastatic potential of transformed cell.

References

1. **103** (5): 653-666, 1956.*Proc. Natl. Acad. Sci. U.S.A.*44 (8): 772–780, 1958.463: 485-492, 2010.Cross SE, Jin YS, Tondre J, Wong R, Rao JY, Gimzewski JK. AFM-based analysis of human metastatic cancer cells, *Nanotechnology*, 19: 384003, 2008.

DEFORMABLE REGISTRATION OF PET IN HEAD AND NECK CANCER TOMOTHERAPY TREATMENT: IS TEXTURE ANALYSIS A GOOD PREDICTOR?

A.CIARMATORI,

*Post-graduate school in medical physics, University of Bologna, via Massarenti 9,
40138 Bologna, Italy.*

ciarmatori.alberto@policlinico.mo.it

N.MAFFEI, C.VECCHI

*Physics Department, University of Bologna, via Irnerio 40
40138 Bologna, Italy*

G. GUIDI, B.FRANZONI, T. COSTI

*Medical Physics Department, University Hospital "Policlinico", Modena Italy, via del Pozzo 71
40121 Modena, Italy*

guidi.gabriele@policlinico.mo.it

¹⁸F-FDG positron emission tomography (PET) is widely used in Head&Neck radiation therapy target definition and tumor staging. In addition to these applications, this retrospective study focuses on the prediction of Texture Analysis respect to BTV (Biological Target Volume) deformation during radiation therapy treatment. 9 patients enrolled for Tomotherapy treatment have been included in this work. BTVs, based on Standardized Uptake Values (SUV), have been copied on treatment planning kVCT. Deformable registration have been performed along the different MVCT executed before each fraction of the treatment. SUV related texture features have been linked with tumor size variation. 8 of the 9 patients showed a substantial reduction of the size of the BTVs during the Tomotherapy treatment (range 8.6% - 33%). SUVmean and SUVmax, corrected for Partial Volume Effects, correlated ($r>0.9$) in case of BTVs greater than 7cc. For small lesion (<7cc) no relevant correlations have been founded.

1. Introduction

Many studies suggest that ¹⁸F-FDG positron emission tomography (PET) may bring important advantages for staging and radiotherapy planning in Head & Neck cancer patient[1]. Image guided radiation therapy (IGRT) and adaptive radiotherapy (ART) are relatively new techniques that consider tumor motion and tumor deformation during radiation therapy planning and during intra-fraction and inter-fraction radiation treatment[2]. This is very important not only for the reproducibility of patient position between subsequent fraction but also for organ at risk and target dimensions evaluation. Tumor regression is, in fact, a major feature in radiotherapy treatment response evaluation[3]. In these context texture analysis of PET images, a tool that reflects the underlying spatial variation and heterogeneity of voxel intensities within a tumour, may yield important predictive and prognostic information[4].

The first part of this retrospective study focused on the procedure for biological target volumes (BTVs) definition on PET images of 9 patients enrolled for fractionated Tomotherapy IGRT treatment. The second step consisted on BTVs structure deformation over the different fraction and on tumor regression evaluation. The last section focuses on the prediction power of standardized uptake value (SUV) related texture features for tumor regression

Keywords: Deformable registration, PET, Texture Analysis

2. Material and methods

Nine patients were enrolled in this study. Eligible patients had to have a pathologic diagnosis of head-and-neck cancer, be treated with definitive external beam RT, and had have FDG avid gross primary lesion. Patient underwent radiotherapy with simultaneous integrated boost (SIB) using IMRT techniques and a protocol comprising 66 Gy to the PTV66 (planning target volume; region of macroscopic tumour) and 60 Gy and 54 Gy to the regions with high risk (PTV60) and low risk (PTV54) of subclinical disease in 30-33 fractions in 6 weeks.

BTVs were defined, by a novel software with deformable registration and ROI mapping capability, starting from SUV_{max} thresholding. An IQ NEMA phantom filled with ^{18}F -FDG (4:1 ratio – hot spheres/background) was scanned with DSTE PET/CT (GE, Milwaukee, USA) and the images were reconstructed with the standard clinical protocol: OSEM – 2 Iteration – 20 Subsets – heavy Filter (Same for the enrolled patients). BTV_{20} (20% of SUV_{max}), BTV_{40} , BTV_{50} , BTV_{60} , BTV_{80} were drawn and the volumes of each ROIs were compared to the real volume of the relative hot sphere. IQ phantom scan was also used for partial volume effect (PVE) [5] and contrast recovery coefficient evaluation.

PET/CT images were then co-registered to the CT used for treatment planning and the BTVs were overlaid to last CT. BTVs, PTVs and CTVs were propagated on the MVCT, acquired during the pre-treatment fraction. Each MVCT per fraction were registered to the planning kVCT for following the size trend of irradiated volume during the Tomotherapy course.

SUV related texture feature were obtained for BTV_{20} , and BTV_{40} using CGITA [6] open software and then correlated with the angular coefficient of linear regression of tumor size vs day from first MVCT.

3. Results:

Target Definition: 40% of SUV_{max} is the threshold that minimize the difference between the measured and the real volume for lesion $> 2cm^3$ (all lesion considered were larger than $2 cm^3$).

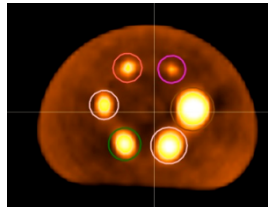


Figure 1 IQ NEMA Phantom PET Scan (4:1 - Ratio Hot Spheres/Background)

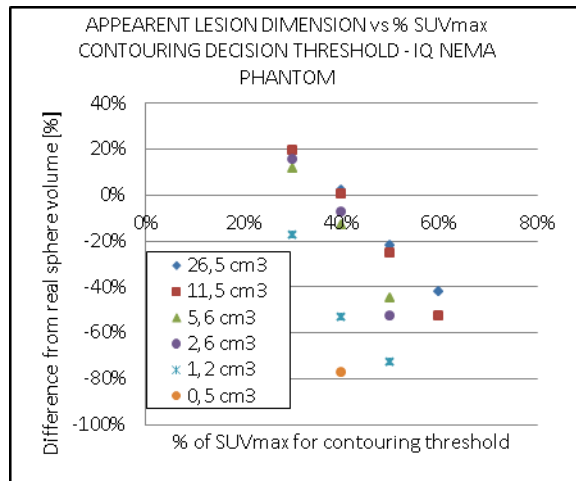


Figure 2 SUVmax thresholding

- As reported in literature [5] PVE has a non-negligible effects on real uptake estimation. The difference between measured and real concentration varies between -49,5% and -2,4% (0,5 cm³ – 26,5 cm³) for the maximum uptake inside a lesion and between -63.5% and -5,8% (0,5 cm³ – 26,5 cm³) for the average uptake.

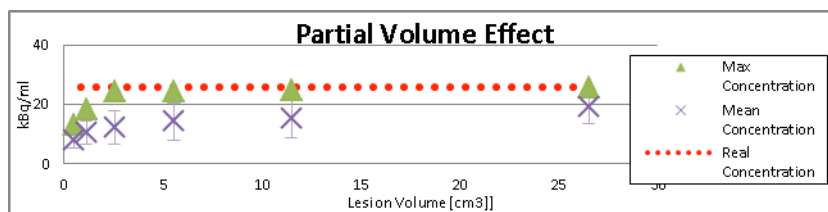


Figure 3 Partial Volume Effect

- ROI definition and ROI size distribution

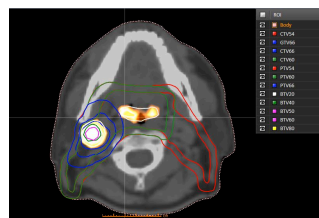


Figure 4 BTV and PTV contouring

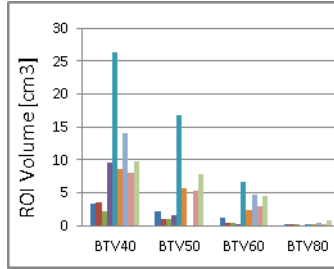


Figure 5 BTV size distribution

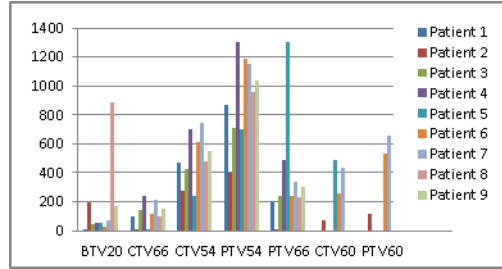


Figure 6 CTV & PTV size distribution

Patient were stratified according to lesion dimensions. Three groups have been defined :

1. BTV40>7cc → 6 subjects
2. BTV40<7 cc → 3 subjects
3. Totality → 9 subjects

- Tumor size trend was evaluated every about 6-7 fraction.

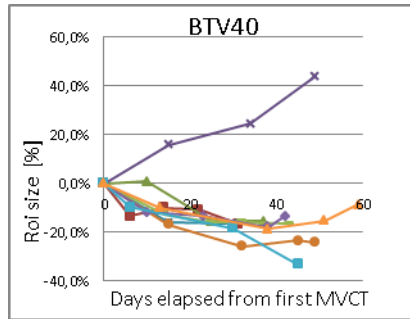


Figure 7 BTV40 size trend

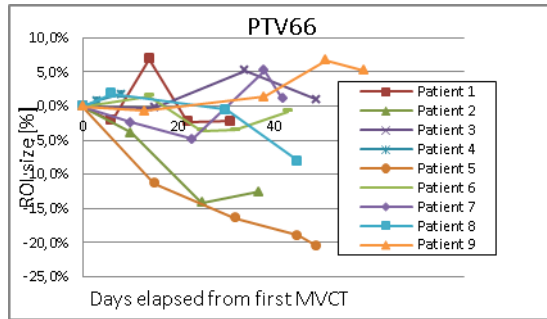


Figure 8 PTV66 size trend

- SUV related texture feature were extracted for BTV40 for each patient. In table 1 are resumed the feature analyzed.

Correlations between angular coefficient of linear regression of ROI size vs Days Elapsed from first MVCT (s. fig.7-8) for each patient and extracted texture feature were calculated in accordance with equation 1.

$$\text{Correl}(x, y) = \frac{\sum(x-\bar{x})(y-\bar{y})}{\sqrt{(\sum(x-\bar{x})^2)(\sum(y-\bar{y})^2)}} \quad (1)$$

No relevant correlation were found for the group 2(BTV<7cc) and 3(all patient) but group 1 (BTV>7cc) seems to show interesting result. Correlation matrix for Group 1 is reported in table 1.

BTV40>7cc	SUV Max	SUV Mean	SUV SD	SUV Skewness	SUV Kurtosis	SUV Entropy	SUV Variance	Vol
BTV40 regression	-0,91	-0,91	-0,85	-0,70	-0,61	-0,89	-0,68	-0,59
PTV66 regression	-0,64	-0,42	-0,71	-0,65	-0,40	-0,35	0,44	-0,28

Table 1 Correlation Matrix for Group 1 (BTV40 >7 cc)

4. Conclusions:

This study confirmed that threshold on 40% of SUV_{max} may lead to reliable results and that partial volume effect plays an important role on quantitative measurement in nuclear medicine. BTVs deformation/regression have been studied for 9 patient underwent to Tomotherapy treatment. Finally SUV related texture feature (in particularly PVE corrected SUV_{max} and PVE corrected SUV_{mean}) seems to have a good prediction power on 18F-FDG-avid zone of lesion regression larger than 7cc. However a larger number of patient is needed to validate the result before implementation in clinical practice.

5. Acknowledges:

The research is partially co-funded by the MoH (GR-2010-2318757) and Tecnologie Avanzate S.r.l.(Italy)

References

- 1 J.L Barker et al. FDG-PET/CT–GUIDED INTENSITY MODULATED HEAD AND NECK RADIOTHERAPY: A PILOT INVESTIGATION Wiley Periodicals, Inc. Head Neck 27: 478–487, 2005
- 2 L. Xing et al OVERVIEW OF IMAGE-GUIDED RADIATION THERAPY Medical Dosimetry, Vol. 31, No. 2, pp. 91-112, 2006
3. *Patrick Therasse et Al.* New Guidelines to Evaluate the Response to Treatment in Solid Tumors J Natl Cancer Inst 2000;92:205–16
4. S. Chicklore et. al Quantifying tumour heterogeneity in 18F-FDG PET/CT imaging by texture analysis Eur J Nucl Med Mol Imaging (2013) 40:133–140
5. O.G. Russel et al. Correction for Partial Volumes Effects in PET: Principle and Validation. Journal of Nuclear Medicine 1998, 39:904-911
6. Yu-Hua Dean Fang, Chien-Yu Lin, Meng-Jung Shih, et al., “Development and Evaluation of an Open-Source Software Package “CGITA” for Quantifying Tumor Heterogeneity with Molecular Images,” BioMed Research International, vol. 2014, Article ID 248505, 9 pages, 2014. doi:10.1155/2014/248505

SCRIPTING AUTOMATION AND BIOMECHANICAL MODELING FOR ADAPTIVE RADIATION THERAPY

C.VECCHI¹, G.GUIDI^{1,2}, N.MAFFEI¹, G.M.MISTRETTA, A.CIARMATORI², G.BALDAZZI¹, T.COSTI²

1: Physics Department, University of Bologna, 40138 Bologna, Italy

2: Medical Physics Department, University Hospital "Policlinico", Modena Italy

claudio.vecchi88@gmail.com, guidi.gabriele@policlinico.mo.it

Scripting automation offers the possibility to reduce involved resources in order to apply Adaptive Radiation Therapy (ART) in the clinical day routine. We used a Treatment Planning System (TPS) to achieve the goal of ART and speed up the whole process by script development. Nowadays, due to automation we could follow biomechanical organ motion and reduce time consuming. We presented the time gain and advantages between scripting automation and user interface approach. Using python scripting approach, we collected statistical volume-dose data of 51 patients (Head and neck, Prostate, SBRT Lung) treated by Tomotherapy. As novel biomechanical approach in radiation oncology, we focused on H&N results and we used script to analyze parotids organ variations of 23 patients during the course of therapy. We evaluated properties and motion of parotids system and we quantified the displacement of those glands during the treatment sessions compared to clinical aspects.

Keywords: script automation; biomechanics; radiotherapy.

1. Introduction

Adaptive Radiation Therapy (ART) technique begin to be a new standard for advanced radiotherapy treatment because offers the possibility to personalize and adapt the patient treatment plan based on anatomical organs deformation due to diagnostic imaging.

This technique needs to be investigated and automatized in order to apply it, in the clinical routine [1], limiting the request of resources. Our study is based on Treatment Planning System (TPS) that it allows the application of ART and the development of IronPython script (IS) in order to automatize and speed the inner operations of ART process [2]. The automatized approach has allowed collecting and evaluating statistical dose-volume data of 51 patients from Tomotherapy treatments.

As well as ART, biomechanics aspect in radiotherapy have grown in importance in the last decades. The major step was to focus on H&N pathology, which have such a critical aspects in clinical routine, caused by typical motion of the glands (e.g. parotids) during the therapy treatments [3]. We evaluated and analyzed the variations and displacement of parotids compared to the first treatment session, laying the foundation for an important research in the field of radiation therapy in the future also applicable to other diseases.

2. Materials and methods

2.1. Scripting automation in ART process

A mix of 23 H&N, 20 prostate and 8 Lung SBRT cases, amounting to 1340 MVCT were imported and post processed using TPS and python scripting. Each H&N patients received an MVCT (Mega-Voltage CT) for setup purpose. The course of treatment consists in 30 daily fractions (equivalent to 30 CT studies). Performing Adaptive RT workflow such import DicomRT studies, make rigid registration, copy ROI (Region Of Interest) from CT_n to CT_1 , perform deformable image registration (DIR), mapping ROI and extract the statistical data of the deformable doses and ROIs volume it is possible to follow the mechanical motion of the glands during therapy. We compare time consuming to perform both manual and automatic ART operations. We create a large patients database with the improvement effort by the scripting.

2.2. Scripting automation in biomechanics

During H&N treatments, parotids could have important quantitative variations in both dimension and position. Using scripts development, we analyzed the distance variations between these organs from therapy session to session.

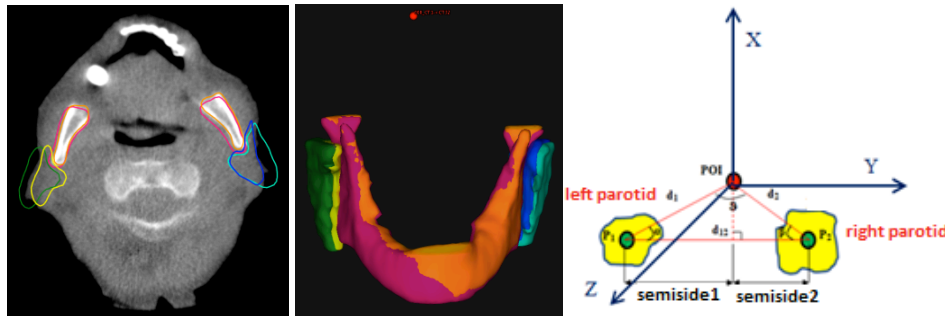


Fig. 1 – At left side: hybrid deformation of parotids and mandible for H&N patient. Right side: parotids problem modeled.

The script is launched in each patient after the deformation process occurs and it creates in automatic way a point of interest (POI) in the planning image (kVCT) exactly in the absolute coordinates point (0,0,0). The origin and points are to the other images (MVCT) but in different coordinates, based on the deformable grids. POIs are useful as a reference point in order to simulate the real system as a triangulation problem (e.g. See Fig. 1) and to calculate variables of system.

3. Results and Discussion

3.1. Script: time comparison between manual and automatic approach

Time consumption is related to HW and code optimization. Using IS, human tasks can be completed in nighttime, when the consoles are out of service, so to provide operators with important partial results and warning indicators during morning. ART results for each pathology are reported here as mean time for each operation groups.

	H&N			Prostate			SBRT Lung		
	A (min)	M (min)	Time gain (%)	A (min)	M (min)	Time gain (%)	A (min)	M (min)	Time gain (%)
CT/MVCT import - Rigid registration	30	50	40	43	55	22	7	10	30
CopyROI – Hybrid deformation – Mapping ROI	180	240	25	140	240	42	15	50	70
Statistical data extraction	60	350	83	60	360	83	3	70	96
Total time	270	640	148%	243	655	147%	25	130	196%

Table 1 – Time for ART in comparison.

The average time gain for the 3 pathology analyzed: H&N, Prostate and SBRT Lung is respectively of 370, 412 and 105 minutes. In terms of percentage, the time gain stands almost at 164%, equivalent to 5 hours for each patient processing.

3.2. Biomechanics: evaluation of parotids motion

$\Delta d_{12} = d_{12n} - d_{12_1}$: Average difference between parotid-parotid distance $|d_{12}|$ in the n_{th} session and the same distance in the first day of treatment. This quantity could give us information about the displacement of the system “Left Parotid” and “Right parotid”. A negative value means that parotids in the n_{th} session have decrease distance from the first session and vice versa.

$\Delta semiside = semiside_n - semiside_1$: Average difference between the semi side of one parotid in the n_{th} session and the same parotid semi side but in the first session. $\Delta semiside$ gives information about the displacement of one parotid independently to other parotid, because it is an asymmetric system.

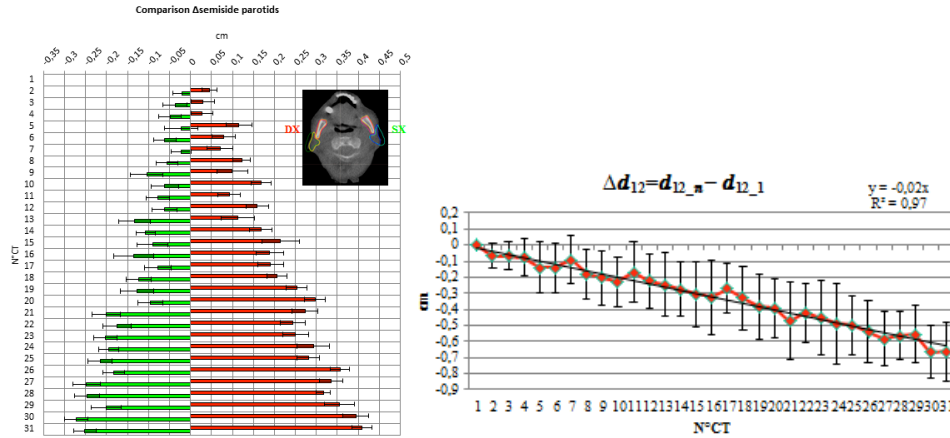


Fig. 2 – Left side: Δsemiside average trend for right parotid (red) and left parotid (green) Vs session numbers. Right side: Δd_{12} trend Vs session numbers.

4. Conclusions

ART automation involves in 3 main advantages:

1. Time reduction for patient and treatment post-process.
2. Limited user operation (only the dose warping operation are not automatized).
3. Saving labor costs and possible human errors during the manual approach.

The improvement in terms of time was significantly high, though some tasks need to be checked out by user. We report some critical aspects:

- Rigid transform matrix with rotation > 5 degrees need to be revised, due to abnormal ROIs and doses deformation.
- Copy ROIs operation sometimes failed and ROIs are copied outside the external body of the patient.

The above errors are detectable through some script for checking results.

- If DIR is carried out in studies with cranio-caudal slices < 6 cm in width, results are affected by errors (e.g. due to limited CT study used during the rigid registration).
- Limited MVCT FOV (Field-Of-View) for large patients can introduce errors during mapping ROI and dose warping (DW) for lateral structures.
- Prosthesis implants can produce artifacts both in DIR and DW.

The biomechanical results are: parotids have an asymmetric trend through sessions. The right parotid have a larger displacement than left one, and may be this need to be investigated if is imputable to the clock-wise rotation of the Tomotherapy and to some reconstruction algorithms.

The average distance between left / right parotid is decreasing with sessions number due the efficacy of radiotherapy treatment and because patients, usually, lose weight during treatments. This biomechanical analysis can help to understand the motion of the glands during course of therapy. Many tumor tissues decrease during the treatment and are replaced by the healthy tissue and organs that appear in motion.

5. Acknowledges

The research is partially co-funded by the MoH (GR-2010-2318757) and Tecnologie Avanzate S.r.l.(Italy)

6. References

1. R.W.J. Janssen, K.H. van der Boom, Development of a protocol-Driven Script Content Management System for a Commercial Radiation Therapy Treatment Planning System, *International Journal of Radiation Oncology* **87**:S619, 2013.
2. Clay Holdsworth, Sharon M. Hummel-Kramer et al., Scripting in Radiation Therapy: An Automatic 3D Beam-Naming System, *Medical Dosimetry* **36**:272-275, 2011.
3. Paul J. Keall, Sarang Joshi et al., Four-dimensional radiotherapy planning for DMLC-based respiratory motion tracking, *Med. Phys.* **32**:942-951, 2005.

AN ARTIFICIAL NEURAL NETWORK TO PREDICT TIME OF REPLANNING FOR TOMOTHERAPY TREATMENTS

N.MAFFEI¹, G.GUIDI^{1,2}, C.VECCHI¹, G.M.MISTRETTA, A.CIARMATORI², G.BALDAZZI¹, T. COSTI²

1: Physics Department, University of Bologna, 40138 Bologna, Italy

2: Medical Physics Department, University Hospital "Policlinico", Modena Italy

maffei.nicola87@gmail.com , guidi.gabriele@policlinico.mo.it

Abstract

The study has analyzed and validated methods for Adaptive Radiation Therapy (RT), whose goal is the optimization of the daily radiation treatment based on the anatomical variations and patient dosimetry. Using IGRT (Image-Guided Radiation Therapy) techniques, was conducted an analysis of 51 patients treated by Tomotherapy, subdivided by three pathology: Head and Neck (H & N), Prostate Adenocarcinoma (ADK) and Lung Stereotactic Body Radiation Therapy (SBRT).

Neural networks, developed and implemented in this work, allow to identify, within the statistical sample, the cases that reveal criticality not in line with the average trend of the patients. Getting information about the complex anatomy affected by deviations from the initial constraints and setting them from the time point of view, it becomes possible to plan the clinical activity and make the methods of warping usable for correction of the daily treatment delivery.

Among the various anatomical regions analyzed, the use of Adaptive RT techniques proved to be especially useful for parts subject to temporal variations in the course of the therapy. In particular, parotid glands, rectum, bladder, and lungs were sensitive organs for the study. The work lays the foundation for research studies regarding deformation of organ through biomechanical approach to validate a method intended, presumably in the near future, the real clinical practice.

Keywords: Adaptive Radiation Therapy, Neural Network, IGRT, Tomotherapy, Biomechanics.

1. Introduction

Volumetric-spatial changes of Organs At Risk (OAR) and tumor target, during Tomotherapy treatment, can alter the dose distribution with respect to the constraints outlined in the planning stages, causing possible recurrence of toxicity in short and long term. Mathematical methods for the evaluation of organ motion and registration algorithms make it possible to automatically generate hybrid Region Of Interest (ROI) on deformed Megavoltage CT (MVCT) images. To correct these anatomical and dosimetric differences compared to the original plan, it is necessary re-planning therapy. However, taking into account the time and cost for a daily re-planning, it is not, generally, sustainable for all patients in busy clinic. The neural networks presented in this work allow to identify cases that have developed critical volumetric and/or dosimetric variation, during the weeks of radiation treatment, making the Adaptive Radiation Therapy techniques truly applicable and sustainable.

2. Methods and materials

2.1 Clinical Data

The work is part of a research project funded by the Ministry of Health and has been developed at the Medical Physics and Radiation Oncology Department of the University Hospital of Modena. The study focuses on the technique of Image Guided Radiation Therapy (IGRT) through analysis of 51 patients divided into three pathologies: H & N, Prostate ADK and Lung SBRT. Within a dedicated experimental software, a hybrid algorithm of deformation automatically generates a mesh grid on the deformed ROI on daily MVCT images, starting from the contours on the kVCT image planning. The data are used to extract the volume and dose evolution during the course of therapy.

2.2 Neural Network Architecture

To quantify the added value of Adaptive RT techniques, an algorithm has been developed in which the volume and dose differences are identified in comparison with the first day of treatment. The statistical divergence, between the classical treatment plan and its daily optimization, is investigated. We used an unsupervised procedure on the dataset. In the research, a Cluster Analysis plays a discovery role of latent structures, in order to infer the most likely partition; then, Support Vector Machines (SVM) functions are used to identify its optimal separation hyper-plane. The algorithm was developed and implemented in MATLAB and it is structured in such a way to be able to identify three main phases (Figure 1). The parameters accounted for the analysis of each ROI are the volume (V) and the dose (D). In order to have all the information available, in addition to $D_{average}$, were considered also the percentages of D relative to the total volume fractions: D_{99} , D_{98} , D_2 , D_1 .

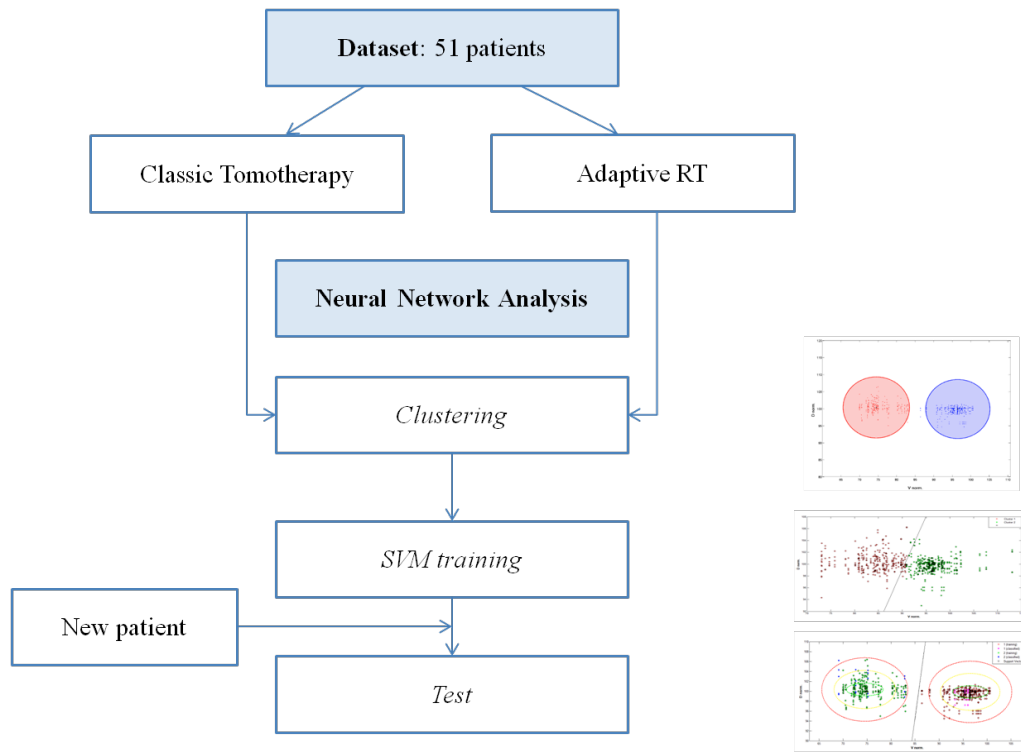


Figure 1 Neural Network architecture flow chart

- Step 1: Clustering

Weekly matrices of all patients analyzed are given in input and, by setting the ROI and parameters of the k-means algorithm (number of K clusters and distance metric), is obtained an output division of data into K groups, with information of the centroid coordinates, distances between each point from them and the Similarity Index.

- Step 2: SVM training

It instructs the classifier to generate a curve of optimal separation hyper-plane D / V and generate acceptance ranges around the centroids of the clusters. The hyper-plane has been obtained by setting the kernel as a linear function, with a compromise between the complexity of the decision rules based on the learning and performance on generalized samples not yet analyzed.

- Phase 3: Testing

New normalized patient data (in course of therapy) are initialized as input to the classifier. According to the arrangement of the latter in the plane, the algorithm assigns a class to new couples and quantifies the percentage changes in terms of D and V with respect to the patients' behavior, emerged during the learning process.

2.3 Predictive output cases

The output of new patient may reveals 4 different placement cases (

Table 1) of the parameters compared to 2 cluster: classical treatment plan and simulation of Adaptive RT, identified by the classifier based on the training.

- A. Predictive. The new patient will follow a weekly trend that is reasonably comparable with the average values of V and D obtained from gold patients post-processed.
- B. Adaptive. The warping methods highlighting differences in the morpho-dosimetric plan, provide added value not obtainable with the current gold standard. A physicist-physician meeting would be advisable to discuss a possible therapeutic intervention to reschedule re-planning.
- C. Error. Output unlikely, due to a bias of the software.
- D. Warning. The present patient should be monitored carefully. The latter may be characterized by an anatomical behavior or delivered dose out of the ordinary; otherwise, there may be a systematic error of patient positioning during treatment setup. The latter possibility can be identified with a multiple blinds on the behavior of other ROI of the same patient.

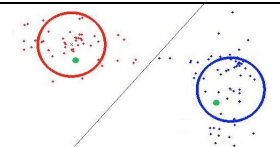
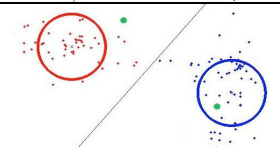
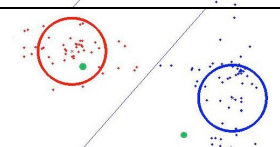
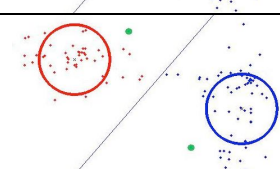
Case	Cluster A: not Deformed (Blue)	Cluster B: Deformed (Red)	Example images
A	Inside	Inside	
B	Inside	Outside	
C	Outside	Inside	
D	Outside	Outside	

Table 1 Neural Network Output cases

3. Results

Neural networks have given information related to the usefulness and applicability of the Adaptive RT techniques in the clinical setting. Given the learning phase, obtained by the morphological information of 1500 MVCT analyzed, the implemented algorithm was validated on test patients during treatment: 8 test cases of H&N region and prostate treatment were used.

Regarding H&N patients, the Figure 2 shows that in the first 3 weeks of therapy we can be predictive. At least 75% of patients exhibits an output in line with the average behavior of the patients analyzed. From the third week onwards occurs a reversal of the trend. In the last two weeks of therapy, all test patients would need a re-plan intervention due to changes on the body and especially in the parotid glands. The parotid glands are the evidence of a volume reduction of 30%, with an increase in the mean dose of approximately 10%.

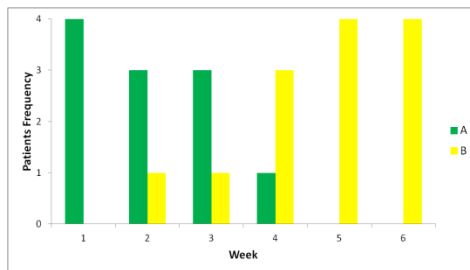


Figure 1 Test Patients Frequency vs. Week (H&N)

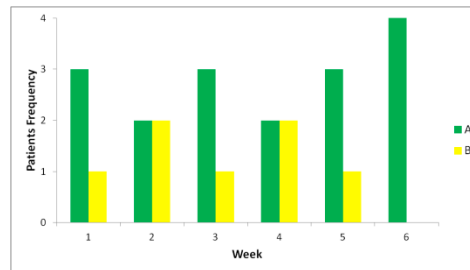


Figure 3 Test Patients Frequency vs. Week (ADK)

In the case of Prostate ADK is not possible to identify a clear time dependence (Figure 3) due to the fact that this anatomical region is characterized by OAR, as the rectum and bladder, where changes are strictly dependent by the arbitrary degree of readiness with which the individual patient comes to the therapy session (Figures 4 and 5). The methods of warping assume even greater importance in this context since, in the absence of predictive techniques for monitoring, would not be possible to notice any changes if not after the successful delivery of the dose to the patient. Volumetric changes of over 30% and 40% respectively for the rectum and bladder were found for 25% of the patients already in the mid-course of treatment.

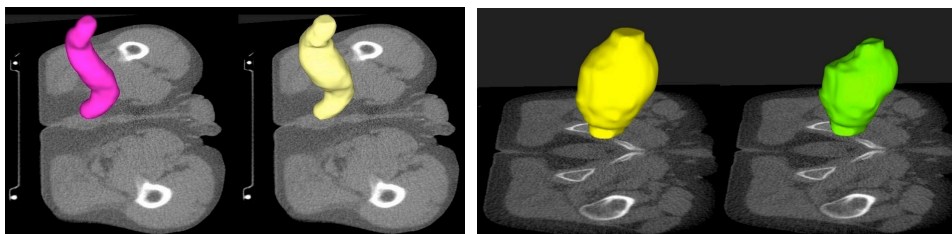


Figure 4 3D rectum reconstruction with/without adequate clinical preparation

Figure 5 3D bladder reconstruction with/without adequate clinical preparation

4. Conclusion

The research work conducted provides a tool that discriminates individuals or treatments not in line with the average patient trend and allows predicting an event or anomaly. The added value inherent the techniques of Adaptive RT, becomes in this way useful in clinical practice, applying it not to the totality of patients undergoing radiation oncology treatments, but targeted to a subset of these. Adaptive RT techniques have proved most useful for organs subject to temporal variations in the course of the therapy. These morphological changes can be analyzed and simulated in order to test the biomechanical prediction of moving target and to validate the clinical data in real-time Radiation Therapy. The realization of anthropomorphic phantoms that simulate the processes of organ deformation and the creation of realistic models relating to the dynamic movement of organs such as the parotid glands, rectum, bladder, ribs and lungs are currently under develop in the areas of experimental research activities suited to a steady increase in accuracy and efficiency for clinical practice of radiotherapy.

5. Acknowledges

The research is partially co-funded by the MoH (GR-2010-2318757) and Tecnologie Avanzate S.r.l.(Italy)

6. References

- [1] [Lee 2008] Lee C, Langeon K M, Lu W, *Evaluation of geometric changes of parotid glands during head and neck cancer radiotherapy using daily MVCT and automatic deformable registration*, Radiotherapy and Oncology 89, 81-88.
- [2] [Gulliford 2004] Gulliford S L, Webb S, Rowbottom C G et al., *Use of artificial neural networks to predict biological outcomes for patients receiving radical radiotherapy of the prostate*, Radiotherapy and Oncology 71, 3–12.
- [3] [Murphy 2008] Murphy M J, *Using Neural Networks to Predict Breathing Motion*, 7th International Conference on Machine Learning and Applications.
- [4] [Schwartz 2013] Schwartz D L, Garden A S, Shah S J et al., *Adaptive Radiotherapy for Head and Neck Cancer: Dosimetric Results from a Prospective Clinical Trial*, Radiotherapy and Oncology 106, 80-84.
- [5] [Nishi 2013] Nishi T, Nishimura Y, Shibata T, *Volume and dosimetric changes and initial clinical experience of a two-step adaptive intensity modulated radiation therapy (IMRT) scheme for head and neck cancer*, Radiotherapy and Oncology 106, 85-89.

- [6] [Barker 2004] Barker J L, Garden A S, Ang K K et al., *Quantification of volumetric and geometric changes occurring during fractionated radiotherapy for head and neck cancer using an integrated CT/linear accelerator system*, Int. J. Radiation Oncology Biol. Phys., Vol. 59, No. 4, 960–970.
- [7] [Scalco 2013] Scalco E, Fiorino C, Cattaneo G M et al., *Texture analysis for the assessment of structural changes in parotid glands induced by radiotherapy*, Radiotherapy and Oncology 109, 384–387.

REAL-TIME MODEL FOR ADAPTIVE RADIATION THERAPY: A BIOMECHANICAL APPROACH USING A LEGO MINDSTORMS

G.GUIDI^{1,2}, N.MAFFEI¹, C.VECCHI¹, G.M.MISTRETTA, A.CIARMATORI²,
G.BALDAZZI¹, T. COSTI²

1: Physics Department, University of Bologna, 40138 Bologna, Italy

2: Medical Physics Department, University Hospital "Policlinico", Modena Italy

guidi.gabriele@policlinico.mo.it , maffei.nicola87@gmail.com

ABSTRACT

The development of high complex methods of irradiation in radiotherapy, to avoid divergence of the treatments compared to the constraints outlined in the planning stages, has introduced new fields of research, such as organ motion and deformation.

Taking into account the dynamics of breathing, the four-dimensional computed tomography (4DCT) allows to follow these steps, involving different anatomical conditions at progressive time steps. However, it remains crucial, the analysis of the artifacts in the breathing phase caused by the irregularity of the respiratory of patients undergoing radiation treatments.

This study represents a first approach to the biomechanical evaluation breathing using humanoid robot. For Adaptive Radiation Therapy (RT) purpose, an anthropomorphic phantom was built using LEGO Mindstorms and programmed in LabVIEW to simulate the processes of breathing, tumors and organ motion in the lung district. The intent is to simulate the human physiology to follow and predict changes in the morpho-dosimetry of patients in order to increase the accuracy and improve efficiency of clinical radiotherapy

Keywords: Biomechanics, LEGO Mindstorms, Adaptive Radiation Therapy.

1. INTRODUCTION

The real-time imaging represents one of the greatest challenges in modern radiotherapy. The standard CT acquisition "freeze" images of tumor and Organs at Risk (OAR) in an arbitrary respiratory phase. In this configuration, are possible systematic errors due to incorrect positioning of the patient or random error related to the breathing motion. The lack of knowledge, of the exact location of the tumor and surrounding organs, add degrees of uncertainty during the contouring, planning and delivery of the patient treatment. Information related to respiratory motion can be obtained by means or by a 4DCT study [1]. However, it remains a fundamental understanding of the dynamics of internal organ motion of the rib cage of the patient. If by gating systems it is possible to reconstruct the patient's respiratory route, this is not easily deductible for tumor mass submitted to compressions and expansions related to the breathing sinograms. This uncertainty could be crucial for organs constrains (e.g. rib) in some treatment, such in lung stereotactic treatment (SBRT). The impact of respiratory irregularity is actually taken into account in this preliminary study, through the developing and programming of an anthropomorphic phantom to simulate precisely those trends in real-time during the breathing of patient.

2. METHODS AND MATERIALS

2.1 ADAPTIVE RT

The goal of the Adaptive Radiation Therapy methods is the daily optimization of radiotherapy treatment plan based on the anatomical variations and patient dosimetry or the real-time adaptation to the variance (e.g. due to the organ motion) [2]. To actually make this technology usable in the daily clinical practice, algorithms, hybrid recording, scripting automation processes and predictive analysis made it possible to quantify anatomical and dosimetric differences of patients, during the course of therapy, compared with the original plan. For clinical Adaptive RT, makes the fundamental research in biomechanics of morphological variations, the creation of realistic models of the motion of organs in real-time.

2.2 PHANTOM CONSTRUCTION

Within the project funded by the Ministry of Health, an anthropomorphic phantom was developed at the Medical Physics and Radiation Oncology Department of the University Hospital of Modena. The robot was built using LEGO Mindstorms programmable EV3 , adding to the Core Set of base expansion set main features of the LEGO [3,4] (Figure 1):

Motors and servomotors

- Sensors touch
- Gyro sensors
- Ultrasonic Sensors
- IR Sensors
- Light Sensors
- Remote control
- Programmable CPU .

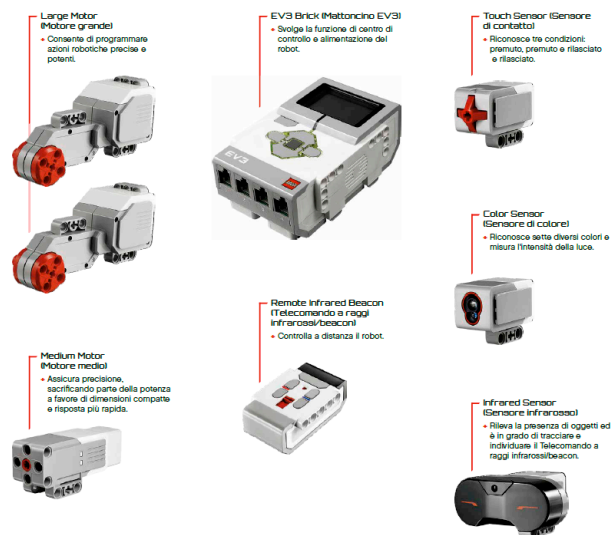


Figure 1 Sample of LEGO Set

By combining these innovations with the complete freedom offered by building bricks, it was possible to achieve a low cost solution for a home-made anthropomorphic phantom (Figure 2) for medical physics purposes that mimics the motion of pulmonary region, in paediatric scale. The gears and robotic parts are generally made of plastic material and this avoids the production of artifacts, of some commercial phantom, during the CT acquisition.

The experimental idea was developed from “zero”, because no instruction is available and it has required to associate knowledge’s of engineering, mechanical, physics and medical physics with added of fantasy, in order to obtain something reliable, reproducible and flexible to simulate of the breathing motion

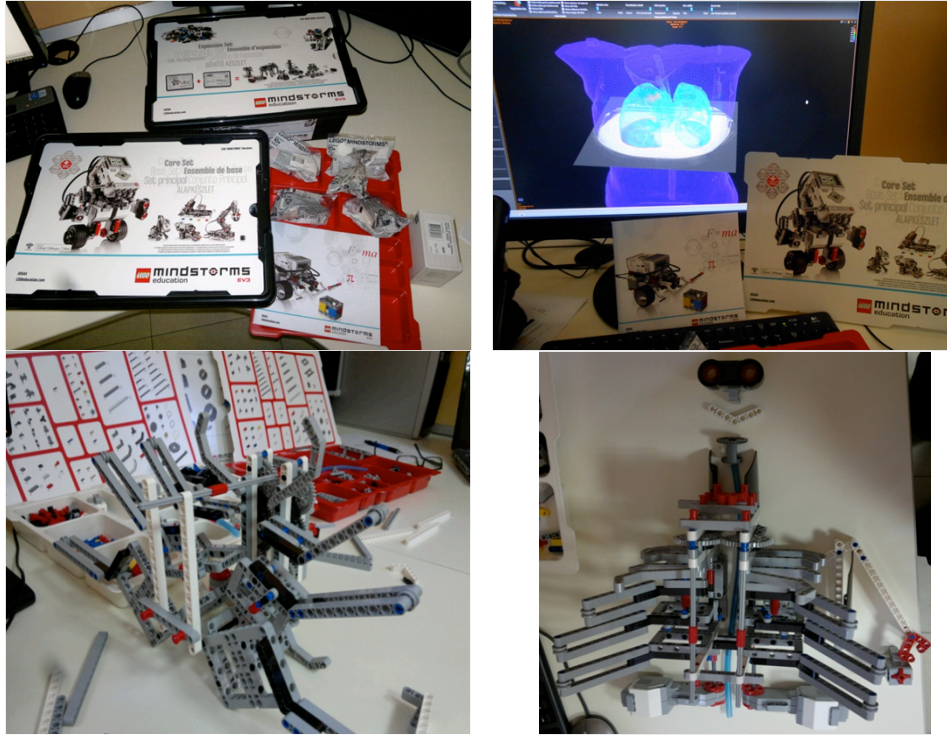


Figure 2 Sample step design of the LEGO Robot

3. RESULTS

To faithfully simulate the dynamics of breathing, the phantom is equipped with a system of mechanical gears that allows the simulation of 4 ribs with simultaneously and independent motion at different angular velocities. As the human breathing, resulting that the lower ribs have a greater opening instead of the upper ribs of the chest. Within the thoracic cavity takes place a housing of two tumor masses whose semi-random movement is monitored by the presence of the markers that allow us to follow and recognize the process of organ motion within the acquired images.

The breathing rate is provided as input by the Intelligent Brick with a LINUX operating system with CPU and 64 MB RAM. The system is fully programmable using LEGO Mindstorms Educational EV3 software based on LabView (Figure 3).

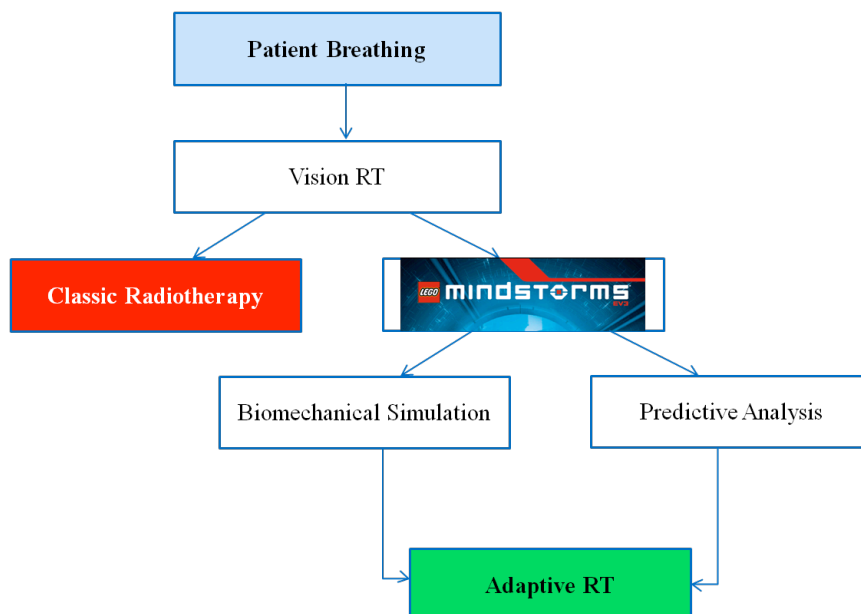


Figure 4 Flowchart of the biomechanical simulation

4. CONCLUSION

Radiation treatment of lung area require adequate representation of the anatomical region of interest, for a correct calculation of the amount of dose delivered. A high degree of sensitivity relative to organs at risk and target tumor becomes so crucial to ensure that the dose distributions are consistently aligned with the therapeutic targets, without introducing additional risks. The creation of realistic models relating to the dynamic movement of organs, real-time tools, in conjunction with predictive analysis related to the Adaptive RT processes, are areas of experimental research activities suited to a steady increase in the accuracy, efficiency of clinical radiotherapy and the development of system in real-time.

5. ACKNOWLEDGES

The research is partially co-funded by the MoH (GR-2010-2318757) and Tecnologie Avanzate S.r.l.(Italy)
The LEGO MINDOSTORM was develop thanks to a donation

6. REFERENCES

- [1] [Malone 2014] Malone C, Rock L, Skourou C, *Efficacy evaluation of retrospectively applying the Varian normal breathing predictive filter for volume definition and artifact reduction in 4D CT lung patients*, Journal of Applied Clinical Medical Physics, vol 15, num 3.
- [2] [Castillo 2014] Castillo S J, Castillo R, Balter P, et al., *Assessment of a quantitative metric for 4D CT artifact evaluation by observer consensus*, Journal of Applied Clinical Medical Physics, vol 15, num 3.
- [3] [Jeong 2011] Jeong H S, Han Y, Kum O et al., *Development And Evaluation of a Phantom for Multi-purpose Dosimetry in IMRT*, Nuclear Engineering And Technology, Vol.43 No.4.
- [4] [Cruz-Martín 2012] Cruz-Martín A, Fernández-Madrigal J A, Galindo C et al., *A LEGO Mindstorms NXT approach for teaching at Data Acquisition, Control Systems Engineering and Real-Time Systems undergraduate courses*, Computers & Education 59, 974–988.

TOWARD AN OPTIMIZATION OF RADIOTHERAPY TREATMENT IN HUMANS GLIOBLASTOMA BASED ON A CANCER STEM CELLS KINETIC MODEL

ANDREA CORAZZA, LUIGI MANCO

*Post-graduate school in medical physics, University of Bologna, via Massarenti 9,
40138 Bologna, Italy.*

GASTONE CASTELLANI, ENRICO GIAMPIERI, DANIEL REMONDINI

*Physics and Astronomy department, University of Bologna, viale Berti Pichat 6/2,
40138 Bologna, Italy.*

ROBERTO SGHEDONI, MAURO IORI

*Medical Physics Unit, Arcispedale Santa Maria Nuova Hospital IRCCS, Viale Umberto I° 50
42123 Reggio Emilia, Italy*

ALESSANDRO TURRA

*Medical Physics Unit, Arcispedale Sant'Anna Hospital, Via Aldo Moro 8,
44124 Cona, Ferrara, Italy*

Glioblastoma are the most common and malignant primary brain tumors and are aggressively treated with surgery, chemotherapy and radiotherapy.

Present radiotherapy treatment plans are based on standard fractionation concepts and don't take into account recent developments in biology, as the discovery of the presence of radioresistant cancer stem cells along with differentiated cells inside the tumor.

Kinetic models involving both these cell populations exist and they can help the evaluation of different dose schedules as well as the research of optimized schedules.

The model implemented considers the radioresistance acquired after a radiation dose and is based on parameters that could be deduced from gene expression data, advanced magnetic resonance techniques as magnetic resonance spectroscopy, or estimates from previous experiences.

Keywords: glioblastoma, radiotherapeutic treatment, kinetic model, stem cells

1. Introduction

Glioblastoma are the most common and malignant primary brain tumors and are aggressively treated with surgery, chemotherapy and radiotherapy.

Present radiotherapy treatment plans are based on standard “radiobiology 4-Rs” (Reassortment, Repair, Repopulation, Reoxygenation), that are the processes that let foresee cellular radioresistance or radiosensitivity according to metabolic pathway expression, cellular cycle, tissue oxygenation and population growth. These 4-Rs are evaluated studying clonogenic curves of differentiated cancer cells and they have led to standard fractionation concepts.

Recent developments in biology showed that in glioma, as well as in other malignancies, cancer stem cells (CSC) exist along with standard and well-studied differentiated cancer cells. CSCs manifest radioresistant phenotype while differentiated sensitive cells (DSC) show greater radiosensitivity.

Increasing evidences of CSCs role in treatments and in the pathology progress/eradication can be found in contemporary literature^{1, 2, 3}. They take account of the fact that CSC need to be treated using specific schedules, and that post-treatment surviving CSC populations can repopulate the tumor.

Among other, CSCs growth can be estimated by mathematical models⁴ that can describe the cell killing after each radiation event, the different radio-resistance of CSC and DSC, the proliferation rate of CSC and DSC, the reversion rate from the differentiated phenotype to the undifferentiated one and the maturation of CSC into DSC. Such a model can lead to innovative treatment plans , adjusted to follow CSC development.

All these processes are driven by experimental/empirical parameters such as proliferation rates, fraction of reverting DSCs , quiescence times and parameters characterizing SLRCs and DSCs response to radiation .

The aim of this study was to adapt to human's glioma the existent model, developed on murine population⁴, in order to compare different radiation dose schedules and find optimized ones.

2. Material and methods

Human's biological parameters used within the model were obtained with different approaches.

Some of the parameters for the kinetic model are based on gene expression data available from public repository. Among various datasets, we selected two experiments, identified by the Accession number : GSE1923 and GSE1128. The first dataset has 15 Samples and is on the Identification of PDGF-dependent patterns of gene expression in U87 glioblastoma cells, while the second experiments has 11 Samples and is on PDGF-induced genes regulated by the PI3K and MEK/ERK signaling pathways. Both experiments contains more than 20000 probesets.

A further approach, that could lead to the evaluation of tumor proliferation parameters, is the ¹H-Magnetic Resonance Spectroscopy (MRS) that can provide in-vivo biochemical information in a non-invasive way^{5, 6, 7}. Although this in-vivo technique can hardly provide information about stem cell (such an evaluation could be properly performed only with high resolution MRS), however it can describe the cancer differentiated population in terms of N-Acetyl Aspartate (NAA), Choline (Cho), Creatine (Cr), Lactate (Lac) and Lypides (Lip) metabolites ratios.

3. Conclusions:

Actual radiotherapeutic plans treating gliomas are based on standard fractionation concepts and don't take into account the differences between sub population of stem and differentiated cells.

Including glioma cancer stem cells contribution in the model used to evaluate treatment plans could help comparing different radiation dose schedules and could help finding optimized ones.

Acknowledgments:

GC,DR and EG acknowledge the INFN project MERIDIAN.

References

1. Bao S, Wu Q, McLendon RE, Hao Y, Shi Q, Hjelmeland AB, Dewhirst MW, Bigner DD, Rich JN. : Glioma stem cells promote radioresistance by preferential activation of the DNA damage response. *Nature* 444(7120):756-60, 2006

2. Chen J, Li Y, Yu TS, McKay RM, Burns DK, Kernie SG, Parada LF. : A restricted cell population propagates glioblastoma growth after chemotherapy. *Nature* 488(7412):522-6, 2012
3. Liu G, Yuan X, Zeng Z, Tunici P, Ng H, Abdulkadir IR, Lu L, Irvin D, Black KL, Yu JS. : Analysis of gene expression and chemoresistance of CD133+ cancer stem cells in glioblastoma. *Mol cancer* 5:67, 2006
4. Leder K, Pitter K, Laplant Q, Hambardzumyan D, Ross BD, Chan TA, Holland EC, Michor F. : Mathematical modeling of PDGF-driven glioblastoma reveals optimized radiation dosing schedules. *Cell* 156(3):603-16, 2014
5. Ramm P, Bettscheider M, Beier D, Kalbitzer HR, Kremer W, Bogdahn U, Hau P, Aigner L, Beier CP. : ¹H-nuclear magnetic resonance spectroscopy of glioblastoma cancer stem cells. *Stem Cells* 20(12):2189-95, 2011
6. Cuperlovic-Culf M, Ferguson D, Culf A, Morin P Jr, Touaibia M. : ¹H NMR metabolomics analysis of glioblastoma subtypes: correlation between metabolomics and gene expression characteristics. *J Biol Chem* 287(24):20164-75, 2012
7. Guidoni L, Ricci-Vitiani L, Rosi A, Palma A, Grande S, Luciani AM, Pelacchi F, di Martino S, Colosimo C, Biffoni M, De Maria R, Pallini R, Viti V. : ¹H NMR detects different metabolic profiles in glioblastoma stem-like cells. *NMR Biomed.* 27(2):129-45, 2014

ADVANCED MRI TECHNIQUES USED TO EVALUATE PARAMETERS FOR A GLIOBLASTOMA GROWTH KINETIC MODEL IN HUMAN

LUIGI MANCO, ANDREA CORAZZA

*Post-graduate school in medical physics, University of Bologna, via Massarenti 9,
40138 Bologna, Italy*

GASTONE CASTELLANI, DANIEL REMONDINI, ENRICO GIAMPIERI

*Physics and Astronomy department, University of Bologna, viale Berti Pichat 6/2,
40138 Bologna, Italy*

ALESSANDRO TURRA

*Medical Physics Unit, Arcispedale Sant'Anna Hospital, Via Aldo Moro 8,
44124 Cona, Ferrara, Italy*

Glioblastoma multiforme is the most common and aggressive primary brain malignancy, with poor prognosis and a lack of effective therapeutic options: after surgical resection (if possible) they are treated with radiotherapy and/or chemotherapy.

Mathematical models can take into account tumor cellular heterogeneity and dynamically acquired radio-resistance to predict the effectiveness of different radiotherapy schedules. The application of kinetic model in human glioblastoma needs a series of specific parameters to describe tumor growth and histology of representative tissue could lead to the determination of such parameters.

Using MRI advanced techniques could help evaluating these parameters non-invasively and in a more local specific way.

Keywords: glioblastoma; magnetic resonance spectroscopy imaging; dynamic susceptibility-contrast magnetic resonance imaging.

1. Introduction

Glioblastoma multiforme (GBM), WHO (World Health Organization) classification name “glioblastoma”, is the most common and aggressive primary brain malignancy, with poor prognosis and a lack of effective therapeutic options (surgical resection followed by radiotherapy and/or chemotherapy). GBM tumors rapidly growing are characterized by the presence of small areas of necrotizing tissue that is surrounded by anaplastic cells. Furthermore, increasing evidences of cancer stem cells role in the pathology progress/eradication can be found in contemporary literature.^{1, 2, 3}

The development of high-field magnetic resonance allowed use of advanced magnetic resonance imaging (MRI) techniques, such as spectroscopy, perfusion and functional imaging to improve the imaging of brain tumors. In addition to the anatomic or structural information available with conventional MRI, advanced MRI techniques also provide physiologic information about tumor metabolism and hemodynamics.

Recent studies on murine population suggested the applicability of mathematical models⁴, based on theoretical and experimental approaches, to describe tumor growth and metabolism. These models can take into account tumor cellular heterogeneity and dynamically acquired radioresistance to predict the effectiveness of different radiotherapy schedules.

The application of kinetic model in human GBM needs a series of specific parameters to describe tumor growth and histology of representative tissue could lead to the determination of such parameters. This can

be made either with a closed CT or MR directed stereotactic needle biopsy or via an open craniotomy. Stereotactic biopsy is often not achievable because of its high risks of morbidity and mortality for the patient. Moreover, the tissue chosen by neurosurgeon during surgery could be too small or it could be not representative of the whole tumor.

The aim of this study is to use functional in vivo techniques MR spectroscopic imaging (MRSI) and dynamic susceptibility-contrast MR imaging (DSC-MRI) to assess tumor metabolism and vasculature characteristics quantitatively, in order to use patient-specific mathematical models to predict radiotherapy effectiveness.

Material and methods

The evaluation of these parameters could be done using advanced MRI techniques as MRSI and DSC-MRI on a 1.5 T scanner (Philips Achieva, Best, The Netherlands) installed at Neuroradiology Unit, Sant'Anna Hospital in Ferrara.

Using MRSI let us evaluate information about brain tumor cellularity and cell membrane breakdown, cellular energetics, neuronal activity, and macroscopic necrosis thanks to its ability to distinguish signals from metabolites such as choline (Cho), creatine (Cr), N-acetylaspartate (NAA), Lactate (Lac). In addition, a multivoxel spectroscopy study enables to characterize metabolism in different tumor region.⁵

DSC-MRI utilizes very rapid imaging to capture the first passage of intravenously injected paramagnetic contrast agent. By kinetic analysis of these data, hemodynamic indices, namely, cerebral blood flow (CBF), cerebral blood volume (CBV), and mean transit time (MTT), can be derived.⁶

Furthermore, it may be possible to use these two techniques in a multi-parametric evaluation in order to better select the region examined with MRSI, to describe region metabolism and estimate proliferative ratio or cellularity.⁷

2. Conclusions:

Currently, parameters used in kinetic models describing tumor growth and metabolism can be obtained by invasive (and even surgical) ways.

MRI advanced techniques could help evaluating these parameters non-invasively and in a more local specific way. At last, mapping tumor metabolism voxel-specifically could help, using mathematical models, the prediction of radiotherapy effectiveness.

Acknowledgments:

GC,DR and EG acknowledge the INFN project MERIDIAN

References

1. Bao S, Wu Q, McLendon RE, Hao Y, Shi Q, Hjelmeland AB, Dewhirst MW, Bigner DD, Rich JN. : Glioma stem cells promote radioresistance by preferential activation of the DNA damage response. Nature 444(7120):756-60, 2006

2. Chen J, Li Y, Yu TS, McKay RM, Burns DK, Kernie SG, Parada LF. : A restricted cell population propagates glioblastoma growth after chemotherapy. *Nature* 488(7412):522-6, 2012
3. Liu G, Yuan X, Zeng Z, Tunici P, Ng H, Abdulkadir IR, Lu L, Irvin D, Black KL, Yu JS. : Analysis of gene expression and chemoresistance of CD133+ cancer stem cells in glioblastoma. *Mol cancer* 5:67, 2006
4. Leder K, Pitter K, Laplant Q, Hambardzumyan D, Ross BD, Chan TA, Holland EC, Michor F. : Mathematical modeling of PDGF-driven glioblastoma reveals optimized radiation dosing schedules. *Cell* 156(3):603-16,2014
5. D.P.Souares, M.Law : Magnetic resonance spectroscopy of the brain: review of metabolites and clinical applications. *Clinical Radiology* 64,12-21,2009
6. Leif Ostergaard : Principles of Cerebral Perfusion Imaging by Bolus Tracking. *Journal of Magnetic Resonance Imaging* 22:710-717,2005
7. Lupo J.M., Cha S., Chang S.M., Nelson S.J. : Analysis of metabolic indices in regions of Abnormal Perfusion in Patients with High-Grade Glioma.*AJNR Am J Neuroradiol* 28:1455-61, 2007

S1C: Cardiovascular - Fluid and Vessels - valves

Chairs: Romano Zannoli, Yos Morsi

ELECTRO-OSMOTIC FLOW OF POWER-LAW FLUIDS AND HEAT TRANSFER IN A MICRO-CHANNEL:APPLICATIONS TO HEMODYNAMICS

AMIT MONDAL

MODELS STUDIES ON THE ROLE OF VIBRATION IN THE DEVELOPMENT OF ANEURYSMS

DIETER LIEPSCH

COMPARISON OF VARIOUS HEMODYNAMIC MODELS FOR APPLICATIONS TO CFD IN STENTED ARTERIES

FATHIA CHABI

THE FULL RADIAL PULSE TRANSIT TIME IS A NEW PARAMETER OF EVALUATION ATHEROSCLEROSIS

QUANYU WU

COLD PRESSURE TEST AND PERIPHERAL VASCULAR RESPONSE IN HEALTHY PATIENTS: TEACHING VASCULAR PHYSIOLOGY TO MEDICINE STUDENTS

CRISTIANO PERON

FORCED OSCILLATION PHASE VELOCITY ON LIVING LARGE VESSEL

EZIO CAROLI

THE INFLUENCE OF STENOSIS ON THE WALL SHEAR STRESS AND FLOW RATE IN THE COMMON CAROTID ARTERY BIFURCATION FOR UNSTEADY FLOW. NUMERICAL ANALYSIS

NADIA ANTONOVA

A LINEAR VISCOELASTIC MODEL FOR ARTERIAL PULSE PROPAGATION

ANDREA GIUSTI

MODELS STUDIES ON THE ROLE OF VIBRATION IN THE DEVELOPMENT OF ANEURYSMS

D.Liepsch¹, A.Balasso², S. Frolov³

¹*University of Applied Sciences Munich and*

²*Interdisciplinary Research Laboratory of the Klinikum rechts der Isar der TU Munich*
³*Chair of Biomedical Technology, TU Tambov, Russia*

Investigations into the development of aneurysms neglect the vibration activity at the blood vessel wall. When considering the development of aneurysm many factors must be considered: flow shear stresses on the vessel wall, wall elasticity, blood pressure, pulsatility, the non-Newtonian flow behavior of blood, and vibration. Vibrational activity arises under a variety of circumstances, e.g., in small aneurysms where vortices are created. Vortices cause velocity fluctuations which cause the wall to vibrate. Initially the vibrational intensity is smaller than the average pulse intensity. However, as the aneurysm increases in size, smaller, additional vortices arise. The energy exchange in these smaller areas increases, resulting in higher wall vibration. Physiological models were used for flow visualization, in addition to velocity measurements with a LDA. Mural vibrations were measured with a high resolution laser vibrometer. To confirm model results, wall vibrations of 2200 Hz were measured in a rabbit at an AV fistula. The vibrations immediately formed an aneurysm. Vibrations with frequencies up to and exceeding 550 Hz must be investigated in more detail in the cerebral arterial system, especially in areas prone to aneurysm. Low shear inside aneurysms may foster the formation of thrombogenesis. It remains to be investigated how these areas are affected by stent placement.

Keywords: Laser vibrometer, vibrations, aneurysm

COMPARISON OF VARIOUS HEMODYNAMIC MODELS FOR APPLICATIONS TO CFD IN STENTED ARTERIES

F. CHABI^{a,*}, S. CHAMPMARTIN^b, C. SARRAF^a, R. NOGUERA^a, B. MAUREL^c

^aENSAM, Arts et Métiers, ParisTech, 151 boulevard d'Hopital, Paris, 75013, France

^bLAMPA, Arts et Métiers, ParisTech d'Angers, 2 boulevard du Ronceray, Angers, 49035, France

^cCHRU Lille, Vascular Surgery, Hôpital Cardiologique, Lille, 59037, France

This work assesses three hemodynamic models for the numerical modeling of intra-stent flows. These are the classical Poiseuille model (PM), the simplified pulsatile model (SPM) and the complete pulsatile model (CPM) based on the analysis of Womersley. They are applied to the physiological flow rate of a stented left coronary artery. The CFD package "Ansys Fluent 14.5" is used to compute the main features of the flows. The results show large differences between the steady and unsteady models notably for the wall shear stress and the re-circulation lengths, which are known to promote intra-stent restenosis. The PM is obviously not pertinent to calculate the flows involved in intra-stent restenosis. The CPM and SPM give close results but the latter model is by far less time-demanding and should be preferred.

Keywords: pulsatile physiologic flow; intra-stent flow; restenosis.

1. Introduction

According to the World Health Organization, 29% of the 56 million deaths worldwide in 2001 could be attributed to cardiovascular diseases. They are often due to a decrease of the diameter of the arterial lumen called stenosis. Available therapeutic means are based on drug delivery or surgery. Nowadays, stent implants are the most widely used angioplasty procedures for cardiovascular diseases. The first implants were bare metal stents, which gave up to 20-30% failure rates (in-stent restenosis)¹. Consecutively, drug-eluting stents were designed in the 2000s and gave good results against restenosis despite a significant additional cost. Intra-stent restenosis is a multifactorial problem. Besides human factors, it depends on the manner cardiologists implement the stents, its design and the drug used. It is also strongly coupled to the blood flow dynamics around the stent struts. Thus it is essential to characterize the features of the in-stent blood flows. In most analytical and numerical approaches found in literature, the blood flow is modeled as a steady Poiseuille flow², or as a Poiseuille flow whose mean velocity is unsteady³. This work presents a comparison of these simplified models with a more complete pulsatile model based on the analysis of Womersley⁴.

2. Hemodynamic models

In this work, we assume that the blood behaves as a Newtonian incompressible fluid and the vascular wall is not deformable and impermeable. For the physiological flow under consideration here, the blood flow is laminar. The seminal model for the steady laminar flow of a Newtonian incompressible fluid (dynamic viscosity μ , density ρ) in a pipe of radius R is the Poiseuille profile:

$$u(r) = 2\bar{V} \left(1 - \frac{r^2}{R^2}\right). \quad (1)$$

where \bar{V} is the average blood flow velocity and r is the radial coordinate. This model (PM) is by far the most used model in the previous studies because of its simplicity but evidently it cannot account for the

pulsatility of real flows. To overcome this problem, many authors utilize a simplified pulsatile model (SPM) based on the previous one:

$$u(r, t) = 2V(t) \left(1 - \frac{r^2}{R^2}\right). \quad (2)$$

where $V(t)$ is the unsteady average blood flow velocity. The main criticism to this model is that it misrepresents the profiles when the pulsatile effects are important. The complete resolution of the pulsatile flow (pulsation ω) in a tube of circular and constant cross section was provided by Womersley⁴ in 1955 and Atabek in 1961⁵.

$$u(r, t) = \frac{A_0 R^2}{4\mu} \left(1 - \frac{r^2}{R^2}\right) + \Re \left\{ \sum_{n=1}^{\infty} \frac{\tilde{a}_n}{i \rho n \omega} \left[1 - \frac{J_0(i^{3/2} \alpha_n \frac{r}{R})}{J_0(i^{3/2} \alpha_n)} \right] e^{i n \omega t} \right\}. \quad (3)$$

where J_0 is the Bessel function of the first kind of zero order, $\tilde{a}_n = A_n - i B_n$ is the complex amplitude of the n th harmonics of the pressure gradient, \Re is the real part of a complex number and $\alpha_n = R \sqrt{n \rho \omega / \mu}$ the generalized Womersley number.

3. Application to the case of flow in a left coronary artery

We applied these models to the case of a left coronary artery with diameter $2R = 3.5 \text{ mm}$. The dynamic viscosity of the blood is $\mu = 3.46 \text{ mPa} \cdot \text{s}$ and its density $\rho = 1050 \text{ kg/m}^3$. The average velocity $V(t)$ in such a vessel is shown in Fig.1 and is reproduced from the thesis work of Bénard⁶ (the period of this waveform is $T = 0.8 \text{ s}$).

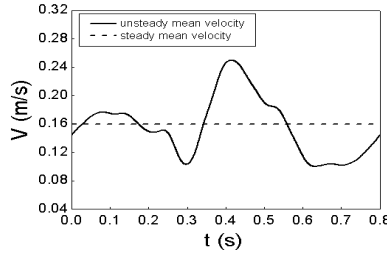


Figure 1: mean velocity in the left coronary artery (Ref. 6).

For the PM, the mean temporal value of this signal is used for \bar{V} in Eq.1. For the SPM, $V(t)$ in Fig.1 is used directly to compute the velocity profile in Eq.2. Finally, for the CPM, the decomposition in Fourier series of $V(t)$ is performed and processed to give the coefficients A_n and B_n in Eq.3. As a first step, we study the flow past a single stent strut with a square cross section of side $a = 100 \mu\text{m}$. The computational domain reduces to the 2D axisymmetric surface shown in Fig.2 below. The size of the computational domain was set to 4 mm upstream and 6 mm downstream of the strut, thereby allowing properly calculating the re-circulation zones around the stent. A structured mesh with variable grid size for a local mesh refinement at the stent is used. The boundary conditions of the three models domain were imposed by User Defined Function programmed in C language. For the unsteady models, the time step is set to $\Delta t = 10^{-3} \text{ s}$.

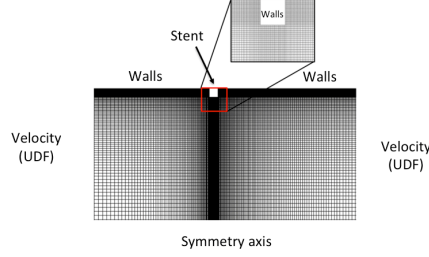


Figure 2: Computation domain of the stented artery.

4. Results and discussion

The flow around the stent is characterized by re-circulation zones upstream and downstream of the strut (Fig.3, left). Inside these re-circulations, very low velocities are observed and are responsible for very low values of the wall shear stresses (Fig.3, right).

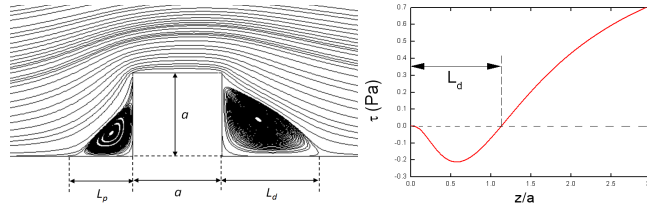


Fig.3: Streamlines (left) and wall shear stress (right) in intra-stent flow.

Let L_p and L_d be the re-circulations lengths in the proximal and distal zones. Fig.4 shows L_p and L_d for the three hemodynamic models. On the average, they scale like the stent size a ($\bar{L}_p \approx 0.6a$ and $\bar{L}_d \approx 1.1a$). L_p is approximately twice as small as L_d . Comparing the SPM and the CPM reveals little differences (at most 3%). This suggests that the SPM is sufficient to calculate the lengths of re-circulation.

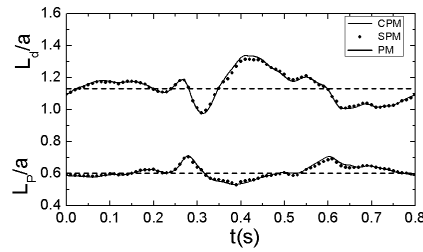


Figure 4: re-circulation lengths upstream and downstream of the stent as a function of time.

The PM is however inaccurate with deviations up to 18% for both L_p and L_d . These re-circulation lengths also have a direct impact on the values of the wall shear stress which is plotted in Fig. 5 as a function of time. It is measured at a distance $\pm a/2$ from the stent strut in the proximal and distal regions and normalized by the steady-state value. We see again that both unsteady approaches are similar. The

difference in the distal region is at most 13%, and occurs at $t = 0.6s$ (diastolic minimum). The maximum difference between the SPM and CPM for the proximal stress is lower (about 8%) and still occurs at $t = 0.6s$. The PM is again clearly insufficient. The stress that it gives is particularly inaccurate at the diastolic and systolic optima (maximum difference of 120% for the distal region). The SPM is again accurate enough for the determination of the wall shear stress in this configuration. Let us finally note that the computational time is roughly 6 times longer for the CPM compared to the SPM.

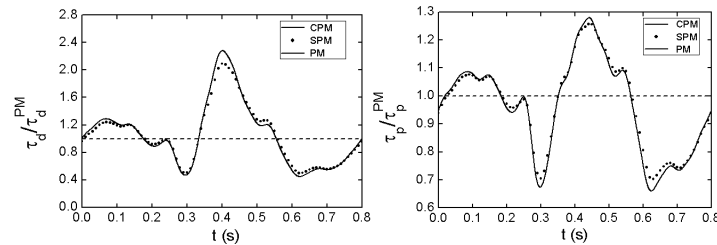


Figure 5: Comparison of wall shear stresses of three models. Distal region (left) and proximal region (right).

5. Conclusion

This work shows that the Poiseuille flow model is insufficient to compute both the re-circulation lengths and the wall shear stress, two of the main causes involved in in-stent restenosis. The SPM and the CPM give quite close results except at times where the peaks of the flow rate occur but the discrepancies are weak (around 10%). Considering the computational times in both unsteady cases, we recommend the use of the SPM for future numerical studies of stented arteries.

6. References

1. Wentzel JJ, krams R, Schuurbiers JCH, Oamen Ja, Kloet J, van der Giessen WJ, Slager CJ, Relationship between neointimal thickness and shear stress after wall stent implantation in human coronary arteries, *Circulation* 103: 1740-1745, 2001.
2. Barakat AI, Tina Cheng E, Numerical simulation of fluid mechanical disturbance induced by intravascular stents, *Proceedings of ICMMB-11, International Conference on Mechanics in Medicine and Biology*, 2000.
3. O'Brien CC, Kolachalama VB, Barber TJ, Simmons A, Edelman ER, Impact of flow pulsatility on arterial drug distribution in stent-based therapy, *Journal of Controlled Release* 186: 115-124, 2013.
4. Womersley JR, Method for the calculation of velocity, rate of flow and viscous drag in arteries when the pressure gradient is known, *Journal of Physiology* 127: 553-563, 1955.
5. Bulent A, Chieh CC, Oscillatory flow near the entry of a circular tube, *Zeitschrift für angewandte Mathematik und Physik* 12: 185-201, 1961.
6. Bénard N, Analyse de l'écoulement physiologique dans un stent coronarien: Application à la caractérisation des zones de resténose pariétale, Ph. D. Thesis, France, 2005.

THE FULL RADIAL PULSE TRANSIT TIME IS A NEW PARAMETER OF EVALUATION ATHEROSCLEROSIS

WU QUANYU^{1,2}, LI ZHIYONG², LI SHU¹, LIU XIAOJIE¹, PAN LINGJIAO¹

¹School of Electrical and Information Engineering, Jiangsu University of Technology, Changzhou 213001, Jiangsu, P. R. China

²School of Biological Science and Medical Engineering, Southeast University, Nanjing 210096, Jiangsu, P. R. China

Abstract: Analysis of different site arterial pulse wave has been proposed as a noninvasive means in assessing arterial stiffness, which has received widespread attention in the medical community at home and abroad. PTT is often used as an indicator of arterial stiffness, and its prognostic value has been repeatedly emphasized. The purpose of the present study was to provide a new parameter, the FRPTT, compare to the other parameters of evaluation atherosclerosis, to determine whether it could be used to assess arterial stiffness with aging. We gained radial pulse wave among adults in the general population (n=248), and measured their height and weight to calculate BMI, measured wrist BP and HR, calculated radial AI, ET and FRPTT. The computer software automatically detects the position of the key points for b and e in sampling wave data of 20 seconds, which algorithm is the second derivative. The calculated mean of FRPTT was analyzed, and compared to the radial AI. The results demonstrated negative correlation significantly between them ($P < 0.001$), but the male group displayed negative correlation weakly compare to the female group. And further finding proved FRPTT is significant correlation with heart rate.

Keywords: radial pulse wave; waveform analysis; FRPTT;

1. Introduction

For the doctors of TCM, wrist pulse diagnosis is one of the four examinations. The different pulse beating could be identified to diagnose the physiological and pathological human body¹. Thus most researchers measured peripheral pulse waveforms objectively and non-invasively, and gained some parameters to assess the elasticity and stiffness of the cardiovascular system²⁻³. But some parameters (pulse wave velocity, PWV) of evaluation arterial stiffness were gained from single radial pulse wave⁴, which was a challenge area in analysis pulse waveforms. So we computed the full radial pulse wave transit time (FRPTT) using one position of the radial pulse wave (Fig. 1), compare to the other parameters

of evaluation atherosclerosis, to determine whether it could be used to assess arterial stiffness with aging. We gained radial pulse wave among adults in the general population ($n=248$), and measured their height and weight to calculate body mass index (BMI), measured wrist blood pressure (BP) and heart rate (HR), calculated radial artery augmentation index (AI)⁵, ejection time (ET) and FRPTT. The computer software automatically detects the position of the key points for b and e in sampling wave data of 20 seconds, which algorithm is the second derivative. The calculated mean of FRPTT was analyzed, and compared to the radial AI. The results demonstrated negative correlation significantly between them ($P < 0.001$), but the male group displayed negative correlation weakly compare to the female group. And further finding proved FRPTT is significant correlation with heart rate.

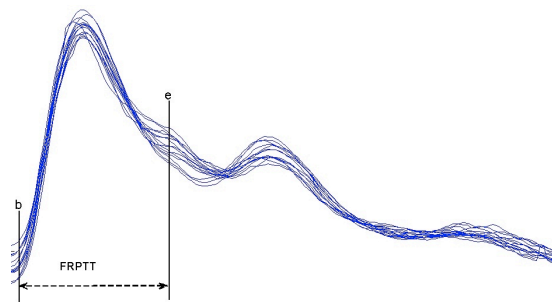


Fig. 1 the superimposed radial pulse wave of 19 years old man

At the same time, we wished to determine whether radial AI and FRPTT are influenced by the other parameters, and with contemporary computer technology analyse the influence of FRPTT on a number of physiological and anatomical indices, such as age, height, weight, BMI, SBP and DBP, PP, HR and ET in healthy old subjects. Furthermore, their relationships were to be better established.

2. Method

Applanation tonometry is a non-invasive, reproducible and accurate representation of the peripheral artery waveforms in human⁶. So an applanation tonometry-based automated vascular testing device (IIM-2010A; Institute of Intelligent of Machines, Hefei, China) was used⁷, and the radial pressure waveform was tested and processed include three steps in our laboratory⁸. In our present study, a sampling-20-second radial pulse waveforms is segmented into superimposed single-period waveform for further analysis (Fig. 1), and the key points of b and e were gained through the second derivative. The automatic computer processing was based on software tools of Matlab and Visual Basic.

3. Result

A total of 248 apparently healthy subjects which have neither record of cardiovascular disease nor regular prescribed medication were chosen by the special operator to take radial pulse waveforms from Feb. 2010 to Oct. 2013. The protocol and informed consent were approved and the written informed consents were obtained from all participants before they enrolled in the study. All subjects were divided into two groups, 17-80 years male (116 individuals, Group 1), 16-77 years old female (131 individuals, Group2).

Table 1 Selected characteristic of the study subjects

Parameter	Male (n = 117)	Female (n = 131)	P values
Age (years)	43.4 ± 16.9	43.9 ± 16.3	0.000
Height (cm)	171.4 ± 5.7	159.7 ± 4.3	0.458
Weight (kg)	66.7 ± 9.8	56.0 ± 8.2	0.480
BMI (kg/m ²)	22.7 ± 3.1	22.0 ± 3.1	0.411
SBP (mmHg)	117.8 ± 13.0	112.3 ± 12.2	0.001
DBP (mmHg)	74.0 ± 9.5	69.6 ± 7.9	0.543
PP (mmHg)	43.6 ± 6.8	42.7 ± 7.7	0.001
HR (bpm)	72.7 ± 10.2	74.0 ± 9.6	0.800
AI (%)	66.7 ± 14.4	78.2 ± 14.7	0.826
ET(s)	0.321 ± 0.030	0.341 ± 0.034	0.644
FRPTT(s)	0.267 ± 0.033	0.273 ± 0.033	0.938

BMI=body mass index; SBP= wrist systolic blood pressure; DBP = wrist diastolic blood pressure; PP= wrist pulse pressure

HR = heart rate; AI=radial augmentation index; ET= ejection time; FRPTT=full radial pulse transit time; Values are mean ± SD.

Associations among anthropometric parameters were evaluated by Pearson correlation. For comparisons among the two groups, a paired two-tailed t-test was used. All values were expressed as the form of mean ± standard deviation. Statistical analyses were performed by using SPSS software, and the probability value of $P < 0.001$ was considered to be statistically significant. Clinical detailed characteristics of the study subjects are listed in Table 1. The mean age was 44.7 ± 17.0 years (range from 16 to 80 years). There was significant difference in height, weight, BMI, diastolic blood pressure (DBP), radial AI, HR, ET and FRPTT. The FRPTT was higher in women than men (0.272 ± 0.033 compared with 0.267 ± 0.033).

3.1. FRPTT and AI

Fig. 2 shows the correlation between FRPTT and radial AI. Fig. 2 (a) shows the relationship between them in 17-80 years old male ($r = -0.459$, $P < 0.001$), there is negative correlation significantly, with increases the radial AI, FRPTT becomes gradually decrease. Fig.2 (b) demonstrates the relationship between them in 16-77 years old female. The coefficient value observed is -0.647 ($P < 0.001$), there is

much stronger negative correlation, but many subjects concentrate into near 90 percent of the radial AI. At the same time, the FRPTT value of the female group changes slowly compare to the male group.

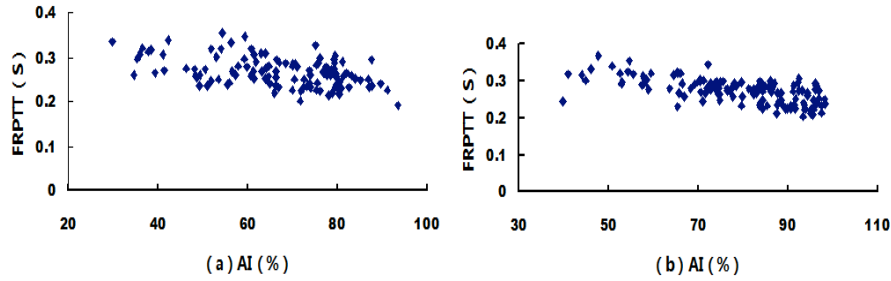


Figure 2. (a) Correlation between FRPTT and radial AI in 17-80 years old male($r = -0.459$, $P < 0.001$); (b) Correlation between FRPTT and AI in 16-77 years old female($r = -0.647$, $P < 0.001$).

3.2. Determinants of FRPTT and AI

Correlations between the two parameters (FRPTT and AI) of arterial stiffness and the other indices are shown in Table 2, among 248 subjects with radial pulse waveforms analysis. FRPTT negatively correlated with AI ($r = -0.503$, $P < 0.001$). Moreover, FRPTT shows stronger relationship with heart rate ($r = 0.643$, $p < 0.001$), and slight negative correlations with two parameters of PP($r = -0.253$, $p < 0.001$), ejection time ($r = -0.276$, $p < 0.001$).

Table 2 Correlations between conventional assessment parameters of arterial stiffness and FRPTT

Parameter	Total (n = 248)	FRPTT	AI
Age (years)	44.7 ± 17.0	$r = -0.114$, $p = 0.067$	$r = 0.418$, $p < 0.001$
Height (cm)	165.2 ± 7.6	$r = -0.005$, $p = 0.938$	$r = -0.403$, $p < 0.001$
Weight (kg)	61.3 ± 10.5	$r = 0.038$, $p = 0.542$	$r = -0.118$, $p = 0.058$
BMI (kg/m ²)	22.4 ± 3.1	$r = 0.038$, $p = 0.539$	$r = 0.124$, $p = 0.047$
SBP (mmHg)	116.0 ± 13.9	$r = -0.119$, $p = 0.056$	$r = -0.248$, $p < 0.001$
DBP (mmHg)	71.9 ± 9.0	$r = 0.059$, $p = 0.344$	$r = 0.121$, $p = 0.052$
PP (mmHg)	44.1 ± 8.5	$r = -0.253$, $p < 0.001$	$r = 0.276$, $p < 0.001$
HR (bpm)	73.2 ± 9.9	$r = 0.643$, $p < 0.001$	$r = -0.246$, $p < 0.001$
AI (%)	73.2 ± 15.7	$r = -0.503$, $p < 0.001$	
ET(s)	0.332 ± 0.034	$r = -0.276$, $p < 0.001$	$r = 0.498$, $p < 0.001$
FRPTT(s)	0.270 ± 0.033		$r = -0.503$, $p < 0.001$

BMI=body mass index; SBP= wrist systolic blood pressure; DBP = wrist diastolic blood pressure; PP= wrist pulse pressure

HR = heart rate; AI=radial augmentation index; ET= ejection time; FRPTT= full radial pulse transit time; Values are mean ± SD

4. Summary

PWV and radial AI are two generally utilized means of assessment atherosclerosis⁹, the former needs two sensors for two separate positions of measurement and the distance between them, besides, experienced personnel is required; the latter needs to calculate the magnitude of the first and another systolic peaks of the radial pressure waveform^{5, 10}. The aim of our present study is to overcome their shortcomings, and find for good parameters in radial pulse wave easily. So we proposed FRPTT of a new parameter, and evaluated the association between FRPTT and radial AI shown in Figure 2, there was the negative correlation between radial AI and FRPTT in men and women ($r = -0.459$ and $r = -0.647$, respectively, $P < 0.001$ for both).

Furthermore, our correlations analysis between FRPTT and the other indices were shown in Table 2, the results revealed that radial AI were associated with the age, height, SBP, PP, HR and ET, except weight and DBP. But the FRPTT was only associated with PP, HR and ET, and the weaker influences of the other parameters in comparison with the AI. The present study supported use of the FRPTT as a measure of arterial stiffness. It provides important information of the cardiovascular as AI.

Acknowledgment

This study was supported by the Ph.D. Start-up Fund of Jiangsu University of Technology (Grant No. KYY12004). Authors appreciate the volunteers involved in this study for allowing us to collect and analyse their data.

Reference

1. Wang BH, Xiang JL. Detecting system and power-spectral analysis of pulse signals of human body. *Proceedings of ICSP'98*. 1998;1646-1650
2. Millasseau S, Kelly RP, Ritter JM, Chowienczyk PJ. Determination of age-related increases in large artery stiffness by digital pulse contour analysis. *Clinical Science*. 2002;103:371-377
3. Huang CM, Wei CC, Liao YT, Chang HC, Kao ST, Li TC. Developing the effective method of spectral harmonic energy ratio to analyze the arterial pulse spectrum. *Evidence-Based Complementary and Alternative Medicine*. 2011;2011:1-7
4. Moses RM, Abhayaratna WP. Pulse wave velocity as a marker of cardiovascular risk in an elderly population: A community-based study. *Journal of the American College of Cardiology*. 2013;61:E2063
5. Sugawara J, Komine H, Hayashi K, Maeda S, Matsuda M. Relationship between augmentation index obtained from carotid and radial artery pressure waveforms. *Journal of Hypertension*. 2007;25:375-381
6. Rajzer MW, Wojciechowska W, Kloczek M, Palka I, Brzozowska-Kiszka M, Kawecka-Jaszcz K. Comparison of aortic pulse wave velocity measured by three techniques: Complior, sphygmocor and arteriograph. *Journal of Hypertension*. 2008;26:2001-2007
7. Zhang YL, Zheng YY, Ma ZC, Sun YN. Radial pulse transit time is an index of arterial stiffness. *Hypertension Research*. 2011;34:884-887
8. Wu Q-Y, Ma Z-C, Sun Y-N. Noninvasive power spectrum analysis of radial pressure waveform for assessment of vascular system. *Journal of Mechanics in Medicine and Biology*. 2012;12:1250021

9. Xu D, Ryan KL, Rickards CA, Zhang GQ, Convertino VA, Mukkamala R. Robust pulse wave velocity estimation by application of system identification to proximal and distal arterial waveforms. *32nd Annual International Conference of the IEEE EMBS*. 2010:3559-3562
10. Zheng YY, Lung CW, Zhang YL, Li XQ, Ma ZC, Sun YN. Radial diastolic augmentation index is a useful predictor of arterial stiffness. *Journal of Mechanics in Medicine and Biology*. 2011

COLD PRESSURE TEST AND PERIPHERAL VASCULAR RESPONSE IN HEALTHY PATIENTS: TEACHING VASCULAR PHYSIOLOGY TO MEDICINE STUDENTS

GIACOMO FELICIANI,

*Post-graduate school in medical physics, University of Bologna, via massarenti 9,
40138 Bologna, Italy.
giacomo.feliciani@studio.unibo.it*

A. LA ROCCA, C. PERON, A. MALAVOLTA, M. F. SCUPPA,

*School of Medicine, University of Bologna, via massarenti 9
40138 Bologna, Italy*

ROMANO ZANNOLI

*Experimental, Diagnostic and Specialty Medicine Department, University of Bologna, Italy , via massarenti 9
40138 Bologna, Italy
romano.zannoli@unibo.it*

1. Introduction

There is evidence in literature that temperature, pressure and other environmental stressors affect Heart Rate (HR) and Blood Pressure (BP)¹. Painful Cold for example is a stressor often used to induce changes in the parameters cited before. These changes are caused by the sympathetic nervous system and are already employed in clinical practice to screen diseases like hypertension or for ventricular function monitoring. This procedure is commonly called Cold Pressure Test (CPT). Moreover the cold pressure test is also used to evaluate cardiac and vascular autonomic function and as an experimental pain stimulus². For example it has been shown that normal subjects undergoing the test exhibit a dilation of coronary arteries whereas hypertensive ones exhibit a constriction³. The objective of this study is to show students of medicine in first years of study basic procedures of signal monitoring and acquisition. Our method improves Dee U. Silverthorn⁴ one with a system for non-invasively monitor the response of the peripheral vascular system (PVS) in healthy subject undergoing the test. In addition to follow HR and BP during the test, strain gauge are applied at the upper part of the forearm of volunteers to analyze the response of the PVS. Finally data coming from groups of students can be scored and analyzed.

1.1. Learning Objectives

1. Monitor basal condition of patients through ECG, oscillometric pressure and continuous pressure
2. Verify constancy and repeatability of physiological parameters measurements such as vascular blood flow and vascular compliance.
3. Evaluate physiological changes in the subject undergoing the CPT, in particular associated to isothermal condition.
4. Collect data from different subjects and develop a statistics to make consideration about measurements acquired

2. Methods

2.1. Required equipment:

1. Task Force Monitor or equivalent for oscillometric blood pressure and HR recording.
2. Finger blood pressure monitor for continuum blood pressure measurement.
3. Light work station or equivalent for signals acquisition and amplification.
4. Water pan and ice (-15°C)

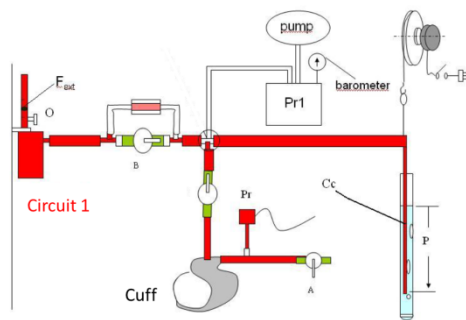


Fig. 1. Inflatable cuff pressure circuit

5. Low pressure Inflatable cuff: schematic example of the system is given in fig. 1. Pressure is generated inflating the cuff through the air source in O. The air flow pushing against the column of water in F generates a stable idrostatic pressure $P = \rho gh$ with h being the length of the column Cc inside the water
6. Pressure transducer to follow pressure changes in P.
7. Strain gauge for peripheral vascular flow measurements through venous occlusion technique realized with the system described in 5.

2.2. Procedure:

Electrodes for ECG acquisition are placed on the thorax of the patient together with the cuff for oscillometric pressure measurements. The patient has to be placed in supine position waiting for him to relax. Strain gauges are then connected to the patient forearm as can be seen in fig.2.

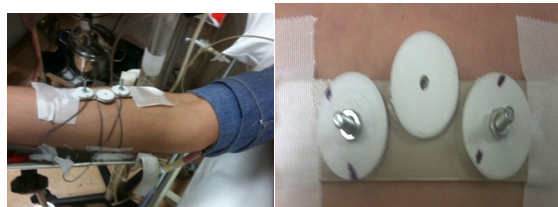


Fig. 2. Strain gauges in measurement position (left) and strain gauge support detail on forearm (right)

- Repeatability measurement of peripheral flux: we acquired at least 4 basal flux in every patient inflating the cuff at a pressure higher than 40 mmHg to stop venular blood circulation. As an example we show two kind of this acquisition in figure 3.

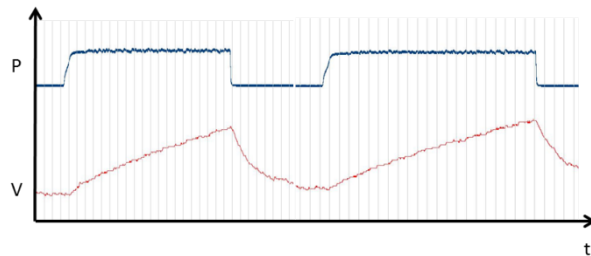


Fig. 3. Example of peripheral ematic fluxes acquisition

- Repeatability measurement of peripheral vascular compliance: progressively inflating the cuff from 0 to 50 mmHg we observe the variation of the elastic component of vascular walls.
- Start of the cold pressure test
- We augmented the pressure to a stable level of 20 mmHg waiting for the basal condition of the patient to stabilize. In this conditions we acquire again peripheral fluxes to show that the new basal condition doesn't influence flux values
- The hand of the patient is then immersed inside cold water to observe peripheral vasoconstriction registering variation of forearm vascular tone. During this phase we also acquired hematic fluxes occluding venous return.
- After that vascular compliance is measured through the procedure described before to observe its variation during the cold pressure test.

3. Results:

- Basal fluxes in different patients were acquired and numerical results agree with each other within experimental errors
- During cold pressure test a reduction of volume was observed in every patient producing a variation in the acquired signal as in fig.4

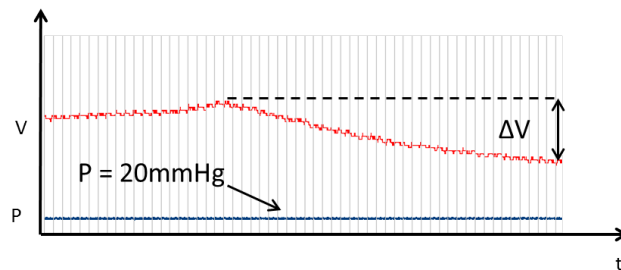


Fig.4 Cold pressure test effect on forearm volume

- After this phase a reduced peripheral flux is registered and increasing gradually the pressure in the cuff the arterovenular compartment showed a decrease in its compliance. At the same time an augmented HR and BP is registered accordingly.

4. Conclusions:

The aim of this study is to introduce medicine student to real practice signal acquisition, processing, result interpretation and drawing conclusions from them . Moreover the procedure can stimulate reasoning on basic physiology of the vascular system such as vasoconstriction and vasodilation as CPT causes stimulation of sympathetic system that leads to:

- At central level an augmented HR and BP
- At peripheral level (skin and muscles in forearm), vasoconstriction of arterioles with consequent diminishing of peripheral perfusion of tissues and a reduced vascular compliance

All this phenomena can be quantitatively recorded and analyzed by the students.

Finally augmenting the number of healthy patients to create a baseline study, this procedure can be applied in clinical research protocols for non-invasively monitor vascular diseases progression.

References

1. Mourot L, Bouhaddi M, Regnard J. Effects of the cold pressor test on cardiac autonomic control in normal subjects. *Physiol Res*. 2009;58(1):83–91. Available at: <http://www.ncbi.nlm.nih.gov/pubmed/18198985>.
2. Monahan KD, Feehan RP, Sinoway LI, Gao Z. Contribution of sympathetic activation to coronary vasodilatation during the cold pressor test in healthy men: effect of ageing. *J Physiol*. 2013;591(Pt 11):2937–47. doi:10.1113/jphysiol.2013.251298.
3. Wood DL, Sheps SG, Elveback LR, Schirger a. Cold pressor test as a predictor of hypertension. *Hypertension*. 1984;6(3):301–306. doi:10.1161/01.HYP.6.3.301.
4. Silverthorn DU, Michael J. Cold stress and the cold pressor test. *Adv Physiol Educ*. 2013;37(1):93–6. doi:10.1152/advan.00002.2013.

FORCED OSCILLATION PHASE VELOCITY ON LIVING LARGE VESSEL

ISABELLA BARBIERI

*Dept. of Mathematics, University of Bologna,
P.zza di Porta S. Donato 5, Bologna, 40100, Italy
e-mail: isabella.barbieri@unibo.it*

EZIO CAROLI

*IASF-Bologna, INAF,
Via Gobetti 101, Bologna, 40129, Italy
caroli@iasfbo.inaf.it*

GIOVANNI PALLOTTI

*Dept. of Physics and Astronomy, University of Bologna,
Via Bertini Pichat 6/2, Bologna, 40127, Italy
e-mail: giovanni.pallotti@unibo.it
Clare Hall, Herschel Road
Cambridge, CB3 9AL, U.K.*

Starting from experimental data, this work exploits the similarity of pressure and axial wave's propagation of both pressure and axial waves in large vessel (e.g. aorta) with the solution of a mathematical model developed to describe the motion of acoustic waves in solid. In particular, we show how the motion parameters derived by fitting the experimental data measured in living dog arteries are related to mechanical properties of the vessel tissue.

Key words: wave propagation, large arteries, radial and axial impedance, viscoelasticity in tissue

1. Introduction

The problem approached in the present work is a further development of the investigation of the tissues mechanical properties of the large vessels in the cardiovascular system. In particular, in the following section we will show how a mathematical model developed to explain the motion of seismological wave propagation could explain experimental results obtained in living large arteries tissue.

The present work starts from the “*in vivo*” experiments made by M. Anliker and collaborators on the transmission of axial, pressure and torsion forced waves in the large vessels of wolf dogs^{1,2}. These animals were used owing to the great similarity of their large vessels with the human ones and because the measurements were possible to be made on living tissues of living bodies. Further motivation of our data selection belongs to comparative medicine and we have preferred to perform our work starting from Anliker's results instead of considering other data obtained during autopsies, because these samples present a large variability due to the quite different variety of both pathological and test preparation conditions.

2. Experimental Results versus Theoretical Model

The results obtained by Anliker's group in their “*in vivo*” experiment on large vessels² are summarized in Fig. 1 that shows, respectively, the velocities and the attenuation measured for two induced mechanical

waves types: along the axis (y direction) of the vessel (axial) and transversal (i.e. orthogonal) to the same axis (pressure) oscillations.

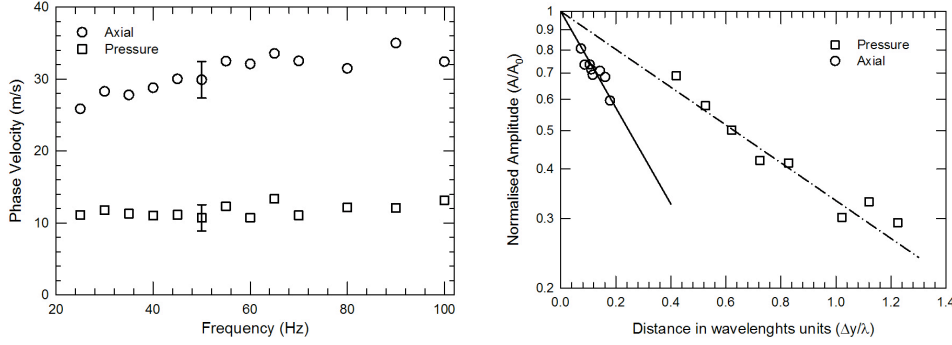


Fig. 1. Summary of Anliker experiment results for axial and pressure forced wave: (left) Phase velocity as function of forced wave frequency; (right) Wave amplitude attenuation as function of distance in wavelength units. Each data point represent the average of six independent experiments. The experimental error is given by the standard deviation of these measures for each point.

The behavior (Fig. 2) of the results of Anliker's work on wave transmission along arteries give two fundamental results: the wave propagation velocity is essentially constant (i.e. independent from the wave frequency) and the wave amplitude is attenuated exponentially with distance.

Using a chi-square test, we confirmed that the Phase velocity data measured in the “in vivo” experiment are compatible with constant values. In fact we obtain a confidence greater than 95% for the case of pressure waves, while for axial ones the statistical confidence is slightly less than 90%. Indeed in the case of axial waves the experimental data in Fig. 2 (left) show a weak frequency dependence, however, is that within the experimental errors. In particular the measured average phase velocities are 11.7 ± 0.2 m/s and 30.8 ± 0.7 m/s for pressure and axial waves respectively.

In the Fig. 2 (right), the attenuation of the two wave types is reported, showing that the amplitude exponential attenuation is function of the forced oscillation wavelength for both types of mechanical waves. The two data set can be fitted by a simple exponential function. The fit give a value of 1.1 and 3.6 for the attenuation constant of pressure and axial wave respectively, with a significance larger than 95%.

These characteristics of wave propagation, suggest that we can consider live large vessel tissue as a Knopoff body³ and try to analyses the propagation of pressure and axial waves similarly to the propagation of acoustic wave in solid. With this assumption for blood vessel tissue, the pressure wave (e.g. shear waves in Knopoff nomenclature) motion could be described by the following differential equation:

$$\rho \frac{\partial^2 \bar{u}}{\partial t^2} = \mu_E \frac{\partial^2 u}{\partial y^2} + \mu_v \frac{\partial^3 \bar{u}}{\partial t \partial y^2} \quad (1)$$

where ρ is the density (g/cm^3), t is the time (s) and x the linear coordinate (orthogonal to the vessel axis), while μ_E and μ_v are the medium elastic and viscosity constant respectively. In Eq. (2), $\bar{u} = \bar{u}(t, y)$ represent the total displacement given by $\bar{u} = u_p + u$, where u_p is the permanent (irreversible) displacement and u the recoverable displacement. Since the permanent displacement (i.e. deformation) is

negligible with respect to the elastic deformation for low attenuation factor, in the wave motion equation we can use only the elastic displacement u .

Following Knopoff, Eq. (1) with the assumption of elastic displacement only can be rewritten as an equation that combines a linear term, corresponding to a Kelvin Voigt Maxwell solid, with a nonlinear term which takes into account the interaction between the two processes (elastic and viscous). If the loss due to each of these mechanisms separately can be considered small even the effect of their interaction of will be very small and therefore the non-linear term can be simplified and the wave motion equation can be rewritten as:

$$\frac{\partial}{\partial y} \left[\frac{\partial^2 u}{\partial y^2} - \frac{1}{V_p^2} \frac{\partial^2 u}{\partial t^2} + \frac{\mu_v}{\mu_E} \frac{\partial^3 u}{\partial y^2 \partial t} - 2\mu_c \rho \frac{\partial u}{\partial t} \right] = 2\eta_c \rho \frac{\partial}{\partial t} \left[\left| \frac{\partial^2 u}{\partial y \partial t} \right| \text{sgn} \left(\frac{\partial u}{\partial y} \right) \right] \quad (2)$$

where, in addition to already defined parameters, μ_c is a constant having the dimension of inverse of viscosity, η_c represents the Columbian deformation impedance and finally V_p is the elastic pressure wave velocity:

$$V_p = \sqrt{\frac{\mu_E}{\rho}} \quad (3)$$

If in Eq. (2) we can assume that the non-linear term is negligible in comparison with the elastic wave propagation term, a quasi-harmonic solution can be obtained using the Krylov and Bogoliubov method assuming a solution of the form^{4,5}.

$$u = A(t, y) \sin(ky - \omega t + \phi(t)) \quad (4)$$

If we consider the amplitude $A(t, y)$ and the phase $\phi(t)$ slowly variable in time we can then obtain the following solution for the pressure elastic displacement:

$$u(t, y) = A_0 e^{-\left(\frac{\mu_v}{\mu_E} \frac{\omega^2}{2V_p} + \frac{2}{\pi} \eta_c \rho V_p \omega + \eta_c \rho V_p \right) y} \sin(ky - \omega t + \phi_0) \quad (5)$$

As discussed in ³, there are some condition (i.e ranges of frequency) for which both the second power term in frequency and the constant are negligible with respect to the ω first order one in the exponential argument. In fact Eq. (5) describe the behavior of pressure wave motion in the Anliker experiment if we assume that the frequency range of the forced induced waves satisfied the previous condition, as the same equation can be simply rewritten as:

$$u(t, y) = A_0 e^{-4\eta_c \rho V_p \frac{y}{\lambda}} \sin(ky - \omega t + \phi_0) = A_0 e^{-\frac{\alpha_p y}{\lambda}} \sin(ky - \omega t + \phi_0) \quad (6)$$

where $\alpha_p = 4\eta_c \rho V_p$ is a constant that depend on the Columbian impedance of the vessel tissue and on its elastic coefficient that define the pressure wave velocity. In Eq. (6) A is the wave amplitude and λ ($\omega/2\pi$) its wavelength.

Always following the model developed by Knopoff, we can solve in a similar manner the equation of motion for the axial waves (i.e. longitudinal waves). As before in defined condition of frequency range, the solution of motion can be described by the following function:

$$u(t, y) = A_0 e^{-\frac{8}{3}\psi_c \rho V_A \frac{y}{\lambda}} \sin(ky - \omega t + \phi_0) = A_0 e^{-\frac{\alpha_A y}{\lambda}} \sin(ky - \omega t + \phi_0) \quad (7)$$

where A , ρ and λ have been already defined, while ψ_c is a constant having the dimension of the invers of stress. As for the pressure wave case, the axial wave attenuation α_A depend on their phase velocity V_A that is defined by:

$$V_A = \sqrt{\frac{\lambda_E + 2\mu_E}{\rho}} \quad (8)$$

in which λ_E represent the volume compressibility and μ_E is the elastic coefficient of the vessel tissue.

Eq. (3) and (8) for phase velocity are constant or slowly variable with frequency because of the physical parameters characteristics on which they depends. Therefore, the phase velocity expressions derived from the Knopoff model are consistent with the experimental results reported above. Furthermore, the two Equations (6) and (7) that represent the modification of the deformation for pressure and axial wave respectively exhibit exponential attenuation of the amplitude as function of the wave frequency. This, being the phase velocity constant, means that the amplitude attenuation depend on the oscillation wavelength as observed in the experimental data. Using the phase velocities measured by Anliker in the Eq. (3) and (9), obtained by solving the motion equations for axial and pressure waves obtained using Knopoff et al. model, we can derive the values for the vessel wall elastic constant μ_E and volume compressibility λ_E . In particular we obtain $\sim 0.151 \text{ N/m}^3$ and $\sim 6.63 \text{ N/m}^3$ respectively for these two material characteristics.

References

1. M. Anliker, "Toward a nontraumatic study of the circulatory system", from *Biomechanics: its Foundation and Objectives*, Y.C. Fung, N. Perrone and M. Anliker Editors, Prentice Hall, Englewood Cliffs, New Jersey, (1972).
2. W.E. Moritz and M. Anliker, "Wave transmission characteristics and anisotropy of canine carotid arteries", *J. Biomechanics*, Vol. 7, pp. 151-154 (1974).
3. L. Knopoff and J.F. MacDonald, "Attenuation of small amplitude stress waves in solids", *Reviews of Modern Physics*, Vol. 30, No 4, pp. 1178-1192 (1958).
4. N. Minorsky, *Introduction to non linear mechanics*, Edwards Brothers, Inc., Ann Arbor, pp. 186 and seq. (1947)
5. N. M. Krylov; N. N. Bogoliubov, *Introduction to non-linear mechanics*, Princeton Univ. Press. ISBN 9780691079851 (1947)

THE INFLUENCE OF STENOSIS ON THE WALL SHEAR STRESS AND FLOW RATE IN THE COMMON CAROTID ARTERY BIFURCATION FOR UNSTEADY FLOW. NUMERICAL ANALYSIS

N. ANTONOVA ^A, X. DONG ^B, P. TOSHEVA ^A, E. KALIVOTIS ^C, I. VELCHEVA ^D

^a Department of Biomechanics, Institute of Mechanics, Bulgarian Academy of Sciences, 1113 Sofia Acad. G. Bonchev str., bl. 4, Bulgaria, antonova@imbm.bas.bg

^b School of Civil Engineering, Tianjin University, China. postcode 300072.

^c Department of Engineering, University College London, London, UK

^d Department of Neurology, University Hospital of Neurology and Psychiatry "St. Naum", Medical University. Sofia, Bulgaria, velchevairena@gmail.com

Blood flow in carotid artery bifurcation is studied on the basis of Navier-Stokes equations performing numerical simulations by a finite volume method and considering one wave period. Four different cases of the common carotid bifurcation were examined: without stenoses, with one, two and three stenoses. Based on geometry reconstruction a mesh generation is done. The case studies are based on different anatomies presented by the one, two or three stenoses of common carotid bifurcation vessel. The physiological geometry can be imported into a CFD solver.

The numerical results of the blood flow in the common carotid bifurcation give detail picture of the axial velocity and WSS distribution. For the case of carotid bifurcation without stenoses results for the axial velocity distribution are presented in six characteristic time points $T=0$ s, 0.1s 0.2s, 0.3s, 0.4s, 0.5s. The results investigate the influence of the stenoses on the blood flow in the bifurcation and deposition processes around it. The recirculation zone behind the stenosis is the area of low WSS. Thus this area is the most probable one for monocytes and platelet aggregation and thrombosis formation.

The results show that the blood flow in the carotid bifurcation is unsteady and the flow disturbances depend on the time and type of the stenoses. The pattern of the velocity and the WSS are obtained and comparison of the peak Wall shear stress (WSS) is done for the four considered cases. The recirculation zone behind the bifurcation and stenosis is the area with low shear stress. The peak WSS are increasing and the maximum is being achieved earlier with increase of the number of stenoses. The relationship between the peak wall shear stress and time for one pulse wave, has 4 inflection points at which the [curvature](#) changes its [sign](#). The dependence of the peak WSS on time reflects the changes due to the velocity of the pulse wave. Comparison of the peak wall shear stress for the four different cases (without stenoses and with 1, 2 and 3 stenoses correspondingly) reveals the peak WSS maximum value at the characteristic point of $T=0.2$ s for the cases with two and three stenoses. In the case of a bifurcation without or with one stenosis, the maximum WSS is achieved with a delay of 0.02 seconds compared to the other two cases. The differences in the maximal WSS value (1.8 Pa) for the cases with 1, 2 and 3 stenoses in comparison to the case without stenosis (1.5 Pa) are observed at the characteristic point of the pulse wave at $T=0.45$ s.

The results play an important role in understanding the formation, growth, rupture and prognosis of damage of the vessel wall and may be a practical tool for planning treatment and follow-up of patients after neurosurgical or endovascular interventions with 3D angiography. The results also present the potential of using numerical simulation to provide existing clinical prerequisites for diagnosis and therapeutic treatment. The numerical results from the changes in the hemodynamic profile could also guide the therapeutic plan in the examined patients.

A LINEAR VISCOELASTIC MODEL FOR ARTERIAL PULSE PROPAGATION

ANDREA GIUSTI

*Department of Physics and Astronomy, University of Bologna,
Via Irnerio 46, Bologna, I-40126 Italy,
andrea.giusti91@gmail.com*

FRANCESCO MAINARDI

*Department of Physics and Astronomy, University of Bologna, and INFN
Via Irnerio 46, Bologna, I-40126 Italy
francesco.mainardi@bo.infn.it
<http://www.fracalmo.org/mainardi>*

The purpose of this paper is to evaluate the effects of blood viscosity on the distortion of the arterial pulse as it propagates within the framework of a linear, one-dimensional theory. In order to single out these effects, we consider the propagation of a pulse generated at the accessible end of a semi-infinite, uniform elastic tube, where the effect of the viscosity of fluid inside (the blood) is taken into account according to the Womersley model for a pulsatile rigid-tube flow. In the framework of this linear model, the evolution equation for any response variable is derived by using the technique of Laplace transforms and turns out to be an integro-differential one of convolution type in analogy with the stress wave propagation in linear viscoelasticity. In particular, the resulting wave equation is analogue to that for a particular viscoelastic solid which exhibits rheological properties similar to those of a fractional Maxwell model (of order 1/2) for short times and of a standard Maxwell model for long times.

Keywords: Linear Viscoelasticity; Biofluid Dynamics; Transient Waves.

1. Introduction to the Mathematical Model

In the present analysis we attempt to consider the blood viscosity in a proper manner for non stationary flows as it occurs in the well established in Womersley theory for pulsatile flow in rigid tubes, see e.g. [1]-[2]. Usually, a number of authors (see e.g. [3-4]) consider the one-dimensional momentum equation with a friction term according to the formula of the Poiseuille steady flow in a rigid tube, whereas surely it is more appropriate to evaluate the friction term according to the formula of a sinusoidal flow. The approach of the paper begins with the continuity equation and two Navier-Stokes equations for an incompressible Newtonian fluid in cylindrical coordinates; motion in the circumferential direction is neglected. The flow is assumed to be quasi-one-dimensional, which implies that the radial velocity w is very small with respect to the axial velocity u [5]. The basic equations are then integrated over the radial coordinate r , reducing the number of independent variables to two (time t and axial distance x) and the dependent variables are then three: the averaged (uniaxial) velocity U (the quantity measured in most experiments) the cross-sectional area A and the pressure p (or its gradient Δ). A pressure - area relation for a uniform, elastic tube, longitudinally tethered, is then used to eliminate one of the dependent variables. In the framework of a linear, uniaxial theory, however, the final system of two equations contains an additional unknown function (the friction term $f_0(x; t)$) which depends on the variation of the axial velocity u with r . In fact, linearising the basic equations (14), (15) in [5], we get the following systems of partial differential equations (denoting the partial derivatives with subscripts):

$$\begin{cases} A_t + A_0 U_x = 0, \\ U_t + p_x/\rho = f_0(x, t), \end{cases} \implies \begin{cases} A_t + A_0 U_x = 0, \\ A_0 U_t + c_0^2 A_x = A_0 f_0(x, t), \end{cases} \quad (1)$$

with

$$f_0 = \frac{2\nu}{R_0} \left. \frac{\partial u}{\partial r} \right|_{R_0}, \quad c_0 = \left(\frac{A_0}{\rho} \left. \frac{dp}{dA} \right|_0 \right)^{1/2}. \quad (2)$$

Above, $A_0 = \pi R_0^2$ denotes the undisturbed cross-sectional area, ρ and ν the density and the kinematic viscosity of the fluid inside the tube (the blood), and c_0 the Moens-Korteweg velocity (for pressure waves in elastic tubes filled of inviscid fluid). We recall that the first equation in (1) is derived from the conservation of the flow (continuity equation) whereas the second one in the LHS system provides the perturbation of the viscosity to the Euler equation for inviscid fluids relating the acceleration with the pressure gradient. In general, the friction term f_0 depending on the velocity profile cannot be properly determined without carrying out a full two-dimensional, non-linear treatment of the problem [5]. However, in the case of a parabolic profile (Poiseuille approximation of steady flow), we get

$$u = 2U (1 - r^2/R_0^2) \implies f_0 = -8U/\tau, \quad \tau = R_0^2/\nu. \quad (3)$$

In order to eliminate the velocity component in the radial direction in the framework of a linearized theory and evaluate f_0 in terms of the dependent variables for unsteady flows, we find it reasonable to assume the velocity profile to be described as in the case of an unsteady flow in a rigid tube of radius R_0 , as required in the Womersley theory. Because of the linearity we can easily compute the friction term corresponding to a sinusoidal pressure-gradient, $\Lambda = \Lambda_0 \exp(i\omega t)$ and we get for $s = -i\omega$:

$$f_0 = \tilde{\Phi}(s\tau) \frac{\Lambda_0}{\rho}, \quad \text{with} \quad \tilde{\Phi}(s\tau) = \frac{2}{\sqrt{s\tau}} \frac{I_1(\sqrt{s\tau})}{I_0(\sqrt{s\tau})}, \quad (4)$$

where I_0, I_1 denote the modified Bessel functions of order 0, 1, respectively. If s is now interpreted as the parameter entering the Laplace transform, we can formally obtain the friction term corresponding to any time history of the pressure-gradient $\Lambda(x, t)$ by a convolution integral. Indeed we get:

$$f_0 = \Phi(t) * \Lambda(x, t)/\rho \implies U_t(x, t) = -[1 - \Phi(t) *] \Lambda(x, t)/\rho, \quad (5)$$

where $\Phi(t)$ denotes the inverse Laplace Transform of $\tilde{\Phi}(s\tau)$ and $*$ denotes the time Laplace convolution. So doing we have properly modified the relation between acceleration U_t and pressure gradient Λ for inviscid flow (the Euler equation) in terms of a Laplace convolution in order to take into account the memory effects of the viscosity.

After simple manipulations, by denoting with $Y = Y(x, t)$ any response variable, such as $\{U, A, p, \Lambda\}$, we get the evolution equation

$$Y_{tt} = c_0^2 [1 - \Phi(t) *] Y_{xx} . \quad (6)$$

which reduces in the absence of viscosity ($\Phi(t) = 0$) to the classical D'Alembert wave equation $Y_{tt} = c_0^2 Y_{xx}$

Eq. (6) is an integro-partial differential equation, which is to be solved for $x \geq 0, t \geq 0$ with a known input condition $Y(0; t) = Y_0(t)$, assuming that the tube is initially quiescent, and there are no waves coming from $x = \infty$. These simplifying assumptions, however, are expected to explain the qualitative features of the distortion of the arterial pulse generated in the heart ($x = 0$) as it propagates along the aorta, that are due to the viscosity of the blood but neglecting other effects like the tapering.

2. Linear Viscoelastic Analogy

From Eq. (6) we note an analogy with the wave equation of linear viscoelasticity in the Relaxation Representation (see e.g. [6]). As a consequence, methods to treat transient viscoelastic waves described in [6] can be used to solve our initial-boundary value problem ("signalling" problem) for the arterial pulse. Basing on the Laplace transform these methods allow us to obtain approximate solutions, suitable for different ranges of the time elapsed from the wave-front and the distance. It is also known (see e.g. [6]) that a linear viscoelastic model could be expressed in two different representations, namely the Creep and the Relaxation Representation. In our case, we can easily recover the Creep Representation using the well known relation for the material functions $J(t)$ (the Creep Compliance) and $G(t)$ (the Relaxation Modulus) that represent respectively the strain response to a unit step of stress and the stress response to a unit step of strain:

$$s\tilde{J}(s) = 1 + \tilde{\Psi}(s) = [1 - \tilde{\Phi}(s)]^{-1} = [s\tilde{G}(s)]^{-1} . \quad (7)$$

Then, in Creep Representation, we obtain the wave equation

$$[1 + \Psi(t) *] Y_{tt} = c_0^2 Y_{xx} . \quad (8)$$

Now, it is very interesting to take a look at the asymptotic behavior of both functions $\Phi(t)$ (the rate of relaxation) and $\Psi(t)$ (the rate of creep) in order to estimate the effect of the viscosity on the material functions $G(t)$ and $J(t)$ for short and long times and, consequently, for the profile of the flow and for the distortion of the arterial pulse:

$$\Phi(t) \sim \begin{cases} (2/\tau) \exp(-4t/\tau), & t \rightarrow \infty \\ (2/\sqrt{\pi\tau}) t^{-1/2}, & t \rightarrow 0 \end{cases} ; \quad \Psi(t) \sim \begin{cases} 8/\tau, & t \rightarrow \infty \\ (2/\sqrt{\pi\tau}) t^{-1/2}, & t \rightarrow 0 \end{cases} . \quad (9)$$

From these results we can easily conclude that:

(1) for the long-time approximation, i.e. $s\tau \rightarrow 0$, we recover the parabolic Poiseuille profile that corresponds to the Maxwell model of viscoelasticity;

(2) for the short-time approximation, i.e. $s\tau \rightarrow \infty$, we get a boundary layer profile that corresponds to the Fractional Maxwell model of order $1/2$.

In the long version of the paper we will provide the details of the above analysis along with illuminating plots.

References

- [1] J.R. Womersley: Method for the calculation of velocity, rate of flow and viscous drag in arteries when the pressure gradient is known, *J. Physiol.*, 127, (1955) 127, 553{563 (1955).
- [2] J.R. Womersley: An Elastic Tube Theory of Pulse Transmission and Oscillatory Flow in Mammalian Arteries, Wright Air Development Center, Technical Report, WADC-TR 56-614 (1957).
- [3] H.W. Hoogstraten, G.H. Smit: A mathematical theory of shock-wave formation in arterial blood flow, *Acta Mech.*, 30, 145{155 (1978).
- [4] D.W. Barclay, T.B. Moodie and V.P. Madan: Linear and non-linear pulse propagation in fluid-filled compliant tubes, *Meccanica*, 16, 3{9 (1981).
- [5] A.C.L. Barnard, W.A. Hunt, W.P. Timlake and E. Varley: A theory of fluid flow in compliant tubes, *Biophys. J.*, 6, 717{724 (1966).
- [6] F. Mainardi: *Fractional Calculus and Waves in Linear Viscoelasticity*, Imperial College Press - World Scientific , London - Singapore (2010).

S4M: Orthopaedics and prosthetics: lower extremities

Chairs: Rita Stagni, Nicola Lopomo

ORIENTATION OF THE TROCHLEAR GROOVE

KYUNG JIN CHO

THE FAST WAVE IS SIMPLY DETERMINED BY THE FABRIC TENSOR

YOUNG JUNE YOON

COMPARING FLEXION AND EXTENSION MOVEMENTS IN ESTIMATING KNEE FUNCTIONAL
AXIS

FRANCESCA COLLE

COMPARISON BETWEEN SINGLE RADIUS AND J-CURVE TOTAL KNEE ARTHROPLASTY
DESIGNS: A FINITE ELEMENT ANALYSIS

HECTOR ROBLEDY YAGUE

POST-CAM CONTACT MECHANISM DURING SEVERAL ACTIVITIES IN PRIMARY AND SEMI-
CONSTRAINED TOTAL KNEE ARTHROPLASTY DESIGN: A FINITE ELEMENT STUDY

RAQUEL ALARIO BERNABÈ

RESTORATION OF THE SEAL FUNCTION OF THE ACETABULAR LABRUM: A CADAVERIC
STUDY

CECILIA SIGNORELLI

HOW REPRODUCIBLE IS THE LOCALIZATION OF ACL INSERTION POINTS BY USING MRI?

PASQUALE SALANDRA

PROBABILISTIC MODEL OF LIGAMENTS AND TENDONS: QUASI-STATIC, LINEAR STRETCHING

MARCO BONTEMPI

ORIENTATION OF THE TROCHLEAR GROOVE

K.J. CHO

*Department of Mechanical and Mechatronic Engineering, Stellenbosch
University, Private Bag X1, Matieland 7600, South Africa
16421140@sun.ac.za*

J.H. MÜLLER

*Department of Mechanical and Mechatronic Engineering, Stellenbosch University,
Private Bag X1, Matieland 7600, South Africa
cobusmul@sun.ac.za*

P.J. ERASMUS

*Department of Orthopaedics, Stellenbosch University,
Private Bag X1, Matieland 7600, South Africa
pieter@orthoclinic.co.za*

C. SCHEFFER

*Department of Mechanical and Mechatronic Engineering, Stellenbosch University,
Private Bag X1, Matieland 7600, South Africa
cscheffer@sun.ac.za*

Achieving correct rotational alignment of the patellofemoral prosthesis is important in patellofemoral arthroplasty (PFA) for an optimal result of the procedure. The trochlear groove alignment was measured in an axial and a coronal view in respect to the posterior condylar plane, the distal condylar plane, and the anatomical axis, using three dimensional computer models segmented from computed tomography (CT) images. The knees with a deeper groove and a higher trochlear facet asymmetry ratio (TFA) were more externally aligned in the axial plane and valgus aligned in the coronal plane, although the standard deviations of the alignments were as high as 3.8° and 5.4° respectively. The trochlear inclination angle (TIA) showed more linear correlation with the axial groove angle when measured from the line perpendicular to the axial groove line than measuring from the posterior condylar plane. In the coronal plane, the correlation between the anatomical and the mechanical angles was more linear when measured from the coronal groove line than measuring from the line perpendicular to the distal condylar plane. The groove alignments in the axial and the coronal planes can be measured preoperatively and are definable during the surgery using the anatomical landmarks. This allows using the groove lines as the guideline to select the most appropriate patellofemoral prosthesis design that fits the patients' trochlear anatomy.

Keywords: Patellofemoral arthroplasty; trochlear groove angle; trochlear groove orientation

1. Introduction

Patellofemoral arthroplasty (PFA) is indicated for patients with patellofemoral osteoarthritis, changing the articulating geometry between the patella and the femur, while the tibiofemoral geometry is unchanged. The rotational alignment of the femoral component influences the patellar tracking and the patellofemoral joint contact after a patellofemoral arthroplasty (PFA).^{1,2} The trochlea design and the alignment were identified to be the factors that determine the success of the procedure.

The alignment of the anterior cut in the axial plane influences the prosthesis' internal-external rotational alignment of the femoral component in the axial plane. Two options exist to achieve correct

femoral rotation of a PFA in the axial plane. Option 1 is based on the derivation of an axis that is based on femoral anatomical landmarks, such as the epicondylar axis,³ the Whiteside's line,⁴ and the posterior condylar axis.⁵ Option 2 is based on the tibial referencing, in which the anterior cut is made perpendicular to the tibial anatomical axis at 90° flexion.⁶ Once the anterior cut is made, the femoral component is aligned in the coronal plane to ensure a smooth transition between the prosthesis and the cartilaginous surface of the natural distal femur. To cater for the trochlear groove alignment of the natural femur, some prostheses have built-in trochlear alignment in the coronal plane, such as the HermesTM prosthesis (CeraverTM) and the GenderTM prosthesis (ZimmerTM), all having 7° valgus alignment. On the other hand, the AvonTM prosthesis (StrykerTM) has a neutral groove alignment and has a symmetrical design, where the prosthesis is designed to fit both left and right femurs.

The aim of this study is to quantify the trochlear orientation relative to the posterior and the distal condylar planes. The difference in groove alignment between the normal knees and the knees with trochlear dysplasia was identified in this study. The normal femurs had a more external and valgus aligned trochlear groove than the dysplastic femurs. The advantage of this method is that the groove orientation can be defined relatively easily on the axial and the coronal planes, using the posterior and the distal condyles as the references during surgery. This study offers a potentially useful preoperative guideline for selection of an appropriate patellofemoral prosthesis design in terms of the patient's trochlear anatomy.

2. Materials and Methods

2.1. Materials

In 18 volunteers between the age of 19 and 65, the lower extremities were scanned from the hip to the ankle with a computed tomography (CT) scanner (Siemens Emotion 16; 130 kV) after informed consent. In accordance with the Declaration of Helsinki, ethical consent was acquired from the Committee for Human Research at Stellenbosch University with a project number N08/02/029. None of the volunteers complained of knee pain or had any prior surgery performed on their knees. The femur and the tibia were segmented from the CT scans to build three dimensional computer models with mimics (Materialise). The segmented models were imported to 3matic (Materialise) for the measurements.

2.2. Referencing method

The femoral reference system was defined (Fig. 1): The sagittal plane is perpendicular to the posterior plane and the distal condylar plane. The coronal plane is parallel to the posterior condylar plane and the axial plane is parallel to the distal condylar plane. The posterior condylar plane touches the most posterior points of the medial and lateral condyles and is parallel to the anatomical axis of the femur. The anatomical axis was defined as the axis of the cylinder that fits to the femoral shaft. The distal condylar plane is perpendicular to the posterior condylar plane while touching the distal points of both condyles. The origin (C_0) of the reference system was defined as the deepest point of the groove, measured from the distal condylar plane in the coronal view. The posterior and the distal condyles were used as the anatomical landmarks for referencing. PFA is indicated for isolated patellofemoral osteoarthritis.⁷ In this situation, the surfaces of the femoral condyles are normal.

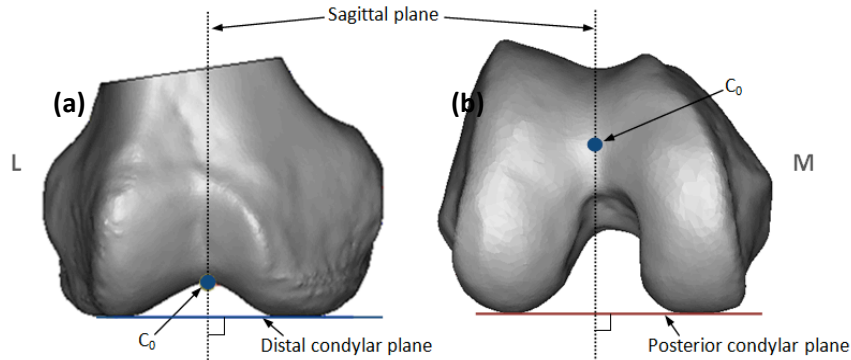


Fig. 1. Femoral reference system (a) coronal view (b) axial view.

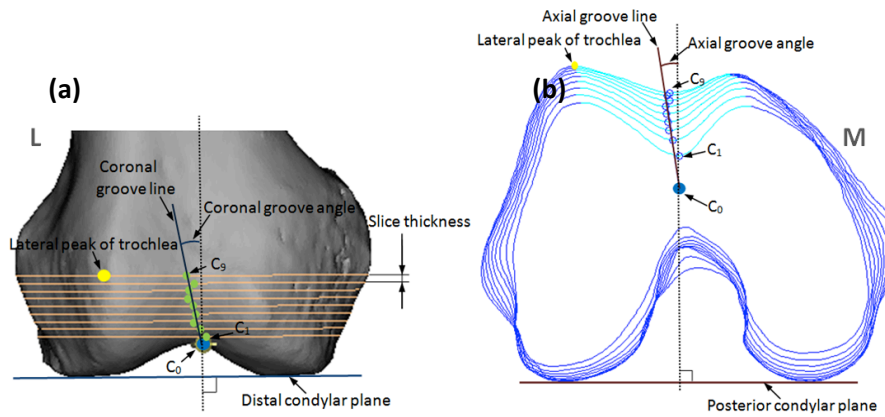


Fig. 2. Measurement of (a) Coronal groove angle (b) axial groove angle.

2.3. Groove line fitting

Nine equidistance axial slices were generated parallel to the distal condylar plane starting from the origin (C_0) to the lateral peak of the trochlea (Fig. 2 (a)). The surface curves were generated from the axial slices and analyzed (Matlab, Mathworks). The deepest groove points (C_1 to C_9 starting from the most distal slice to the most proximal slice) were identified from each axial slice. The axial and the coronal groove lines were then fitted to these deepest points by approximating the slope of the lines using the least squares theorem, with the starting point constrained to the origin (C_0). The axial groove line was fit on the axial plane and the coronal groove line was fit on the coronal plane. A positive axial groove angle was defined to be externally rotated relative to the line perpendicular to the posterior condylar plane in the axial view (Fig. 2(b)). A positive coronal groove angle was in valgus relative to the line perpendicular to the distal condylar plane in the coronal view (Fig. 2(a)).

2.4. Measurements in axial view

The trochlear inclination angles (TIA)⁸ were measured on the most proximal slice, the slice that goes through C₉ (Fig. 3). The TIA1 is the angle between the line connecting the lateral and medial peaks of the trochlea and the posterior condylar line. The TIA2 is the angle between the line connecting the lateral and medial peaks of the trochlea and the line perpendicular to the axial groove. The sulcus angle, the trochlear depth, the lateral trochlear inclination (LTI) and the trochlear facet asymmetry (TFA) were also measured.⁹

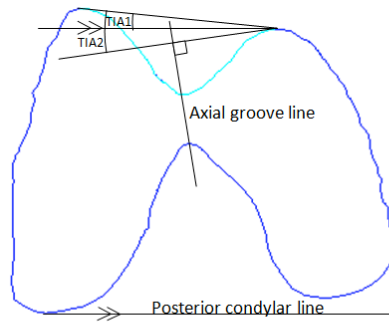


Fig. 3. Measurement of trochlear inclination angles (TIA).

2.5. Measurements in coronal view

The mechanical axis was drawn joining the centre of the femoral head and the origin (C₀). The angular position of the mechanical and the anatomical axes were then measured on the coronal plane. The mechanical angle1 and the anatomical angle1 were measured from the line perpendicular to the distal condylar plane to the mechanical and the anatomical axes respectively (Fig. 4(a)). The mechanical angle2 and the anatomical angle2 were measured from the coronal groove line (Fig. 4(b)).

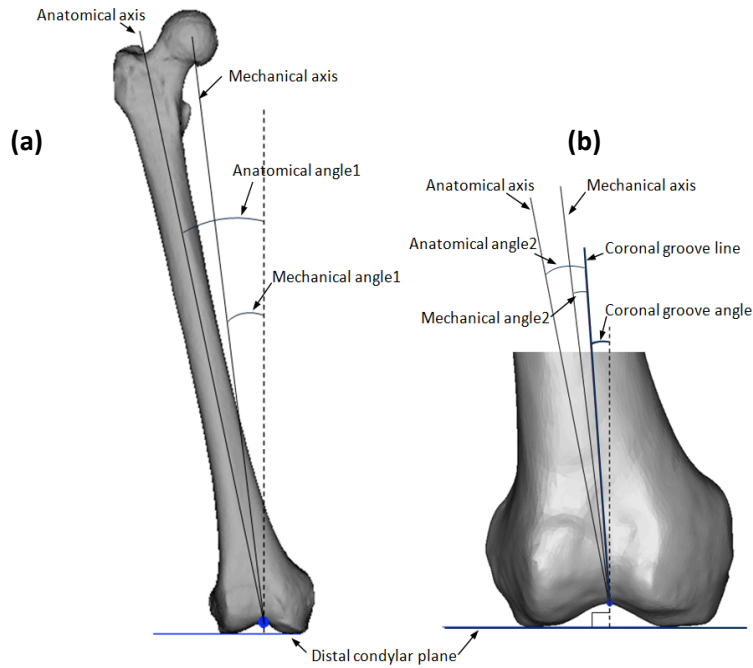


Fig. 4. Mechanical angle and anatomical angle measurement on the coronal plane relative to (a) the line perpendicular to the distal condylar plane (b) the coronal groove line.

2.6. Statistical study

The knees with any sign of trochlear dysplasia (trochlear depth < 5 mm, sulcus angle > 142° or TFA < 50 %) were grouped as the dysplastic group and the rest was the control group. Unpaired one way student's t-test was performed on the two groups to test the statistical significance.

3. Results

3.1. Measurements in axial view

The axial groove line was fit to the groove points on the axial plane with an average root mean square error (RMS_{error}) of 0.53 mm and the maximum RMS_{error} of 0.80 mm. The linear correlation between the axial groove angle and the TIA2 was higher than the TIA1, with an increased R^2 of 0.58 from 0.02 (Fig. 5). The TIA2 increases linearly as the axial groove angle increases, i.e., as aligns more externally.

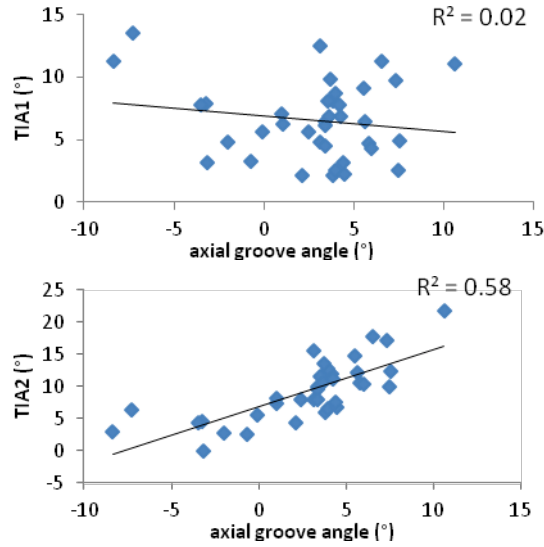


Fig. 5. Trochlear inclination angle (TIA) vs. axial groove angle measured from different reference line.

3.2. Measurements in coronal view

The average RMS_{error} between the coronal groove line and the groove points on the coronal plane was 0.55 mm with the maximum of 1.16 mm. The linear correlation between the mechanical angle and the anatomical angle increased when they were measured from the coronal groove line than measuring from the line perpendicular to the distal condylar plane. The R^2 between the mechanical angle1 and the anatomical angle1 was 0.59, which was increased to R^2 of 0.97 when the mechanical angle2 was plotted against the anatomical angle2 (Fig. 6).

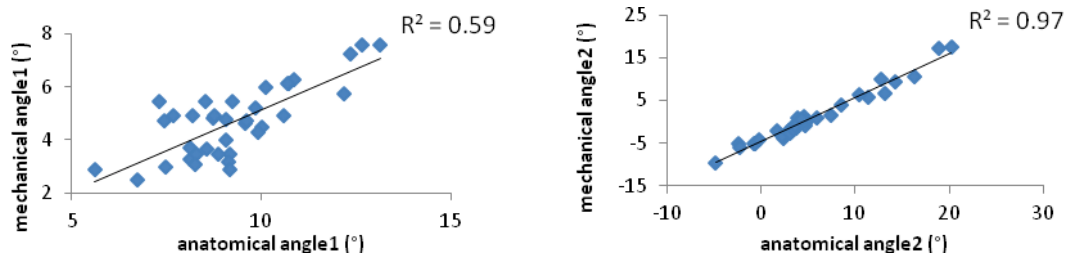


Fig. 6. Angular position of the mechanical axis vs. angular position of the anatomical axis measured from different reference line.

3.3. Statistical study

20 out of the 36 knees had at least one sign of trochlear dysplasia (trochlear depth < 5 mm, sulcus angle > 142° or TFA < 50 %) and the rest were classified as the control group.

The axial groove lines of the control group were significantly more externally rotated in relation to the axial groove lines of the dysplastic group (mean axial groove angle = 4.3° vs 1.9°, $p = 0.02$, Table 1). When the trochlear inclination angle was measured from the posterior condylar line, no significant difference was shown between the control and the dysplastic group (mean TIA1 = 6.9° vs 6.4°, $p = 0.11$, Table 1). However, when the trochlear inclination angle was measured from the line perpendicular to the axial groove line, it was significantly increased in the control compared with the dysplastic group (TIA2 = 11.1° vs 7.8°, $p = 0.02$, Table 1).

The coronal groove line was aligned in more valgus in the control group than in the dysplastic group (mean coronal groove angle = 5.9° vs 2.1°, $p = 0.03$, Table 1). The mechanical angle1 and the anatomical angle1 showed no significant difference between the control and the dysplastic groups ($p = 0.50$ and 0.47 respectively, Table 1). When the angles were measured from the coronal groove line, both the mechanical angle and the anatomical angle showed statistically significant difference between the two groups ($p = 0.03$ for both the mechanical angle2 and the anatomical angle2).

Table 1. Femoral parameter measurements for control and dysplastic groups.

		control group	dysplastic group	t-test
		mean	mean	p value
axial groove angle	[°]	4.3	1.9	0.02
TIA1	[°]	6.9	6.4	0.11
TIA2	[°]	11.1	7.8	0.02
coronal groove angle	[°]	5.9	2.1	0.03
mechanical angle1	[°]	4.7	4.7	0.50
anatomical angle1	[°]	9.2	9.3	0.47
mechanical angle2	[°]	1.2	2.6	0.03
anatomical angle2	[°]	3.4	7.3	0.03
trochlear depth	[mm]	6.9	4.4	<0.001
sulcus angle	[°]	135.5	147.7	<0.001
LTI	[°]	22.7	17.8	<0.001
TFA	[%]	71.8	56.7	<0.001

4. Discussions

In most knees with a deeper and more symmetrical groove, with a higher trochlear depth, a lower sulcus angle, a higher lateral trochlear inclination (LTI), and a higher trochlear facet asymmetry (TFA), the trochlear groove was more externally aligned in the axial view and more valgus aligned in the coronal view than the knees with a shallow trochleas. There were however some exceptions. In some knees with the normal and deep trochlear grooves without any sign of dysplasia, the trochlea was internally rotated and varus aligned. The range of the axial groove angle for the control group was -3.5° to 10.6°, with a standard deviation of 3.8°, having the mean groove angle of 4.3°. The range of the coronal groove angle was -5.3° to 13.3° with an average of 5.9° for the control group, with a standard deviation of 5.4°. In cases with an extreme internal and varus alignment of the trochlear groove, correcting the groove to

external rotation and valgus alignment during PFA may result an over correction. This might negatively affect the soft tissue tension in the ligaments and muscles resulting in abnormal patellofemoral kinematics. The high variability of the natural groove angle might explain the PFA prostheses with a more constraining groove design has poorer results than the ones with less constraining trochlear groove.¹⁰ This indicates that more attention should be given to the patient's natural trochlear groove alignment during PFA surgery. The prostheses having a deep groove with a built-in coronal alignment might over constrain the femoral trochleas with an internally rotated and varus aligned groove.

PFA is also indicated for the patients with trochlear dysplasia.¹⁰ When the dysplastic group is included, the standard deviations of the axial and the coronal groove angles increase to 4.1° and 6.0°, increasing the variability of the groove alignment. As a result of this high variability in the groove alignment of the femur, prosthesis with single fixed axial or coronal alignment angle might not fit all femurs. For example, a more internally aligned knee may need more symmetrical and flatter prostheses. On the other hand, prostheses having deeper groove with embedded varus alignment may produce good result for the patients with a more externally aligned and deeper trochlear groove. Measuring the orientation of the patient's natural trochlear groove preoperatively should help the surgeons select a prosthesis design that best suits the patient.

There are limitations with this research: We employ a different referencing technique to what has been used previously. Comparison to other studies will therefore be challenging, but our referencing technique was shown to be reliable and repeatable.⁹ We illustrated this technique on a population who can be considered to have normal patellofemoral anatomy. Thus we plan to increase our database with a more representable abnormal population in our follow-up studies.

References

1. Amis AA, Senavongse W, Darcy P, Biomechanics of patellofemoral joint prostheses, *Clin Orthop* **436**:20-9, 2005.
2. Boucher HR, Patellofemoral arthroplasty, *Curr Opin Orthop* **17**:47-50, 2006.
3. Berger RA, Rubash HE, Seel MJ, Thompson WH, Crossett LS, Determining the rotational alignment of the femoral component in total knee arthroplasty using the epicondylar axis, *Clin Orthop* **286**:40-7, 1993.
4. Middleton FR, Palmer SH, How accurate is Whiteside's line as a reference axis in total knee arthroplasty? *Knee* **14**:204-207, 2007.
5. Nagamine R, Miura H, Inoue Y, Urabe K., Matsuda S, Okamoto Y, Nishizawa M, Iwamoto Y, Reliability of the anteroposterior axis and the posterior condylar axis for determining rotational alignment of the femoral component in total knee arthroplasty, *J Orthop Sci* **3**: 194-198, 1998.
6. Stiehl JB, Cherveney PM, Femoral rotational alignment using the tibial shaft axis in total knee arthroplasty. *Clin Orthop Relat Res* **331**: 47-55, 1996.
7. Lonner JH, Patellofemoral arthroplasty: Pros, cons, and design considerations, *Clin Orthop Relat Res* **428**:158-65, 2004.
8. Kamath AF, Slattery TR, Levack AE, Wu CH, Kneeland JB, Lonner JH, Trochlear inclination angles in normal and dysplastic knees, *J Arthroplasty* **28**:214-9, 2013.
9. Cho K, Müller JH, Scheffer C, Erasmus PJ, Application of an artificial neural network for the quantitative classification of trochlear dysplasia, *J Mech Med Biol* **13**:1350059, 2013.

10. Lustig S, Magnussen RA, Dahm DL, Parker D, Patellofemoral arthroplasty, where are we today? *Knee Surg Sport Tr A* **20**:1216-26, 2012.

THE FAST WAVE IS SIMPLY DETERMINED BY THE FABRIC TENSOR

YOUNG JUNE YOON

*Division of Mechanical Engineering, Hanyang University
17 Haengdang-dong, Seongdong-gu, Seoul 133-791, Korea
yjoon@hanyang.ac.kr*

The fabric tensor is a good measure to determine the anisotropy of a cancellous bone. Ultrasound is one method to determine the mechanical properties of a cancellous bone. We start from the fact that the fast wave in poroelastic theory is identical to the bulk wave velocity, and then, we formulate the equation of fast wave in terms of fabric tensor for the calcaneus.

Keywords: Biot theory, Ultrasound, Bar equation, Fabric tensor, calcaneus

1. Introduction

The fabric tensor is a good measure to determine the anisotropy of a cancellous bone. There are three types of methods to measure the fabric tensor of a cancellous bone – the mean intercept length (MIL)^{1,2}, the volume orientation (VO) method³, and the star volume distribution (SVD) method^{4,5}.

Ultrasound is one method to determine the mechanical properties of a cancellous bone^{6,7}. It was found that the elastic modulus measured by ultrasound is almost equal to the mechanically tested and measured elastic modulus^{7,8}. Recently Biot theory⁹⁻¹¹ was employed to characterize the mechanical properties of a cancellous bone. Experimentally and theoretically two waves were observed in cancellous bone ultrasound measurements (Hosokawa and Otani 1997; Wear et al. 2005). It is reported that the fast wave is identical to the bulk wave.

For an anisotropic porous material, Cowin and Cardoso¹², and, Cardoso and Cowin¹³ expanded the wave equation of Biot theory by employing the fabric tensor illustrated in Cowin¹⁴. However, there are too many unknown parameters to be determined in order to calculate the speed of sound (or wave velocity).

We believe that the speed of a fast wave in Biot theory is identical to the speed of the bulk wave because the elastic modulus measured by ultrasound is identical to the mechanically tested and measured elastic modulus. Thus we expand the bulk wave equation by using the fabric tensor and propose a simple equation for further experiments.

2. Method

The fabric tensor is related to the elastic modulus when the bone matrix is assumed to be isotropic, which is given by

$$E_i = E_s [m_1 + m_2 I + m_3 F_i + m_4 F_i^2] \quad , \quad (1)$$

Where E_i is the elastic modulus in i direction and F_i is the fabric tensor in i direction. The coefficients m_1 , m_2 , m_3 , and m_4 are determined by

$$m_1 = d_2 \left[(1-\phi)^n + d_1 \phi (1-\phi)^n \right] \quad , \quad (2)$$

and

$$m_2 = m_3 = m_4 = -d_1 \phi (1-\phi)^n \quad . \quad (3)$$

Then the equation (1) can be written as

$$E_i = E_s \left[d_2 (1-\phi)^n + d_1 \phi (1-\phi)^n (d_2 - II - F_i - F_i^2) \right] \quad , \quad (4)$$

Where d_1 and d_2 are unknown coefficients to be determined. ϕ is the porosity. II is the second invariant, which is given by

$$II = \frac{1}{2} \left((tr F)^2 - tr F^2 \right) \quad . \quad (5)$$

The bone matrix elastic modulus E_s should be equal to the elastic modulus in i direction, E_i when the porosity ϕ is zero, then the unknown coefficient d_2 becomes 1 (i.e., $d_2 = 1$). The equation (4) is simplified to

$$E_i = E_s (1-\phi)^n \left[1 + d_1 \phi (1 - II - F_i - F_i^2) \right] \quad . \quad (6)$$

Here the anisotropy of the elastic modulus E_i is determined the term, $d_1 \phi (1 - II - F_i - F_i^2)$. For isotropic material, the elastic modulus E_i is simply determined by the equation $E_i = E_s (1-\phi)^n$ without considering the anisotropic behavior. By comparing it to Wear¹⁵, we can conclude that the exponent n is 1.75 (i.e., $n = 1.75$) for human calcaneus. In Wear¹⁵, 53 human calcaneus samples were tested and the best fit for the curve between the speed of sound (SOS) and the porosity was found, of which exponent n is 1.75. By employing the bar equation, we can simply conclude the relationship between the speed of sound (SOS) of the fast wave and the fabric tensor F_i ,

$$v_i = \sqrt{\frac{E_s (1-\phi)^{1.75} \left[1 + d_1 \phi (1 - II - F_i - F_i^2) \right]}{(1-\phi) \rho_s + \phi \rho_w}} \quad , \quad (7)$$

Where ρ_s is the bone matrix density and ρ_w is the density of water. For numerical calculation, the

fabric tensors for human calcaneus F_1 , F_2 , and F_3 are given by $F_1 = 0.398 \pm 0.016$, $F_2 = 0.319 \pm 0.014$, and $F_3 = 0.286 \pm 0.011$ ¹⁶. From equation (5), we can obtain the second invariant II as 0.331. The porosity ϕ is 83.2%. Since the wave equation indicates the fast wave in poroelasticity, Eq. (7) should be identical to the bulk wave equation for isotropic case, which is given by

$$\bar{v} = \sqrt{\frac{K}{(1-\phi)\rho_s + \phi\rho_w}} \quad (8)$$

When we average Eq. (7) for isotropic case and the Poisson's ratio is selected to be 0.32, the unknown parameter d_1 is obtained to be 0.112. Here K is the bulk modulus for calcaneus.

3. Results And Discussion

We simply formulate the fast wave velocity with respect to the porosity and fabric tensor as

$$v_i = \sqrt{\frac{E_s (1-\phi)^{1.75} [1 + 0.112\phi(1 - II - F_i - F_i^2)]}{(1-\phi)\rho_s + \phi\rho_w}} \quad (9)$$

It is a theoretical formulation, but we need further experiments for validating the given equation.

Acknowledgement

This work was supported by the National Research Foundation of Korea (2010-0023070).

References

1. Harrigan T, Mann RW, Characterization of microstructural anisotropy in orthotropic materials using a second rank tensor. *J. Mat. Sci* 19:761-769, 1984.
2. Whitehouse WJ, The quantitative morphology of anisotropic trabecular bone. *J. Microsc* 101: 153-168, 1974.
3. Odgaard A, Kabel J, van Rietbergen B, Dalstra M, Huiskes R, Fabric and elastic principle directions of cancellous bone are closely related. *J. Biomech* 30:487-495, 1997.
4. Cruz-Orive LM, Karlsson LM, Larsen SE, Wainstein F, Characterizing anisotropy: a new concept. *Micron Microscopica Acta* 23: 75-76, 1992.
5. Karlsson LM, Cruz-Orive LM, Application of the start volume distribution to characterize structural anisotropy of a duplex stainless steel. In *Stereology in Materials Science: Demonstration of Some Methods*. Royal Institute of Technology, Stockholm, 1993.
6. Rho JY, An ultrasonic method for measuring the elastic properties of human tibial cortical and cancellous bone. *Ultrasonics* 34: 777-783, 1996.
7. Turner CH, Cowin SC, Rho JY, Ashman RB, Rice JC, The fabric dependence of the orthotropic elastic constants of cancellous bone. *J. Biomech* 23:549-561, 1990.

8. Ashman RB, Corin JD, Turner CH, Elastic properties of cancellous bone: Measurement by an ultrasonic technique. *J. Biomech.* 20: 979-983, 1987.
9. Haire TJ, Langton CM, Biot theory: a review of its application to ultrasound propagation through cancellous bone. *Bone* 24: 291-295, 1999.
10. Williams JL, Ultrasonic wave propagation in cancellous bone and cortical bone: Prediction of some experimental results by Biot's theory. *Journal of the Acoustical Society of America* 91: 1106-1112, 1992.
11. Yoon YJ, Chung JP, Bae CS, Han SY, The speed of sound through trabecular bone predicted by Biot theory. *J. Biomech.* 45: 716-718, 2012.
12. Cowin SC, Cardoso L Fabric dependence of wave propagation in anisotropic porous media. *Biomech Model Mechanobiol* 10: 39-65, 2011.
13. Cardoso L, Cowin SC (2011) Fabric dependence of quasi-waves in anisotropic porous media. *Journal of the Acoustical Society of America* 129: 3302-3316
14. Cowin SC, The relationship between the elasticity tensor and the fabric tensor. *Mechanics of Materials* 4: 137-147, 1985
15. Wear KA, Laib A, Studber AP, Reynolds JC, Comparison of measurements of phase velocity in human calcaneus to Biot theory. *J. Acoustic Soc. Am.* 117: 3319 – 3324, 2005.
16. Sourzanchi MF, Palacio-Mancheno P, Borisov YA, Cardoso L, Cowin SC, Microarchitecture and bone quality in the human calcaneous: Local variations of fabric anisotropy. *Journal of Bone and Mineral Research* 27(12) 2562-2572, 2012

COMPARING FLEXION AND EXTENSION MOVEMENTS IN ESTIMATING KNEE FUNCTIONAL AXIS

FRANCESCA COLLE^{*,†,‡}, NICOLA FRANCESCO LOPOMO^{*,†}, DANILO BRUNI^{*}, FRANCESCO IACONO^{*}, STEFANO ZAFFAGNINI^{*}, MAURILIO MARCACCI^{*,†}

^{*}Laboratorio di Biomeccanica ed Innovazione Tecnologica, Istituto Ortopedico Rizzoli, via di Barbiano 1/10
40136 Bologna, Italy

[†]Laboratorio NaBI, Istituto Ortopedico Rizzoli, via di Barbiano 1/10
40136 Bologna, Italy

[‡]The BioRobotics Institute, Scuola Superiore Sant'Anna, Polo Sant'Anna Valdera, Viale Rinaldo Piaggio, 34
56025 Pontedera (Pisa), Italy
f.colle@biomec.ior.it

www.ior.it/biomec

Proper rotational alignment of femoral component in total knee arthroplasty (TKA) is mandatory to achieve correct kinematics, good ligament balance and proper patellar tracking. Starting from the hypothesis that the function flexion axis (FFA) can thoroughly describe knee kinematics, the purpose of this study was to analyse which factors could affect the FFA estimation by separately focusing on flexion and extension movements. FFA was estimated on 79 patients undergoing TKA. Internal-external (IE) rotations and the angle between the FFA and the transepicondylar axis, in axial and frontal plane, were separately analysed for flexion and extension in both pre- and post-implant conditions. The IE rotation showed a statistically significant difference in pre-implant condition, between 25° and 35° of flexion ($p < 0.05$). The angle showed statistical differences between paths in both pre- and post-implant conditions and in both frontal and axial plane. Analogously, pre- and post-operative conditions presented statistically significant difference. The estimation of the functional axis changed in the frontal plane in relation to flexion and extension movements, above all considering pre-operative conditions, therefore from a clinical point of view it is important to consider the only flexion movement for functional axis estimation during navigated TKA.

Keywords: Functional Flexion Axis; Total Knee Arthroplasty; Computer Aided Medicine.

1. Introduction

Providing proper rotational alignment of femoral component in total knee arthroplasty is mandatory to achieve correct kinematics, good ligament balance and proper patellar tracking. The femoral component malpositioning is indeed a critical aspect in TKA because it may cause several problems such as joint instability, excessive wear of the polyethylene component and joint stiffness, which may lead to the early failure of the implant [1, 2].

Recently functional references, like the function flexion axis (FFA), have been introduced to achieve this goal and to overcome the issues related to the use of the anatomical landmarks. This method is inherently joint- and patient-specific and it is based on the identification of a functional landmark estimated through the knee joint Mean Helical Axis (MHA) [3].

Several studies reported the benefits of using the FFA to describe the tibio-femoral flexion-extension movement [3, 4, 5, 6, 7] and also to assess the rotational alignment of the femoral component [2, 8, 9, 10, 11, 12], but, on the other hand highlighted that further analyses are required to better verify the FFA

applicability to the general clinical practice. Some works focused on assessing the reliability of the FFA compared to the anatomical landmarks [2, 8, 9, 11] as first step to prove its applicability. Starting from the hypothesis that the FFA can thoroughly describe knee kinematics but that the joint kinematics itself can be different from flexion to extension movements, the purpose of this study was to analyse which factors could affect the FFA estimation by separately focusing on flexion and extension movements.

2. Materials and Methods

A cohort of consecutive subjects presenting osteoarthritic knees was prospectively enrolled for the evaluation of FFA study between September 2008 and September 2010. Inclusion criteria consisted in primary osteoarthritis (OA), Kellgren-Lawrence score up to 4 and BMI < 40 kg/m². Exclusion criteria included all with post-traumatic and rheumatoid arthritis. Seventy-nine patients were thus included in the analysis, presenting an average age of 72 ± 5 years (range 56 - 82 years). All patients received a cemented TKA with patellar resurfacing. All the surgeries were guided by a commercial navigation system (BLUGS, Orthokey LLC, Delaware, USA) that neither did alter the original surgical technique nor affect knee kinematics. The navigated protocol and the accuracy of the method have been already widely reported in literature [13, 14]. A software specifically designed for kinematic analysis (KLEE, Orthokey LLC, Lewes, Delaware, USA) [14] allowed to acquire kinematic data in both pre-implant and post-implant condition.

After skin incision and before meniscal and Anterior Cruciate Ligament (ACL) removal, femoral and tibial trackers were fixed, with patella reduction, and anatomical and pre-implant kinematic data were acquired. Post-implant kinematic data were collected after definitive prosthesis implantation. The joint coordinate reference system (JCS) was specifically defined by means of anatomical landmarks acquisitions, performed on femur and tibia, as proposed by Cole et al. [15] and Grood and Suntay [16]. Passive flexion and extension movements, from 0° to 120°, were separately acquired three times for each subject, both before and after implant positioning. All the information acquired by the navigation system were off-line processed with proprietary routines (Matlab, Mathworks, Natick, MA, USA).

The relative motion of tibia with respect to femur was analysed with Grood and Suntay algorithm [16]. Rotations during the passive range of motion (PROM) were computed and described in terms of instantaneous flexion–extension (FE) and internal-external (IE) rotations.

The angle between FFA and TEA was studied in two different anatomical planes (specifically axial and frontal) in order to more easily compare the obtained results from a clinical point of view (Figure 1).

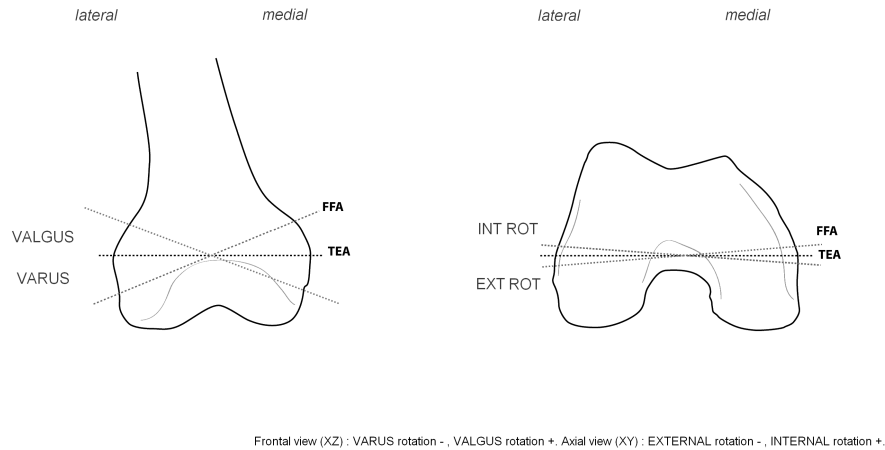


Fig. 2. The angle between the FFA and the TEA in frontal (left) and axial (right) plane.

The statistical analysis was performed considering flexion (0° - 120°) and extension (120° - 0°) movements, separately.

Difference in internal-external rotations during flexion and extension paths in pre- and post-operative conditions were tested with independent and two-tailed paired Student t-test respectively, thus to evaluate any statistical difference between flexion and extension movements at each frame of PROM. Independent Student t-test was performed on the angles identified by FFA with respect to TEA in both the planes, to evaluate any statistical difference in the estimation of FFA between flexion and extension movements. These inferential statistics was also individually performed on both pre- and post-implant data. Moreover paired Student t-test was executed between pre-operative and post-operative estimation of FFA analysing the corresponding angles between FFA and TEA, in order to identify the differences introduced by the implant in the FFA estimation.

Statistical significance was set to 95% ($p = 0.05$) for all the tests.

Analyse-it software (Analyse-it Software, Ltd., The Tannery 91 Kirkstall Road, Leeds, LS3 1HS, United Kingdom) was used to perform the reported statistical analysis.

3. Results and discussion

The analysis of IE rotation during flexion and extension both in pre- and post-implant condition reported a statistically significant difference between the two paths in pre-implant condition, between 25° and 35° of flexion ($p < 0.05$) (Figure 2).

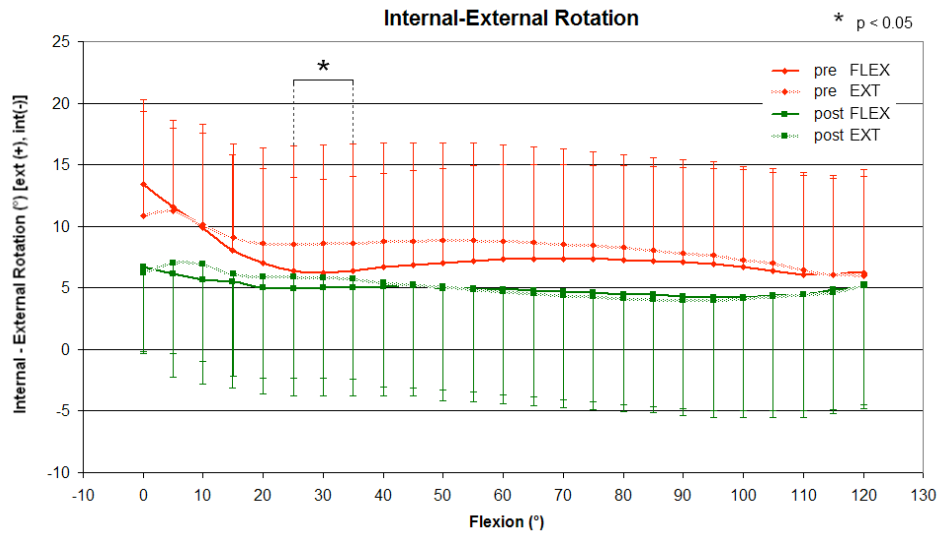


Fig. 2. Internal-External (IE) rotation during PROM in pre- and post-implant conditions for flexion and extension paths.

The independent Student t-test of FFA-TEA angle in frontal (XZ) and axial (XY) planes, showed significant statistical differences ($p < 0.0001$) between flexion and extension movements in both pre- and post-implant conditions and in both frontal and axial plane (Figure 3). Analogously, the paired Student t-test, on pre- and post-operative conditions, presented statistically significant difference ($p < 0.0001$) as showed in Figure 4.

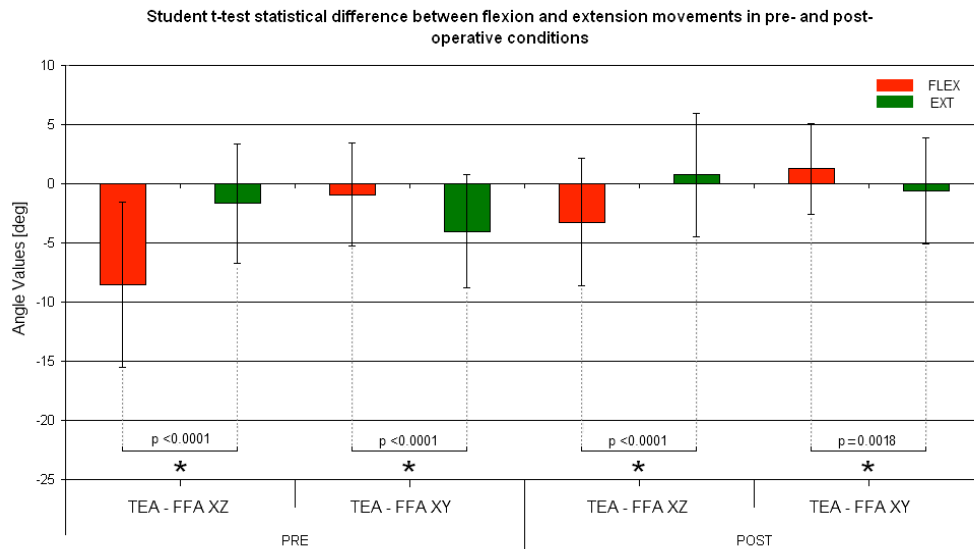


Fig. 3. Student t-test statistical difference between flexion and extension movements in pre- and post-operative conditions (XZ (frontal plane): varus -, valgus +; XY (axial plane): internal +, external -).

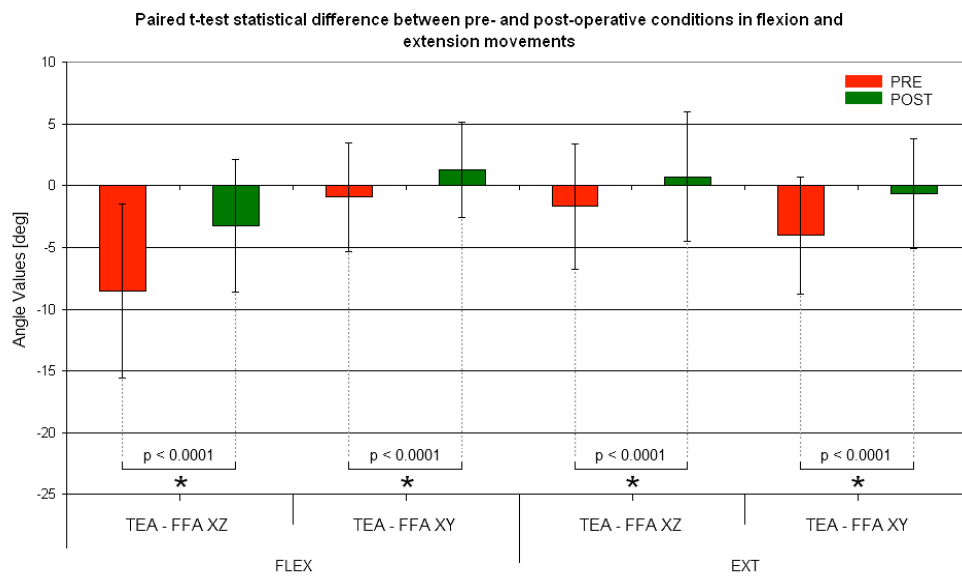


Fig. 4. Paired t-test statistical difference between pre- and post-operative conditions in flexion and extension movements (XZ (frontal plane): varus -, valgus +; XY (axial plane): internal +, external -).

The estimation of FFA, identified through the FFA-TEA angle, changed in the frontal plane in relation to flexion and extension movements, above all considering pre-operative conditions. Specifically pre-implant FFA, computed during flexion movements, significantly differed from TEA, whereas the FFA-TEA angle resulting from extension movements was closer to zero. Moreover, the orientation of FFA changed significantly after TKA both in flexion and extension, mostly in frontal plane, while the correspondence between FFA and TEA was generally maintained in axial plane. Given more details, in pre-operative conditions the FFA computed in the frontal plane by flexion movements, showed a greater distance from TEA and an higher variability ($-8.5^{\circ} \pm 7.0^{\circ}$), while in the axial plane a greater distance derived from the analysis of the extension movements ($-4.0^{\circ} \pm 4.7^{\circ}$). These values reduced in post-operative conditions mainly due to the influence of the prosthesis: the FFA-TEA angle was specifically $-3.2^{\circ} \pm 5.4^{\circ}$ in the frontal plane for flexion movements, and $-0.6^{\circ} \pm 4.5^{\circ}$ in the axial plane for extension movements.

Both pre-operative and post-operative results were in agreement with those reported by Colle et al. [17], but the present study better highlighted the differences during flexion and extension movements that could be due to different factors, first of all, the presence of the screw-home mechanism, that occurs in the first 30° of PROM and that was more evident in the frontal plane during flexion movement, whereas the FFA estimation resulted less stable in the axial plane during extension. These results could be also due to the differences involuntarily introduced by the surgeon in passively performing flexion or extension movements. In fact, it is possible that an abnormal external rotation was maintained during extension, especially during the first 30° of motion, due to a temporary loss of contact of the articular surfaces and therefore causing the absence of the screw home mechanism in frontal plane and the FFA unusual variation in axial plane, as suggested by the results of IE rotation during flexion and extension movements which showed a statistically significant difference between 25° and 35° of PROM.

4. Conclusion

This study demonstrated that the FFA requires further analyses in order to allow its application to the daily clinical practice. In particular, its estimation in the frontal plane remains crucial. The pre-implant FFA-TEA angle showed in fact a greater value in the frontal plane with respect to axial plane for both flexion and extension movements. This was probably due to the influence of osteoarthritis on altering the proper condyles shape that did not occur in axial plane. Moreover the present work demonstrated that the FFA computation was significantly influenced by the different paths of motion, i.e. flexion and extension, suggesting the importance of considering the only flexion movements for FFA estimation during navigated TKA.

References

1. Aglietti P, Sensi L, Cuomo P, Ciardullo A. Rotational Position of Femoral and Tibial Components in TKA Using the Femoral Transepicondylar Axis, *Clin Orthop* **466**:2751–2755, 2008.
2. Oussedik S, Scholes C, Ferguson D, Roe J, Parker D. Is femoral component rotation in a TKA reliably guided by the functional flexion axis?, *Clin Orthop* **470**:3227–3232, 2012.

3. Woltring HJ, Huiskes R, de Lange A, Veldpaus FE. Finite centroid and helical axis estimation from noisy landmark measurements in the study of human joint kinematics, *J Biomech* **18**:379–389, 1985.
4. Blankevoort L, Huiskes R, De Lange A. Helical axes of passive knee joint motions. *J Biomech*. 1990;23:1219–1229.
5. Van den Bogert AJ, Reinschmidt C, Lundberg A. Helical axes of skeletal knee joint motion during running, *J Biomech* **41**:1632–1638, 2008.
6. Dennis DA, Mahfouz MR, Komistek RD, Hoff W. In vivo determination of normal and anterior cruciate ligament-deficient knee kinematics, *J Biomech* **38**:241–253, 2005.
7. Sheehan FT. The finite helical axis of the knee joint (a non-invasive in vivo study using fast-PC MRI), *J Biomech* **40**:1038–1047, 2007.
8. Colle F, Lopomo N, Bruni D, Visani A, Iacono F, Zaffagnini S, Marcacci M. Analysis of knee functional flexion axis in navigated TKA: identification and repeatability before and after implant positioning, *Knee Surg Sports Traumatol Arthrosc* **22**:694–702, 2014.
9. Doro LC, Hughes RE, Miller JD, Schultz KF, Hallstrom B, Urquhart AG. The reproducibility of a kinematically-derived axis of the knee versus digitized anatomical landmarks using a knee navigation system, *Open Biomed Eng J* **2**:52, 2008.
10. Eckhoff D, Hogan C, DiMatteo L, Robinson M, Bach J. AN ABJS BEST PAPER: Difference Between the Epicondylar and Cylindrical Axis of the Knee, *Clin Orthop* **461**:238, 2007.
11. Siston RA, Cromie MJ, Gold GE, Goodman SB, Delp SL, Maloney WJ, Giori NJ. Averaging different alignment axes improves femoral rotational alignment in computer-navigated total knee arthroplasty, *J Bone Joint Surg Am* **90**:2098–2104, 2008.
12. Walker PS, Heller Y, Yildirim G, Immerman I. Reference axes for comparing the motion of knee replacements with the anatomic knee, *The Knee* **18**:312–316, 2011.
13. Casino D, Zaffagnini S, Martelli S, Lopomo N, Bignozzi S, Iacono F, Russo A, Marcacci M. Intraoperative evaluation of total knee replacement: kinematic assessment with a navigation system, *Knee Surg Sports Traumatol Arthrosc* **17**:369–373, 2009.
14. Martelli S, Zaffagnini S, Bignozzi S, Bontempi M, Marcacci M. Validation of a new protocol for computer-assisted evaluation of kinematics of double-bundle ACL reconstruction, *Clin Biomech Bristol Avon* **21**:279–287, 2006.
15. Cole GK, Nigg BM, Ronsky JL, Yeadon MR. Application of the joint coordinate system to three-dimensional joint attitude and movement representation: a standardization proposal, *J Biomech Eng* **115**:344–349, 1993.
16. Grood ES, Suntay WJ. A joint coordinate system for the clinical description of three-dimensional motions: application to the knee, *J Biomech Eng* **105**:136–144, 1983.
17. Colle F, Lopomo N, Bruni D, Visani A, Iacono F, Zaffagnini S, Marcacci M. Analysis of knee functional flexion axis in navigated TKA: identification and repeatability before and after implant positioning, *Knee Surg Sports Traumatol Arthrosc* **22**:694–702, 2014.

COMPARISON BETWEEN SINGLE RADIUS AND J-CURVE TOTAL KNEE ARTHROPLASTY DESIGNS: A FINITE ELEMENT ANALYSIS.

HÉCTOR ROBLEDO YAGÜE

*BEAMS Department, Université Libre de Bruxelles, Franklin Rooseveltlaan 50, 1050 Brussels, Belgium
hrobledo@ulb.ac.be*

SILVIA PIANIGIANI

*IRCCS Istituto Ortopedico Galeazzi
Via R. Galeazzi 4, 20161
Milano, Italy*

BERNARDO INNOCENTI

*BEAMS Department, Université Libre de Bruxelles, Franklin Rooseveltlaan 50, 1050 Brussels, Belgium
bernardo.innocenti@ulb.ac.be*

Nowadays the number of instantaneous centers of knee flexion/extension rotation is not known with absolute certainty. For that reason, different Total Knee Arthroplasty (TKA) femoral components models are available in the market; there are designed under different hypotheses. In the surgery field there is no agreement about the veracity of the theoretical advantages of a single radius design with respect to a multiple radii one, like the J-curve and no literature study compares in deep these two solutions for TKAs. For that reasons, a finite element analysis was carried out. Two models were generated to analyze a single radius design and a J-curve design; a standard gait cycle and the downward movement of a squatting activity were simulated for both models. The kinematics, the contact area and the force due to the contact pressure were obtained and compared.

After comparing the results, no significant differences are detected during a gait cycle whereas during the squat task, differences are shown up especially in the post engagement.

Keywords: TKA; J-curve; single radius, kinematics, kinetics.

1. Introduction

Until the last decade native knee joints were thought to present multiple instantaneous centers of knee flexion/extension (KF/KE) rotation,^{1,2} therefore the femoral components designed for total knee arthroplasty (TKA) purposes were designed with a progressive increase of the radius of curvature from the posterior to the anterior part of the knee. Among these multiple radii of rotation designs, the J-Curve (JC) has been one of the most widely used, providing successful results as a method for avoiding the reduction in mobility and pain caused by usual diseases such as osteoarthritis, rheumatoid arthritis or post-traumatic arthritis.

However, recent studies have suggested the presence of only one KF/KE axis fixed within the femur leading to the manufacture of the so called single radius (SR) femoral components.³

This change in the geometry may induce changes in the functional performance of

the artificial joint. In fact, it has been observed that the KF/KE axis of the SR is more posterior to those of the JC design, hence the extensor moment arm is larger, the quadriceps forces are lower and then, daily life activities are easier to carry out.⁴ Moreover, this reduction in quadriceps forces leads to a lower load induced in the patella and then, smaller anterior knee pain and patellar component wear.

As these theoretical advantages remains without being proved, this study aims to make a comparison between a SR and a JC design, working with the same posterior stabilized tibial component, during daily life activities such as walking and squatting. In particular, the tibio-femoral kinetics and kinematics will be analyzed by means of a finite element analysis (FEA).

2. Materials and Methods

Only the femoral component and the tibial bearing insert (along with the upper part of the tibial tray) have been used for developing this study. The influence on the loads of the other elements present in the knee joint such as the patella and ligaments was already taken into account in the data obtained from the standard ISO 14243-1, in the case of the gait cycle, and from a cadaver knee motion test, in the case of the downward movement of the squat cycle.

2.1. Design of the SR component

Starting from a JC design, a SR femoral component was created with the aid of a CAD software. For carrying out this operation, the rear part of the piece which was beyond the point at which the first change of radius appeared was removed. After that, the piece was symmetrically reproduced in order to get condyles with a fixed radius, the surplus of this operation was removed and the original cam was reinserted.

2.2. Development of the finite element analysis

The same procedure was followed for both femoral designs. First, the upper part of the tibial tray was added to the tibial bearing and the system femur-tibia was properly assembled. Secondly, the corresponding materials were created and assigned to each piece: pure titanium for the tibial tray, polyethylene for the tibial bearing and an alloy of cobalt-chrome for the femoral component.⁵

Next, the conditions for performing an explicit analysis were fixed, including a mass scaling of $5 \cdot 10^{-5}$ that optimized the binomial accuracy-computerization time.

After that, the interaction between surfaces of femoral and tibial components was defined and a friction coefficient of 0,1 was included to simulate real conditions of movement. At this point, the loads and boundary conditions were assigned. Whereas the loads defining the gait cycle were directly applied, the

data for the squat cycle, which came from an experimental test, were submitted to a filtering task and a polynomial approximation of the trend before being entered into the software. The boundary conditions were common for both activities: the lower part of the tibial component was embedded.

Finally, both components were meshed with regular and tetrahedral elements of different global sizes (3mm vs 1,5mm) to better fit each geometry.

2.3. Outputs of the finite element analysis

The outputs selected in order to analyze the models were the contact area in both compartments and the post, the total force due to contact pressure and the center of this total force. The most determinant results are presented in the next section.

3. Results

Figure 1a shows the trend of kinematics of the center of total force in the Anterior-Posterior (AP) direction during a standard gait cycle. No significant difference is observed between the two TKA designs for all the observed directions.

Figure 1b shows the magnitude of the total force due to contact pressure in different regions of the model. In comparison with the JC design, the total force exerted on the back side of the post in the SR design is around 0,8% lower; in the lateral compartment of the tibia, the force is 0,53% higher and in the medial compartment it is 0,42% lower. In both medial and lateral sides of the post, no force is exerted by any model.

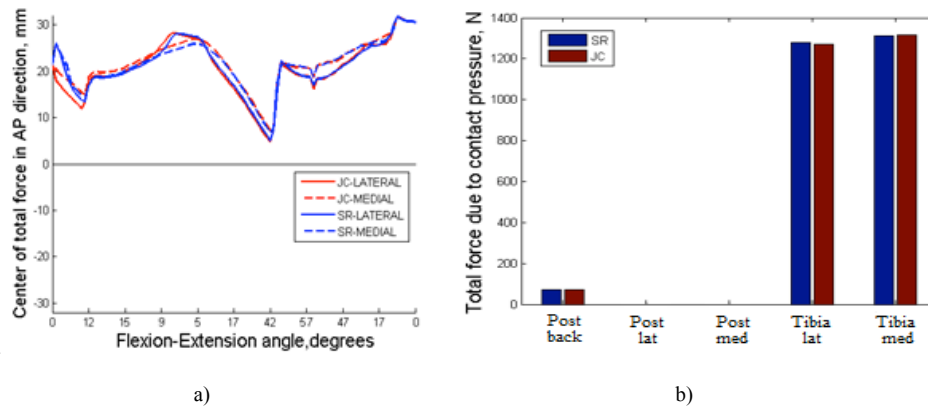


Fig. 1. a) Position of the center of total force in AP direction during gait cycle; b) Total force in post and tibial compartments during gait cycle .

Figure 2a shows the trend of kinematics of the center of total force in the Anterior-Posterior (AP) direction during the downward movement of a squatting task. The behaviour of both design is very similar until they reach an angle of 80°. At this point, the trend of the SR has a more pronounced drop. In the other analyzed directions, SR presents less uniform fashion with respect to the JC design after 80°.

Finally, figure 2b shows again the magnitude of the total force due to contact pressure. In the case of the squat task higher differences can be observed. Again comparing the SR design with respect to the JC design, the total force exerted on the back side of the post is 2,33% higher; on the lateral compartment of the tibia, the force is 3,69% higher and on the medial compartment it is 0,36% lower. In both medial and lateral sides of the post, no force is exerted by model.

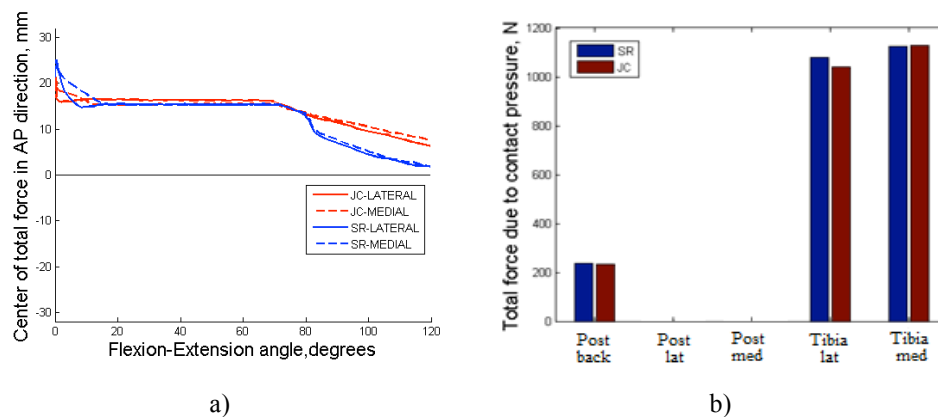


Fig. 2. Position of the center of total force in AP direction during squatting; b) Total force in post and tibial compartments during squatting.

4. Conclusions

After considering all the results, different conclusions can be set depending on the movement.

If we take into account the gait cycle, where the flexion angle is always lower than 60°, there are no benefits in using the SR or the JC design, as the evolution is quite similar and the exerted force difference is lower than 1%. Then, their response will be almost identical.

However, during high flexion, such as in the squat task, some stability problems can appear in knees with SR femoral components due to those changes that it experiences after 80° in all the directions and the general increase in the forces exerted on the polyethylene tibial component.

References

1. Gunston FH, Polycentric knee arthroplasty, Prosthetic simulation of normal knee movement. J Bone Joint Surg Br 1971, 53(2):272-277.
2. Frankel VH, Burstein AH, Brooks DB, Biomechanics of internaderangement of the knee Pathomechanics as determined by analysis of the instant centers of rotation. J Bone Joint Surg Am 1971, 53:945-962.1. Beeson MJ,

Foundations of Constructive Mathematics, Springer, Berlin, 1985.

3. Pinskerova V, Iwaki H, Freeman MA, The shapes and relative movements of the femur and tibia at the knee. *Orthopade* 2000, 29(Suppl 1):3-5.
4. D'Lima DD, Poole C, Chadha H, Hermida JC, Mahar A, Colwell CWJ, Quadriceps moment arm and quadriceps forces after total knee arthroplasty, *Clin Orthop Rel Res* 2001, 392:213-220.
5. F Farizon, J L Aurelle, J Rieu, G Bousquet, Wear characteristics of different metal-polyethylene bearing surfaces. An experimental study of a new model of knee prosthesis, Centre d'Orthopédie-Traumatologie, CHRU de Saint-Etienne.

POST-CAM CONTACT MECHANISM DURING SEVERAL ACTIVITIES IN PRIMARY AND SEMI-CONSTRAINED TOTAL KNEE ARTHROPLASTY DESIGN: A FINITE ELEMENT STUDY

RAQUEL ALARIO BERNABÉ
*BEAMS Université Libre de Bruxelles
Franklin Rooseveltlaan 50, 1050 Brussels, Belgium
ralariob@ulb.ac.be*

SILVIA PIANIGIANI
*IRCCS Istituto Ortopedico Galeazzi
Via R. Galeazzi 4, 20161 Milano, Italy*

BERNARDO INNOCENTI
*BEAMS, Université Libre de Bruxelles, Franklin Rooseveltlaan 50, 1050 Brussels, Belgium
bernardo.innocenti@ulb.ac.be*

During last three decades, Posterior-Stabilized (PS) prostheses have been widely used reporting generally good results in long-term studies. However, conventional PS may not be enough for some patients who require larger constrain in order to manage knee instability. Thus, semi-constrained PS versions have been designed by means of enlarging the size of the post to be more restrictive. Nevertheless, there is a lack of confidence from surgeons on this last version, based on the belief that its larger degree of constraint could lead to the premature failure of the prosthesis. Therefore, both TKA solutions have been studied by means of a finite element analysis in order to analyze the efforts supported by the prosthesis, and more exactly, the post-cam engagement during two daily activities: gaiting and squatting. After analyzing both designs it was observed that a change on the contact between the two components, especially in the medio-lateral direction, took place, giving as a result also a variation of the kinematics of the knee joint.

Keywords: primary, TKA, semi-constrained, TKA, FEM, posterior-stabilized

1. Introduction

In 1978, the Posterior-Stabilized (PS) knee joint was introduced in order to solve the problems related to instability and subluxation of the tibia for those patients with degenerative or absent posterior-cruciate ligament (PCL) ¹. It includes a cam on the femoral component, which articulates with a post located on the tibial insert, replacing in that way the function of the PCL that should be removed.

Such prostheses have been widely used for three decades and they have reported satisfactory results since they provide an increased predictability in restoration of knee kinematic as well as greater range of motion. Nevertheless, when a conventional PS prosthesis is not enough for management of instability, it arises the need of a larger degree of constraint. So that, PS semi-constrained tibial insert has been introduced. This one limits the internal and external rotation to 2° – 3° ², providing an additional stability with respect to the conventional design. The main difference between the two solutions remains on the post shape: while for conventional PS it is slightly rounded, for the semi-constrained model it is almost rectangular and has larger dimensions, especially in the medio-lateral direction. This is an alternative solution for those patients whose soft tissue is compromised and greater constraint is required, but for whom a hinge TKA is too invasive ³.

However, there is a general distrust on semi-constrained prosthesis since it is presupposed that its larger dimensions of the post and its increased restriction results in larger stresses that may lead the prosthesis to experience the failure earlier than the conventional design. For those reasons, the aim of this study is to perform an analysis about the performances of the two solutions. The study has been conducted through a finite element analysis (FEA) simulating daily activities such as gaiting and squatting.

2. Materials and methods

The model in analysis consists of the femoral and tibial components. The influence on the loads of the rest of components affecting the behavior of the knee joint, such as the patella and the knee envelope, are already taken into account in the standard ISO 14243-1 in case of the gait, and in the experimental data in case of the squat, that are used as boundary conditions of the models.

2.1. Design of the semi-constrained tibial insert

The semi-constrained tibial insert was obtained from the design of the primary insert. By means of an extrusion, the width of the post was increased and it was given a squared shape. Moreover, in order to avoid collisions between the front part of the femur and the post, a small slope was given to the anterior part of the post.

2.2. Development of finite element method

After assembling the femoral and the tibial components, following the manufacture's instruction, commonly used materials for TKAs were assigned to each one of the parts. So that, to femoral component Cobalt-Chrome properties were attributed following linear model while to the tibial tray, Titanium was attributed and for the tibial insert, polyethylene was chosen⁴.

In order to get closer to the real behavior, interactions with a friction coefficient of 0.1 between femoral and tibial surfaces were established.

After that, boundary conditions were defined: the lower part of the tibial tray was embedded and on the other hand, the evolution of the flexion-extension angle during gaiting and squatting was assigned to each model. Loads acting during each activity were applied on a single point which was attached to the entire femoral component. For the gait, axial force, anterior-posterior force and torque were considered, while for the squat, only an axial force was applied.

Finally, both components were meshed with tetrahedral elements with a final element global size of 1.5mm.

3. Results

The aim of the study was to analyze the influence of the post's geometry on the stresses withstood by the tibial component. Thus, the study was mainly focused on the variation of the contact area and contact forces experienced by the post as well as those in the lateral and medial compartments of the tibial insert. The outputs for the gait are depicted in Figure 1.

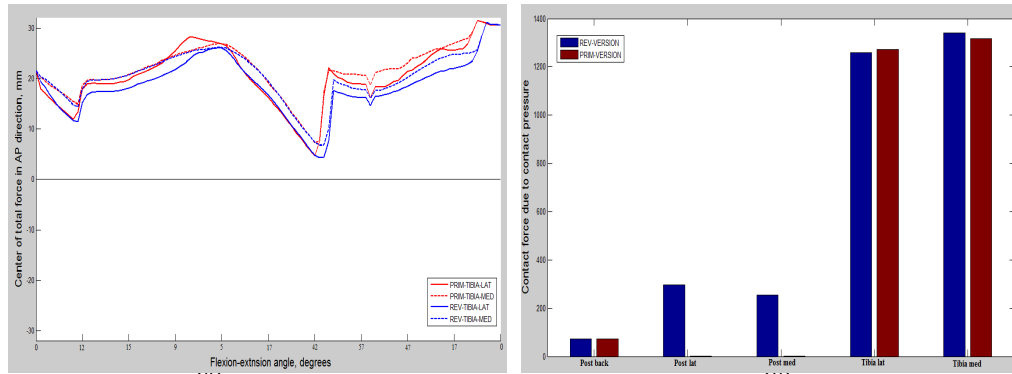


Fig. 1 (a) Center of the total force in AP direction in lateral and medial sides of the tibial component during the gait; (b) comparison of the contact force due to contact pressure between the two designs

Due to the enlargement of the post in the medio-lateral direction, larger contact forces are experienced by lateral and medial sides of the post in the semi-constrained version compared to those in the conventional one, where no contact forces can be observed (Figure 1b). The increment of the contact force in the back side of the post and in the medial side of the tibia is around 1.5%, while for the lateral compartment it decreases 1%, being these variations almost negligible.

By comparing the position of the total force in the AP direction between the lateral and medial compartments of the tibial component, it is possible to observe larger difference between both positions on the semi-constrained version in comparison with the conventional design. This larger difference, which results from the higher restriction of the post, gives as a result a bending moment on the post when the rotation between both components tries to take place.

On the other hand, the simulation of the squat provided the following results (Figure 2):

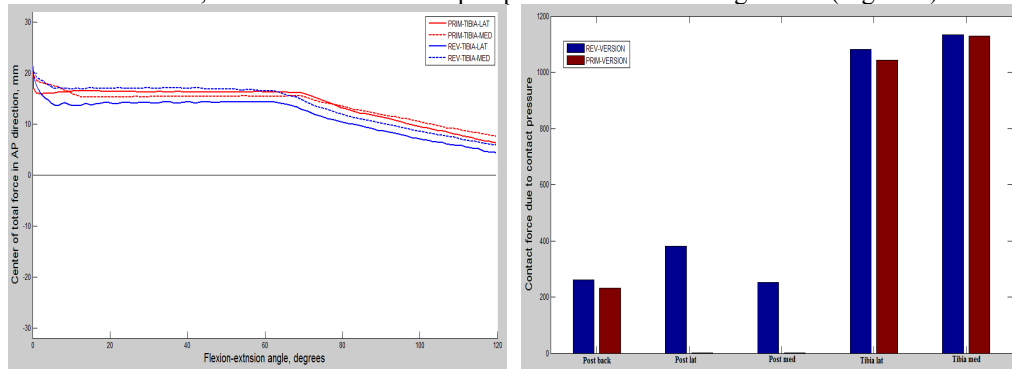


Fig. 2 (a) Center of the total force in AP direction in lateral and medial sides of the tibial component during the squat; (b) comparison of the contact force due to contact pressure between the two designs

Similarly to the gait, contact forces for the medial and lateral surfaces of the post become increased due to the larger restriction that limits the rotation of the femoral component (Figure 2b). With respect to the

post back, it can be seen that for both designs the contact force is higher than during the gait. That can be explained due to the larger range of flexion-extension angle which will put more in contact the back side of the post with the cam of the femoral component. However, the variation of the force with respect to the conventional version is more pronounced, having in that case an increase of 12.5%.

Regarding the position of the total force on lateral and medial compartments, although the tendency is also similar, the difference between both positions remains also higher for the semi-constrained version. However, in that case the difference is more pronounced, which results in larger forces experienced by the post.

4. Conclusions

By means of this study it has been shown that the modification of the geometry of the post varies the way in which the femoral component contacts the tibial one. The main difference is observed in the post, which establishes larger contact with the femoral component especially on its medial and lateral sides.

The rotation of the knee becomes also limited, which leads to a change on the position of the contact force on the tibial compartments. Thus, the kinematics of the knee prosthesis are modified and as a result an increase of the bending movement exerted on the post takes place.

5. References

1. Fabio O., Alvin O., Posterior Stabilized Total Knee Arthroplasty, Thomas Jefferson University, Philadelphia, Pennsylvania, USA.
2. Bryan R. King et al., Range of motion and function are not affected by increased post constraint in patients undergoing posterior stabilized total knee arthroplasty, Department of Orthopaedic Surgery, Hospital for Special Surgery, United States.
3. Frey, Rebecca. "Knee Revision Surgery." Gale Encyclopedia of Surgery: A Guide for Patients and Caregivers. 2004.
4. Jack E. Uellendahl, CPO, Prosthetic Primer: Materials Used in Prosthetics Part II

RESTORATION OF THE SEAL FUNCTION OF THE ACETABULAR LABRUM: A CADAVERIC STUDY

CECILIA SIGNORELLI[†]

[†] *Laboratorio di Biomeccanica e Innovazione Tecnologica, Istituto Ortopedico Rizzoli,
Via Di Barbiano 1/10, Bologna, 40136 / Italy
c.signorelli@biomec.ior.it*

NICOLA LOPOMO[‡], STEFANO ZAFFAGNINI[‡],
MARC R SAFRAN[‡]

[‡] *Orthopaedic Surgery - Medical Center, Stanford University, USA*

Abstract: The study analyzes *if* and *how* a labral-chondral separation of the acetabular labrum affects the *seal function* of the labrum itself and if the surgery is able to restore the function of the intact labrum. Three different treatment options have been analyzed: labrectomy, vertical mattress repair and cerclage. The study was conducted on 6 cadavers after removing the soft tissue from the joint and leaving the capsuloligamentous structures intact. Tracker with passive markers were fixed to the pelvis and the femur for the kinematics analysis using a surgical navigation system during 12 different movements. In the medullary canal of each femur was fixed a triaxial load cell for the control of the applied load. The displacement of the Hip Joint Centre (HJC) was calculated in five different conditions: intact labrum, after causing a labral - chondral separation, after vertical mattress repair, after cerclage repair and after labrectomy. The results confirm that a labral - chondral separation increases the HJC respect to the intact condition compromising the function of the labrum. Among the proposed surgical techniques, labrectomia is the one that provokes the highest values of HJC displacement.

Keywords: *acetabular labrum, seal, HJC displacement.*

Running Heads: *Seal Function of the acetabular labrum.*

1. Introduction

The acetabular labrum increases socket depth and articular surface, as well ¹. A biomechanical study performed by Konrath and colleagues ², assessed the role of the acetabular labrum in load transmission.

In particular, the intact acetabular labrum has been shown to create a seal between the peripheral and central compartment of the hip joint. The such called “seal function” of the labrum contrasts the synovial fluid flow from the central compartment achieving a negative pressure within the joint that increases resistance and stability of the femoral head ^{3,4}.

Labral tears commonly cause disabling intra-articular hip pain and are usually treated with hip arthroscopy ⁵. This latter may help in the preservation of the hip of young and active adults.

Current surgical techniques, defined labrectomy, to treat unreparable labral tears include removal of the loose torn tissue ¹. Anyway, restoration and maintenance of the labrum seems appropriate with the knowledge that it possesses important mechanical properties at the hip. Given that, repair should be undertaken to restore the seal function of the labrum.

While recent studies have clarified the anatomy of the acetabular labrum ⁶, its biomechanical and kinematics behaviour as well as the most effective treatment option have lagged behind.

This current study was performed with the intention to help determine when and how the seal function of the labrum is restored, by comparing the results of different surgical techniques including labrectomy and two different labral repairs: Vertical Mattress repair and Cerclage repair.

2. Methods

2.1 Testing set-up

Six cadaveric hips (3 female and 3 male, average age 87 years) without labral tears or arthritis were included in the study.

Specimens presenting evidence of either any previous surgery, or soft tissue pathology were excluded from the analysis.

The femurs were transected at the level of the knee joint, to eliminate the mechanical influence of the knee position on the hip, due to the biarticular muscles. After thawing the hemicorpses for 48 hours at room temperature, skin, subcutaneous muscle and soft tissues were removed, leaving the bones and the hip capsuloligamentous structures intact. The tests were carried out at the “Bone and Joint Center” – Veterans Affairs Palo Alto Health Care System – Stanford University (Palo Alto, CA, USA).

A commercially available system for intra-operative kinematic assessment (BluIGS/KLEE, Orthokey Ltd, Delaware, DE, USA) based on an optoelectronic localizer, was used to acquire kinematics and anatomical data. In order to track the relative motion between the femur and the pelvis, a tracker equipped with passive optical markers was mounted on the iliac crest, and a corresponding tracker was fixed on the femoral diaphysis, about 100 mm distal to the lesser trochanter toward the anterolateral femur. The acquisition of additional anatomical landmarks was necessary in order to define the anatomical system of references and perform the kinematics analysis.

Into the canal of each distal cut femur a 6-axis load cell (MC3A, AMTI, Lynchburg, Virginia, US) was fixed. This latter was used for controlling the applied load when performing the test. A suitable graphical interface was designed in LabView (National Instruments, Austin, Texas, US) for having a real-time feedback during the maneuvers execution and for recording the values of the applied load. The limit of the range of motion (ROM) of each maneuver was determined as the position at which 2Nm of torque was applied to the hip to generate both an abduction/adduction and flexion/extension maneuver. 1Nm was the limit for internal/external rotation. The load was manually applied by the testing surgeon, he was also the one who performed the surgery.

The pelvis was fixed stationary on a special set-up by eight Steinmann pins in a neutral alignment as the hip was tested. The wooden base was fastened at the end of a sturdy table to stabilize the pelvis without affecting the motion of the hips and femurs.

Figure 1 shows the set-up used for the analysis.

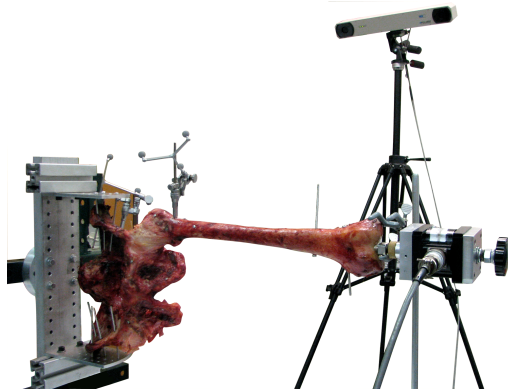


Figure 1. Set-up used for the kinematics acquisition: navigation system and load cell.

2.2 Testing protocol

The hips were passively taken through 12 different tests to study hip kinematic behavior throughout the hip ROM.

Each test was repeated 3 times to assess test-retest repeatability.

The kinematics tests were performed in 5 different conditions, each time modifying the status of the acetabular labrum. In particular we tested:

- Intact labrum
- Labral-Chondral Separation (*a # 11 scalpel blade was used to separate the labrum from its acetabular attachment centered anterolaterally at the labrum for a 15 mm length detachment*)
- Vertical Mattress repair
- Cerclage repair
- Labrectomy

Table 1 shows the tested position

Table 1. Tested positions.

TEST	FLEXION/EXTENSION	ADDUCTION/ABDUCTION	ROTATION
Test 1	NEUTRAL	NEUTRAL	Int-Neu-Ext
Test 2	NEUTRAL	ADUCTION	Int-Neu-Ext
Test 3	NEUTRAL	ABDCTION	Int-Neu-Ext
Test 4	90 FLEXION	NEUTRAL	Int -Neu-Ext
Test 5	90 FLEXION	ADUCTION	Int -Neu-Ext
Test 6	90 FLEXION	ABDUCTION	Int-Neu-Ext
Test 7	FULL FLEXION	NEUTRAL	Int-Neu-Ext
Test 8	FULL FLEXION	ADUCTION	Int -Neu-Ext
Test 9	FULL FLEXION	ABDUCTION	Int -Neu-Ext
Test 10	EXTENSION	NEUTRAL	Int-Neu-Ext
Test 11	EXTENSION	ADUCTION	Int-Neu-Ext
Test 12	EXTENSION	ABDUCTION	Int-Neu-Ext

2.3 Surgical procedure

The surgical techniques were performed following the procedures reported by Freehill and Safran ¹.

Figures 2 reports the acquired anatomical points in order to define the anatomical system of references.

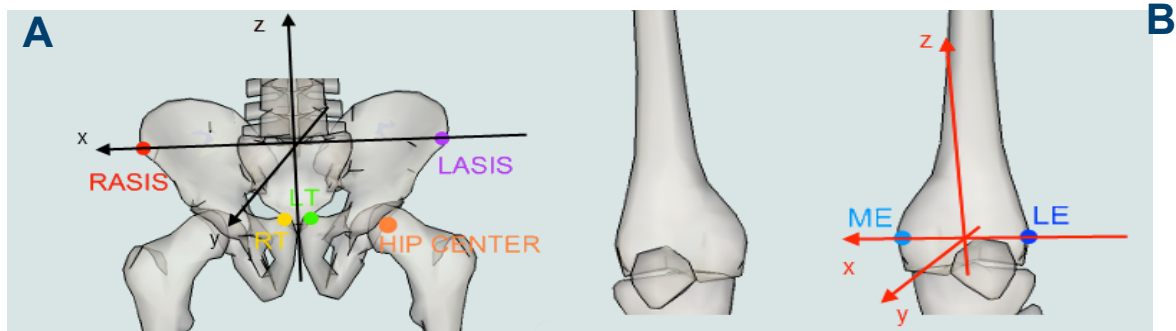


Figure 2. Pelvis Anatomical Reference System and Femur Anatomical Reference System. X-axis defines the medial-lateral direction passing through LASIS and RASIS for the pelvis and through ME and LE for the femur, Y-axis the posterior-anterior direction, while Z-axis defines the proximal-distal direction.

Standard surgical equipment was used to perform both the hip labrum repairs. The purposed surgical techniques were not modified by the introduction of the navigation system and the load cell, as well.

2.4 Data and Statistical Analysis

A direct comparison could be made among the intact state and all the following states for internal consistency to reduce inter-specimen variation. In particular we computed the displacement of the Hip Joint Center (HJC) to assess the effect of the labral-chondral separation to the acetabular labrum seal function, and whether it can be retrived with different surgical approaches. The whole set of kinematic data was acquired and off-line elaborated using MATLAB (The Mathworks Inc., MA, USA).

Interclass Correlation Coefficient (ICC) was calculated over the total amount of data in order to quantify the repeatability of the test results.

3. Results.

The inter-subject repeatability was good with an ICC value equal to 0.6. No statistically significant difference among the values of HJC displacement was identified ($p > 0.05$ for all the states) during the 5 steps analysed.

The greatest displacement of the femoral head centre was after the labral-chondral separation for all the 12 performed tests. In particular we found a mean increase of 0.8 mm as compared with intact condition.

After labrectomy we found a displacement 0.7 mm greater of the value acquired with the intact labrum. While, when the labrum was repaired by vertical mattress and cerculage technique we found a displacement that deviates from the initial value of 0.4 mm and 0.3 mm, respectively.

Holding the hip in an abducted position seems to better underline difference between the tested conditions.

Table 2 reports the average (\pm std) values of HJC displacement. The values have been organized according to the level of hip flexion.

Table 2. HJC displacement at different values of flexion/extension.

FLEX/EXT	INTACT (avg \pm SD) mm	LAB_CH (avg \pm SD) mm	VERT MAT (avg \pm SD) mm	CERCLAGE (avg \pm SD) mm	LABRECTOMY (avg \pm SD) mm
0° Flex	2.38 \pm 0.31	2.69 \pm 0.54	2.26 \pm 0.76	2.33 \pm 0.58	2.41 \pm 0.69
90 ° Flex	2.84 \pm 0.12	2.93 \pm 0.21	2.76 \pm 0.06	2.84 \pm 0.13	3.26 \pm 0.19
Full Flex	3.31 \pm 0.40	3.47 \pm 0.41	3.10 \pm 0.20	3.07 \pm 0.31	3.53 \pm 0.44
Full Ext	2.35 \pm 0.20	2.91 \pm 0.28	2.27 \pm 0.27	2.42 \pm 0.15	3.18 \pm 0.43

4. Discussion.

The most important finding of the present work was the exact quantification of the HJC displacement throughout the hip ROM.

The aim of this was therefore to determine if surgical techniques including labrectomy and two different labral repairs (Cerclage and Vertical Mattress) are able to restore the seal function of the hip labrum.

This was done taking the hip through 12 different hip positions applying a controlled load while a navigation system was recorded kinematic and anatomical data, as well.

To the best of our knowledge this is the first study to quantify HJC displacement in five different labral conditions in a controlled configuration with specific physical examination maneuvers.

According to the starting hypothesis, the results confirm that a labral-chondral separation of the labrum increases the HJC displacement respect to the intact condition compromising the “seal function” of the labrum itself. Among the analyzed surgical techniques, the labrectomia has showed the highest values of HJC displacement when compared to the intact condition.

Since the articular cartilage is optimally configured to resist compressive forces, increased translation of the femoral head within the acetabulum may result in accelerated wear of the cartilage. This fact according with the findings of our study suggest that labral repair is preferable to labrectomy.

This study does have some limitations. First is use of cadaveric specimens, which, by necessity, lacks muscular forces, and thus joint reactional forces, which likely influence the tests outcome. Moreover, a greater amount of specimens are required to discern which one of the two analyzed surgical repairs allow for a better recovery.

However, with all these limitations, from the clinical point of view this study may allow for better understanding which surgical treatment, labrectomy or repair, is optimal in case of hip labrum tear.

References.

1. Freehill MT1, Safran MR. *The labrum of the hip: diagnosis and rationale for surgical correction*. Clin Sports Med. 2011 Apr;30(2):293-315. doi:10.1016/j.csm.2010.12.002.
2. Konrath GA, Hamel AJ, Olson SA, et al. *The role of the acetabular labrum and the transverse acetabular ligament in load transmission in the hip*. J Bone Joint Surg Am 1998;80(12):1781–8.
3. Takechi H, Nagashima H, Ito S. Intra-articular pressure of the hip joint outside and inside the limbus. Nippon Seikeigeka Gakkai Zasshi 1982; 56(6):529–36.
4. Terayama K, Takei T, Nakada K. *Joint space of the human knee and hip joint under a static load*. Eng Med 1980;9:66–74.
5. Safran MR, Giordano G, Lindsey DP, Gold GE, Rosenberg J, Zaffagnini S, Giori NJ. *Strains across the acetabular labrum during hip motion: a cadaveric model*. Am J Sports Med. 2011 Jul;39 Suppl:92S-102S. doi: 10.1177/0363546511414017
6. Kelly BT, Shapiro GS, Digiovanni CW, Buly RL, Potter HG, Hannafin JA. *Vascularity of the hip labrum: a cadaveric investigation*. Arthroscopy. 2005 Jan;21(1):3-11.

HOW REPRODUCIBLE IS THE LOCALIZATION OF ACL INSERTION POINTS BY USING MRI?

PASQUALE SALANDRA

*Università Politecnica delle Marche , Via Brecce Bianche
Ancona, 60131, Italy
pas.sal788@gmail.com*

SILVIA PIANIGIANI

*IRCCS, Istituto Ortopedico Galeazzi, Via Galeazzi 4
Milano, 20161, Italy
silvia.pianigiani84@gmail.com*

ENRICO PRIMO TOMASINI

*Dipartimento di Meccanica, Università Politecnica delle Marche , Via Brecce Bianche
Ancona, 60131, Italy
e.p.tomasini@univpm.it*

BERNARDO INNOCENTI

*BEAMS Department, Université Libre de Bruxelles, Av. F. Roosevelt 50
Bruxelles, Belgium
bernardo.innocenti@ulb.ac.be*

The Anterior Cruciate Ligament (ACL) is a soft-tissue subjected to extreme mechanical stress especially during high performance activities, and it is fundamental for the knee stability. To provide information on the status of the ligament, especially when the patient complains pain, the use of MRI images became a common practice. The position of the insertion of the ACL on the tibia could be correlated with possible pathologies, as ACL fracture, but, up to now, no literature study provides this information.

For these reasons, this work focuses on the determination of the reproducibility and repeatability of a new technique aimed to identify the ACL insertion position. Particularly, the Anterior and Posterior attachment of ACL (respectively ACLa and ACLp) were identified and normalized on MRI images. INTRA and INTER-Class-Correlation (ICC) were determined to prove the reproducibility and repeatability of this new procedure.

Results show excellent agreement both for the ACLa ($ICC_{-Inter} = 0,923$, $ICC_{-Intra} = 0,867$) and the ACLp ($ICC_{-Inter} = 0,901$, $ICC_{-Intra} = 0,851$).

Accordingly, the proposed procedure can be considered suitable to define the position of ACL for a specific patient.

Keywords: Knee, ACL, insertion point, Reproducibility, Repeatability, ICC.

1. Introduction

The Anterior Cruciate Ligament (ACL) is one of the four main ligaments in the knee joint. It is located deep within the joint, between the tibia and the femur. Its primary biomechanical function is to stabilize the joint, preventing the forward displacement of the tibia in relation to the position of the femur and it is crucial to guarantee the stability of the knee joint¹. Secondary biomechanical function of the ACL is to control the internal rotation of the knee in synergy with the collateral ligaments².

Anatomically, in the sagittal plane, the anterior part of the ACL is attached on the proximal tibia, beneath the transverse ligament, which unites the anterior horns of the medial and lateral meniscus, with some

fibers attaching to the anterior horn of the lateral meniscus. Medially, the ACL attachment is bound by the articular cartilage border of the medial tibial plateau. Laterally, the ACL attachment is located near the articular cartilage border of the lateral tibial plateau³.

When a patient suffers pain, MRI images, usually achieved under low irradiation dose³, are used to assess the position, quality and shape of the ACL, aiming to find a possible explanation to the patient's issue. Another use of the analysis of MRI images is to reconstruct ligament geometries for the development of patient specific models for kinetics and kinematics investigations^{3,4,5}. But, unlike MRI for scientific use, the MRIs for clinical use have lower resolution that sometimes make difficult the correct localization of the ACL.

Therefore, for the present research purpose, a new method is proposed and tested. This method is aimed to determine the identification of the ACL position on the tibial plateau with the use of MRI for clinical use and to normalize it according to specific patient anatomical landmarks.

2. Materials and methods

The proposed technique is based on the use of a series of clinical MRI images of healthy patients, however could be applied even to pathological MRI without lacking significance. The procedure is divided into two main steps:

1. identification of a reference system on the tibial plateau;
2. identification of the ACL insertion points.

For the identification of the reference system four anatomical landmarks⁸ were considered:

- CM: center of the best circle around the edge of the tibial plateau on the medial side (Fig. 1b);
- CL: center of the best circle around the edge of the tibial plateau on the lateral side (Fig. 1b);
- RA: the rightmost point of the largest proximal antero-posterior tibial outline (Fig. 1a);
- LP: the leftmost point of the largest proximal antero-posterior tibial outline (Fig. 1a).

Once these points are identified the patient reference system is fully defined: the axis passing through CM and CL determine the medio-lateral axis of the patient, the orthogonal axis is the antero-posterior axis of the patient. LA and RA are therefore projected to the Antero-posterior axis to determine the patient AP total length.

For the identification of the ACL insertion point on the tibial plateau two distinct points were considered:

- ACLa: the anterior point of the insertion of ACL on the tibial plateau (Fig. 1a);
- ACLp: the posterior point of the insertion of ACL on the tibial plateau (Fig. 1a).

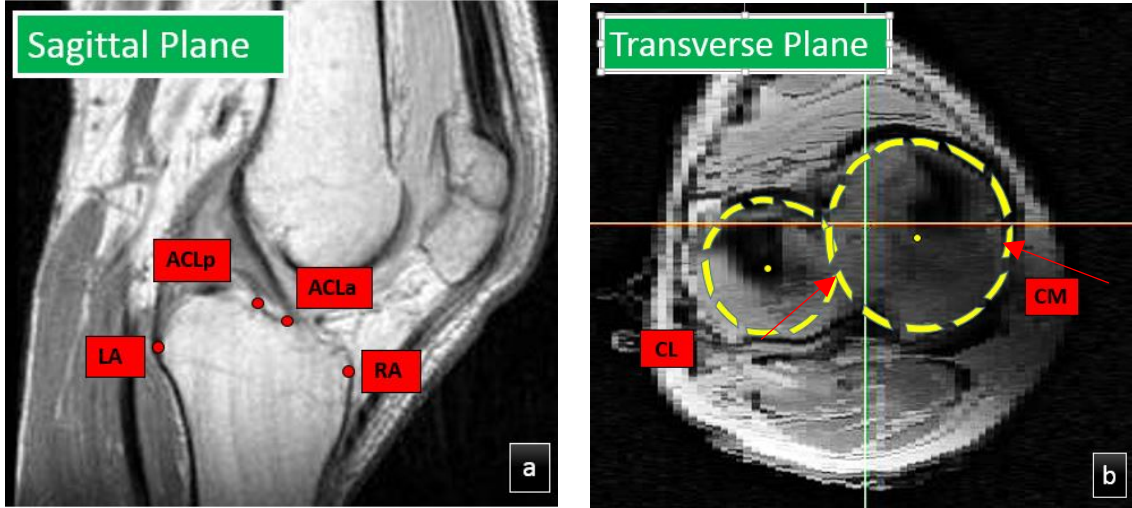


(Fig.1) Identification of points required to obtain Reference System

- CM: center of the best circle around the edge of the tibial plateau on the medial side;
- CL: center of the best circle around the edge of the tibial plateau on the lateral side;
- RA: the rightmost point of the largest proximal antero-posterior tibial outline;
- LP: the leftmost point of the largest proximal antero-posterior tibial outline.

Once these two points were identified the antero-posterior distances between ACLa and LP and between ACLp and LP were extracted and normalized using the patient AP total length calculated before.

To check the reproducibility and repeatability of the proposed technique, the Intra and Inter class correlation coefficients (ICC_{Inter} and ICC_{Intra}) were calculated for the normalized antero-posterior distances ACLa-LP and ACLp-LP.

To calculate these coefficients, three different operators applied the same procedure on 3 specimens, repeating the trial for 3 times.

By definition, the ICC is evaluated according to the following formulation⁶:

$$ICC_{Intra} = \frac{\sigma_p^2}{\sigma_t^2} ;$$

$$ICC_{Inter} = \frac{\sigma_p^2}{\sigma_p^2 + \sigma_e^2};$$

where

- σ_t^2 is the total variance of measurements by different observers on different subjects;

- σ_p^2 is the variance between subjects;

- σ_e^2 is the error variance of measurements by the same observer on different subjects⁶.

ICC values range from 0 to 1, indicating better agreement as the value approaches 1. An ICC values higher than 0.75 indicates excellent agreement⁶.

3. Results

Figure 2 reports an example of the position of the points identified with the previous technique. In details, all the normalized points are plotted in graphs that shows the transverse plane of the tibial plateau.

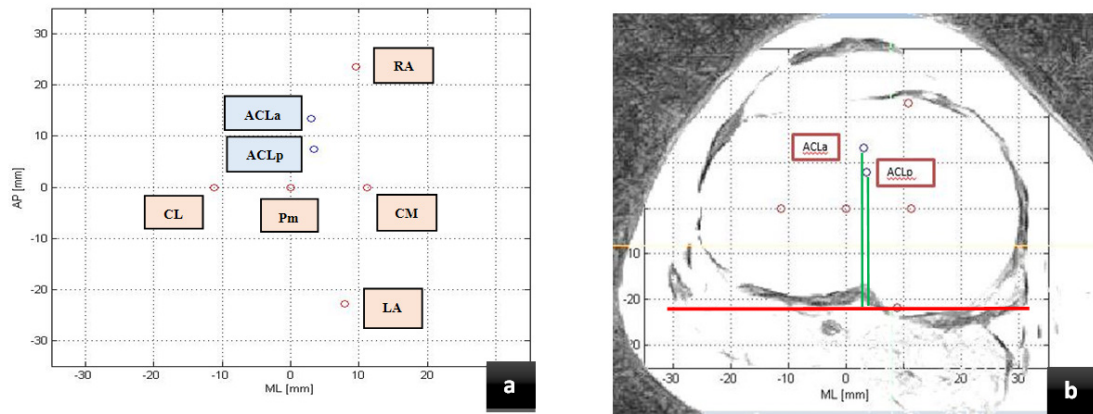


Fig.2 - Normalized values (The Pm point is defined as the midpoint between CM-CL) without (a) and with (b) a tibial MRI transversal image. The red line represent the lower tibial margin and the two green lines the antero-posterior normalized distances

As regards to the INTER-Class Correlation Coefficient:

- For the ACLa-LP distance is equal to 0,923;
- For the ACLp-LP distance is equal to 0,908.

As regards to the INTRA-Class Correlation Coefficient:

- For the ACLa-LP distance is equal to 0,867;
- For the ACLp-LP distance is equal to 0,851.

4. Discussion

To provide information on the status of the ACL, especially when the patient complains pain, the use of MRI images became a common practice. Several technique could be used with different accuracy but, up to now, no literature study provides this information.

For these reasons, this work focuses on the determination of the reproducibility and repeatability of a new technique aimed to identify the ACL insertion positions. In particular, the ACLa and ACLp were

identified and normalized on MRI images. ICC-Inter and ICC-Intra were determined to prove the reproducibility and repeatability of this new procedure.

Results show excellent agreement both for the ACLa ($ICC_{\text{-Inter}} = 0,923$, $ICC_{\text{-Intra}} = 0,867$) and the ACLp ($ICC_{\text{-Inter}} = 0,901$, $ICC_{\text{-Intra}} = 0,851$).

Accordingly, the proposed procedure can be considered suitable and efficient to define the position of ACL for a specific patient.

5. References

1. H.-U. Stäubli, W. Rauschning. Tibial attachment area of the anterior cruciate ligament in the extended knee position. *Knee Surg, Sports Traumatol, Arthroscopy* (1994) 2:138-146.
2. S Plaweski, D Petek, S Saragaglia. Morphometric analysis and functional correlation of tibial and femoral footprints in anatomical and single bundle reconstructions of the anterior cruciate ligament of the knee. *Orthopedics and Traumatology: Surgery & Research* (2011) 97S,S75-S79.
3. B.Innocenti, S.Pianigiani, L.Labey, J.Victor, J.Bellemans. Contact forces in several TKA designs during squatting: A numerical sensitivity analysis. *Journal of Biomechanics* (2011) 1573-158.
4. S.Pianigiani, Y.Chevalier, L. Labey. V. Pascale, B. Innocenti. Tibio-femoral kinematics in different total knee arthroplasty designs during a loaded squat: A numerical sensitivity study. *Journal of Biomechanics* (2012) 2315-2323.
5. B.Innocenti, G.Van Lenthe. Load sharing and ligament strains in balanced, overstuffed and understuffed UKA. A validated Finite Elements analysis. *J Arthroplasty* (2014) S0883-5403.
6. J. Victor, D. Van Donick, L. Labey, B. Innocenti, P.M. Parizel, J. Bellemans. How precise can bony landmarks be determined on a CT scan of the knee. *The Knee* (2009).

PROBABILISTIC MODEL OF LIGAMENTS AND TENDONS: QUASI-STATIC LINEAR STRETCHING

MARCO BONTEMPI

*Laboratorio di biomeccanica ed Innovazione Tecnologica, Istituto Ortopedico Rizzoli,
via di Barbiano 1/10, 40136, Bologna, Italy
m.bontempi@biomec.ior.it*

MAURILIO MARCACCI

*Laboratorio di biomeccanica ed Innovazione Tecnologica, Istituto Ortopedico Rizzoli,
via di Barbiano 1/10, 40136, Bologna, Italy
m.marcacci@biomec.ior.it*

Abstract

Ligaments and tendons have a significant role in the musculoskeletal system and are frequently subjected to injury. This study presents a model of collagen fibers, based on the study of a statistical distribution of fibers when they are subjected to quasi-static linear stretching. With respect to other methodologies, this model is able to describe the behavior of the bundle using less ad hoc hypotheses and is able to describe all the quasi-static stretch-load responses of the bundle, including the yield and failure regions described in the literature. It has two other important results: the first is that it is able to correlate the mechanical behavior of the bundle with its internal structure, and it suggests a methodology to deduce the fibers population distribution directly from the tensile-test data.

Keywords: ligaments, tendon, constitutive equations, linear stretching

Ligament and tendon injury can be very serious both for non-athletes and athletes, and when it happens, it is fundamental that physicians do their best to ensure a correct repair of the injury. The literature presents many clinical articles concerning hypotheses and proposals about techniques useful to repair ligaments correctly. Pioneers in this field are Fung¹ and Woo^{2,3} who used constitutive equations to model the collagen fibers and predict the stress-strain behavior. These models work well during fiber recruitment and linear elastic deformation phases^{4,5} but nothing is said about bundle failure. Although these models are effective at describing the force-stretch behavior of bundles, ad hoc hypotheses need to be made about the equations to insert into the models, and the result could vary greatly depending on the change of equations. Another approach, that can be used to model a collagen bundle, is to look at collagen fibers as a statistic population and correlate the single fiber dynamics through the population^{6,7,8}. This is the core of the model presented here. It is based on the assumption that the Nature creates ligaments and tendons with a specific structure according to the specific function. For this reason this model wants to avoid, as much as possible, a priori hypotheses on the internal structure, because it wants to suggest methods to create specific models for specific bundles.

Collagen fibers have a very complex anatomical structure, both concerning their molecular composition and their structural organization, as shown in figure 1.

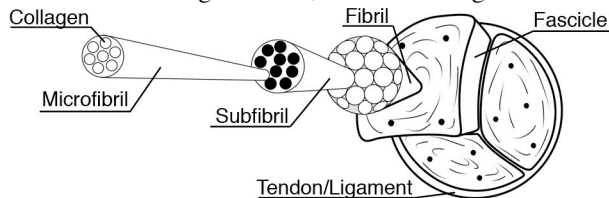


Figure 1: Representation of the hierarchical structure of tendons and ligaments.

The model here described analyses what happens to a collagen bundle when it is quasi-statically stretched and, for this reason, the spatial distribution of fibers can be ignored. Each collagen fiber is considered as a one-dimensional string characterized by a rest length (x_r), and a maximal length (x_b), after which it fails and it is supposed to have a force response to stretching $f(x)$, so that $f(x) \neq 0$ if $x \in [x_r, x_b[$ and $f(x) = 0$ otherwise. Because of the presence of the rest length, the model takes into account only the stretch length ($L \geq 0$). In the phase of recruitment, the fiber population can be characterized by the numbers of fibers (N_0) distributed according to a certain probability density of the rest lengths, with a mean and standard deviation of the population: $r(x; \bar{x}_r, \sigma_r)$. Collagen fibers have their own failure length and, as above, it is possible to consider the distribution of the failure lengths: $b(x; \bar{x}_b, \sigma_b)$. Thus the behavior of a ligament in quasi static-linear stretching can be expressed as:

$$F(L) = N_0 \int_{-\infty}^L r(x; \bar{x}_r, \sigma_r) f(L - x) [1 - B(L - x)] dx \quad (1)$$

where $B(L - x) = \int_{-\infty}^{L-x} b(\lambda; \bar{x}_b, \sigma_b) d\lambda$ is the probability of failure after a fiber stretch of $L - x$. The “ $-\infty$ ”, at the lower bound of the integral, takes into account the *pretension*, i.e. the bundle could have a physiological initial tension, so it can have a non-zero force when $L = 0$.

The correctness of the model was tested fitting data generated by a MonteCarlo simulation. Figure 2 shows the results of the simulation of 10^6 linear fibers with a force response of $f(x) = k(x - x_r)$ if $x \in [x_r, x_b[$ and $f(x) = 0$ otherwise.

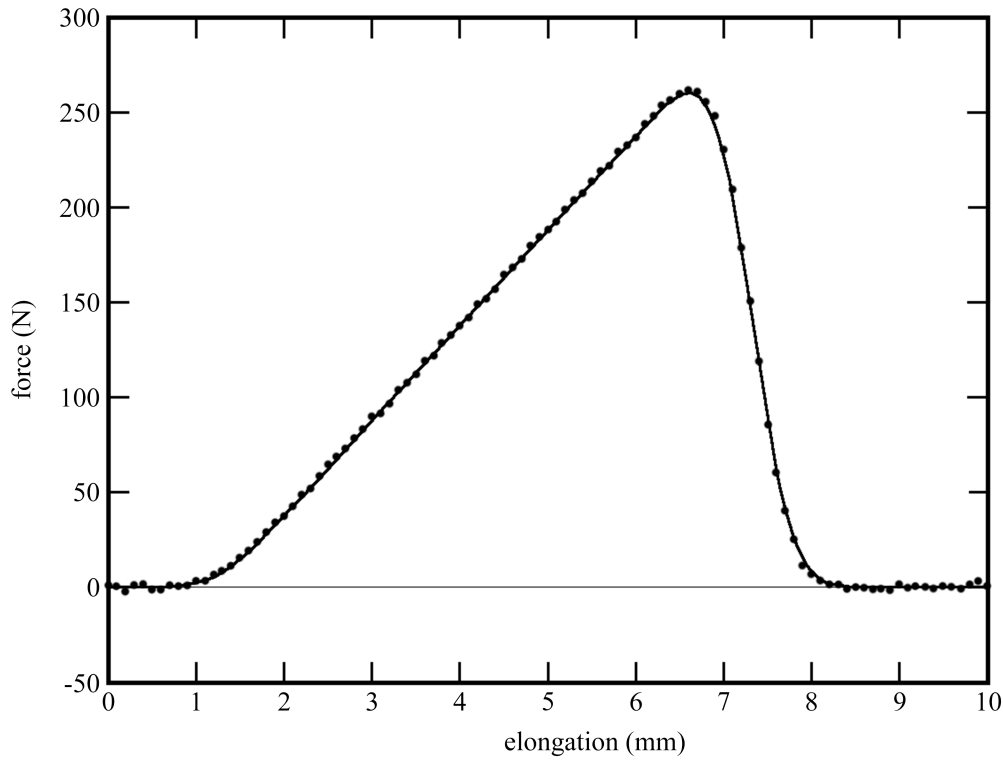


Figure 2: Plot of experimental data and the model fitting.

All the simulation's parameters were randomly generated and both the rest length of each fiber (x_r) and the break length (x_b) were gaussian distributed, including the *extra*-noise added to the total fiber's force.

The data set was fitted according to the model in equation 1.

The originality and the advantage of the approach used here is that it can describe all the behaviors presented in the literature, including the yield and part of the failure phases, thus avoiding many ad hoc hypotheses, and it can neglect the accuracy of the geometry description. Despite to other probabilistic models this does not need the a priory knowledge of the probability functions and it suggests a methodology to extract these information from the experimental data, opening the opportunity to make specific models according to the bundle characteristics, as expected. It could have several applications in biomechanics to correlate ligament and tendon functions to anatomical parameters and to understand better how macroscopic behavior is correlated to the microscopic structure of the bundle, and evaluations can be made about the physiological and pathological structure and behavior of the bundle.

References

1. Y. C. Fung, Biomechanics: mechanical properties of living tissues (Springer, New York, 1993).
2. S. L.-Y. Woo, S. D. Abramowitch, R. Kilger, and R. Liang, J Biomech 39, 1 (2006), ISSN 0021-9290 (Print).
3. S. L. Y. Woo, M. B. Fisher, and A. J. Feola, Mol Cell Biomech 5, 49 (2008), ISSN 1556-5297 (Print).

4. Y. Lanir, J Biomech 16, 1 (1983), ISSN 0021-9290 (Print).
5. Y. Lanir, Biophys J 24, 541 (1978), ISSN 0006-3495 (Print).
6. A. J. Rapoff, D. M. Heisey, and R. J. Vanderby, J Biomech 32, 189 (1999), ISSN 0021-9290 (Print).
7. C. Hurschler, P. P. Provenzano, and R. J. Vanderby, J Biomech Eng 125, 415 (2003), ISSN 0148-0731 (Print).
8. C. Hurschler, B. Loitz-Ramage, and R. J. Vanderby, J Biomech Eng 119, 392 (1997), ISSN 0148-0731 (Print)

S4P: Modelling and diagnosis - Models and numerical analysis

Chairs: Gastone Castellani, Francesco Mainardi

STOCHASTICAL MODELING OF THE GUT MICROBIOTA ECOLOGICAL SYSTEM

CLAUDIA SALA

A MECHANO-PHYSIOLOGICAL MODEL OF METABOLIC AUTOREGULATION IN EYE RETINAL
MICROCIRCULATION

PAOLA CAUSIN

BAGGED NEAREST NEIGHBOR CLASSIFIERS IN SEMI SUPERVISED LEARNING

NESMA SETTOUTI

DYNAMIC PRUNING FOR RANDOM FOREST

MOSTAFA EL HABIB DAHO

RETINAL IMAGE ANALYSIS FOR CONTENT BASED IMAGE RETRIEVAL APPLICATIONS USING
MULTILEVEL THRESHOLDING

SIVAKAMASUNDARI JOTHI

MULTIFRACTAL BASED SEGMENTATION AND ANALYSIS OF HUMAN RETINAL BLOOD
VESSELS IN FUNDUS IMAGES

SRI MADHAVA RAJA NADARADJANE

METABOLIC NETWORK MODELS FOR THE CHARACTERIZATION OF PATHOLOGICAL
CELLULAR STATES

GABRIELE FONTANAROSA

MULTIOMICS NETWORK ANALYSIS OF HEARTH DISEASE RISK

ENRICO GIAMPIERI

DEVELOPMENT OF A DYNAMIC MODEL OF THE ALVEOLAR INTERFACE FOR THE STUDY OF
AEROSOL DEPOSITION

DANIELE CEI

STOCHASTICAL MODELING OF THE GUT MICROBIOTA ECOLOGICAL SYSTEM

CLAUDIA SALA, SILVIA VITALI, ENRICO GIAMPIERI, DANIEL REMONDINI, GASTONE CASTELLANI
*Physics and Astronomy department, University of Bologna, viale Berti Pichat 6/2,
40138 Bologna, Italy.*

Alterations in intestinal microbiota composition are associated with several chronic conditions, including metabolic diseases, inflammatory diseases and ageing [1, 2]. We described the gut microbiota as an ecological system and model its Relative Species Abundance (RSA) distribution. We applied our stochastic model to the microbiota of young and elderly people from which we also had dietary informations [2]. We showed that our model, describes well the gut microbiota, and, furthermore, seems able to discriminate between people with different age, diet and health state.

1. Introduction

The human body is home to roughly 10 times more microbial cells than human cells. The collective genomes of these symbiotic microorganisms (called human microbiome) constantly interacts with the human genomes, making humans ‘superorganisms’ harboring these two integrated genomes. It is through their interaction with our living environment that the human health phenotype is defined; than, it is this interaction that we should consider in the study of systemic diseases [1].

In healthy adults, the composition of the human intestinal microbiota is individual-specific and stable over time, but in older people (> 65 years) is extremely variable between individuals, and significantly different from that of younger adults [2].

Compositional changes in the gut microbiota have been linked with inflammatory and metabolic disorders, including obesity in adults, type 2 diabetes and ageing [2].

Considering the gut microbiota as an ecological system, we described its biodiversity through the Relative Species Abundance distribution (RSA).

According to the neutral theory of ecosystems, the RSA distribution can be described by a gamma distribution [3] in the continuous case, or by a negative binomial [4] in the discrete case, both with biologically meaningful parameters. We used the continuous description to study the dynamics of the GUT microbiota:

(1)

We found out that rare and abundant species obey different ecological laws and can be treated as competitive species. We thus applied a chemostat-like model with competing bacteria populations, adding an influx term as in [3] and [4]. This new model led to a mixture of gammas as stationary distribution for the RSA. The model seems able to describe our data (Figure 1) and to discriminate between people with different age, diet and health state.

2. Material and methods

We analysed the data from Claesson et al [2] (available in MG-RAST under the Project ID 154), which include 16S rRNA data from 178 elderly and 13 control young adults with informations about their diet and residence settings. We obtained the RSA distribution of the GUT ecological system through a clustering procedure. In particular we clustered the sequences with UCLUST [5], using different

similarity thresholds (93%, 95%, 97% and 99%) in order to study the system at different phylogenetic levels.

We computed the abundances of the obtained clusters (Operational Taxonomic Units), we represented their RSA distribution in the form of Preston plot and we fitted them with our model (Figure 1).

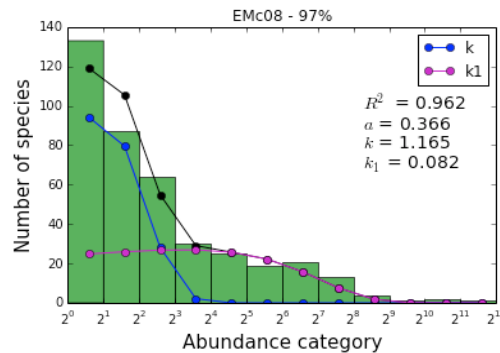


Figure 1: RSA distribution at 97% of similarity of one young gut microbiota sample and fit with a mixture of gammas (k and k_1 are the gammas shape parameters and a is the mixture coefficient).

3. Conclusions

The gut microbiota behaves like an organ in the human body and strictly interacts with that. Previous studies showed that diet, life style, age and health are linked to the gut microbiota composition in a reciprocal interaction [1, 2].

We showed that the gut microbiota can be described as an ecological system and that this description can help to understand this interaction.

The gut microbiota ecological system is not simply neutral, but rare and abundant species obey different laws. We computed a model which takes into account the competition among these two subsystems. Considering a further influx term, the stationary distribution of this model is given by a mixture of gammas.

This distribution fits well our data and, furthermore, seems able to discriminate between people with different age, diet and health state.

References

1. D. Marco. Metagenomics. Current Innovations and Future Trends. Caister Academic Press, 2011.
2. M. J. Claesson, I. B. Jeffery, S. Conde, S.E. Power (2012). Gut microbiota composition correlates with diet and health in the elderly. Nature, 488 (7410), pp.178-184.
3. Volkov, I., Banavar, J. R., Hubbell, S. P., Maritan, A. (2007) . Patterns of relative species abundance in rainforests and coral reefs. Nature, 450 (7166), pp. 45-49.
4. S. Azale, S. Pigolotti, J.R. Banavar, A. Maritan (2006). Dynamical evolution of ecosystems. Nature, 444 (7121), pp. 926-928.
5. UCLUST, extreme high-speed sequence clustering, alignment and database search, 2010. URL <http://www.drive5.com/uclust>.

A MECHANO-PHYSIOLOGICAL MODEL OF METABOLIC AUTOREGULATION IN EYE RETINAL MICROCIRCULATION

PAOLA CAUSIN

*Dept. of Mathematics, Università degli Studi di Milano
via Saldini 50 - 20133 Milano, Italy
paola.causin@unimi.it*

FRANCESCA MALGAROLI

*Dept. of Mathematics, Politecnico di Milano
piazza Leonardo da Vinci 32 - 20133 Milano, Italy
francesca.malgaroli@polimi.it*

FRANCESCA ZORZAN

*Dept. of Mathematics, Università degli Studi di Milano
via Saldini 50 - 20133 Milano, Italy*

Retinal circulation is a complex system, characterized by a blood flow strictly tailored to metabolic demands, and -at the same time- able to supply a constant blood flow over a pretty wide range of ocular perfusion pressure values. Variation of blood flow is mainly attained by the variation of diameter of resistance arterioles, a mechanism known as autoregulation. In this work, we present a mathematical model of autoregulation, where blood flow and nutrient transport occur in compliant microvessels, whose diameter is actively regulated according to solute levels in the vessel wall and in the metabolically active surrounding tissue.

Keywords: microcirculation; vessel autoregulation; oxygen delivery; tissue perfusion; eye retina.

1. Introduction

The eye retina receives its blood supply from two separate circulatory systems: i) the retinal vessels consisting in a network of arterioles and venules embedded in the retinal tissue at the boundary with the vitreous. These vessels are charged to supply nourishment/remove waste in the inner retinal layers; ii) the choroidal vessels embedded in a layer adjacent to the sclera. These vessels are charged to supply by diffusion nutrient to the retinal outer layers. While choroidal circulation is characterized by a high blood flow, inner retinal circulation is tightly regulated to the demand. Increased oxygen (O_2) demand due to metabolic activity in the retinal tissues proportionally increases retinal blood flow (metabolic autoregulation¹); conversely, at constant metabolic rate, an altered arterial oxygen content reciprocally alters retinal blood flow, leaving total oxygen delivery constant. In addition, blood flow to the inner retina remains constant over a certain range of ocular perfusion pressure values (myogenic autoregulation¹). The interaction of these two autoregulatory mechanisms results into a complex vascular dynamics, mediated by vasoactive substances, mainly nitric oxide (NO) released by the vascular endothelium². Impaired autoregulation is thought to be also a major risk factor for serious retinal pathologies like glaucoma³. Several mathematical models exist addressing vascular response to brain activation, most of which are based on lumped parameter representations (see, e.g.,⁴ and references therein). However, very few mathematical works address the retinal vascular response, among which we cite the very recent⁵. Ref.5 addresses, via the use of empirical correlations, autoregulatory mechanisms in the retina, highlighting the importance of the metabolic contribution. In this work, we present a coupled mathematical model of

metabolic regulation response based on an artificial anatomically-reasonable network representing the inner retinal circulation. Blood flow and nutrient transport are supposed to occur in compliant microvessels, whose diameter is actively regulated according to solute (O_2 , NO) levels in the vessel wall and in the metabolically active surrounding tissue.

2. Mathematical model

2.1. Anatomical Model of the Microvessel Network

We consider an artificially constructed geometry of the arteriolar/venular network (AVT), based on the well-recognized similarity of retinal vessels to a fractal tree. The network is generated through an algorithm of Diffusion Limited Aggregation (DLA), which leads to describe the arterial and venous sides of the AVT as two trees, each consisting of cylindrical segments which branch out in bifurcation points. More details on the network generation are given in⁶, see also Fig.1(left). We denote by L length of each segment, by R the lumen radius and by h the thickness of the vessel wall. Each segment is endowed with a local system of cylindrical axes, $s \in (0, L)$ and $r \in (0, R + h)$ being the radial and longitudinal coordinates, respectively. The vessel radius is a function of time t , while the vessel length is kept constant.

2.2. Model of Blood Flow

Blood (b) is modeled in the lumen $(r, s) \in (0, R) \times (0, L)$ of each vessel as an incompressible fluid using the axisymmetric Navier-Stokes equations. After averaging across the vessel section as in⁷, the problem reads: find the volumetric blood flow rate Q_b , the blood pressure p_b and the blood hematocrit H_D such that

$$\frac{\partial(H_D Q_b)}{\partial s} = -\frac{\partial(H_D A)}{\partial t}, \quad \frac{\partial Q_b}{\partial s} = -\frac{\partial A}{\partial t}, \quad Q_b = -\frac{\pi R^4}{8\mu_b} \frac{\partial p_b}{\partial s}, \quad (1)$$

where $A = \pi R^2$ is the vessel cross-section area and $\mu_b = \mu_b(H_D)$ is the hematocrit-dependent blood viscosity⁶. If the time variation of A is slow enough, the right hand side terms in the first two equations of system (1) can be neglected⁸. Extension to the network requires adding branch nodes with no blood volume, simply modeled by conservation of flow and continuity of pressure equations. At the inlet (arteriolar side) and outlet (venular side) of the network blood pressure is prescribed.

2.3. Model of O_2 transport and delivery in the AVT

Let $u_b = Q_b/A$ be the cross-sectional averaged blood axial velocity and S blood saturation (C_{Hb} being hemoglobin carrying capacity), supposed to be related to oxygen tension by Hill's formula. Oxygen tension $p_{O_2, b}$ in each vessel lumen is given by

$$\begin{aligned} \frac{\partial J_s}{\partial s} &= -\frac{2}{R} L_p (\alpha_b p_{O_2, b} - \alpha_w p_{O_2, et}) \omega_2, \\ J_s &= u_b (\alpha_b \omega_1 p_{O_2, b} + C_{Hb} S) - \frac{\partial}{\partial s} (D_b \alpha_b p_{O_2, b} + D_{Hb} C_{Hb} S), \end{aligned} \quad (2)$$

where ω_1, ω_2 are shape factors⁶, D_b and D_{Hb} are O_2 diffusion coefficients in blood and red blood cells, α_b, α_w are O_2 solubility coefficients in blood and in arterial wall and L_p is a permeability coefficient. Prescribed O_2 concentration is assigned at the arterial entry, while a no flux-condition is assigned at the venous outflow. An equation similar to (2) holds for NO transport in the vessel lumen (see Ref.9 for details).

2.4. Model of O_2 and NO transport across the vessel wall

We model solute profiles across the wall of the arterioles, considered to be composed of an endothelial (*et*, external radius R_{et}) and a smooth muscle cell (*smc*, external radius R_{smc}) layer. Oxygen tension $p_{O_2,j}$ and nitric oxide concentration $c_{NO,j}$ in layer $j=et, smc$ are described, for $r \in (R, R_{et})$ if $j=et$ and $r \in (R_{et}, R_{smc})$ if $j=smc$, by:

$$\frac{\partial p_{O_2,j}}{\partial t} - \frac{1}{r} \frac{\partial}{\partial r} \left(r D_{O_2} \frac{\partial p_{O_2,j}}{\partial r} \right) + \frac{M_{O_2,j}}{\alpha_w} = 0, \quad \frac{\partial c_{NO,j}}{\partial t} - \frac{1}{r} \frac{\partial}{\partial r} \left(r D_{NO} \frac{\partial c_{NO,j}}{\partial r} \right) + M_{NO,j} = 0, \quad (3)$$

where, for $X=O_2, NO$, D_X is the O_2 or NO diffusion coefficient, the O_2 solubility in vessel wall and where the source/sink terms $M_{X,j} = M_{X,j}(p_{O_2}, c_{NO})$ are defined as in⁹. Mass conservation across the interface of adjacent layers requires continuity of the concentrations/tensions and of the diffusive fluxes. No flux is imposed at $r=R_{smc}$.

2.5. Model of smooth muscle cell contraction (muscular tonus)

Contraction in the smooth muscle cells is determined by the activity level of the myosin heads, represented here as the concentration f of phosphorylated bridges. This latter, in turn, depends on the intracellular concentration of calcium ions $c_{Ca^{2+}}$, related to NO levels. We describe in each vessel the two kinetics as in Ref.8, to which we refer for the equations and precise definition of all the coefficients.

2.3. Vessel wall mechanics

We assume the arterioles to be incompressible elastic solids exhibiting active and passive responses to blood flow, and the capillaries and venules to be passive compliant vessels. Let $R_m=R+h/2$ be the radius of the average surface of the vessel; its time evolution is given by $R_m(t)=R_{m,0}+\eta(t)$, η being the (small) radial displacement from the reference configuration with mean vessel radius $R_{m,0}$, given by

$$\rho_w h_0 \frac{d^2 \eta}{dt^2} + \lambda h_0 \frac{d\eta}{dt} + \kappa \eta = p_b - p_{out} + \frac{h_0}{R_0} k_2 F, \quad (4)$$

where $F = \frac{2}{R_{smc}^2 - R_{et}^2} \int_{R_{et}}^{R_{smc}} f(r, t) r dr$ provides active feedback in the arterioles, p_{out} is the interstitial pressure and the other coefficients are defined in⁸.

3. Numerical algorithm and simulation results

Equations (1)-(4) are solved in a decoupled manner adopting a fixed point algorithm, with internal iterations performed where nonlinearities (e.g. due to the saturation function or metabolic consumption)

are present. In Fig.1 (left), we show the preliminary results of simulations carried out without autoregulation/compliance mechanisms.

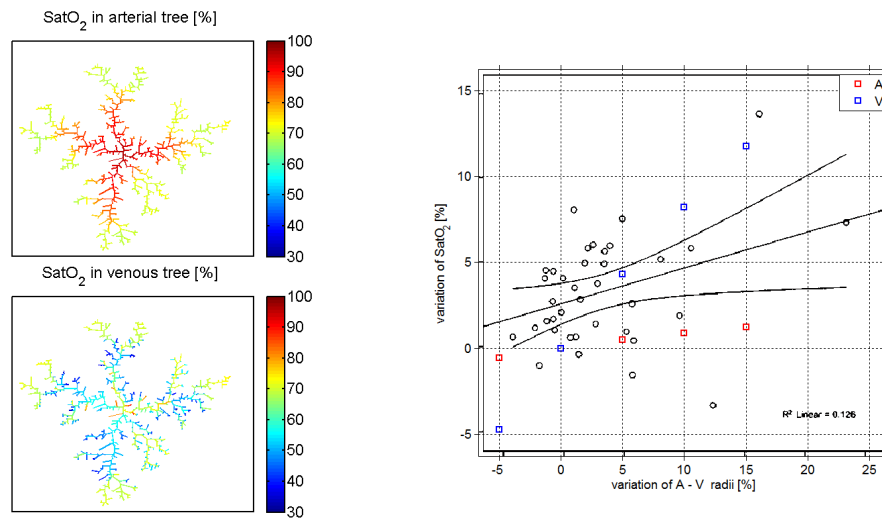


Fig. 1. Left: oxygen saturation in the AVT. Right: change in oxygen saturation in arteries and venules versus an imposed vasodilation. Black circles are experimental data from¹⁰.

Acknowledgements

This work has been conducted in the framework of a joint research activity with R.Sacco (Politecnico of Milano, Italy), G.Guidoboni and J.Arciero (IUPUI, USA) and A. Harris (Indiana School of Medicine, USA).

References

1. Harris A, Ciulla TA, Chung H, Martin B. Regulation of Retinal and Optic Nerve Blood Flow. *Arch Ophthalmol.* **116**(11):1491-1495. doi:10.1001/archoph.116.11.1491, 1998.
2. Pournaras CJ, Rungger-Brändle E, Riva CE, Hardarson SH, Stefansson E. Regulation of retinal blood flow in health and disease. *Prog Retin Eye Res.* **27**(3): 284-330, 2008.
3. Ocular blood flow in glaucoma. Weinrab & Harris Eds., Consensus Series-6, Kugler Publications, 2009.
4. Boas D et al. A vascular anatomical network model of the spatio-temporal response to brain activation. *NeuroImage* **40**(3): 1116-1129, 2007.
5. Arciero J, Harris A, Siesky B, Amireskandari A, Gershuny V, Pickrell A, Guidoboni G. Theoretical analysis of vascular regulatory mechanisms contributing to retinal blood flow autoregulation. *IOVS* **54**(8):5584-93, 2013.
6. Kudryashov NA, Chernyavskii IL. Numerical simulation of the process of autoregulation of the arterial blood flow. *J Fluid Dynamics*, **43**(1):32-48, 2008.
7. Gundersen SI, Chen G, Palmer AF. Mathematical model of NO and O₂ transport in an arteriole facilitated by hemoglobin based O₂ carriers. *Biophys Chem.* **143**(1-2):1-17, 2009.
8. Hammer M et al. Retinal vessel oxygen saturation under flicker light stimulation in patients with nonproliferative diabetic retinopathy. *IOVS* **53**(7):4063-8, 2012.
9. Causin P, Guidoboni G, Malgaroli F, Sacco R, Harris A. Mathematical modeling of retinal microcirculation and oxygen delivery, to appear, Kugler Publications, 2014.

10. Canić S, Hartley CJ, Rosenstrauch D, Tambaca J, Guidoboni G, Mikelić A. Blood flow in compliant arteries: an effective viscoelastic reduced model, numerics, and experimental validation. *Ann Biomed Eng.* **34**(4):575-92, 2006.

BAGGED NEAREST NEIGHBOR CLASSIFIERS IN SEMI SUPERVISED LEARNING

Nesma SETTOUTI, Mohamed Amine BECHAR, Mostafa EL HABIB DAHO, Mohamed Amine LAZOUNI, Mohamed Amine CHIKH

Biomedical Engineering Laboratory Tlemcen University Algeria nesma.settouti@mail.univ-tlemcen.dz;

am.bechar@gmail.com;mostafa.elhabibdaho@gmail.com;aminelazouni@gmail.com; mea-chikh@mail.univ-tlemcen.dz

In this paper, the *co-Bagged k-NN* algorithm is proposed. It has the ability to take advantage of unlabeled samples to improve the performance of the system formed from labeled samples. By extending the *Bagged k-NN* paradigm, *co-Bagged k-NN* harnesses the power of *Bagging* an overall method well known to tackle: the problem of more confident unlabeled samples' selection for the re-learning of each classifiers.

Keywords: Bagging, Nearest Neighbor Classifiers, Semi Supervised Learning, Ensemble methods

1. Introduction

The idea of semi-supervised learning is to combine labeled and unlabeled data to develop a classifier that is more accurate than the one built solely on the labeled data. Thus, a first model will be based from the labeled data and will be refined subsequently through unlabeled data.

Many semi-supervised learning algorithms have been developed. Roughly speaking, they can be categorized into four categories, i.e., generative methods ¹, S3VMs (Semi-Supervised Support Vector Machines) ², graph-based methods ³, and Ensemble methods in SSL (disagreement based methods) ^{4, 5, 6, 7}.

The last few years' disagreement based methods semi-supervised learning has become an important learning paradigm. The key of Ensemble Methods in SSL is to generate multiple learners, let them collaborate to exploit unlabeled examples, and maintain a large disagreement between the base learners. In ensemble learning, a group of methods is employed and its results are combined to form the final results of the system. Gaining the higher accuracy rate is the main advantage of this system.

Bagging or "bootstrap aggregation" ⁸, is the first effective ensemble method in supervised learning which can be used with any classifier. In this paper, the K nearest neighbors (k -NN) is used as the main classification technique and Bagging as the classification methods in semi supervised Learning. A major attraction of the nearest neighbor classifiers is their simplicity. For implementation they require only a measure of distance in the sample space, along with samples of training data; hence their popularity as a starting-point for refinement and improvement. The *bagged k-NN* in Supervised Learning has been seen different applications ^{9, 10, 11} they used to be very interesting and been seen multiple improvements ^{12, 13}.

In this article, a *Bagged k-NN* approach in Semi Supervised Learning called *co-Bagged k-NN* is proposed. The content is as follows: First, the principle of *co-Bagged k-NN* is explained by describing how the confidence measure is used in the semi supervised context by using labeled and unlabeled data. Experiments using Medical and Biological data-sets are presented in Section 3. In section 4, we exhibit and discuss the different results of our methods in comparison with other techniques in SSL. Finally, a conclusion is conducted to summarize the contribution of this work.

2. Material and Method

2.1. Co-Bagged k-NN Algorithm

In semi-supervised ensemble methods, this line of research started from Blum & Mitchells seminal work ⁴. They proposed the *co-Training* Algorithm for semi-supervised classification of web pages. In the paradigm of *co-Training* ⁴, two classifiers are first formed from L , and then each of them chooses the most confident examples U (unlabeled examples) from his point of view, and updates other classifiers with these new labeled examples. But the inefficient confidence estimation significantly reduces the applicability of the extent of *co-Training* algorithm in applications such as computer aided diagnosis.

However, if a set of N classifiers, denoted by H^* , are used in the *co-Training* instead of two classifiers, so confidence can be estimated efficiently. When determining the most confident labeled for the entire classifiers h_i ($i = 1...N$), each classifier is used except h_i . These classifiers form a new entity, which is called concomitant ensemble, denoted by H_i . Note that H^* differs from H_i only by the absence of h_i . Now, confidence for unlabeled example can be simply estimated by the degree of agreement on labeling, i.e. the number of classifiers that agree on the label assigned by H_i . Using this method, *co-Bagged* inspired from *Co forest* ¹⁴ covers a whole set of classifiers on L , and then it refines each component classifier with unlabeled examples chosen by the concomitant ensemble.

More specifically, in each iteration of learning around *co-Bagged*, the concomitant ensemble of h_i will test each example in U . For an unlabeled example x_u , if the number of classifiers that agree on a particular label exceeds a threshold θ predefined, this new label is assigned to the example and then it will be copied in the new set L^0 . In the next iteration, L^0 is used for refining h_i . Hereafter, it will be appreciated that the unlabeled examples are not deleted from U , so they can be selected by other H_j ($j \neq i$) in the following iterations.

3. Experimentations

Five Medical and Biological datasets mainly selected from the UCI Machine Learning Repository ¹⁵, and ASU feature selection Repository ¹⁶. These are used to evaluate the performance of *co-Bagged k-NN* and their characteristics are described in Table 1.

For each dataset, a 5 cross validation is carried out for evaluation. The training data are randomly divided into two sets: L labeled and unlabeled U determined by an unlabeled rate (μ), which is calculated by the size of U on the size of $L \cup U$. To simulate different amounts of unlabeled data, four different

levels of "unlabeled rate" $\mu = 90\%$, 80% , 70% , 60% , 40% and 20% , are studied. In the following experiments, the value of N is 20 Nearest Neighbor, we

Table 1.	Description of experimental bases		
Bases	#instances	#variables	#class
Heart	270	13	2
Hypothyroid	3163	25	2
Ovarian	54	1536	2
Prostate	102	12533	2
Images	2310	19	7

apply the nearest neighborhood (3-NN) classifiers using the *prtools* toolbox ¹⁷. The Confidence level θ is set at 0.75, i.e. a newly labeled example is considered trusted if more than three quarters of the trees are agreements on its assigned label.

For each set, the algorithm is evaluated on its ability to correctly predict the labels of unlabeled examples. The labeled examples were selected randomly; with the only constraint to have at least one example of each class present in each set.

To compare the performance of *co-Bagged k-NN* with *Bagged k-NN*, improvements are averaged over all datasets in all unlabeled instances, and improving the overall performance is obtained.

4. Results and discussion

Co-Bagged k-NN seems best to combine labeled and unlabeled data for the task of classification in semi supervised learning; it is more interesting to the large data size that has the characteristics of few examples depending on thousands of variables. Specifically, the good performance on the basis *Ovarian* and *Prostate* is noticed. More importantly, *co-Bagged k-NN* outperforms *Bagged k-NN* on most datasets mainly when the unlabeled rate is increasing. These results confirm the effectiveness of confidence measure for the labeling process in *co-Bagged k-NN* which permits our approach to be more efficient in various data sets.

Table 2. Classification rates of the compared algorithms under different unlabeled rate μ

Unlabel %	Techniques	Heart	Hypothroid	Ovarian	Prostate	Images
$\mu=90\%$	Bagged k-NN	0,5311	0,8874	0,4556	0,5086	0,9249
	Co Bagged k-NN	0,5667	0,9449	0,7111	0,5714	0,9577
	Improv.%	3,56	5,75	25,55	6,29	3,27
$\mu=80\%$	Bagged k-NN	0,4844	0,9039	0,5556	0,52	0,9442
	Co Bagged k-NN	0,6133	0,9457	0,7778	0,6114	0,9719
	Improv.%	12,89	4,18	22,22	9,14	2,77
$\mu=70\%$	Bagged k-NN	0,5378	0,9179	0,5778	0,5714	0,9457
	Co Bagged k-NN	0,6067	0,9476	0,7444	0,7429	0,9751

	Improv. %	6,89	2,97	16,66	17,15	2,94
$\mu=60\%$	Bagged k-NN	0,5333	0,9187	0,6556	0,5943	0,9545
	Co Bagged k-NN	0,5867	0,9454	0,7889	0,7029	0,9836
	Improv. %	5,34	2,67	13,33	10,86	2,91
$\mu=40\%$	Bagged k-NN	0,5178	0,9237	0,5333	0,6171	0,9696
	Co Bagged k-NN	0,5889	0,9411	0,6556	0,7029	0,9855
	Improv. %	7,11	1,74	12,23	8,58	1,59
$\mu=20\%$	Bagged k-NN	0,5533	0,929	0,6333	0,5829	0,981
	Co Bagged k-NN	0,5911	0,939	0,7111	0,6629	0,9878
	Improv. %	3,78	1	7,78	8	0,68

5. Conclusion

Since the proliferation of partially labeled databases, semi-supervised methods have seen an important development in machine learning. In this paper, we proposed to address this problem with ensemble method of *bagged k-NN* type. This model is based on semi-supervised classification to select the most confident example from the unlabeled data to enrich the labeled set. Experiments performed on several medical and biological databases show very large effective *co-Bagged k-NN* and confirm its ability to improve the performance of the learned hypothesis on a small amount of labeled samples in exploiting unlabeled samples.

References

1. Kamal Nigam, Andrew Kachites McCallum, Sebastian Thrun, and Tom Mitchell, "Text classification from labeled and unlabeled documents using em", *Mach. Learn.*, vol. 39, no. 2-3, pp. 103–134, May 2000.
2. Yves Grandvalet and Yoshua Bengio, "Semi-supervised learning by entropy minimization.", in *CAP*, Francois Denis, Ed. 2005, pp. 281–296, PUG.
3. Mikhail Belkin, Partha Niyogi, and Vikas Sindhwani, "Manifold regularization: Ageometric framework for learning from labeled and unlabeled examples", *J. Mach. Learn. Res.*, vol. 7, pp. 2399–2434, Dec. 2006.
4. Avrim Blum and Tom Mitchell, "Combining labeled and unlabeled data with co-training", in *Proceedings of the eleventh annual conference on Computational learning theory*, New York, NY, USA, 1998, COLT' 98, pp. 92–100.
5. Zhi-Hua Zhou and Ming Li, "Tri-training: Exploiting unlabeled data using three classifiers", *IEEE Trans. on Knowl. and Data Eng.*, vol. 17, no. 11, pp. 1529–1541, Nov. 2005.
6. Jiao Wang, Siwei Luo, and Xianhua Zeng, "A random subspace method for co-training.", in *IJCNN*. 2008, pp. 195–200, IEEE.
7. Zhi-Hua Zhou and Ming Li, "Semi-supervised learning by disagreement", *Knowl. Inf. Syst.*, vol. 24, no. 3, pp. 415–439, Sept. 2010.
8. Leo Breiman, "Bagging predictors", *Mach. Learn.*, vol. 24, no. 2, pp. 123–140, Aug. 1996.
9. Peter Hall and Richard J. Samworth, "Properties of bagged nearest neighbour classifiers", *Journal of the Royal Statistical Society Series B*, vol. 67, no. 3, pp. 363–379, 2005.
10. Brian M. Steele, "Exact bootstrap k-nearest neighbor learners.", *Machine Learning*, vol. 74, no. 3, pp. 235–255, 2009.
11. Guohua Liang, Xingquan Zhu, and Chengqi Zhang, "An empirical study of bagging predictors for different learning algorithms.", in *The Twenty-Fifth AAAI Conference on Artificial Intelligence*, Wolfram Burgard and Dan Roth, Eds. 2011, AAAI Press.

12. Amer J. AlBaghdadi and Fuad M. Alkoot, "Bagging knn classifiers using different expert fusion strategies.", in *PRIS*, Hugo Gamboa and Ana L. N. Fred, Eds. 2005, pp. 219–224, INSTICC Press.
13. Fuad M. Alkoot, "Investigating methods for improving bagged k-nn classifiers", in *7th WSEAS Int. Conf. on ARTIFICIAL INTELLIGENCE, KNOWLEDGE ENGINEERING and DATA BASES (AIKED'08)*, University of Cambridge, UK., Feb 20-22, 2008.
14. Ming Li and Zhi-Hua Zhou, "Improve computer-aided diagnosis with machine learning techniques using undiagnosed samples", *Trans. Sys. Man Cyber. Part A*, vol. 37, no. 6, pp. 1088–1098, Nov. 2007.
15. D.J. Newman, S. Hettich, C.L. Blake, and C.J. Merz, "Uci repository of machine learning databases", 1998.
16. Reza Zafarani and Huan Liu, "Asu repository of social computing databases", 1998.
17. R. P. W. Duin, "Prtools version 3.0: A matlab toolbox for pattern recognition", in *Proc. of SPIE*, 2000, p. 1331.

DYNAMIC PRUNING FOR RANDOM FOREST

M. EL HABIB DAHO, N. SETTOUTI, M. A. LAZOUNI, M. A. CHIKH

Biomedical Engineering Laboratory Tlemcen University Algeria mostafa.elhabibdaho@mail.univ-tlemcen.dz;

A Dynamic Pruning method for Random Forests algorithm is proposed in this paper. Our procedure of trees selection is based on the Out Of Bag (OOB) error. This approach is therefore tested on four data bases from the UCI Machine Learning Repository. Results show that using few best trees, selected by our proposed Pruning method, improve the performance of each dataset comparing to classical Random Forests.

Keywords: Ensemble Pruning, Dynamic Pruning, Ensemble methods, Random Forest, Supervised classification.

1. Introduction

The aim of ensemble methods (see, for example ¹) is to build a collection of predictors, and then aggregate all of their predictions. In classification, aggregation returns, for example, a majority vote among the classes provided by predictors. The objective is that the final model will be better than each individual predictor. In this work, one of the most used ensemble methods called RF (Random Forest)² is used. A Random Forest consists of a set of prediction trees. Using this set, a significant improvement in prediction compared with the conventional techniques (like CART) is believed to be obtained. Despite the efficiency of the random forests, several researchers have tried to improve the accuracy using only the best trees of the forest. This method is called Tree Selection or Pruning. There are two kinds of Pruning: Static Pruning, where a subset of trees is selected for the whole test set, and Dynamic pruning, where the selection is made for each test sample individually. In this paper, the main interest is therefore to study the ability of dynamic tree selection on random forests. Our new proposed method for tree selection attempts at improving accuracy. For that, this work has been framed as follows: in section 2, methods that we use in our algorithm are introduced. Then, our results tested on four benchmarks from the UCI Machine Learning Repository are exposed. At last, a general summary is given.

1

2. Material and Method

2.1. Random Forest

The Random Forests algorithm ² is one of the most popular achievements of research devoted to the aggregation of randomized trees. Synthesizing the approaches developed, respectively by ³ and ⁴, RF generates a set of trees doubly disrupted using a randomization operating both at the training sample (using bootstrapping samples) and internal partitions. Each tree is thus generated at first from a subset of the complete training set. Then, the tree is constructed using the CART methodology where, at each node, the selection of the best split based on the Gini index is performed not on the complete set of attributes but on a randomly selected subset of it. The tree is then developed to its maximum size without pruning. During the prediction phase, the instance to be classified is spread in every tree of the forest and labeled according to a simple majority vote among all the individual decisions. In addition

to building a predictor, the algorithm of Random Forests calculates an estimate of its generalization error: the error Out-Of-Bag (OOB). “Out-Of-Bag” here means “outside the bootstrap”. This error was already calculated by the Bagging algorithm.

2.2. *Dynamic Pruning*

Dynamic Pruning (also called Dynamic Ensemble Selection or Instance-based Ensemble Selection) aims at selecting the best subset of classifiers dynamically (ie: for each test example) from the original set. The selected classifiers are aggregated afterward by a majority vote. The subset should lead to a greater accuracy compared to the whole set. This type of selection is best suited for offline problems where we privilege accuracy over computation time because there is an additional cost in the testing phase. ^{5 6} are said to be among the first authors who were interested in dynamic selection. Their methods consist in using for each instance of the test base, the best classifiers of its neighborhood (using KNN). Among the most recent works, one may find that of ⁷. The authors proposed four different versions of a method called KNORA (K-nearest Oracle). The proposed algorithms use the KNN to select neighbors of each test instance. In ⁸, authors have proposed a dynamic classifier selection that tries to avoid the non-competent classifiers when their output is probably not of interest. This method considers the neighborhood of each instance to decide which classifier may correctly classify this instance.

2.3. *Proposed method*

It has been noticed that all the works previously cited, in the section dynamic pruning, are based on KNN for the choice of the neighborhood. Noting that this method is not effective if we do not use all the space of attributes. Indeed, instances may be far in the complete space and close in a part of it. As a solution to this problem, a method based on a different notion of neighborhood is suggested. In this work, the nodes of the trees are used as a heuristic neighborhood. Indeed, two instances are adjacent if they pass through the same nodes in a given tree. Our algorithm of Dynamic Pruning involves three steps:

- The creation of a set of classifiers using the Random Forest method.
- For each tree in the forest, the classification of its OOB elements (with this tree) is launched and their paths are saved.
- To classify a new instance, the score of each tree for this instance should be calculated. The class is obtained by a majority vote among the K-best trees.

The principle of calculating the score of a tree, for an instance, is very simple. It is based on a Boolean function which weights the distance between the test instance and each OOB of this tree. This function returns “1” if the element OOB is well classified by the tree, otherwise “0”. The notion of neighborhood here is a binary distance that depends on the leaf of the instance and the OOB. A distance between a test instance and an OOB equals to “1” means they have gone together through all the nodes of the tree, otherwise “0”. For a test instance, the score of a tree is a value comprised between “0” and “1”. A score equals to “1” means that the tree is very efficient and will ensure a correct classification for this test instance. A tree with a score equals to “0” has a high chance to give a false classification for the instance.

3. Results and discussion

To test our algorithm, four databases from the UCI Machine Learning Repository⁹ were used.

Table 1. Description of experimental bases				
Databases	Breast	Liver	Pima	Vehicle
Instances	699	345	768	846
Features	9	6	8	18
Class	2	2	2	4

In what follows, 100 trees for each method were used. Our goal in this work is to study the evolution of the performance of the forests according to the number of trees they contain. For that, a comparison of our Proposed Dynamic Pruning method and RF was established. Groups of selections were organized to which, each time, five trees to the group were added. In the first experiment, a random tree selection for RF where, trees are selected and aggregated according to their order of appearance and without condition, was processed. For the Dynamic Pruning, our proposed algorithm is used.

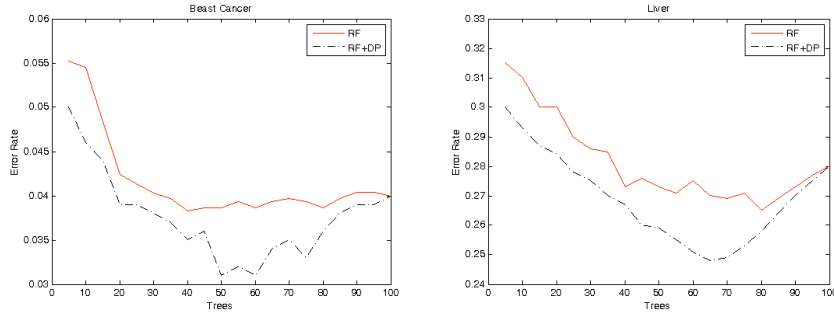


Fig. 1. Error rates of different algorithms

Figures 1 show error rates of different methods as the number of selected trees increases. It may be observed that our algorithm of dynamic pruning gives best result for all databases. DP seems to give better results than RF: it leads globally a lower error rate than RF and it also reaches its optimum for a smaller set of trees.

4. Conclusion

In this paper, a new Dynamic Pruning method, which uses the neighborhood in the tree, has been essentially hypothesized. This method has, in fact, proven effective on Random Forest. For this, it sounds quite important to investigate the efficiency of trees selection. For that reason, our approach on ten UCI databases was experimentally tested. Results display that our approach is almost competitive with Random Forest, which uses the whole ensemble of trees, or with random selection.

References

1. T. Dietterich, "Ensemble methods in machine learning", *Lecture Notes in Computer Science*, vol. 1857, pp. 1–15, 2000.
2. L. Breiman, "Random forests", *Machine Learning*, vol. 45, pp. 5–32, 2001.
3. Leo Breiman, "Bagging predictors", *Machine Learning*, vol. 24, no. 2, pp. 123–140, 1996.
4. Yali Amit and Donald Geman, "Shape quantization and recognition with randomized trees", *Neural Computation*, vol. 9, no. 7, pp. 1545–1588, 1997.
5. Kevin Woods, W. Philip Kegelmeyer, Jr., and Kevin Bowyer, "Combination of multiple classifiers using local accuracy estimates", *IEEE Trans. Pattern Anal. Mach. Intell.*, vol. 19, no. 4, pp. 405–410, Apr. 1997.
6. Giorgio Giacinto and Fabio Roli, "Adaptive selection of image classifiers", in *Image Analysis and Processing*, Alberto Bimbo, Ed., vol. 1310 of *Lecture Notes in Computer Science*, pp. 38–45. Springer Berlin Heidelberg, 1997.
7. Albert H.R. Ko, Robert Sabourin and Alceu Souza Britto, "From dynamic classifier selection to dynamic ensemble selection", *Pattern Recognition*, vol. 41, no. 5, pp 1718–1731, 2008.
8. Mikel Galar, Alberto Fernndez, Edurne Barrenechea, Humberto Bustince, and Francisco Herrera, "Dynamic classifier selection for one-vs-one strategy: Avoiding non competent classifiers", *Pattern Recognition*, vol. 46 no. 5, pp. 3412-3424, 2013.
9. K. Bache and M. Lichman, "UCI machine learning repository", <http://archive.ics.uci.edu/ml>, 2013.

RETINAL IMAGE ANALYSIS FOR CONTENT BASED IMAGE RETRIEVAL APPLICATIONS USING MULTILEVEL THRESHOLDING

SIVAKAMASUNDARI. J¹, KAVITHA. G², NATARAJAN. V¹ and RAMAKRISHNAN. S³

¹*Department of Instrumentation Engineering, Madras Institute of Technology, Anna University, Chennai-600 044, India.*

²*Department of Electronics Engineering, Madras Institute of Technology, Anna University, Chennai-600 044, India.*

³*Non-Invasive Imaging and Diagnostics Laboratory, Biomedical Engineering Group, Department of Applied Mechanics, Indian Institute of Technology Madras, Chennai-600 036, India.*

sivakamasundarij17@gmail.com

The automated segmentation of the vasculature in retinal images is critical to the detection of diabetic retinopathy. In this work, an attempt has been made to analyze retinal images using Content Based Image Retrieval (CBIR) system based on multilevel thresholding (MLT). Otsu and Tsallis MLT based segmentation methods are employed on different normal and abnormal preprocessed fundus images. The vessel segmentation is validated using various similarity measures. Texture and structural features are extracted from the segmented vessels. The Tsallis method detected most of the major and thin vessels better than Otsu method and also shows high similarity values with its corresponding ground truth. Features obtained from the segmented images of Tsallis method differentiate normal and abnormal images with high statistical significance. The retrieval efficiency of Tsallis MLT based CBIR system shows average precision and recall of 94% and 71% respectively. It appears that the Tsallis MLT based CBIR system is useful for automated diabetic retinopathy detection and mass screening.

Keywords: content based image retrieval; Tsallis multilevel thresholding; retinal blood vessels; diabetic retinopathy; similarity measures.

1. Introduction

Diabetic Retinopathy (DR) is the leading ophthalmic pathological cause of blindness and affects the morphology of the retinal blood vessel tree due to abnormal blood glucose level elevation.¹ The visual loss can be prevented when it is detected in early stages. Digital retinal fundus images are widely used for large scale detection and diagnosis of several eye diseases. The increasing number of DR cases demands an automated system for mass screening and image-guided treatments.²

Otsu threshold selection technique is a non-parametric image segmentation method that can be extended to multilevel thresholding.³ Tsallis thresholding method has been used to separate object and the background using the luminance value.⁴ This method is extended to multilevel thresholding for multi objects segmentation.

CBIR in medical image retrieval applications are used to assist physicians in clinical decision-support techniques and research fields.⁵ CBIR has also been used in medical image annotation and retrieval system for X-ray images such as skull, spine, arm and elbow.⁶ In this work, Tsallis and Otsu MLT based methods are applied on preprocessed retinal fundus images for the segmentation of blood vessels. A CBIR system is implemented based on the performance of these MLT based methods.

2. Methodology

Retinal images used for the study are obtained from publicly available database such as

DRIVE, DR database1 and HRF images. Preprocessed images are segmented using Tsallis and Otsu MLT methods.

2.1. Otsu's multilevel thresholding

Otsu applies the between-class variance to threshold an image. An optimal thresholds $\{t_1^*, t_2^*, \dots, t_{M-1}^*\}$ are chosen by maximizing the between-class variance σ_{BC}^2 is given as:

$$\{t_1^*, t_2^*, \dots, t_{M-1}^*\} = \text{Arg} \max_{t_1, \dots, t_{M-1} < L} \{\sigma_{BC}^2(t_1, t_2, \dots, t_{M-1})\} \quad (1)$$

where t_1, t_2, \dots, t_{M-1} represents different threshold levels.³

2.2. Tsallis multilevel thresholding

The Tsallis entropy $S_q(t)$ of each individual class is maximized and the luminance level t is considered to be the optimum threshold value.⁷ Tsallis entropy criterion is extended to multilevel thresholding and is given as:

$$f(t) = \text{Arg} \max \{S_q^A(t) + S_q^B(t) + S_q^C(t) + \dots + S_q^M(t) + (1-q)S_q^A(t)S_q^B(t)S_q^C(t)\dots S_q^M(t)\} \quad (2)$$

where q is an entropic index, $S_q^A(t)$, $S_q^B(t)$, $S_q^C(t)$, ... are the individual classes A, B, \dots, M . In this work, three levels of thresholds are considered for segmentation of the blood vessels, optic disc and background in the retinal fundus images for both the methods.

Validation of segmentation is carried out by comparing the vessels with its corresponding ground truth. Retinal vessels information is extracted and evaluated using various binary similarity measures.⁸ Image retrieval is carried out using query image. The query image is segmented and its features are extracted. Tamura features such as directionality, likeliness, contrast and coarseness are obtained. Statistical texture features such as energy, entropy, homogeneity, mean, median and standard deviation are extracted. The structural feature namely the ratio of vessel to vessel free area is also extracted from the segmented binary images. The matching is carried out between features of query and database images using Hausdorff distance.⁹ The retrieved images are ranked. Statistical analysis is performed on all the features using t-test.

3. Results and Discussion

The preprocessed images are subjected to Otsu and Tsallis MLT segmentation techniques. The segmentation results are shown in Fig. 1 and 2. Tsallis method identifies the primary and small vessels up to complete length with continuous vessels as shown in Fig. 1 (b). Otsu method identifies major vessels and also less small vessels with more discontinuities as shown in Fig. 1 (a). In abnormal images, it is observed from Fig. 2 (b) that the lesions due to DR conditions are also detected along with vascular networks. The thin vessels are not detected in Otsu method and major vessels have more discontinuity as shown in Fig. 2 (a). The lesion pixels which are later removed when compared with the corresponding ground truth vessels as shown in Fig. 1 (c) and 2(c).

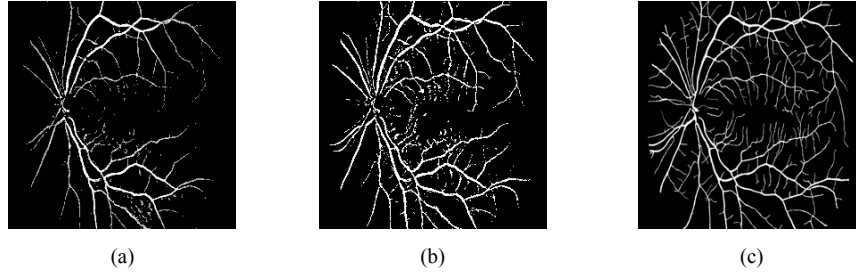


Fig. 1 Segmentation of normal images, (a) Otsu method (b) Tsallis method and (c) ground truth images

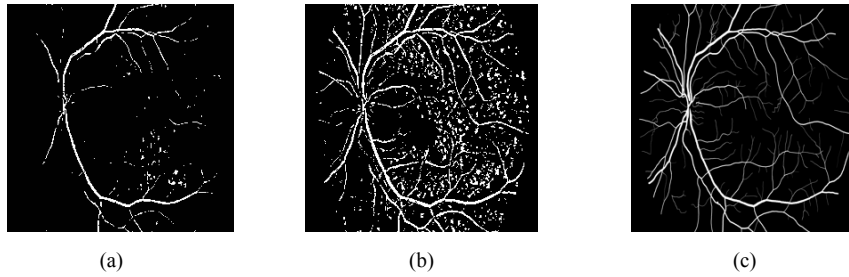


Fig. 2 Segmentation of abnormal images, (a) Otsu method (b) Tsallis method and (c) ground truth images

The validation of Otsu and Tsallis MLT based segmentation results are evaluated by significant binary similarity matching measures. The similarity values close to one are represented in Fig. 3 (a) and (b) using box plots. It is observed that the two similarity measures such as Sokal-Sneath-2 and Goodman-Kruskal Lambda have higher magnitude. The Jaccard measure shows very less similarity value (0.7) in Otsu method which is better (0.85) for Tsallis method. Other measures exhibit higher similarity values for Tsallis method with ground truth than Otsu method.

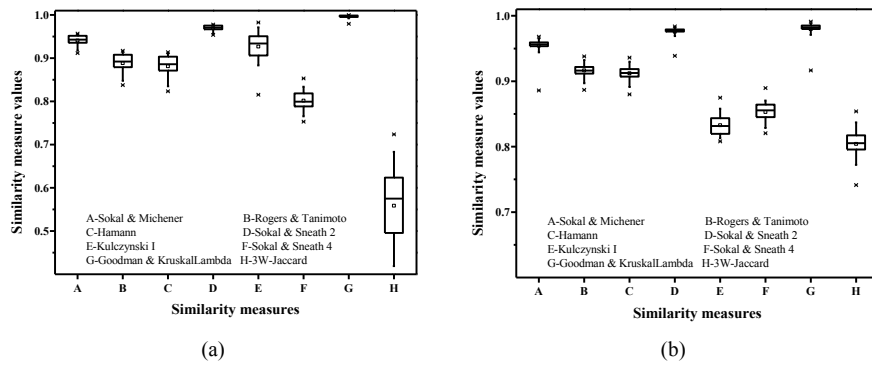


Fig. 3 Validation of segmentation with ground truth using binary similarity measures, (a) Otsu and (b) Tsallis MLT methods

The statistical analysis of features such as Tamura, statistical texture and ratio of vessel to vessel free area derived from segmented images using Tsallis and Otsu MLT methods. The p - values are obtained for features of both the methods. It is found that the p - values of all features are statistically significant ($p < 0.0001$) for Tsallis MLT method and differentiates normal and disease affected retinal images significantly than Otsu method. Hence it could be concluded that these features are used for the Tsallis MLT based CBIR system. The performance of this CBIR system is found to be high precision of 94% and recall of 71%.

4. Conclusion

In this work, MLT based CBIR system for retinal images is attempted for automated screening of diabetic retinopathy. Otsu and Tsallis MLT based methods are employed for segmentation of retinal blood vessels. Tsallis method identifies major and thin blood vessels and performs better than the Otsu method. Based on the quantitative analysis, it is observed that the p -values obtained for the features of Tsallis method are highly significant and show better difference of normal and abnormal images. The retrieval performance of Tsallis based CBIR system such as precision and recall are found to be 94% and 71% respectively. It appears that the Tsallis MLT based CBIR approach is effective and suitable to implement in the computer-aided diabetic retinopathy screening system for better accuracy.

References

1. Abramoff MD, Garvin MK, and Milan Sonka, Retinal imaging and image analysis, *IEEE Trans. Med. Imaging* **3**:169-208, 2010.
2. Reza AW, and Eswaran C, A decision support system for automatic screening of non-proliferative diabetic retinopathy, *J. Med. Syst* **35**:17-24, 2011.
3. Liao PS, Chen TS, and Chung PC, A fast algorithm for multilevel thresholding, *J. Inf. Sci. Eng* **17**:713-727, 2001.
4. Portesdealbuquerque M, Esquef I, and Gesualdimello A, Image thresholding using Tsallis entropy, *Pattern. Recogn. Lett.* **25**:1059-1065, 2004.
5. Muller H, Michoux N, Bandon D, and Geissbuhler A, A review of content-based image retrieval systems in medical applications – clinical benefits and future directions, *Int. J. Med. Inform* **73**:1-23, 2004.
6. Mueen A, Zainuddin R, and Sapiyan Baba M, MIARS: a medical image retrieval system, *J. Med. Syst.* **34**:859-864, 2010.
7. Sathya PD, and Kayalvizhi R, PSO-based Tsallis thresholding selection procedure for image segmentation, *Int. J. Comput. Appl. T* **5**:39-46, 2010.
8. Choi SS, Cha SH, and Tappert C, A survey of binary similarity and distance measures, *J. Systemics. Cybernetics and Informatics* **8**(1): 43-48, 2010.
9. Huttenlocher DP, Klanderman GA, and Rucklidge WJ, Comparing images using the Hausdorff distance, *IEEE T. Pattern. Anal* **15**(9): 850-863, 1993.

MULTIFRACTAL BASED SEGMENTATION AND ANALYSIS OF HUMAN RETINAL BLOOD VESSELS IN FUNDUS IMAGES

SRI MADHAVA RAJA NADARADJANE*, KAVITHA GANESAN†, SRINIVASAN SUBRAMANIAN*, SWAMINATHAN RAMAKRISHNAN††

*Dept of Instrumentation Engg, Madras Institute of Technology Campus, Anna University, Chennai., India

† Dept of Electronics Engg, Madras Institute of Technology Campus, Anna University, Chennai., India

††Non- Invasive Imaging and Diagnostics Laboratory, Biomedical Engineering Group, Dept of Applied Mechanics, Indian Institute of Technology Madras, Chennai, India

‡nsrimadhavaraja@gmail.com

In this work, an attempt has been made to segment and analyze human retinal vasculature using multifractal based method. The retinal images acquired under standard protocols are subjected to segmentation for extraction of retinal vasculature both in normal and abnormal cases. Different performance measures are obtained from the segmented vessels by comparing the segmented image with ground truth images. These measures are able to differentiate normal and abnormal images. The proposed study seems to be useful in assisting clinical interventions related to retinal disorders.

Keywords: Retinal fundus images, Multifractal, Performance measure.

1 Introduction

Retina is a light-sensitive tissue lining the inner surface of the eye. It can be directly visualized non-invasively. Vessels, fovea and optic disk form the important structures of the human retina. Of these, blood vessel is the prime feature that directly manifests the state of the eye. Many retinal diseases are characterized by changes in retinal vessels [1]. The blood vessels of a normal retina are straight or gently curved, but they become dilated and tortuous in many pathological conditions such as high blood flow and angiogenesis [2]. Staal et al have [3] applied ridge-based vessel segmentation in color retinal images. Fourier fractal dimension has also been attempted to compute the fractal dimension of the retinal images [4]. Assessment and optimization approaches of retinal vasculature abnormalities have been attempted by Raja et al [5, 6]. Multifractal (MF) is extension of fractals used to describe signal singularity and its information is not lost by any smoothing process [7]. MF analysis has found widespread applications in medical diagnosis and image processing applications [8-10]. In this work, retinal blood vessel segmentation has been attempted using MF. The measures extracted from the segmented images are used to differentiate normal and abnormal images.

2 Methods

Retinal fundus images (N=40) are considered from STARE, DRIVE, DIABRET [3] public database. The green channel of images is subjected to segmentation using MF. The MF box counting analysis gives the description of a measure over a region both locally and globally. The local exponent also called Hölder exponent are discretized into number of α sub-ranges. The alpha image is created with the one-to-one correspondence of image pixels. E_α represents the region to be partitioned into subsets where the local dimension is α . When these sets E_α are non-empty and fractal over a range of α , it is called as MF measure. The spectrum is calculated as:

$$f_\epsilon(\alpha_i) = -\frac{\ln(N_\epsilon(\alpha_i))}{\ln(\epsilon)} \quad (1)$$

where, $N_e(\alpha_i)$ is the number of boxes containing particular value α_i . The limiting values of the MF spectrum $f(\alpha)$ is obtained from the slope of bi-logarithmic plot. Using a suitable MF value as threshold, the segmentation of the blood vessel is carried out [4]. The segmentation results are compared with their corresponding ground truth to obtain different measures [9]. These measures include structural content, peak signal to noise ratio, normalized cross correlation, normalized absolute error, mean square error, maximum difference, and average difference. These are used for quantitative analysis to differentiate normal and abnormal conditions [11].

3 Results and Discussion

Representative normal and abnormal retinal images are shown in Figures 1(a) and 2(a). Figures 1(b) and 2(b) shows their corresponding segmented images. These images are subjected to segmentation using threshold obtained by MF method. The thin vessels along with their branching patterns are clearly visualized. It is also found that the information pertaining to pathological state is clearly extracted along with the blood vessels in case of abnormal subjects.

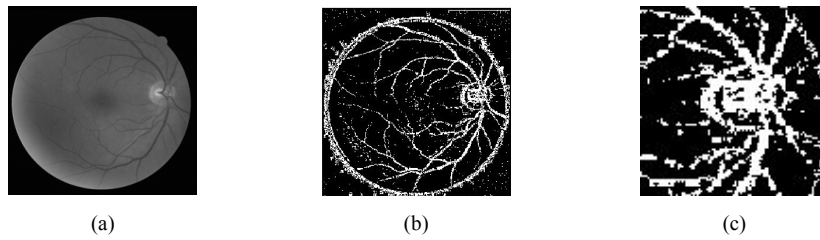


Fig. 1 Representative normal (a), Corresponding Segmented (b) and Region of interest (100x 100)(c)

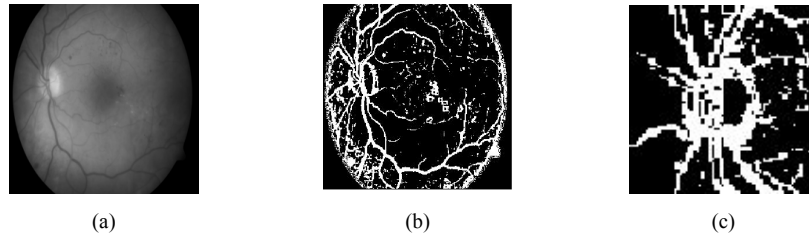


Fig. 2 Representative abnormal (a), Corresponding Segmented (b) and Region of interest (100x 100)(c)

This could be used to grade the different stages of pathological condition of retinal images. The regions of interest enclosing the optic disc of normal and abnormal images are shown in Figures 1(c) and 2(c). The vessels present around the optic disc region show considerable variations between normal and abnormal images. To validate the segmentation, the normalized values of different quantitative parameters are obtained by comparing segmented images with ground truth and are shown in table 1.

Table 1. Performance measures for the segmented normal and abnormal images using multifractal method

Sl. No	Parameters	Normal	Abnormal
1	Structural Content	0.57	0.50
2	Peak Signal to Noise Ratio	0.89	0.78
3	Normalized Cross-Correlation	0.53	0.44
4	Normalized Absolute Error	0.88	0.93
5	Mean Square Error	0.16	0.30
6	Maximum Difference	0.97	0.88
7	Average Difference	0.09	0.02

It is observed that high value of the structural content is obtained for normal images when compared to abnormal images. This could be attributed to the reason that more edge information of the vessels are obtained in normal images. Similarly, peak signal to noise ratio which corresponds to useful information of the vessel is high in the case of normal segmented images. Due to presence of more noise pixels in abnormal images, peak signal to noise ratio is found to be low. The normalized absolute and mean square error are greatly reduced in normal images. This shows that most of the vessels are correctly detected and spurious ones are not detected in abnormal images. It is also observed that there exist distinct variations between normal and abnormal images.

4. Conclusion

In this work, an attempt has been made to analyze retinal vasculature using MF method. From the subjective analysis, it has been observed that the MFs are able to effectively segment even the small blood vessels along with their branching patterns. It is also found that significant variations are observed between normal and abnormal images. And also, the parameters obtained by comparing segmented images with the ground truth show distinct variation between normal and abnormal subjects. In addition, various performance measures provide better differentiation between normal and abnormal. This study seems to be clinically relevant as automated analysis of retinal vasculature is important to identify manifestation of diseases such as diabetes and hypertension.

References

1. Patton N, Aslam, TM, MacGillivray, T, Deary IJ, Dhillon, B, Eikelboom, RH, Yogesan K & Constable IJ, Retinal image analysis: concepts, applications potential *Journal of Prog Retinal Eye Research* 25, **1**, pp.99-127, 2006.
2. Nirmala, SR, Nath MR Dandapat S, Retinal Image Analysis: A Review *International Journal of Computer & Communication Technology* 2, **6**, pp.11-15,2011.
3. Staal, J, Abramoff, MD, Niemeijer, M, Viergever MA & Ginneken BV, Ridge-based vessel segmentation in color images of the retina *IEEE Trans Med Imag* 23,4, pp. 501–509, 2004.
4. Kawasaki, R, Azemin, CMZ, Kumar, MK, Tan, AK, Liew, G, Wong, TY, Mitchell P & Wang, JJ, Fractal dimension of the retinal vasculature and risk of stroke: a nested case-control study *J Neurology* 76, **20**, pp.1766-67, 2011.

5. Sri Madhava Raja N, Kavitha G, Ramakrishnan S, Analysis of vasculature in human retinal images using particle swarm optimization based tsallis multi-level thresholding and similarity measures, *Swarm, Evolutionary, and Memetic Computing, Lecture Notes in Computer Science* **7677**, pp. 380-387, 2012.
6. Sri Madhava Raja N, Kavitha G, Ramakrishnan S, Assessment of Retinal Vasculature Abnormalities using Slantlet Transform based Digital Image Processing, *Biomedical Sciences Instrumentation*, **46**, pp.93-99, 2011.
7. Lopes R & Betrouni N, Fractal and multifractal analysis: A review *Journal of Medical Image Analysis* 13, **4**, pp. 634–649, 2009.
8. Soares, F, Sousa, I, Janela, I, Seabra, J, Pereira M & Freire M, Multifractal analysis of arterial spin labeling functional magnetic resonance imaging of the brain *IEEE Proceedings of International Workshop on Medical Measurements and Applications*, Ottawa, ON, Canada, pp. 161-165, 2010.
9. Stojic T, Reljin I, Reljin B, Adaptation of multifractal analysis to segmentation of microcalcifications in digital mammograms *Stat Mech and its Phy Appl* **367**, pp.494–508, 2006.
10. Vehel JL & Mignot P, Multifractal segmentation of images, *Fractals*, 2, **3**, pp.379–382, 1994.
11. Poobal S & Ravindran, The Performance of Fractal Image Compression on Different Imaging Modalities Using Objective Quality Measures, *International Journal of Engineering Science and Technology*, 3, **1**, pp.525-530, 2011.

METABOLIC NETWORK MODELS FOR THE CHARACTERIZATION OF PATHOLOGICAL CELLULAR STATES

GABRIELE FONTANAROSA, ENRICO GIAMPIERI, GIULIA MENICHETTI, GASTONE CASTELLANI, DANIEL REMONDINI

*Physics and Astronomy department, University of Bologna, viale Berti Pichat 6/2,
40138 Bologna, Italy.*

We introduce the formalism for the characterization of cellular states at the level of metabolic activity. We describe the state of the art knowledge about human metabolic network, as obtained from publicly available databases. Moreover, by means of mathematical models (such as Flux Balance Analysis and Markov chains) we show how this network can be used to characterize perturbations to cellular activity (eg. by removal of compounds or reactions from the network) that can mimic the effect of drugs or of pathologies.

Keywords: metabolic network, flux balance analysis, Markov chain, multidrug treatment, Warburg effect, cellular metabolism, constraint-based method

1. Introduction

A metabolic network is the complete set of metabolic and physical processes that determine the physiological and biochemical properties of a cell. These networks comprise the chemical reactions of metabolism, the metabolic pathways, as well as the regulatory interactions that guide these reactions. With the sequencing of complete genomes the metabolic reconstructions are built nowadays in a bottom-up fashion, starting from the genome scale to the whole molecular physiology of the cell and allowing for an in-depth insight in to the mechanisms of a particular organism's metabolism. Once a reconstruction is complete, the model is converted into a robust mathematical/computational representation, which constitutes the ground for subsequent in-silico simulations. Some recent applications of these “virtual cells” include innovative treatments analysis (i.e. multidrug combinations) or entire disease simulations, such as cancer or metabolic syndromes. It is thus possible to study a whole series of modifications on the metabolism network of an organism without any intervention on the actual cell. With the refinement of the techniques used to characterize the metabolic networks of biological tissues we expect continuous improvements in the reliability of these models, allowing in-silico simulations to become a valuable tool in the biomedical research field.

2. Material and methods

RECON2¹ is a community-driven global reconstruction of human metabolism and represents the most comprehensive model applicable to computational simulations: it is composed of almost 7.5k different reactions and 5.4k unique metabolites. Reactions are divided in 100 human major metabolic pathways and each metabolite is further partitioned in 8 cellular compartments. It is based on a protocol² describing each step necessary to build a high-quality genome-scale metabolic reconstruction, which allows further coherent revisions. The reconstruction is fully semantically annotated with references to persistent and publicly available chemical and gene databases, unambiguously identifying its components and increasing its applicability for third-party users. The model is freely available in the Systems Biology Markup Language format (SBML) at <http://humanmetabolism.org>. The core of Recon consists of a matrix in which each row represents a metabolite and each column a reaction: the values of the matrix represent the stoichiometric coefficients for the metabolites in the reactions. If we imagine the reactions exchanges

as fluxes, we presume the cell to be in a steady state (a well justified assumption) and we provide upper and lower bounds to the reactions capacity (the constraints), then the metabolism can be simulated by Flux Balance Analysis, which is a linear-programming constraint-based technique (eg by the COBRA toolbox³, COntstraint Based Reconstruction Analysis) capable to solve the vector of the unknown metabolic fluxes. The fundamental step in applying FBA is the definition of the constraints: it is necessary to identify an objective function to be maximized (ie ATP production, or the global cell biomass) while imposing inequalities on the other fluxes. Recent interesting efforts have been made towards the simulation of multidrug treatments on cancer cells⁴: in this case the FBA algorithm finds the optimal combination of drugs which guarantees the inhibition of an objective function, while minimizing the side effect on the other cellular processes. Two different applications were considered: finding drug synergisms for human metabolic diseases (like diabetes, obesity and hypertension) and finding antitumoral drug combinations with minimal side effect on the normal human cell. Another application of FBA in the field of cancer research is the simulation of the most common hallmarks of all tumoral diseases: the Warburg effect⁵ which, in oncology, is the observation that most cancer cells predominantly produce energy by a high rate of glycolysis followed by lactic acid fermentation in the cytosol, rather than by a comparatively low rate of glycolysis followed by oxidation of pyruvate in mitochondria as in most normal cells. Malignant, rapidly growing tumor cells typically have glycolytic rates up to 200 times higher than those of their normal tissues of origin; this occurs even if oxygen is plentiful. In this case FBA minimizes pyruvate oxidation, provides unlimited glucose intake and maximizes glycolysis: this kind of simulations could highlight the role of single reactions or entire pathways and even explain the mechanism behind this effect, leading to novel anti-cancer strategies. Another approach in studying the metabolic network that we are pursuing consists in extracting and studying the pathway-pathway network from the Recon stoichiometric matrix: each node represents a subsystems and one node is linked to another only if the pathways are connected in the original network (ie: the product of a pathway is the reactant in another). The weighted and directed network thus obtained (a 100x100 adjacency matrix) can be seen as a stochastic transition matrix for a Markov process: each value of the matrix can be mapped to the transition probability between pathways. With this approach we can characterize the stationary distribution of the process, related to the basal state of the cell metabolism, and evaluate the relevant changes in the steady states due to modifications such as removal of reactions, metabolites or whole pathways without biological limitations (such as the objective function in the FBA).

3. Conclusions:

At the core of all these techniques lies the reconstructed model of the metabolism network: such element is by far the most important brick in building good simulations. All the predictive and descriptive power arises from the quality of the reconstruction. The stoichiometric matrix must be coherent, chemically balanced and capable of capturing at least the fundamental reactions that happen inside the cell. While there's plenty of room for the improvement of the reconstructions, COBRA method as FBA or stochastic analysis are mature tools ready to be applied to the vast majority of metabolic and genomic problems.

References

1. Ines Thiele, Neil Swainston, Ronan M T Fleming, et al. A community-driven global reconstruction of human metabolism. *Nature Biotechnology* 2013, 31:5
2. Ines Thiele& Bernhard Ø Palsson, A protocol for generating a high-quality genome-scale metabolic reconstruction. *Nature Protocols* 2010, 5:1
3. Schellenberger J, Que R, Fleming RM, Thiele I, Orth JD, Feist AM, Zielinski DC, Bordbar A, Lewis NE, Rahmanian S, Kang J, Hyduke DR, Palsson BØ, Quantitative prediction of cellular metabolism with constraint-based models: the COBRA Toolbox v2.0. *Nat Protoc.* 2011, 6(9)
4. Giuseppe Facchetti, Mattia Zampieri, and Claudio Altafini, Predicting and characterizing selective multiple drug treatments for metabolic diseases and cancer. *BMC Systems Biology* 2012, 6:115
5. Vineet Sangar, James A. Eddy, Evangelos Simeonidis, Nathan D. Price, Mechanistic modeling of aberrant energy metabolism in human disease. *Front Physiol.* 2012, 3:404

MULTIOMICS NETWORK ANALYSIS OF HEARTH DISEASE RISK

GIULIA MENICHETTI (1), ENRICO GIAMPIERI (1), DANIEL REMONDINI (1), ETTORE MOSCA (2) AND GASTONE CASTELLANI (1)

1: Physics and Astronomy department, University of Bologna, viale Berti Pichat 6/2, 40138 Bologna, Italy

2: Bioinformatics Group, Istituto di Tecnologie Biomediche, CNR, Via Fratelli Cervi, 93, 20090, Segrate (Milano), Italy

Recent developments of data collection in medicine are generating a huge amount of data for each subject in a study. This amount of data creates problems for the data analysis, as the number of variables is greater than the number of subjects, and a statistical procedure that does not include biological knowledge in an automated way is bound to overfit. One method to avoid this problem is using network theory in the form of multiplex analysis. This approach allows to combine information deriving from different sources and compare them. The multiplex approach consists in creating several, overlapping, networks on the same nodes, using informations on the relationships between these networks to improve the following analysis. We demonstrate two possible uses of this information analyzing the DILGOM database (Dietary, life style, and genetic determinants of obesity and metabolic syndrome). We study a possible natural clustering of subjects based on a multiplex network of the subjects. This multiplex is composed by two layers describing the similarities between subjects, both using metabolites amount and RNA expression. Varying the threshold value on these correlation we see the natural formation of two clusters with a strong relationships between them and with several relevant phenotypical informations. With a similar approach we develop a network between metabolites as regressors for the Framingham risk score, a phenomenological assessment of the probability of having heart diseases in the following 5 years. Combining this network with information from the genetic mutation of the subjects, we can infer a robust estimator of this probability based on non-local relationships between the regressors.

Keywords: Multiplex, Multiomics, cardiac disease, outcome prediction, clustering

Introduction:

Recent advancement in medical and biological analysis is producing an incredible amount of data, describing each subject in great detail[1]. Such this dataset include, alongside with physiological and clinical observations:

- RNA expression level
- metabolites spectrography
- gene expression
- DNA sequencing
- methylation level of the genetic material
- immunity status
- glycosilation of blood proteins
- profiling of the composition of blood fatty acid
- the genetic profile of the microbiome in the gut or the environment
- the amount and modification of proteins

These data can be collected in a continuously faster, cheaper and accurate way, and the biggest hindrance to the use of these data in clinical practice is now being able to correctly interpret them. Being the amount of data per subject orders of magnitude greater than the number of subjects, classical exploratory analysis has a great risk of overfitting the noise implicit in these measurements as signal, and no amount of significant value correction can avoid this pitfalls.[4, 5]

A classic correction method involves machine learning approaches of train-test splitting of the database,

but this method has its own shortcoming, as the number of splits required to understand if the results is a simple effect of noise can grows more than quadratically in the number of subjects and variables.

A different take on this problem (that can be used together with the train-test split) is taking into consideration the current biological knowledge in form of relationships between the entities under study. This information can often be represented in the form of network of pair relationship between the variable or the subjects. The information from these networks can be joined in a multiplex, where each network create a layer of a super-structure of information. From the relationships between these layers additional information on the properties of each layer and the node that constitute it can be deducted [6].

Methods:

As a case study for this approach we used the DILGOM (Dietary, life style, and genetic determinants of obesity and metabolic syndrome) dataset, from the MimoMimics European Project. This database contains information about lifestyle and phenotypes, biochemical analysis, RNA expression and SNP from around 600 subjects[3].

We performed the analysis on the subjects of the study as nodes of the networks, considering a network of similarities calculated with two different parameter sets, using a non-parametric correlation between the subjects as index of similarity. One network is based on similarity from metabolites profiles, while the other is based on the RNA expression level. These networks have been discretized as binary, undirected network with a filtering on the correlation value, and the superposition between the networks. Varying the binarization threshold for each network we can study what happens to the structure of the network. We observe that the thresholding over the correlation network induces a spontaneous division of the network in two separate, almost equal size cluster. We checked this natural clustering against gender, age, BMI, WHR and Framingham risk score (FRS), a phenomenological assessment of the probability of having heart diseases in the following 5 years. We found that this division is significant for all of these categories, and so further steps to identify the nature of the division are required.

A similar approach can be used to predict the FRS on individual patients based on metabolic and genetic information, under the assumption that the probability of having heart diseases in the 5 years period varies slowly between before the observation and after. To perform this estimation we began with creating a network of relationships between the various variables. A connection was created between two variables based on a likelihood based score for the regression of the FRS. We used the generated network as a basis to find a subset of regressors that accurately predict the score. Elements with low correlation and high clustering are most likely to contains relevant informations about the systems. This approach allows to include non local information in the variable selection.

Conclusions:

The network analysis is gaining traction as a fundamental technique in data analysis for biological data, especially with multiplex that allows to encompass information from different sources. These methods allow to avoid mistaking noise as information using the superposition of several related structures[2]. Given the relevance multiomics measurements are gaining in evidence-based medicine, we think that multiplex network analysis of these variables will be a central toolkit in the data analysis process.

Acknowledgments:

GC, DR, GM and EG acknowledge the European project MimoMics (grant 305280), FIBEBiotics (grant 289517) and the INFN project MERIDIAN

References

- [1] M. Inouye et al Novel Loci for Metabolic Networks and Multi-Tissue Expression Studies Reveal Genes for Atherosclerosis. PLoS Genet 2012 8(8): e1002907. doi:10.1371/journal.pgen.1002907
- [2] B. Barzel A. Barabási Network link prediction by global silencing of indirect correlations. nature biotechnology (2013) VOLUME 31 NUMBER 8, doi:10.1038/nbt.2601
- [3] M. Inouye et al Metabonomic, transcriptomic, and genomic variation of a population cohort. Molecular Systems Biology (2010) 6; Article number 441; doi:10.1038/msb.2010.93
- [4] V.n E. Johnson Revised standards for statisticevidence. PNAS (2013), vol. 110, no. 48, 19313–19317, doi:10.1073/pnas.1313476110
- [5] G. Shmueli To Explain or to Predict? . Statistical Science (2010), Vol. 25, No. 3, 289–310, doi: 10.1214/10-STS330
- [6] G. Menichetti et al Weighted multiplex networks. PloS one (2014), Vol. 9, No. 6: e97857. doi: 10.1371/journal.pone.0097857

DEVELOPMENT OF A DYNAMIC MODEL OF THE ALVEOLAR INTERFACE FOR THE STUDY OF AEROSOL DEPOSITION

D. CEI

*Research Center "E. Piaggio", University of Pisa
Largo Lucio Lazzarino 2, 56126 Pisa, Italy
daniele.cei@for.unipi.it*

A.D. AHLUWALIA

Department of Information Engineering, University of Pisa, via Caruso 2, 56126 Pisa, Italy

O. SCHMID

*Comprehensive Pneumology Center, Helmholtz Zentrum Muenchen, Ingolstadter Landstrasse 1
D-85764 Neuherberg, Germany*

Nano and micro particles are largely used in different industrial, household and medicinal applications. However their effect on human tissue, in terms of toxicity or induction of pathologies is not well understood. Because it is one of the first organs to come into intimate contact with airborne particles from smoke or aerosols. The study of nano and micro material-tissue interaction in a physiological context is of interest. The aim of this project is study nanoparticle deposition on and passage through a porous membrane which mimics lung motion during breathing. A Moving Air-Liquid Interface (MALI) bioreactor is a new in-vitro model of the alveolar epithelia and blood capillary interface that allows investigation of the short and long term effects of nanoparticles on alveolar epithelial cells. A layer of pulmonary tissue is regenerated inside a bioreactor and mechanically stimulated using an activated polymeric membrane.

Keywords— Bioreactor, Air-Liquid Interface, Nanoparticle, Moving Membrane.

1. Introduction

Every day lungs are in contact with the air, potentially charged with dispersed particles, which cause inflammation and stress, contributing to the development or exacerbation of diseases such as asthma or chronic obstructive pulmonary disease (COPD). Epidemiological studies show an association between the concentration of fine and ultrafine particles (PM₁₀, PM_{2.5}, PM_{0.1}) in the atmosphere and the rate of mortality or morbidity due to respiratory and cardiovascular diseases.¹

The interaction of nano and micro particles with pulmonary epithelia is a complex process, mediated by the humidity of the alveolar environment as well as the rhythmical contraction of the diaphragm, which generates a periodic change in alveolar volume accompanied by displacement of the alveolar wall. How this movement contributes to nanoparticle deposition and uptake by the epithelial wall, or to downstream inflammatory processes is not clearly understood, partly because of the lack of appropriate models which can recapitulate the alveolar microenvironment.²

Measurements of small molecule transport across epithelial cell monolayers in tissue culture are routinely performed in pharmaceutical research laboratories to predict the absorption properties of drug candidates.²

Those systems cannot fulfil the entire complexity of the alveolar interface, especially change in lung

permeability to small particles and drugs due to mechanical cyclic strain.³⁻⁵

This effect was attributed to a concomitant increase in the pulmonary blood flow and increased movement of drug across the alveolar membranes due to opening of the epithelial cell tight junctions and hence increased permeability.^{6, 7}

To study the long and short terms effects of aerosol phase nanoparticles on pulmonary tissue in the presence of cyclic motion of the interface we developed an air-liquid interface bioreactor with a mobile elastic membrane to simulate physiological lung muscle stretching. Known as MALI, (Moving Air Liquid Interface bioreactor) the system consists of an aerosol generator and a bioreactor with a moving membrane placed between an air-liquid interface to study drug and nanoparticles deposition and passage.

2. Material and Methods

Lung tissue is cultured on the stretchable porous membrane. The membrane, electrospun poly (carbonate)urethane scaffold with a mean fiber diameter of about 3 μ m (Bionate II 80A, Electrospinning UK) is sandwiched between the two compartments of the bioreactor. The mechanical properties of the membranes were evaluated in dry and wet conditions to evaluate the ability to undergo reversible cyclic deformation and to ensure the biomaterial can be used in the bioreactor for long term experiments.

As shown in *figure 1*, the bioreactor is composed of three main parts: a mesh membrane aerosol generator (Aeroneb Pro[®], Aerogen, USA) and a two-chamber PDMS bioreactor. The working principle is very simple: briefly an external electro-pneumatic regulator induces an increase of pressure in the apical chamber of the bioreactor, while culture medium flows in the basal chamber. The difference between air pressure and hydrodynamic pressure reflects in membrane deformation. The entity of the stimulus mainly depends on fluid velocity (flow rate) and air pressure.

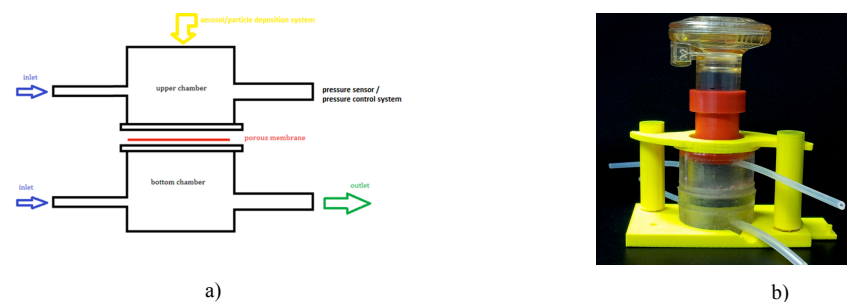


Fig. 1. Bioreactor schematic (a) and prototype (b): the MALI Bioreactor is composed of two chambers, one filled with cell medium and one with air for membrane movement and particle deposition. The top of the bioreactor holds a casing for the nebulization system. The system dimensions and free volume are based on a 6-well transwell insert

The system was also characterized in terms of aerosol deposition efficiency. Two different fluorescent solution were nebulised into the apical chamber to evaluate aerosol deposition efficiency and homogeneity: respectively a 15 μ g/mL fluorescein sodium salt solution in PBS (Sigma-Aldrich Chemie GmbH Munich, Germany) and a 0,05% (w/V) SkyBlue polystyrene nanoparticles (Kisker Biotech GmbH

&CoKg, Steinfurt, Germany) were used. Fluorescein solution was also used to evaluate particle concentration on the Bionate membrane and in the liquid compartment. Efficiency and aerosol distribution were evaluated at different nebuliser duty cycle.

Human epithelial-like cell line from lung adenocarcinoma (A549, ATTC, Manassas, VA, USA) were cultured in Dulbecco Modified Eagle's Medium (DMEM), supplemented with 10% (v/v) of Fetal Calf Serum (FCS), 4 mM- L- glutamine, 100 Unit/mL penicillin and 100 µg/mL streptomycin. Cells were seeded on Bionate membrane disc (surface area 4,9cm², 5·10⁶ cells/sample), coated with Matrigel (*see Appendix A*).

3. FEM Model

A FEM (Finite Element Method) model was used to design the bioreactor and study the dynamics of the membrane between a liquid and gas phase chamber. Medium flow in the basal chamber was modelled using Navier Stokes's equations to provide nutrients and oxygen to the cells. Air flow in the apical chamber was modelled as a boundary load condition, with the assumption of a quasi-static condition of membrane stretching. Membrane stretching magnitude and displacement field was evaluated with a two-way coupled analysis and a moving mesh modelling: membrane displacement resulted as a balance between pressure field in the wet compartment and boundary load due the air pressure (*Figure 2*).

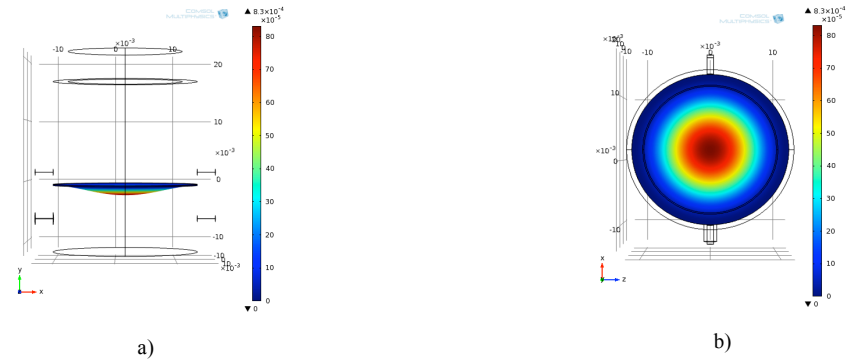


Fig. 2. FEM model of MALI Bioreactor; lateral (a) and superior view (b). Colorbar represent membrane displacement in z direction (max 1.5mm, air pressure is 1kPa)

4. Discussion

Membranes ability to undergo reversible cyclic deformation and for long term experiments were evaluated in this work. Mechanical test at different incubation time (0, 1, 2, 4, 7 days in DMEM @ 37°C, *Figure 3*) showed no evident effect (tested with ANOVA test, $p < 0.05$) of hydrolytic degradation on apparent elastic modulus. After 24h continuous cyclic stress Bionate also do not change significantly its characteristics (room temperature ~25°C, tested with ANOVA test, $p < 0.05$).

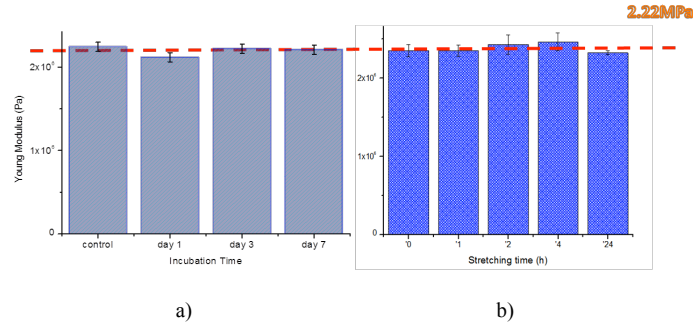
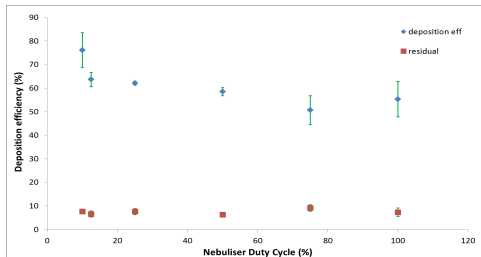


Fig. 3. Electrospun Bionate II 80A tensile test in wet condition (DMEM at 37°C , $\epsilon=1-5\%$, $f=0.4\text{Hz}$): membrane apparent elastic modulus do not change significantly after seven day of incubation (a) and after 24h of continuous cyclic stress (b) (ANOVA test, $p<0.05$)

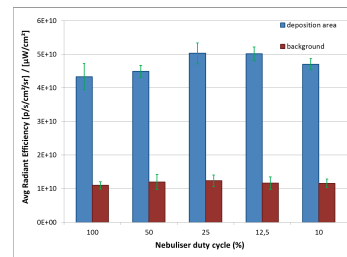
The MALI bioreactor was tested in terms of water tightness and membrane stretching reliability and repeatability. The Bioreactor is air and watertight for over 24 hours. Maximum strain levels in the membrane were similar to physiological values (5% strain at 0.4 Hz^{8,9}).

Our results show that the bioreactor can maintain physiologically relevant flows and pressure driven cyclic membrane motion which recapitulates the dynamic alveolar environment.

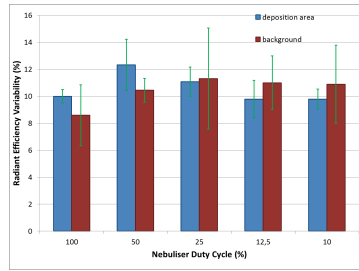
Fluorescent particle nebulisation showed a good repeatability and reliability of the system. Nebulised fluorescein solution results in the deposition of a near-uniform layer of material on the membrane, with small losses (efficiency close to 90% of the initial solution). Moreover Sky-Blue nanoparticles deposition showed that homogeneity does not change significantly with duty cycle, while efficiency increase ($\sim 80\%$ at $\delta=10\%$) (figure 4a and 4b).



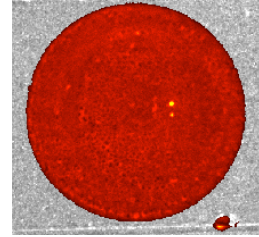
a)



b)



c)



d)

Fig. 4. Aerosol deposition into MALI Bioreactor: aerosol deposition efficiency (a) and homogeneity (b-d) have been evaluated with Fluorescein sodium salt and SkyBlue nanoparticles respectively for different nebuliser duty cycles (δ , fractional on-time). Deposition homogeneity (~10%) does not change significantly with duty cycle, while efficiency increases with decreasing δ (from 60 to ~80% at $\delta=10\%$).

Preliminary viability test showed that the Bionate II 80A membrane can support lung derived epithelial cells: A549 cells seeded and grown on Bionate membrane show adequate adhesion and good viability, making the system suitable for cell testing in dynamic environment (*figure 5*).

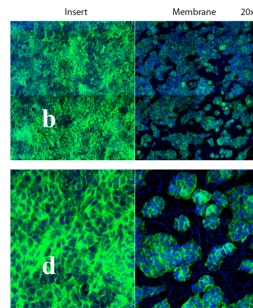


Fig. 5. Confocal microscopy image of A549 cells cultured at the air-liquid interface on (a,c) the membrane of a standard transwell insert and (b,d) a stretchable Bionate II 80A membrane coated with Matrigel (Magnification: a, b 20X; c, d 40X; Blue: Dapi Staining for nuclei, Green: Actin Staining for Cytoskeleton)

5. Conclusion

A prototype of the alveolar interface model has been realised and tested in terms of air and water tightness of the bioreactor. The control system for membrane motion allow us to apply a physiological stress field on cells and preliminary mechanical and adhesion test proved that Bionate II 80A is a suitable material for a cyclic stressing system.

Moreover quantitative nanoparticle deposition tests are being conducted to determine deposition system reliability, repeatability and homogeneity.

Further studies are being conducted on the effects of nanomaterial exposure in the system, focusing on

the impact of biomimetic cyclic motion on nanoparticle endocytosis.

Appendix A: Membrane Coating

The Matrigel coating was prepared using a 8.6 mg/mL protein solution in DMEM medium. The solution was then kept in ice and 1mL Matrigel solution was added for each membrane, once treated with 15% ethanol to render it hydrophilic. After 1 hour at room temperature membranes were put at 37°C for 30 minutes. Finally the supernatant liquid was removed by suction.

References

1. A. Peters, J. Heyder, *American Journal of Respiratory and Critical Care Medicine*, 155:1376, 1997
2. K.A. Min, G.R. Rosania, "The extracellular microenvironment explains variations in passive drug transport across different airway epithelial cell types", *Pharm Res*, 30:2118–2132, 2013
3. B. Schnekel, "Exercise increases the rate of pulmonary absorption of inhaled terbutaline", *Chest*, 101: 742-45, 1992
4. K.J. Cavanaugh, T.S. Cohen, S.S. Margulies, "Stretch increases alveolar epithelial permeability to uncharged micromolecules", *Am J Physiol Cell Physiol*, 290: 1179-1188, 2006
5. U. Savla, C.M. Waters, "Cyclic stretch of airway epithelium inhibits prostanoid synthesis", *The American Physiological Society*, pp L1013-L1019, 1997
6. E.N. Vlahakis, R.D. Hubmayr, "Stretch induces cytokine release by alveolar epithelial cells in vitro", *The American Physiological Society*, 1999
7. KJ Jr Cavanaugh, J Oswari, SS. Margulies, "Role of stretch on tight junction structure in alveolar epithelial cells", *Am J Respir Cell Mol Biol*, 25: 584–591, 2001
8. TS Cohen, KJ Cavanaugh, SS Margulies, "Frequency and peak stretch magnitude affect alveolar epithelial permeability", *Eur Respir J*, 32: 854–861, 2008
9. J.P. Vande Geest, E.S. Di Martino, D.A. Vorp, "An analysis of the complete strain field within Flexercell™ membranes", *Journal of Biomechanics*, 37, 12: 1923-1928, 2004

S2C: Cardiovascular -hearts, signals analysis, reflexes

Chairs: Felix Blyakman, Dieter Liepsch

CARDIAC APEX ROTATION: A VALUABLE INDEX OF GLOBAL MYOCARDIAL PERFORMANCE IN
ACUTE ISCHEMIA

LAURA CERCENELLI

VENTRICULAR CONTRACTILITY AND VENTRICULAR-ARTERIAL MATCHING IN DIASTOLIC
HEART FAILURE

LIANG ZHONG

HEART RATE VARIABILITY ANALYSIS THROUGH WAVELET DECOMPOSITION

STEFANO GIANCATERINO

MERGING INTER-BEAT MODELS WITH INTRA-BEAT HAEMODYNAMICS TO INVESTIGATE
STABILITY AND RESPONSIVENESS OF THE CARDIOVASCULAR SYSTEM

ANDREA DUGGENTO

ANALYSIS OF CHRONIC OBSTRUCTIVE PULMONARY DISEASE USING SPIROMETRIC
INVESTIGATIONS AND QUANTUM PARTICLE SWARM OPTIMIZATION

MYTHILI ASAITHAMBI

USEFULNESS OF $^{99\text{M}}$ TC-3,3-DIPHOSPHONO-1,2-PROPANODICARBOXYLIC ACID ($^{99\text{M}}$ TC-DPD)
IN AMYLOIDOTIC CARDIOMYOPATHY

SIMONE LONGHI

SLANTLET TRANSFORM BASED STEGANOGRAPHY IN ECG SIGNAL USING LEAST
SIGNIFICANT BIT WATERMARKING ALGORITHM

EDWARD JERO

SPECKLE TRACKING IN 3D ULTRASOUND IMAGES FOR STRAIN ANALYSIS OF CARDIAC
TISSUES

IMAGING AND QUANTIFICATION OF RIGHT VENTRICULAR REMODELING IN REPAIRED LIANG

SIMONE MASETTI

TETRALOGY OF FALLOT FOR CLINICAL DECISION MAKING

LIANG ZHONG

CARDIAC APEX ROTATION: A VALUABLE INDEX OF GLOBAL MYOCARDIAL PERFORMANCE IN ACUTE ISCHEMIA

LAURA CERCENELLI

*Experimental Diagnostic and Specialty Medicine Dept., University of Bologna,
via Massarenti 9, 40138 Bologna, Italy*
laura.cercenelli@unibo.it
www.dimes.unibo.it/it

EMANUELA MARCELLI

*Experimental Diagnostic and Specialty Medicine Dept., University of Bologna,
via Massarenti 9, 40138 Bologna, Italy*
emanuela.marcelli@unibo.it

Cardiac Apex Rotation (CAR) is a key component of cardiac mechanics. We evaluated the potential of CAR index to detect changes of global myocardial performance during experimentally induced acute ischemia on animals. In 2 sheep, CAR was assessed using a miniature gyroscopic sensor positioned on the epicardial site at LV apex. Acute ischemia was induced by ligation of coronary artery. CAR signal was continuously recorded along with the LV pressure (LVP). A myocardial performance index obtained from LVP measurements (MPI_{LVP}) was calculated and it was correlated with the CAR parameter. A strong negative correlation was observed between CAR and MPI_{LVP} during consecutive ligations-releases of the coronary artery. CAR reduced even before changes in $LVdP/dt_{max}$, thus showing good potential to predict acute hemodynamic changes.

Keywords: cardiac rotation; coronary ligation; myocardial performance index; acute ischemia, heart failure.

1. Introduction

Cardiac apex rotation (CAR) is the major determinant of left ventricular (LV) systolic twist and the apical back-rotation also plays the dominant role in the subsequent diastole¹. Despite many investigators have focused on cardiac rotation as a sensitive marker of LV function¹, no studies have been specifically aimed to evaluate the correlation of CAR with the Myocardial Performance Index (MPI), a parameter that combines systolic and diastolic measurements. The value of MPI, which is obtained from echo Doppler measurements of cardiac time intervals², has been shown in various heart disorders, including heart failure^{3,4}. A strong correlation has been demonstrated between the cardiac time intervals used for calculating the MPI and the hemodynamic invasive measurements of LV pressure first derivative ($LVdP/dt$)⁵.

The aim of this study was to evaluate the potential of CAR index to reflect changes of global myocardial performance by correlating it with a myocardial performance index calculated from LV pressure assessments (MPI_{LVP}), during acute ischemia experimentally induced on animals.

2. Material and Methods

2.1 Experimental protocol

Two adult sheep were used for the study. All surgical procedures were performed following a standardized and approved protocol. The animal was placed in a right lateral decubitus position and

surgically treated to have full access to the heart. To assess CAR, a miniaturized gyroscopic sensor (XV-3500CB, Epson Toyocom, Tokyo, Japan), inserted in a rigid hermetic capsule, was glued on the epicardial site at LV apex. The angle of rotation (Angle), obtained by integrating the angular velocity (AngV) measured by the gyroscopic sensor, was continuously recorded. Simultaneously, the ECG was recorded and the LV pressure (LVP) was assessed by a pigtail catheter incorporating a pressure transducer (CD-Leycom, Zoetermeer, The Netherlands) inserted in the left ventricle. LVP was used to obtain LVdP/dt signal and to calculate LV peak positive dP/dt (LVdP/dt_{max}) and LV peak negative dP/dt (LVdP/dt_{min}). All signals were acquired at baseline, during acute ischemia induced by ligation of left anterior descending coronary artery, and after release of ligation (Fig.1).

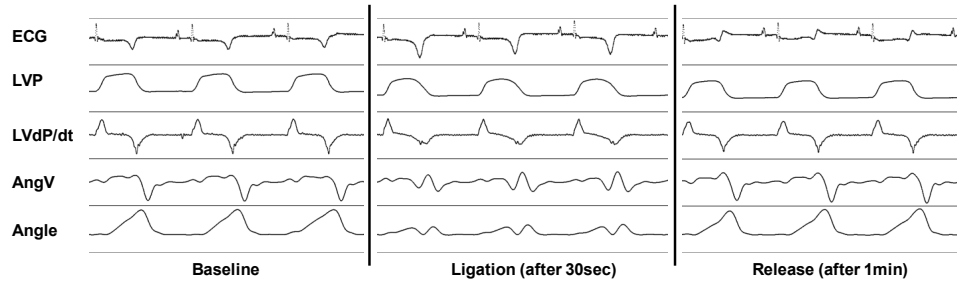


Fig. 1. Example of the acquired signals.

2.2 Calculation of MPI_{LVP}

The Doppler-derived MPI is defined as the sum of the Isovolumic Contraction Time (ICT) and the Isovolumic Relaxation Time (IRT), divided by Ejection Time (ET)¹. Following the previously demonstrated⁵ inverse correlation between the echo-derived ICT, IRT intervals and LVdP/dt_{max}, LVdP/dt_{min}, respectively (Fig.2), the cardiac time intervals (ICT_{LVP}, IRT_{LVP}, ET_{LVP}) were estimated from LVP measurements as reported in (1)-(3):

(1)

(2)

(3)

$$ICT_{LVP} = \frac{1}{\frac{LVdP/dt_{max}}{LVP(T_{max})}} [\text{sec}] \quad IRT_{LVP} = \frac{1}{\frac{LVdP/dt_{min}}{LVP(T_{min})}} [\text{sec}] \quad ET_{LVP} = T_{min} - T_{max} [\text{sec}]$$

and the MPI_{LVP} was calculated as follows:

$$(4) \quad MPI_{LVP} = \frac{ICT_{LVP} + IRT_{LVP}}{ET_{LVP}}$$

2.3 Data Analysis

Linear correlation ($p < 0.001$) between the peak-to-peak value of the Angle during the cardiac cycle (CAR) and the calculated MPI_{LVP} was evaluated at baseline and during sequences of ligation-release of the coronary artery. Changes in CAR was also compared with $LVdP/dt_{max}$ and $LVdP/dt_{min}$.

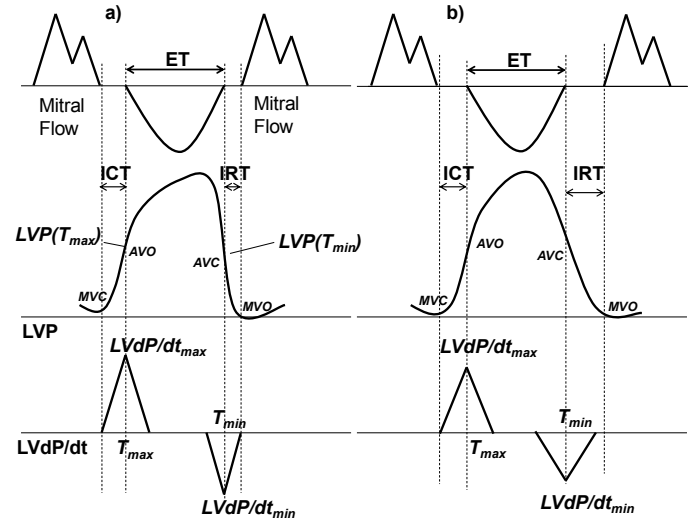


Fig.2. Schematic example of the inverse relationship between echo cardiac time intervals (ICT, IRT) and $LVdP/dt$ measurements used to calculate the MPI_{LVP} : a prolonged IRT corresponds to a reduced $LVdP/dt_{min}$ (b) if compared with a shorter IRT (a). MVC: mitral valve closing; AVO: aortic valve opening; AVC: aortic valve closing; MVO: mitral valve opening; T_{max} : time at $LVdP/dt_{max}$; T_{min} : time at $LVdP/dt_{min}$.

3. Results and Discussion

CAR significantly reduced after coronary ligation and it recovered after release of ligation, while MPI_{LVP} showed an inverse trend. A strong negative correlation ($r = -0.79$ (Sheep 1); $r = -0.81$ (Sheep 2), $p < 0.001$) was found between CAR and MPI_{LVP} (Fig.3). Increase of MPI_{LVP} during coronary ligation was in accordance with the previously reported prolonged ICT and shortened ET in acute myocardial infarction⁶, which tend to increase the formula $(ICT + IRT)/ET$. Acute ischemia reduced CAR even before changes in $LVdP/dt_{max}$. Indeed, 30sec after ligation, a marked decrease of CAR was observed, while $LVdP/dt_{max}$ showed minor changes (Fig. 4). $LVdP/dt_{min}$ exhibited a more similar trend to CAR (Fig.5).

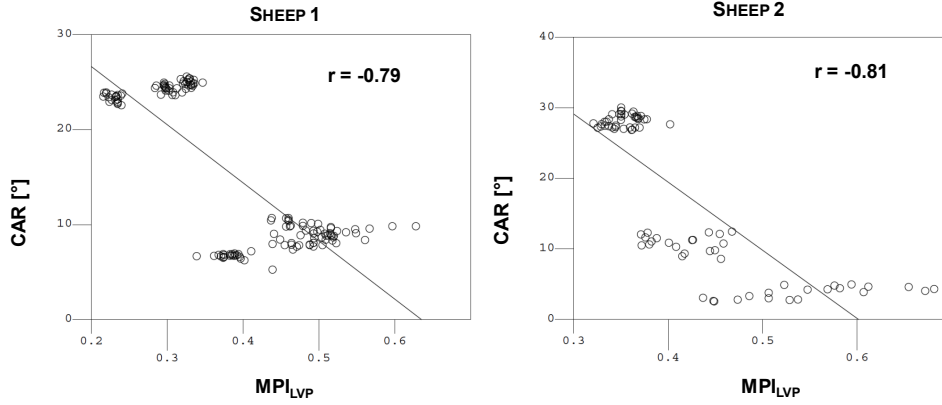


Fig. 3. Correlation between CAR and MPI_{LVP}.

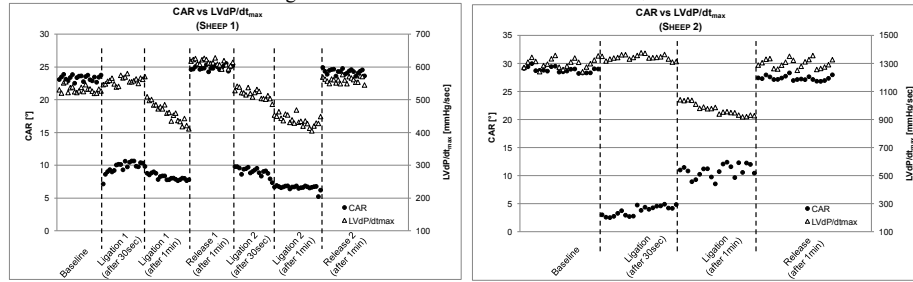


Fig. 4. CAR against LVdP/dt_{max} during consecutive ligation-release of the coronary artery.

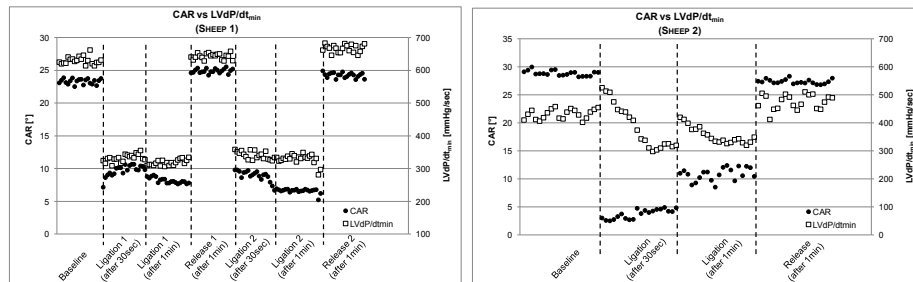


Fig. 5. CAR against LVdP/dt_{min} during consecutive ligation-release of the coronary artery.

4. Conclusions

Acute ischemia had a pronounced effect on CAR. The demonstrated strong correlation between CAR and MPI_{LVP}, which accounts for both systolic and diastolic myocardial performance, suggests that cardiac apex rotation may be a useful marker of global cardiac function in acute myocardial infarction. These preliminary data should be confirmed in other experimental settings including left bundle branch block, chronic myocardial infarction and chronic heart failure. Moreover, CAR index seems to early detect the

hemodynamic changes caused by an acute impairment of cardiac function. This potential may be extremely interesting to predict cardiac function deterioration in heart failure patients.

References

1. Rüssel, I.K. et al. Left ventricular torsion: an expanding role in the analysis of myocardial dysfunction. *JACC Cardiovasc Imaging*. 2009;2(5):648-55.
2. Tei, C. New non-invasive index for combined systolic and diastolic ventricular function *J. Cardiol* 1995; 26: 135-136.
3. Lakoumentas, J.A., et al. The Tei index of myocardial performance: Application in Cardiology. *Hellenic J Cardiol* 2005; 46: 52-58.
4. Meric, M. et al. Tissue doppler myocardial performance index in patients with heart failure and its relationship with haemodynamic parameters. *Int J Cardiovasc Imaging*. 2014.
5. Tei, C., et al. Noninvasive Doppler-derived myocardial performance index: correlation with simultaneous measurements of cardiac catheterization measurements. *J Am Soc Echocardiogr* 1997;10:169e78.
6. Poulsen, S.H., et al. Value of the Doppler index of myocardial performance in the early phase of acute myocardial infarction. *J Am Soc Echocardiogr* 2000;13:723-30.

VENTRICULAR CONTRACTILITY AND VENTRICULAR-ARTERIAL MATCHING IN DIASTOLIC HEART FAILURE

LIANG ZHONG, FEI-QIONG HUANG, THU-THAO LE, DAVID SIM, RU-SAN TAN

*Bioengineering, National Heart Research Institute of Singapore, Singapore
zhong.liang@nhcs.com.sg*

Heart failure (HF) is a major health care burden on society and suffering for the individual. In the United States, HF affects 5 million patients, and it is the leading cause of hospitalization for people 65 years and rates of hospital readmission within 6 months range from 25% to 50%. In Singapore, between 1991 and 1998, it accounted for 4.5% of all hospital admissions and 2.5% of overall mortality in the geriatric age group. It confers an annual mortality of 10%. HF can occur with either normal or reduced left ventricular (LV) ejection fraction (EF), depending on different degrees of ventricular remodeling. Both heart failure with normal ejection fraction (HFNEF) and heart failure with reduced ejection fraction (HFREF), also commonly known as diastolic and systolic heart failure respectively, have equally poor prognosis.

We have developed a novel LV contractility index, $d\sigma^*/dt_{max}$, and ventricular-arterial coupling and developed the methodology for its derivation from echocardiographic data. 115 heart failure (HF) patients based on clinical diagnosis and 43 age and sex-match normal controls were prospectively recruited. We found that 24% of HF patients had normal left ventricular ejection fraction (EF) (e.g., $EF \geq 50\%$). $d\sigma^*/dt_{max}$ was $5.28 \pm 1.79 \text{ s}^{-1}$ in control subjects; reduced in HFNEF, $2.81 \pm 0.95 \text{ s}^{-1}$, and HF with reduced EF (HFREF), $1.55 \pm 0.59 \text{ s}^{-1}$ (ANOVA $P < 0.001$). In comparison with normal subjects, $d\sigma^*/dt_{max}$ was found to be the significant indicator to differentiate HFNEF and HFREF. The area under the curve of the receiver operating characteristics (ROC) in detecting HFNEF compared with normal controls ($d\sigma^*/dt_{max} < 3.69 \text{ s}^{-1}$) was 0.932 ($P < 0.0001$) (sensitivity=0.88 and specificity=0.88), and in detecting HFREF compared with HFNEF ($d\sigma^*/dt_{max} < 1.87 \text{ s}^{-1}$) was 0.87 ($P < 0.0001$) (sensitivity=0.81 and specificity=0.75). Hence we see a great potential for application of this novel index to evaluate heart function in HFNEF and HFREF.

HEART RATE VARIABILITY ANALYSIS THROUGH WAVELET DECOMPOSITION

STEFANO GIANCATERINO

Student enrolled in specialty school of Medical Physics, University of L'Aquila, L'Aquila, Italy

IVAN CORAZZA and ROMANO ZANNOLI

Experimental, Diagnostic and Specialty Medicine Department, University of Bologna, Bologna, Italy

The autonomic nervous system (ANS) is responsible for controlling the cardiovascular parameters (heart rate and blood pressure) at rest and in response to external stimuli. It is composed of two subsystems: the sympathetic and parasympathetic (or vagal) ones, acting simultaneously but at different rates, the first for increasing and the second one for decreasing the heart rate (HR). To evaluate the activities of the two subsystems spectral analysis of HR variability is traditionally used. Standard methods (Fourier and autoregressive analysis) require stationary signals and do not allow to analyze short and transitory periods. But applying the wavelet analysis, it is possible to make a multi-resolution evaluation (in time and frequency) of the activation of the two subsystems and quantify their variations.

Since a validated methodology for spectral analysis of transient periods does not exist, we tested the wavelet approach by analysing the Valsalva manoeuvre in healthy and pathologic patients. The physiology of this cardiovascular test is well known and it represents the good target to evaluate the wavelet approach and its feasibility in quantifying sympathetic and vagal activations.

The obtained results demonstrate the goodness of wavelet approach: in healthy subjects the different activations were quantified properly with the right sequence. In pathological patients, our analysis demonstrated the absence of some activations and the results are statistically different from the normal ones.

Keywords: wavelet analysis, Valsalva maneuver, autonomic nervous system evaluation

Introduction

The autonomic nervous system (ANS) consists of cells and fibres innervating the internal organs, regulating the functions not controlled by the voluntary nervous system. ANS consists of two subsystems, the sympathetic (SS) and parasympathetic (or vagal - VS) ones, acting simultaneously with different periodicities (Sympathetic: 0.04-0.4 Hz; Vagal: 0.4-1.4 Hz) [1]. The ANS function can be evaluated in different ways: the easiest one is to study the effects of ANS on heart rate variability: the sympathetic activation increases heart rate while vagal stimulation lowers the rate. (Figure1)

By studying the heart rate variability (HRV) during well known physiological stimuli (i.e. tilt test, Valsalva maneuver, deep breathing, etc), it is possible to quantify the two subsystems activation and to compare the results with normal values [2] [3].

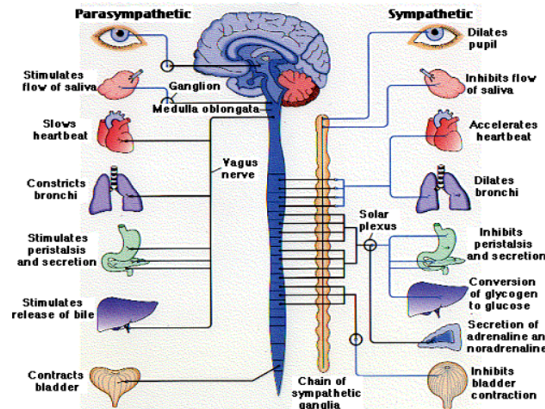


Figure 1. Innervation by the autonomic nervous system of different organs.

HRV is commonly performed through Fourier Analysis (FA) or Autoregressive modeling (AR) and produces quantitative estimates of VS and SS activity. However, signal nonstationarity poses significant applicability limits in a number of preclinical and clinical settings.

Time-variant spectral estimation can be performed through Wavelet analysis (WA), hence lifting the stationarity requirement and producing time-dependent band-power estimation. However, the deployment of this novel approach requires rigorous validation.

In a previous work, we validated the new approach by comparing the results of WA and traditional FA analysis on stationary tachographic signals acquired during tilt tests on normal subjects [4]. By using the same mathematical set up, in this work we tested the wavelet approach to non stationary signals of short duration.

Methods

A multiresolution analysis was then performed (Daubechies-16 form), closely matching the FWHM boundaries of dilated wavelet spectra to the HF and LF band transition frequencies. Squared level specific amplitude coefficients were summed across appropriate decomposition levels and relevant time intervals, computing total band powers (LF: 0.04 - 0.08 Hz, HF: 0.17 - 0.34 Hz).

Since it is not possible to compare WA to already validated techniques, HRV was performed on 18 normal subjects (12 males, 6 females, age 16 ÷ 74 year) who underwent to standard Valsalva maneuver (VM): during this procedure, the subjects have to blow into a mouthpiece attached to a mercury manometer, in order to maintain a pressure of 40 mmHg for 15 s. VM has a well-known physiology and provide the serial activation of both sympathetic and vagal systems [5] (figure 2):

- In phase I, there is a transient rise in blood pressure and a fall in heart-rate due to compression of the aorta. The hemodynamic changes during this phase are secondary to mechanical factors and are not accompanied by an increase sympathetic activity.

- Phase II consists of an initial fall in blood pressure (2a) with a subsequent late recovery of blood pressure (2b). These changes are accompanied by an increase in heart rate. The fall in cardiac output due to impaired venous return to the heart results in compensatory cardioacceleration and an increase in muscle sympathetic activity and peripheral resistance.
- In phase III, there is a fall in blood pressure and increase in heart rate that occurs with cessation of expiration due to release of expiratory pressure.
- Phase IV of the maneuver is characterized by an early increase in blood pressure above the baseline value (the overshoot) due to the residual vasoconstriction and normal venous return. Vagal activities increases with a persistent sympathetic activation.

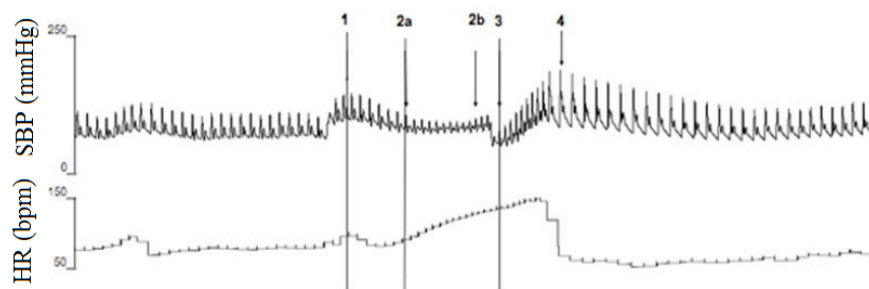


Figure 2. Normal response during the Valsalva manoeuvre.

Knowing the correct order of activation of SS and VS, it is easy to verify whether the results of the wavelet analysis are correct or not.

Moreover, 3 pathologic patients, with dysautonomia, (males, age $58 \div 65$ year) were then analysed to evaluate the differences with the normal subjects .

For each subject (normal and pathologic ones), ECG was recorded with Light System (Sparkbio SRL, Bologna, Italy) with a resolution of 12 bit and a sampling rate of 1000Hz. Then, R waves were extracted and HRV was performed on tachograms resampled at 10 Hz through cubic spline interpolation [4].

To better highlight the changes in LF and HF amplitudes during the manoeuvre, the basal values (measured 30s before the manoeuvre beginning, during a stationery period) were subtracted.

A skilled neurologist evaluated the results in order to verify the feasibility of wavelet approach.

Results

Figures 3 show the LF and HF amplitude with respect to the basal condition in 4 normal subjects. The sequence of vagal and sympathetic activations is correct and the clinical evaluation of the specialists does not highlight any abnormalities.

Figures 4 show the result of the pathological subjects. ANS response is different from subject to subject and with respect the normal ones. The incorrect sequence of sympathetic and parasympathetic activations are the consequence of the pathologies.

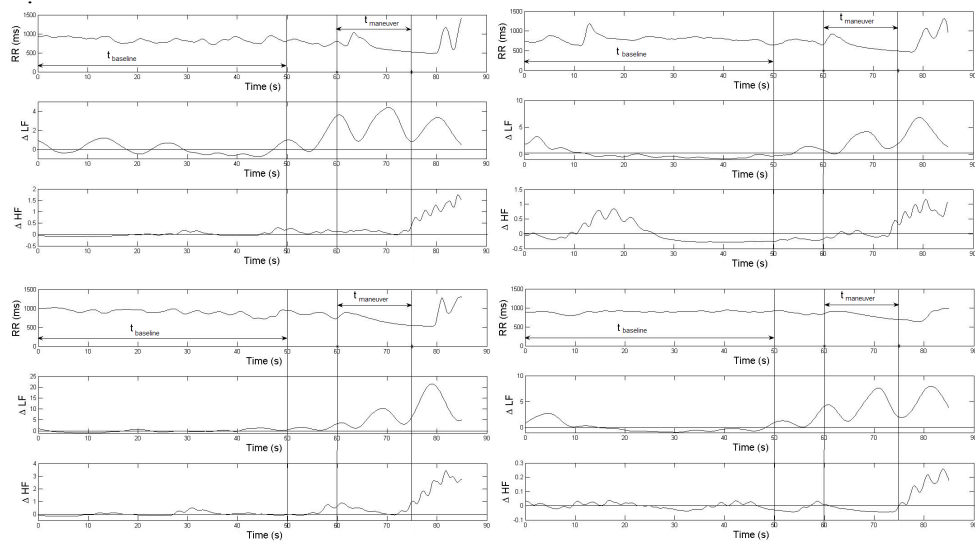


Figure 3. Example of spectrum in the time of the bands on LF, HF and their relationship during the Valsalva maneuver in four different normal subject. Between time zero and first marker have the period in which baseline is calculated (t_b), between the last two markers maneuver occurs.

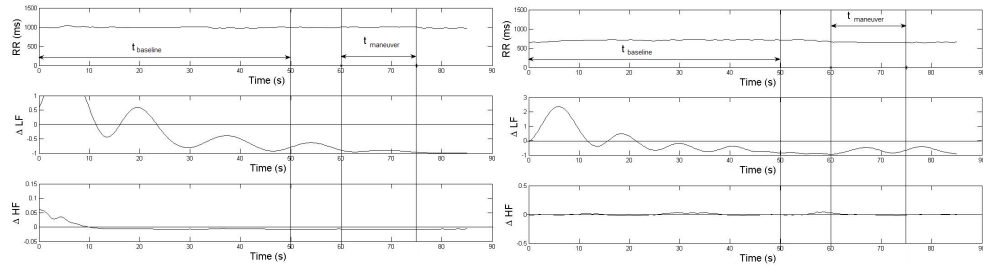


Figure 4. Example of spectrum in the time of the bands on LF, HF and their relationship during the Valsalva maneuver in three different pathological subject.

Discussion

Wavelet analysis demonstrated, in both healthy and disautonomic subjects, good results in terms of repeatability and feasibility. Wavelet approach is able to quantify the sympatho-vagal activations, highlighting possible abnormalities. The method could be improved by studying different families of wavelets and optimizing the analysis but the way is correct and should be followed. The next step is represented by the in-depth analysis of the different pathologies to discriminate between different kinds of dysautonomia.

References

- [1] "Heart Rate Variability - Standards of Measurement, Physiological Interpretation, and Clinical Use", *Task Force of the European Society of Cardiology the North American Society of Pacing Electrophysiology*. Circulation. 1996;93:1043-1065;
- [2] Guaraldi P., Cortelli P., "Il sistema vegetativo: valutazione clinica e strumentale", Clinica Neurologica, Dipartimento di Scienze Neurologiche, Università di Bologna;
- [3] M. Malik, A. J. Camm, "Heart Rate Variability", Futura Publishing Company, Inc., 1995;
- [4] Toschi N, Corazza I, Barletta G, Cecere A, Calandra-Buonaura G, Guerrisi M, Cortelli P. Heart Rate Variability analysis through wavelet decomposition: validation and new perspectives. European Federation of Autonomic Societies (EFAS) Congress, 12-15 Maggio 2010, Giardini Naxos, Italy.
- [5] Freeman R. Assessment of cardiovascular autonomic function. Clinical Neurophysiology **117** (2006) 716-730.
- [6] Xavier R., et al, "The Valsalva maneuver revisited by Wavelets", Rev Port Cardiol 2008; **27**(4): 435-441.
- [7] Press W. H. et al, "Numerical Recipes", Cambridge, 2007;
- [8] Kimm K.K., et al, " The effect of missing RR-interval data on HRV analysis in the frequency domain", Physiol Meas 2009; **30**:1039-50;

MERGING INTER-BEAT MODELS WITH INTRA-BEAT HAEMODYNAMICS TO INVESTIGATE STABILITY AND RESPONSIVENESS OF THE CARDIOVASCULAR SYSTEM

ANDREA DUGGENTO, NICOLA TOSCHI, ANTONIO CANICHELLA ITALO VANNUCCI, MARIA GUERRISI

Medical Physics Section, Faculty of Medicine

University of Rome "Tor Vergata", via Montpellier 1, 00133 Roma, Italy

duggento@med.uniroma2.it

We investigate the Seidel-Herzel model of the human baroreflex feedback control mechanism in terms of parameter choices and its use to mimic heart rate physiology. We demonstrate the potential of a re-parameterization of the model in order to reproduce features commonly observed human physiology in health and in disease, make critical considerations about potential pitfalls in parameter choices.

Keywords: Haemodynamics control; Baroreflex; Bifurcations in dynamical system.

1. Introduction

The Seidel-Herzel model [1,2,3] has been proposed to describe the basic physiological mechanisms that regulate the heart pace-maker response to aortic pressure. Currently, while the pneumo-mechanics of the heart is fairly well understood, models that describe the feed-back control are largely based arbitrary assumptions and hypotheses. The Seidel-Herzel model tries to merge these two aspects: the pneumo-mechanics, and the feedback control. The pneumo-mechanics is the part of the model that produces the flow and pressure of the blood in a particular segment of the cardiovascular system as a time-dependent observable. The feedback control describes the information that the central nervous system receives through the afferent pathways and the signals that are sent back through the efferent nerves as well as the 'grey-box' which represents information processing in the brain.

The Seidel-Herzel model, while describing mechanisms that are not fully explained, has many desirable features: i) the state variables of this model have a direct physiological interpretation; ii) the model is surprisingly parsimonious in the number of parameters. Despite this relative tightness, there is so much room for an *ad-hoc* re-parameterization that any previous attempt to determine a set of parameters which reproduces selected features of human physiology can be questionable. In this contribution we review of the context and limitations of this otherwise excellent model and discuss the features it lacks when aiming for a meaningful description of all the salient properties of human heart rate and its control.

2. The Model

The baroreceptor afferent tone has a linear response to both the aortic pressure and its derivative:

$$\nu_b(t) = k_1(p(t) - p_0) + k_2 \frac{dp}{dt} \quad (1)$$

The baroreceptor tone is then reprocessed by the medullary regions of the brain and the parasympathetic control. This is the most crucial part of the model because it is the part where most of physiological knowledge is almost entirely based on intuitions. Accordingly to Seidel and Herzel, the linear approximation is the safest guess, with a zero-threshold to take into account the non-negativity of the firing rates:

$$\begin{aligned} \nu_s(t) &= \max(0, \nu_s^{(0)} - k_s^b + \nu_b + k_s^r |\sin(\phi_{\text{resp}}(t) + \Delta_s)|) \\ \nu_p(t) &= \max(0, \nu_p^{(0)} + k_p^b + \nu_b + k_p^r |\sin(\phi_{\text{resp}}(t) + \Delta_p)|) \end{aligned} \quad (2)$$

where the sinus term in eq.(2), which contains the respiratory phase ϕ_{resp} , is a term that explicitly

models the Respiratory Sinus Arrhythmia (RSA). The sympathetic tone controls the release of noradrenaline, whose dynamics is described as

$$\frac{dc_{\text{cNa}}}{dt} = -\frac{c_{\text{cNa}}}{\tau_{\text{ccNa}}} + k_{\text{cNa}} v_s(t - \theta_{\text{cNa}}) \quad (3)$$

where τ_{cNa} is the decay constant of noradrenaline at the myocardium and θ_{cNa} is a delay term. The heart is seen as a integrate and fire system. The ventricular contraction begins when the cardiac phase ϕ reaches the threshold one, then the systolic phase of the heart is initiated and the phase reset to zero.

$$\frac{d\phi}{dt} = \frac{1}{T^{(0)}} f_s f_p \quad (4)$$

The cardiac phase is driven by sympathetic and parasympathetic contributions, respectively f_s and f_p

$$\begin{aligned} f_s &= 1 + k_{\phi}^{\text{cNa}} \left[c_{\text{Na}} + (\hat{c}_{\text{Na}} - c_{\text{Na}}) \frac{(c_{\text{Na}})^{n_{\text{cNa}}}}{(\hat{c}_{\text{Na}})^{n_{\text{cNa}}} + (c_{\text{Na}})^{n_{\text{cNa}}}} \right] \\ f_p &= 1 - k_{\phi}^p \left[v_p(t - \theta_p) + (\hat{v}_p - v_p(t - \theta_p)) \frac{(v_p(t - \theta_p))^p}{(\hat{v}_p)^p + (v_p(t - \theta_p))^p} \right] F(\phi) \\ F(\phi) &= \phi^{1.3} (\phi - 0.45) \frac{(1 - \phi)^3}{(1 - 0.8)^3 + (1 - \phi)^3} \end{aligned} \quad (5)$$

where $F(\phi)$ is a mathematical model that take into account the effectiveness of the sympathetic contribution as a function of the heart phase.

To obtain a synthetic pressure signal a pneumo-mechanics model is adopted. In [1] the Windkessel model is was chosen for simplicity. In [4] a 21-compartment model [5] based largely on the circuit analogous representation of a vascular segments was used. In [4] the 21-compartment model was used to model physiological state relevant in critical care patient management.

3. RR return maps, bifurcations and role of time constants

While the Seidel-Herzel model is parsimonious in the number of parameters, the behaviour of the generated RR sequences varies considerably with respect to almost any of the parameter of the model. RR sequences can exhibit chaotic behaviour (see [2]). On Fig. 1 the RR return map are presented for various parameter choices. We conduct extensive research to determine which parameters of the model might determine chaotic RR behaviour. We demonstrate that varying almost any parameter around its physiologically plausible values might trigger bifurcation phenomena and chaotic dynamic onset. On Fig. 2 some route-to-chaos pattern are shown with respect to parasympathetic gain k_p^p and Windkessel relaxation parameter τ_v . It is then possible to imagine that the classical bifurcation figure is formed in as many direction as the number of chaos-inducing parameters, to form a sort of multidimensional “sponge”.

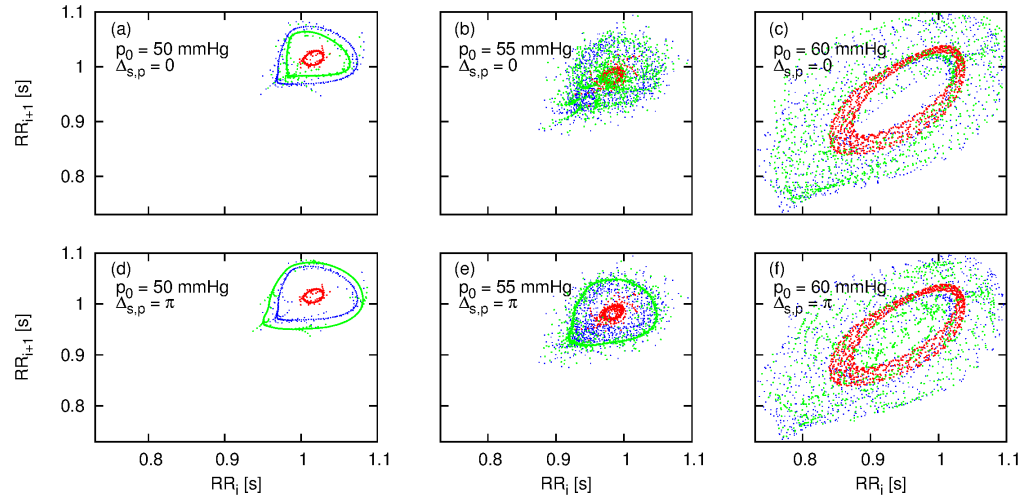
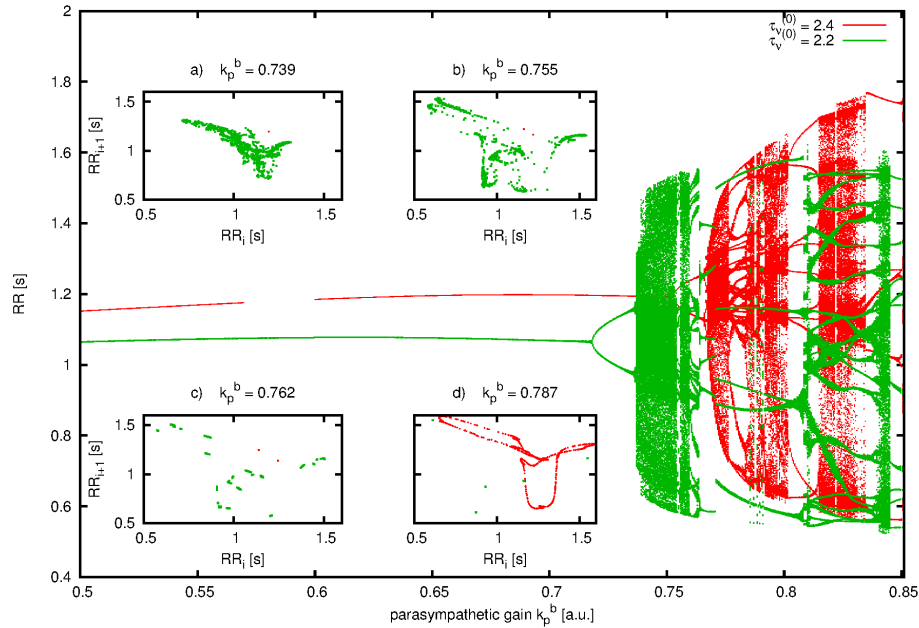


Fig. 1: (Color on line) RR return map plot of the Seidel-Herzel model with the Windkessel pressure model. The values for parameters are the same as in [3]. Parameter p_0 (baroreceptor set-point) varies: a,d) $p_0=50$ mmHg; b,e) $p_0=55$ mmHg; c,f) $p_0=60$ mmHg. The phase between the mechanical coupling and the medullary modulation shown is at the extrema of the phase difference (results also resemble extrema in the behaviours): (a,b,c) $\Delta_{s,p}=0$; (d,e,f) $\Delta_{s,p}=\pi$.

Fig. 2: (Color on line) In green, in the main pictures and in the insets a),b),c) and d), RR intervals resulting from the integration



of the Seidel-Herzel model and with parameters set as in [3]. Parameters k_s^r and k_p^r are set to zero to "disengage" RSA phenomena.

4. Parameter sensitivity and modelling for physiological states

With an adequate re-parameterization of the Seidel-Herzel model with the detailed 21-compartment model for the vascular bed the hybrid model models might be useful a patient-care setting as a tool that provides a major access pathway to information which may be readily re-cast into clinically useful form. However it is challenging to choose the model parameter that should be allowed to vary to accurately describe a several clinically relevant physiological states. To this porpuse we performed a parameter sensitivity test to select the most informative parameters for each simulated clinical condition. Observable outputs are expected to vary with respect to every model parameter. This property is called sensitivity of the model. If there are parameters whose change produces negligible change in the observable, the model is over-parameterized. Observable outputs could be the RR distribution, systolic and diastolic pressures, and statistical index that can be derived by those. A local sensitivity analysis allows us to quantify this reasoning numerically. Given a certain state $\Psi^{(0)}$ in the parameters space, and denoting $H^{(0)}$ the corresponding vector containing average values of the measurable outputs at equilibrium, we can compute the "normalized" Jacobian J as

$$J_{ij}^{(0)} = \frac{\psi_j^{(0)}}{H_i^{(0)}} \frac{dH_i^{(0)}}{d\psi_j^{(0)}} \quad (6)$$

where i and j sequentially label respectively all the input parameters' values and all the measurable outputs.

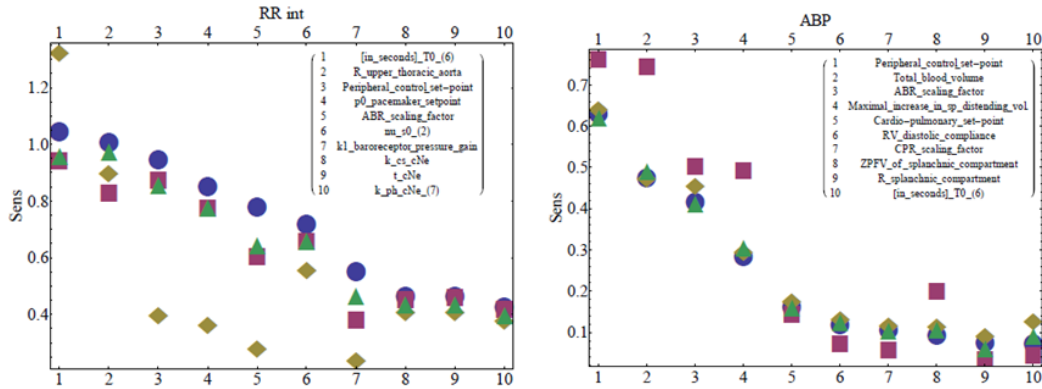


Fig. 3: (Color online) Sensitivity of (a) the mean heart period and (b) the mean systolic values in respect of all the model parameters. Blue dots, red squares, yellow diamonds and green triangles show sensitivity for different physiological states, respectively: baseline, fluid deprived subject, reduced baroreceptor gain and increased left-ventricular compliance.

6. Conclusions

Combining an accurate structural model for baroreflex response with a lumped-parameter model of varying complexity to represent the cardiovascular system allows to explore the stability/instability transitions on a physiological meaningful manner. Additionally, sensitivity analysis provides a global picture of which paramters may represent actionable points for efficient modification of global haemodynamics.

References

1. H. Seidel and H. Herzel. *Physica D*, 115:145–160, 1998.
2. A. Dudkowska and M. Danuta. *Journal of mathematical biology* 57.1:111-137, 2008.
3. A. Duggento, et Al. *Fluctuation and Noise Letters* 11.01, 2012.
4. N. Toschi, et al. *Engineering in Medicine and Biology Society, EMBC, IEEE*, 2011.
5. T. Heldt, et Al. *The Open Pacing, Electrophysiology & Therapy Journal*, 3:45-54, 2010.

ANALYSIS OF CHRONIC OBSTRUCTIVE PULMONARY DISEASE USING SPIROMETRIC INVESTIGATIONS AND QUANTUM PARTICLE SWARM OPTIMIZATION

MYTHILI ASAITHAMBI*,†, SRINIVASAN SUBRAMANIAN* SUJATHA C MANOHARAN† SWAMINATHAN RAMAKRISHNAN††

**Dept. of Instrumentation Engg, Madras Institute of Technology Campus, Anna University, Chennai,, India*

†Dept. of Electronics and Communication Engg, CEG Campus, Anna University, Chennai – 600 025, India

††Non- Invasive Imaging and Diagnostics Laboratory, Biomedical Engineering Group, Dept. of Applied Mechanics, Indian Institute of Technology Madras, Chennai, India

‡mythiliasaithambi@gmail.com

Chronic Obstructive Pulmonary Disease (COPD) is the leading cause of morbidity and mortality worldwide and represents an important public health challenge. Spirometric pulmonary function test is the most common method used to assess COPD. However, spirometric investigation often prone to false positive rate due to large interdependency of dataset. Also, there is a requirement that too many parameters are to be analyzed by the physician. In this study, an attempt is made to identify most significant features using Quantum Particle Swarm Optimization (QPSO) to enhance the diagnostic relevance of spirometry. Then these selected feature set is evaluated based on the error in prediction of FEV₁ and PEF using back propagation neural network model. Results show that QPSO is able to identify most significant features in both normal and obstructive subjects. This feature selection is useful in mass screening of pulmonary function test in the case of missing data due to incomplete test.

Keywords: Pulmonary function test; spirometry; quantum particle swarm optimization

1. Introduction

Pulmonary Function test is the most important screening test to assess the dynamics of pulmonary function. Spirometry is the most commonly performed reproducible test and is recommended for diagnosis of respiratory diseases.¹ The major concern of the spirometry is that there is a requirement that a large database is to be analyzed.² Hence, it is very essential to identify the most representative features of pulmonary function crucial for disease diagnosis. The feature selection process in medical data processing removes irrelevant, redundant data, and results in acceptable classification and prediction accuracy.³ Feature selection is a process that selects a subset of original features.⁴ Particle Swarm Optimization (PSO) techniques appeared as promising algorithms for handling the optimization based feature selection problems. PSO, inspired by the social behaviour of bird flocking or fish schooling.⁵ However, premature convergence is one of the major shortcomings of PSO. Recently, the concept of quantum behaved particles is introduced in PSO to enhance global search ability of the particle which is known as Quantum behaved Particle Swarm Optimization (QPSO).⁶ In this work, quantum particle swarm optimization based wrapper algorithm has been attempted to identify most significant features of spirometric pulmonary function data. Each feature subset generated using QPSO is evaluated by observing its performance on prediction of FEV₁ and PEF using back propagation based neural network learning model.

2. Methods

The spirometer recordings are carried out on adult volunteers ($N = 300$) according to ATS/ERS guidelines for spirometry.⁷ Feature selection is performed using quantum particle swarm optimization. In the quantum model of a PSO, the particle's position can be generalized to the d dimensional space where each particle position is updated independently. Mean best (mbest), defined as the mean of the best positions of all particles, is calculated using

$$mbest = \frac{1}{M} \sum_{i=1}^M P_i^j = \left(\frac{1}{M} \sum_{i=1}^M P_{i1}^j, \frac{1}{M} \sum_{i=1}^M P_{i2}^j, \dots, \frac{1}{M} \sum_{i=1}^M P_{id}^j \right) \quad (1)$$

where M is the population size; d is dimension of particle; P_i^j is the Personal best (pbest) position of j^{th} component of particle i . The centre of potential of particle i at n^{th} iteration $p_{i,n}^j$ is calculated so that all particles converge to the global best position. The position of particle i is updated at the $(n+1)^{\text{th}}$ iteration using evolution equation:

$$X_{i,n+1}^j = p_{i,n}^j \pm \frac{L_{i,n}^j}{2} \ln \left(\frac{1}{u_{i,n+1}^j} \right), \quad u_{i,n+1}^j \sim u(0,1), \quad (2)$$

where $p_{i,n}^j$ is the j^{th} component of the centre of potential p_i^n of particle i at the n^{th} iteration. $u_{i,n+1}^j$ is a sequence of random numbers uniformly distributed on $(0,1)$. The fitness value of each particle is calculated using two different benchmark functions namely Ackely and Griewank. Each feature subset generated using QPSO is evaluated observing its performance on prediction of FEV₁ and PEF using back propagation based neural network learning model.⁸ A performance evaluation function is introduced to accommodate the constraints namely number of selected features and the prediction error of neural network.⁹ The selected best subset is validated using two different classifier models which include decision stump and ensembler.¹⁰

3. Results and discussion

The optimum combination of feature set for the defined number of selected features is determined using the selection pressure α . The variation of prediction error with different values of selection pressure is shown in Figure 1 and the optimum value of selection pressure value is chosen as 0.4. The variation of mean best fitness value of QPSO algorithm with Ackely and Griewank functions with number of iterations is plotted in Figure 2. It is found that QPSO with Griewank function performs better with least fitness value and converges at 3000 iterations.

The variations of performance evaluation function with number of features for different values of k are plotted in Figure 3. When $k = 0$, the performance evaluation function is equivalent to that of the prediction error. The curve for $k = 1$ corresponds to the original evaluation function without weighing the number of features which demonstrates the tendency of restricting the search space to very small feature sets.

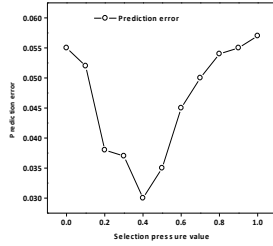


Figure. 1 Variation of prediction error with varying selection pressure (α) value

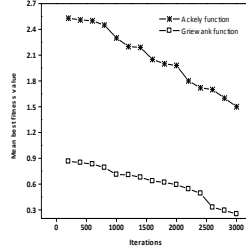


Fig. 2 Variation of mean best fitness value of QPSO with Griewank and Ackley function for varied number of iterations

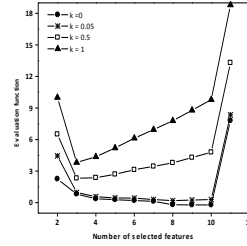


Fig. 3 Variations of performance evaluation function with number of selected features for various k values

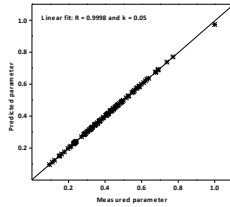


Fig.4 Linear regression analysis between the actual FEV1 and the predicted FEV1 given with the best feature set.

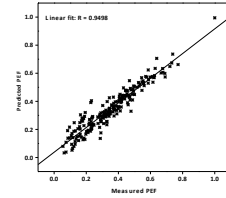


Fig.5 Linear regression analysis between the actual PEF and the predicted PEF with the best feature set.

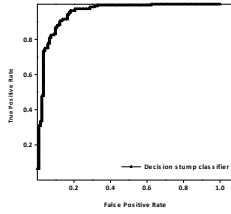


Fig.6 Receiver operating characteristics curve of decision stump classifier with 3 significant features

The feature set which yield least prediction error and highest correlation on regression model is considered to be the optimal one. The accuracy of feature selection is evaluated using prediction of significant parameters FEV_1 and PEF using back propagation neural network model and it is shown in Figures 4 and 5. The predictions of both the parameters seem to be accurate as predicted values follow measured values with minimum variation. Hence, linear and high degree of correlation is observed. The feature selection is further validated using two different classifiers such as ensemble based classifiers and decision stump. It is observed that feature set 3 for decision stump classifier achieves higher classification accuracy, sensitivity and specificity. Receiver operating characteristics curve estimated for decision stump classifier achieves higher area under the curve as shown in Fig. 6.

4. Conclusion

The clinical utility of spirometer depends on the accuracy, performance of the subject, measured and predicted values. It is also reported that a large database is to be analyzed by the physician to investigate the pulmonary function abnormalities. Hence there is a need for identification of significant feature selection of the pulmonary function data to differentiate normal and obstructive subjects. In this work, QPSO is employed for the feature selection procedure, which preserves the data interpretability. Results show that four set of features are obtained using QPSO. Optimal feature set consisting of FEV_1 , FVC and

PEF is selected by tuning the selection pressure value of 0.4. It is also observed that the classifier with optimal feature set achieves higher classification accuracy of 98%. Results demonstrate that this method could be useful to enhance diagnostic relevance of pulmonary function test and mass screening.

References

1. Cope S, Donohue JF, Jansen JP, Kraemer M, Niggli GC, Baldwin M, Buckley F, Ellis A Jones P, Comparative efficacy of long-acting bronchodilators for COPD a network meta analysis. *Respiratory Research*, 14, **100**: pp. 1-18, 2013.
2. Kavitha A and Ramakrishnan S, prediction of forced expiratory volume (fev6) in flow-volume spirometry using support vector machines and radial basis function neural networks, *Journal of Mechanics in Medicine and Biology*, 10, **4**: pp. 683-693, 2010.
3. Chung JT, Li YC, Jun YC, Cheng HY, Feature Selection using PSO - SVM. *International Journal of Computer Science*, 33, **1**: pp. 1-18, 2007.
4. Kohavi R, John GH, Wrappers for feature subset selection. *Artificial Intelligence*, 97, **1-2**: pp. 273-324, 1997.
5. Kennedy J, Eberhart RC, Particle swarm optimization. *Proceedings of the IEEE International Conference on Neural Networks*, 4, pp. 1942-1948, 1995.
6. Jun Sun, Wei F, Vasile P, Xiaojun W, Wenbo Xu, Quantum-behaved particle swarm optimization with Gaussian distributed local attractor point. *Applied Mathematics and Computation*, 218, pp. 3763-3775, 2011.
7. American Thoracic Society, Standards for the diagnosis and care of patients with chronic obstructive pulmonary disease *American Journal of Respiratory Critical Care Medicine*, 152, pp. 77-121, 1995.
8. Mahesh V, Sujatha C. M and Ramakrishnan S, Experimental analysis on human respiratory dynamics using flow-volume spirometry and combined neural networks, *Journal of Mechanics in Medicine and Biology*, vol. 8, no. **4**: pp. 541-548, 2008.
9. Monteiro ST, Kosugi Y, Particle Swarms for Feature Extraction of Hyperspectral Data, *IEICE transaction on Information and systems*, 90, **7**: pp. 1038-1046, 2007.
10. Stephan, C., Marine, D. and Nicolas, V, Ranking Forests, *Journal of Machine Learning Research*, 14, pp. 39-73, 2013.

USEFULNESS OF ^{99m}Tc-3,3-DIPHOSPHONO-1,2-PROPANODICARBOXYLIC ACID (^{99m}Tc-DPD) IN AMYLOIDOTIC CARDIOMYOPATHY

SIMONE LONGHI¹, PIER LUIGI GUIDALOTTI², MASSIMILIANO LORENZINI¹, CHRISTIAN GAGLIARDI¹, AGNESE MILANDRI¹, CANDIDA CRISTINA QUARTA¹, LISA MANUZZI¹, ILARIA GALLELLI¹, MICHELE MARIO CINELLI¹, ELENA BARBARESI¹, MARCO MASETTI¹, CLAUDIO RAPEZZI¹.

¹ Cardiology, Department of Experimental, Diagnostic and Specialty Medicine – DIMES, Alma Mater Studiorum, University of Bologna, Bologna, Italy. ² Nuclear Medicine Unit, Department of Experimental, Diagnostic and Specialty Medicine – DIMES, Alma Mater Studiorum, University of Bologna, Bologna, Italy.

^{99m}Tc-DPD has a strong affinity for transthyretin (TTR)-infiltrated myocardium. In the last 15 years our centre has applied this finding with different aims: 1) Differential diagnosis between TTR-related amyloidosis and light-chain (AL) form 2) Early identification of TTR-related disease and prognostic significance of myocardial DPD uptake 3) Differential diagnosis between TTR-related amyloidosis and other forms of unexplained left ventricular hypertrophy.

1) We evaluated 45 patients with TTR-related amyloidotic cardiomyopathy (AC): 28 hereditary form (ATTR) and 17 senile systemic amyloidosis (SSA). Heart retention (HR) and heart to whole-body retention ratio (H/WB) of late ^{99m}Tc-DPD uptake were higher among TTR-related disease (HR 7.8%; H/WB 10.4) compared with both unaffected controls (HR 3.5%; H/WB 5.7; $p < 0.0001$) and the AL form (HR 4.0%; H/WB 6.1; $p < 0.0001$). 2) Examining 63 patients with ATTR we found that all patients with AC showed moderate-to-severe myocardial tracer uptake. In the subgroup without AC, 4 patients showed myocardial tracer uptake and subsequently underwent endomyocardial biopsy that showed amyloidotic infiltration in all cases. LV wall thickness >12 mm in combination with H/WB >7.5 was associated with a higher event rate. We also reexamined the scintigraphies from 12,400 patients who underwent the exam for oncologic or rheumatological reasons and found that incidental myocardial tracer uptake was present in 45 subjects (0.36%) that all went on to receive a final diagnosis of TTR-related disease. 3) We retrospectively examined the findings from 57 patients (25 SSA, 20 ATTR, 12 hypertrophic cardiomyopathy, HCM) who underwent DPD-scintigraphy for a suspicion of TTR-related AC. Strong myocardial uptake was present in all patients with SSA and ATTR and in none of the HCM patients.

^{99m}Tc-DPD scintigraphy allows an early and accurate diagnosis of TTR-related AC as well as a differential diagnosis with the AL form of the disease and HCM.

Keywords: amyloidosis; DPD; scintigraphy.

SLANTLET TRANSFORM BASED STEGANOGRAPHY IN ECG SIGNAL USING LEAST SIGNIFICANT BIT WATERMARKING ALGORITHM

EDWARD JERO S, PALANIAPPAN RAMU, and RAMAKRISHNAN S

*Indian Institute of Technology Madras,
Chennai-600 036, India.*

E-mail address: edwardjero@gmail.com, palramu@iitm.ac.in, and sramki@iitm.ac.in

The proposed work is Slantlet Transform based ECG signal steganography. Patient's ECG signal is used as cover signal for steganography. The selected cover ECG signal is decomposed using Slantlet Transform and patient personal information are embedded into its coefficients using threshold based Least Significant Bit watermarking algorithm. Threshold values are selected based on the low distortion level of watermarked ECG through experiments. The performance assessment of Slantlet Transform based ECG steganography and diagnosability measurement of watermarked ECG is calculated using validation metrics such as Peak Signal to Noise Ratio, Percentage Residual Difference. In addition we have introduced two metrics, area metrics and Kullback-Leibler divergence. The former two metrics calculate the distortion level in time domain information, whereas latter two measures distortion level in frequency domain.

Keywords: Slantlet Transform; ECG steganography; watermarking; validation metrics; Area Metrics; Kullback-Leibler divergence

1 Introduction

Steganography is a technique used to embed secret information into a cover signal. In ECG steganography patient's ECG signal is used as cover signal and personal information of the patient like name, age and locations are the secret data. Classically, the secret data is embedded into the cover signal using watermarking algorithms. Least Significant Bit (LSB), threshold level, patchwork and assignment based algorithms are the few existing watermark embedding algorithms. Performance of each watermark embedding algorithms varies with selection of cover signal and size of secret information. Upon embedding the secret data, the cover signal is prone to distortion. One of the performance metric of watermarking algorithms is to measure the distortion between the cover and watermarked signal. Lesser the distortion, better it is.

In frequency domain, the cover signal is decomposed using transforms such as Discrete Cosine Transform (DCT), Short Time Fourier Transform (STFT), Fast Fourier Transform (FFT), Discrete Fourier Transform (DFT) and Integer Wavelet Transform (IWT) etc. Discrete Wavelet Transform (DWT) based ECG steganography scheme is proposed in Ibaida A et al.'s work.¹ where DWT is used to decompose the cover ECG, and scrambling matrix based LSB watermark embedding algorithm is used to embed the secret information into the DWT coefficients. The inverse transform of watermarked coefficients gives the watermarked ECG signal. Distortion less data hiding based on Slantlet Transform (SLT) for image steganography is proposed in Thabit R et al.'s work.³ Robust reversible watermarking scheme using SLT matrix is presented in Kumar S et al.'s work.⁴ Image watermarking using slantlet transform is presented in Mohammed RT et al.'s work.⁵ The diagnostic measurement of watermarked ECG and the reliability of retrieved secret information assessments give the distortion level in watermarked ECG and performance assessment of SLT based steganography.

We propose the SLT based ECG steganography technique using LSB and threshold watermark embedding algorithm. Here, the secret data is embedded into the SLT coefficients based on the selected

threshold value. Typically the secret data is hid in the high frequency components. This is under the assumption that they don't carry information that is critical for diagnosis. Hence, researchers use metrics that measure the distortion in the low frequency components. However, sometimes information in the high frequency components also needs to be preserved. In such cases, different metrics in frequency domain are required. Therefore, the distortion need to be measured in both time and frequency domain. The performance evaluation is obtained using the validation metrics of Peak Signal to Noise Ratio (PSNR), Percentage Residual Difference (PRD), Area Metric (AM) and Kullback-Leibler (KL) divergence. Validation metrics calculates the distance using time domain information in PSNR and PRD. AM and KL uses frequency information to measure the distance between the cover and watermarked ECG signal.

The organization of the paper is as follows, the outline of SLT and the methodology of SLT based steganography is explained in section 2. The validation metrics are explained in section 3. The result and discussion section is presented in section 4. The conclusion of the work is presented in section 5.

2 Methods

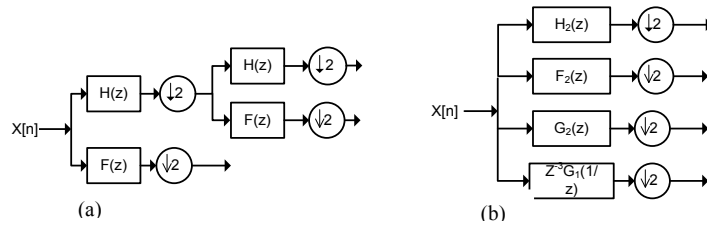
2.1 Slantlet transform

Slantlet transform is the diagonal DWT constructed using parallel structure of different filters for each scale instead of iteration of filters for each levels of DWT as shown in the Fig. 1. The filters used to design the Slantlet filter bank are $h_i(n)$, $f_i(n)$ and $g_i(n)$. The L scale filter bank has $2L$ channels. $h_L(n)$ is the lowpass filter and $f_L(n)$ filter is adjacent to the lowpass filter. The required down sampling order after the filters $h_L(n)$ and $f_L(n)$ are 2^l [1]. The output $y_i(n)$ of filters $g_i(n)$ is computed as follows:

$$y_i(n) = \sum_{k=0}^{2^{i+1}-1} x(2^{i+1}n+k)g_i(k) \quad (1)$$

SLT provides better time localization that causes the degradation of frequency selectivity because of shorter length of SLT filter bank causes less frequency selective than the DWT filter bank. Slantlet filter banks are orthogonal and has two zero moments. The slantlet filters are piecewise linear.

In ECG signal steganography, Slantlet transform is applied to the cover ECG signal using convolution with the coefficients of SLT filter bank. The selected watermarking algorithm is applied to the SLT coefficients to embedding the personal information and applying inverse slantlet transform results the watermarked ECG signal. The original cover ECG and watermarked ECG signal are shown in Fig. 2.



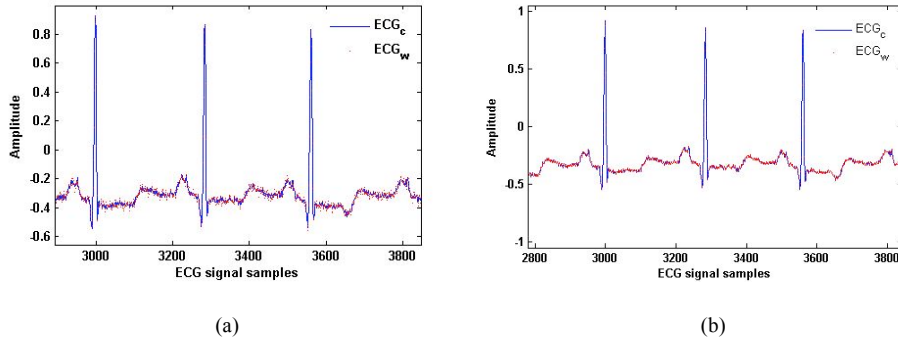


Fig. 2. Cover ECG (ECG_c) and watermarked ECG (ECG_w) for two different thresholds
Filter bank structure of (a) DWT (b) SLT

Fig. 1.

2.2 LSB and threshold watermarking

The patient information is embedded into the Slantlet Transform (SLT) coefficients of cover ECG. The location of embedding the data is identified based on the threshold value T . The distortion level of the watermarked cover ECG signal is based on the selection of threshold value T . T is selected based on, not to distort the ECG features. T is compared with SLT coefficients of cover ECG, and data is embedded where SLT coefficients are lesser than T . Least Significant Bit (LSB) watermark embedding algorithm is applied to embedding the patient information into the SLT coefficients of cover ECG as shown in the Fig. 3, taking inverse SLT gives the watermarked ECG. Pseudo watermark embedding algorithm:

1. Patient's ECG data is selected as cover signal for ECG steganography
2. Apply Slantlet transform on cover ECG
3. Find threshold value T for SLT coefficients
4. Select patient information needed to be sent, secret data
5. Apply LSB watermarking algorithm on,
6. Take inverse Slantlet transform after LSB watermarking
7. Evaluate performance of ECG watermarking

Watermark extraction:

1. Apply SLT on watermarked ECG
2. Extract secret information from LSBs of SLT coefficients
3. Calculate the reliability of extracted data

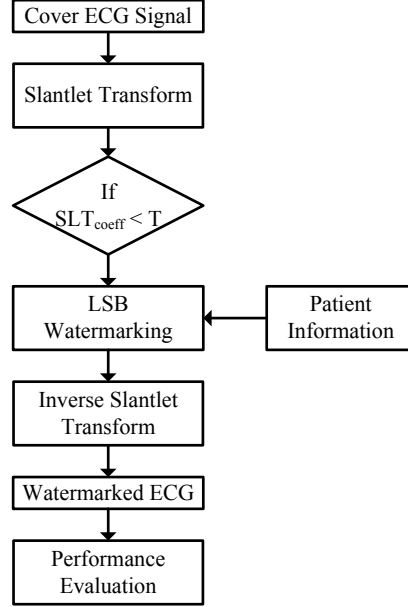


Fig. 3. SLT based ECG steganography

3 Validation Metrics

The performance of SLT based ECG steganography using LSB and threshold watermarking algorithm is evaluated using various validation metrics such as PSNR, PRD, AM and KL divergence. Where PSNR and PRD are calculated from the amplitude values of cover and watermarked ECG directly. AM and KL divergence are calculated using the CDFs and PDFs of the cover and watermarked ECG respectively. Gaussian kernel is used to construct the CDFs and PDFs of ECG signal. PRD gives the measure of the distance between cover (x_i) and watermarked ECG (y_i) in time domain as follows:

$$PRD = \sqrt{\frac{\sum_{i=1}^N (x_i - y_i)^2}{\sum_{i=1}^N (x_i)^2}} \quad (2)$$

Area metric is the measure of distance between the cover and watermarked ECG using CDFs. $F(x)$ is the CDF of cover ECG and $F'(x)$ is the CDF of watermarked ECG.

$$d(F, F') = \int_{-\infty}^{\infty} |F(x) - F'(x)| dx \quad (3)$$

Kullback-Leibler divergence (D) is the measure of distance between the cover and watermarked ECG using PDFs. $p_1(x)$ is the PDF of cover ECG and $p_2(x)$ is the PDF of watermarked ECG. The KL divergence is calculated using the formula as follows:

$$D(p_1, p_2) = \int p_1(x) \log \frac{p_2(x)}{p_1(x)} dx \quad (4)$$

The distance measurement techniques are used to analyze the diagnosability measurement of watermarked ECG.

4 Results and Discussion

The watermarked ECG obtained through Slantlet transform is evaluated through the measurements of PSNR, PRD, AM and KL divergence methods and the results are listed in Table 1 & 2, for the selected threshold value of 0.048 and -0.03 respectively. The metrics shows the similarity between cover ECG and watermarked ECG. The CDF values to calculate the area metric is plotted in Fig. 4

The CDF, CDF difference and PDFs of cover ECG and watermarked ECG for the secret data of size 1000 bytes is shown in the Fig. 4. The CDF difference plotted in Fig.4 c and Fig 5c gives the variations in frequency information between ECG_c and ECG_w. Sum of absolute CDF difference gives the overall distance between the cover and watermarked ECG. The PDFs plotted in Fig. 4 d and Fig. 5 d shows the distortion in PDFs of watermarked ECG where the distortion level is high for two reasons of threshold value and size of secret data.

Embedding the secret information into SLT coefficients may distorts the features of the ECG signal, selection of threshold values for embedding prevents the alteration due to watermarking in sensitive SLT coefficients. The results are listed for two threshold values 0.048, -0.03 in Table 1 & 2 respectively. The PRD measurement gives the distance between cover and watermarked ECG in time domain with respect to time and amplitudes of ECG signal. AM and KL divergence gives the distortion in cover ECG due to watermarking based on frequency information using differences in CDFs and PDFs of ECG signals respectively. The listed result shows that the metrics gave large difference when the increase in size of secret information. The secret data is embedded in the cover ECG signal of sample size 8192 bytes.

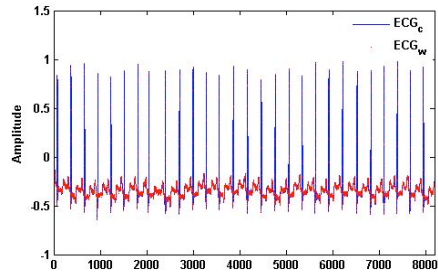
TABLE 1 METRICS FOR THRESHOLD VALUE = 0.048

Bytes	PSNR	PRD	AM	KBL
10	112.79	0.0016	1.68	0.000044
20	110.98	0.002	1.84	0.000064
30	110.14	0.0022	2.77	0.0001
40	108.37	0.0027	3.11	0.00016
50	107	0.0032	3.18	0.00018
60	106.66	0.0033	3.46	0.0002
70	106.06	0.0035	3.51	0.00024
80	105.1	0.0039	5.71	0.00042
90	104.7	0.0041	5.72	0.00043

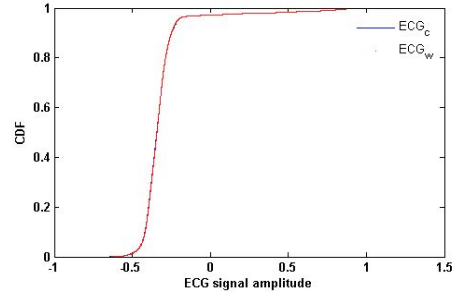
100	104.05	0.0044	5.74	0.00043
200	100.93	0.0063	7.13	0.00066
400	97.76	0.0091	9.92	0.0012
600	95.95	0.0113	9.92	0.0011
800	94.61	0.0131	4.67	0.00055
1000	93.69	0.0146	38.87	0.0099

TABLE 2 METRICS FOR THRESHOLD VALUE = - 0.03

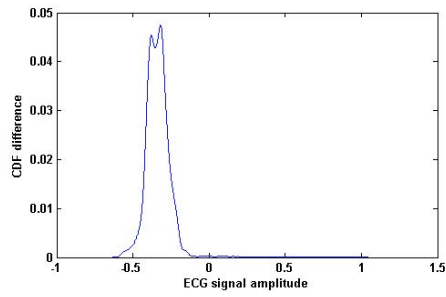
Bytes	PSNR	PRD	AM	KBL
10	113.69	0.0015	1.8750	0.000045
20	111.34	0.0019	2.93	0.0001
30	110.66	0.0021	2.96	0.00011
40	108.12	0.0028	3.31	0.00017
50	107.41	0.003	3.38	0.00019
60	106.91	0.0032	3.46	0.00022
70	105.85	0.0036	5.61	0.0004
80	105.25	0.0039	5.65	0.00043
90	104.52	0.0042	5.67	0.00043
100	103.76	0.0046	5.73	0.00046
200	100.94	0.0063	7.23	0.00072
400	97.63	0.0093	36.14	0.0089
600	95.77	0.0115	29.58	0.0059
674	95.26	0.0122	29.61	0.0061



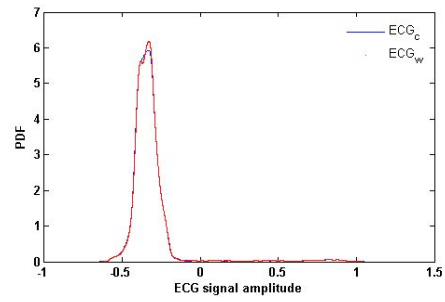
(a)



(b)

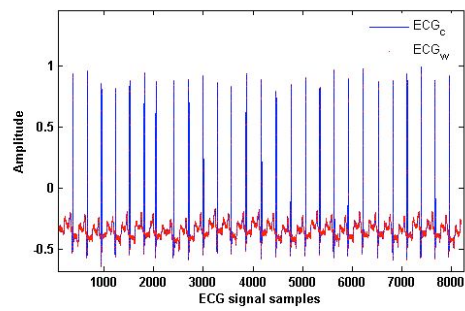


(c)

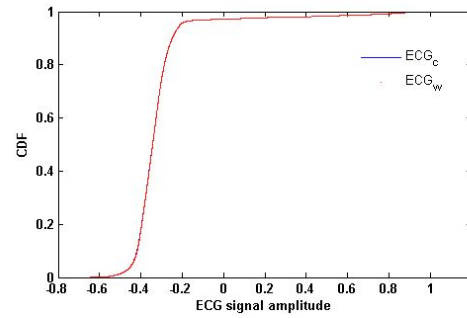


(d)

Fig. 4. Plots of cover Vs watermarked ECG for secret data size 50 bytes and threshold value of 0.048 (a) ECG signal (b) CDFs (c) Difference between CDFs (d) PDFs

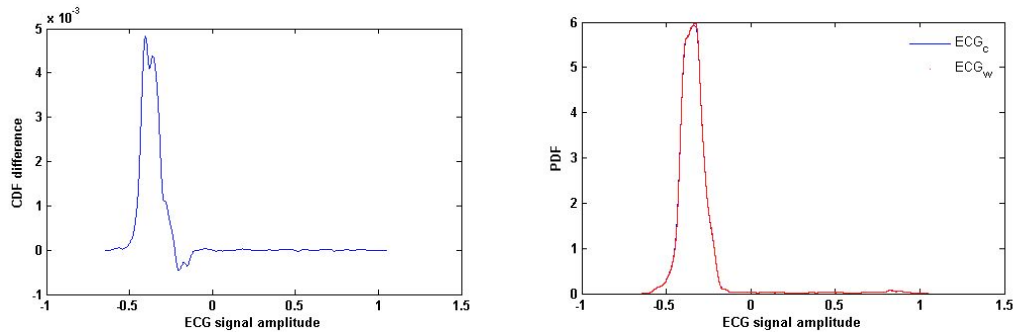


(a)



(b)

Fig. 5. Plots of cover Vs watermarked ECG for secret data size 50 bytes and threshold value of -0.03



(c) (d)
Fig. 5. Plots of cover Vs watermarked ECG for secret data size 50 bytes and threshold value of -0.03
(a) ECG signal (b) CDFs (c) Difference between CDFs (d) PDFs

4 Conclusion

ECG steganography using slantlet transform provides personal information security of a patient through combined LSB and threshold based watermarking algorithm in transform domain using SLT. The watermarked ECG has been evaluated for diagnosability measurement using various metrics. Threshold based LSB watermarking gives less distortion in watermarked ECG signal for the specific amount of secret data size and the selected number of LSBs for watermarking. The distortion levels are calculated using validation metrics of PSNR, PRD, AM and KBL, the result shows that the better similarity and diagnosis measurement of watermarked ECG is possible in ECG steganography using slantlet transform.

5 References

1. Ibaida A, Khalil I, Wavelet-Based ECG Steganography for Protecting Patient Confidential Information in Point-of-Care Systems. *IEEE Trans. Biomed. Eng.*, 60(12):3322–3330, 2013.
2. Selesnick I W, The Slantlet Transform. *Proceedings of the IEEE-SP International Symposium on Time-Frequency and Time-Scale Analysis*, 1998.
3. Thabit R, Khoo B E, Robust reversible watermarking scheme using Slantlet transform matrix. *J Syst Software*, 88:74–86, 2014.
4. Kumar S, Muttou S K, Distortionless Data Hiding Based on Slantlet Transform. *2009 International Conference on Multimedia Information Networking and Security*, 2009.
5. Mohammed RT, Bee Ee Khoo, Image watermarking using slantlet transform, *2012 IEEE Symposium on Industrial Electronics and Applications (ISIEA)*, 281-286, 2012.
6. Raftari N, Moghadam A M E, Digital Image Steganography Based on Assignment Algorithm and Combination of DCT-IWT. *2012 Fourth International Conference on Computational Intelligence, Communication Systems and Networks*, 295-300, 2012.
7. Natgunanathan I, Xiang Y, Zong T, Patchwork-based stereo audio watermarking against de-synchronization attack. *2012 5th International Congress on Image and Signal Processing*, 1601-1605, 2012.
8. Dai Y, Wang C, Digital Watermarking Algorithm Based on Wavelet Transform. *2011 International Conference on Control, Automation and Systems Engineering (CASE)*, 1-3, 2011

9. Farooq O, Vyas AL, Datta S, Mulvaney D, Watermarking biomedical signal for authentication using integer wavelet transform. 2011 4th International Conference on Biomedical Engineering and Informatics (BMEI), 892-896, 2011
10. Kozat S S, Vlachos M et al., Embedding and Retrieving Private Metadata in Electrocardiograms. J Med Syst 33(4):241–259, 2009
11. Santini S, Jain R, Similarity measures. IEEE Transactions on Pattern Analysis and Machine Intelligence, Institute of Electrical and Electronics Engineers (IEEE), 21(9):871–83, 1999
12. Basseville M, Distance measures for signal processing and pattern recognition, Signal Processing, 18(4): 349-369, 1989
13. Ferson S, Oberkampf W L, Validation of imprecise probability models, Int. J. Reliab. Saf., 3:3-22, 2009

SPECKLE TRACKING IN 3D ULTRASOUND IMAGES FOR STRAIN ANALYSIS OF CARDIAC TISSUES

SIMONE MASETTI, NICO LANCONELLI

*Alma Mater Studiorum – University of Bologna,
Department of Physics and Astronomy, I-40127 Bologna, Italy
nico.lanconelli@unibo.it*

PAOLA NARDINOCCHI

*Dipartimento di Ingegneria Strutturale e Geotecnica
Sapienza Università di Roma
I-00184 Roma, Italy*

LUCIANO TERESI

*LaMS – Modeling & Simulation Lab
Università degli Studi Roma Tre
I-00146 Roma, Italy*

PAOLO EMILIO PUDDU, CONCETTA TORROMEIO

*Dipartimento di Scienze Cardiovascolari, Respiratorie, Nefrologiche, Anestesiologiche e Geriatriche
Sapienza Università di Roma,
I-00161 Roma, Italy*

VINCENZO GIGLIO

*Unione Italiana Lotta alla Distrofia Muscolare (Uildm), I-00167 Roma, Italy
Divisione di Cardiologia ed UTIC Osp. San Paolo, I-00053 Civitavecchia, Italy.*

Abstract — In this paper we are presenting a method for achieving strain analysis of cardiac tissues from 3D ultrasound images. First of all, the left ventricle was segmented by an iterative snake algorithm which exploits the gradient vector flow field estimated from the 3D images. Once the ventricle was segmented, a set of points located on the external surface of the ventricle was selected. The movement of all these points along the entire cardiac cycle was calculated by using speckle tracking techniques. The strain of all the segments connecting two of the considered points was computed, together with the rotation of the points along the long axis of the ventricle. The method was tested on images acquired from 10 subjects: 3 with heart pathologies, 5 healthy subjects, and 2 patients with mild hypertrophy. Preliminary results showed the feasibility of characterizing healthy subjects and patients with well-defined heart pathologies by using the outcomes achieved with the strain analysis.

Keywords—speckle tracking; 3D ultrasounds; strain analysis; echocardiography.

1. Introduction

Three-dimensional (3D) echocardiography offers the ability to improve and expand the diagnostic capabilities of cardiac ultrasound [1]. 3D ultrasounds theoretically can provide what 2D echocardiography cannot. For instance, a comprehensive and time-volume analysis of cardiac chamber geometry and function can be obtained throughout the cardiac cycle from a single 3D data set.

The mechanical properties of tissue have long been recognized as a useful indicator of disease. In what is a natural development of manual palpation, the analysis of the elasticity involves the imaging of tissue deformation induced by some sort of applied mechanical stress. The measured deformation, taken alongside any knowledge of the stress, allows estimation of the tissue's mechanical properties. Strain can measure myocardial deformation, which is an intrinsic mechanical property of the myocardium. Because assessment of the myocardial mechanical parameters has proven to be a crucial step in the detection of

cardiac abnormalities, the analysis of the elasticity of the tissues should have a significant impact in this field by measuring the mechanical response of the cardiac muscle at the various steps of the cardiac cycle. The occurrence of myocardial disease can precede structural myocardial changes shown by traditional imaging techniques. Myocardial strain by speckle tracking echocardiography has demonstrated to be a sensitive tool for assessing ventricular function in early myocardial disease. The change in tissue characteristics could be done through an elaboration of the 3D echocardiography images where specific chamber strains are defined [2]. In presence of lesions the tissue is strongly impaired and the elasticity of the tissue is altered. This elasticity may be related to the strains of the tissue and, hence, could be described through a change in the strains. The establishment of a digital map corresponding to the elasticity values could be used to monitor the possible reduction in tissue contractility related to the presence of lesions. In healthy individuals, the absolute value of the average peak systolic left ventricular strain assessed by speckle tracking technique is in the range of 18-22% [3]. Strain is frequently attenuated in cardiomyopathy and can be utilized for the evaluation of disease progression and the effect of therapeutic interventions.

Speckle-tracking echocardiography is able to provide accurate and robust measurements of regional tissue motion and deformation. The image-processing algorithm tracks user-defined regions of interest containing stable patterns that are described as *speckles* [4,5]. Being caused by the interference of near placed ultrasound reflectors, speckle pattern will give every different region of the myocardium a unique pattern which will only change slightly from one frame to another. Speckles are tracked consecutively frame to frame to resolve angle-independent 2D and 3D sequences of tissue motion and deformation. The tracking system is based on grayscale B-mode images and is obtained by automatic measurement of the distance between two pixels of a segment during the cardiac cycle [6].

2. Materials and methods

The data files provided by the clinical partners of the EU project CHIRON were ten DICOM 4D images of a human heart. The images were acquired with a Philips iE33 Ultrasound Machine and exported as *Cartesian DICOM* from a total of ten subjects (three patients with heart pathology, five healthy subjects, *i.e.* without known pathologies, and two patients presenting mild hypertrophy). Temporal resolution was between 8 and 20 frames per cardiac cycle, depending on heart rate.

The segmentation of the left ventricle was realized by using an active contours algorithm, which needs an initial seed point provided by the user. This point should be positioned manually for each patient within the left ventricle only in the first frame. The first step of the segmentation consists in the computation of the GVF, which was used for modifying the shape of the segmented ventricle in an iterative way. Snakes, or active contours, are curves or surfaces defined within an image domain that can evolve under the influence of internal forces, defined upon the characteristic of the snake itself, and external forces derived from the image data. The internal and external forces are defined in order to make the snake converge to an object boundary. Snakes were firstly introduced by Kass et al. [7]. An important advance was made by Xu and Prince [8], who introduced a new external force, which they called *Gradient Vector Flow* (GVF), computed as a diffusion of the gradient vectors of a gray-level or binary edge map derived from the image. The resultant field has a large capture range and forces active contours into concave regions. In this paper we adopt the 3D formulation for the GVF active contours method. Once the left ventricle was segmented, a certain number of points were extracted along the external surface of the ventricle. Each point was considered as a *speckle* and its movement through the different frames was tracked. The essence of this technique lies in the comparison of two successive frames of the heart 3D image to determine where the speckle of interest has moved. In this paper the tracking of the speckle was realized through a Sum of Absolute Difference (SAD) method [9].

Regional strain is a dimensionless measurement of deformation, expressed as a percentage change from an object's original dimension. The strain was calculated by measuring the deformation of all the segments connecting two of the extracted speckles. That allowed the computation of the strain of the various sections of the heart. We also estimated the left ventricle rotation around its long axis, as the angular displacement expressed in degrees. In fact, the base and the apex of the ventricle normally rotate in opposite directions, whereas different kind of angular displacement could occur in presence of some pathologies. From an anatomical point of view, the heart can be divided into three sections (apical, medial and basal). Here, we estimated separately the global strain for these three sections, as the average of all the segments located in that particular section. The same applies for the angular displacement of the speckles.

3. Results

In figures 1 and 2 we report an example of the strain and the angular displacement calculated for the three heart sections for a healthy subject (figure 1), and a patient suffering from hypertrophic cardiomyopathy (figure 2). We can note that in both cases, starting from end diastole, the strain decreases to a minimum value reached during the systole (shortening of tissues), and increases again approaching the end of the cardiac cycle, as expected. It is worth noting that for the healthy subject the apical section of the ventricle rotates clockwise during systole and counter-clockwise during diastole; the base of the ventricle rotates in the opposite direction, as expected. The patient considered in figure 2 is affected by hypertrophic cardiomyopathy, which is usually characterized by myocardial fiber disarray, resulting in left ventricle systolic and diastolic dysfunction. As a consequence, marked differences can be observed, both in terms of strains and of angular displacement. A clear reduction of all the strain values is present, together with a completely different angular displacement of the three sections of the ventricle.

Table I. Average peak strain estimated for all the 10 patients composing our dataset. Patients #0, 4, 5, 6, and 9 are healthy subjects, patients #1 and 2 suffer from dilated cardiomyopathy, patient #3 suffers from hypertrophic cardiomyopathy, and finally patients #7 and 8 present mild concentric hypertrophy.

We can note that all the healthy subjects, together with the two patients presenting mild concentric hypertrophy have strain values compatible with those reported in the literature for the healthy population. On the contrary, the three patients suffering from cardiomyopathy have markedly reduced strain values. That confirms the feasibility of using strain analysis for deriving some indexes to estimate the typical distribution for healthy subjects, and second we could follow how these indexes vary in time for patients with known pathologies.

Patient ID	Average peak strain [%]
# 0	-22±5
# 1	-5±4
# 2	-8 ±4
# 3	-11 ±4
# 4	-16±5
# 5	-20±5
# 6	-19±5
# 7	-20±5
# 8	-19±5
# 9	-16±5

4. Conclusions

In this paper we presented a method for obtaining a strain analysis of cardiac tissues in 3D ultrasound images. Our algorithm first segments the left ventricle with an iterative technique which exploits the GVF

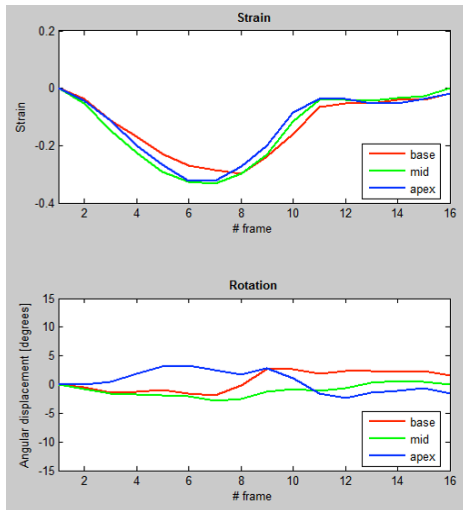


Fig. 1. Strain and rotation values estimated along the entire cardiac cycle on the three cardiac sectors for a healthy subject.

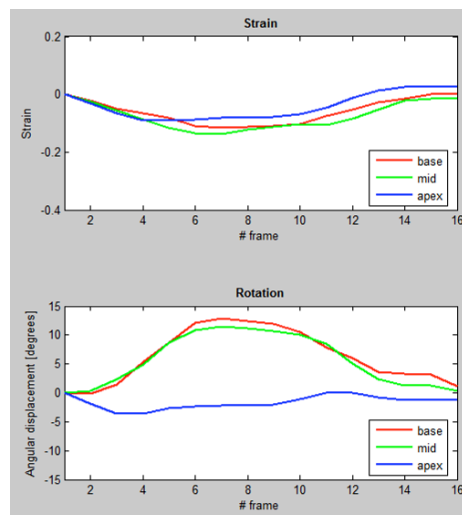


Fig. 2. Strain and rotation values estimated along the entire cardiac cycle on the three cardiac sectors for a patient with hypertrophic cardiomyopathy.

field. The speckle tracking is achieved through the minimization of the SAD coefficient. Preliminary results on an initial small set of patients show the feasibility of characterizing healthy subjects and patients with well-defined heart pathologies by using strain analysis.

Acknowledgment

This work was supported by the European project CHIRON co-funded by the ARTEMIS Joint Undertaking program under grant agreement n° 100228.

References

- [1] J Hung, R Lang, F Flachskampf, SK Shernan, ML McCulloch, DB Adams, J Thomas, M Vannan, T Ryan, 3D Echocardiography: A Review of the Current Status and Future Directions, *J Am Soc Echocardiogr*, 20(3), 213–233, 2007.
- [2] H Geyer, G Caracciolo, H Abe, S Wilansky, S Carerj, F Gentile, HJ Nesser, B Khandheria, J Narula, PP Sengupta, Assessment of Myocardial Mechanics Using Speckle Tracking Echocardiography: Fundamentals and Clinical Applications, *J Am Soc Echocardiogr*, 23(4), 351–369, 2010.
- [3] TH Marwick, Consistency of myocardial deformation imaging between vendors, *European Journal of Echocardiography*, 11(5), 414–416, 2010.
- [4] SA Reisner, P Lysyansky, Y Agmon, D Mutlak, J Lessick, Z Friedman, Global longitudinal strain: a novel index of left ventricular systolic function, *J Am Soc Echocardiogr*, 17, 630–633, 2004.
- [5] M Leitman, P Lysyansky, S Sidenko, V Shir, E Peleg, M Binenbaum, Two-dimensional strain-a novel software for real-time quantitative echocardiographic assessment of myocardial function, *J Am Soc Echocardiogr*, 17, 1021–1029, 2004.
- [6] AK Comess, KW Beach, T Hatsukami, DE Strandness, W Daniel, Pseudocolor displays in B-mode imaging applied to echocardiography and vascular imaging: an update, *J Am Soc Echocardiogr*, 5, 13–32, 1992.
- [7] M Kass, A Witkin, D Terzopoulos, Snakes: Active contour models, *Int J of Comput Vision*, 1(4), 321–331, 1988.
- [8] C Xu, JL Prince, Snakes, Shapes, and Gradient Vector Flow, *IEEE Trans Image Process*, 7(3), 359–369, 1998.
- [9] DI Barnea, HF Silverman, A class of algorithms for fast digital image registration, *IEEE Trans Comput*, C-21(2), 179–186, 1972.

IMAGING AND QUANTIFICATION OF RIGHT VENTRICULAR REMODELING IN REPAIRED TETRALOGY OF FALLOT FOR CLINICAL DECISION MAKING

LIANG ZHONG, JU-LE TAN, XIAO-DAN ZHAO, THU-THAO LE, YI SU, CALVIN LIM, RU-SAN TAN
Bioengineering, National Heart Research Institute of Singapore, Singapore
zhong.liang@nhcs.com.sg

Tetralogy of Fallot (TOF) has an incidence of 6% to 10% among patients with congenital heart disease. Good long term survival and the quality of life are possible after surgical repair. However, long-term complications such as pulmonary regurgitation (PR), right ventricular (RV) volume overload, residual pulmonary stenosis, ventricular septal defect, ventricular outflow tract (RVOT) aneurysm, arrhythmias and sudden death may occur post repair. Among these, severe PR is the most prevalent. It may initially be well-tolerated for many years, but may eventually lead to severe RV dilation, impaired RV function, and increased risk for ventricular arrhythmias. Repeat surgery with pulmonary valve replacement (PVR) may be necessary to preempt RV functional deterioration and malignant ventricular arrhythmias. In the presence of severe PR, optimal timing of PVR, before irreversible RV functional deterioration, is critical.

We have developed a new cardiac MRI-based patient-specific quantitative method in 3-dimensional format to derive comprehensive measures of RV remodeling. We determined the mechanisms of RV remodeling and analyzed the effects of RV remodeling on clinical status in 60 repaired TOF patients, prospectively. (175 words)

S5M: Biomechanical clinical application - Strain, fatigue and posture

Chairs: Luca Cristofolini, Marco Bontempi

APPLICATION OF DIGITAL VOLUME CORRELATION (DVC) TO INVESTIGATE THE STRAIN
DISTRIBUTION IN AUGMENTED VERTEBRAL BODY

VALENTINA DANESI

USE OF DIGITAL IMAGE CORRELATION TO INVESTIGATE THE BIOMECHANICS OF VERTEBRA

MARCO PALANCA

EFFECTS OF 6 WEEKS BALANCE AND MOBILITY TRAINING ON POSTURAL CONTROL IN
HEALTHY SUBJECTS

GUIDO BELLI

NEWLY WALKING TODDLERS: HOW DO DIFFERENT STRATEGIES COMBINE WHEN
DEVELOPING PENDULUM MECHANISM

MARIA CRISTINA BISI

TKA KINEMATICS OR KINETICS: WHAT IS BEHIND KNEE PERFORMANCES?

SILVIA PIANIGIANI

METHODS OF ASSESSMENT BIOMECHANICS IN CYCLING: FROM POSTURAL DISORDER TO
THE DISEASE

LEYDI NATALIA VITTORI

APPLICATION OF DIGITAL VOLUME CORRELATION (DVC) TO INVESTIGATE THE STRAIN DISTRIBUTION IN AUGMENTED VERTEBRAL BODY

VALENTINA DANESI¹

¹ Dipartimento di Ingegneria Industriale, Università di Bologna, Viale Risorgimento
Bologna, 40136, Italy
valentina.danesi4@unibo.it

GIANLUCA TOZZI²

² School of Engineering, University of Portsmouth Anglesea Road
Portsmouth, PO1 3DJ, United Kingdom
gianluca.tozzi@port.ac.uk

LUCA CRISTOFOLINI¹

¹ Dipartimento di Ingegneria Industriale, Università di Bologna, Viale Risorgimento
Bologna, 40136
luca.cristofolini@unibo.it

There is a need to investigate the strength of the vertebral body after reinforcement treatments such as vertebroplasty (VP). With the advent of high-resolution micro-CT imaging (μ CT), digital volume correlation (DVC) techniques emerged as a novel tool for the measurement of 3D deformation fields throughout entire volumes. For bones such as the vertebra, the use of DVC allows the detection of the onset and progression of failure. Application of DVC to whole bones was recently exploited to examine yield and post-yield deformations in vertebral compression experiments. In this perspective, the aim of the present study was to investigate the biomechanical efficacy of prophylactic augmentation in preventing fracture of non-fractured vertebral bodies. In conjunction with high-resolution μ CT imaging, this study applied DVC to investigate the strain distribution of augmented porcine vertebrae during compression testing, to assess the effect of different types of augmentation materials.

Keywords: biomechanics, *in vitro* test, digital volume correlation (DVC), strain measurement, vertebral body, augmentation.

1. Introduction

There are cases in which vertebrae are at high risk of fracture, such as with low bone mineral density or metastatic lesion. These vertebrae are weak because their micro- and/or macro-structure are pathologically compromised. If untreated, they might fracture, causing severe pain and even paralysis. One strategy that has recently been proposed for reducing the fracture risk is the mechanical reinforcement of the vertebral body, by injection of a synthetic augmentation material (prophylactic augmentation). This treatment is meant to increase the strength of selected weaker vertebrae.¹ While many studies have been undertaken to investigate the biomechanical effects of vertebroplasty on fractured single vertebral bodies^{2,3} or spine segments,^{4,5} very little data exist regarding the efficacy of prophylactic augmentation on non-fractured vertebrae. It must be noted that most such studies focused on the overall behaviour of the treated vertebral body, without analyzing the strain distribution. Recently the strain distribution was measured *in vitro* for a variety of loading configurations, using a large number of strain sensors.⁶ However, traditional experimental techniques such as strain gauges are restricted to the surface of specimens where no internal strain distribution could be interrogated. With the recent and rapid progress of micro-focus computed tomography (μ CT) in conjunction with *in situ* mechanical testing,^{7,8}

DVC has become a powerful tool to examine full-field deformations in trabecular bone,^{9,10} whole bones,¹¹ cellular scaffolds¹² and recently bone-cement composites.¹³

2. Material and Methods

Thirty-two single lumbar vertebrae (L2, L3, L4 and L5) were harvested from eight porcine thoracolumbar spines provided by a local butcher. The samples were divided in four groups:

- Augmentation was performed with three types of augmentation material on twenty-four vertebrae (3 groups of 8 vertebrae each).
- The remaining eight specimens were tested without any treatment, as a control.

All the surrounding soft tissues will be removed, including the ligaments. The endplates of each vertebra will be potted in PMMA using a 6-degrees-of-freedom clamp for alignment, similar to Danesi et al.¹⁴ The posterior arch was subsequently removed. Augmentation was performed on the selected specimens, which were subsequently CT-scanned to assess the distribution of cement inside the vertebral body. Each specimen was placed in a custom-designed and loading device. The sample as a whole was constrained against rotation inside the loading device. *In situ* destructive tests were conducted by means of a novel micromechanical loading device, equipped with a 5kN load cell. The specimen was compressed axially in a stepwise fashion. μ CT imaging was carried out at each step, following a relaxation period of ~15min to reach a stable state of stress relaxation in the sample. The combination of step-wise loading and μ CT imaging was repeated until the ultimate force was achieved. DVC analysis was performed on the reconstructed volumes to obtain the full-field displacement and strain distribution, in order to identify the onset and progression of bone failure in the augmented vertebral body. LaVision DVC software was used to compute the 3D displacements and strain fields in both controls and augmented samples.

3. Expected Outcomes

The study will enable a better understanding of the failure process in augmented vertebrae. Moreover, the suitability of different biomaterials, in improving the post-operative performance of the treatment will be investigated.

Acknowledgements

The Authors wish to thanks Marco Palanca and Kavin Morellato for the technical support. Funding from the European Union for the Osteoporotic Virtual Physiological Human Project (VPHOP FP7-ICT2008-223865) is gratefully acknowledged.

References

1. Tancioni, F., et al., *Percutaneous vertebral augmentation in metastatic disease: state of the art*. J Support Oncol, 2011 **9**(1): p. 4-10
2. Brandolini, N., L. Cristofolini, and M. Viceconti, *Experimental methods for the biomechanical investigation of the human spine: a review* Journal of Mechanics in Medicine and Biology, 2014. **14**(1): p. 1430002 (33 pages).

3. Belkoff, S.M., et al., *An ex vivo biomechanical evaluation of an inflatable bone tamp used in the treatment of compression fracture*. Spine (Phila Pa 1976), 2001. **26**(2): p. 151-6.
4. Ananthakrishnan, D., et al., *The effect on anterior column loading due to different vertebral augmentation techniques*. Clin Biomech (Bristol, Avon), 2005. **20**(1): p. 25-31.
5. Oakland, R.J., et al., *The biomechanical effectiveness of prophylactic vertebroplasty: a dynamic cadaveric study*. J Neurosurg Spine, 2008. **8**(5): p. 442-9.
6. Cristofolini, L., et al., *Biomechanical effectiveness of prophylactic augmentation: an in vitro study*. under review Clinical of Biomechanics, 2014.
7. Nazarian, A. and R. Muller, *Time-lapsed microstructural imaging of bone failure behavior*. J Biomech, 2004. **37**(1): p. 55-65.
8. [Buffière, J.Y., et al., *In Situ Experiments with X ray Tomography: an Attractive Tool for Experimental Mechanics*. Experimental Mechanics, 2010. **50**(3): p. 289-95.
9. Gillard, F., et al., *The application of digital volume correlation (DVC) to study the microstructural behaviour of trabecular bone during compression*. J Mech Behav Biomed Mater, 2014. **29**: p. 480-99.
10. Liu, L. and E.F. Morgan, *Accuracy and precision of digital volume correlation in quantifying displacements and strains in trabecular bone*. J Biomech, 2007. **40**(15): p. 3516-20.
11. Hussein, A.I., P.E. Barbone, and E.F. Morgan, *Digital Volume Correlation for Study of the Mechanics of Whole Bones*. Procedia IUTAM, 2012. **4**: p. 116-125.
12. Madi, K., et al., *Computation of full-field displacements in a scaffold implant using digital volume correlation and finite element analysis*. Med Eng Phys, 2013. **35**(9): p. 1298-312.
13. Tozzi, G., Q.-H. Zhang, and J. Tong, *Microdamage assessment of bone-cement interfaces using in situ testing, digital volume correlation and finite element analysis*. under revision Journal of Biomechanics, 2014.
14. Danesi, V., et al., *Reproducible reference frame for in vitro testing of the human vertebrae*. Journal of biomechanics, 2014. **47**(1): p. 313-318.

USE OF DIGITAL IMAGE CORRELATION TO INVESTIGATE THE BIOMECHANICS OF VERTEBRA

MARCO PALANCA, VALENTINA DANESI, LUCA CRISTOFOLINI

Department of Industrial Engineering, University of Bologna,

Via Terracini 28, Bologna, 40131, Italy

marco.palanca2@unibo.it

1. Introduction

In the last years, the vertebra is the focus of a lot of biomechanical studies. There is a need for a tool, like the Digital Image Correlation (DIC), that measures the displacement and strain of surface, full field and contactless is essential.

Before using the DIC to draw any clinically relevant conclusions, a focused optimization is necessary to obtain the best results (minimum error and noise). The main problem initially is an average error of 100 microstrain and a noise of 500 microstrain. Because of this problem the DIC is neither sufficiently accurate nor exact. Such errors are far away from the performances of strain gauges that are currently the golden standard in the biomechanical area.

2. Materials and methods

2.1 Optimization of the speckle pattern

The first step is optimizing the preparation of the specimen surface. The aim was to define the optimal airbrush settings to produce the optimal pattern for five different measurement windows chosen for biomechanical specimens. Different patterns were obtained, using an airbrush, with different pattern sizes. Each specimen was acquired with the DIC camera: the speckle size and the black and white ratio has been evaluated with a dedicated MatLab script (Lionello, Submitted).

2.2 Optimization of the software parameters

We subsequently analyzed the following software parameters:

- Facet size,
- Grid spacing,
- Contour smoothing.

A factorial design permitted to establish a link between the software parameters and the errors. An unloaded flat specimen (Fig. 1) with a dedicated pattern for the specific measurement window was used to evaluate the effects produced by the alteration of software parameters on the strain measurement (as

the specimen is not subjected to any real strain, any readout different from zero is an indicator of measurement error).

Subsequently, tests were carried out applying a real strain. The strain distribution in a specimen with a simplified geometry was measured using DIC, while two strain gauges were bonded on the opposite face, as a reference.

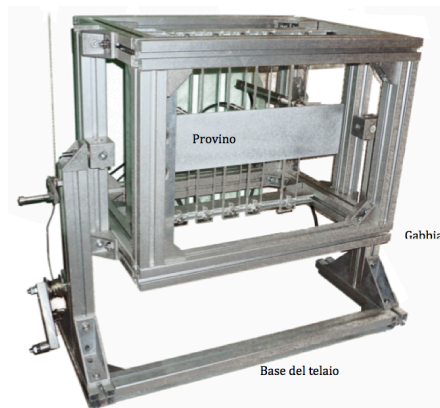


Fig. 1 - flat specimen with tiltable loading frame (Lionello, Submitted)

2.3 Optimization of the hardware parameters

The hardware parameters examined were:

- the camera gain;
- the shutter time.

Using the result of the previous tests it was possible to investigate the effect produced by the alteration of the hardware parameters. The same unloaded flat specimen was used in these tests. In the first test, different gain levels and a fixed exposure (controlled with external software) were used. The aim was evaluate the effects produced by the alteration of gain level on the errors affecting the measured strain. In the second test, the best gain level was fixed, and the best exposure was evaluated to obtain the minimum error and noise.

2.4 Application to a real vertebra

Ended the optimization section, the work moves on the measurement of vertebral strain. The DIC was used to measure the mechanical strength of physiological vertebrae (fig. 2) and vertebrae with augmentation. On this way, the best surgery, to increase the mechanical strength of pathological vertebrae, is identified and chosen through the DIC.

In the end, the features of the DIC was used to measure strain in complex geometry, anisotropic, not homogeneous specimens with a lot of strain concentration, like vertebrae.

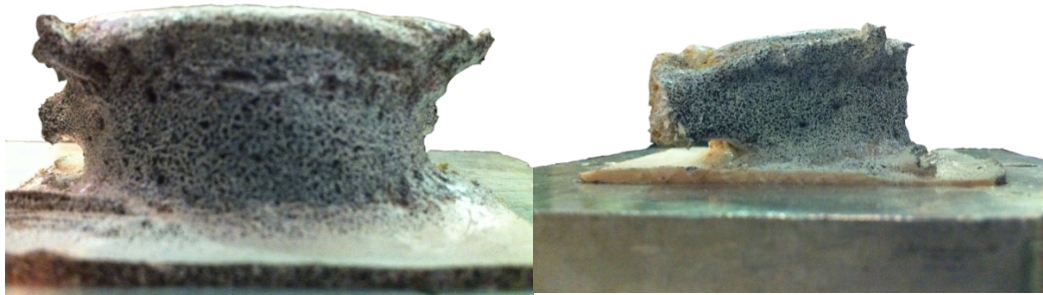


Fig. 2 – Left: front view of prepared vertebra. Right: sagittal view of prepared vertebra.

3. Results and Discussion

The improvements due to this work are remarkable.

Starting from an average error of 100 microstrain and a noise of 500 microstrain, using the knowledge developed during these tests, the error decreased to 10 microstrain and the noise to ± 100 microstrain (Fig. 3).

The software tests allowed the determination of the error and the noise in relationship with the necessary resolution. Since the demanded range of resolution is known, it is possible select the best setting software parameters.

Finally, the knowledge of the gain level and the exposure with which the system works better is basic to allow the best output without any losses or compromises.

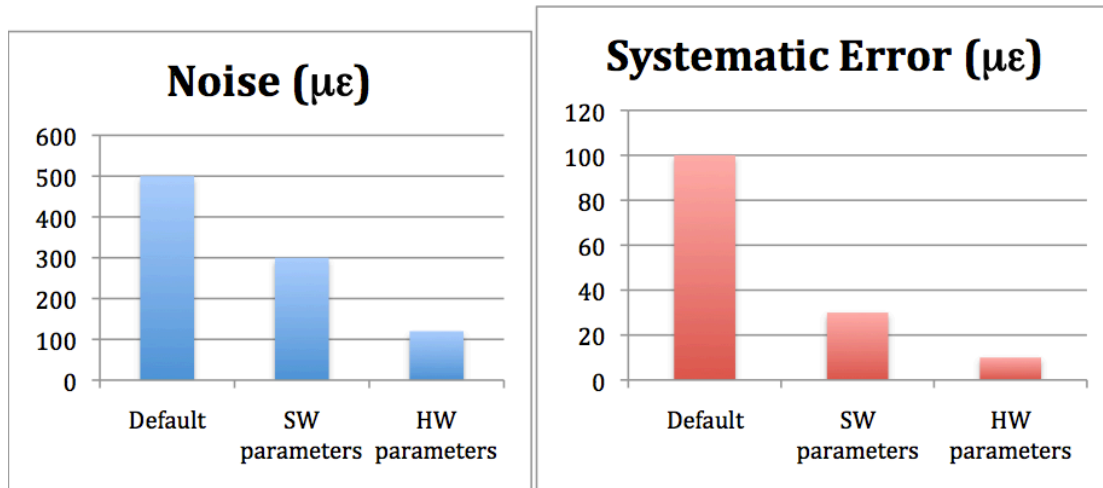


Fig. 3 – Left: reduction of random noise. Right: reduction of systematic error.

References

Lionello, G., Cristofolini, L., SUBMITTED. Optimization of the preparation of speckle patterns for digital image correlation. Measurement Science and Technology

EFFECTS OF 6 WEEKS BALANCE AND MOBILITY TRAINING ON POSTURAL CONTROL IN HEALTHY SUBJECTS

BELLI GUIDO

*School of Pharmacy, Biotechnology and Motor Sciences,
University of Bologna, Italy*

MAIETTA LATESSA PASQUALINO

*Department of Sciences for Quality of Life,
University of Bologna, Italy*

FOSCHI ELIA

*School of Pharmacy, Biotechnology University of Bologna, Italy
and Motor Sciences,*

EMILIANI FILIPPO

Manual Therapy Center, Ravenna, Italy

TENTONI CLAUDIO

*Department of Biomedical and Neuromotor Sciences,
University of Bologna, Italy*

Postural training is commonly performed in clinical, fitness and sport fields to improve performance and wellness. Despite his wide diffusion for healthy and unhealthy people, confusion still exist about focus, time and kind of training and many different techniques are currently suggested.

The aim of this study is to analyze the effect of 6 weeks training time using Bosu Balance Trainer® and Pancafit ® tools on postural control in healthy subjects.

Nineteen healthy subjects volunteered for the study. They were divided in training (TG - n:10) and control (CG - n:9) group. TG trained for 6 weeks, 3 times per weeks, 60 minutes per session with focus on balance and mobility (30 minutes each one). Training program was settled with specific progression in both components to continuously stress the neuromuscular system. Postural control using stabilometric platform in eyes open (EO) and closed condition (EC) and spine mobility (SPINE) were assessed pre and post training.

TG improved center of pressure (COP) area and displacement in EO and EC conditions, while CG in EO condition only. TG showed better improvements compared to CG for both COP measures, even if not significantly. TG improved SPINE in lumbar region and during trunk flexion, even if not significantly ($p>0.05$), while no improvements were observed in CG.

These findings suggest that a short time (6 weeks) training time with same focus on balance and mobility could lightly improve postural control and spine mobility in healthy subjects. Bosu Balance Trainer® and Pancafit ® are efficient tools for this kind of training.

Keywords: postural training, Bosu, Pancafit

NEWLY WALKING TODDLERS: HOW DO DIFFERENT STRATEGIES COMBINE WHEN DEVELOPING PENDULUM MECHANISM?

MARIA CRISTINA BISI

Department of Electrical, Electronic and Information Engineering "Guglielmo Marconi", University of Bologna,
mariacristina.bisi@unibo.it

RITA STAGNI

Department of Electrical, Electronic and Information Engineering "Guglielmo Marconi", University of Bologna,
Health Sciences and Technologies, Interdepartmental Center for Industrial Research (HST-ICIR),
Ozzano dell'Emilia, Italy
rita.stagni@unibo.it

During the first months of independent walking toddlers use different gait strategies and then converge to more similar walking forms, developing manifestation of the pendulum mechanism. The extreme modes of walking usually used by toddlers are three: twister, faller and stepper. The aim of this work was to analyze quantitatively how toddlers explore those strategies and combine them when developing the pendulum mechanism. Twenty healthy infants participated in the study. Each infant performed 5 tests in 6 months after the onset of walking. Preliminary results on three toddlers (an initially twister, an initially faller and an initially stepper) showed that each infant explored only two of the three mode of walking: faller and stepper strategies appeared to be alternative in the development of mature gait.

Keywords: Toddlers; gait strategies; pendulum mechanism.

1. Introduction

Many studies have analyzed infants at the onset of independent walking in order to evaluate the development of different strategies and coordination^{1,2}. In particular, Mc Collum et al³ described qualitatively the mechanical strategies that toddlers use during the first few weeks of independent locomotion. Three basic forms of walking were presented:

- the Twister, who dominantly exploits trunk twist for progression;
- the Faller, who dominantly exploits gravity for progression;
- the Stepper, who dominantly controls the balance of the center of mass during progression.

Toddlers use a mixture of these mechanical strategies during the first weeks of walking experience and then converge to more similar walking forms over the first few months of independent locomotion, when also they begin to develop and show some manifestation of the pendulum mechanism.

It could be argued that the pendulum mechanism is the result of the superimposition of the three basic walking forms: this assumption could be confirmed analyzing objectively biomechanical data of toddlers during their first months of independent walking.

In this work, longitudinal gait data were collected on toddlers from the onset of independent walking for six months using wireless inertial sensors. Data were used to quantitatively observe and analyze the

mechanical strategies used by toddlers and analyze how those strategies develop into the pendulum mechanism.

The aims of this work were:

- to identify the major characteristics of toddler gait strategies using inertial sensors;
- to evaluate data collected on toddlers during their first months of walking and quantify objectively how the gait strategies change towards a pendulum mechanism;
- to preliminary verify the hypothesis that the pendulum mechanism results the composition of the three presented gait strategies.

2. Materials & Methods

Twenty healthy infants ($77\pm 3\text{cm}$, $10\pm 2\text{kg}$, $13\pm 2\text{months}$) were included in the study. All of the infants were full-term at birth and had no known developmental delays. Tests on the infants were scheduled once a month after the onset of independent walking for three months (T1, T2, T3) and one after six months (T6). When possible, a test during the very first week of independent walking was performed (T0) (twelve infants). Two tri-axial wireless inertial sensors (OPALS, Apdm, USA) were mounted respectively on the lower back and on the right leg. The participants were asked to freely walk in the room. For all the participants 10 consecutive strides were analyzed. Right heel strike (HS) and toe off (TO) instants were estimated from the angular velocity of the lower limb⁴.

First, gait strategies used at the first week of independent walking were identified both visually during the test and from the trends of accelerations and angular velocities. Based on the theoretical description presented by McCollum et al³ the following characteristics have been searched for in the data:

- Twister strategy was expected to show an high angular velocity around L5 vertical axis;
- Faller strategy was expected to show an high peak to peak L5 acceleration range along the AP axis;
- Stepper was expected to show low peak to peak range at L5 acceleration and angular velocities in all directions. The rapid movement of the foot were expected to show high accelerations of the legs happening in a small percentage of the stride.

Data at T0 were grouped for strategy and a typical parameterized waveform, reproducing the characteristics described above, was designed for each one.

Each waveform was fitted into toddler data and then subtracted from the signals. Percentage of signal power left was calculated as an indication of how much the gait deviated from the intended strategy.

3. Results

The identified waveforms representative of the principal toddler gait strategies were:

- Twister: a sinusoidal function on the angular velocity around the vertical axis of L5 (Fig. 1a)

$$A \sin(Bx + C) + D \quad (1)$$

- Faller: an inverted saw-tooth waveform on the antero-posterior acceleration of L5 (Fig.1b)

$$A * \left(-\frac{t}{B} + \text{round} \left(\frac{t}{B} + \frac{1}{2} \right) \right) + C \quad (2)$$

- Stepper: a sinusoidal function on the vertical acceleration of the foot for 20% of the stride and then a constant value (Fig.1c).

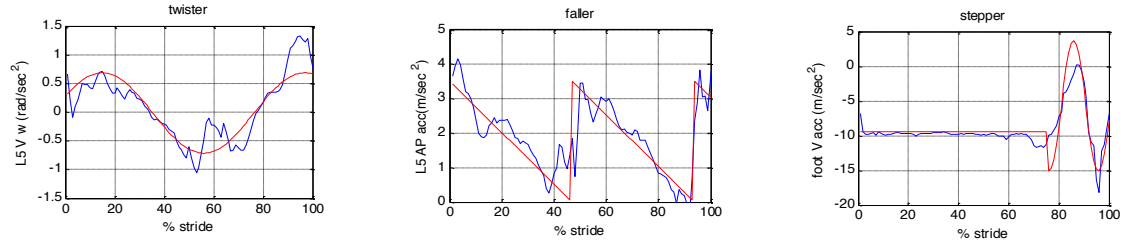


Fig. 1. Measured signal (blue) and estimated waveform (red) for (a) twister, (b) faller, (c) stepper.

Preliminary results of signal power analysis are shown in Figure 2a, 2b and 2c for three toddlers, each one showing at T0 a different gait strategy.

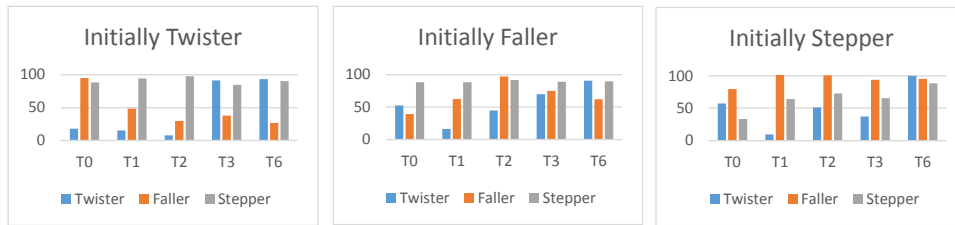


Fig. 2. Percentage of signal power left after removing the estimated trend of each gait strategies (twister in blue, faller in orange and stepper in grey) at different stage of gait development. Figures show results of 3 toddlers who manifested during the first week a twister (a), faller (b), stepper (c) strategy.

Assuming that the percentage of signal residual power indicates of how much the gait deviated from the intended strategy, the “initially stepper” toddler used the twister strategy from T0 to T2 and then left it, while from T1 to T6 explored also the faller strategy. Stepper strategy was almost not used.

The “initially faller” toddler used the faller strategy less and less from T0 to T2 and the twister strategy from T1 to T3. Stepper strategy was not used.

The “initially stepper” toddler explored at first the stepper strategy and then the twister one (from T1). Faller strategy was not used.

The major characteristics of pendulum mechanism⁵ appeared in most of the toddlers data at T1 and became more and more evident from T1 to T6.

4. Discussion

In this work gait strategies used by toddlers were investigated using inertial sensors. Three different waveforms, characteristics of different toddler strategies were identified. Preliminary results showed that each toddler explored and combined mostly two of the three strategies presented when developing the pendulum mechanism. The two combinations found were twister and faller or stepper and twister: faller and stepper strategies appeared to be alternative in the development of mature gait.

The analysis of more data will confirm this first conclusion. Further work is needed to understand how the different strategies combine in order to create the pendulum mechanism.

References

1. Ivanenko, Y. P., Dominici, N., Cappellini, G., Dan, B., Cheron, G., & Lacquaniti, F. Development of pendulum mechanism and kinematic coordination from the first unsupported steps in toddlers. *The Journal of experimental biology*, 207(Pt 21), 3797–3810, 2004.
2. Looper, J., Wu, J., Angulo Barroso, R., Ulrich, D., & Ulrich, B. D. Changes in step variability of new walkers with typical development and with Down syndrome. *Journal of motor behavior*, 38(5), 367–372 2006.
3. McCollum, G., Holroyd, C., & Castelfranco, A. M. Forms of early walking. *Journal of theoretical biology*, 176(3), 373–390, 1995.
4. Aminian K, Najafi B, Büla C, Leyvraz PF, Robert P., Spatio-temporal parameters of gait measured by an ambulatory system using miniature gyroscopes. *J Biomech* 35(5): 689-99, 2001.
5. Zijlstra, W., & Hof, A. L. Assessment of spatio-temporal gait parameters from trunk accelerations during human walking. *Gait & posture*, 18(2), 1–10, 2003.

TKA KINEMATICS OR KINETICS: WHAT IS BEHIND KNEE PERFORMANCES?

SILVIA PIANIGIANI

*IRCCS Istituto Ortopedico Galeazzi
Via R. Galeazzi 4, 20161 Milano, Italy
silvia.pianigiani@grupposandonato.it*

LUC LABEY

*Biomechanics Department, KU Leuven
Cemestijnenlaan 300, 3001, Leuven, Belgium
luc.labey@mech.kuleuven.be*

WALTER PASCALE

*IRCCS Istituto ortopedico Galeazzi
Via R. Galeazzi 4, 20161 Milano, Italy
wal.pascale@gmail.com*

BERNARDO INNOCENTI

*BEAMS Department, Université Libre de Bruxelles,
Franklin Rooseveltlaan 50, 1050 Brussels, Belgium
bernardo.innocenti@ulb.ac.be*

Total Knee Arthroplasty (TKA) is a successful surgical treatment; however failures, as pain and patient dissatisfaction still persist. Sometimes, surgeons are not able to understand or explain these bad performances because the patient “looks good, but feels bad”.

Apart from X-Rays, conventionally used follow-up methods are mainly based on the analysis of knee kinematics, but even if kinematics remains close to “normal”, the patient may still complain about pain and functional limitations.

To provide more insight in this paradox, a better quantitative understanding of TKA mechanics must be established. Therefore, our hypothesis is to check if kinetics information needs to be improved, i.e. integrating with kinematic, in conventional TKA follow-up.

To prove this hypothesis, an analysis on several TKA designs was performed investigating mal-alignments and different soft tissues configurations. As output, the relative differences in tibio-femoral kinematics and in tibio-femoral and patello-femoral contact forces (kinetics) induced by the altered configurations were extracted and compared with the reference configuration.

Results show that surgical errors influence more kinetics outputs (forces) than kinematics, confirming our hypothesis. Therefore, knee forces are fundamental in the analysis of knee performance and patient follow-up. Such information should be integrated in the clinical practice together with knee motion.

Keywords: TKAs kinematics, TKAs kinetics, knee pain, patient follow-up

1. Introduction

Total Knee Arthroplasty (TKA) is a very successful surgical procedure, but patients with difficulties or pain during motion still persist. TKA patient outcomes can be affected not only by the implant design, but also by implant position and by patient-related anatomical factors. During standard clinical follow-up, conventional activities are usually performed by the patient and clinical scores are determined and compared with standard data of healthy subjects^{1,2}. Rarely, and usually only for research purposes, more thorough investigations of patient joint kinematics such as fluoroscopy^{3,4} or 3D motion analysis⁵, can be performed to assess patient function. As convincing explanations for patients with knee pain after TKA that present “normal” gait pattern are not reported yet in the literature and standard follow-up techniques includes only analysis of their kinematics. Our hypothesis is that alterations in contact forces are more important for knee performance than kinematics changes, in terms of implant motion, and that they could be related to the pain.

To prove this hypothesis, an analysis on several TKA designs was performed investigating mal-alignments and different soft tissues configurations. As output, the relative differences in tibio-femoral kinematics and in tibio-femoral and patello-femoral contact forces (kinetics) induced by the altered configurations were extracted and compared with the reference configuration.

2. Materials and methods

Physiological bone models were obtained from a CT of a cadaver leg and the physiological soft tissue insertion points were taken from the literature^{6,7}. Four TKA designs were implanted in the same physiological model according to their surgical guidelines (conventional fixed bearing, posterior stabilized (PS) design; fixed bearing high flex design; mobile bearing design; hinge prosthesis design).

The following configurations were analyzed:

- (1) the theoretical configuration corresponding to the optimal surgical technique and physiological locations of the soft tissue insertion points;
- (2) a change in position of the tibial component in medio-lateral (ML) and antero-posterior (AP) directions;
- (3) a change in orientation of the tibial component in flexion-extension (FE), abduction-adduction (AA) and internal-external (IE) orientation;
- (4) patella alta and baja;
- (5) tilting of the patellar component (IE rotation);
- (6) a change in location of the two collaterals in ML, AP and proximo-distal (PD) directions.

For each prosthesis and configuration, loaded squat up to 120° of flexion was simulated using LifeMOD/KneeSIM 2007.0.5 (LifeModeler, Inc., San Clemente, California) following the same procedure as used in experimental tests⁸. TF kinematics along IE, AA and AP axes and TF and PF maximal contact forces are observed and compared for all the configurations. A total number of 98 configurations were investigated.

3. Results

The frequencies, with which deviation from the reference kinematics occurs due to tibial component mal-positioning, patellar mal-positioning and the soft-tissues anatomy, are listed in Tab 1. We made a distinction between three levels of deviation in terms of TF kinematics (2°, 3° and 4° and 2 mm, 3 mm and 4 mm) and TF and PF contact forces (10%, 20% and 30%).

Tab.1 The table shows the frequency [%] of affected configurations, with respect to the total number of analyzed mal-configurations.

	Tibial component	Patellar component	Collateral ligaments
Difference in IE rotation $\geq 2^\circ$	11	1	11
Difference in IE rotation $\geq 3^\circ$	2	1	6
Difference in IE rotation $\geq 4^\circ$	1	1	4
Difference in AA tilting $\geq 2^\circ$	5	0	1
Difference in AA tilting $\geq 3^\circ$	4	0	0
Difference in AA tilting $\geq 4^\circ$	1	0	0
Difference in AP translation ≥ 2 mm	10	0	0
Difference in AP translation ≥ 3 mm	2	0	0
Difference in AP translation ≥ 4 mm	0	0	0
PF contact force $\geq 10\%$	6	12	0
PF contact force $\geq 20\%$	3	6	0
PF contact force $\geq 30\%$	2	3	0
Medial TF contact force $\geq 10\%$	7	7	12
Medial TF contact force $\geq 20\%$	4	2	9
Medial TF contact force $\geq 30\%$	4	0	2
Lateral TF contact force $\geq 10\%$	4	4	14
Lateral TF contact force $\geq 20\%$	1	0	9
Lateral TF contact force $\geq 30\%$	0	0	4

4. Conclusions

In this project the effects of tibial mal-positioning, patellar mal-positioning and soft-tissues anatomies on knee kinematics and kinetics were numerically analyzed and correlated for different TKA designs.

The used model has been validated both for the contact force analysis⁶ and for the kinematics analysis⁹. Deviations in kinematics are usually quite small (smaller than 5° or 4 mm)⁹, thus proportional to the applied changes in alignment, while changes in contact forces can reach much higher values⁶. The same small changes in configuration which lead to the small changes in kinematics, can cause dramatic differences in contact forces.

Results show that surgical errors influence more kinetics outputs (forces) than kinematics, confirming our hypothesis. Therefore, knee forces are fundamental in the analysis of knee performance and patient follow-up. Such information should be integrated in the clinical practice together with knee motion.

5. References

1. Hurwitz DE, Ryalsa AB, Block JA, Andriacchi T P. The knee adduction moment during gait in subjects with knee osteoarthritis is more closely correlated with static alignment than radiographic disease severity, toe out angle and pain. *Journal of orthopaedic research*. 2002; 20:101-107.
2. Papadopoulos K, Noyes J, Jones J G, Thom J M, Stasinopoulos D. Clinical tests for differentiating between patients with and without patellofemoral pain syndrome. *Hong Kong Physiotherapy Journal*. 2013.
3. Acker S, Lia R, Murray H, John P S, Banks S, Mu S, Wyss U, Deluzio K. Accuracy of single-plane fluoroscopy in determining relative position and orientation of total knee replacement components. *Journal of Biomechanics*. 2011;44:784-787.
4. Moewis P, Wolterbeek G, Valstar E, Heller M O, Taylor WR. The quality of bone surfaces may govern the use of model based fluoroscopy in the determination of joint laxity. *Medical Engineering and Physics*. 2012.
5. Broström E W, Esbjörnsson A, von Heideken J, Iversen M. Gait deviations in individuals with inflammatory joint diseases and osteoarthritis and the usage of three dimensional gait analysis. *Best practice & Research Clinical Rheumatology*. 2012;26:409-422.
6. Innocenti B, Pianigiani S, Labey L, Victor J, Bellemans J. Contact forces in several TKA designs during squatting: A numerical sensitivity analysis. *Journal of Biomechanics*. 2011; 44:1573-1581.
7. Victor J, Van Doninck D, Labey L, Innocenti B, Parizel PM, Bellemans J. Reproducibility CT: How precise can bony landmarks be determined on a CT scan of the knee?. *The Knee*. 2009; 16: 358-365.
8. Victor, J ,Van Glabbeek ,F, Vander Sloten, J, Parizel, P M, Somville, J, Bellemans, J, 2009c . An experimental model for kinematic analysis of the knee. *J Bone Joint Surg. Am*. 91, 150-163.
9. Pianigiani S, Chevalier Y, Labey L, Pascale V, Innocenti B. Tibio-femoral kinematics in different total knee arthroplasty designs during a loaded squat: A numerical sensitivity study. *Journal of Biomechanics*. 2012; 45:2315-2323.

METHODS OF ASSESSMENT BIOMECHANICS IN CYCLING: FROM POSTURAL DISORDER TO THE DISEASE

*LN VITTORI, *F. PEGREFFI, *M. PAGANELLI, *G. BELLI, **P. MAIETTA

**School of Pharmacy, Biotechnology and Sport Science; University of Bologna, Bologna, Italy ; ** Department for Life Quality, University of Bologna, Bologna, Italy.*

During leisure time, the bicycle is used a lot as an instrument to keep moving, because of it improves the function of the cardiovascular and pulmonary, blood pressure control and especially because it encourages the development of well-being. While in the sports world is used and studied in all its forms, and from here comes the requirement of a study on the biomechanical evaluation of the cyclist, to improve the quality of the performance and to prevent all the diseases related to incorrect posture on the middle, such as low back, low back pain, neck pain, knee's tendonitis.

Laboratory studies of cycling were launched when it was built the first cycle ergometer in the early 20th century and their development was accompanied by improvements in software for data acquisition and for the consequent data analysis. The evaluation of the athlete includes a complete analysis of the static morphology, joint mobility, and possible paramorphisms or dysmorphism.

The acquisition systems are many, a lot software houses have developed programs able to carry out this function, differing for their functionality.

Idmatch ® is the first patented system in cycling and can be used for the analysis of step, the support and the foot pressure, and the support of the two ischial bones in a sitting position.

Stabylopro is mainly used to highlight the rider's foot support and analyze any imbalances of the foot.

Bikesys is a custom system able to perform the detection of cyclist's pressure on the seat during pedaling.

The main software allows, in a completely non-invasive way, the acquisition in numerical form, the processing and the integrated representation of kinematic and dynamic data related to posture and movement of persons. Bikesys is also used in medical and rehabilitation field for postoperative evaluation or analysis of the results of a training program in sports.

Kinovea is a software for the acquisition and evaluation of movement; it's very valuable to analyze the technique of motion and improve the performance of the sportsman.

Key words: biomechanics analysis, postural disorder, cycling, joint mobility

S5P: Imaging -dosimetry - interaction radiation-matter - thermography

Chairs: Daniel Remondini, Gabriele Guidi

CONTENT-BASED MEDICAL IMAGES RETRIEVAL

IMANE NEDJAR

DETERMINATION OF BIOLOGICAL TISSUE PARAMETERS FROM LINEAR ATTENUATION
COEFFICIENT MEASUREMENTS

PIER LUCA ROSSI

APPLICATION OF PIN DIODES IN RADIO DIAGNOSTIC: IMAGING AND DOSIMETRIC
PROPERTIES

LUCIA ANDREANI

ASYMMETRY ANALYSIS OF BREAST THERMOGRAMS USING MINKOWSKI FEATURES

PRABHA SRINIVASAGAM

SEGMENTATION OF BREAST TISSUES IN INFRARED IMAGES USING FRACTIONAL GAUSSIAN
NOISE MODEL AND LEVEL SETS

SALEM SRINIVASAN SUGANTHI

FEASIBILITY STUDY OF A NECK COLLAR FOR CEREBRAL COOLING

IVAN CORAZZA

CONTENT-BASED MEDICAL IMAGES RETRIEVAL

IMANE NEDJAR

*Biomedical Engineering Laboratory, Tlemcen University
Tlemcen , Algeria
imane.nedjar@yahoo.fr*

SAID MAHMOUDI

*Department of Computer Science, Mons University
Mons, Belgium
said.mahmoudi@umons.ac.be*

MOHAMED AMINE CHIKH

*Biomedical Engineering Laboratory, Tlemcen University
Tlemcen , Algeria
mea_chikh@mail.univ-tlemcen.dz*

Abstract The need for automatic medical images retrieval is now getting more and more attention in the world. Medical image classification is a technique used for assigning a medical image to a class among a number of image categories, and due to its computational complexity this task is one of the major current challenges in the field of content-based image retrieval (CBIR). In this paper a medical image retrieval approach is proposed. This method is composed of two main phases: a pre-processing phase, where a vector of features is extracted from the texture and shape, then a classification process is achieved by using a supervised multi-class classifier based on the support vector machine (SVM). After that a selection process is achieved by using the euclidean distance in order to retrieve the most images similar to a given query.

Keywords— Content-based image retrieval, Medical X-ray image, features extraction, SVM.

1. Related Works

Content-medical based image retrieval (CMBIR) techniques are used for retrieving similar images to a query from large medical databases. In medical X-ray image classification, several schemes and algorithms have been presented in the literature.

In [1] a merging-based hierarchical classifier is proposed. This method use a supervised classification and unsupervised clustering techniques combined to semantic medical X-ray image classification. The proposed algorithm was evaluated on a database composed of 9100 medical X-ray images, and the accuracy rate provided for 17 classes was 94%.

In [2] an algorithm for medical image classification according to visual contents was proposed. This method used a multiple kernel learning (MKL) approach that combine different visual features, and learn the optimal mixing weights for each class adaptively. This method was evaluated on a medical X-ray image dataset composed of 1400 images divided into 14 categories. The accuracy rate produced by using Gabor feature and Modsift with MKL were 96.68%.

In [3] a novel content based medical image retrieval method consisting of combination of deducible and traditional retrieval was proposed. The goal of deducible retrieval was to retrieve the label that a user expects while the aim of traditional retrieval was to retrieve the images with the same label in the database. The deducible retrieval is achieved by using the semi-supervised Semantic Error-Correcting output Codes (SEMI-SECC). This method has given accuracy rate of 84.9%.

In [4] a classification scheme was presented in order to classify medical images into 80 categories describing the imaging modalities and directions. This scheme was evaluated on the basis of 6231 reference images from X-ray images, and 85.5% correctness was obtained by combining global texture features with scaled images.

2. Material And Methods

2.1. Data base

In our experimentation, we have constructed a database by selecting 15 categories from the ImageCLEFmed2005 annotation dataset. This database has been divided into two parts: the first for training (5951 images) and the second for test (671 images). All the images are X-ray images. The images have different sizes before the normalization.

2.2. Medical X-ray image classification

Our search system is composed of two phases:

- *Classification phase*: the goal of this process is to detect the class of the query image; Fig. 1 shows the framework.
- *Selection phase*: in this second step, the system retrieves the 10 more similar images to the query image.

2.2.1. The classification phase

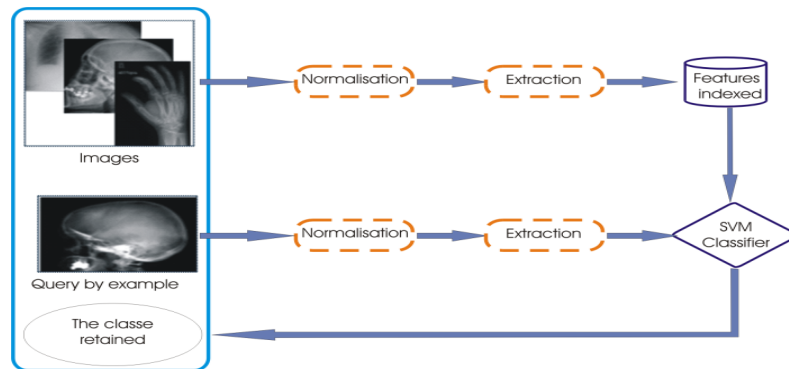


Fig 1. The framework of phase 1.

- *Features extraction and description*
 - **Texture features**: we have tested two global texture features, which are the gray level co-occurrence matrix (GLCM), and the Gabor wavelet transform.
 - **Gabor Wavelet Transform* it defined in equation (1) as follows [5]

$$\psi_{u,v}(z) = \frac{\|K_{u,v}\|^2}{\sigma^2} e^{\left(\frac{\|K_{u,v}\|^2 |z|^2}{2\sigma^2} \right)} \left[e^{ik_{u,v}z} - e^{-\sigma^2/2} \right] \quad (1)$$

Where u and v define the orientation and the scale of the Gabor kernels, and $\|\cdot\|$ denotes the norm operator, and the wave vector K_{uv} is defined as follows:

$$K_{u,v} = K_v e^{i\theta_u} \quad (2)$$

Where $K_v = K_{\max}/f^v$; $\theta_u = \pi u / 8$, $Z=(x,y)$ and K_{\max} is the maximum frequency, and f is the spacing factor between kernels in the frequency domain. We have used $\sigma = 2\pi$, $K_{\max} = \pi/2$, and $f = 2^{1/2}$.

Let $I(x,y)$ be the gray level distribution of an image, the convolution of the image I and a Gabor kernel $\psi_{u,v}$ is defined as follows:

$$O_{u,v} = I(z) * \psi_{u,v}(z) \quad (3)$$

Where $*$ denotes the convolution operator, and $O_{u,v}(z)$ is the convolution result corresponding to the Gabor kernel at orientation u and scale v . Therefore, the set $S \{O_{u,v}(z): u \in \{1, \dots, 5\}, v \in \{1, \dots, 3\}\}$ forms the Gabor wavelet representation of the image $I(z)$.

The energy information of the image $I(x, y)$ can be expressed as follows [6]:

$$E(u, v) = \sum_x \sum_y |O_{u,v}| \quad (4)$$

In this work, we propose to use the mean and the standard deviation as texture features. Suppose that $I(x,y)$ denotes an image of $M \times N$ pixels, $\mu_{uv}(x)$ and $\sigma_{uv}(x)$ denote its mean and standard deviation computed from the scale v and the direction u , respectively, $\mu_{uv}(x)$ and $\sigma_{uv}(x)$ can be computed as follows [6].

$$\mu_{u,v} = E_{u,v} / MN \quad (5)$$

$$\sigma_{u,v} = \sqrt{\frac{\sum_x \sum_y (\psi_{uv}(z) - \mu_{u,v})^2}{MN}} \quad (6)$$

With five orientations and three scales the feature vector includes 15 elements for the means and 15 elements for deviation. Therefore, the feature vector is composed of 30 features.

**Co-occurrence Matrices* the spatial gray level co-occurrence estimate image properties related to second-order statistics. Proposed by Haralick [7] the gray level co-occurrence matrices (GLCM) is a common method for texture feature extraction which have become one of the most well-known and widely used.

In this paper, we propose to use the following features extracted from the gray level co-occurrence matrix: contrast, entropy, sum of squares (variance), correlation [7].

And the energy, autocorrelation, dissimilarity, cluster shade and cluster prominence and homogeneity proposed in [8].

We have calculated the gray level co-occurrence matrix for four different directions ($\theta \in \{0^\circ, 90^\circ, 45^\circ, \text{ and } 135^\circ\}$) and the distance $d=1$. Therefore, the feature vector includes 40 elements.

- **Shape features:** as shape features, we propose to use the two features the centroid and area of the shape; feature vector includes 3 elements corresponding to x and y coordinates of the centroid and the area value.

***Preprocessing**

We have used the active contours model proposed in [9]. This model can detect the objects whose boundaries are not necessarily defined by gradient or with very smooth boundaries. This model is based on Mumford–Shah segmentation techniques and the level set method [9]. The objective of this process is to minimize an energy which can be seen as a particular case of the minimal partition problem. After applying snakes, we extract the area and the centroid from object.

- **Classification**

The Support Vector Machine (SVM) active learning is one popular and successful technique for relevance feedback in content-based image retrieval (CBIR) [10]. SVM method is well suited for the treatment of high dimension data such as images, so we have chosen SVM multiclass in our application; also we have used the Radial Basis Function (RBF) Kernel, RBF is nothing more than a low-band pass filter, well known in signal processing as a tool to smooth images¹.

- **Discussion and analysis**

From the results of the first phase, we found that combining GLCM features and shape features give the best performance among all other possible features combinations. The table 1 gives the classification accuracy.

TABLE 1. THE CLASSIFICATION RATES FOR EACH DESCRIPTOR

Number of category	Descriptor n°1 <i>Co-occurrence matrix + Shape feature (length is 43)</i>	Descriptor n°2 <i>Gabor +Shape feature (length is 33)</i>	Descriptor n°3 <i>Combined features GLCM + Gabor+ Shape (length is 73)</i>
	<i>Accuracy%</i>		
15	79.4337%	39.0462%	47.2429%

^a http://charlesmartin14.wordpress.com/2012/02/06/kernels_part_1/

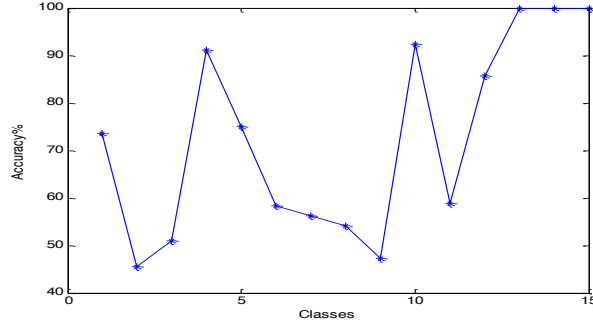


Fig 2. Classification results of 15 classes for descriptor n°1.

From the results obtained and presented in Figure5, we can see that:

- 53.33% of the classes have a classification rate > 70%.
- 33.33% of classes have a classification rate > 50%.
- 13.33% of the classes having a classification rate < 50%.
- Note that the class 2 has the lowest classification: 45%.
- The highest rate was achieved for class n°: 13, 14, 15 100%.

2.2.2. The selection phase

After the classification process that consists of assigning a specific class to the query, we achieve a selection phase by using the euclidian distance measure (EDM) in order to retrieve the 10 more similar images to the query image.

$$Dist(Im_{req}, Im_{cur}) = \left(\sum_{k=1}^K |V(k)_{imreq} - V(k)_{imcur}|^2 \right)^{1/2} \quad (7)$$

$imreq$ is the query image and $imcur$ is the current image. $V(k)_{imreq}$ the descriptor vector of the query image.

$V(k)_{imcur}$ the descriptor vector of the current image.

The results of this search phase return the similar radiographs acquired from the same region of the same patient within the same orientation but with different radiation [4].

3. Conclusion

In this paper, a knowledge extraction and classification approach applied to medical X-ray image was presented. We have used 15 categories of images extracted from the ImageClef 2005 annotation dataset. The experimental results showed the efficiency of a descriptor vector with 43 features, containing just the

features of the co-occurrence matrix (40 features) and of shape (3 features). In our future work, we plan to use more image features, and to extend the medical image dataset by adding more categories, and introduce an automatic annotation process.

References

- [1] H.Pourghassem and H.Ghassemian, "Content-based medical image classification using a new hierarchical merging scheme," *Computerized Medical Imaging and Graphics*, vol. 32, pp. 651–661, 2008.
- [2] W.Hong, Z.Hao, and L. Chao, "Medical Image Classification with Multiple Kernel Learning.," in *ICIMCS'10*, Harbin, China., December 30-31, 2010, pp. 189-192.
- [3] J.Yao, Z.Zhang, S.Antani, R.Long, and G.Thoma, "Automatic medical image annotation and retrieval," *Neurocomputing elsevier*, vol. 71, pp. 2012–2022, 2008.
- [4] TM.Lehmann et al., "Automatic categorization of medical images for content-based retrieval and data mining," *Computerized Medical Imaging and Graphics*, vol. 29, no. 2, pp. 143-155, March 2005.
- [5] C.Liu and H.Wechsler, "Gabor Feature Based Classification Using the Enhanced Fisher Linear Discriminant Model for Face Recognition," *IEEE Transactions on Image Processing* , vol. 11, no. 4, pp. 467-476, 2002.
- [6] G.Zhang, ZM.Ma, and L. Deng, "Texture Feature Extraction and Description Using Fuzzy Set of Main Dominant Directions of Variable Scales in Content-Based Medical Image Retrieval," in *SAC '08 Proceedings of the ACM symposium on Applied computing*, Fortaleza, Ceará, Brazil, March 16-20, 2008, pp. 1760-1761.
- [7] R.M.Haralick, k. Shanmugam, and I. Dinstein, "Textural Features for Image Classification," *IEEE Transaction on Systems ,Man and Cybernetics*, vol. 3, no. 6, pp. 610-621, November 1973.
- [8] L.K.Soh and C.Tsatsoulis, "Texture Analysis of SAR Sea Ice Imagery Using Gray Level Co-Occurrence Matrices," *IEEE transactions on Geoscience and Remote Sensing*, vol. 37, no. 2, MARCH 1999.
- [9] F.T.Chan and L. A. Vese, "Active Contours Without Edges," *IEEE Transactions on Image Processing* , vol. 10, no. 2, FEBRUARY 2001.
- [10] H.HOI, R.JIN, J.ZHU, and R.LYU, "Semisupervised SVM Batch Mode Active Learning with Applications to Image Retrieval," *ACM Transactions on Information Systems*, vol. 27, no. 3, pp. 1-16, May 2009.
- [11] M.Tuceryan and A K. Jain, *"The Handbook of Pattern Recognition and Computer Vision"*, 2nd ed., P. S. P. Wang (eds), pp. 207-248, World Scientific Publishing Co, 1998.

DETERMINATION OF BIOLOGICAL TISSUE PARAMETERS FROM LINEAR ATTENUATION COEFFICIENT MEASUREMENTS

^{1,2}PIER LUCA ROSSI, ¹SIMONE MASETTI, ^{1,2}NICO LANCONELLI, ³DAVID BIANCHINI, ³IVAN CORAZZA,
²ALESSANDRO LOMBI, ³ROMANO ZANNOLI, ^{1,2}GIUSEPPE BALDAZZI

¹*University of Bologna, Physics and Astronomy Dept. - DIFA, Viale Berti-Pichat 6/2, Bologna, Italy*

²*INFN Bologna, Viale Berti Pichat 6/2, Bologna, Italy*

³*University of Bologna, Experimental, Diagnostic and Specialty Medicine Dept. – DIMES, Via Massarenti 9, Bologna, Italy*

The possibility to classify pathological tissues – for example tumor neo-angiogenesis pattern-, using new X-ray imaging technique (such as Quasi-Monochromatic Multi-Energy X-ray Imaging) is strictly related to an accurate knowledge of their X-ray absorption coefficients $\mu(E)$.

Unfortunately, tissues $\mu(E)$ values are studied and known only for a little number of pathologies and are typically obtained via mathematical analysis, such as Monte Carlo simulations.

So, an experimental study of the tissue attenuation properties was started in order to investigate, define and classify not only different organ tissues, but also parameters that probably exalt differences between normal and neoplastic tissues.

In particular, X-ray attenuation curves of biological tissues are measured with an experimental setup based on a Bragg monochromator - to produce quasi monochromatic X-ray beams in the range 10-90 keV - and a CdTe detector to collect attenuated X-ray spectra.

To investigate tissues characteristics, different analysis methods are implemented, starting from algorithms that can extract chemical-physical information from X-ray absorption measurements, such as effective atomic number and electron density.

Our results are then compared with previously published values for normal (both experimental and theoretical) and carcinoma tissues, to test the potential usage of the X-ray characterization and classification between pathological and normal tissues.

Keyword: linear attenuation coefficient, classification, Multi-Energy X-ray Imaging

APPLICATION OF PIN DIODES IN RADIO DIAGNOSTIC: IMAGING AND DOSIMETRIC PROPERTIES

LUCIA ANDREANI

*Department of Physics and Astronomy, University of Bologna,
Viale Berti-Pichat 6/2, 40127 Bologna, Italy
INFN, Bologna Section,
Viale Berti Pichat 6/2, 40127 Bologna, Italy
lucia.andreani4@unibo.it*

MARCO BONTEMPI

*Laboratorio NaBi, Istituto Ortopedico Rizzoli,
via di Barbiano 1/10, 40136, Bologna, Italy
m.bontempi@biomec.ior.it*

PIER LUCA ROSSI

*Department of Physics and Astronomy, University of Bologna,
Viale Berti-Pichat 6/2, 40127 Bologna, Italy
INFN, Bologna Section,
Viale Berti Pichat 6/2, 40127 Bologna, Italy
pierluca.rossi@unibo.it*

LUIGI PIO RIGNANESE

*Department of Physics and Astronomy, University of Bologna,
Viale Berti-Pichat 6/2, 40127 Bologna, Italy
luigipio.rignanese@studio.unibo.it*

GIUSEPPE BALDAZZI

*Department of Physics and Astronomy, University of Bologna,
Viale Berti-Pichat 6/2, 40127 Bologna, Italy
INFN, Bologna Section,
Viale Berti Pichat 6/2, 40127 Bologna, Italy
giuseppe.baldazzi@unibo.it*

Abstract

Amorphous Si-PIN diodes are commonly used as imaging X-ray detectors in conventional radiology and showed interesting applications in detector research. The responses of a bare Si-PIN diode and a Si-PIN diode + CsI(Tl) scintillator to the measurement of gray levels and X-ray total air KERMA are compared and presented. The goal is the possibility to calibrate selected pixels of an image detector in dose. Both detector outputs were calibrated using a reference image detector (HAMAMATSU PHOTONICS K.K. C10900D) in order to analyze and discuss the gray level response and the energy dependence of the detectors at a different tube voltages (from 50 kVp to 100 kVp) and anode currents (from 1.0 to 7.0 mA). The diode outputs were then calibrated in dose using a secondary reference standard (UNFORS Mult-O-Meter mod. 510), in order to use the same devices for the imaging and the calculation of the dose administered to the patients.

Keywords: PIN diodes, X-rays, CsI(Tl).

Summary

Si-PIN diode and CsI(Tl) scintillator are commonly used as imaging X-ray detectors in conventional radiology and showed interesting applications in detector research.^{1,2,3,4,5,6,7} The possibility to calibrate selected pixels of an image detector in dose was investigated, in order to use the same device for the two fundamental aspects of the clinical procedure: the imaging and the dose evaluation.

Two small silicon PIN diodes of $2.7 \times 2.7 \text{ mm}^2$ were used, one of them was coupled to a 5 mm thick CsI(Tl) crystal. A very thin layer of transparent epoxy resin was used to attach the polished CsI(Tl) to the

PIN diode. These diodes were selected because of their low dark current @ 2 nA. Detector outputs (mV) were calibrated, in order to analyze and discuss both the gray level and the dose response of the detectors at a different tube voltages and anode currents.

In order to analyze the use of Silicon PIN diode – with or without CsI(Tl) scintillator coupled – as image detector and real-time dosimeter during radiological procedure, the diode outputs (mV) were initially calibrated in gray level using a reference image detector (HAMAMATSU PHOTONICS K.K. C10900D, JAPAN). Pictures of the detector prototypes are shown in figure 1, in both configurations.

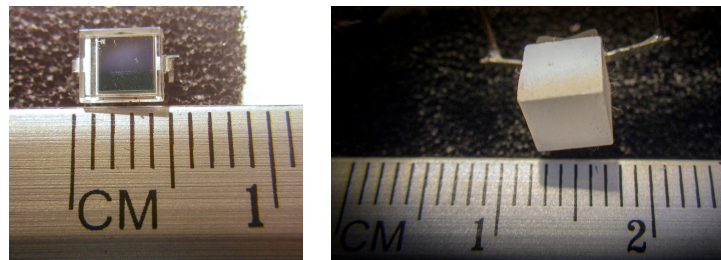


Fig. 1. An image of the Si-PIN diode (left) and the Si-PIN + CsI(Tl) scintillator detector (right).

The X-ray facility is represented by an X-ray radiological tube. The characteristics are summarized in Table 1. This X-ray tube is very common and it was considered a good device to calibrate and test the Si-PIN diode configuration. All the internal filters were removed - so the inherent filtration was the only type of filtration present.

Table 1. Characteristics of the X-ray tube utilized.

Model	XRT-160, liquid cooled
Generator	XRG120IT-.501
Manufacturer	Bosello High Technology srl Gallarate (VA), Italy
Total filtration	2.6 mm Al
Nominal focal spot size	0.8 mm
Current range	Up to 10 mA
Tension range	20 – 120 kVp

The aim of the first sets of measurements was substantially the comparison of the detector responses for the evaluation of the gray levels. Semiconductor PIN diodes are, in fact, very sensitive to visible or infrared light; the detection efficiency is approximately 100% for photons of few keV, decreasing to approximately 2% at 60 keV for a 300 μm thick PIN diode.⁸ The CsI(Tl) inorganic scintillator increases the detector efficiency in the energy range of interest⁹ but is more bulky for in vivo applications. The diode was mounted on a custom-made electronic readout implementing a classical transimpedance amplifier circuit (figure 2) to read the X-ray output and in a charge sensitive configuration to extend the dynamical range. The same dedicated circuit was used for both detectors.

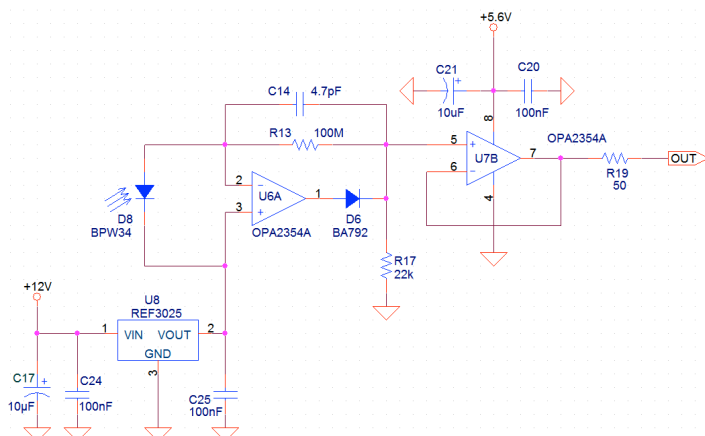


Fig. 2. Schematic of transimpedance detector readout

To obtain an accurate characterization, the tension waveform was measured using a current preamplifier applied to the diode and the signal was digitized using a data acquisition device NI USB-6366 (National Instruments Inc, Austin, TX, USA). The calibration measurements of the Si-PIN and the Si-PIN + CsI(Tl) were performed at a different tube voltages (from 50 kVp to 100 kVp) and anode currents (from 1.0 to 7.0 mA). The diode response (mV*s) was calculated as the area under the measured waveform. Data were then normalized to a distance of 1m from the focal spot size. The calibration between the gray level and the diode output (mV*s) was calculated. The plots were fitted with the least square linear method and the uncertainties regarding the calibration parameters were evaluated.¹⁰ Moreover, a second sets of measurements were performed under the same radiological conditions. The aim was substantially the comparison of the detectors efficiency for the evaluation of the air KERMA, in order to use the same devices as real-time dosimeter during radiological procedure. The total air KERMA was also acquired using a multimeter (UNFORS Mult-O-Meter mod. 510), calibrated with an ISO X-ray series to obtain a traceable secondary standard. The calibration was performed by comparing the detector with a primary detector standard at the Calibration Centre LAT n. 065, accredited by ACCREDIA, appointed by the Italian Government as the National Accreditation Body, in compliance with International and European Standards. We will present and discuss the results obtained.

References

1. A.R. Cowen, A.G. Davies, M.U. Sivananthan, The design and the imaging characteristics of dynamic, solid state, flat panel x-ray image, detectors for digital fluoroscopy and fluorography, *Clinical radiology* 63, 1073-1085 (2008).
2. C.C. Bueno et al., Response of PIN diodes as room temperature photon detectors, *Applied Radiation and Isotopes* 61, 1343-1347 (2004).
3. F.J. Ramirez-Jiménez et al., Application of PIN diodes in Physics Research, *AIP Conference Proceedings* 857, 395-406 (2006).
4. F.J. Ramirez-Jiménez et al., Considerations on the measurement of practical peak voltage in diagnostic radiology, *The British Journal of Radiology* 77, 745-750 (2004).
5. F. Rego and L. Peralta, Si-PIN photodiode readout for a scintillating optical fiber dosimeter, *Radiation measurements* 47, 947-950 (2012).

6. M. Hoheisel et al., Amorphous silicon X-ray detectors, *Journal of Non-Crystalline Solids* 227 - 230 p. 1300 – 1305 (1998).
7. M. Marrs et al., Flexible amorphous silicon PIN diode x-ray detector, *Proc. SPIE 8730, Flexible Electronics 87300C* (May 29, 2013).
8. G.F. Knoll, *Radiation Detection and Measurement*, fourth ed., Wiley, New York (2010).
9. I. Valais et al., A systematic study of the performance of the CsI: Tl single-crystal scintillator under X-ray excitation, *Nuclear Instruments and Methods in Physics Research A*(571), 343-345 (2007).
10. J.R. Taylor, *An Introduction to Error Analysis: The Study of Uncertainties in Physical Measurements*, University Science Books, Sausalito (1996).

ASYMMETRY ANALYSIS OF BREAST THERMOGRAMS USING MINKOWSKI FEATURES

S. PRABHA, C. M. SUJATHA

*Department of ECE, CEG Campus, Anna Univeersity
Chennai - 600025, India. Email: harprabha@gmail.com*

S. RAMAKRISHNAN

*Non-Invasive Imaging and Diagnostics Laboratory
Biomedical Engineering Group, Department of Applied Mechanics
Indian Institute of Technology Madras, India
Email: sramki@iitm.ac.in*

Breast cancer diagnosis using thermograms entirely depends on the identification of asymmetrical thermal patterns. In this work, topology based Minkowski features are used for the analysis of breast tissues which include normal and pathological conditions of breast tissues. Breast tissues are extracted from background tissue by multiplying ground truth masks with raw images. The corresponding left and right breasts are delineated. The separated regions are grouped into normal and abnormal tissues. Minkowski features such as area, perimeter and Euler number are extracted from the segmented breast tissues. Results show that this topology based image analysis method is capable of differentiating the change in structural information due to varied metabolic conditions. Minkowski features such as area provide better discrimination of normal and abnormal subjects. It appears that these features could be used efficiently to identify normal and abnormal tissues and hence, improves the diagnostic relevance of breast thermography in early detection of breast cancer.

Key words: Biceps Breast thermogram; Minkowski functional; Area; Asymmetry analysis

1. Introduction

Breast thermography is a functional imaging technique which records and displays thermal patterns emitted by human skin.¹ Statistics on incidence of breast cancer among women reveals that there is a need for early detection of the disease. Mammography which is the current gold standard technique has high false positive rate and less sensitivity in dense breast tissue. Thermography being non-invasive, non-contact and radiation free procedure is reported as an adjunct tool due to its high sensitivity and specificity.² Asymmetry in thermal pattern is one of the contributing factors in the identification of abnormality. Statistical features³, histogram based features⁴ and fractal measures⁵ were found to be useful in identification of pathological conditions of breast tissues. There is a need for an efficient feature extraction technique that could effectively analyze the structural changes in an image. Minkowski functionals (MFs) capture structural and topological properties of gray level pattern using different threshold levels. Abnormality detection is analyzed using Minkowski functional in several medical application such as bone and breast.^{6,7} In this work, an attempt has been made to analyze structural and topology changes in breast thermography using Minkowski functionals.

2. Methods

Breast thermal images for this study are obtained from online database of the project PROENG. FLIR ThermoCam S45 camera was used to capture images at University Hospital of Federal University of Pernambuco. The acquisition procedure and protocol details have already been reported elsewhere.⁸ 42 breast images are considered for this analysis.

2.1 Minkowski Functionals

Minkowski functionals are computed by binarizing the segmented breast regions through the application of several threshold levels lying between minimum and maximum intensity limits. The following three MFs are calculated as

$$\text{Area} = \text{Number of white pixels} \quad (1)$$

$$\text{Perimeter} = 4 * \text{Area} + 2 * \text{Number of open edges} \quad (2)$$

$$\text{Euler number} = \text{Area} - \text{Number of open edges} + \text{Number of open vertices} \quad (3)$$

The Minkowski area and perimeter represents the structural changes in the image and Euler number represents the connectivity in the image which accounts for the topology changes. The threshold levels of 0-255 values are divided into 10 windows of equal width. The different windows considered for this analysis are denoted as W1-W10.

3. Results and Discussion

A typical gray scale breast thermogram is shown in Fig. 1(a). This thermogram depicts asymmetry pattern which is due to the presence of carcinoma condition in the left breast. Fig. 1(b) and (c) show the ground truth mask and the segmented breast tissues. Right and left regions are separated using midpoint of inframammary folds and corresponding results are shown in Fig. 2 (a) and (b). The right breast region is normal and left breast region is carcinoma condition.



Fig. 1. (a) Typical breast thermogram (b) Ground truth mask (c) Segmented breast tissues

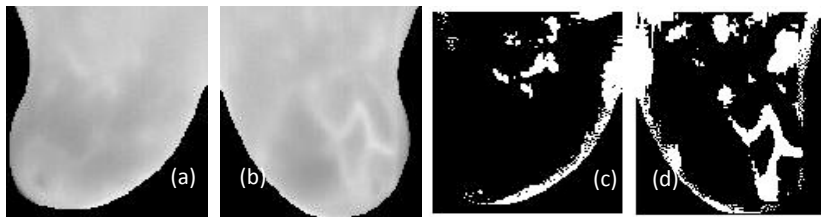


Fig. 2. (a) Delineated right breast tissue and (b) Left breast tissue (c) & (d) Binarization of breast tissue (a) & (b) using threshold level of Minkowski functional

MF	Normal (N = 14)	Abnormal (N = 28)		
		Carcinoma	Nodule	Fiberadenoma
	Mean \pm Stdev	Mean \pm Stdev	Mean \pm Stdev	Mean \pm Stdev

Perimeter	4.41 ± 1.754	4.66 ± 1.165	4.39 ± 1.72	4.36 ± 2.03
Area	4.46 ± 1.791	5.34 ± 1.109	4.66 ± 1.99	4.55 ± 2.38
Euler number	6.51 ± 1.295	6.42 ± 1.048	6.39 ± 1.31	6.37 ± 1.15

Table 1. Mean and standard deviation of Minkowski Features

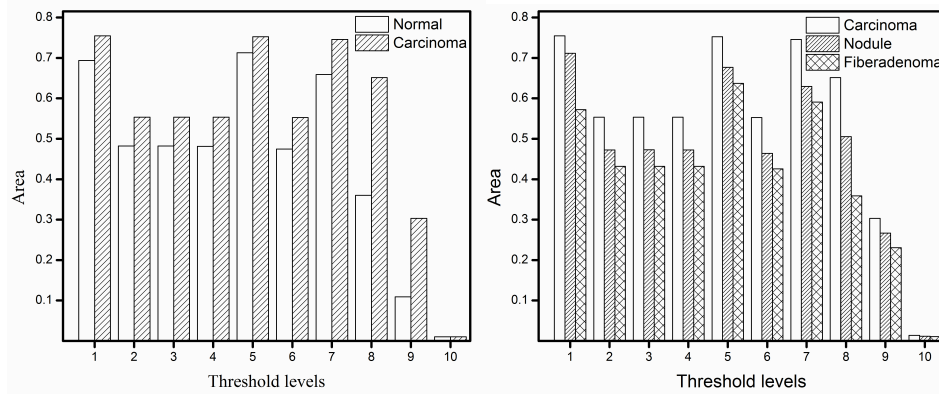


Fig. 3. Minkowski functional area of segmented breast tissue with different threshold levels

Binarization of segmented breast tissues is performed through the application of different threshold levels lying between minimum and maximum intensity limits. Fig. 2(c) and (d) show binarization of segmented breast tissues of 8th window in which minimum and maximum gray level intensity values are 178 and 204.

Table.1 shows mean and standard deviation of Minkowski Features. The obtained mean value is the summation of normalized mean value at all different threshold levels. The mean values of Minkowski features such as perimeter and area are high for carcinoma subjects since thresholded blood vessel area (hot spot area) is high in abnormal regions compared to normal region (shown in Fig. 2 (c) & (d)). The mean value of Euler number is low for carcinoma subjects which may be due to structural changes associated in pathology condition.

Fig. 3 shows Minkowski functional area of 10 increasing threshold levels throughout the whole gray level spectrum. T_{test} is performed in each window. It is found that among these windows, W8 shows discriminative potential to bring out the asymmetry patterns present in the image. These chosen window provides distinct variation between normal and abnormal conditions with high statistical significance.

4. Conclusion

In this work, an attempt is made to analyze the breast infrared images using Minkowski Features. For this study, normal and abnormal conditions such as carcinoma, fibro adenoma and nodule are considered. Features such as perimeter, area and Euler number are extracted. The obtained results are analyzed for normal and various abnormal conditions. It is observed that the Minkowski functionals show the structural changes due to different vascularized nature of the various tissues. Further, the area feature

seems to be highly significant ($p<0.005$) in differentiating normal and carcinoma tissues. Hence, it appears that the Minkowski functionals can be used effectively in asymmetry analysis of breast thermograms in early detection of breast cancer.

Reference

1. Ng E, Sudharsan N, Numerical computation as a tool to aid thermographic inter-pretation, *International Journal of Medical Engineering and Technology*, **25**:53-60, 2001.
2. Ng EYK, A review of thermography as promising non-invasive detection modality for breast tumor, *International Journal of Thermal Sciences*, **48**: 849-859, 2009.
3. Lipari CA, Head J, Advanced infrared image processing for breast cancer risk assessment, *Proceedings for 19th International Conference of the IEEE Engineering in Medicine and Biology Society*, **2**:673-676, 1997.
4. Kuruganti PT, Qi H, Asymmetry analysis in breast cancer detection using thermal infrared images, *Proceedings of Second Joint EMBS/BMES Conference*, **2**: 1129–1130, 2002.
5. Serrano RC, Ulysses J, Ribeiro S, Lima, RCF, Using hurst coefficient and Lacunarity for diagnosis of breast diseases considering thermal images, *Proceedings of 17th International Conference on Systems, Signals and Image Processing*, **4**:550-553, 2010.
6. Boehm HF et al. Differentiation between post-menopausal women with and without hip fractures: enhanced evaluation of clinical DXA by topological analysis of the mineral distribution in the scan images, *Osteoporosis international*, **18**:779-787, 2007.
7. Nagarajan, Mahesh B et al, Classification of small lesions in dynamic breast MRI: eliminating the need for precise lesion segmentation through spatio-temporal analysis of contrast enhancement, *Machine vision and applications*, **24**:1371-1381, 2013.
8. NBCF, National Breast Cancer Foundation, Inc., 2010. Available: <http://visual.ic.uff.br/proeng/>

SEGMENTATION OF BREAST TISSUES IN INFRARED IMAGES USING FRACTIONAL GAUSSIAN NOISE MODEL AND LEVEL SETS

S. S. SUGANTHI

*Non-Invasive Imaging and Diagnostics Laboratory
Biomedical Engineering Group, Department of Applied Mechanics
Indian Institute of Technology Madras, India
Email: suganthiss@gmail.com*

LUCA SABA

*Department of Radiology
O. U Cagliari – Polo di Monserrato,
S 554 Monserrato (CA), Italy
Email: lucasaba@tiscali.it*

S. RAMAKRISHNAN

*Non-Invasive Imaging and Diagnostics Laboratory
Biomedical Engineering Group, Department of Applied Mechanics
Indian Institute of Technology Madras, India
Email: sramki@iitm.ac.in*

JASJIT S. SURI

*Point of Care Devices, Global Biomedical Technologies, Inc., Roseville, CA, USA and
AtheroPoint™ LLC, Roseville, CA, USA and
Department of Electrical Engineering, Idaho State University, ID, USA
Email: jasjit.suri@atheropoint.com*

In this work, an attempt is made to segment the breast tissues using the modified level set method after performing denoising and contrast enhancement of infrared images. Phase information is used as an edge map for evolution of the level set function. The segmented results are compared and validated against ground truth images using similarity measures. Further it is also compared with the performance of reported segmentation methods. Results show that the unified approach of phase map integration into level sets is able to drive the level set function towards the true boundaries. The segmented and ground truth areas show a high correlation of 0.98. Compared to the intensity gradient based edge map, the segmented result of the proposed method seems to be significantly consistent among all overlap measures irrespective of inter person's observations. The results show 2% improvement in the segmentation accuracy and specificity when compared to the existing segmentation methods. The accurate segmentation of breast tissues helps to improve the performance of asymmetry analysis in the automated diagnosis of early breast abnormalities using medical thermography.

Key words: Breast infrared images; Denoising; Contrast enhancement; Modified level sets; Segmentation

1. Introduction

Medical thermography measures infrared radiations that are constantly emitted from skin surface and converts that into electrical impulses that are visualized as image called as thermogram. It is non contact, non invasive, radiation free, painless, and low cost.¹ It is most widely accepted as an adjunct tool for breast cancer diagnosis.² Due to the inherent limitations of medical thermal images, the accurate and symmetrical segmentation of the breast tissues remains challenging.³ The complexity involves in the detection of lower breast boundaries and infra mammary folds. Thermal images are low in contrast and

signal to noise ratio.^{1,4} In this work, a unified approach is used in which the phase map of denoised and contrast enhanced images are integrated into the modified level set method. A clinical score is obtained from a radiologist to validate the improvement in the edge enhancement. The segmented results are compared against ground truth images and validated by computing similarity measures.

2. Methods

Images are obtained from online database PROENG (<http://visual.ic.uff.br/>).⁵ Total 72 images are considered. Anscombe transform is used to convert the Poisson distributed data to Gaussian.⁶ A wavelet based soft thresholding is performed in which the coefficients are modeled as fractional Gaussian noise.⁷ Denoised images are generated by applying inverse wavelet transform and Anscombe transform. The denoised images are subjected to contrast-limited adaptive histogram equalization to improve the local contrast of the image. A modified level set method is adopted to segment the breast tissues.⁸ Phase map of denoised and enhanced images are used as edge indicator in order to avoid the spurious and false edges during curve evolution. The corresponding the phase based modified level set evolution equation can be written as

$$\frac{\partial \varphi}{\partial t} = \tau \left\{ \mu g_{\text{new}} [\nabla^2 \varphi - \text{div} \left(\frac{\nabla \varphi}{|\nabla \varphi|} \right)] + v g_{\text{new}} \delta_\varepsilon(\varphi) \right\} \quad (1)$$

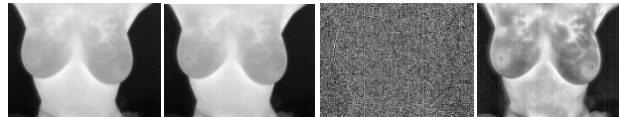
where φ is the manual initial contour, μ , τ and v are constants, g_{new} is the new phase based edge indicator function and is given as⁹

$$g_{\text{new}} = \frac{\sum_o (W_o(x)(E_o(x) - T_o))}{\sum_o \sum_n (A_{no}(x)) + \text{eps}} \quad (2)$$

where 'o' defines the orientation, 'E' is the energy, 'W' is the weighting function, T_o is the noise threshold, A_{no} are the amplitude of frequency components and eps is a small constant. The segmented results are compared and validated against ground truth images using similarity measures. The performance of proposed segmentation framework is also compared against intensity based level set method and segmentation methods based on Cubic Spline Method (CSM)¹⁰ and Quadratic B spline Method (QBM)¹¹.

3. Results and Discussion

A representative gray scale breast thermal image is shown in Fig. 1 (a). The denoised and the corresponding noise image are shown in Fig. 1 (b) and 1 (c). The denoised image is observed to be smoothed and preserved with edges. The contrast enhanced image is shown in Fig. 1(d). The breast and background tissues are distinguishable particularly inner breast regions when compared to the raw image. The figure of merit calculated from the obtained clinical scores are found to be 8 % higher for contrast enhanced images and 3 % for denoised images compared to raw images.



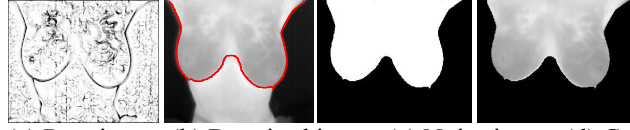


Fig. 2 Representative (a) Raw image (b) Denoised image (c) Noise image (d) Contrast enhanced image (e) Phase map (f) Initial contour (g) Segmented mask and (h) Segmented image

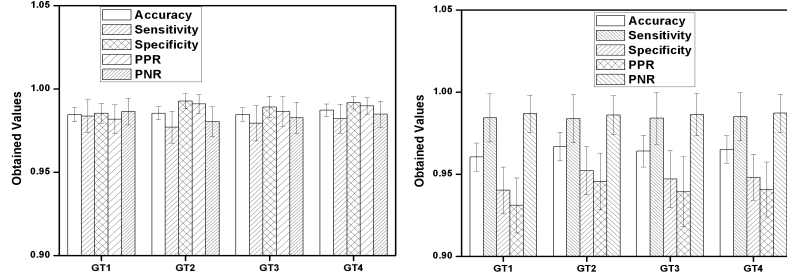


Fig. 2 Average variation in similarity measures using (a) Phase edge map and (b) Intensity edge map

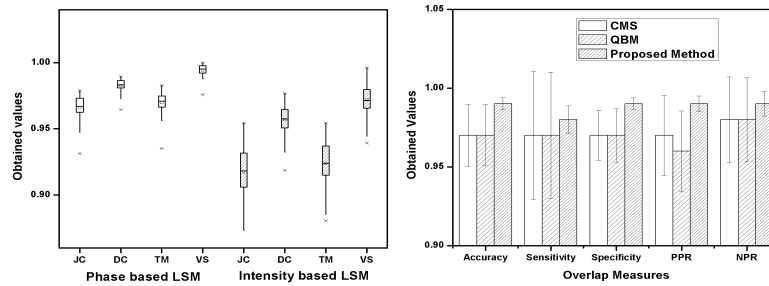


Fig. 3 (a) Average variation in overlap measures (b) Comparison of different segmentation methods

The phase map that is used to evolve the initial contour is shown in Fig. 1 (e). The thin and continuous edges are observed near lower breast boundaries and infra mammary folds. The final evolved contour is shown in Fig. 1 (f). The generated segmented mask and segmented image are shown in Fig. 1 (g) and 1 (h). High correlation of 0.98 is observed with the calculated segmented and ground truth areas.

Figure 2 shows that the performance of proposed segmentation framework is consistent with all measures when compared to segmentation results using intensity edge map.

Figure 3 (a) shows that the volume similarity results in the maximum (0.99) overlap with the ground truth images using the proposed segmentation framework. Also, dice index gives maximum difference of 6% improvement using phase map. The performance of intensity edge map seems to be distributed sparsely. Figure 3 (b) shows consistent performance improvement of a maximum of 2 % in terms of accuracy and specificity using proposed method.

4. Conclusion

In this work, breast tissues in thermal images are extracted using a pipeline approach integrating denoising, edge enhancement and phase map into the modified level set framework. The segmented results validated against ground truth images and are compared against the conventional level set, CSM

and QBM methods. The results show that the proposed method is able to delineate the breast tissues appropriately. On average, the segmented areas are found to be highly correlated (0.98) with the all ground truth images. The sensitivity measure do not show much improvement against conventional method which may be due to the over segmentation. But noticeable improvement is observed with Jaccard and Dice measure between the proposed and conventional LSM. Hence, the proposed segmentation method appears to be helpful in improving the clinical relevance of medical thermography in the early diagnosis of breast pathologies.

Reference

1. Minikina W, Dudzik S, *Infrared thermography, Error and Uncertainties*, 1st edition. A John Wiley and Sons Ltd. Publication, 2009, ch. 2.
2. Ng E Y K, A review of thermography as promising non-invasive detection modality for breast tumor, *Int J Therm Sci.*, **48**:849-859, 2009.
3. Borchardt T B, Conci A, Lima R C F, Resmini R, Sanchez A, Breast thermography from an image processing viewpoint: A survey, *Signal Process.*, **93**:2785–2803, 2013.
4. Zhou Q, Li Z, Aggarwal J K, Boundary extraction in thermal images by edge map, *Pro. of the 2004 ACM symposium on Applied computing*. ACM, 2004.
5. PROENG (2012). Image processing and image analyses applied to mastology. <http://visual.ic.uff.br/en/proeng/>
6. Kafieh R, Rabbani H, Wavelet- based medical infrared image noise reduction using local model for signal and noise, *IEEE Stats Signal Process Workshop*, pp.549 – 552, 2011.
7. Gonzaga A, Wavelet-based algorithm for attenuation of spatially correlated noise, *Pro. of the 10th WSEAS Int. Conf. on Multimedia Systems & Signal Processing*, pp. 31-34, 2010.
8. Kuo H C, Giger M L, Reiser I, Boone J M, Lindfors K K, Yang K, Edwards A, Level Set Segmentation of Breast Masses in Contrast-Enhanced Dedicated Breast CT and Evaluation of Stopping Criteria. *J of digit imaging*, 1-11, 2013.
9. Kovess P, Image Features from Phase Congruency, *J of Comput Vis Res*, 1:1-26, 1999.
10. Motta L, Conci A, Lima R, Diniz E, Luís S, Automatic segmentation on thermograms in order to aid diagnosis and 2D modeling, *Pro. of 10th Workshop em Informática Médica*, pp.1610-1619, 2010.
11. Marques R S, Segmentação automática das mamas em imagens térmicas, M.S. dissertation, IC-UFF, 2012.

FEASIBILITY STUDY OF A NECK COLLAR FOR CEREBRAL COOLING

IVAN CORAZZA, FRANCESCA CAPORUSSO, ENRICO GIULIANI and ROMANO ZANNOLI

*Experimental, Diagnostic and Specialty Medicine Dept., University of Bologna
Via Massarenti, 9, 40138 Bologna, Italy
ivan.corazza@unibo.it

Hypothermia is an important neuro-protective strategy for patients with acute brain damage following traumatic brain injury, stroke or sudden cardiac death. Nowadays, cooling therapy is performed inside the intensive care units with non-invasive systems applied to the body and head surface or invasively through cooling catheters inserted in the femoral vein. Full body cooling presents criticism still unresolved and a therapy localized in the brain is more effective. External systems (i.e. cool helmets) have a very low efficiency due to the need to overstep the cranial cap. For this reason we tested the feasibility to reduce the temperature of brain tissues by cooling the blood inside carotid and cervical artery through the neck. A simple mathematical model of heat transfer between neck surface, tissue, blood in the carotid and cervical arteries and then brain was studied and then in-vitro simulated. Cooling was performed with peltier cells opportunely conditioned. Results demonstrate the possibility to reduce the temperature of the brain of 2°C in about 50 minutes. Temperature's decrease and process duration fit good together with actual first aid times and medical procedures. Moreover, an earlier intervention makes it faster the cooling transfer administered in the intensive units.

Keywords: stroke, hypothermia, carotid arteries

1. Introduction

Hypothermia represents a gold standard in intensive care units to improve the neurological outcome of patients after cardiac arrest. Its benefits are related to the slowing of cerebral metabolism^{1,2} and the reduction of apoptosis^{3,4}; the increased stability of cellular membrane and the reduction of intracranial pressure^{5,6}. Actually, tissue cooling is performed both invasively and not. The first technique is based on the insertion of a catheter in femoral vein and the continuous injection of a cold saline solution. Despite this technique is very efficient and decrease the temperature of the full body, it could lead to adverse events like bleeding, infection and deep vein thrombosis⁷. Non-invasive systems are based on the cooling of the body surface (legs, head, torso) and solves the problem related to invasive approach but they have a very low efficiency. Moreover, some problems are related to the cooling of other organs than the brain⁷. All these solutions can be adopted only in the intensive care units but are unwieldy and not portable in the place of the accident when the first aid is administered.

A different approach could be to decrease only the temperature on the brain tissues by cooling the blood in the carotid and cervical arteries. These vessels are quite superficial (from 1.57 to 1.80 cm for the carotid arteries) and reach all the tissues of interest. Moreover, neck cooling could be obtained with a dedicated collar which contribute to the immobilization of the patient and does not encumber medical

staff during first aid procedures. On the market, a collar with pocket for ice insertion are actually present⁸. These devices are very useful but do not allow the control of the heat transfer process, the temperature of the collar and are limited by the temperature of the ice that progressively increases depleting the cooling efficiency.

Our proposal is to produce brain hypothermia (with a temperature decrease ΔT of 3°C) through the controlled cooling of the carotid and cerebral arteries blood with a portable neck collar. The main objective of the present study is to validate the feasibility of this proposal and has been divided into two steps: (1) theoretical evaluation of the heat transfer processes to evaluate the temperature of the neck cooling system to obtain the desired brain ΔT ; (2) in-vitro verification of the numerical model. To simplify the problem, we chose to consider the heat transfer through only one carotid artery, neglecting the other one and the cervical arteries.

2. Methods

The system brain, vessels and neck was divide into 3 subsystems (fig. 1): (1) brain arteries-brain tissue; (2) external carotid wall-blood flowing inside; (3) external neck wall- carotid wall.

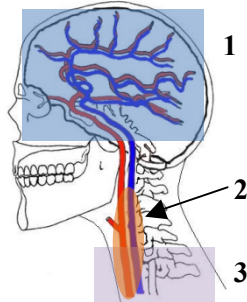


Figure 1: Schematization of the whole system and of the 3 subsystems: (1) brain arteries-brain tissues; (2) external carotid wall-blood flowing inside; (3) external neck surface-carotid wall.

2.1 Numerical models

2.1.1 Brain arteries-tissues

Considering the high vascularization of the brain, we hypothesize that heat transfer happens by mixing of blood and tissues, considering physiological inflow and outflow values (F).

Being m the brain mass, T_0 the initial temperature (37°C), T_i the target temperature (34°C), it is possible to evaluate the temperature at the time t .

$$T = (T_0 - T_i) \cdot e^{-(F/m) \cdot t}$$

2.1.2 External carotid wall-blood flowing inside

Considering the heat exchange across the carotid wall (q) and the convection transfer due to the flowing blood (fig. 2), we calculated, through successive approximations, the external temperature T_w necessary to decrease the blood temperature from T_1 (37°C) and T_2 (calculated from the previous model).

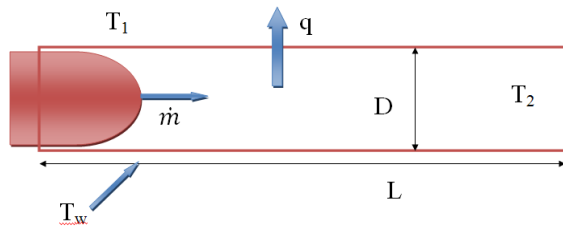


Figure 2: carotid artery with blood flowing inside.

$$\begin{aligned} \dot{m} \cdot c_p \cdot \Delta T &= h_L \cdot A_i \cdot \Delta T_{LM} \\ \dot{m} \cdot c_p \cdot (T_2 - T_1) &= h_L \cdot A_i \cdot (T_w - T_m) \end{aligned}$$

\dot{m} represents the mass flow rate, D the arterial diameter and L the length of the artery's portion that could be cooled. An uniform cooling was supposed through all the artery lateral surface (A_i). h_L is the convective heat transfer coefficient and c_p the specific heat transfer at constant pressure. Physiological values were used^{9,10,11}.

2.1.3 External neck wall-carotid wall

Applying the Newton model for heat transfer and considering three external temperature values T_e (20°C, 10°C, 5°C) the relationship between carotid wall temperature (T_w) and time (t) was evaluated (fig. 3).

$$T = (T_0 - T_e) \cdot e^{-(q/Q) \cdot t} \text{ where } q = (k/L) \cdot A_i \cdot (T_w - T_0) \text{ and } Q = m_c \cdot c_p \cdot (T_w - T_0)$$

T_0 =initial temperature (37°C); k = thermal conductivity of tissues; L = carotid length; A_i =carotid surface exposed to cooling; m_c = considered tissue mass; C_p = specific tissues heat transfer coefficient at constant pressure.

2.2 In vitro validation

2.2.1 Brain arteries-tissues

To simulate the brain tissues, we used an insulated glass bottle containing 1 liter of water at the initial temperature of 37°C. Brain was inserted in a closed circuit together with a continuous pump connected to a reservoir containing cold water at the temperature calculated from the numerical model (fig. 3). The temperature inside the brain was then plotted against time and compared with the results of the theoretical model. All temperatures were measured with a digital thermometer (K-type, Amprobe, Everett, Washington, US) with an accuracy of 0.1°C.

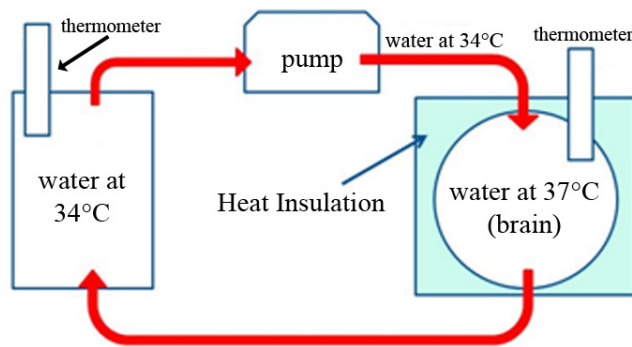


Figure 3: In vitro simulator of the brain circulation.

2.2.2 External carotid wall-blood flowing inside

To simulate the carotid artery, a latex tube (length: $(15,0 \pm 0,5)$ cm; diameter: $(0,50 \pm 0,05)$ cm) was used. The carotid was inserted in a water tank with the same volume of neck tissues and then connected to cardiovascular system mock filled with water at 37°C (fig 4). Tank water temperature was settled according the results of numerical simulation and the carotid outflow temperature was measured.

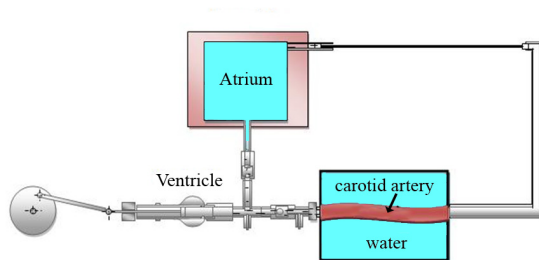


Figure 4: cardiovascular mock. Atrium contains water at 37°C. The carotid artery is inside a tank containing cold water.

2.2.3 External neck wall- carotid wall

For this preliminary phase, we chose to cool the water in the tank with a Peltier cell (power supply: 12V; maximal power 80W) connected with a fan-cooled heat sink. The cell was able to produce a surface temperature of 0°C. The temperature on the carotid surface was measured along time.

3. Results

3.1.1 Brain arteries-tissues

Both numerical and in-vitro simulation demonstrated that, with an incoming blood temperature of 34°C, a complete cooling of brain tissues is performed after about 600 s.

3.2.2 External carotid wall-blood flowing inside

To decrease the blood temperature from 37°C to 34°C, the numerical model predicted an external temperature of 19°C.

In vitro simulation gave different results: in fact, with an external temperature of 19°C, we produced a decrease of 1.4°C instead of 3°C. For this reason we simulated other conditions with different external temperature. The best result was obtained with an external water temperature of 17°C, producing an internal cooling of 2.1°C.

3.2. 3 External neck wall- carotid wall

Since the Peltier cell we have used can reach and maintain stable a temperature of 0°C, the in-vitro tests focalized only on this condition. Experimentally we reached a temperature of 17°C in about 2700 s comparable to the theoretical value (2600 s).

Combining the results obtained for each subsystem, a global cooling time could be estimated and results about 50 minutes.

Discussion

The proposed models are very simple, are based on the use of water instead biological tissues and refers only to one carotid. In the numerical models, we did not consider any heat exchange but for the ones

described: for example, in the first subsystem (brain-vessels) we did not consider the convective currents inside the brain; moreover no dissipation through surrounding tissues were calculated and this is probably the reason for the discrepancies between the numerical and in-vitro models in the second system. Moreover, the temperature decrease calculated in the model (-3°C) is bigger than the one measured in the experimentation (-2.1°C) because of a non perfect cooling through the whole vessel surface due to system geometry and to the position of the latex vessel leaned on the water tank bottom. Despite these problems, our theoretical was able to adequately describe the heat exchange in the first and last subsystems. Globally, a real temperature decrease of 2.1°C in an estimated time of 50 minutes is a very good results, being compatible with first aid procedures time. This results will be improved by adding the cooling of the other carotid and of the cervical arteries, building a neck collar with more than one cooling element to optimize the process.

References

1. Erlich MP, McCulloch JN, Zhang N, et al. *Effect of hypothermia on cerebral blood flow and metabolism in the pig*, Ann Thorac Surg.; 2002; 73; p. 191-197.
2. Erecinska M, Thoresen M, Silver IA. *Effects of hypothermia on energy metabolism in Mammalian central nervous system*, J Cereb Blood Flow Metab.; 2003; 23; p. 513-530.
3. Povlishock JT, Buki A, Koizumi H, Stone J, Okonkwo DO. *Initiating mechanisms involved in the pathobiology of traumatically induced axonal injury and interventions targeted at blunting their progression*, Acta Neurochir Suppl.; 1999; 73; p. 15-20.
4. Lecker RR, Constantini S. *Experimental models in focal cerebral ischemia: are we there yet?*, Neurosurgery; 2001; 83; p. 1128-1135.
5. Smith SL, Hall ED. *Mild pre- and posttraumatic hypothermia attenuates blood brain barrier damage following controlled cortical impact injury in the rat*, J Neurotrauma; 1996; 13; p. 1-9.
6. Jurkovich GJ, Pitt RM, Curreri PW, Granger DN. *Hypothermia prevents increased capillary permeability following ischemia-reperfusion injury*, J Surg Res.; 1988; 44; p. 514-521.
7. Rivera-Lara L, Zhang J, Muehlschlagel S. *Therapeutic Hypothermia for Acute Neurological Injuries*, The American Society for Experimental NeuroTherapeutics; 2012; 9; p. 73-86.
8. Aqeel A. Sandhu, *Cervical Immobilization Collar with Arterial Cooling Elements and Methods of Using The Same*, Pub. No.: US 2011/0040244 A1, Pub. Date: Feb. 17, 2011.
9. Krejza J et al. *Carotid Artery Diameter in Men and Women and the Relation to Body and Neck Size*, Stroke; 2006; p. 1103-1105.
10. Holmes Kenneth R. <http://users.ece.utexas.edu/~valvano/research/Thermal.pdf>, 24 Gennaio 2013.
11. Ing. Magnani L. http://www-3.unipv.it/ingegneria/copisteria_virtuale/magnani/termofluido/1%20-20convezione.pdf, Termofluidodinamica applicata - convezione, 1 marzo 2010.

S3C: Cardiovascular - Heart

Chairs: Liang Zhong, Francesco Grigioni

THE EFFECTS OF THE ANGLES BETWEEN THE MITRAL AND AORTIC ORIFICES IN LEFT VENTRICLE (LV) USING FLUID STRUCTURE INTERACTION (FSI) DURING FILLING PHASE

YOS MORSI

THE IMPACT OF FALSE TENDONS ON THE REGIONAL MECHANICS OF LEFT VENTRICLE IN YOUNG SPORTSMEN WITH THE SYNDROME OF CONNECTIVE TISSUE DYSPLASIA

KAMILIYA MEKHDIEVA

DEVELOPMENT OF THE LEFT VENTRICLE 3D MODEL TO DETERMINE THE TOPOLOGY OF FALSE TENDONS

SERGEY SOKOLOV

CHARACTERIZING THE CARDIOVASCULAR FUNCTIONS DURING ATRIAL FIBRILLATION THROUGH LUMPED-PARAMETER MODELING

STEFANIA SCARSOGLIO

MITRAL VALVE REGURGITATION: CORRELATION BETWEEN QUANTITATIVE AND SEMI-QUANTITATIVE METHODS

ELENA BARBARESÌ

BLOOD RHEOLOGICAL PROPERTIES AND CHANGES OF OSCILLATIONS IN SKIN TEMPERATURE AFTER COLD TEST IN PATIENTS WITH TYPE 2 DIABETES

NADIA ANTONOVA

THE EFFECTS OF THE ANGLES BETWEEN THE MITRAL AND AORTIC ORIFICES IN THE LEFT VENTRICLE (LV) USING FLUID STRUCTURE INTERACTION (FSI) DURING FILLING PHASE

MD. SHAMSUL AREFIN

Biomechanical and Tissue Engineering Laboratory, Swinburne University of Technology, Hawthorn, Victoria-3122, Australia
marefin@swin.edu.au

YOS S. MORSI

Biomechanical and Tissue Engineering Laboratory, Swinburne University of Technology, Hawthorn, Victoria -3122, Australia
ymorsi@swin.edu.au

It is well known that slight variations in the geometry of the LV can significantly change hemodynamic characteristics. There are numerous imaging tools which can distinguish the flow dynamics inside the LV qualitatively, but the effects of the angles between the mitral and aortic orifices are still to be determined. Therefore, by using the FSI scheme, this paper highlights the variations in the hemodynamic and physiological characteristics of the LV, varying the angles (50° , 55° and 60°) between the mitral and aortic orifices during the filling phase. The time-dependent and incompressible viscous fluid, along with the stress tensor equations, are combined with the Navier-Stokes equations, including the Arbitrary Lagrangian Eulerian and the elasticity for the structural region. The results are examined using velocity mapping, intraventricular pressure (I_p) distributions and structural displacement using total mesh displacement (TMD). From the results, it is evident that, during the peak E-wave, a ring shaped vortex exists near the aortic orifice for the 55° and 60° angles. Also, during the diastolic period, the magnitude of the I_p in the ventricle apex is found to be higher than at its base. Consequently, maximum displacement is observed to be in the apex during the peak E-wave for the 50° than that of 55° and 60° .

Keywords: Hemodynamic, FSI, aortic orifice, mitral orifice, filling phase

1. Introduction

Medical imaging technology tools can be widely used to acquire qualitative data regarding the flow dynamics inside the cardiac structure, but they are unable to offer a detailed picture of the physiological variations, and the influence of the structural deformation, on the hemodynamics of the cardiac structure. The Fluid Structure Interaction (FSI) scheme is broadly used to investigate the flow dynamics and variations in the physiological properties of the structure in different studies [1-3]. The FSI method is also used to examine the changes in hemodynamics, including the progression and amalgamation of the vortices in the LV as well as structural variations [4-6].

Substantial research has been conducted to understand and determine the hemodynamic behaviour of the heart using computational fluid dynamics (CFD). Jones and Metaxas, 1998, examined the blood flow dynamics inside the LV chamber using CFD solver. They utilised the wall motion of the ventricle in a patient specific-case for the first time as the boundary conditions [7]. Afterwards, the boundary conditions were further refined and, using the Immersed Boundary Conditions [8], Vierendeels et al. 2000, analysed the flow pattern and pressure gradients during the filling phase based on a 2D axisymmetric CAD model [9]. Subsequently, Watanabe et al. 2004 simulated the flow dynamics in the cavity using FSI, where the researchers investigated the influence of the angle between the aortic and mitral orifice. However, they did not consider the dynamic characteristics of the LV model [10]. Moreover, Adib et al., 2013, investigated the flow characteristics inside the LV during the filling phase using FSI [11]. Recently, using FSI, Arefin and Morsi, 2014, investigated the hemodynamic behaviour and structural displacement of the LV during diastolic conditions, but the variations in the angles between the mitral and aortic orifice were not reported [12]. On the other hand, literature still recommends that proper structural information needs to be implemented to simulate the precise functioning characteristics of the ventricle, which incorporates multi-scale, multi-physics simulations [13-15].

The abovementioned investigations concentrated largely on the hemodynamic behaviour of the LV with different degree of success but, to the best of our knowledge, none of them considered the variations in the angular differences between the mitral and aortic orifices. Therefore, this paper reports on research that simulates the flow pattern, including the generation, elongation, amalgamation and merging of vortices and structural displacement using FSI during the diastolic flow conditions.

2. Mathematical Approaches

The Navier-Stokes equations for the incompressible viscous fluid (time-dependent) combined with the continuity equation, were utilized in this computational approach as described in [12, 16]. Furthermore, by considering smaller deformation, the stress tensor equation was also utilized, which is documented in [12]. Also, ANSYS 14.5 was used for the whole FSI simulations.

3. Computational Procedures

3.1 Geometry

The details of the simplified 3D geometry of the LV using SolidWorks 2012 have been described in our previously published work [12]. Briefly, during the diastolic flow simulation, the inlet (mitral orifice) of the LV was considered completely open and the outlet (aortic orifice) was considered completely closed. Additionally,

the angular difference of 50°, 55° and 60° was varied between the mitral and aortic region of the ventricle. Due to space limitations in this paper, only the 50° and 55° case results are presented herein.

3.2 Boundary conditions

The inlet velocity waveform/ transmitral flow velocity (U) was implemented through the mitral region of the LV during the simulations. This was adapted from [4, 12] containing the early filling wave (E-wave); the atrial contraction wave (A-wave), and the middle phase, known as the diastasis/ slow filling phase[12]. Moreover, the ventricle wall was considered to be isotropic and homogenous with the value of ventricle wall density set to be 1.2 g/cm³; the fluid density was 1050 kg/m³ and the viscosity was 0.0035 Pa.s incorporating the no-slip boundary stipulations [4, 5, 12, 17].

4. Results

4.1 Velocity mapping for the angular difference of 50°

Fig.1 represents the velocity distributions for the angular variation of 50°, where the velocity vectors were mapped on the XY cross-sectional plane of the LV cavity during the filling phase. Fig. 2 represents the 55° case.

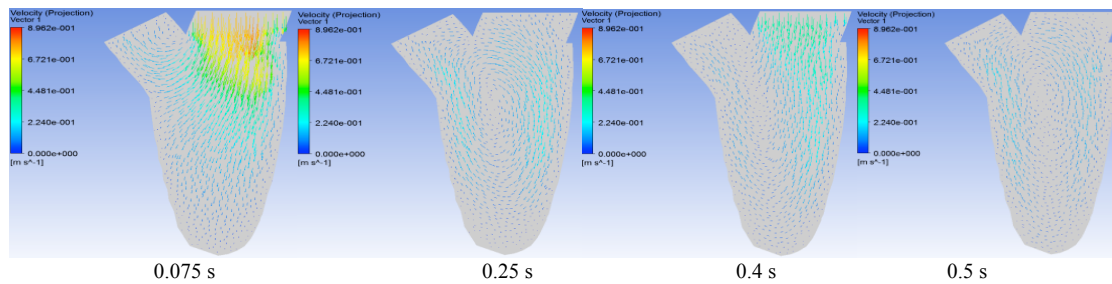


Fig.1: Angular difference of 50°

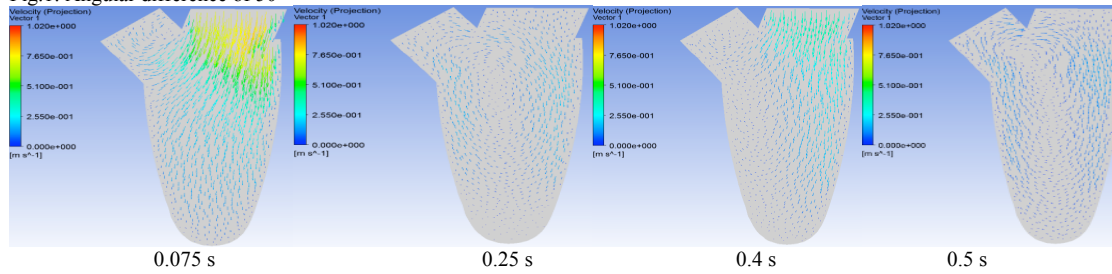


Fig.2: Angular difference of 55°

4.2 Structure simulation using total mesh displacement (TMD) for the angular difference of 50°

Once again, structural variations were also observed using XY cross-section plane in the LV cavity as shown in Fig. 3 and Fig. 4.

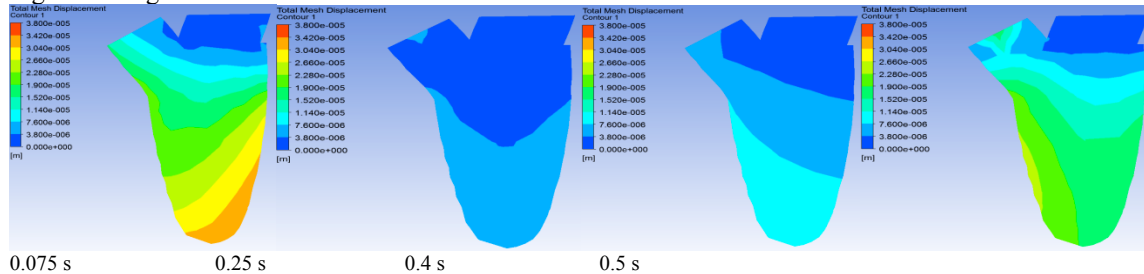


Fig.3: Angular difference of 50°

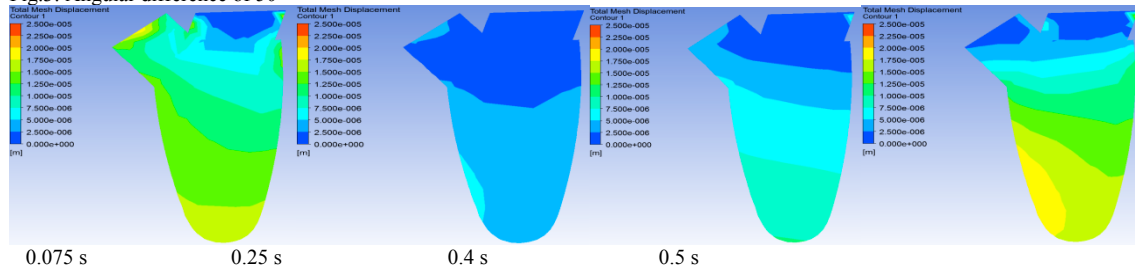


Fig.4: Angular difference of 55°

5. Discussion

From the simulation results it can be stated that; when the inlet velocity waveform (U) reached the peak of the E-wave (approximately, $t = 0.075$ s), maximum fluid velocity entered through the inlet region. From Fig.1 and Fig.2, it was found that a weaker vortex, which was ring shaped and clockwise (CW), developed near the aortic orifice for the 55° but for 50° no clear vortex was found. After reaching the peak of the E-wave, inlet velocity entered into the diastasis phase (approximate, $t = 0.25$ s) where the flow was minimal through the inlet region. In general, during this phase, the adherence vortices for all cases were found to be enlarging and changed their location towards the centre of the chamber. This could be attributed to the fact that the posterior part of the vortex slightly moved forward and the anterior part shifted in the reverse direction to the posterior part, which then developed the adherence vortex. Subsequently, with the rise in the inlet velocity due to atrial contraction wave (A-wave) (for example, approximately $t = 0.4$ s) inlet velocity began to rise once again and the vortices slowly amalgamated with the propagation of the flow. However, at the end of the filling phase ($t = 0.5$ s), a ring shaped vortex was found at the core of the LV chamber for all cases. Maximum velocity of $9.39\text{E-}1$ m/s was found during the peak of the E-wave for 60° in the ventricle base. The general trends of the flow dynamics which consisted of the generation, progression, amalgamation and shifting of vortices were in line with previously published research [4, 5, 10, 12, 17]. Moreover, for the I_p distributions it was found that a much higher magnitude of I_p was evident in the apical region of the ventricle than its basal region.

Subsequently, from Fig.3 and Fig.4, due to the peak of the E-wave ($t = 0.75$ s), the volume inside the LV chamber elevated but the displacement generally occurred at the apical region. The maximum displacement of $3.42\text{E-}5$ m was in the apical region of the ventricle during the peak E-wave for the 50° case. Once more, with the deceleration in the inlet velocity, as it entered into the diastasis phase ($t = 0.25$ s) minimal inflow velocity propagated through the mitral region. Because of this, the volume inside the chamber decelerated which, in turn, decreased the magnitude of the displacement in the apical and basal region. However, the magnitude in the apical region was still found to be slightly higher compared to the ventricle base for all cases (50° , 55° and 60°). Once again, due to the rise in the A-wave ($t = 0.4$ s), the volume started to increase inside the cavity and the magnitude of the displacement in the ventricle apex started to rise. At the end of the filling phase ($t = 0.5$ s), due to the increased volume inside the chamber, the magnitudes of the displacement for all cases elevated in the apical region. It should be noted that, due to the limitations of the pages, all the results could not be documented here.

6. Conclusion

Based on the simulation results and the findings, it is evident that, during the peak of the E-wave, a ring shaped and CW vortex developed near the aortic orifice for the 55° and 60° cases but, for 50° , no clear vortex was found. Moreover, the magnitude of the I_p in the ventricle apex was higher during the filling phase compared to its basal region. Precisely, at the peak E-wave, a much higher magnitude of I_p was found at the apical region for the 50° case than for the 60° and 55° cases. Subsequently, maximum displacement was in the apical region, due to the increased volume during the peak E-wave for the 50° case compared to the 55° and 60° cases.

References

1. Kouhi, E., *An Advanced Fluid Structure Interaction Study of Tri-leaflet Aortic Heart Valve*, in *Faculty of Engineering & Industrial Sciences*. 2011, Swinburne University of Technology: Melbourne.
2. Do, H.V., *Design And Optimization Of Coronary Arteries Bypass Graft Using Numerical Method*, in *Faculty of Engineering and Industrial Sciences*. 2012, Swinburne University of Technology.
3. Morsi, Y., et al., *Graft-Artery Junctions: Design Optimization and CAD Development*, in *Computer-Aided Tissue Engineering*, M.A.K. Liebschner, Editor. 2012, Humana Press. p. 269-287.
4. Cheng, Y., H. Oertel, and T. Schenkel, *Fluid-Structure Coupled CFD Simulation of the Left Ventricular Flow During Filling Phase*. *Annals of Biomedical Engineering*, 2005. **33**(567-576).
5. Lassila, T., et al., *Multiscale fluid-structure interaction simulation of patient-specific left ventricle fluid dynamics with fictitious elastic structure regularization*. *Int. J. Numer. Meth. Biomed. Engng.*, 2012. **00**: p. 1-23.
6. Nordsletten, D., et al., *Fluid-solid coupling for the investigation of diastolic and systolic human left ventricular function*. *International Journal for Numerical Methods in Biomedical Engineering*, 2011. **27**(7): p. 1017-1039.
7. Jones, T. and D. Metaxas, *Patient-specific analysis of left ventricular blood flow*, in *Medical Image Computing and Computer-Assisted Intervention — MICCAI'98*, W. Wells, A. Colchester, and S. Delp, Editors. 1998, Springer Berlin Heidelberg. p. 156-166.
8. McQueen, D.M. and C.S. Peskin, *A three-dimensional computer model of the human heart for studying cardiac fluid dynamics*. *ACM SIGGRAPH Computer Graphics*, 2000. **34**(1): p. 56-60.
9. Vierendeels, J., et al., *Computer simulation of intraventricular flow and pressure gradients during diastole*. *J Biomech Eng.*, 2000. **122**(6): p. 667-74.
10. Watanabe, H., et al., *Multiphysics simulation of left ventricular filling dynamics using fluid-structure interaction finite element method*. *Biophys J.*, 2004. **87**(3): p. 2074-85.

11. Adib, M.A.H.M., et al., *Prediction on Behaviour of Blood Velocity and Mitral Leaflet Displacement in the Different Shapes of Heart Valve during Cardiac Cycle*. Journal of Biomimetics, Biomaterials & Tissue Engineering, 2013. **17**: p. 79-85.
12. Arefin, M.S. and Y. Morsi, *Fluid structure interaction (FSI) simulation of the left ventricle (LV) during the early filling wave (E-wave), diastasis and atrial contraction wave (A-wave)*. Australasian Physical & Engineering Sciences in Medicine, 2014: p. 1-11.
13. Lee, J., et al., *Coupling contraction, excitation, ventricular and coronary blood flow across scale and physics in the heart*. Phil. Trans. R. Soc. A, 2009. **367**(1986): p. 2311-2331.
14. Nordsletten, D.A., et al., *Coupling multi-physics models to cardiac mechanics*. Progress in Biophysics and Molecular Biology, 2011. **104**(1-3): p. 77-88.
15. Sugiura, S., et al., *Multi-scale simulations of cardiac electrophysiology and mechanics using the University of Tokyo heart simulator*. Progress in Biophysics and Molecular Biology, 2012. **110**(2-3): p. 380-389.
16. Temam, R., *Navier-Stokes Equations: Theory And Numerical Analysis*. 2001: AMS Chelsea Publishing.
17. Vierendeels, J.A., et al. *Computer simulation of left ventricular filling flow: impact study on echocardiograms*. in *Computers in Cardiology*, 1999. 1999.

THE IMPACT OF FALSE TENDONS ON THE REGIONAL MECHANICS OF LEFT VENTRICLE IN YOUNG SPORTSMEN WITH THE SYNDROME OF CONNECTIVE TISSUE DYSPLASIA

MEKHDIEVA K.R.*

**Sports and Health-improving Technologies Lab., Ural Federal University named after the first President of Russia B.N.Yeltsyn
Yekaterinburg, 620078, Russian Federation
kamilia_m@mail.ru*

TIMOKHINA V.ED.*

**Pediatric Dept, Ural State Medical University
Yekaterinburg, 620028, Russian Federation
varvaratim@yandex.ru*

SOKOLOV S.YU.^{#,+}

*#Biomedical Physics Dept., Ural State Medical University
Yekaterinburg 620028, Russian Federation*

*+Physics Dept., Ural Federal University named after the first President of Russia B.N.Yeltsyn
Yekaterinburg 620053, Russian Federation
sergey.sokolov@urfu.ru*

BLYAKHMAN F.A.^{#,+}

*#Biomedical Physics Dept., Ural State Medical University
Yekaterinburg 620028, Russian Federation*

*+Physics Dept., Ural Federal University named after the first President of Russia B.N.Yeltsyn
Yekaterinburg 620053, Russian Federation
feliks.blyakhman@urfu.ru*

Abstract

The aim of the study is to test a cause-effect relation between the false tendons (FT) in left ventricle (LV) structure and the myocardial function. The focus was on LV regional wall motion with respect to the mechanical asynchrony. Twenty-six young athletes (mean age 20.7 ± 3.0 years) with the syndrome of connective tissue dysplasia underwent the transthoracic echocardiography. On average, 4.0 ± 1.0 FT with different localization and orientation in LV were determined. Cardiac wall function was estimated by the motion of 12 regions at LV long-axis section in the course of complete heart cycle. Standard deviation of the systolic motion duration for 12 regions (dt) was served as a measure of the mechanical asynchrony. Wide range of dt from 10.7 to 99.3 ms with the mean value of 38.1 ± 18.0 ms was found. Meanwhile, the higher extent of asynchrony ($dt > 30$ ms) associated with the transverse and oblique FT mainly located at basal and/or medial portions of LV chamber while FT located at apical portions of LV showed no effect on the asynchrony extent. We concluded that the FT occurrence in LV stricture results in the decrease of mechanical interaction efficiency in the cardiac wall.

Keywords: Connective tissue dysplasia, left ventricle, false tendons, regional wall mechanics, mechanical asynchrony.

Introduction

False tendons (FT) in the left ventricle (LV) are a phenotypic marker of the connective tissue dysplasia (CTD), associated with mutations in genes responsible for collagen synthesis.¹ According to the epidemiological findings, the occurrence of CTD associates with the increase of anthropogenic load. For example, in Russian industrial regions like the Ural, the CTD frequency among young people is about 70%.

Typically, the CTD people are tall individuals with the asthenic type and the hypermobility of joints so these features make them highly needed for the sports. Meanwhile, the intensive sport training implies the high level of heart adaptation to the physical load. Therefore, strong assessment of the myocardial function in young athletes with CTD is critically important.

In fact, the appearance of FT in LV is an adaptive phenomenon aimed to increase the stability of chamber structure with impaired collagen. As heart structure and function are integrally linked, the constructive anomalies in LV may negatively affect the myocardial function.² The aim of the study is to test a cause-effect relation between the FT in LV structure and the myocardial function.

This paper presents the data of echocardiographic examination of CTD young sportsmen, members of the student teams of the Ural Federal University. Obtained results demonstrate an important role of FT in the LV regional function determining.

Methods

Twenty six young athletes, (mean age 20.76 ± 3.02 years, height 184.9 ± 13.07 cm, body weight 79.35 ± 15.7 kg) were recruited for this investigation. All sportsmen signed the consent to participate in the study. The ultrasound diagnostic system HD15 (Phillips, USA) was used for the LV transthoracic visualization from parasternal and apical views. To formalize FT topology, the 3D-model of LV geometry was reconstructed based on three short-axis sections and one long-axis section of LV images recorded at the heart end-diastole. Global LV function was estimated according to ACC/AHA Guidelines for the Clinical Application of Echocardiography 2012.

LV regional function was assessed by means of the frame-by-frame image processing (46 frames per sec) of LV long-axis section in the course of complete cardiac cycle. With use the «DICOR» software («Rospatent» № 2002610607), LV endocardial contour was outlined by hand. The area of delineated figure was divided into 12 sectors using radii connecting to the center of mass of the respective LV section. Finally, 12 triangles were obtained, and the relative area change of triangle was chosen as a measure of regional motion. The duration of systolic wall-motion for 12 regions was estimated with further calculation of the mean value and standard deviation (dT). The value of dT (ms) served as a measure of mechanical asynchrony.³

Figure 1 presents the typical example of regional wall-motion. Upper plot corresponds to some region owned the LV free wall, medium plot - LV apex, lower plot - interventricular septum. The relative area change is marked with the ordinate, 100% corresponds to the area of respective region obtained at the end of LV diastole. The time (frames) with scale bar of about 22 ms plotted with abscissa. The vertical line marked in the middle of picture corresponds to the beginning of LV diastolic period.

The statistic software package “SPSS Statistics 17.0” was used for statistical analysis. Mean value and standard deviation were calculated, *t-test* was applied for comparative analysis. The level of significance was set at $P < 0.05$.

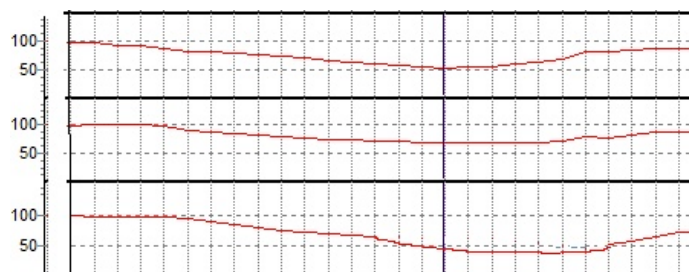


Fig. 1. The example of regional wall-motion (see explanation in the text).

Results

According to the standard ultrasound examination, all athletes had normal values of the major indices of LV global systolic and diastolic function. All athletes had FT from 2 to 6 (4.0 ± 1.0) units. Figure 2 demonstrates the examples of FT localization in LV.

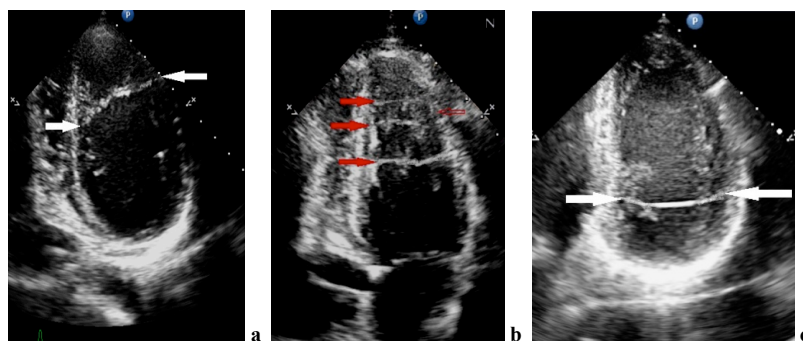


Fig. 2. Examples of FT visualization in LV: a – median-apical oblique FT; b – multiple median and apical transverse FT, c – basal transverse FT (arrows indicate the points of FT fixing to LV wall).

Tendons were classified in the accordance with two criteria: i - the points of FT fixing to LV regions, ii - FT orientation. The following distribution of FT was found: apical oblique - 22.5%, apical transverse - 27.5%, median oblique - 14.7%, median transverse - 3.9%, basal oblique - 9.8%, basal transverse - 2.9%, median-basal oblique - 6.9%, median-apical oblique 7.8%, basal-apical oblique - 3.9%. Thus, FT were located across the LV long axis at apical and median portions of LV chamber.

The analysis of regional wall motion showed complex mechanics as it was displayed in the example with Figure 1 (see above). At the beginning of LV systole, the motion of interventricular septum regions

appeared with delay (up to 151.9 ms) relatively to the free wall regions. At the beginning of LV diastole, the free wall regions demonstrated diastolic lengthening while the septum regions still showed the systolic shortening (up to 195.3 ms). On average interventricular septum regions showed the systolic delay of 37.5 ± 40.8 ms and diastolic delay of 90.8 ± 60.5 ms.

The value of asynchrony parameter (dT) varied widely from 10.7 to 99.3 ms (38.1 ± 18.0 ms). To estimate the impact of FT on the extent of mechanical asynchrony, the studied group was divided into 2 subgroups by criteria of dT threshold value of 30 ms. Essentially, the Group I ($dT > 30$ ms) was represented the athletes with high level of asynchrony, and Group II ($dT < 30$ ms) – low level of asynchrony.

The comparative analysis of FT distribution in groups showed: i - in Group I the number of the median oblique FT was significantly higher, than in Group II (0.8 ± 0.6 and 0.3 ± 0.5 units, $P < 0.01$); ii – in Group I the relative number of transverse basal FT was equal to 4.9% while in Group II these FT were not distinguished.

Discussion

From the medical point of view, the connective tissue dysplasia is not a “disease”, and even individuals with FT in the heart are healthy people in the terms of cardiology. The most important argument to support this solution based on the data set of clinical observations where no significant effects of FT on the global heart function was evidenced. In this context, the data obtained here are in a good agreement with the common results so that we confirmed in athletes the normal values for key parameters of the LV global systolic and diastolic function.

Meanwhile, we found an anomalous function in the LV wall regions. Generally, the systolic motion of interventricular septum was highly delayed relatively to the most regions owned the LV free wall. Furthermore, the most regions of LV septum demonstrated the systolic motion at the beginning of LV diastolic filling. Presented data show high extent of the mechanical asynchrony in LV wall.

According to the FT topology, the higher extent of asynchrony associated with the transverse and oblique FT mainly located at basal and/or medial portions of LV chamber while FT located at apical portions of LV showed no effect on the asynchrony extent. Noteworthy, FT attached to the LV septum and free wall were represented as strictures with increased echogenicity and thickness (> 2 mm), and mainly oriented at a small angle to the LV long axis.

Thus, the occurrence of FT in LV structure as a response to the connective tissue dysplasia development accompanies by the increase of myocardium mechanical asynchrony. It is logical to assume that this phenomenon associates with complex mechanical interaction between the opposite portions of LV chamber connected by false tendons. Obviously, the FT occurrence results in the decrease of mechanical interaction efficiency in the cardiac wall.

Acknowledgments

The study is supported by the Russian Foundation for Basic Research (grant #12-08-00789a).

References

1. Grahame R, Heritable disorders of connective tissue, *Best. Pract. Res. Clin. Rheumatol*, **14**: 345–361, 2000.
2. Blyakhman F, Left ventricular inhomogeneity and the heart's functional reserve, in: Ghista D (ed), *Cardiac Pumping and Perfusion Engineering*, World Scientific Press, Singapore, pp. 17-56, 2007.
3. Blyakhman FA, Naydich AM, Kolchanova SG et al, Validity of ejection fraction as a measure of myocardial functional state: impact of asynchrony, *Eur J Echocardiogr* **10**(5): 613-618, 2009.

DEVELOPMENT OF THE LEFT VENTRICLE 3D MODEL TO DETERMINE THE TOPOLOGY OF FALSE TENDONS

SOKOLOV S.YU.^{#,+}

[#]*Biomedical Physics Dept., Ural State Medical University,
Yekaterinburg, 620028, Russian Federation*

⁺*Physics Dept., Ural Federal University named after the first President of Russia B.N.Yeltsyn
Yekaterinburg 620083, Russian Federation*
sergey.sokolov@urfu.ru

MEKHDIEVA K.R.*

**Sports and Health-improving Technologies Lab., Ural Federal University named after the first President of Russia B.N.Yeltsyn,
Yekaterinburg, 620078, Russian Federation*
kamilia_m@mail.ru

ZINOVYEVA YU.A.[×]

[×]*Diagnostics Dept., Ural State Hospital №2,
Yekaterinburg, 620000, Russian Federation*
ciklon@olympus.ru

BLYAKHMAN F.A.^{#,+}

[#]*Biomedical Physics Dept., Ural State Medical University,
Yekaterinburg, 620028, Russian Federation*

⁺*Physics Dept., Ural Federal University named after the first President of Russia B.N.Yeltsyn
Yekaterinburg 620002, Russian Federation*
feliks.blyakhman@urfu.ru

This research is devoted to the development of algorithms for assessing the topology of false tendons in the heart. Video-image sequences of left ventricle obtained by the transthoracic echocardiography were used as the input data, and the method of thin plate splines was applied for ventricular chamber reconstruction. The method enables to produce three-dimensional model of the left ventricle of the examined heart and correctly visualize position and orientation of the false tendons. Using these possibilities, we evaluated the distribution of false tendons for 29 individuals with the syndrome of connecting tissue dysplasia.

Key words: left ventricle, 3D reconstruction, false tendon, echocardiography.

1. Introduction

To estimate the effects of false tendons on the left ventricle (LV) function, the correct assess of their topology is necessary. Three-dimensional (3D) representation of the LV inner surface is most suitable approach for this purpose. Generally, there are several medical imaging techniques such as MRI or CT originally able to produce the heart 3D reconstruction. However, these methods are still quite expensive for now and not as widely distributed as a technique for ultrasound (US) cardiac examinations.

Since the most common transducer for heart echolocation is a probe with an external (transthoracic) location, it is appeared the task of developing algorithms of 3D reconstruction of the LV surface for a limited number of ultrasonic sections. To interpolate the missing sections, these methods use either interpolating polynomials^{1,2} or finite element model³.

Recently, for the interpolation of elastic surfaces deformed by external forces, the method of thin plate splines (TPS) is widely used⁴⁻⁶. This algorithm we have used for restoration (interpolation) of missing sections for 3D imaging of the left ventricle.

2. Methods

2.1 Initial sections acquisition

Image sequences obtained by ultrasound examination of the heart using a transducer with a sector scanning and outer (transthoracic) access were used as the input data. For 2-3 cardio cycles, data are recorded for four sections: one section along the long axis of the heart (the standard four-chamber view) and three cross sections - along the short. In each frame of each of the four sections the inner and outer surface boundaries LV are traced. To trace LV boundaries, we used semi-automated method developed by us on the basis of speckle tracing techniques⁷. Fig. 1A shows the initial sections, and Fig. 1B shows the same sections, arranged in three-dimensional space taking into account their mutual orientation.

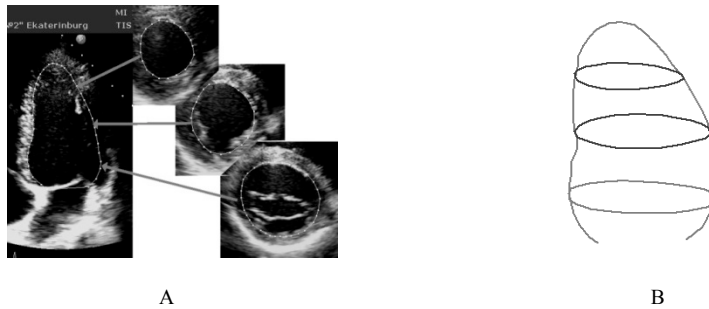


Fig. 1 Initial LV sections (A) and their arrangement to 3D view (B).

2.2 Thin plate splines method

To construct the sections in the intervals between the initial sections of the thin plate splines algorithm is used. TPS are an interpolation and smoothing technique, the generalization of splines so that they may be used with two or more dimensions^{5, 6}. The TPS arises from consideration of the integral of the square of the second derivative - this forms its smoothness measure. In the case where x is two dimensional (x_1 and x_2), for interpolation, the TPS fits a mapping function $f(x)$ between corresponding point-sets $\{y_{ij}\}$ and $\{x_{ij}\}$ that minimizes the following bending energy function:

$$E = \iint \left[\left(\frac{\partial^2 f}{\partial x_1^2} \right) + 2 \left(\frac{\partial^2 f}{\partial x_1 \partial x_2} \right) + \left(\frac{\partial^2 f}{\partial x_2^2} \right) \right] dx_1 dx_2 \quad (1)$$

Here $\{y_{ij}\}$ and $\{x_{ij}\}$ are the points of intersection of long-axis contour with three short-axis's contours (x and y are points on initial and interpolated contours correspondently). In Fig. 2A, there are shown an initial (thick curve) and interpolated by TPS technique (thin curve) long-axis LV contours. After TPS interpolation, new contour is added to the 3D model of the LV with consideration of its spatial orientation (Fig. 2B). So, by use the TPS method we can fill all "holes" between initial LV sections with required accuracy.



Fig. 2. An initial (thick curve) and interpolated by TPS technique (thin curve) long-axis LV contours (A); the new interpolated contour added to 3D representation of the LV (B).

Now we can use obtained 3D model of the LV for more accurate positioning of false tendons inside the heart's chamber.

3. Results

An example of use of developed 3D model of the LV is shown in Fig. 3. An initial image (for-chamber view) of the LV with oblique chorda (false tendon) is displayed in fig. 3A. After implementation of the 3D reconstruction of the LV and specifying the chord attachment points to the myocardium surface we obtain the 3D model of the LV with correct position of the chorda (Fig. 3B).



Fig.3. An initial image (for-chamber view) of the LV with oblique chorda (A) and 3D model of the LV with correct position of the chorda (B).

Using the developed model, we have analyzed data from echocardiography of 29 people with the chords in the left ventricle (they were all sportsmen - basketball and mini football). This allows us to classified chords in LV according to their positions and orientation (Fig. 4).

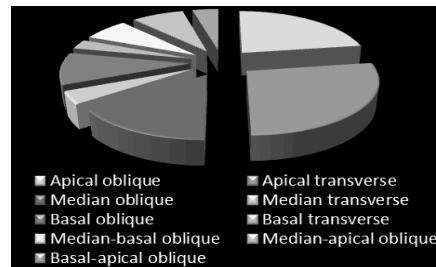


Fig. 4. Distribution of chords in position and orientation (according to echocardiography of 29 persons).

4. Conclusion

Thus, we have developed a method which enables to build 3D model of the LV taking into account data (image sequences) obtained during echocardiographic study of person with false tendons in the heart. This allowed us to determine correctly topology of the false tendons and obtain distribution of chords in position and orientation.

Acknowledgement

The study was supported by the Russian Foundation for Basic Research (project #12-08-00789a).

References

1. Kolchanova S.G., Grinko A.A., Sokolov S.Yu., et al. The regional elastic properties analysis of myocardium based on echocardiographic 3D reconstruction of the left ventricle. *J. Ultrasound in Medicine and Biology*, **30(3)**:311-320, 2004.
2. O. Nilsson, D.E. Breen, and K. Museth. Surface reconstruction via contour metamorphosis: An Eulerian approach with Lagrangian particle tracking. *In Proc. IEEE Visualization*, 2005, pp. 407–414.
3. F. Dorri , P. F. Niederer & P. P. Lunkenheimer A finite element model of the human left ventricular systole, *Computer Methods in Biomechanics and Biomedical Engineering*, **9(5)**:319-341, 2006.
4. J. Lim, M.-H. Yang A Direct Method for Modeling Non-rigid Motion with Thin Plate Spline. *Proceedings of the 2005 IEEE Computer Society Conference on Computer Vision and Pattern Recognition (CVPR'05)*. pp. 1196-1202.
5. Yin-Chiao Tsai, Hong-Dun Lin, Yu-Chang Hu, et al. Thin-Plate Spline Technique for Medical Image Deformation. *Journal of Medical and Biological Engineering*, **20(4)**: 203-210 2000.
6. Gianluca Donato, Serge Belongie. Approximate Thin Plate Spline Mappings. *Lecture Notes in Computer Science*. **2352**:21-31, 2002.
7. Sokolov S. Yu. Improving the Accuracy and Stability of the Speckle Tracking Technique in Processing Images Obtained in Echocardiographic Examinations. *Pattern Recognition and Image Analysis*, **23(4)**:536–540, 2013.

CHARACTERIZING THE CARDIOVASCULAR FUNCTIONS DURING ATRIAL FIBRILLATION THROUGH LUMPED-PARAMETER MODELING

STEFANIA SCARSOGGIO

*Department of Mechanical and Aerospace Engineering, Politecnico di Torino
Corso Duca degli Abruzzi 24 Torino, 10129, Italy
stefania.scarsoglio@polito.it*

ANDREA GUALA, CARLO CAMPOREALE, LUCA RIDOLFI

*Department of Environment, Land and Infrastructure Engineering, Politecnico di Torino
Corso Duca degli Abruzzi 24, Torino, 10129, Italy
andrea.guala@polito.it, carlo.camporeale@polito.it, luca.ridolfi@polito.it*

Atrial fibrillation (AF), causing irregular and rapid heartbeats, is the most common arrhythmia. Due to the widespread impact on the population and the disabling symptoms related to rapid heart rate, AF is a subject of growing interest under several aspects: statistical analyses on the heartbeat distributions, risk factors, impact on quality of life, correlation with other cardiac pathologies. However, several key points on the consequences induced by AF on the cardiovascular system are still not completely understood. The proposed work aims at quantifying the impact of AF on the most relevant cardiovascular parameters by means of a lumped-parameter modeling, paying particular attention to the stochastic nature of the irregular heartbeats and the reduced contractility of the heart. The global response leads to a rather impressive overall agreement with the clinical state-of-the-art measures regarding AF: reduced cardiac output with correlated arterial hypotension, as well as higher left atrial volume and pressure values are some of the most representative outcomes emerging during AF. Moreover, new insights on hemodynamic parameters such as cardiac flow rates, which are difficult to measure and almost never offered in literature, are here provided.

Keywords: Atrial fibrillation; lumped-parameter modeling; cardiovascular dynamics.

1. Modeling Description

In the lumped parameterization, the anatomical details are neglected and the cardiovascular system is described through a Windkessel model by a set of electrical components¹. The lumped model here adopted extends the Windkessel approach to the whole (pulmonary and systemic) circulation system, and is combined to an active atrial and ventricular representation, through four time-varying elastance functions, for the left and right heart chambers. The present model consists of a network of compliances, resistances and inductances describing the pumping heart coupled to the systemic and pulmonary systems, along with an accurate description of the valve motion mechanisms². The viscous effects are taken into account by the resistances, R , the inertial terms are considered by the inductances, L , while the elastic vessel properties are described by the compliances, C . Three

cardiovascular variables are involved at each section: the blood flow rate, Q , the volume, V , and the pressure, P .

The main aim of the present work is to characterize the cardiovascular functions during AF with respect to the normal sinus rhythm (NSR). The fibrillated beating is simulated paying particular attention to the stochastic modeling of the irregular heartbeats and the reduced contractility function of the heart. The stochastic modeling of the heartbeat allows to have long fibrillated time series (e.g. 5000 cardiac cycles), thereby yielding statistically significant results.

The proposed approach has a double advantage. First, AF conditions can be analyzed avoiding the presence of other side pathologies, which usually accompany AF. Therefore, the outcomes should be read as purely consequent of a fibrillated cardiac status in a healthy young adult. Second, the main cardiac variables and hemodynamic parameters can all be obtained at the same time, while clinical studies usually focus only on a few of them at a time.

2. Results

In Fig. 1 we first report, through time series, some cardiovascular outcomes showing a striking agreement³ with the state-of-the-art in vivo data regarding AF. During AF, there is a consistent reduction of both cardiac output (-9%) and stroke volume (-26%), with a consequent moderate arterial hypotension (diastolic: -7%, systolic: -11%), while the mean left atrial pressure increases by 13%.

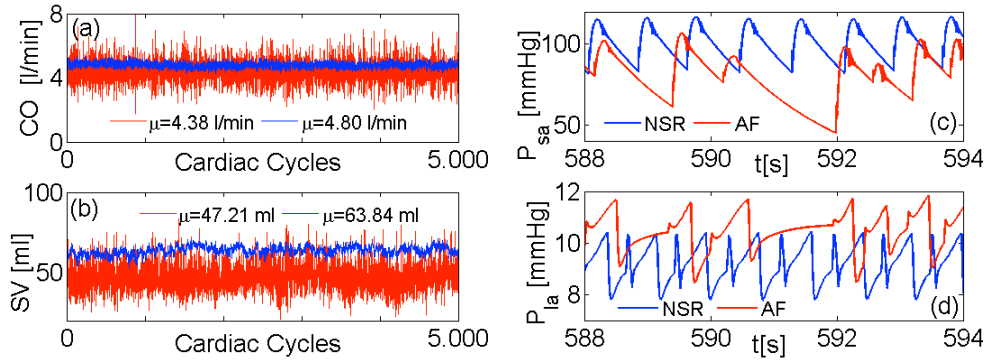


Fig. 1: (a)-(b): Cardiac output (CO) and stroke volume (SV) over 5000 cardiac cycles (average values are indicated with μ). (c)-(d) Systemic arterial (P_{sa}) and left atrial (P_{la}) pressure series. Blue: NSR, red: AF.

Among all the cardiovascular variables obtained through the present model, we here focus on hemodynamic parameters, such as cardiac flow rates, which are not easily measured during AF. In fact, to the best of our knowledge, there are no available trends or data of cardiac flow rates during AF in literature. However, the four valve flow rates can provide precious information to understand the effects of fibrillation events.

The time series of both mitral and tricuspid flows evidence the absence, in the fibrillated configuration, of the peaks due to atrial contraction in late diastole (see Fig. 2, panels a and d). A deeper investigation (see Fig. 2, panels b and e) highlights that short heartbeats lead to higher peaks of regurgitant mitral and tricuspid flows, while longer beats cause a decrease of the reflux (we recall that RR is the temporal range between two consecutive heartbeats). For the direct flow, the contrary holds for the tricuspid flow: there is an inverse proportionality between the beat length and the value of direct flow peak (Fig. 2f). For the mitral flow, instead, the sparsity of values impedes to identify a clear trend between RR and the maxima of Q_{mi} (Fig. 2c). Therefore, the greater amount of regurgitant flow due to a rapid beat is in large part compensated by a greater amount of direct flow for the tricuspid valve. The situation is different for the mitral valve, where the increased portion of regurgitant flow during short beats is not systematically accompanied by a higher contribute of direct flow. Although the mean flow rates of mitral and tricuspid flows experience a similar decrease during AF (mitral flow: NSR $\mu=79.81$, AF $\mu=71.10$; tricuspid flow: NSR $\mu=79.80$, AF $\mu=71.09$), the net mitral flow

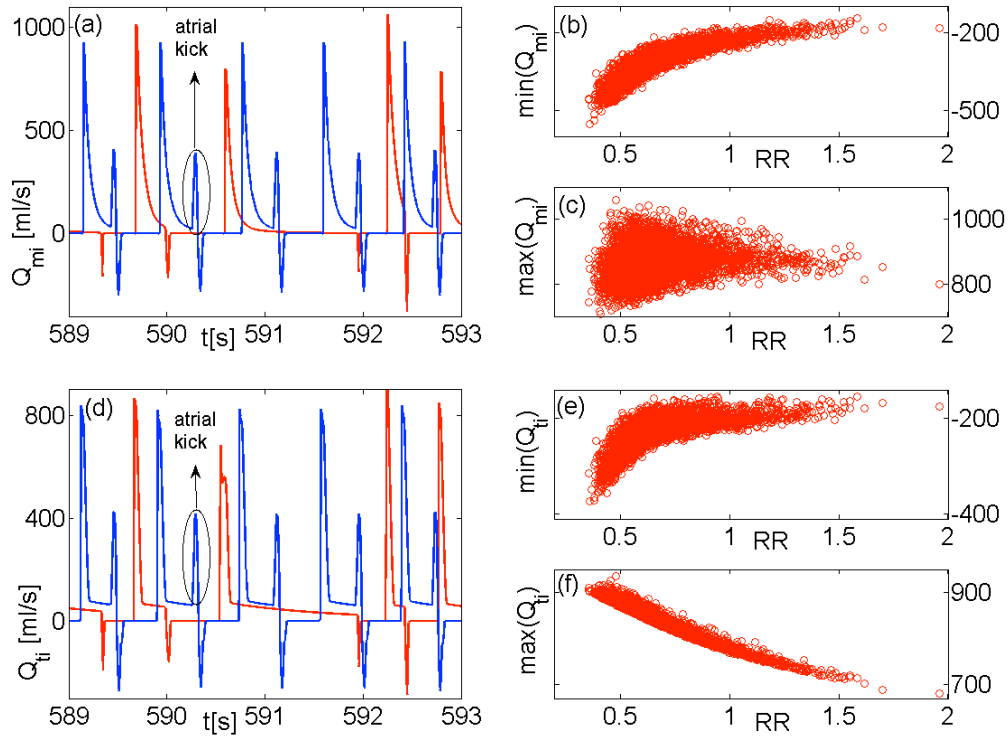


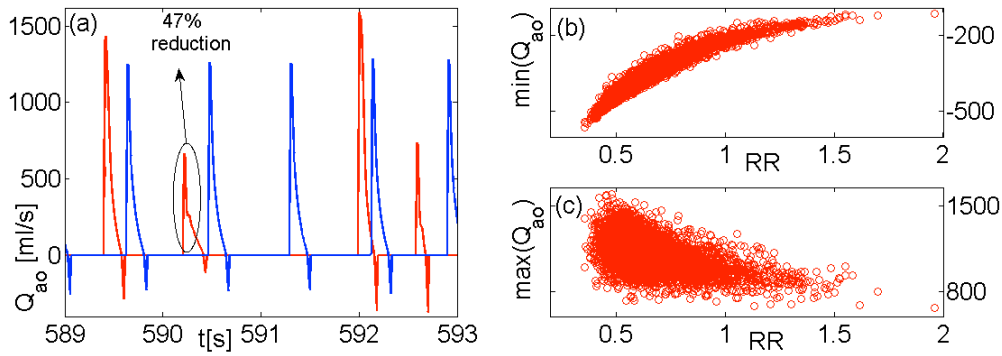
Fig. 2: Mitral (Q_{mi}) and tricuspid (Q_{ti}) flow rates. (a) Q_{mi} series. (b) AF: mitral flow regurgitant peak values as function of the heartbeat, $\min(Q_{mi})(RR)$. (c) AF: mitral flow direct peak values as function of the heartbeat, $\max(Q_{mi})(RR)$. (d) Q_{ti} series. (e) AF: tricuspid flow regurgitant peak values as function of the heartbeat, $\min(Q_{ti})(RR)$. (f) AF: tricuspid flow direct peak values as function of the heartbeat, $\max(Q_{ti})(RR)$. Blue: NSR, red: AF.

can be insufficient during rapid heartbeats, leading thereby to significant functional mitral regurgitation, as recently observed^{4,5}.

For the flows out of the left and right ventricles (aortic and pulmonary valve flows, respectively), the scenario partially reflects what happens in the corresponding atria. For both flows there is a marked positive correlation between the heartbeat length and the regurgitant peak (see Fig. 3, panels b and e). For the direct maximum peaks, the aortic flow rate presents an inverse but more sparse relation between RR and the maxima of Q_{ao} (Fig. 3c), while for the pulmonary flow dispersion of data is lower and the decreasing trend is better highlighted (Fig. 3f). These results may suggest that, due to AF, aortic valve insufficiency is more likely to occur than pulmonary valve insufficiency.

3. Conclusions

The main goal of characterizing the global response of the cardiovascular system during AF has been achieved by means of a lumped-parameter approach. Although some fine details as well as the spatial cardiovascular description are here missing, the present stochastic modeling turns out to be a synthetic and powerful tool for a deeper comprehension of the arrhythmia impact on the whole cardiovascular system. Furthermore, the current modeling can provide new comprehension on hemodynamic parameters (such as, for example, cardiac flow rates), which are difficult to measure and almost never treated in literature. The proposed approach can be exploited to predict the response to AF with the combined presence of altered cardiac conditions (e.g., left atrial appendage clamping), therefore recovering a clinical framework which often occurs in medicine.



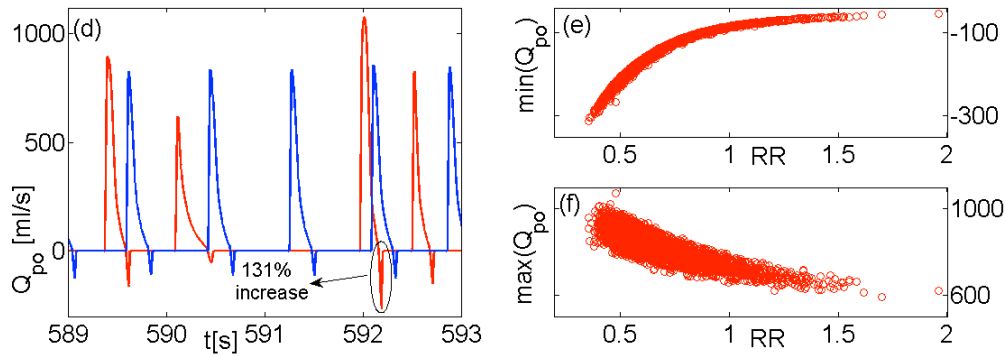


Fig. 3: Aortic (Q_{ao}) and pulmonary (Q_{po}) flow rates. (a) Q_{ao} series. (b) AF: aortic flow regurgitant peak values as function of the heartbeat, $\min(Q_{ao})(RR)$. (c) AF: aortic flow direct peak values as function of the heartbeat, $\max(Q_{ao})(RR)$. (d) Q_{po} series. (e) AF: pulmonary flow regurgitant peak values as function of the heartbeat, $\min(Q_{po})(RR)$. (f) AF: pulmonary flow direct peak values as function of the heartbeat, $\max(Q_{po})(RR)$. Blue: NSR, red: AF.

References

1. Westerhof N, Stergiopulos N, Noble MIM, *Snapshots of Hemodynamics*, Springer, 2010.
2. Korakianitis T, Shi Y, Numerical simulation of cardiovascular dynamics with healthy and diseased heart valves, *J Biomech* **39**: 1964-1982, 2006.
3. Scarsoglio S, Guala A, Camporeale C, Ridolfi L, Impact of atrial fibrillation on the cardiovascular system through a lumped-parameter approach, under review for *Med Biol Eng Comput*, 2014.
4. Vohra HA, Whistance RN, Magan A, Sadeque SA, Livesey SA, Mitral valve repair for severe mitral regurgitation secondary to lone atrial fibrillation, *Eur J Cardio-Thorac* **42**: 634-637, 2012.
5. Gertz ZM, Raina A, Saghy L, Zado ES, Callans DJ, Marchlinski FE, Keane MG, Silvestry FE, Evidence of atrial functional mitral regurgitation due to atrial fibrillation, *J Am Coll Cardiol* **58**: 1474-1481, 2011.

MITRAL VALVE REGURGITATION: CORRELATION BETWEEN QUANTITATIVE AND SEMI-QUANTITATIVE METHODS

ELENA BARBARES¹, ANTONIO RUSSO¹, MARINA CANNIZZO¹, MATTEO SCHINZARI¹, SIMONE LONGHI¹, MARCO MASETTI¹, FRANCESCO GRIGIONI¹, CLAUDIO RAPEZZI¹

¹ Cardiology, Department of Experimental, Diagnostic and Specialty Medicine – DIMES, Alma Mater Studiorum, University of Bologna, Bologna, Italy

Echodoppler quantification of mitral regurgitation (MR) is still controversial, in particular little is known about correlation between quantitative and semi-quantitative methods.

78 patients (pts) aged 58 +/- 13 years (47 M and 31 F) with at least moderate organic MR were enrolled in the period between oct 2006 and may 2012. The etiology of MR was prolapse/flail 73 pts (93%), rheumatic 2 pts (3%), post-endocarditis 3 pts (4%). Regurgitant Volume (RV) and Effective Regurgitant Orifice (ERO) quantified by PISA (RV 57± 16,7 ml, ERO 0,32 ± 0,09 cm²), Doppler (RV 58 ± 17 ml, ERO 0,34 ± 0,12cm²) and Volumetric (RV 49,9±17,5 ml, ERO 0,28±0,09 cm²) methods, were similar, particularly Doppler and PISA (R 0,89, p<0,01). A satisfactory correlation was also found between quantitative and semi-quantitative methods (jet area 9,5 ± 4,7 cm², jet area/left atrium (LA) area 41 ± 20, vena contracta (VC) (4,6 ± 1,2 mm): RV mean and jet area (R 0,5, p<0,01), RV mean and jet area/LA area (R 0,33, p = 0,002), RV mean and VC (R 0,74, p < 0,01); ERO mean and jet area (R 0,4; p 0,003), ERO mean and jet area/LA area (R 0,22, p = 0,04), ERO mean and VC (R 0,69, p <0,001).

In the evaluation of MR, quantitative methods were well correlated each other. A weaker but sufficient correlation was also detected between quantitative and semiquantitative methods, particularly with VC.

Keywords: effective regurgitant orifice area; mitral regurgitation; proximal isovelocity surface area; regurgitant volume, transthoracic echocardiography; vena contracta;

BLOOD RHEOLOGICAL PROPERTIES AND CHANGES OF OSCILLATIONS IN SKIN TEMPERATURE AFTER COLD TEST IN PATIENTS WITH TYPE 2 DIABETES

N. ANTONOVA*, V. KOSTOVA*, I. VELCHEVA**, S. PODTAEV***, N. CHAUSHEV**

** Institute of Mechanics, Bulgarian Academy of Sciences, Sofia, Bulgaria*

*** University Hospital of Neurology and Psychiatry, Medical University, Sofia, Bulgaria*

**** Research Center "FM Diagnostics", Perm, Russia*

Diabetes mellitus has high social and economic importance and accompanied with vascular degenerative complications, leading to the change in the mechanical properties of vessels of the microcirculation (capillaries, arterioles, venules and the like). It is one of the major risk factors of cardiovascular diseases.

The aim of the study is to evaluate the relationships between rheological properties of blood and dynamics of changes of the temperature oscillations corresponding to the myogenic, neurogenic and endothelial regulation of vascular tonus in patients with type 2 diabetes.

Skin temperature was measured on the palm surface of the distal phalanx of the second (index) finger with two closely-spaced sensors and were continuously measured under basal conditions (10 min), during contralateral hand immersion in cold water (3 min) and thereafter (10 min) in patients with type 2 diabetes and in control group of healthy persons by a Microtest device (Russia).

The wavelet transformation analysis was used to study the localized variations of the low amplitude oscillations of skin temperature in accordance with myogenic (0.05 – 0.14 Hz), neurogenic (0.02 – 0.05 Hz), and endothelial (0.0095 – 0.02 Hz) control mechanisms and their association with skin blood flow changes during indirect cold test in 10 patients with diabetes mellitus type 2 and 10 healthy age and sex matched controls. Dynamics of changes of oscillations in skin (cutaneous) temperature were evaluated through the root mean square values of the amplitudes obtained by the wavelet analysis in the frequency range corresponding to the mechanism of myogenic, neurogenic and endothelial regulation of vascular tonus. The measured average amplitudes in three frequency ranges were estimated by a box plot diagram.

A rotational viscometer Contraves Low Shear 30 (Switzerland) was used to measure whole blood viscosity at shear rates of 0, 0237s⁻¹ to 128,5s⁻¹ in both groups. The basic hemorheological constituents: hematocrit (HT), whole blood (WBV) and plasma viscosity (PV) were also investigated. Increased blood viscosity in patients versus controls was correlated with the amplitudes of myogenic, neurogenic and endothelial vasomotor reactivities, determined by the wavelet analysis.

5 September

S6M: Biomaterials - Prosthesis, gel, coatings and porous media

Chairs: Sara Ferraris, Feng Xu

BIOMECHANICAL STUDY USING TOTAL OSSICULAR REPLACEMENT PROSTHESIS OF THE
MIDDLE EAR
FERNANDA GENTIL

ZIRCONIA-TOUGHENED-ALUMINA COATINGS REALIZED BY MEANS OF PULSED PLASMA
DEPOSITION TECHNIQUE: PRELIMINARY RESULTS
NICOLA LOPOMO

FLUID DYNAMICS IN POROUS SCAFFOLDS STIMULATED WITH CYCLIC SQUEEZE PRESSURE
IN THE S2PR BIOREACTOR
MARCO FERRONI

FRACTIONAL-ORDER GENERALIZATION OF TRANSPORT EQUATIONS IN FRACTAL POROUS
MEDIA
MASSIMILIANO ZINGALES

HARD ZIRCONIA THIN FILMS REALIZED BY MEANS OF PULSED PLASMA DEPOSITION FOR
HIGH-PERFORMANCE UHMWPE INSERTS
MICHELE BIANCHI

EVALUATION OF DIFFERENT FIXATION MATERIALS FOR MANDIBULAR CONDYLE
FRACTURES
YUNUS ZIYA ARSLAN

AGE-RELATED CHANGES IN MECHANICAL PROPERTIES OF POLYPROPYLENE HERNIA
MESHES
MIGLENA K. DONEVA

NANOMECHANICAL EVALUATION OF BONE TISSUE REGENERATED BY MAGNETIC
SCAFFOLDS
MARCO BOI

BIOMECHANICAL STUDY USING TOTAL OSSICULAR REPLACEMENT PROSTHESIS OF THE MIDDLE EAR

FERNANDA GENTIL

*IDMEC, Clinica ORL-Dr. Eurico Almeida, Widex, ESTSP, Portugal
fernanda.fgnanda@gmail.com*

MARCO MARQUES¹, CAROLINA GARBE², MARCO PARENTE³, PEDRO MARTINS⁴, CARLA SANTOS⁵, RENATO NATAL JORGE⁶

*IDMEC, Faculdade de Engenharia da Universidade do Porto, Campus da FEUP: Rua Dr. Roberto Frias, 404
Porto, 4200-465, Portugal*

*¹marco.costa.marques@gmail.com, ²carolinagarbe@hotmail.com, ³mparente@fe.up.pt, ⁴palsm@fe.up.pt,
⁵fsantos.carla@gmail.com, ⁶rnatl@fe.up.pt*

The main goal of the present study is to analyze and characterize the behavior of the middle ear when a total ossicular replacement prosthesis (TORP) is used in the ossicular chain, in order to troubleshoot transition deafness. Using a finite element model, a dynamic study of the middle ear was made. The displacements values were obtained at the umbo and stapes footplate, for different levels of sound pressure applied at the tympanic membrane, when a cartilage in membrane-prosthesis interface of different diameters and thicknesses was used. The results were compared with the healthy middle ear model. The usage of this model aims to achieve a set technique that promotes the best possible performance of prostheses in the middle ear. The present study allows to conclude that the rehabilitation of the middle ear with TORP type prosthesis can lead to the best results when used with 4 mm diameter cartilages, with a thickness between 0.3 mm and 0.4 mm.

Keywords: biomechanics; finite element method; middle ear; TORP.

1. Introduction

The major function of the auditory system is to convert pressures variations, created by wave sound propagation, into bioelectrical signals. Problems in the normal functionality of the human ear make that this normal conversion do not happen and so is created a deafness problem. This deafness problem is related to hearing loss, which is a full or partial decrease in the ability to detect or understand sounds. Hearing impairment is a condition that can occur at any period of life, to any gender and to any race, with many origins, having a significant repercussions in human lifestyle.¹ It can be define according to its severity, lesion foci, uni or bi laterality and to according to the frequencies that are lost.² Conductive hearing loss occurs when there is a pathology in the outer or/and in the middle ear. Those pathologies can be identified as the presence of earwax, malformations in the ossicular chain, otosclerosis, tumors, otitis or tympanic membrane perforation, among other.²

In conductive hearing loss, when there is an ossicular chain malformation, the Austin-Kartush classification defines the ossicular impairment in seven classes and the corresponding ossicular chain reconstruction technique.³

The type of the prosthesis used in the rehabilitation of the middle ear, total ossicular replacement prosthesis (TORP) or a partial ossicular replacement prosthesis (PORP) depends of the level of the ossicular impairment.³

In case of a TORP, the cartilage must be interposed between the tympanic membrane and the prosthesis.⁴⁻⁷ This cartilage can be extracted from tragus.^{6, 7} The placement of the cartilage has the intention to reduce de extrusion rate of the TORP thru the tympanic membrane. The fixation of this cartilage can be done by using sutures, “glued,” placed on an available peg, or simply overlaid as a dome.⁷ According to various authors it can held in place by water adhesion forces, but still this methodology leads to a unsatisfying hearing, caused by unwanted displacements of the prosthesis.^{8,9} This methodologies can be characterized by the usage of a centered holed cartilages fixed in the base of the stapes, prosthesis with sharpened superficies that anchor in the base of the stapes and even pieces that make the connection of the prosthesis with the stapes, like the Ω Connector produced by Heinz Kurz GmbH Medizintechnik.^{8,10}

The first study related to the biomechanical behavior of the middle ear, using the finite element method (FEM), was made in 1978 relative to the middle ear cat.¹¹ Using FEM, the present study has the meaning to evaluate the sound transmission in the middle ear, when a TORP type prosthesis replaces the ossicular chain in order to solve problems of deafness transmission in a class D procedure of the Austin-Kartush classification. This class is characterized by the absence of the ossicular chain, except the stapes footplate.³ Thus, in order to understand the behavior of the middle ear when it is replaced by a TORP, a dynamic study was performed, using the ABAQUS program. In this study of forced vibrations, for frequency range between 100 Hz and 10 kHz, different sound pressures at the tympanic membrane were applied. The audible sound pressure levels applied on the membrane were 0 dB SPL (2.0×10^{-5} Pa), 60 dB SPL (2.0×10^{-2} Pa), 80 dB SPL (0.2 Pa), 90 dB SPL (0.632 Pa) and 130 dB SPL (63.246 Pa), pressures between 0 dB, considered the minimum audibility and 130 dB, the pain threshold.

2. Finite element analysis

2.1. Finite element model

The finite element model of the eardrum and ossicles (malleus, incus and stapes) of the normal ear used, was built by F. Gentil et al.^{12, 13} based on images of a 65-years-old woman. This initial model was used as the template for the model of this study, where the ossicular chain and respective muscles and ligaments are not present, and were added components as the cartilage and the TORP. This model was created in order to be within the specification of surgical techniques used and described by many authors.⁴⁻⁹ The default ABAQUS direct solver for sparse matrices was used to solve the system of equations resulting from the FEM.

The cartilage, since there were experiments for various diameters and thickness, also various models were created. The elements of cartilage for all models are of type C3D4.

Various length TORP finite elements models were created. TORP foot and head have always the same dimensions, but TORP rod has to have different sizes because of different thickness of the cartilage.

The mechanical properties of the tragal cartilage were obtained in the literature according to Wen et al. 2006.¹⁴ The material of the TORP is characterized as being titanium grade 2. The glue properties were obtained in the literature according to Schimidt 2000.¹⁵

3. Results and conclusions

The results gathered in these models are relative to the displacements in two nodes, one node from the membrane and other from the stapes base. For all pressures of models with TORP, the results were compared with a model of the healthy middle ear.

Having all the results for all the models and for all the pressures, one can say that the behaviour of a specific model in all the applied pressures is very similar, changing as expected the value of the displacement being this proportional to the pressure applied. The results were obtained for the umbo displacements (and stapes displacements) considering the diameters of 4mm and 5 mm for the cartilage and also the values of 0.3 mm and 0.7 mm for the thickness.

In the Figure 1, one can see the stapes footplate, comparing the normal model of the middle ear with the models where the ossicular chain was replaced by TORP of the 4 and 5 mm of diameter with thickness of 0.3 and 0.7 mm.

As conclusion one can say that the best results were the obtained with 4 mm of diameter and not having great importance the thickness.

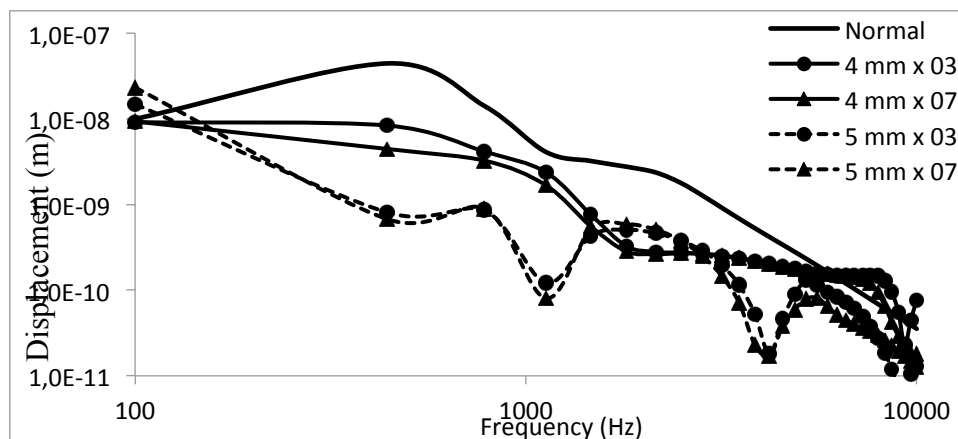


Fig. 1. Stapes footplate displacements.

References

1. Gentil F, *Estudo Biomecânico do Ouvido Médio*, Faculdade de Engenharia da Universidade do Porto, Porto, 2008.
2. Canalis RF, Abemayor E, Shulman J, Blunt and penetrating injuries to the ear and temporal bone. In: Canalis RF, Lambert PR, ed. *The ear: comprehensive otology*. Philadelphia: Lippincott Williams & Wilkins, pp. 785–800, 2000.
3. Wiet RJ and Wiet RM, Experience-driven ossiculoplasty, *Operative Techniques in Otolaryngology-Head and Neck Surgery*, vol. 21, **3**: 211–216, 2010.
4. Cavaliere M, Mottola G, Rondinelli M, Iemma M, Tragal cartilage in tympanoplasty: anatomic and functional results in 306 cases, *Acta Otorhinolaryngologica Italica*, vol. 29, **1**: 27, 2009.
5. Dornhoffer J, Cartilage tympanoplasty: Indications, techniques, and outcomes in a 1,000 patient series, *The Laryngoscope*, vol. 113, **11**: 1844-1856, 2003.
6. Neff BA, Rizer FM, Schuring AG, Lippy WH, Tympano-Ossiculoplasty Utilizing the Spiggle and Theis Titanium Total Ossicular Replacement Prosthesis, *The Laryngoscope*, vol. 113, **9**: 1525–1529, 2003.
7. Pyle GM, Ossicular sculpting for conductive hearing loss, *Operative Techniques in Otolaryngology-Head and Neck Surgery*, vol. 14, **4**: 237–242, 2003.
8. Beutner D, Hüttenbrink KB, Passive and active middle ear implants, *GMS Curr Top Otorhinolaryngol Head Neck Surg*, vol. 8, Mar. 2011.
9. Beutner D, Luers JC, Huttenbrink KB, Cartilage ‘shoe’: A New Technique for Stabilisation of Titanium Total Ossicular Replacement Prosthesis at Centre of Stapes Footplate, *The Journal of Laryngology & Otology*, vol. 122, **7**: 682-686, 2008.
10. © Heinz Kurz GmbH Medizintechnik, “Ω CONNECTOR,” Ω CONNECTOR. [Online]. Available: <http://www.kurzmed.com/en/products/otology/middle-ear-prostheses / tympanoplasty / connector/>. [Accessed: 21-Mar-2012].
11. Funnell WR, Laszlo CA, Modeling of the cat eardrum as a thin shell using the finite-element method, *J. Acoust. Soc. Am.*, vol. 63, **5**: 1461-1467, May 1978.
12. Gentil F, Natal R, Parente M, Martins P, Ferreira A, Estudo Biomecânico do Ouvido Médio, *Clínica e Investigação em Otorrinolaringologia*, vol. 3, pp. 24-30, 2009.
13. Gentil F, Garbe C, Parente M, Martins P, Ferreira A, Natal R, Santos C, Paço J, Analysis of eardrum pathologies using the finite element method. *Journal of Mechanics in Medicine and Biology*, **3**:14, 2014, World Scientific Publishing Company DOI: 10.1142/S0219519414500341
14. Wen YH, Hsu LP, Chen PR, Lee CF, Design Optimization of Cartilage Myringoplasty using Finite Element Analysis, *Tzu Chi Medical Journal*, vol. 18, **5**: 370–377, 2006.
15. Schmidt J, Bergander H, Eng L, Experimental and theoretical analysis of shear–force interaction in the non-contact regime with 100 pN force resolution, *Applied Surface Science*, vol. 157, **4**: 295-301, Apr. 2000.

ZIRCONIA-TOUGHENED-ALUMINA COATINGS REALIZED BY MEANS OF PULSED PLASMA DEPOSITION TECHNIQUE: PRELIMINARY RESULTS

NICOLA LOPOMO^{*,†}, MICHELE BIANCHI[†], MARCO BOI[†], MARIA CRISTINA MALTARELLO[°],
ANDREA VISANI^{*}, MAURILIO MARCACCI^{*}, ALESSANDRO RUSSO[†]

^{*}Laboratorio di Biomeccanica ed Innovazione Tecnologica, Istituto Ortopedico Rizzoli, via di Barbiano 1/10,
40136 - Bologna , Italy

[†]Laboratorio di NanoBiotecnologie - NaBI, Istituto Ortopedico Rizzoli, via di Barbiano 1/10,
40136 -Bologna , Italy

[°]Laboratorio di Biologia Cellulare Muscoloscheletrica, Istituto Ortopedico Rizzoli, via di Barbiano 1/10,
40136 -Bologna , Italy

n.lopomo@biomec.ior.it
www.ior.it/biomec

Protective hard coatings are appealing for several technological applications like solar cells, organic electronics, fuel cells, cutting tools and even for orthopaedic implants and prosthetic devices. Hard ceramic materials have been in fact reported to show high strength, fracture toughness, elasticity, hardness, and wear resistance. The main goal of this study was to directly deposit Zirconia-Toughened-Alumina (ZTA) coating by using a novel sputter-based electron deposition technique, namely Pulsed Plasma Deposition (PPD). The realized coatings have been preliminary characterized from the point of view of morphology, wettability, adhesion and friction coefficients. The preliminary results obtained by this novel approach suggested the feasibility of realizing ZTA coatings by means of PPD technique. Well-adherent ZTA films deposited directly on the surface of the prosthetic components of a joint implant would then allow a drastic improvement of their actual mechanical and wear performance.

Keywords: Pulsed Plasma Deposition; Zirconia-Toughened-Alumina; Ceramic Coatings; Physical Vapour Deposition.

1. Introduction

Protective hard coatings are appealing for several technological applications like solar cells, organic electronics, fuel cells, cutting tools and even for orthopaedic implants and prosthetic devices. At present for what concerns the application to prosthetic components, the coating of the surface of the metallic part with low-friction and low-wear materials has been proposed [1, 2].

Parallely, concerning the use of ceramic materials in joint arthroplasty, the zirconia-toughened-alumina (ZTA) ceramic material has been reported to show high strength, fracture toughness, elasticity, hardness, and wear resistance [3, 4]. The main goal of this study was to directly deposit ZTA coating by using a novel sputter-based electron deposition technique, namely Pulsed Plasma Deposition (PPD) [5].

The realized coatings have been preliminary characterized from the point of view of morphology, wettability, adhesion and friction coefficients.

2. Materials and Methods

Zirconia-toughened-alumina coatings were deposited by PPD technique, which is able to maintain the stoichiometry of the starting target. In this case we started from a cylindrical ZTA target (30 mm diameter x 5 mm thickness, 75% alumina / 25% zirconia) and followed the procedure described by Bianchi et al [5].

The morphology, micro-structure and chemistry of deposited coatings were characterized by Scanning Electron Microscopy (SEM) equipped with Energy Dispersive X-ray Spectroscopy (EDS) and Atomic Force Microscope (AFM).

Coating-substrate interface quality were investigated by microscratch tests. The degree of wetting was estimated by measuring the contact angle between a drop of 1 ml of ultrapure water and the surface of the sample.

Preliminary ball-on-disk tribological tests were carried out in air and deionized water coupling ZTA-coated stainless steel ball (AISI 420, 3 mm radius) against medical grade UHMWPE to evaluate the friction of the proposed coupling.

3. Results and discussion

Deposited ZTA films exhibited a smooth nanostructured surface. Coatings up to several microns thick have been deposited by PPD (Fig. 1).

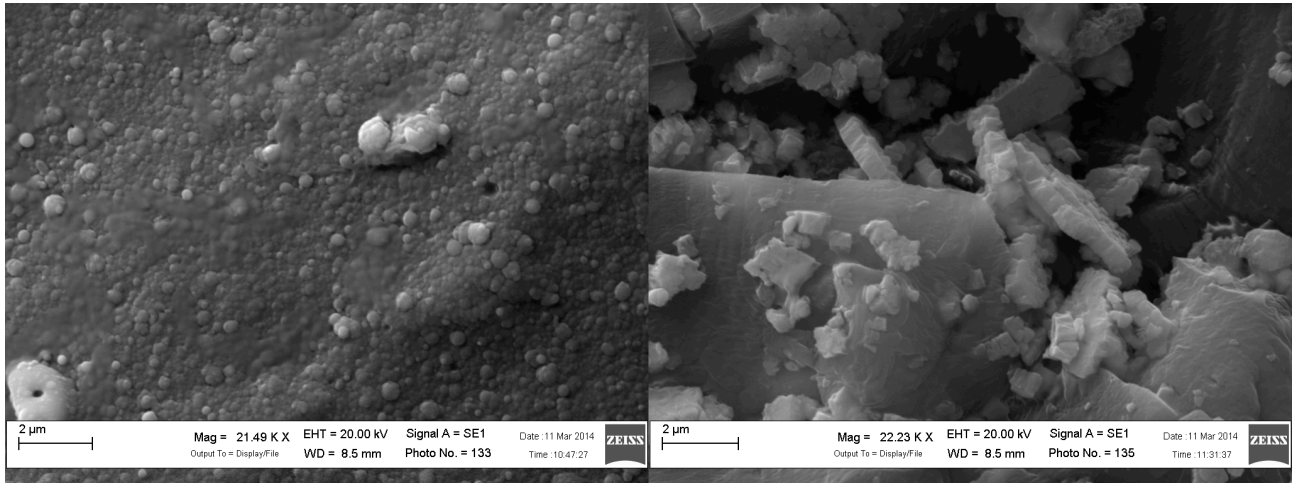


Figure 1. SEM image of the coating (left) and of a cross section of a thick ZTA film in a user-produced crack (right).

Mechanical tests showed a well-adherent films were deposited. In particular, the good interface adhesion was assessed by scratch tests, reporting at about 0.8 N the first formation of cracking in the coating during testing.

The contact angles revealed an hydrophobic behaviour of the coating (average contact angle $116^\circ \pm 2^\circ$), probably due to the nano-roughness of the coating itself.

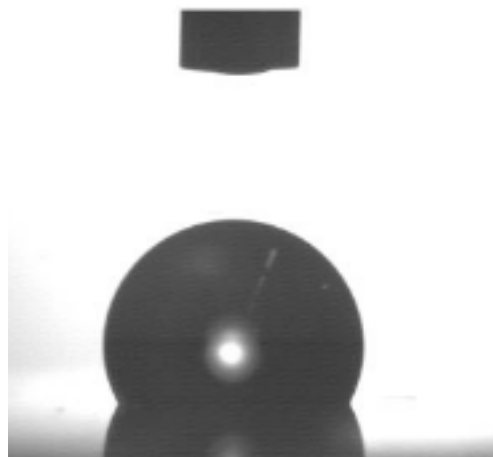


Figure 2. Contact angle test on ZTA coating.

Preliminary tribological tests carried out in deionized water after up to 10000 m tracks showed good average friction coefficient ranging from 0.12 to 0.15 (figure 3).

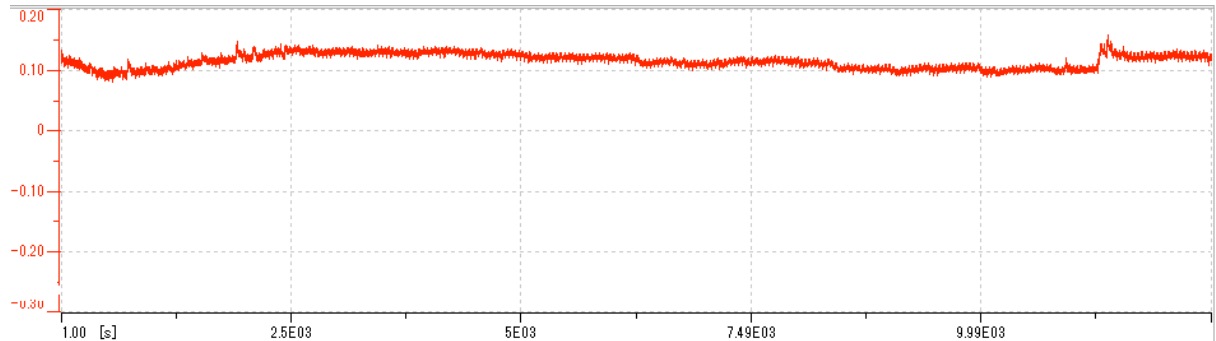


Figure 3. Friction coefficient in a tribological testing example with deionized water.

4. Conclusion

We have presented the preliminary results of a novel approach aiming to the drastically improve the performance of prosthetic couplings by introducing hard ceramic coating. The results showed suggested the feasibility of pursuing this approach of realizing ZTA coatings by means of PPD technique.

Further analyse on mechanical properties, nanoroughness and tribology should be performed. Well-adherent ZTA films deposited directly on the surface of prosthetic components of a joint implant would then allow a drastic improvement of the actual prosthetic behaviour.

Acknowledgments

This study was partially supported by the "5x1000" (2009) funding, provided by Istituto Ortopedico Rizzoli, Bologna (Italy). The authors would like to particularly thank Emil Ferretti for his remarkable contribution in laboratory IT management.

References

1. Zywieli MG et al. EXP REV MED DEV 2011, 8:187-207.
2. Rahaman MN et al. J AM CERAM SOC 2007, 90:1965-1988
3. Kurtz SM et al. J MECH BEHAV BIOMED MATER 2014, 31:107-16.
4. Fabbri P et al. DENT MATER 2014, 30(2):138-42.
5. Bianchi M. et al. J MATER CHEM 2013;1:310-318.

FLUID DYNAMICS IN POROUS SCAFFOLDS STIMULATED WITH CYCLIC SQUEEZE PRESSURE IN THE S²PR BIOREACTOR

MARCO FERRONI, GRAZIA SPATAFORA, FEDERICA BOSCHETTI

*Laboratory of Biological Structure Mechanics, Chemistry Materials and Chemical Engineering Department "Giulio Natta",
Politecnico di Milano, Piazza Leonardo Da Vinci 32
Milano, 20133, Italy*

marco.ferroni@mail.polimi.it; federica.boschetti@polimi.it; grazia.spatafora@polimi.it

SERENA GIUSTI, ARTI AHLUWALIA

*Research Center E. Piaggio, University of Pisa, Via Diotisalvi 2
Pisa, 56126, Italy*

serena.giusti@centropiaggio.unipi.it; arti.ahluwalia@unipi.it

In cardiac tissue engineering, the use of bioreactors is fundamental for applying controlled mechanical stimuli on the cells and recreate a physiological environment for cardiomyocytes cultures. This work is focused on an innovative Sensorized Squeeze Pressure (S²PR) bioreactor, able to apply a periodic contactless hydrodynamic pressures on 3D porous constructs. The fluid-dynamic environment inside the bioreactor was fully characterized using computational models, focusing on the pressures and fluid velocity profiles generated in the porous scaffold during the cyclic stimulation.

Keywords: CFD models, bioreactor, 3D porous cryogel, cardiac tissue engineering.

1. Introduction

Culture conditions are an important aspect of engineering myocardial tissue. In fact, the heart is a dynamic organ subjected to several physiological stimuli (e.g. mechanical stretch, electrical stimulation, pressure, perfusion) that impact on the tissue, its growth and function.

In cardiac tissue engineering, several studies demonstrated the role of mechanical forces and fluid movement on the organization and function of cardiomyocytes. In particular, fluid movement can increase the oxygen and nutrient transport, whereas mechanical forces can activate mechanotransduction pathways and induce cell alignment and cytoskeleton re-organization. In this work, we present Computational Fluid-Dynamical (CFD) models of the Sensorized Squeeze Pressure bioreactor (S²PR), used for studying the effect of hydrodynamic stimuli on neonatal cardiomyocytes seeded in porous 3D constructs. This bioreactor has already been tested on different cell cultures (i.e. chondrocytes, cardiomyocytes), demonstrating the ability of the squeeze stimulus to induce changes in the ECM synthesis and cytoskeletal organization of cells.

The fluid dynamic environment created around and inside the porous scaffold was fully characterized using 2D axial symmetric macro-scaled models of S²PR bioreactor. Then, the fluid dynamics predicted by the 2D models was applied to 3D micro-scaled sub-models of gelatin porous cryogels, in order to evaluate the fluid-induced forces in the porous construct during stimulation in the S²PR bioreactor.

2. MATERIAL AND METHODS

2.1 S²PR Bioreactor

The S²PR bioreactor is an innovative stimulation chamber which imposes a cyclic, hydrodynamic and contactless overpressure on cell cultures, using a simple vertical piston movement. The entity of the stimulus mainly depends on the piston velocity and the distance between the two approaching surfaces,

called meatus. In addition, during the cyclic piston movement, culture media flows through the cell-seeded construct enhancing the diffusion of oxygen and nutrients. To precisely apply the desired stimulus on a cell culture, the S²PR is provided with a force and a position sensor, assuring high precision and control of the piston movement, with a resolution of 5 μm .

The S²PR is a highly automated system with a dedicated GUI from which the user can set all the stimulation parameters such as the maximum value of the hydrodynamic pressure applied, the frequency of the stimulus and the duration of the experiment.

2.2 Gelatin Cryogel

Porous gelatin cryogels were fabricated using the freeze-dry method from gelatin 5% w/v chemically crosslinked with glutaraldehyde (GTA) 100 mM, as previously reported. Gelatin cryogels have a porosity of 90%, a permeability of $13 \times 10^{-12} \text{ m}^2$ and an elastic modulus of around 12 kPa.

2.3 Computational Model

Computational models were implemented using the commercial software Comsol Multiphysics in order to characterize the local fluid dynamics applied on the scaffold with the S²PR bioreactor, using the same conditions defined in *De Maria et al. (2011)* and *Giusti et al. (2013)*. At first, time-dependent 2D models of the transverse section of the bioreactor chamber were implemented, assuming an axial symmetric geometry in the system.

Navier-Stokes equations for incompressible fluid were used for the fluid flow in the bioreactor chamber, whereas Brinkman equations are applied for the flow in the porous scaffold. The velocity profile, evaluated by the laminar flow mode, is considered as a boundary condition of the Brinkman module, whereas the arbitrary Lagrangian-Eulerian (ALE) method is used to model the piston movement to apply the moving mesh mode to specify stationary or transient deformation of the simulation domain.

Then, two time-dependent 3D models are built idealizing the geometry of a 10 degrees section of the cylindrical scaffold fluid domain. Starting from the porosity and permeability values of these scaffold, previously defined, we estimated the average fiber dimension of 50 μm and the average pore diameter of 150 μm .

The first model (3D-T1) represents the culture of cardiomyocytes in static conditions, whereas the second one (3D-T2) is referred to a the dynamic conditions applied by the bioreactor. Starting from the 2D sub-models, we exported the pressure and velocity profiles of the fluid around the porous scaffold in order to apply these conditions to the 3D models. The surface density of cardiomyocytes ρ_{sup} was set at 30000 cells/cm².

Moreover, the oxygen consumption was implemented as an outflow ($R(c_1)$) from the solid-fluid interface, following the Michaelis Menten kinetics.

3. RESULTS

2D sub-models were used to analyse the flow conditions around the scaffold, evaluating the pressure and flow velocity at specific time-points. Figure 1 shows the changes in direction and intensity of the fluid velocity in the bioreactor chamber according to the piston movement. In fact, the fluid goes out from the meatus when the piston moves down, reaching the highest velocity when it is at the lowest position (time 1, Fig. 1 on the left), whereas the culture medium flows slowly into the meatus from the lateral sides of the chamber when the piston recedes from the scaffold (time 2, Fig. 1 on the right).

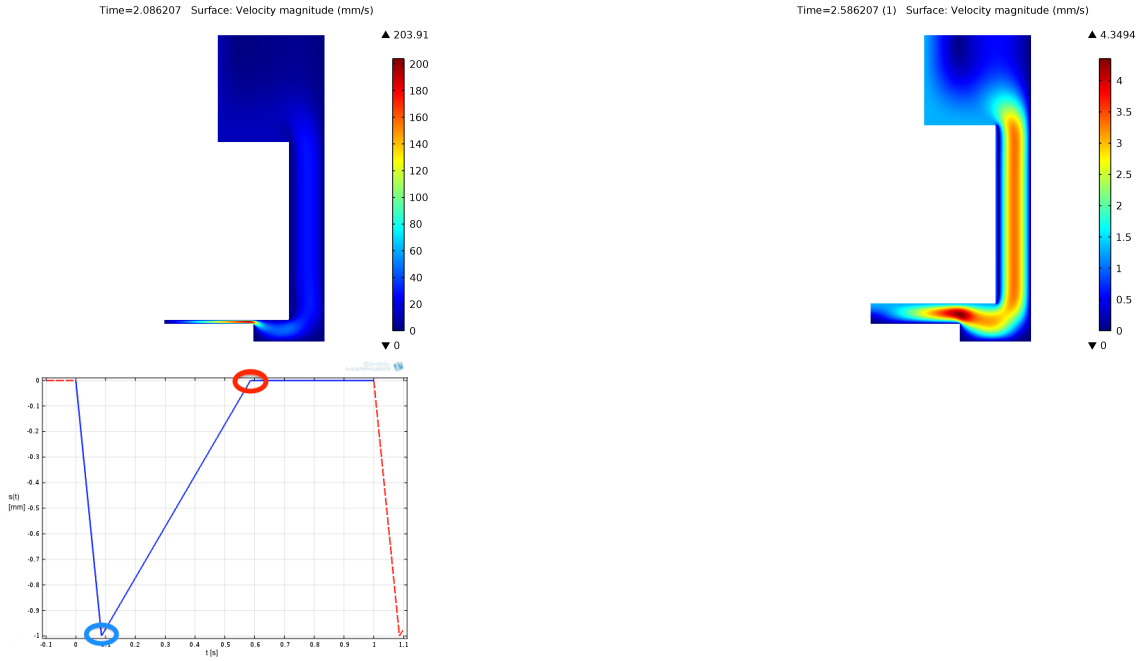


Fig. 1 Two velocity profiles at different time-points of the cyclic piston movement: when the piston is in the lowest (blue circle and profile on the left) and in the highest (red circle and profile on the centre) position with respect to the base of the bioreactor.

The fluid pressure on the upper face of the scaffold presents a parabolic profile, with the maximum value at time 1 of about 341 Pa. Results showed that the pressure values and distribution also change as a function of the time.

In figure 2 we can see the ideally reconstructed geometry of the scaffold inside the chamber, according to the real value of porosity (90%), pore diameter ($150 \cdot 10^{-3}$ mm) and permeability ($13 \cdot 10^{-12}$ m²).

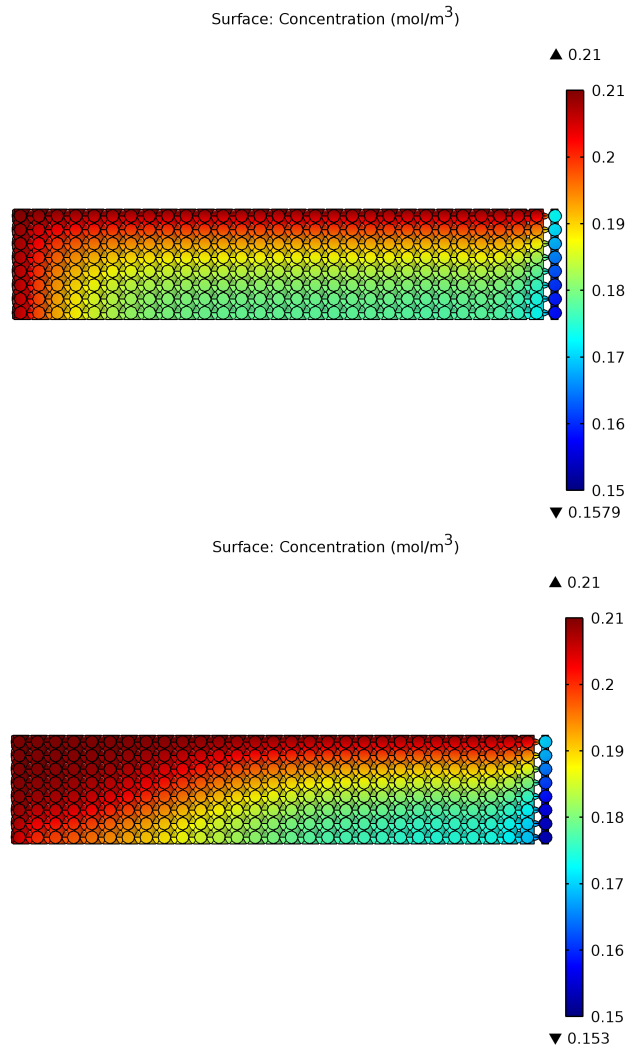


Fig. 2 Oxygen concentration distribution in the scaffold after 200 seconds of simulation in static (on the left) and dynamic conditions (on the right).

4. Conclusion

Results from 2D axial symmetric models highlighted the importance of characterizing time-dependent movement of the piston in the presence of porous cryogels, even considering just the macro-properties of the scaffold (permeability and porosity). Moreover, pressure and velocity profiles around to the scaffold are in accordance with our stationary models and pressure measurements reported in *De Maria et al. (2011)*. As previously outlined, these results are used as boundary conditions for 3D scaffold micro-scale sub-models, in order to evaluate the oxygen concentration distribution inside the scaffold, which is directly linked to the oxygen consumption of the cells seeded in the construct. A model in static condition

is developed to confirm that the hydrodynamical stimuli permit a better transport in the external part of the structure (Fig. 2). The micro-scaled models are developed as a simplified geometry of the actual scaffold, from 3D reconstructions of the sample. Moreover, the fluid-dynamic environment created in the 3D scaffolds by the S²PR bioreactor improves oxygen transport without damaging the cells only where the porous structure is perfused by an adequate flow of culture medium (Fig. 3).

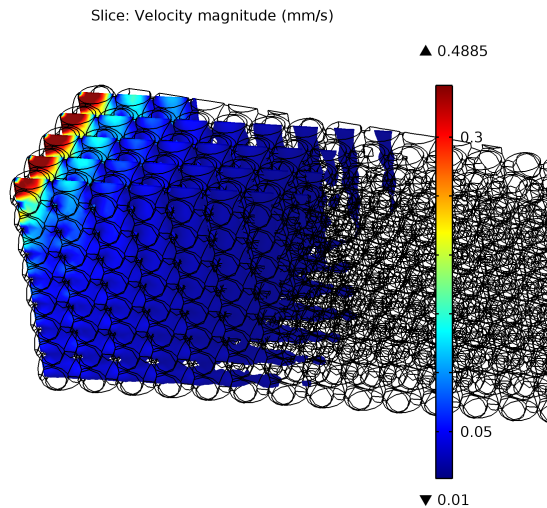


Fig. 3 Velocity field inside the scaffold, underlining the part where the fluid is in motion ($v > 0.01$ mm/s).

Acknowledgments

The study was co-funded by the Italian Ministry of Education, University & Research (MIUR) (Project PRIN 2010, MIND).

References

1. Ye KY, Black LD, Strategies for tissue engineering cardiac constructs to affect functional repair following myocardial infarction, *J Cardiovasc Transl Res*, 4:575–91, 2011.
2. Vunjak-Novakovic G, Radisic M, Obradovic B, Cardiac tissue engineering: effects of bioreactor flow environment on tissue constructs, *J Chem Technol Biot*, 81:485–90, 2006.
3. Shimko VF, Claycomb WC, Effect of mechanical loading on three-dimensional cultures of embryonic stem cell-derived cardiomyocytes, *Tiss Eng*, 14:49–58, 2008.
4. Shachar M, Benishti N, Cohen S, Effect of mechanical stimulation induced by compression and medium perfusion on cardiac tissue engineering, *Biotech Progress* 28:15519, 2012.
5. DeMaria C, Giusti S, Mazzei D, Crawford A, Ahluwalia A, Squeeze pressure bioreactor: a hydrodynamic bioreactor for noncontact stimulation of cartilage constructs, *Tiss Eng Part C* 17:75764, 2011.
6. Giusti S, Pagliari F, Vozzi F, Tirella A, Mazzei D, Cabiati M, Del Ry S, Ahluwalia A, SQPR 3.0: A Sensorized Bioreactor for Modulating Cardiac Phenotype, *Procedia Engineering* 59:219225, 2013.
7. Bigi A, Cojazzi G, Panzavolta S, Rubini K, Roveri N, Mechanical and thermal properties of gelatin films at different degrees of glutaraldehyde crosslinking, *Biomaterials* 22:7638, 2001.
8. Spinelli A, Vinci B, Tirella A, Matteucci M, Gargani L, Ahluwalia A, Domenici C, Picano E, Chiarelli P, Realization of a poro-elastic ultrasound replica of pulmonary tissue, *Biomatter* 2:3742, 2012.
9. DeMaria C, Giusti S, Mazzei D, Crawford A, Ahluwalia A, Squeeze pressure bioreactor: a hydrodynamic bioreactor for noncontact stimulation of cartilage constructs, *Tiss Eng Part C* 17:75764, 2011.

10. De Maria C, Giusti S, Mazzei D, Crawford A, Ahluwalia A, Squeeze pressure bioreactor: a hydrodynamic bioreactor for noncontact stimulation of cartilage constructs, *Tiss Eng Part C* 17:75764, 2011.

FRACTIONAL-ORDER GENERALIZATION OF TRANSPORT EQUATIONS IN FRACTAL POROUS MEDIA

MASSIMILIANO ZINGALES

DICAM, University of Palermo

Viale delle Scienze ed.8, Palermo, Italy 90128

massimiliano.zingales@unipa.it

Biomechanics and Nanomechanics in Medicine Laboratory, (BNM2)-Lab

Viale delle Scienze ed.18, Palermo, Italy 90128

massimiliano.zingales@unipa.it

GIANLUCA ALAIMO

Biomechanics and Nanomechanics in Medicine Laboratory, (BNM2)-Lab

Viale delle Scienze ed.18, Palermo, Italy 90128

gianluca.alaimo@unipa.it

The anomalous flux of a viscous fluid across a porous media with power-law scaling of the geometrical features of the pores is dealt with in the paper. It has been shown that, assuming a linear force-flux relation for the motion in the porous solid, then a generalized version of the Darcy equation has been obtained with the aid of Riemann-Liouville fractional derivative. The order of the derivative is related to the scaling property of the considered media yielding an appropriate physical picture of the use fractional-order Darcy equation recently used in scientific literature.

Keywords: Anomalous diffusion; Fractional derivative; Hausdorff dimension; Transport equations.

1. Introduction

Mass diffusion across porous media is usually dealt with by means of linear force-flux relations that relating the mass transfer rate to the gradient of pressure. However modern applications in coupled multi-field problems encountered in recent problems of biological mechanics require, however, the introduction of more complete operators to account for scale as well as of non-uniform geometrical features of the considered domain. In this regard the use of fractional-order differential calculus proved to be one of the most powerful

method to handle physical complexity (1). In the paper it will be assumed that the flow occurs in a self-similar porous volume with prescribed fractal dimension d and it will be shown that in presence of flow of a viscous

fluid in the Poiseuille laminar regime, the flux of the initially contained fluid is related to the pressure gradient fluctuations by means of a Riemann-Liouville fractional-order derivative. The differentiation-order is related to the fractal dimension of the porous volume yielding a direct connections among fractals and fractional differential operators.

2. Materials and methods

Let us assume that the flux of a Newtonian fluid occurs in a fractal-like three-dimensional porous media with anomalous dimension of the cross sectional area $[A_F] = L^d$ where $1 \leq d \leq 2$ is the Hausdorff dimension of the fractal set (2). The overall volume of the porous solid is assumed as a subset of the 3d Euclidean volume V_E that is $VF \subseteq VE$ with dimension $[V_F] = L^{1+d}$. If, instead, the usual Euclidean measure is used, then the cross-section area measure $AF = 0$ and the volume measure $VF = 0$. Let us assume that a coordinate system $\{O; x_1, x_2, x_3\}$ is attached to the Euclidean volume surrounding VF and let us define l and h , respectively, the Euclidean length of the solid and the Euclidean measure of a

characteristic dimension of the generator. Under these circumstances the cross-sectional area and the volume measure of the medium reads,

respectively, $A_F \propto h^d$ and $V_F \propto h^d l$ with an appropriate proportionality coefficient that depends on the shape of the cross-sectional area. Let us assume that the velocity field of the moving fluid across the material pores is $\mathbf{v}^T(x_1; x_2; x_3) = [0; 0; v(X; t)]$ where $\mathbf{x}^T = [x_1; x_2; x_3]$ is the coordinate vector. The gravity is neglected for the considered motion and the driving force of the moving fluid is the pressure gradient $\Delta p(t)$ that is maintained in range with values of the Reynolds number $Re = v\delta/\nu$ where δ is the hydraulic diameter and ν is the kinematic viscosity ($\nu = \mu/\rho$), lower than the value corresponding to the transition regime for the assumed fluid motion. We assume that the fluid motion occurs in a self-similar fractal set with cross-sectional area $A_f^{(k)}$ given as $A_f^{(k)} = \xi_F \left(\frac{h}{a^k}\right)^2 b^{g_k}$ where ξ_F is a shape factor that depends on the shape of the self-similar object, b^{g_k} is the number of pre-fractal at resolution k , a^{f_k} is the scale resolution factor of the k^{th} pre-fractal that is the division factor of the k^{th} length to yield an object self similar to the parent set and a , b , f_k and g_k depend on the fractal construction rule; for instance, the Sierpinski Triangle yields $a = 3$, $b = 2$, $f_k = k$ and $g_k = 3k$.

As we assume a self-similar fractal set, without any non-linear transformations among different scales, the geometric dependent exponents f_k and g_k may be defined as appropriate linear functions of the resolution level k , as $f_k = rk$; $g_k = sk$ where $r, s \in \mathbb{N} - \{0\}$ are the resolution factors. The lack of the geometric invariance of the Euclidean metric yields that the outgoing flux across the different channels of the porous medium is not uniform at any resolution scale. This consideration yield that the overall outgoing flux is provided by the algebraic contribution of the outgoing fluxes at $x_3 = l$ from the channels with cross-sections represented by the material pores as:

$$q(t) = \sum_{k=0}^{\infty} q_k(t) = \sum_{k=0}^{\infty} A_f^{(k)} \bar{v}_k(t) \quad (1)$$

where $\bar{v}_k(l, t)$ is the mean velocity field at cross-section $x_3 = l$

Under the assumption of small Reynolds number and the purely viscous linear fluid flow we assume a linear relation among the mean velocity field and the pressure gradient as from the Hagen-Poiseuille law:

$$\bar{v}_k = \frac{\alpha_s \Delta p R^2}{\mu l} = \frac{\alpha_s \alpha_r \Delta p}{\mu l} \left(\frac{h}{a^{rk}}\right)^2 \quad (2)$$

where α_s is an appropriate coefficient depending upon the shape of the channel cross-section and R is the scale-dependent hydraulic radius of the fluid channel. The hydraulic radius may be always expressed as proportional to the characteristic dimensions (base, height) of the cross-section by a proper radius factor

$$\alpha_r \text{ as in latter eq. (2) } R = \frac{h\sqrt{\alpha_r}}{a^{rk}}$$

In the following we will restrict our attention to the volume of fluid that leaves the porous solid at the time instant t , namely $q_E(t)$. Neglecting inertia forces, the outgoing time in which the fluid columns at scale k reaches the right side at $x_3 = l$ may be evaluated as $t_k = \left|\frac{l}{\bar{v}_k}\right| = \frac{\mu l^2}{\alpha_s \alpha_r h^2 \Delta p} a^{2rk}$ after straightforward manipulations, the effective volume of fluid abandoning the solid reads

$$q(t) = \sum_{k=0}^{\infty} q_k(t) \langle t_k - t \rangle^0 = \frac{\alpha_s \alpha_r h^4 \Delta p \xi_F}{\mu l} \sum_{k=0}^{\infty} \left(\frac{b^s}{a^{4r}} \right)^k \langle t_k - t \rangle^0 \quad (3)$$

where $\langle \cdot \rangle^0$ is a zero-order singularity function. The expression of the outgoing flux may be continualized for every time t in the control volume as

$$q_E(t) = f(x) = \begin{cases} 0, & 0 < t \leq t_0 \\ \propto \left(\frac{\Delta p}{l} \right)^{1-\beta} t^{-\beta}, & t \geq t_0 \end{cases} \quad (4)$$

that is depicted in fig. 1 for the Sierpinsky triangle porous solid. The exponent of the power law is related to the fractal dimension of the set as

$$\beta = \frac{2-d}{2} \quad (5)$$

3. Results

The experimental data showed in previous section allow for a fractional order generalization of the transport equation. Indeed, assuming a continualized counterpart for $f_k = r\varepsilon$ and $g_k = s\varepsilon$ where r and s are real order resolution factors, the outgoing flux reads:

$$q_E(x_3, t) \propto \left(\frac{\partial p}{\partial x_3} \right)^{1-\beta} \quad (6)$$

that, upon a proper linearization of the pressure gradient term as a perturbation of the pressure field $p(x_3, t) = p_0(x_3, t) + \bar{p}(x_3, t)$ where \bar{p} is the pressure perturbation, it reads

$$q_E(x_3, t) \propto \left(\frac{\partial p_0}{\partial x_3} \right)^{-\beta} \left(D_0^\beta + \frac{\partial \bar{p}}{\partial x_3} \right)(t) \quad (7)$$

that represents a linear type force-flux relation across a porous fractal media in terms of Riemann-Liouville fractional derivative (3;4).

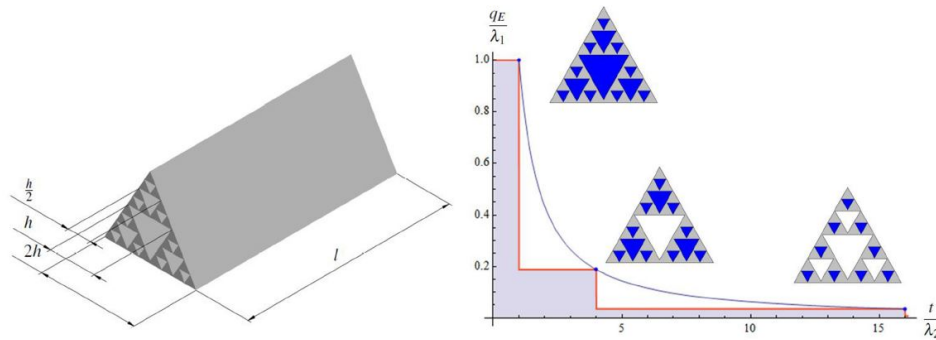


Fig. 1. Left: Sierpinsky triangle-like fractal porous solid. Right: non-dimensional outgoing flux across the fractal porous media

4. Conclusions

In the present study it has been shown that the mechanics involved in the outgoing flux of a viscous fluid in a laminar regime across a fractal porous media is capable to describe the state curdling described in previous papers 5. Fractional-order operators have been obtained under three main assumptions: i) the existence of a continualized scale parameter ϵ to describe the self-similar fractal pores of the media; ii) a proper linearization of the non-linear force-flux relation around an initial value of the pressure gradient and iii) the local form of the force-flux relation obtained as the length of the control volume tends to zero. As far as these three assumptions have been introduced in the model, a fractional-order generalization of laminar transport equation is obtained in terms of the Riemann-Liouville fractional-order operators with differentiation order related to the fractal dimension of the porous set.

References

1. Podlubny I, Fractional Differential Equations, Accademic Press, 1993 .
2. Le M'ehaute A, Crepy G, Introduction to transfer and motion in fractal media: The geometry of kinetics, Solid State Ionics, 9-10:17-30, 1983.
3. Nigmatullin RR, Le M'ehaute A, Is there geometrical/physical meaning of the fractional integral with complex exponent?, J Non-Cryst Solids, 351:2888-2899, 2005.
4. Samko SG, Kilbas AA, Marichev OI, Fractional Integrals and Derivatives: Theory and Applications, Taylor & Francis, 1987.
5. Alaimo G, Zingales M, Fractional order generalization of laminar transport equations, Comm Nlin Sci Num Sim, in press.

HARD ZIRCONIA THIN FILMS REALIZED BY MEANS OF PULSED PLASMA DEPOSITION FOR HIGH-PERFORMANCE UHMWPE INSERTS

MICHELE BIANCHI, NICOLA LOPOMO, MARCO BOI

*Laboratory of NanoBiotechnologies (NaBi), Rizzoli Orthopaedic Institute,
via di Barbiano 1/10, 40136 Bologna, Italy
m.bianchi@biomec.ior.it*

<http://www.ior.it/en/laboratori-tecnopolo/lab-nabi/nabi-laboratory>

MARIA CRISTINA MALTARELLO

*Laboratory of Musculoskeletal cell biology, Rizzoli Orthopaedic Institute,
via di Barbiano 1/10, 40136 Bologna, Italy*

FABIOLA LISCIO

*Institute for Microelectronics and Microsystems (IMM), National Research Council,
via Gobetti 101, 40129 Bologna, Italy
liscio@bo.imm.cnr.it*

ANDREA VISANI, MAURILIO MARCACCI, ALESSANDRO RUSSO

*Laboratory of Biomechanics and Technology Innovation – Rizzoli Orthopaedic Institute,
via di Barbiano 1/10, 40136 Bologna*

Plastic deformation and wear of the ultra-high molecular weight polyethylene (UHMWPE) insert have been pointed out as major issues relating to the long-term stability of an orthopaedic implant. Several solutions have been proposed to overcome this issue, including also to metal-on-metal and ceramic-on-ceramic couplings. Our hypothesis was that a hard ceramic thin film realized on the plastic component (i.e. UHMWPE) could improve the friction and wear performance in a prosthetic coupling. The main goal of the presented study was therefore to characterize this ceramic-coated plastic component from the point of view of structure and mechanical performance. The thin films were specifically realized by means of the novel Pulsed Plasma Deposition (PPD) technique.

Keywords: Pulsed Plasma Deposition; zirconia; UHMWPE; nanoindentation, wear.

1. Introduction

When a traumatic or degenerative disease leads a healthy joint to develop osteoarthritis (OA), total joint prosthesis is frequently necessary. At present, the main reason for prosthesis failure is related to the UHMWPE wear debris that leads to osteolysis and aseptic loosening of the implant itself.^{1, 2} Different solutions have been proposed to overcome this issue, including also to metal-on-metal and ceramic-on-ceramic couplings. Our hypothesis was that a hard ceramic thin film realized on the plastic component (i.e. UHMWPE) could improve the friction and wear performance in a prosthetic coupling. The main goal of the presented study was therefore to characterize this ceramic-coated plastic component from the point of view of structure and mechanical performance. The thin films were specifically realized by means of the novel Pulsed Plasma Deposition (PPD) technique.³ PPD exploits the ablation of the target material by a highly energetic (up to 25 kV) pulsed (1-100 Hz) electron beam, in order to obtain a dense hot plasma plume that is directed towards the defined substrate, preserving the target stoichiometry.⁴ The high energy involved in the generation of the plasma plume and the pulsed nature of the electron beam, are responsible for the strong adhesion, high fidelity in the transfer of the target chemical composition and for good mechanical properties of the coatings, even at room temperature and without post-deposition

treatments.⁵ The above-mentioned features, together with the high electrical efficiency (up to 30%), the ability of ablating transparent or highly reflective materials and lower scaling-up costs, when compared for example to the conceptually-similar Pulsed Laser Deposition technique, are envisaged to open the way for the development of functional coatings on heat-sensitive materials like plastics useful in several technological fields.⁶

2. Materials and Methods

3%Yttria-stabilized zirconia films were deposited by PPD technique on medical-grade UHMWPE substrates. The morphology and micro-structure were characterized by Scanning Electron Microscopy (SEM) equipped with Energy Dispersive X-ray Spectroscopy (EDS), X-ray diffraction (XRD) and X-ray Photoelectron Spectroscopy (XPS). Mechanical properties were investigated by nanoindentation and scratch tests. Ball-on-disk tribological tests were carried out in air, deionized water and physiological solution against alumina balls (6 mm diameter, grade 200) used as counterpart to evaluate the friction of the proposed approach and the corresponding worn track were analyzed by SEM-EDS. Starting from the aforementioned working hypothesis, the main goal of this study was to perform an extended investigation concerning the tribo-mechanical behavior of zirconia thin films deposited on UHMWPE substrate comparing the obtained results - i.e. strength to plastic deformation, creep behavior and wear - with the properties of pristine UHMWPE.

3. Results

Deposited zirconia films up to several micron thickness exhibited a fully cubic structure and a smooth nanostructured surface (Fig. 1).

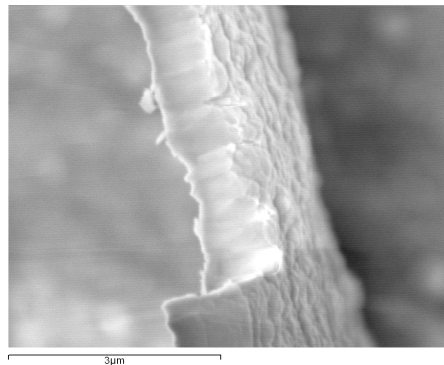


Figure 1. SEM image of the cross section of a thick YSZ film deposited on UHMWPE.

Nanoindentation tests revealed good high hardness and Young's modulus values (17 GPa and 154 GPa respectively, Fig. 2), while critical fracture tests revealed no radial cracks, spalling or pile-up phenomena were observable. The very strong interface adhesion was also assessed by scratch tests (with initial delamination at about 2 N load).

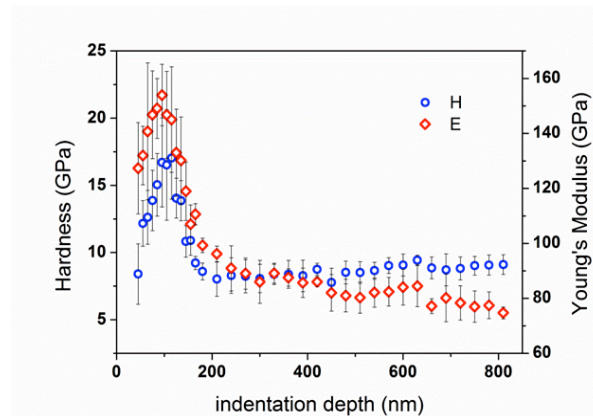


Figure 2. Nanoindentation curve reporting hardness and elastic modulus of YSZ film deposited on UHMWPE.

An indentation depth reduction of about 330% was registered when the UHMWPE substrate was covered by a ceramic film as thin as 1.5 micron. Further, the material yielding under an applied constant load (creep) was larger for UHMWPE compared to coated UHMWPE, whose total creep being only the 19% of the total creep of UHMWPE, respectively. Finally, preliminary tribological tests carried out in air against an alumina ball counterpart showed wear rate as low as $3.2 \cdot 10^{-6} \text{ mm}^3 \text{ N}^{-1} \text{ m}^{-1}$ after 500.000 cycles, showing an average friction coefficient evaluated on unpolished materials ranging from 0.15 to 0.3 in air.

4. Conclusions

The proposed approach was able to directly coat the plastic insert of a commercial implant joint with hard ceramic materials, thus providing specific additional mechanical and superficial properties, while preserving the well-established mechanical properties of UHMWPE. The results of this study showed an alternative and promising approach to improve UHMWPE mechanical properties in arthroplasty.

Acknowledgments

This study was supported by the project “Nanostructured Coatings Enhancing Material Performances in Joint Arthroplasty” (project code: 2012-1838), co-funded by the Italian Ministry of Health. This study was partially supported also by the “5x1000” (2010) funding, provided by Istituto Ortopedico Rizzoli, Bologna (Italy). The authors would like to thank Emil Ferretti and Carmelo Carcasio for their contribution to the management of IT and mechanical workshop.

References

1. Sobieraj MC, Rimnac CM, Ultra high molecular weight polyethylene: mechanics, morphology, and clinical behavior, *J Mech Behav Biomed Mater* **2**:433-443, 2009.
2. Dumbleton J, Manley MT, Edidin AA, A literature review of the association between wear rate and osteolysis in total hip arthroplasty, *J Arthrop* **17**:649-661, 2002.
3. Nistor M, Mandache NB, Perrière J, *J Phys Appl Phys* **41**:165205, 2008.

4. Yarmolich D, Nozar P, Gleizer S, Krasik YE, Mittica G, Ancora C, Brillante A, Bilotti I, Taliani C, *Jpn J Appl Phys* **50**:08JD03, 2011.
5. Bianchi M, Russo A, Lopomo N, Boi M, Maltarello MC, Sprio S, Baracchi M, Marcacci M, *J Mater Chem B* **1**:310-318, 2013.
6. Mathis JE, Christen HM, *Phys C* **459**:47-51, 2007.

EVALUATION OF DIFFERENT FIXATION MATERIALS FOR MANDIBULAR CONDYLE FRACTURES

EROL CANSIZ

*Department of Oral and Maxillofacial Surgery, Faculty of Dentistry,
Istanbul University, Capa, Istanbul, Turkey 34093
erol.cansiz@istanbul.edu.tr*

SUZAN CANSEL DOGRU

*Department of Mechanical Engineering, Faculty of Engineering
Istanbul University, Avcilar, Istanbul, Turkey 34320
cansel.gurcan@istanbul.edu.tr*

YUNUS ZIYA ARSLAN

*Department of Mechanical Engineering, Faculty of Engineering
Istanbul University, Avcilar, Istanbul, Turkey 34320
yzarslan@istanbul.edu.tr
<http://yunusziya.wix.com/biomechanics>*

In this study, comparative evaluation of the mechanical properties of resorbable and titanium miniplates, which are used for the fixation of the mandibular condyle fractures, was carried out using finite element analysis (FEA). To do so, first two dimensional computed tomography images of mandibles recorded from ten adult patients were converted into three-dimensional solid body models. Then these models were transferred to the finite element software. In the finite element stage of the study, a condyle fracture was created onto the mandible and double-titanium and double-resorbable miniplates were separately fixed to the mandible surface such that the fractured sites to be firmly attached. Stress distribution over the plates and interfragmentary displacements between adjacent surfaces, which stem from the clenching force applying to the mandible, were calculated using FEA. It was observed from the results that maximum tensile stresses occurred in the titanium miniplates were significantly higher than those obtained from resorbable miniplates ($p<0.01$). Higher maximum displacements between fractured surfaces were observed in the case of resorbable plate systems ($p<0.01$). Maximum stress and displacement values obtained from both titanium and resorbable plate systems were under clinically acceptable limits. According to results, resorbable plates showed a similar reliability with titanium miniplates in terms of withstanding various stress and strain deformations.

Keywords: Mandibular condyle fracture; titanium miniplate; resorbable miniplate; finite element analysis.

1. Introduction

The condylar process is one of the most frequently fractured regions after traumatic injuries involving the mandible and its treatment is technically challenging.¹ There are two main treatment methods as conventional intermaxillary fixation and rigid internal fixation by surgical approach. Rigid internal fixation, which is providing functional stability during healing process, is now accepted as routine procedure for surgical management of mandible fractures.² It is well known that ideal reduction is the main point of the healing process and the ideal rigid fixation hardware must provide strong and rigid reduction.³

There are many different types of rigid fixation hardware systems used for mandibular condyle fractures and each of these systems has the specific pros and cons.⁴ Titanium miniplates and screws have been widely used for rigid fixation of the mandibular condyle fractures⁵. The main drawback of these metallic fixations is to require a second surgery to be removed from the body. The development of resorbable materials has proposed an effective remedy for this problem. However, the reliability of the resorbable materials in fixation of different jaw sites after fractures remains controversial.⁶ The miniplates used for fixation of the mandibular fractures must i) withstand various stress and strain deformations due to tensile forces, ii) have to be malleable for easy adaptation to bone surface and, iii) have minimal dimensions to be covered by mucosa.

In this study, biomechanical properties of miniplates used for mandibular condylar neck fractures, fabricated from resorbable and titanium materials, were comparatively evaluated by using finite element analysis (FEA).

2. Materials and Method

2.1 Data Collection and Study Design

Computed tomography images of mandibles from ten adult patients, which were recorded previously for different reasons rather than a pathology effecting ramus and condyle, with an axial thickness of 0.5 mm were used for the construction of three dimensional (3D) mandible models. In order to observe the effect of topographic features of mandible on biomechanical behaviors, 10 different 3D models were used to obtain statistical results. Initially, mandibles were isolated from whole CT data and 3D computer models were reconstructed. The cortical layer was designed all around the mandibles in 1 mm thickness. Then, diagonal fracture lines starting from mandibular notch and reaching to the posterior border of the ramus, completely separating the condyle and the vertical ramus, were simulated (Fig. 1). The fracture line designed completely dislocated and boundary conditions were not implemented between fracture parts. Two four-hole isotropic and homogenous miniplates, which are made of titanium and resorbable (copolymer of L-lactide (17%), D-lactide (78.5%), and TMC monomers (4.5%)) materials with 1 mm thickness, were designed. Double-titanium and double-resorbable miniplates were separately placed onto the appropriate positions between the fractured parts in 3D construction software (Fig. 1). Four isotropic and homogenous miniscrews, with 1.55 mm in diameter, were also designed and placed into the bone passing through the miniplate's screw holes. It was considered that the fixation of the screws to the bone is rigid and the functional forces were transferred from bone to the miniplate via screws completely. Anisotropic properties of mandible were negligible.

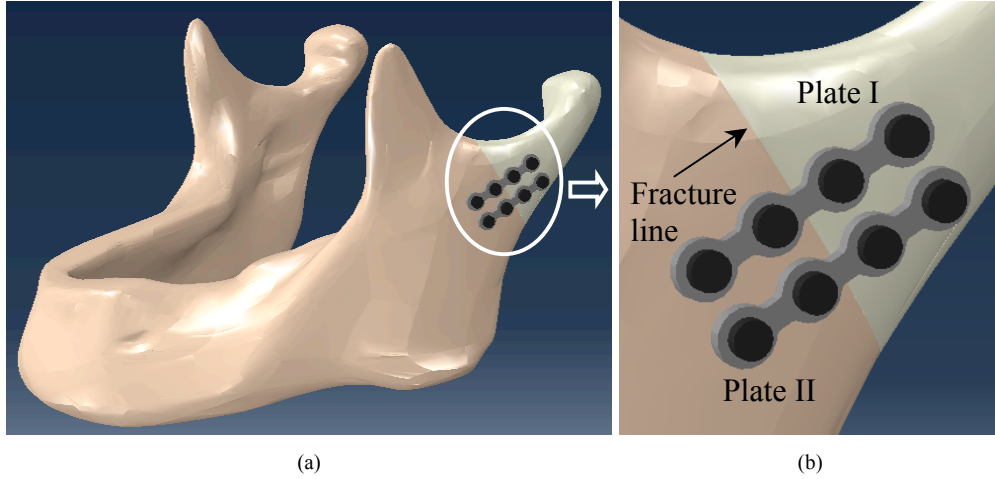


Fig.1 A typical representation of a mandible with miniplates which are used as fixators for healing of the mandibular condyle fracture.

(a) General perspective view, (b) zoom-in view.

2.2 Finite Element Analysis

Since the spongy layer of bone does not provide meaningful stiffness and nearly all strength of the bone is compensated by the cortical layer, all mandibles were modeled as a shell, which consist of cortical bone layer with 1 mm thickness. Double miniplate system, which has been well accepted as standard procedure in maxillofacial surgery,⁵ were applied to fix the simulated mandibular condylar fracture. Hereafter the miniplates, which were placed on the superior and inferior condyle neck, are referred to as Plate I and Plate II, respectively (Fig 1). All plates were assumed to have linearly elastic - isotropic behavior and their mechanical properties can be described by the Young's modulus and Poisson's ratio. The mechanical properties of the cortical bone, titanium and resorbable miniplates were given in Appendix A.

Global edge length of 0.75 mm and quadratic tetrahedral element type were assigned for the miniplate and screw meshing. For the cortical meshing, 1.5 mm global edge length and 3-node triangular shell element type were chosen. All ten models had 46560 elements and 28959 nodes in average, thereby enabling the model has a high accuracy.

Each screw was determined to be bounded (no slip and clearance) with miniplates and cortical bone, which enables miniplates to be fixed firmly to the cortical bone. The bone surfaces between fracture lines were considered to be frictional.

A clenching force of 62.8 N, which is vertical to the occlusal plane of molar region at the same site of fracture line, were applied for the simulation of the unilateral molar clenching forces and different pairs of parallel vectors were preferred for the realistic simulation of clenching movements.⁷ The condylar heads were constrained to all translation movement and only allowed for rotational movement. For all cases, the load and analysis were assumed static.

3. Results

Von-Misses stress distribution and interfragmentary displacements were comparatively evaluated according to the results obtained from FEA.

Maximum stresses over the miniplates and maximum displacements between the fracture surfaces for each mandible were given in Table 1. Maximum stress values observed in the titanium miniplates are higher than those in the resorbable miniplates for all cases. Also, maximum displacement values occurred in the resorbable plate system are higher than those in the titanium plate system for all cases. To observe whether the stress and displacement differences observed between titanium and resorbable plate systems are statistical significant, one way ANOVA was employed. The differences were evaluated at a level of significance of 0.01.

Table 1. Maximum stress and displacement values obtained from double-titanium and double-resorbable miniplate systems.

Number of mandible model	Maximum stress value in the plates (MPa)				Maximum displacement between fractured surfaces (μm)	
	Titanium plate I	Titanium plate II	Resorbable plate I	Resorbable plate II	Titanium plate system	Resorbable plate system
Model 1	37	20	8	5	0.046	0.458
Model 2	36	30	11	7	0.398	1.750
Model 3	33	33	6	6	0.545	1.690
Model 4	33	38	7	8	0.528	1.440
Model 5	42	14	12	6	0.541	2.150
Model 6	33	44	2,8	10	0.600	3.040
Model 7	45	45	9	10	0.762	3.870
Model 8	28	13	7	2,3	0.333	0.973
Model 9	40	20	11	6	2.700	5.880
Model 10	38	55	4	26	0.226	3.650

It was observed that the maximum stress and displacement differences between titanium and resorbable plate systems were statistically significant (Fig 2). Averages of maximum stresses were calculated as 36.5 MPa and 8.63 MPa for titanium and resorbable fixators, respectively (Fig. 2a). Averages of maximum displacements were calculated as 0.66 μm and 2.49 μm for titanium and resorbable materials, respectively.

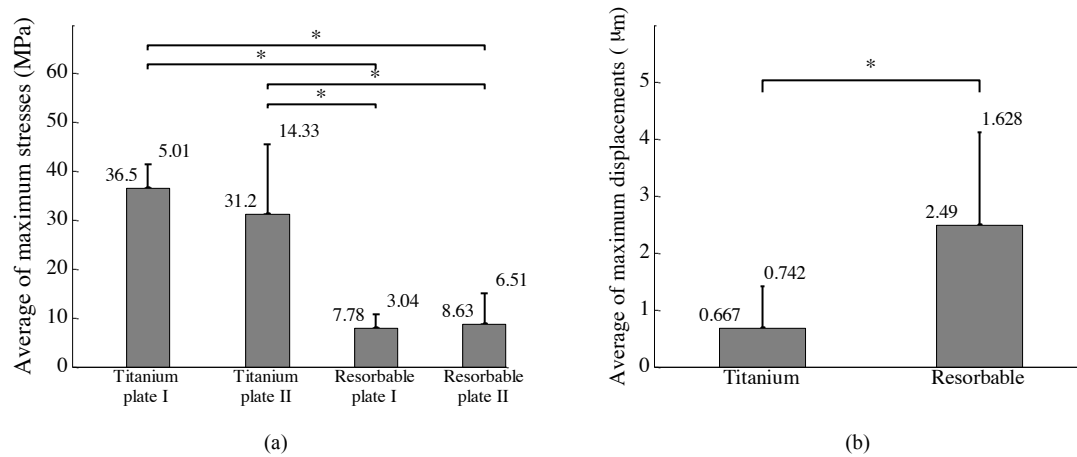


Fig. 2. Average (\pm standard deviation) values of (a) maximum stresses over titanium and resorbable plates and (b) displacements between fractured surfaces for all ten cases. * $p < 0.01$

4. Discussion

Mandibular condyle fractures are one of the most common fracture types of the maxillofacial region⁸ and the ideal treatment protocol for condylar fractures are still controversial. The conventional method, i.e. the intermaxillary fixation and functional treatment combination, is still used.⁹ On the other hand, rigid fixation by open reduction has become popular thanks to the developments in the field of osteosynthesis technologies.¹⁰

Intermaxillary fixation is not a comfortable choice and has side effects mostly on periodontal tissues. Also it causes function loss during healing period. By the open reduction, patients can return to function earlier than intermaxillary fixation significantly.¹¹ Otherwise, need to surgical approach and, in some cases, second surgery to remove fixation hardware are the basic disadvantages of open reduction.

The utilization of resorbable osteosynthesis systems is useful for the elimination of second surgery to remove rigid fixation hardware, but we are not still sure the mechanical qualifications of this kind of resorbable rigid fixation materials.¹² In addition, resorbable rigid fixation hardware is more expensive than the non-resorbables and they are also thicker to compensate the mechanical inability.

The utilization of double 4-hole titanium miniplates and 8 miniscrews is the material of choice for the rigid fixation of mandibular condyle fractures by open reduction.¹³ In this research, biomechanical properties of resorbable fixation hardware were compared with the conventional titanium miniplates. For this aim, maximum Von-Mises stress distribution on the miniplates and displacement between fractured surfaces during loading were evaluated.

Advantages of the two-titanium miniplate placement system for the treatment of mandibular condylar fractures by open reduction were experienced in clinical and in in-vitro studies and this method has become a standard protocol.⁵ For this reason, fixation by double 4-hole titanium miniplates were considered as control group and compared with fixation by double resorbable 4-hole miniplates in this study.

The mechanical characteristics of resorbable material are directly related to the Young's modulus and the Poisson's ratio. Therefore, to evaluate the material-based differences between titanium and resorbable miniplates, all parameters other than Young's modulus and Poisson's ratio, which are affecting mechanical behavior of fixations, were kept stable.

Considering the maximum Von-Mises stress results, statistically significant difference was found between resorbable and titanium materials. All maximum stresses occurred over both material types stayed clearly below the plastic deformation limits of the materials (see Appendix A for the yield stress values of materials). Although the titanium is more resistant to the tensile stress than the resorbable material, both the titanium and resorbable materials are suitable for rigid fixation of mandibular condyle fractures.

Because of its more flexible characteristics, displacements between fracture lines were found significantly higher in resorbable material fixation system than those in the titanium system. On the other hand, both displacement values of titanium and resorbable materials were below the acceptable gap healing values.¹⁴

5. Conclusion

The actual forces being applied to the condyle have not yet been completely identified and scientists are still searching the ideal rigid fixation material to deal with functional forces. Today's biomaterial technology brings us titanium as a biocompatible, mechanically resistant, cheap and reliable material, but not as effective as it is expected. Due to the necessity of removal surgery for titanium plate, it can be concluded that resorbable miniplates can be a convenient alternative to the titanium material for the rigid fixation of mandibular condyle fractures.

Acknowledgements

This research was supported by The Research Fund of the Istanbul University, Project No. YADOP-42672.

Appendix A

Model parameters

Table A.1. Mechanical properties of the cortical bone and miniplates evaluated in this study.

	Young's modulus (MPa)	Poisson's ratio	Yield Strength (MPa)
Cortical bone	15000	0.33	-
Titanium miniplate	115000	0.34	462
Resorbable miniplate	3150	0.46	72

References

1. Scolozzi P, Richter M, Treatment of severe mandibular fractures using AO reconstruction plates. *J. Oral Maxillofac. Surg.* **61**:458-461, 2003.

2. Moreno JC, Fernandez A, Ortiz JA, Montalvo JJ, Complication rates associated with different treatments for mandibular fractures. *J. Oral Maxillofac. Surg.*, **58**:273-280, 2000.
3. Mathog RH, Toma V, Clayman L, Wolf S, Nonunion of the mandible: an analysis of contributing factors. *J. Oral Maxillofac. Surg.*, **58**:746-752, 2000.
4. Pilling E, Eckelt U, Loukota R, Schneider K, Stadlinger B, Comparative evaluation of ten different condylar base fracture osteosynthesis techniques, *Br. J. Oral Maxillofac. Surg.*, **48**:527-531, 2010.
5. Haug RH, Peterson GP, Goltz M, A biomechanical evaluation of mandibular condyle fracture plating techniques. *J Oral Maxillofac. Surg.*, **60**:73-81, 2002.
6. Bayram B, Araz K, Uckan S, Balcik C., Comparison of fixation stability of resorbable versus titanium plate and screws in mandibular angle fractures, *J. Oral Maxillofac. Surg.*, **67**:1644-1648, 2009.
7. Arbag H, Korkmaz HH, Ozturk K, Uyar Y, Comparative evaluation of different miniplates for internal fixation of mandible fractures using finite element analysis. *J. Oral Maxillofac. Surg.*, **66**:1225-1232, 2008.
8. Santler G, Karcher H, Ruda C, Köle E, Fractures of the condylar process: surgical versus nonsurgical treatment. *J. Oral Maxillofac. Surg.*, **57**:392-397, 1999.
9. Ellis E, Throckmorton G, Treatment of mandibular condylar process fractures: Biological considerations. *J. Oral and Maxillofac. Surg.*, **63**:115-134, 2005.
10. Zachariades N, Mezitis M, Mourouzis C, Papadakis D, Spanou A. Fractures of the mandibular condyle: review of 466 cases. Literature review, reflections on treatment and proposals. *J. Craniomaxillofac. Surg.*, **34**:421-432, 2006.
11. Baker AW, McMahon J, Moos KF, Current consensus on the management of fractures of the mandibular condyle: A method by questionnaire. *Int. J. Oral Maxillofac. Surg.*, **27**:258-266, 1998.
12. Kulkarni RK, Moore EG, Hegyeli AF, Leonard F, Biodegradable poly(lactic acid) polymers. *J. Biomed. Mater. Res.*, **5**:169-181, 1971.
13. Cutright DE, Hunsuck E, The repair of fractures of the orbital floor using biodegradable polylactic acid. *J. Oral Surg.*, **33**:28-34, 1972.
14. Augat P, Margevicius K, Simon J, Wolf S, Suger G, Claes L, Local tissue properties in bone healing: influence of size and stability of the osteotomy gap. *J. Orthop. Res.*, **16**:475-481, 1998.

AGE-RELATED CHANGES IN MECHANICAL PROPERTIES OF POLYPROPYLENE HERNIA MESHES

MIGLENA KIRILOVA-DONEVA^{1,2}

*Faculty of Pharmacy, Medical University-Sofia, Dunav Str.2,
Sofia 1000, Bulgaria¹
miglena_doneva@abv.bg*

DESSISLAVA PASHKOULEVA²

*Institute of Mechanics, Bulgarian Academy of Sciences,
Acad.G.Bonchev Str., Bl. 4, Sofia 1113, Bulgaria²
dessip@imbm.bas.bg*

VASIL KAVARDZHIKOV²

*Institute of Mechanics, Bulgarian Academy of Sciences,
Acad.G.Bonchev Str., Bl. 4, Sofia 1113, Bulgaria²
kavarj@imbm.bas.bg*

The purpose of this study was to assess age-related changes in mechanical properties of hernia meshes Surgimech (SM), Tecnomesh (TM) and Surgipro (SP). Tensile test was applied to mesh specimens cut along the rows of loops (T direction) and parallel to the column of loops (L direction). From the stress - stretch ratio curves the secant modulus at 5% strain, maximum stress and maximum stretch were determined.

The results indicated an increase in elasticity of TM in both directions and of SM in longitudinal direction. Elasticity of SP was not altered significantly after 4 years. The ultimate stress and stretch of meshes remain practically unchanged.

Age-dependent variations in elasticity of polypropylene meshes were compared with the elasticity of human abdominal fascia. The elastic properties of hernia meshes in L direction approaches the elastic properties of the fascia in direction parallel to fibers for 45-64 years old patients. In T direction the value of secant modulus for all meshes exceeds considerably the physiological elasticity of investigated fascia. SP samples cut in T direction approach elastic properties of fascia in L direction for 65-80 years old donors. The results suggested a necessity of further improvement of mechanical properties of these meshes.

Keywords: hernia meshes; mechanical compatibility; age-related changes.

1. Introduction

The decrease of number of re-operations is real challenge for health care system. One of the problems which influences the outcome of operations is age-related variability of mechanical properties of hernia meshes. The effects of age on the mechanical properties of hernia meshes depend on their structure, pore size, type of used material, filament diameter, coatings of the surface or number of layers.¹ The long-term mechanical properties of polypropylene hernia meshes were evaluated from many authors in animal models.^{2,3,4} Dora reported about variations in polypropylene (PP) mesh SPARC explanted after two, six and 12 weeks post implantation and the changes of tensile strength, stiffness, shrinkage and distortion were evaluated. It was observed that the stiffness of polypropylene mesh increased from its baseline values.³

Ferrando et al. evaluate the post implantation changes in biomechanical response of Marlex placed in the abdominal wall of rats for 30 days.² He reported that no difference in stiffness of the samples before and after implantation was found. Cobb et al. performed textile analysis of three of polypropylene meshes - Marlex, Prolene Soft and Ultrapro in porcine model. He assessed their stiffness pre-implantation and five months post-implantation and reported that only one mesh – Ultrapro exhibited significant reduction

of its stiffness.⁴ The big diversity of the reported results after using animal models imposed necessity of evaluation of the age-related changes in hernia meshes according to mechanical properties of human tissue. The aim of the study is to quantify the long-term changes in mechanical properties of three commercially available hernia meshes and to assess their mechanical compatibility with human abdominal fascia.

2. Materials and Methods

Polypropylene knitted reinforcement monofilament hernia mesh Surgimech (Aspi Medical, France), Tecnomesh (TecnoMedic GmbH, Germany) and Surgipro (USSC, USA) were investigated. The mesh specimens (10x70mm) were cut in two perpendicular directions - along the rows of loops (T - transversal direction) and parallel to the column of loops (L - longitudinal direction). Ten samples before and ten samples up to four years after expiration date (ED) were used in tensile tests. Uniaxial tests were performed using a testing machine FU1000/e at 0.13 mm/sec rate of elongation. After mechanical testing load and displacement data were converted to stress and strain. From the stress - stretch ratio curves the secant modulus at 5% strain - $E_{(5)}$, maximum stress T_{max} and maximum stretch λ_{max} were determined. $\lambda_{max} = (L_0 + \Delta L) / L_0$, where L_0 is initial length of sample and ΔL is elongation of sample.

For the purposes of this study the results from tensile testing of 84 samples of human umbilical and inguinal abdominal fascia from 13 donors were used. Experimental protocol was described in Ref. 5. Samples were cut parallel to fibers - L direction and perpendicular to fibers - T direction. The average age of the subjects was 66.3 years in the range of 45 - 87 years. The specimens were divided into three age groups - up to 64 years (group A- 8 samples cut in L direction and 8 samples in T direction), between 65-80 years (group B- 14 samples in L and 14 samples in T direction) and between 81-90 years (group C - 23 samples in L direction and 17 samples in T direction). Samples of umbilical and inguinal fascia were combined because of preliminary results which stated that there are no statistically significant differences in the mechanical properties of abdominal fascia according to localization. The median values of secant modulus and absolute median deviation for investigated samples were calculated and compared with mechanical parameters of hernia meshes. The differences between groups were assessed by paired *t* test and ANOVA. A *p*-value of less than 0.5 was considered to be statistically significant for all comparisons.

3. Results

The values of main mechanical parameters for investigated meshes-maximal stress T_{max} , maximum stretch λ_{max} and secant modulus of samples are presented in Table 1. The values for λ_{max} exceeds 1.88 for all meshes with the exception of the SP samples in T direction where λ_{max} is 1.74. Maximum stress is greater than 8 MPa. Maximal stress and stretch of investigated meshes remain practically unchanged for investigated period. The differences between values of T_{max} and λ_{max} before and after expiration date are not statistically significant except the value for λ_{max} in T direction for TM (*p*=0.027) and for SM (*p*=0.07).

The secant modulus $E_{(5)}$ for SM and TM decreases about 30% in direction parallel to the column of loops but along the rows of loops (transversal direction) only modulus of TM decreases. The value of $E_{(5)}$ for SP and SM remain constant.

Table 1. The values of mechanical parameters for Surgimech, Tecnomesh and Surgipro before and after expiration date (ED).

Type of mesh	Direction	T_{\max} [MPa]	λ_{\max}	$E_{(5)}$ [MPa]
SM				
Before ED	L	9.56±1.17	1.94±0.057	7.06±1.09
Before ED	T	8.54±0.85	1.95±0.03	7.46±1.34
1 year after ED	L	8.17 ±0.9	2.3±0.11	5.12±0.59
1year after ED	T	8.05±0.16	2.08±0.18	7.44±0.52
TM				
Before ED	L	9.83±1.35	2.15±0.07	6.18±0.34
Before ED	T	10.92±1.11	1.86±0.07	12.63±2.53
3 years after ED	L	9.55±2.19	2.04±0.19	4.39±0.37
3 years after ED	T	10.74±1.45	1.99±0.04	6.87±1.61
SP				
Before ED	L	8.22±0.98	1.97±0.04	4.36±1.04
Before ED	T	8.17±0.72	1.74±0.03	8.3±0.75
4 years after ED	L	9.07±0.72	2.08±0.17	4.33±0.38
4 years after ED	T	9.79±0.64	1.887±0.02	8.09±0.38

The secant modulus $E_{(5)}$ of fascia samples divided in three age groups is presented in Table 2. Modulus $E_{(5)}$ for group A is more than two times lower than $E_{(5)}$ for B and C group in bought directions (4.94 MPa vs. 8.49 or 8.102 MPa for L direction and 1.11 MPa vs. 3.52 or 2.32 MPa for T direction). The statistical analysis was performed and was obtained that there are no statistically significant differences between the values of $E_{(5)}$ for B and C group in longitudinal direction ($p=0.61$) and in transversal direction ($p=0.09$).

Table 2. The values of secant modulus $E_{(5)}$ for fascia (Median values ± AMD)

Direction	$E_{(5)}$ for group A* [MPa]	$E_{(5)}$ for group B* [MPa]	$E_{(5)}$ for group C* [MPa]
L	4.94±2.50	8.49±3.42	8.102±3.86
T	1.11±0.49	3.52±1.76	2.32±1.06

*Group A - up to 64 years, group B between 65-80 years, group C between 80-90 years, AMD – absolute median deviation

The mechanical compatibility between fascia and hernia meshes was accessed on the basis of their elasticity. The trend of elastic modulus for hernia meshes before and up to four years after ED is plotted in Fig.1. There is the influence of age on the elasticity of investigated hernia mesh in both directions for TM and in longitudinal

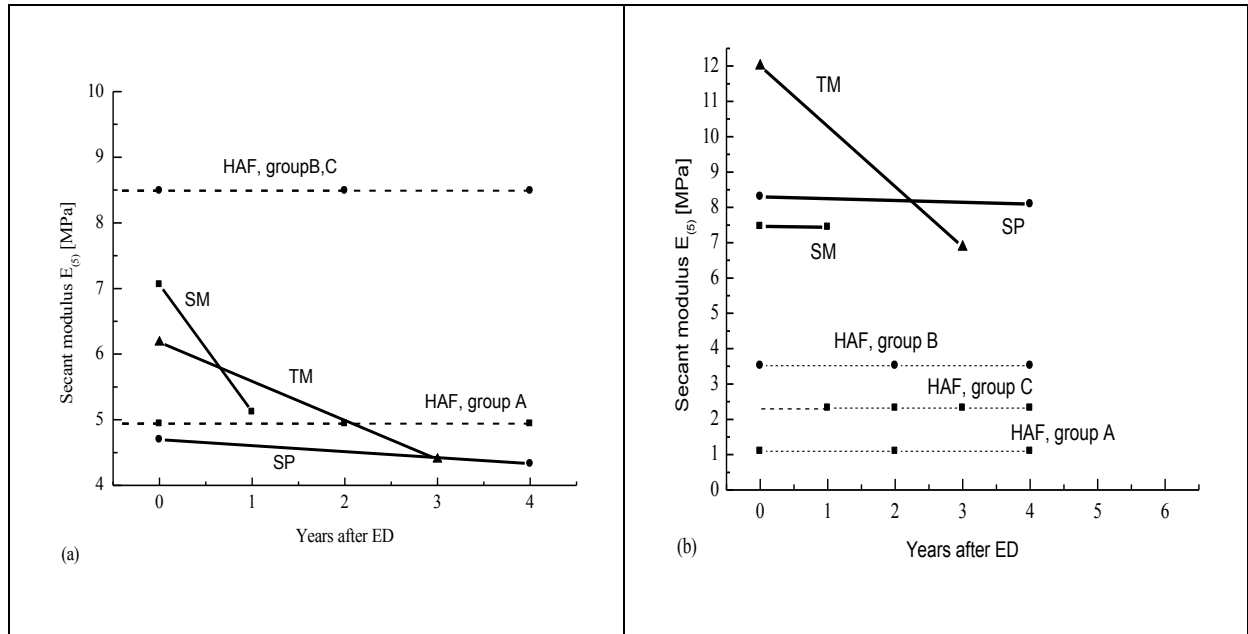


Fig. 1a(left) - Effects of age on elastic properties of SM, TM, SP samples cut in L direction. Fig. 1b(right) - Effects of age on elastic properties of SM, TM, SP samples cut in T direction. Trend of $E_{(s)}$ for human abdominal fascia (HAF) is presented with dashed line, while trend of $E_{(s)}$ for meshes with straight line.

direction for SM and SP. TM become more elastic in both directions, SM become elastic in L direction and SP does not change significantly its elasticity.

The elastic properties of hernia meshes in L-direction do not approach the elastic properties of the fascia from 65-80 years old donors in the same direction after long-term implantation. They are close to elastic properties of the abdominal fascia of group A. In transversal direction the value of $E_{(s)}$ for all investigated meshes exceeds considerably the physiological elasticity of fascia from all groups. $E_{(s)}$ of hernia meshes exceeds values for HAF of group A between 7-12 times and between 2-3 times values for samples from group B and C. It should be noted that elastic properties of mesh samples from SM and SP cut in T direction are close to elastic properties of fascia samples from group B,C cut in L direction.

4. Discussion

It is commonly accepted that for good clinical results the mechanical properties of biomaterials need to match the properties of tissues. This means that the mechanical compatibility of hernia meshes and abdominal layers is important condition for success of operation.^{6,7} Very often implanted meshes remain in the abdominal wall for years and during this period they changed their mechanical properties. The necessity of implantation of more physiologically relevant meshes imposed this investigation which continue the study presented in Ref.8.

Usually as a consequence of long-term implantation of meshes authors reported for reduced compliance of abdominal wall and increased stiffness because of dense unorganized scar plate formation.^{4,9} The encapsulation of PP mesh by connective tissue contributes to stiffness not only of

abdominal wall but of hernia meshes. The tensile moduli values and their changes with age showed different trend according to brand of mesh. Pascual et al. showed that modulus of elasticity of SP increase from about 12 MPa after three months to 20 MPa 6 months of implantation in rabbits. These values are much larger than reported values of 4,3-8,3 MPa measured in our study probably because of scar formation.¹⁰ Cobb et al. reported for decreased stiffness of Prolene Soft and Ultrapro mesh after five months implantation in porcine.⁴ Ferrando presented results for 6 months implantation of Bard Complex mesh, constructed of two layers of PP and one layer of ePTFE in rats. The modulus of elasticity decreased from 5.22 to 1.5 MPa for 6 months.¹¹ The increasing trend of tensile moduli values measured in this study and their changes with age were generally consistent with the results reported in Ref. 4.

The samples do not change their strength and deformability with age. Actually these results are consistent with the investigations of Ref. 10 and 11. Results of Pascual indicated a greater tensile strength for SP after 6 months of implantation but differences were not significant compared with previous results after 3 months of implantation.¹⁰ Ferrando showed that, tensile strength of Bard Complex mesh increased from 0.2 MPa to 0.36 MPa but the values again are not significantly different.¹¹

The elastic moduli at L direction for fascia are higher than in T direction reflecting the structure of samples. It is known that the elasticity of human abdominal wall is higher in the longitudinal direction than in the transverse direction by approximately 2:1 in proportion.^{5,12} This requirement is met in the design of TM and SP but after years their modulus of elasticity decreases or remain constant. The secant modulus of TM decreases in both direction, the secant modulus of SM decreases in L direction, while SP elasticity remain nearly constant.

The study emphasize the differences in material properties between hernia meshes and human abdominal fascia. Although the elasticity of TM increase in both directions, while SM and SP hernia meshes become more elastic only in L directions, their elastic properties are closer to elastic properties of the fascia samples only in direction parallel to fibers. The elastic properties of SP mesh in the L-direction approaches the elastic properties of the fascia in the same direction for 45-64 years old patients and elastic properties of fascia in T direction for 65-80 years old donors. In transversal direction the value of $E_{(5)}$ for all meshes exceeds considerably the physiological elasticity of fascia from all groups. This difference decrease with time only for TM mesh as can see from the results in Fig1.

Our results indicated that only SP is able to mimic the elastic response of the healthy abdominal fascia from 65-90 aged donors after expiration date. The mechanical compatibility of this mesh will be improved if rows of loops of the mesh are implanted parallel to collagen fibers of the tissue.

Our study has some limitations. The long-term changes in mechanical properties of hernia meshes were not determined for the same period. They should be investigated increasing interval after expiration date. Only three commercial meshes was investigated. The textile analysis of other hernia meshes would be useful to find those meshes which mechanical properties matched the properties of human abdominal fascia.

5.Conclusions

The results presented in this article are important for evaluating the mesh ability to match abdominal elasticity over a length of time. The study revealed mechanical behavior of hernia meshes SM, TM and SP before and after expiration date. The influence of age on elastic properties of SM and TM is clearly demonstrated. The secant modulus of SM decreases in the process of aging in longitudinal direction and its elastic properties approach the mechanical properties of the fascia samples from younger group A. The secant modulus of TM decrease in longitudinal and transversal direction. The results suggested that

further ageing of SM and TM will affect its long-term elasticity. Probably the best mesh of all three is SP which mechanical properties are close to properties of fascia samples from all groups. This study adds new data for the mechanical properties of PP hernia meshes which can be applied to mathematical models of long-term implanted meshes in abdominal wall.

References

1. Amid PK, Classification of biomaterials and their related complications in abdominal wall surgery, *Hernia* **1**: 15-21, 1997.
2. Ferrando JM, Vidal J, Armengol M, Huguet P, Gil J, Manero P, Planeli J, Segara M, Schwartz S, Arbos M, Early imaging of integration response to polypropylene mesh in abdominal wall by environmental scanning electron microscopy: comparison of two placement techniques and correlation with tensiometric studies, *World J. Surgery* **25**: 840-847, 2001.
3. Dora C, Dimarco D, Zobitz M, Elliott D, Time dependent variations in biomechanical properties of cadaveric fascia, porcine dermis, porcine small intestine submucosa, PP mesh and autologous fascia in the rabbit model: implications for sling surgery, *J. of Urology* **171**: 1970-1973, 2004.
4. Cobb W, Burns J, Peindl R, Carbonell A, Matthews B, Kercher K, Heiniford T, Textile analysis of heavy weight, mid-weight and light weight polypropylene mesh in a porcine ventral hernia model, *J.Surgical Research* **136**: 1-7, 2006.
5. Kirilova M, Stoytchev S, Pashkouleva D, Kavardzhikov V, Experimental study of mechanical properties of human abdominal fascia, *J. Med. Engin.&Phys.* **33**: 1-6, 2011 .
6. Hernandez-Gason B, Pena E, Pascual G, Long-term anisotropic response of surgical meshes used to repair abdominal wall defects, *J. of the mechanical behavior of biomedical materials* **5**: 257-271, 2012.
7. Kirilova M, About mechanical compatibility of some hernia meshes and abdominal wall layers, *Series on Biomechanic* **25** (1-2): 134-139, 2010.
8. Kirilova M, Pashkouleva D, Kavardzhikov K, A long-term elastic behaviour of hernia meshes, *Series on Biomechanics* **28**(3-4): 24-28, 2013.
9. Klosterhalfen B, Junge K, Klinge U, The Lightweight and Large Porous Mesh Concept for Hernia Repair. *Expert Rev. Med. Devices* **2**(1): 103-115, 2005.
10. Pascual G, Hernandez-Gason B, Rodriguez M, Sotomayor S, Pena E, Calvo B, Bellon J, The long-term behavior of lightweight and heavyweight meshes used to repair abdominal defects is determined by the host repair process provoked by the mesh, *Surgery* **152**: 886-95, 2012.
11. Ferrando JM, Vidal J, Armengol M, Gil J, Manero P, Huguet P, Segara M, Quiles M, Arbos M, Via I, Experimental Evaluation of a New Layered Prosthesis Exhibiting a Low Tensile Modulus of Elasticity: Long-term Integration Response within the Rat Abdominal Wall, *World J. Surgery* **26**: 409-415, 2002.
12. Anurov M, Titkova S, Oettinger A, Biomechanical compatibility of surgical mesh and fascia being reinforced: dependence of experimental hernia defect repair results on anisotropic surgical mesh positioning, *Hernia* **16**: 199-210, 2012.

NANOMECHANICAL EVALUATION OF BONE TISSUE REGENERATED BY MAGNETIC SCAFFOLDS.

M. BIANCHI ¹, M. BOI ¹, M. SARTORI ², G. GIAVARESI ^{2,3}, N. LOPOMO ^{1,4}, A. ORTOLANI ⁴, M. FINI ^{2,3}, A. DEDIU ⁵, A. TAMPIERI ⁶, M. MARCACCI ^{1,4}, A. RUSSO ^{1,4}

¹Laboratory of Nano-Biotechnologies (NaBi), Rizzoli Orthopaedic Institute, via di Barbiano 1/10, 40136 Bologna, Italy.
m.boei@biomec.ior.it

²Laboratory of Biocompatibility, Innovative Technologies and Advanced Therapies (BITTA), Rizzoli Orthopaedic Institute, via di Barbiano 1/10, 40136 Bologna, Italy.

³Laboratory of Preclinical and Surgical Studies, Rizzoli Orthopaedic Institute, via di Barbiano 1/10, 40136 Bologna, Italy.

⁴Laboratory of Biomechanics and Technology Innovation, Rizzoli Orthopaedic Institute, via di Barbiano 1/10, 40136 Bologna, Italy.

⁵Institute for the Study of Nanostructured Materials (ISMN), National Research Council, via Gobetti 101, 40129 Bologna, Italy

⁶Laboratory of Bioceramics and Bio-hybrid Composites, Institute of Science and Technology for Ceramics, National Research Council, Via Granarolo 64, 48018 Faenza, Italy.

Abstract

Since last decade, nanoindentation tests have been used to evaluate the mechanical performance of bone tissue not easily accessible by conventional analyses. However, very few studies are present in literature investigating the nanomechanical properties of regenerating bone. In this study, we show the nanoindentation analysis of newly formed trabecular bone tissue regenerated at 4 and 12 weeks from implantation, by the synergic use of NdFeB magnets and magnetic scaffolds in a critical experimental bone defect of the distal femur of rabbits. The effect of two different magnetic scaffolds has been investigated, being nucleation of biomimetic phase and super magnetic nanoparticle on self-assembling collagen fibrils (MAG-A) and scaffold impregnation in ferrofluid solution leaving magnetic nanoparticles entrapped in the construct (MAG-B), and compared with NdFeB magnet alone (MAG-C) and nonmagnetic biomimetic scaffolds (MAG-D). We assessed the effect of the different magnetization method on bone formation by correlating nanoindentation results with the histological and histomorphometrical findings. The results of this study evidenced highly organized bone tissue regeneration, mediated by collagen fibrils magnetized by magnetic nanoparticles under the effect of permanent magnetic field holding.

Keywords: Bone regeneration; nanoindentation; magnetic scaffolds.

1. Introduction

Instrumented indentation technique has been recently employed with the purpose of addressing the micro- and nanomechanical properties of biological tissues¹. Bone is indeed a highly hierarchically-structured material: for this reason the investigation of the mechanical properties at the micro- and nano-scale can not be achieved by conventional mechanical tests. Nanoindentation measurements allow to estimate bone tissue stiffness that, being strongly correlated to the mineralization degree of the collagen fibrils, provide a reliable estimation of bone tissue maturity, integrating classical qualitative histological data. Thus, during the last decades, several studies have been carried out in order to evaluate the mechanical properties of pristine bone by nanoindentation focusing on bone type, embedding medium, humidity, presence of osteoporotic, pathological conditions or additional ions. However, literature reports relatively few investigations on the mechanical properties of regenerating bone². We have previously showed the positive effect on bone tissue regeneration exerted by the synergic combination of magnetic scaffolds and magnetic forces³. In this study a analysis at 4 and 12 weeks from implantation of the nanomechanical properties (elastic modulus and hardness) of magnetically regenerated bone is reported, providing new insights on bone maturity differences induced by the distinct regenerative medicine approaches and on the contingent correlations between mechanical properties of different maturity bone tissues. The starting

hypothesis of the present study is that mechanical properties (i.e. maturity) of native bone represent the ultimate goal for the mechanical properties of newly-formed bone.

2. Materials and Methods

2.1. Specimens preparation

Four different groups of specimens (MAG-A; MAG-B; MAG-C; MAG-D groups) were obtained from a previously in vivo study³, each group consisting of three rabbit condyles. Briefly, the two magnetic groups under analysis included two different types of magnetic scaffolds - i.e. apatite/collagen scaffolds with magnetic nanoparticles nucleated on the collagen fibers (MAG-A group,⁴) and apatite/collagen scaffolds impregnated with magnetic nanoparticles (MAG-B group,⁵). MAG-D (control group) consisted of not magnetic commercial apatite/collagen scaffolds. All scaffolds were implanted into cylindrical defects (4 mm x 4mm) created bilaterally in the lateral condyle of the distal femoral epiphyses of 12 healthy male rabbits together with a cylindrical titanium-coated NdFeB magnet allocated in a 2 x 12 mm defect adjacent to the scaffold (Fig. 1). A set of specimens with the only NdFeB magnet were used as control group (MAG- group). At 4 and 12 weeks after surgery, the animals were pharmacologically euthanized and the femoral condyles excised; bone segments were fixed in paraformaldehyde, dehydrated, embedded in methyl methacrylate resin (PMMA) and polished with fine alumina powder in order to provide a flat and smooth surface suitable for nanoindentation analysis.

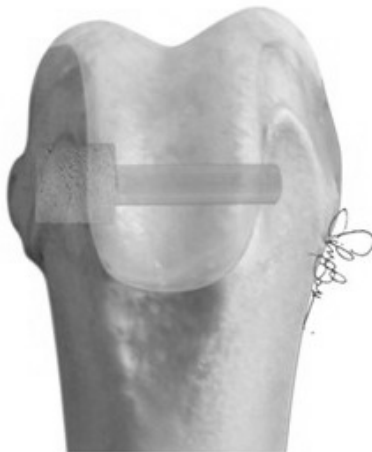


Fig. 1 Sketch of implantation site (magnetic scaffold, left; permanent magnet).

2.2. Selection of the regions of interest (ROIs)

On samples retrieved after 4 weeks from implantation, the nanoindentation analysis was carried out in three different regions of interest (ROI). Two ROIs were selected close to the site of scaffold implantation to evaluate bone formation, i.e. immature bone (I: newly-formed woven bone) and mature bone (M: newly-formed bone showing the onset of lamellae formation). The mechanical properties of bone tissue belonging to I and M regions were compared with that of native trabecular bone (N: not regenerated bone far from the site of implantation). According to histological analyses M and N- ROIs were present at 12 weeks.

2.3. Nanoindentation measurements

A Nanoindentation Tester, (NHT2, CSM, Switzerland), equipped with a diamond Berkovich tip, was employed to assess the contact hardness (H_c) and elastic modulus (E_r) of the different regions of interest. H_c and E_r were calculated according to the Oliver-Parr method⁶. All nanoindentation tests were performed using a linear loading rate profile, up a maximum load (P_{max}) of 10 mN followed by a pause of 100 s to limit the creep phenomenon due to the visco-elastic nature of bone tissue. Loading and unloading rate were set at 30 mN/nm. (Fig. 2)

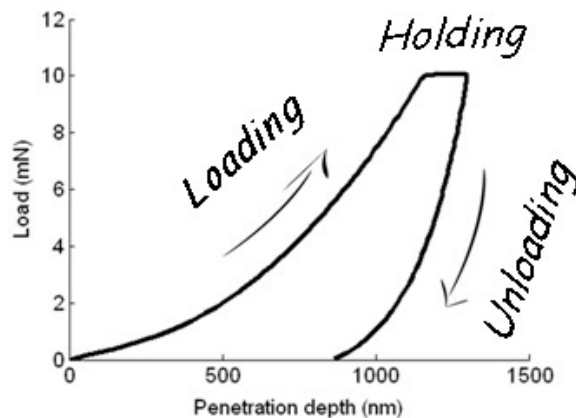


Fig. 2 Typical nanoindentation load depth curve used in this study.

3. Results and Discussion

The results of present study compare the mechanical properties of different-maturity bone tissues after 4 and 12 weeks from surgery of two magnetic scaffolds located close to a permanent magnet. At 4 weeks, Newly-formed woven bone exhibited lower hardness and elastic modulus than mature and native bone (Fig. 3), with MAG-B group exhibiting significantly higher values than MAG-A. Mechanical properties of newly-formed mature bone were closer to that of native bone of MAGB group than MAG-A group and MAG-C. Matching together results from hystomorphometric analyses and nanoindentation studies, it could be concludes that MAG-A group provided faster bone regeneration at 4 weeks from implantation, but the mechanical properties (bone maturity) of the newly-formed bone were still far from that of the native bone (ultimate goal). On the contrary, MAG-B group provided lower amount of regenerated bone, but the latter exhibited mechanical properties significantly closer or even similar to that of native bone, thus indicating a higher level of bone maturity provided by group MAG-B compared to MAG-A. On the contrary bone samples retrieved at 12 weeks from surgery showed higher bone volume (BV/TV %) and smaller gap between the mechanical properties of newly-formed mature and native bone for MAG-A than for MAG-B, MAG-C and MAG-D. The reported results showed that :1) the synergic combination between magnetic scaffolds and magnetic forces has a positive effect on bone tissue regeneration; : 2) nanoindentation tests represent on effective tool to evaluate tissue maturity level on a multiscale easily not accessible through conventional analyses.

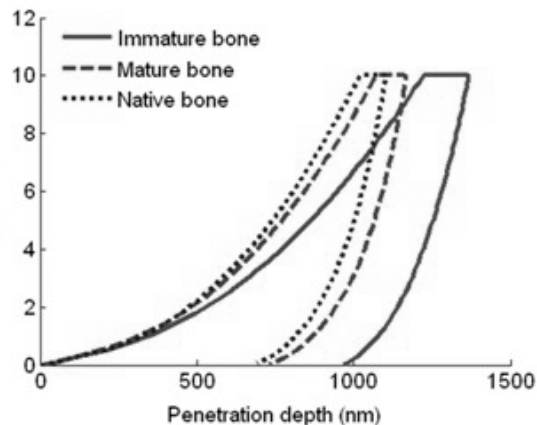


Fig. 3 Representative indentation curves for immature, mature and native bone.

Acknowledgements

This study was supported by the European Project “Magnetic Scaffolds for in vivo Tissue Engineering” (NMP3-LA-2008-214686) and by the project “Nanostructured Coatings Enhancing Material Performances in Joint Arthroplasty” (project code_2012-1838) co-founded by the Italian Ministry of Health.

References

1. Ebenstein DM, et al., Nanoindentation of biological materials. *Nano Today*. 2006;1:26-33.
2. Cipitria A, Lange C, Schell H, Wagermaier W, Reichert JC, Hutmacher DW, et al., Porous Scaffold Architecture Guides Tissue Formation. *J. Bone Miner Res*. 2012;27(6),1275-1288.
3. Panseri S, Russo A, Sartori M, Giavaresi G, Sandri M, Fini M, et al., Modifying bone scaffold architecture in vivo with permanent magnets to facilitate fixation of magnetic scaffolds, *Bone*. 2013;56(2):432-439.
4. Tampieri A, Landi E, Valentini F, Sandri M, D'Alessandro T, Dediu V et al., A conceptually new type of bio-hybrid scaffold for bone regeneration, *Nanotech*. 2011;22:015104.
5. Bock N, Riminucci A, Dionigi C, Russo A, Tampieri A, Landi E et al. A novel route in bone tissue engineering: magnetic biomimetic scaffolds. *Acta Biomater*. 2010;6:786-798.
6. Oliver WC, Parr GM. Measurement of hardness and elastic modulus by instrumented indentation: advances in understanding and refinements to methodology, *J Mater Res*. 2004;19:3-20.

S6P: Modelling and diagnosis - Muscles, ligaments and movement

Chairs: David Manners, Cecilia Signorelli

CHARACTERIZATION AND ANALYSIS OF SEMG SIGNALS UNDER FATIGUE AND NON FATIGUE
CONDITIONS USING MULTISCALE FRACTAL DIMENSION TECHNIQUE

DIPTASREE MAITRA GHOSH

INTENSE INTERVAL TRAINING MODIFIES THE SLOW COMPONENT OF VO₂ IN SEDENTARY
ADULTS

LEYDI NATALIA VITTORI

INTEGRATION OF SURFACE EMG, US IMAGING AND 3D KINEMATIC: NEW FRONTIERS FOR
MUSCLE FUNCTION INVESTIGATION

MARIA CRISTINA BISI

ANALYSIS OF SURFACE EMG SIGNALS UNDER FATIGUE AND NON- FREQUENCY
DISTRIBUTION

PERIYAMOLAPAL AYAM ALLIMUTHU KARTHICK

MUSCLE ACTIVATION UNDER DIFFERENT ANKLE AND KNEE POSITIONS DURING LEG
EXTENSION EXERCISE

MATTEO BOTTEGHI

DIFFERENTIATING SURFACE EMG SIGNALS UNDER FATIGUE AND NON- FATIGUE
CONDITIONS USING RAIN FLOW COUNTING BASED FEATURES

SUSHANT KULKARNI

ANALYSIS OF FATIGUE PROGRESSION DURING DYNAMIC CONTRACTION OF BICEPS BRACHII
MUSCLES USING INTRINSIC MODE FUNCTIONS OF SURFACE EMG SIGNALS AND SPECTRAL
FEATURES

GOPINATHAKAIM AL VENUGOPAL

MUSCLE ACTIVATION DURING PUSH UP EXERCISE UNDER STABLE AND UNSTABLE
CONDITIONS

GUIDO BELLI

FUNCTIONAL EVALUATION OF A METHOD TO SPECIFY AN APPROPRIATE EXERCISE LOAD
FOR WEIGHT LOSS IN OVERWEIGHT SUBJECTS

LEYDI NATALIA VITTORI

CHARACTERIZATION AND ANALYSIS OF SEMG SIGNALS UNDER FATIGUE AND NON FATIGUE CONDITIONS USING MULTISCALE FRACTAL DIMENSION TECHNIQUE

DIPTASREE MAITRA GHOSH and RAMAKRISHNAN S

Non-Invasive Imaging and Diagnostics Laboratory

Biomedical Engineering Group, Department of Applied Mechanics

Indian Institute of Technology Madras, Chennai, Tamil Nadu-600036, India

diptaa2005@gmail.com and sramki@iitm.ac.in

The objective of this work is to distinguish sEMG signal under fatigue and non fatigue conditions by exploring nonlinearity of the process. The signals are acquired from biceps brachii muscle of 50 healthy adult volunteers. The recorded signals are pre-processed and analyzed using Multi-Scale Fractal Dimension (MSFD) technique. Multiple time scales of the signal are obtained by coarse-graining method and Higuchi fractal dimension is calculated for each subject. Statistical parameters such as mean and skewness are calculated from MSFD. Results show that the MSFD values are higher in non fatigue condition. Mean and skewness values are able to separate sEMG signal under fatigue and non fatigue condition. Percentage difference of mean of skewness is found more than 100% between fatigue and non fatigue zones. It appears that this method of analysis can be used in clinical conditions to identify muscle fatigue noninvasively.

Key words: Biceps brachii; muscle fatigue; surface EMG signal; multiscale, Higuchi fractal dimension

1. Introduction

Muscle is one of the important tissues found in human body. There are three types of muscles, skeletal muscle, cardiac muscle and smooth muscle. The main function of muscle is to generate force and motion. Muscle fatigue is a state in which the capability of the muscle contraction and generation of force is decreased.¹ Surface Electromyography (sEMG) is a technique to capture cumulative electric signal acquired from skeletal muscles non invasively.² sEMG signal analysis is one of the method to analyze muscle fatigue. Fractal Dimension (FD) is a mathematical tool to measure the complexity of sEMG signals⁴. FD lies between 1 and 2 for one dimensional signal.⁴ It is a useful method for analyzing the nonlinearity and the state of chaotic systems.³ It has been reported that biomedical signals have multi scale nature.⁷

In this work, sEMG signals are acquired and FDs are computed in multiple scales. Statistical parameters such as mean and skewness are calculated and these are used to analyze the sEMG signal.

2. Methods

Signals are acquired from 50 healthy subjects having no history of neuromuscular disorder. The sEMG signal has been acquired by using Biopac MP36 (24 bit resolution, CMRR 110dB). The sampling frequency of the signal is 10 kHz. In this experiment, the skin preparation is done first and then Ag-AgCl surface electrodes are placed in the middle of biceps brachii muscle. All subjects are asked to maintain upright body position during the experiment. After that each participant is requested to do repetitive flexion and extension of the elbow with a load of 6 kg. The subjects are free to select the cycle

frequency and can continue the experiment until they experience biceps muscle discomfort and are unable to lift the load again.⁵ Signals are passed through a band pass filter (10 Hz to 400Hz) and a (50Hz) notch filter. The duration of the signal depends on the endurance of the subjects so the time axis needs to be normalized. Therefore, the entire signal has been divided into six zones. First zone of the signal is considered as non fatigue zone and the sixth zone is considered as fatigue zone.

2. 1 Multi Scale Higuchi Fractal Dimension

In this technique, signal is taken in various time scales and then Higuchi FD of each rescaled signal has been calculated. The multiple time scales signal are achieved by coarse graining procedure.⁶ Finally, FD is calculated by using Higuchi's method.³

3. Results and Discussion

In this study, sEMG signals are recorded from biceps brachii during dynamic contraction. Fig. 1 and Fig. 2 represent the non fatigue and fatigue zone respectively. It is seen that the amplitude of the signals under fatigue cases is higher than non fatigue cases. This can be due to increased motor unit recruitment in fatigue case. Fig. 3 shows FD versus scales of sEMG signal under non fatigue and fatigue conditions. It is observed that FD values are found to increase in both cases with increase in scale factor. As the scale factor increases the irregularity of the signal increases and becomes more random.⁷ It is also observed that sEMG signal under non fatigue condition has higher FD than sEMG under fatigue condition in all scales. Fractal dimension of sEMG depends on various parameters such as different recruitment of motor unit, firing rate and duration of action potential. FD varies from 1.1 to 1.8 as recruitment number varies.⁸ Motor unit recruitment is more in the case of fatigue than non fatigue but the firing rate of motor unit is lower than non fatigue. Motor unit synchronization and reduction of firing rate of motor unit decreases the complexity of the signal under fatigue condition compared to non fatigue case. It is observed that as complexity of the signal decreases, FD also decreases. Therefore, FD of fatigue is lower than non fatigue. The mean of FD in multi scales for 50 subjects has been shown in Figure 4. It is observed that mean values of non fatigue is higher than mean value of the fatigue. Previously, Figure 3 shows that fractal dimension of sEMG signal of one subject during non fatigue condition is higher than the fatigue condition in each scale.

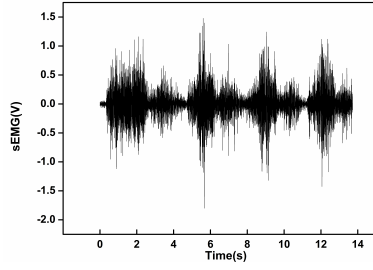


Fig. 1. Non Fatigue zone of the signal

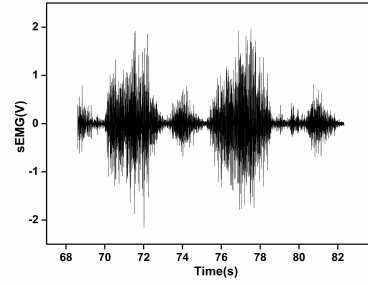


Fig. 2. Fatigue zone of the signal

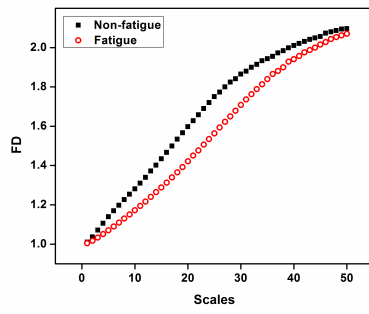


Fig. 3. Fractal dimension of one subject in multiple scales

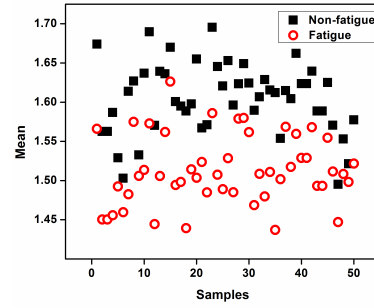


Fig. 4. Mean of 50 different subjects in multiple scales

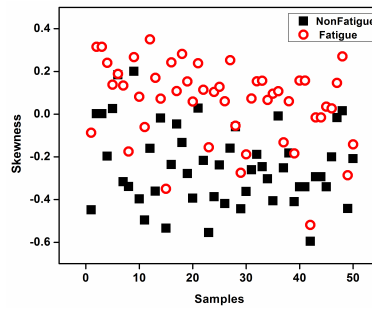


Fig. 5. Skewness of 50 different subjects in multiple scales

Hence the mean values of 50 scales of each sample of non fatigue are also higher than the fatigue. It is also observed that the spread of mean values is more in fatigue than non fatigue condition. This is may be due to increased number of motor unit recruitment in fatigue condition. Figure 5 shows that skewness of FD of sEMG during fatigue is higher than non fatigue. sEMG signal distribution is non-Gaussian at the muscle's maximum contraction stage comparing to its resting stage.⁹ Hence, FD values are high in fatigue. Table 1 shows the mean of mean and skewness of MSFD in the case of non fatigue and fatigue. It is observed that percentage difference is more than 100% in the case of mean of skewness of MSFD between fatigue and non fatigue conditions.

Table 1. Statistical variation of features

	Mean	Skewness
Non Fatigue	1.6042	-0.2413
Fatigue	1.4870	0.1163

4. Conclusion

In this study, multiscale fractal dimension (MSFD) technique is proposed to differentiate sEMG signal during fatigue and non fatigue conditions. Coarse-graining method is used for multiscale analysis. Higuchi's method has been used to compute fractal dimension. The MSFD values are higher in non fatigue condition compared to fatigue condition. Mean and skewness of MSFD have shown clear separability between fatigue and non fatigue zone. This technique can be used to distinguish between sEMG signal under various clinical neuromuscular conditions.

Reference

1. Allen DG, Lamb GD, Westerblad H, Skeletal muscle fatigue: cellular mechanisms, *Physiological Reviews* **88**: 287-332, 2008.
2. Farina D, Negro F, Accessing the neural drive to muscle and translation to neurorehabilitation technologies, *IEEE Rev. Biomed. Eng* **5**: 3-14, 2012.
3. Uthayakumar R, Fractal Dimension in Epileptic EEG Signal Analysis, *Applications of Chaos and Nonlinear Dynamics in Science and Engineering* **3**: 103-157, 2013.
4. Raghavendra BS, Dutt DN, Computing fractal dimension of signals using multiresolution box-counting method, *International Journal of Information and Mathematical Sciences* **6**: 50-65, 2010.
5. Venugopal G, Navaneethakrishna M, Ramakrishnan S, Extraction and analysis of multiple time window features associated with muscle fatigue conditions using sEMG signals, *Expert Systems with Applications* **41**: 2652-2659, 2014.
6. Costa Madalena, Goldberger AL, Peng CK, Multiscale entropy analysis of biological signals, *Physical Review E* **71**: 021906 -1-012906-18, 2005.
7. Raghavendra BS, Dutt DN, Multiscale fractal dimension technique for characterization and analysis of biomedical signals, In: *Digital Signal Processing Workshop and IEEE Signal Processing Education Workshop (DSP/SPE)*, 370-374, 2011.
8. Xu Z, Xiao S, Fractal dimension of surface EMG and its determinants, In: *IEEE Proceedings of the 19th Annual International Conference on Engineering in Medicine and Biology Society* **4**: 1570-1573, 1997
9. Hussain M S, Mamun Md, Effectiveness of the wavelet transform on the surface EMG to understand the muscle fatigue during walk, *Measurement Science Review* **12**: 28-33, 2012.

INTENSE INTERVAL TRAINING MODIFIES THE SLOW COMPONENT OF VO₂ IN SEDENTARY ADULTS

*L.N. VITTORI, *M. ALBONETTI, **D.N. MANNERS, ** C. TENTONI, ***D. MAIONE

School of Pharmacy, Biotechnology and Sport Science; University of Bologna, Bologna, Italy ** Department of Biomedical Sciences and Neuromotor, University of Bologna, Bologna, Italy *Medical and Surgical Sciences Department, University of Bologna, Bologna, Italy*

Keywords: Interval training, incremental test, energy cost, oxygen uptake, oxygen consumption slow component

Introduction

Respired gas volumes equilibrate only slowly to constant load exercise above the anaerobic threshold, in untrained subjects. The reasons for this slow adaptation is still debated, but both central factors such as cardiopulmonary response, and peripheral factors including muscle metabolism and endothelial dysfunction, have been proposed (1, 2). Training of sufficient intensity reduces the time constant of the slow component while increasing VO_{2 max}. The efficiency and safety of different training protocols that reduce the slow component has yet to be established, especially in sedentary populations. In this study the efficacy of a high intensity interval training (HIIT) programme was tested for its capacity to reduce the slow component (SC), increase VO_{2 max} and improve body composition.

Methods

Seven sedentary adults (2 male; age 50 ± 6 years; BMI 25 ± 4) were recruited and agreed to participate in the study. At the start of the study (T0) incremental testing established the anaerobic threshold (AT) and VO_{2 max}, while the SC was investigated during constant load exercise at AT. Participants followed an interval training exercise protocol using a cycle ergometer, and lasting about 60 min, three times a week for 6 weeks. Exercise intensity started at 70% age-derived FC_{max} (3) and increased weekly. The main exercise phase included up to 5 cycles of 3 min programmed load alternated with 5 min minimal load. At the end of the study (T1) initial tests were repeated, and constant load exercise was also performed at AT+10% and AT+20%, on separate days. Data were analysed using purpose-built software, to determine metabolic thresholds and SC parameters, in particular SC-related O₂ consumption during 6 min of constant load exercise (V_{O₂ SC}).

Results

Aerobic capacity increased following training (mean VO_{2 max} ± SD: from 27 ± 6 at T0 to 34 ± 5 ml kg⁻¹ min⁻¹ at T1), as did the maximum load borne (from 212 ± 41 to 266 ± 50 W), although the corresponding HR barely altered. The lactate threshold shifted right in absolute terms (from 180 ± 32 to 206 ± 39 W) but not relative to VO_{2 max}. The slow component of VO₂ recovery, as measured by V_{O₂ SC}, was decreased

following training, at a load corresponding to the initial lactate threshold (from 0.96 ± 0.51 to 0.56 ± 0.29 L), and even at higher loads on average. On average, both body weight and lean body mass remained constant.

Discussion

The test results are consistent with an improvement of peripheral, such as muscle efficiency) rather than central factors. Indeed, the decrease in the slow component of the VO₂ curve suggests that either proportionately more slow fibres were being recruited following training, all that the fibres recruited were funding their activity more aerobically. In conclusion, we have demonstrated an HIIT protocol that is effective in improving SC VO₂ parameters (and VO_{2 max}) in only 6 weeks.

Bibliography

- (1) Koga S, Poole DC, Shiojiri T, et al. Am J Physiol Regul Integr Comp Physiol. 2005;288:R212-20.
- (2) Krstrup P, Jones AM, Wilkerson DP, et al. J Physiol. 2009; 587:1843-56.
- (3) Tanaka H, Monahan KD, Seals DR. J Am Coll Cardiol. 2001 Jan;37(1):153-6.

INTEGRATION OF SURFACE EMG, US IMAGING AND 3D KINEMATIC: NEW FRONTIERS FOR MUSCLE FUNCTION INVESTIGATION

MARIA CRISTINA BISI

*Department of Electrical, Electronic and Information Engineering "Guglielmo Marconi", University of Bologna, Via Risorgimento 2,
Bologna, 40136, Italy*
mariacristina.bisi@unibo.it

ALBERTO BOTTER

*Laboratory for Engineering of the Neuromuscular System (LISiN), Department of Electronics and Telecommunications, Politecnico di Torino, Via Cavalli 22/h,
Torino, 10138, Italy*
alberto.botter@polito.it

RITA STAGNI

*Department of Electrical, Electronic and Information Engineering "Guglielmo Marconi", University of Bologna, Via Risorgimento 2,
Bologna, 40136, Italy*
*Health Sciences and Technologies, Interdepartmental Center for Industrial Research (HST-ICIR),
Via Tolara di Sopra, 50, Ozzano dell'Emilia, 40064, Italy*
rita.stagni@unibo.it

TAIAN VIEIRA

*Laboratory for Engineering of the Neuromuscular System (LISiN), Department of Electronics and Telecommunications, Politecnico di Torino, Via Cavalli 22/h,
Torino, 10138, Italy*
taian.vieira@polito.it

The integration of grids of electrodes, US imaging and 3D kinematics can allow investigating how muscle architectural changes influence surface EMGs, providing novel spatio-temporal information regarding electromechanical function of muscle. The aims of this study were i) to verify whether movements of the US probe lead to artefacts in surface EMGs; ii) to analyse how much muscle architectural changes, induced by changes in joint positions, can influence the amplitude distribution of surface EMGs. While provided with EMG visual-feedback, a participant was asked to recruit a single motor unit of the right tibialis anterior (TA) at two different ankle positions. Surface EMGs, kinematic data and US images were acquired. The spatial distribution of the root mean square amplitude of motor unit action potentials was assessed from collected EMGs. Ankle angles were obtained from 3D kinematics. TA volume was obtained through the segmentation of US images reconstructed in 3D space: width and thickness variations between the two positions were measured. Movements of the US probe over the grid of electrodes did not result in artefacts in surface EMGs. Presuming the same motor unit was recruited for both ankle positions, results indicated a marked effect of TA architecture on the amplitude distribution of action potentials.

Keywords: HD EMG, US system, muscle function.

1. Introduction

Application of two-dimensional surface electrode arrays can provide a means of mapping motor unit action potentials on the skin surface above a muscle. The muscle tissue displacement due to contraction can be quantified, in a single plane, using ultrasound (US) imaging. Recently a material that enables concurrent measurement of two-dimensional surface electromyograms (EMGs) with US images was developed¹. In addition, the possibility of integrating US imaging with 3D kinematics^{2,3} can provide information on architectural and geometrical changes of muscle that occur during contraction not only in a single plane but at the entire volume level. Thus, the integration of grids of electrodes, US imaging and 3D kinematics can provide new spatiotemporal information regarding electromechanical function of muscle that are relevant both for improving basic knowledge and for clinical applications (e.g. to assess the neuro-mechanical progression of muscle injuries). The aim of the present work was to collect preliminary evidence on:

- 1) whether movements of the US probe, necessary for the reconstruction of muscle volume², lead to artefacts in surface EMGs detected with US-transparent electrodes¹;
- 2) how much muscle architectural changes, induced by changes in joint positions, can influence the amplitude distribution of surface EMGs.

2. Materials & Methods

A young healthy subject participated in the study [33 years; 1.78 m; 75.1 kg] after providing informed consent. The Review Board Committee approved this study.

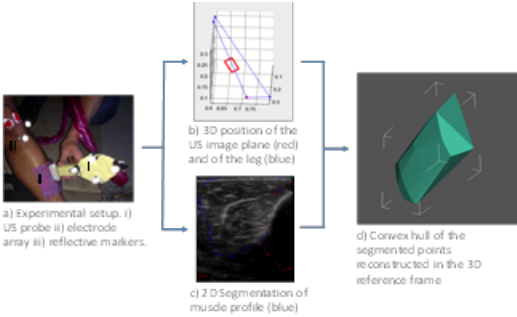
Surface EMGs (W-EMG, Bitron s.p.a. and LISiN-Politecnico di Torino, Italy), kinematic data (SmartD, BTS, Italy) and US images (Echoblaster 128, Telemed, LT) were acquired (experimental setup shown in Figure 1a). A grid of 32 electrodes (8x4; 1 cm inter-electrode distance) transparent to US¹ was placed on the participant right tibialis anterior (TA) muscle. Eight reflective markers were directly placed on anatomical landmarks of the subject's right lower limb (leg and foot). Four reflective markers were attached to the US probe. 3D position of the US image plane in the laboratory reference frame was calibrated through the acquisition of a plate and two edges both with US system (with markers attached) and with a marker stick (as reference). US images were recorded at 25 fps.

The participant performed TA contractions at A) ankle neutral and B) ankle full plantar-flexion. While observing differential EMGs (EMG-feedback), the participant was asked to recruit a single motor unit⁴. Specifically, the participant was instructed to push his foot up into dorsal-flexion until a regular train of action potentials of a single motor unit could be observed (contractions duration: 50 sec; rest period: 5 min).

The spatial distribution of the root mean square amplitude of motor unit action potentials was then assessed⁵. A 2 segment model of the subject's right lower limb was obtained from kinematic data collected at 100 Hz^{6,7}. Ankle angles were calculated⁸. Segmentation of muscle profile was performed manually on 2D US images (Fig. 1c). US images were projected in the 3D laboratory reference frame

using the cluster probe position and the previously performed calibration. Segmented points were reconstructed in the laboratory reference frame, projected in the anatomical reference system of the leg and then used to obtain the convex hull of the muscle surface. A flowchart of the 3D reconstruction of the muscle surface is shown in Figure 1b-d. Muscle volume positioned under the electrode matrix was analysed. The volume was virtually palpated using Multimod DataManager⁹: width and thickness variations between the two ankle positions were measured.

Fig. 1. a) Experimental setup. b), c) and d) Flowchart of the procedure for 3D muscle surface reconstruction



3. Results

Movements of the US probe over the grid of electrodes did not result in artefacts in the surface EMGs. Table 1a shows ankle angles for the two analysed positions. TA width increased of 6 mm at neutral position in respect to full plantar-flexion. Table 1b shows results obtained in a time window of 12 sec.

Tab 1. a) Ankle angle means and standard deviations (deg) for the A) plantar flexion and B) neutral positions. (+ Dorsiflexion (FE), + Eversion (AA), + InternalRotation (IE)).

b) TA variations in width and thickness from plantar-flexed position B) to a neutral position A).

		A		B	
		mean	std	mean	std
FE	mean	-9,41		-36,58	
	std	1,01		0,317	
AA	mean	3,48		-2,9868	
	std	0,17		1,0734	
IE	mean	20,59		27,81	
	std	0,48		0,805	

		Δwidth		Δthickness	
		mean (mm)	std (mm)	mean (mm)	std (mm)
		6,3	1,1	-0,9	0,5
	mean (%)	11,6		-1,4	
	std (%)	1,6		1,4	

At both ankle positions, the largest action potentials were observed in the most distal TA regions. During contractions exerted with the ankle in neutral position, however, the RMS amplitude of action potentials was twice as greater as that obtained with the ankle at plantar flexion position. Moreover, relatively larger RMS amplitudes were observed over a wider skin region for the ankle at neutral position (cf. left and right panels in Figure 2).

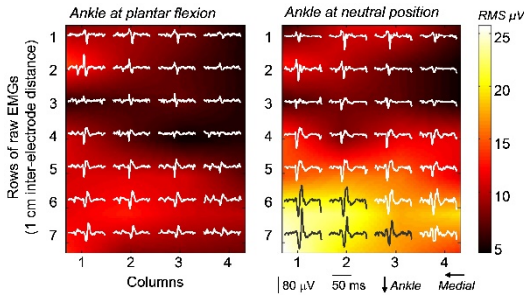


Figure 2. Surface representation of action potentials of presumably the same TA motor unit, elicited during dorsal flexions exerted with ankle at plantar flexion (left) and neutral (right) positions. Potentials are superimposed on images created with the RMS amplitude calculated for each potential.

4. Discussion

Reconstructing the TA volume from US imaging demands moving the US probe over skin regions covering the target, muscle area. Such shifting of the US probe over the matrix of electrodes (Fig. 1a) could potentially result in low frequency artefacts in the surface EMGs. Artefacts were not observed in any of the differential EMGs recorded. Two main factors possibly accounted for the absence of artefacts: i) the pressure between the US probe and the matrix of electrode changed likely marginally when the probe was moved over the matrix; ii) the silicon material and the conductive paste possibly damped any movement induced from the movement of the US probe to the electrodes.

Key results indicate a marked effect of TA architecture on the amplitude distribution of action potentials of a single, TA motor unit. When moving the foot from plantar flexion to a neutral position, TA width increased of 6mm. Interestingly, a corresponding increase in the RMS amplitude and in its spatial distribution was observed for the ankle neutral position. Presuming the same the same motor unit was recruited for both ankle positions (cf. similarities in the shape of action potentials shown in Figure 2), the changes in EMG amplitude reported here were predominantly due to TA architectural changes. If these findings hold for a sample of subjects, then, the effect of muscle anatomical factors on the surface EMGs may be more expressive than previously appreciated.

References

1. Botter A, Vieira TM, Loram ID, Merletti R, Hodson-Tole EF. (2013). A novel system of electrodes transparent to ultrasound for simultaneous detection of myoelectric activity and B-mode ultrasound images of skeletal muscles. *J Appl Physiol* (1985)115(8):1203-14
2. Stagni R, Fantozzi S, Cappello A, Camomilla V. (2006) Ultrasound for identification of anatomical landmarks in stereophotogrammetry: a new method for the calibration of the probe. *J Biomech.* 39 (S1)
3. Bisi MC, Riva F, Stagni R, (2011). A non-invasive protocol to estimate muscle tendon lengths and moment arms through ultrasound images, *GP 33S1, S28-S29.*
4. Basmajian JV. (1963) Control and training of individual motor units. *Science.* 141(3579):440-1.
5. Vieira TM, Merletti R, Mesin L. (2010) Automatic segmentation of surface EMG images: Improving the estimation of neuromuscular activity. *J Biomech.* 43(11):2149-58.
6. Wu G, Cavanagh PR. (1995) ISB recommendations for standardization in the reporting of kinematic data. *J Biomech.* 28(10):1257-61.
7. Cappozzo A, Catani F, Croce UD, Leardini A. (1995). Position and orientation in space of bones during movement: anatomical frame definition and determination. *Clin Biomech.* 10(4):171-178.
8. Grood ES, Suntay WJ. (1983). A joint coordinate system for the clinical description of three-dimensional motions: application to the knee. *J Biomech Eng.* 105(2):136-44.
9. Viceconti M, Taddei F, Montanari L, Testi D, Leardini A, Clapworthy G, Van Sint Jan S. (2007) Multimod Data Manager: a tool for data fusion. *Comput Methods Programs Biomed.* 87(2):148-59.

ANALYSIS OF SURFACE EMG SIGNALS UNDER FATIGUE AND NON-FATIGUE CONDITIONS USING B-DISTRIBUTION BASED QUADRATIC TIME FREQUENCY DISTRIBUTION

KARTHICK P A, VENUGOPAL G, and RAMAKRISHNAN S

*Non-Invasive Imaging and Diagnostics Laboratory
Biomedical Engineering Group, Department of Applied Mechanics
Indian Institute of Technology Madras,
Chennai-600 036, India.*

E-mail address: pakarthick1@gmail.com, venugopalg@gmail.com, and sramki@iitm.ac.in

In this work an attempt has been made to analyze surface electromyography (sEMG) signals under non-fatigue and fatigue conditions using time frequency based features. The sEMG signals are recorded from biceps brachii muscle of fifty healthy volunteers under well defined protocol and preprocessed. The preprocessed signals are divided into six equal epochs. The first and last epochs are considered as non-fatigue and fatigue zones respectively. Further these signals are subjected to B-distribution based quadratic time-frequency distribution. Time frequency based features such as instantaneous median frequency (IMDF) and instantaneous mean frequency (IMNF) are extracted. Spectral entropy is modified to obtain instantaneous spectral entropy (ISPE_n) from the time-frequency spectrum. The results show that all the extracted features are distinct in non-fatigue and fatigue conditions. It is also observed that the values of all features are higher in non-fatigue zones. It appears that, this method is useful in analyzing various neuromuscular conditions associated with muscle movements using sEMG signals.

Keywords: Biceps brachii; B distribution; quadratic time frequency method; instantaneous mean frequency; instantaneous spectral entropy; instantaneous median frequency;

1 Introduction

Muscle fatigue results with progressive reduction in muscle force due to sustained contraction or continuous exercise. Fatigue assessment plays an important role in analysis of various neuromuscular diseases, ergonomics, sports medicine and rehabilitation. The sEMG signals are widely used in muscle fatigue analysis.¹

Surface electromyography is a non-invasive technique that is used to record the electrical activity of neuromuscular system under the vicinity of electrode locations. It depends on several physiological and detection system parameters. The sEMG signal is complex, non-stationary and multicomponent.² Cohen's class time frequency distribution reveals the non-stationary and multicomponent nature of the signal. B-distribution is based on time-frequency distribution (TFD), outperforms Choi-Williams and Wigner-Ville distribution in resolving closely spaced components in the time frequency domain. It provides better time-frequency resolution and suppresses the cross terms.^{3,4}

In this work, sEMG signals are recorded from biceps brachii muscles during dynamic contractions. These signals are subjected to B-distribution based TFD. The three features are extracted from the time frequency spectrum. These features are further used to analyze non-fatigue and fatigue conditions from the recorded sEMG signals.

2 Methods

2.1 Signal acquisition and Protocol

Signals are recorded using Biopac MP36 data acquisition system with a sampling rate of 10 kHz. Fifty subjects with no history of neuromuscular disorders or weight training are participated in this study. Subjects are made to perform biceps brachii flexion-extension exercise with a 6 kg dumbbell until they are unable to lift the load again.¹ Signals are subjected to offline band pass filtering, using a Butterworth filter with cut-off frequencies of 10 Hz and 400 Hz. A notch filter with 50 Hz is used to remove power line interference.¹ The pre-processed signals are segmented into six equal epochs. The first epoch is considered as non-fatigue zone. The last epoch corresponds to fatigue zone where all the subjects failed to perform the exercise further.

2.2 B-distribution based TFD

The B-distribution based time-frequency method is adapted from Boashash B et al.'s work.^{3,4}

2.3 Time frequency based features

Three features namely IMDF, IMNF and ISPE_n are extracted from the B-distribution based TFD of three corresponding zones. The IMDF and IMNF are used in this work are taken from Bonato P et.al. work.⁵

2.3.1 Instantaneous Spectral Entropy (ISPE_n)

Spectral entropy is used to quantify the global regularity of the signal. The high value of spectral entropy corresponds to more complex and less regular property.⁶ Spectral entropy is modified to obtain the instantaneous spectral entropy and it is given in Eq. (1) and Eq. (2)

$$\rho[n, k_i] = \frac{P[n, k_i]}{\sum_{i=1}^N P[n, k_i]} \quad (1)$$

$$ISPE_n = - \sum_{i=1}^N \rho[n, k_i] \log(\rho[n, k_i]) \quad (2)$$

where $P[n, k]$ is a power of time frequency spectrum.

3 Results and Discussion

The time frequency plot of non-fatigue and fatigue zones is presented in Fig.1 and Fig.2. More number of high frequency components with lower power is observed in non-fatigue zone.

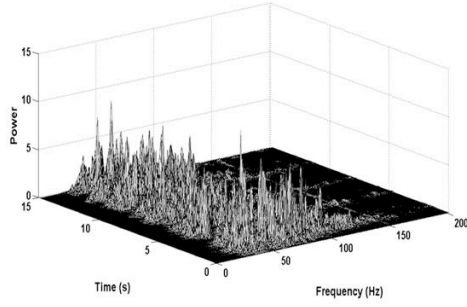


Fig.1. Time frequency plot of non-fatigue zone

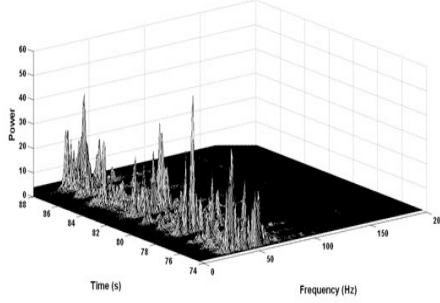


Fig.2. Time frequency plot of fatigue zone

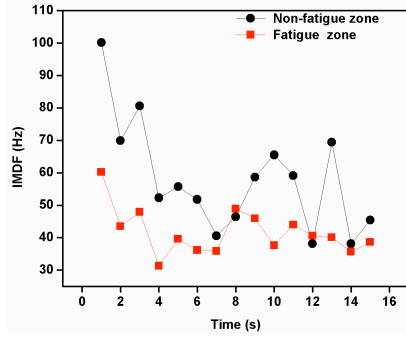


Fig.3. IMDF of non-fatigue and fatigue zone

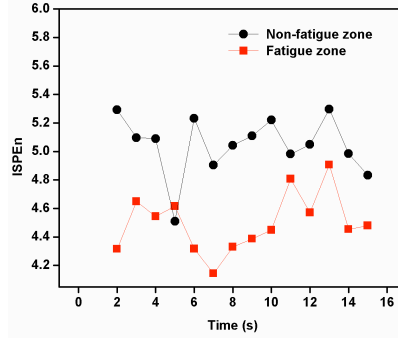


Fig.4. ISPEn of non-fatigue and fatigue zone

This may be attributed to increase in firing rate in this zone. The time frequency plot of fatigue zone indicates the spectral shift towards low frequency regions. Also, these low frequency components are appeared with higher power. This spectral shift may be due to the reduction of firing rate and conduction velocity in this zone. The higher power may be associated with the participation of larger number of motor units during fatigue.

The IMDF and ISPEn are extracted from the time-frequency spectrum of corresponding zones and it is shown in Fig. 3 and Fig. 4 respectively. The IMDF's are found to be higher in non-fatigue zone and it varies from 50 Hz to 100 Hz where as it lies in the range of 30 Hz to 60 Hz in fatigue zone. This variation in IMDF may be due to the reduction in firing rate and conduction velocity of muscle fibers. Similar variations are also seen in IMNF. Also the values of ISPEn are found to be higher in non-fatigue zone. From Fig. 4 it is seen that the complexity reduces during fatigue and it may be attributed to motor unit action potential synchronization. The mean and standard deviation of non-fatigue signals are found to be 65.2356 ± 6.1576 , 70.2327 ± 5.5079 Hz and 5.0187 ± 0.1573 for IMDF, IMNF and ISPEn respectively. The same for fatigue signals are 43.6282 ± 13.8244 , 50.2620 ± 9.0194 and 4.6270 ± 0.1395 . The t-test performed gives a p-value less than 0.0001 implying that the features are extremely significant.

4 Conclusion

Surface EMG signals are complex and non-stationary. In this work an attempt is made to analyze time-frequency based features extracted from the sEMG signals recorded during dynamic contraction of biceps brachii muscle. Signals are acquired from fifty healthy adult volunteers during flexion and extension exercise. Signals are subjected to B-distribution based Cohen class time frequency method. Features such as IMDF, ISPE_n and IMNF are extracted from time-frequency spectrum of non-fatigue and fatigue zones of muscle contraction. All features are found to be distinct in non-fatigue and fatigue zones. The percentage change between non-fatigue and fatigue regions of IMDF is found to be more than 30. It appears that this method is useful in analysis of the sEMG signals associated with various normal and clinical conditions.

5 References

1. Venugopal G, Navaneethakrishna M, and Ramakrishnan S, Extraction and analysis of multiple time window features associated with muscle fatigue conditions using sEMG signals, *Expert Syst. Appl* **41**: 2652–2659, 2014.
2. Olmo FL and Presti LL, Matched wavelet approach in stretching analysis of electrically evoked surface EMG signal, *Signal Process.* **80**: 671-684, 2000.
3. Boashash, Ed., Time-frequency signal analysis and processing: A comprehensive reference. Oxford, UK, Elsevier, 231-278, 2003.
4. Victor S, Braham B and Boashash B, Performance Evaluation of the B-Distribution, *Fifth International Symposium on Signal Processing and its Applications*, ISSPA 22-25, 1999.
5. Bonato P, Serge HR, Knaflitz M, and Luca CJD, Time-frequency parameters of the surface myoelectric signal for assessing muscle fatigue during cyclic dynamic contractions, *IEEE Trans. Biomed. Eng.*, **48**: 765-775, 2001.
6. Bachiller A, Díez A, Suazo V, Domínguez C, Ayuso M, Hornero R, Poza J, and Molina V, Decreased spectral entropy modulation in patients with schizophrenia during a P300 task, *Eur. Arch. Psychiatry Clin. Neurosci.*, 1–11, 2014.

MUSCLE ACTIVATION UNDER DIFFERENT ANKLE AND KNEE POSITIONS DURING LEG EXTENSION EXERCISE

VITALI LUCA

School of Pharmacy, Biotechnology and Motor Sciences, University of Bologna, Italy

BELLI GUIDO

School of Pharmacy, Biotechnology and Motor Sciences, University of Bologna, Italy

TENTONI CLAUDIO

*Department of Biomedical and Neuromotor Sciences,
University of Bologna, Italy*

BOTTEGHI MATTEO

Department of Clinical and Molecular Sciences, Università Politecnica delle Marche, Ancona, Italy

MAIETTA LATESSA PASQUALINO

*Department of Sciences for Quality of Life,
University of Bologna, Italy*

BACKGROUND: The imbalance between vastus medialis oblique (VMO) and vastus lateralis (VL) is one of the main factor for (PFPS) onset, related to improper alignment of the patella. **PURPOSE:** The aim of this study is to investigate the effects of knee flexion, knee rotation and ankle flexion attitudes on the activity of the VMO and VL muscles during unilateral maximal voluntary isometric contraction (MIVC) of the quadriceps femoris. **METHODS:** Ten healthy subjects volunteered for the study. Five conditions for two different knee flexion angles (90°; 30°) were tested: neutral condition, maximal knee medial rotation, maximal knee lateral rotation, maximal ankle plantarflexion and maximal ankle dorsiflexion. Data were normalized in order to calculate the normalized VMO/VL ratio. **CONCLUSIONS:** The normalized VMO/VL ratio for all the conditions occurred at 90° of knee flexion was higher than the same conditions at 30° of knee flexion ($p=0.04$), due to a lower level of activity of the VMO. No statistically differences between conditions at the same knee angle were observed, with only exception for lateral rotation at 30° knee flexion ($p<0.05$). These findings suggest that knee flexion is the main factor to be considered to improve VMO activity during leg extension exercise

Keywords: patello-femoral pain syndrome, leg extension, electromiography

1. Introduction

The patellofemoral pain syndrome (PFPS) is defined as a series of morphological and functional alterations that determine the onset of anterior knee pain. These alterations pertain to an improper joint alignment or to the presence of patella and femoral trochlea dysmorphisms, which achieve an altered sliding of the patella in the trochlear groove and an unequal distribution of the compressive forces on the joint surface. The condition of imbalance between vastus medialis oblique (VMO) and vastus lateralis (VL) shows a positive correlation with the PFPS, as largely documented by many studies.^{1,2,3,4,5,6,7,8,9} Some authors assume that the imbalance is related to a delayed VMO contraction while others reported a lack of strength of this muscle, which depends on a lower nervous activation or on an hypotrophic process.^{1,2,6,7,9}

Great benefits may be achieved performing exercises suitable to establish a prevalent VMO activation in order to restore the proper alignment of the patellofemoral joint by improving muscular tone and trophism.^{1,3,4,7,8,9}

2. Methodology

2.1 Experimental Approach

The aim of this study is to investigate the effects induced by different knee and ankle joint attitudes on VMO and VL activation during maximal voluntary isometric extensions of the knee, in healthy and physically active subjects. The examined variables are: knee flexion angle, knee rotation and ankle flexion. In order to achieve our aim we performed a series of trials that requires to maintain a certain joint attitude during maximal voluntary isometric contractions (MVIC) of the quadriceps.

Five conditions were defined and examined at two different knee flexion angles (90° and 30°): neutral condition (N) characterized by indifferent knee rotation and ankle flexion, maximal medial rotation (MR) and maximal lateral rotation (LR) of the knee, maximal plantarflexion (PF) and maximal dorsiflexion (DF) of the ankle. The altered joint attitudes were voluntarily maintained by participants therefore obtained by muscular activity. EMG data were collected from both muscles in order to calculate the normalized VMO/VL ratio.

2.2 Subjects

The participants to the study had to satisfy some access requirements:

- Aged between 18-40;³
- Presence of a regular physical activity background (two week sessions at least);^{3,10}
- Absence of surgery to the lower limbs;^{7,8,10}
- Absence of recent joint and muscle-tendon injuries of the knee;^{1,3,4,7,9}
- Absence of a recent or past painful symptomatology due to patellofemoral joint dysfunction.^{2,3,4,7,8}

11 subjects volunteered for the study, but only 10 of them (8M, 2F; 25,0 ±2,9 years) satisfied the requirements.

All trials were performed with the dominant limb.^{7,9}

2.3 Warm-up Session

Before performing the test, each subject participated to a warm-up session composed of 5 minutes cardio training (using the bicycle ergometer, Air Machine, Italy) followed by 3 series of 10 repetitions on the leg extension machine (Air Machine, Italy), with a 10Kg load, interspersed by 1 minute of rest.^{3,4,9,10}

The bicycle ergometer resistance was self-adjusted by subjects in order to achieve a pedalling rhythm between 60-70 rpm.

2.4 Skin Preparation and Electrodes Placement

A five minutes resting time was settled between the warm-up session and the test session. During this time, the skin was prepared and the electrodes were placed.⁷

The skin surface was shaved, abraded with fine sandpaper and cleaned with alcohol wipes, in order to remove hair, dead cells and sweat, reducing skin impedance and ensuring good adhesion of the electrodes.

A reference line was drawn between the anterior-superior iliac spine and the center of the patella. The VMO electrode was positioned 4 cm above the superior border of the patella and 3 cm measured medially to the reference line. The VL electrode was placed 10 cm above the superior border of the patella and 6 cm measured laterally to the reference line. To be parallel to the course of muscle fibers, the electrodes were oriented 55° for the VMO and 15° for the VL with respect to the reference line. The ground electrode was fixed to the patella center. All the electrodes used were disposable with pre-applied conducting gel and were placed on each muscle with a preset inter-electrode distance of 20 mm.^{1,3,5,7,10}

Data collection was completed within the day for each participant and the electrodes were left in place during all the test session.

2.5 Subjects positioning and Test Session

Subjects were positioned on the leg extension machine (Air Machine, Italy) with hip flexed at 90°, lateral femoral epicondyle of the knee aligned with the machine's axis, torso adherent to the backrest, hands crossed on chest and resistance applied 3 cm above the malleoli.^{5,7}

Two trials for each condition were performed by all subject. To reduce the order effect, which may be caused by fatigue and previous muscle activation, half of participants have performed first the conditions at 90° of knee flexion then at 30°, while the other half have performed the test with the opposite sequence. For the same reason the order of the conditions occurring at the same angle were randomized.^{2,4,5,7,8,9}

Each contraction has been maintained for 5 seconds followed by 1 minute of rest.⁷

2.6 EMG Data Collection and Statistical Analyses

During the test execution the neuromuscular activity has been detected by using the BTS Pocket EMG device (BTS Bioengineering, Italy). The EMG signals of both muscles were collected during the whole 5 seconds period of isometric contraction, but the first and last second were discarded.^{2,7} Therefore, a 3 seconds window was used for analysis, and the data obtained have been subjected to a 20-400 Hz band pass filter, then full wave rectified and processed with the root mean square amplitude algorithm (RMS) to assess the electrical activity of each muscle.⁷

Since two trials were performed for each condition, data were normalized using as reference contraction the highest one obtained in neutral condition with the knee flexed at 90°, whilst for the other conditions has been calculated the average RMS value, then the percentage activation compared to the reference contraction (NRMS). Finally, it has been calculated the ratio between the muscles, thus achieving the normalized VMO/VL ratio.

An analysis of variance for repeated measures (Repeated ANOVA) was used to assess the effects of the knee flexion angle (30 °, 90 °) and the knee and ankle attitudes (N, RM, RL , FP, FD). The level of significance was defined as $p < 0.05$ and the software used for the analysis is SPSS ver.13.

3. Results

Results are showed in Table 1 ad Fig. 1. None of the tested conditions was able to define a prevailing VMO activation. The normalized VMO/VL ratio for all the conditions occurred at 90° of knee flexion was higher than the same conditions at 30° of knee flexion ($p=0.04$), due to a lower level of activity of the VMO. No statistically differences between conditions at the same knee angle were observed, with only exception for lateral rotation at 30° knee flexion ($p<0.05$), with values close to those obtained at 90° of knee flexion.

Table 1. Muscles activation and normalized VMO/VL ratio

CONDITION	VMO (NRMS) $\pm \sigma$	VL (NRMS) $\pm \sigma$	VMO/VL $\pm \sigma$
90° of knee flexion angle			
Neutral	100,0%	100,0%	1
Medial rotation	96,3% ± 16	96,4% $\pm 13,9$	1,000 $\pm 0,098$
Lateral rotation	93,8% $\pm 20,7$	93,4% $\pm 20,4$	1,012 $\pm 0,131$
Plantarflexion	106,5% $\pm 19,6$	106,0% $\pm 21,0$	1,013 $\pm 0,104$
Dorsiflexion	111,5% $\pm 31,1$	110,1% $\pm 34,4$	1,029 $\pm 0,120$
30° of knee flexion angle			
Neutral	90,6% $\pm 22,5$	103,9% $\pm 33,8$	0,897 $\pm 0,137$
Medial rotation	84,9% $\pm 17,4$	97,2% $\pm 28,3$	0,899 $\pm 0,153$
Lateral rotation	66,2% $\pm 20,7$	76,6% $\pm 35,5$	0,989 $\pm 0,493$
Plantarflexion	95,5% $\pm 26,8$	109,4% $\pm 37,8$	0,894 $\pm 0,142$
Dorsiflexion	88,5% $\pm 31,1$	103,1% $\pm 43,5$	0,889 $\pm 0,145$

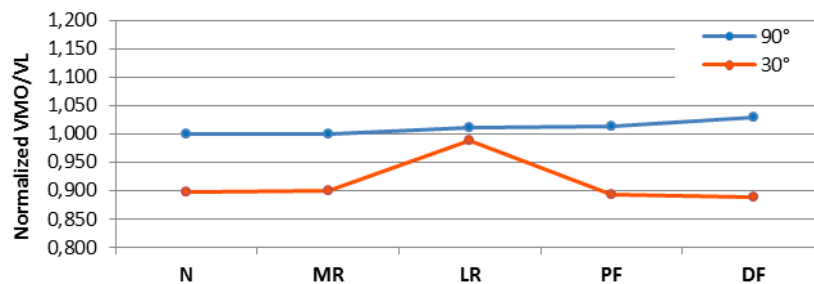


Fig. 1. Normalized VMO/VL ratio comparison under different knee flexion angles

4. Conclusion

These findings suggest that knee flexion is the main factor to be considered to improve VMO activity during leg extension exercise; differently, knee rotation and ankle flexion attitudes does not influence the VMO/VL ratio with exception of lateral rotation during 30° flexion. This should be

considered by clinicians when treating patients affected by PFPS in order to contrast the lateral dislocation of the patella.

References

1. Hertel J, Earl JE, Tsang KKW, Miller SJ, Combining isometric knee extension exercises with hip adduction or abduction does not increase quadriceps EMG activity, *Brit J Sport Med* 38:210-213, 2004
2. Hung Y, Gross MT, Effect of foot position on electromyographic activity of the vastus medialis oblique and vastus lateralis during lowerextremity weight-bearing activities, *J Orthop Sports Phys Ther* 29:93-105, 1999
3. Irish SE, Millward AJ, Wride J, Haas BM, Shum GLK, The effect of closed-kinetic chain exercises and open-kinetic chain exercise on the muscle activity of vastus medialis oblique and vastus lateralis. *J Strength Cond Res* 24:1256-1262, 2010
4. Matheson JW, Kernozek TW, Fater DCW, Davies GJ, Electromyographic activity and applied load during seated quadriceps exercises, *Med Sci Sport Exer* 33:1713-1725, 2001
5. Signorile JF, Kacsik D, Perry A, Robertson B, Williams R, Lowensteyn I, Digel S, Caruso J, LeBlanc WG, The effect of knee and foot position on the electromyographical activity of the superficial quadriceps, *J Orthop Sports Phys Ther* 22:2-9, 1995
6. Smith TO, Bowyer D, Dixon J, Stephenson R, Chester R, Donell ST, Can vastus medialis oblique be preferentially activated? A systematic review of electromyographic studies, *Physiother Theory Pract* 25:69-98, 2009
7. Sousa A, Macedo R, Effect of the contraction of medial rotators of the tibia on the electromyographic activity of vastus medialis and vastus lateralis, *J Electromyogr Kines* 20:967-972, 2010
8. Stoutenberg M, Pluchino AP, Ma F, Hocht JE, Signorile JF, The impact of foot position on electromyographical activity of the superficial quadriceps muscles during leg extension, *J Strength Cond Res* 19:931-938, 2005
9. Zakaria D, Harburn KL, Kramer JF, Preferential activation of the vastus medialis oblique, vastus lateralis, and hip adductor muscle during isometric exercises in females, *J Orthop Sports Phys Ther* 26:23-28, 1997
10. Pincivero DM, Gandhi V, Timmons MK, Coelho AJ, Quadriceps femoris electromyogram during concentric, isometric and eccentric phases of fatiguing knee extensions, *J Biomech* 39:246-254, 2006

DIFFERENTIATING SURFACE EMG SIGNALS UNDER FATIGUE AND NON-FATIGUE CONDITIONS USING RAIN FLOW COUNTING BASED FEATURES

SUSHANT KULKARNI, VENUGOPAL G and RAMAKRISHNAN S
*Non-Invasive Imaging and Diagnostics Laboratory, Biomedical Engineering Group,
Department of Applied Mechanics, Indian Institute of Technology Madras, India
E-mail address: ksushantk@gmail.com, venugopalg@gmail.com and sramki@iitm.ac.in*

In this work, an attempt has been made to discriminate Surface Electromyography (sEMG) signals under non fatigue and fatigue conditions using Rainflow Counting (RC) method. Signals are recorded for isometric contractions from biceps brachii muscle of 50 healthy subjects. RC algorithm is used on sEMG signals for extracting Rainflow cycles and features, namely, mean and amplitude. To quantify the features, root mean square value is used. Results show that the sEMG signal and corresponding RC mean are visually similar except for the length. RMS values of RC mean and amplitude are found to distinct in fatigue conditions. More than 50 % difference is obtained for RMS values of both RC features between fatigue and nonfatigue states.

Key words: Muscle fatigue; Surface EMG signal; Rainflow counting; Rainflow mean; Rainflow amplitude

1. Introduction

Muscle fatigue is a neuromuscular condition in which the ability of muscles to generate force reduces.¹ It occurs due to sustained or intense contractions of muscles and inadequate supply of oxygen and nutrition through blood. It can also arise due to malnutrition, Parkinson's disease and neuromuscular disorders.² Muscle fatigue studies finds applications in clinical analysis of neuromuscular diseases, ergonomics, rehabilitation, occupational and sports medicine studies.³ Surface electromyography (sEMG), a non-invasive technique, is used widely in muscle fatigue studies. sEMG signals are electrical signals generated by skeletal muscles during relaxation or contraction activities and are recorded using surface electrodes.

The identification of prominent signal features is important in muscle fatigue studies. For this purpose researchers have considered various time,¹ frequency⁵ and time frequency domain features.⁶ The Rainflow Counting (RC) algorithm is one of the cycle counting techniques used in health care monitoring of mechanical structures.⁷ This algorithm decomposes the randomly varying stress into a set of cycles which is used for prediction of fatigue and failure analysis.

In this work, sEMG signals are recorded from biceps brachii muscles under fatigue and non-fatigue conditions. The Rainflow cycles are obtained from the pre-processed signal and features such as mean and amplitude of cycles are extracted. These features are used for further analysis.

2. Methodology

2.1 Signal Acquisition and Exercise Protocol

In this study, 50 healthy volunteers with no history of neuro-muscular disorders and experience in weight training have participated. These subjects are having an average age of 25, average height of 1.67 m and an average weight of 60 kg. The signals are acquired using Biopac MP36 at sampling rate of 10k samples per second, gain of 1000 and with 24 bit resolution. Ag-AgCl surface electrodes are placed

on biceps brachii muscle with inter electrode distance of 3 cm after cleaning the skin. The subjects are then asked to stand upright on insulated wood platform holding a weight of 6 kg and perform biceps curl exercise until they experience fatigue. Signals are acquired at the start of the experiment and after getting fatigue, for 2 seconds at 30° angle with respect to vertical axis. The mean removed signal is pre-processed offline using a Butterworth band pass filter of range of 20-400 Hz and a notch filter of 50 Hz.²

2.2 Rainflow Counting Algorithm

The analogy of rainflow counting first described by Matsuishi and Endo, is derived from the rain flowing (dripping) off the pagoda roofs.⁸ The method has become popular as it has small relative error and it provides average value.⁹ Counting is carried out on basis of the variation of signal with time. This algorithm requires only successive extremes, which has to be extracted from the sEMG signal. The algorithm is adapted from the work reported by Deng et al.¹⁰

The pre-processed signals are subjected to rainflow counting and rainflow matrix is calculated, which contains the individual cycles. For each cycle, the mean and amplitude were obtained. The mean of cycle is the mean of all the extremes in that cycle and amplitude of cycle is maximum variation of any extreme from the mean in that cycle. When mean and amplitude of each individual cycle are plotted for all cycles, a new signal with cycles as independent axis results. To quantify these signals, root mean square (RMS) value is extracted and used for further analysis.

3. Results and Discussions

Fig. 1(a) and Fig. 1(b) shows the rainflow mean signal derived from sEMG signals for non-fatigue and fatigue periods after application of Rainflow counting algorithm.

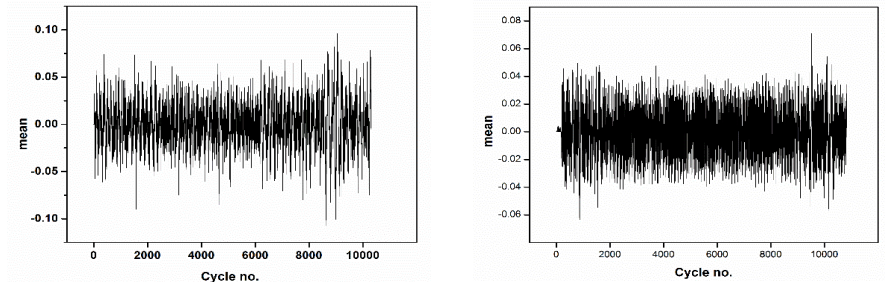


Fig. 1. Mean of rainflow cycles for sEMG signals for non-fatigue and fatigue.

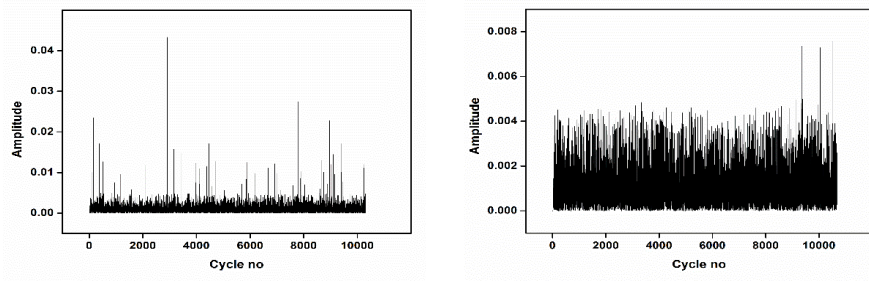


Fig. 2. Amplitude of rainflow cycles for sEMG signals for non-fatigue and fatigue.

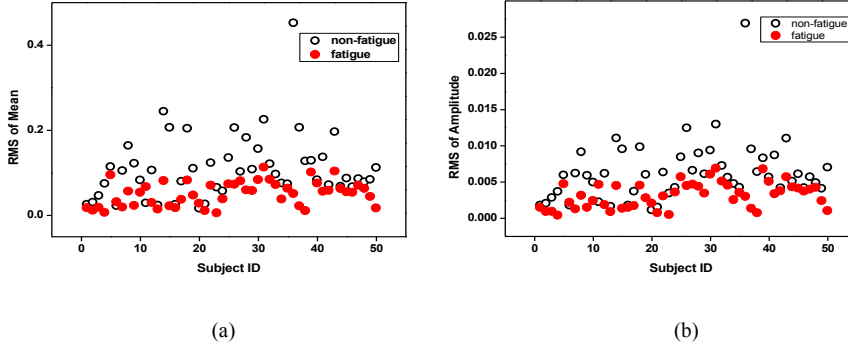


Fig. 3. RMS values of rainflow features (a) mean and (b) amplitude

Fig. 2 shows the rainflow amplitude signal derived from RC cycles for non fatigue and fatigue periods. It is observed that the rainflow amplitude decreases significantly in fatigue conditions. This may be due to the fact that RC of nonfatigue condition has larger number of cycles and it has high variation from the rainflow mean. The reduced value of rainflow amplitude during fatigue condition may be attributed to lower amplitude variations of sEMG signal due to synchronization of the motor units.

Fig. 3(a) and Fig. 3(b) show the scatter plot of the RMS value of rainflow mean and amplitude respectively for all the 50 subjects. In fatigue period, the RMS values of rainflow mean and amplitude are found to be closer to zero. In nonfatigue condition, for both RC mean and amplitude signal, the RMS values are consistently higher compared to fatigue case. The reduction of RMS values for rainflow mean and amplitude during fatigue period may be due to the reduction in the signal energy in the fatigue conditions. Statistical parameters of RMS values of RC mean and amplitude are presented in Table 2. The percentage difference of average value of RMS of RC mean and amplitude is found to be 54 and 50 respectively. The variability of the data is found to reducing in fatigue state.

Table 1. Statistical parameters of RMS value of mean and amplitude of rainflow cycles

	Non-Fatigue		Fatigue	
	Mean	SD	Mean	SD
Rainflow mean	0.111	0.076	0.050	0.028
Rainflow amplitude	0.006	0.004	0.003	0.002

4. Conclusion

In this work, an attempt has been made to differentiate sEMG signals under fatigue and nonfatigue conditions using RC algorithm. Signals are recorded from 50 healthy volunteers and rainflow cycles are calculated. Two features namely RC mean and amplitude are extracted from the cycles. To quantify the RC features, RMS values are calculated and used for further analysis. The results show that the extracted features are distinct in fatigue condition. RC mean signal is found to preserve the energy characteristics of the preprocessed sEMG signal even with less number of samples. RMS values of RC features are found to be separable between fatigue and nonfatigue states. A difference of 54% and 50% is obtained for

the average value of RMS of RC mean and amplitude respectively. It appears that this method can be used to identify muscle fatigue using sEMG signals in normal and varied clinical conditions.

References

1. Dimitrova N A, Dimitrov GV, Interpretation of EMG changes with fatigue: facts, pitfalls, and fallacies. *J. Electromyogr. Kinesiol.* **13**: 13–36, 2003.
2. Venugopal G, Navaneethakrishna M, Ramakrishnan S, Extraction and analysis of multiple time window features associated with muscle fatigue conditions using sEMG signals. *Expert Syst. Appl.* **41**: 2652–2659, 2014.
3. Liang M, Damien C, Fouad B, Wei Z, Bo H, Francois G, A novel approach for determining fatigue resistances of different muscle groups in static cases. *Int. J. Ind. Ergon.* **41**: 10–18 2011.
4. Kumar D K, Arjunan SP, Naik GR, Measuring increase in synchronization to identify muscle endurance limit, *IEEE Trans. Neural Syst. Rehabil. Eng. Publ. IEEE Eng. Med. Biol. Soc.* **19**: 578–587, 2011.
5. Phinyomark A, Phukpattaranont P, Limsakul C, Feature reduction and selection for EMG signal classification, *Expert Syst. Appl.* **39**: 7420–7431, 2012.
6. Bonato P, Roy SH, Knaflitz M, De Luca CJ, Time-frequency parameters of the surface myoelectric signal for assessing muscle fatigue during cyclic dynamic contractions, *IEEE Trans. Biomed. Eng.* **48**: 745–753, 2001.
7. Bai S, Li X, Xie Z, Zhou Z, Ou J, A wireless fatigue monitoring system utilizing a bio-inspired tree ring data tracking technique, *Sensors* **14**: 4364–4383, 2014.
8. Matsuichi M, Fatigue of metals subjected to varying stress, *Japan society of mechanical engineering*, 1968.
9. Mainka K, Thoben M, Schilling O, Lifetime calculation for power modules, application and theory of models and counting methods, *Proc. 2011-14th Eur. Conf. Power Electron. Appl.*, pp. 1–8, 2011.
10. Deng Q, Yuan H J, The Algorithm for Graphic Method of Rain-Flow Counting in Programming, *Adv. Mater. Res.* **225**: 1157–1161, 2011.

ANALYSIS OF FATIGUE PROGRESSION DURING DYNAMIC CONTRACTION OF BICEPS BRACHII MUSCLES USING INTRINSIC MODE FUNCTIONS OF SURFACE EMG SIGNALS AND SPECTRAL FEATURES

VENUGOPAL G and RAMAKRISHNAN S
*Non-Invasive Imaging and Diagnostics Laboratory
Biomedical Engineering Group, Department of Applied Mechanics
Indian Institute of Technology Madras, India
E-mail address: venugopal@gmail.com and sramki@iitm.ac.in*

In this work, an attempt has been made to analyze progression of fatigue in biceps brachii muscles using surface electromyography (sEMG) signals considering the nonlinearity and nonstationary of the process. The recorded signals are pre-processed and subjected to empirical mode decomposition to derive Intrinsic Mode Functions (IMF). Further analysis is carried out by dividing the entire duration of the exercise into six zones. Analytic functions are calculated in each IMF using Hilbert transform for estimating power spectrum. Features namely Spectral Peak (SP), Peak Frequency (PF), Spectral Entropy (SE) and Spectral Energy (SEN) are extracted from the power spectrum and used for analysis. The results show significant amplitude and frequency variations in IMF1 and IMF2 during dynamic contractions. All features of IMF1 and IMF2 except PF are found to be distinct in all zones. It appears that, this method is useful in analyzing progressive changes associated with muscle mechanics in fatigue conditions using non-invasive sEMG recordings.

Key words: Biceps Brachii; Muscle Fatigue; Surface EMG signal; Empirical Mode Decomposition; Analytic Function; Spectral Features

1. Introduction

Sustained, intense or continuous muscle contraction results in muscle fatigue.¹ Fatigue assessment is important in patients with neuromuscular disorders, sports medicine, ergonomics and myoelectric controls. Surface electromyography (sEMG) is a widely used technique for muscle fatigue studies.² sEMG signals are recorded using surface electrodes placed over the skin and provide information about the electrical activity of contracting skeletal muscles.² During dynamic contractions and fatigue conditions, non-stationarity and nonlinearity of the sEMG signal varies due to many physiological reasons.³ Time, frequency and time-frequency domain methods are used to analyze sEMG signals.⁴ Empirical Mode Decomposition (EMD) is a novel signal processing tool used to analyze non-linear and non-stationary data. This technique decomposes the sEMG signals into its constituent Intrinsic Mode Function (IMF) using adaptive basis function.⁵ Kang et al. suggests IMF1 component of EMD is best suited for evaluating muscle fatigue using sEMG signals.⁶

In this work, sEMG signals are recorded from biceps brachii muscles during curl exercise and are decomposed into IMFs using EMD. Each IMF is converted into analytic functions using Hilbert transform and spectral features are extracted from the power spectrum of the same. These are further used to analyze the progression of muscle fatigue.

2. Methods

2.1 Signal Acquisition and Protocol

Signals are recorded using Biopac MP36 data acquisition system.⁴ It has a minimum common mode rejection ratio of 110dB and an ADC with 24 bits resolution. The gain of the system is set as 1000 and

sampling rate is fixed as 10 kHz. Fifty subjects with no history of neuromuscular disorders or weight training participated in this study. Ag-AgCl disc type disposable electrodes with 3 cm inter-electrode distance are placed over the belly of biceps brachii muscle in differential configuration. Subjects are made to perform curl exercise with a 6 kg dumbbell until they are unable to lift the load again. The instances of first muscle discomfort and task failure are noted. Signals are subjected to band pass filtering using a Butterworth filter with cut-off frequencies of 10 Hz and 400 Hz. A notch filter with 50 Hz is used to remove power line interference.⁴

2.2 Spectral feature extraction from IMFs

EMD algorithm is used to decompose the sEMG signal into IMFs.⁵ In this work first two IMFs are considered for analysis. Each IMF is divided into six zones to normalize the time axis and hence to analyze the progression of muscle fatigue. Further, IMFs are converted into analytic function using Hilbert transform to understand amplitude and frequency modulated frequencies. Power spectrum of analytic functions are calculated using Welch's method. Following spectral features are extracted from IMF1 and IMF2 for further analysis.

Spectral Peaks (SP)

The maximum value in the power spectrum series. This feature can be used as a measure of shift in spectral power due to muscle fatigue.

Peak Frequency (PF)

The frequency corresponding to the spectral peak. This feature can be used as a measure of shift in the frequency due to muscle fatigue.

Spectral Entropy (SE)

It is a measure of unpredictability of a time series. Here, the power spectrum is considered as the time series and its predictability is analyzed.

$$SE = - \sum_{f=0}^{f_s/2} P_{XX}(f) \log |P_{XX}(f)| \quad (1)$$

where, $P_{XX}(f)$ is the normalized power spectral density and f_s is the signal sampling frequency.

Spectral Energy (SEN)

Spectral energy provides a measure of signal energy and its variation due to muscle fatigue. This feature depends on the muscle force production during contraction.

$$SEB = \frac{1}{N} \sum_{f=0}^{f_s/2} P_{XX}(f) \quad (2)$$

where, N is the total number samples in frequency. In this work, MATLAB software with custom made functions are used for pre-processing, EMD and extraction of features.

3. Results and Discussion

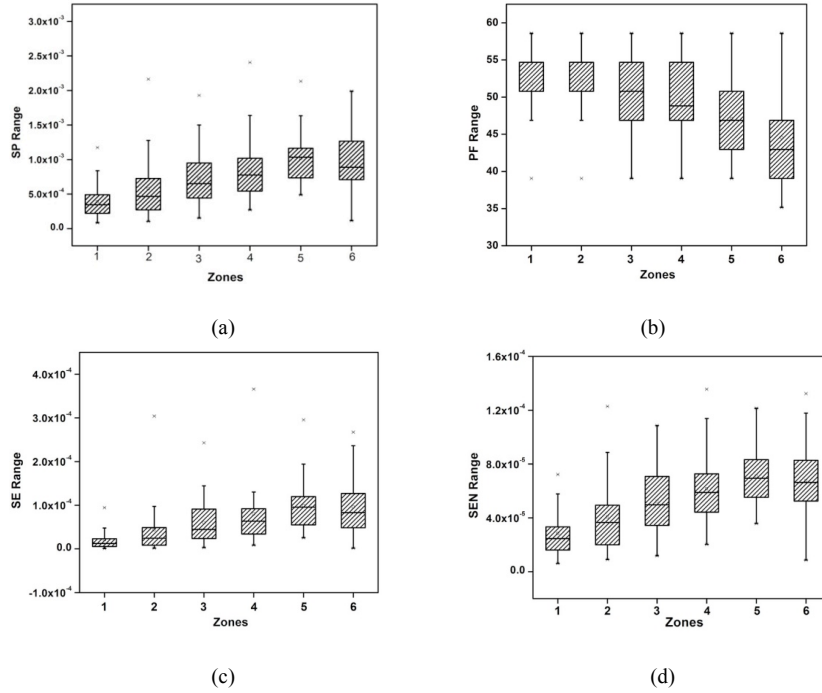


Fig. 1. Spectral features of IMF1 (a) SP (b) PF (c) SE and (d) SEN

The statistical characteristics of spectral features extracted from IMF1 of 50 subjects is shown in Fig. 1(a-d). The mean value of SP is found to be increasing with respect to the progression of fatigue (Fig. 1(a)). It is observed that variability of SP is higher in fatigue zone. From Fig. 1(b) it is observed that PF is stable in first two zones but from third zone onwards it is decreasing. The mean PF is found to be less in sixth zone and this may be attributed to the reduction of motor unit firing frequency in fatigue condition.

The signal randomness, expressed using SE, is found to be increasing in IMF with progression of fatigue as shown in Fig. 1(c). It may be due to the recruitment of more motor units and biomechanical instabilities of hand joints. Fig. 1(d) shows the variations in SEN due to cyclic contractions. It is observed that the IMF1 energy is increasing with respect to the progression of fatigue and it may be ascribed to the increase in the effort level of subject and recruitment of more motor units.

The percentage difference of features for IMF1 and IMF2 is found to be decreasing with progression of muscle fatigue. Maximum percentage difference value is obtained for SE feature in both IMF1 and IMF2. This could be attributed to the reduction in signal predictability with fatigue. Among all features, PF provides minimum percentage difference.

4. Conclusion

In this work, an attempt is made to analyze spectral features extracted from IMF of sEMG signals during dynamic contraction of biceps brachii muscle. Signals are recorded from 50 healthy volunteers during curl exercise. Further they are subjected to EMD and each IMF is divided into six zones to normalize the variability of endurance time among subjects. Spectral features such as SP, PF, SE and SEN are extracted and analyzed. It is observed that PF of IMF1 is differentiable in all the zones. It appears that this method of analysis is useful in dealing with nonlinearity and non-stationarity of the sEMG signals associated with various normal and clinical conditions.

Reference

1. Enoka RM, Duchateau J, Muscle fatigue: what, why and how it influences muscle function, *Journal of Physiology* **586**: 11-23, 2008.
2. Vladimir M, Stanko T, Sasa O, Surface EMG based muscle fatigue evaluation in biomechanics, *Clinical Biomechanics* **24**: 327–340, 2009.
3. Daniel J, Wolfgang IS, Karl MN, Jorg MJ, Franz R, Katrin V, Diagnosing fatigue in gait patterns by support vector machines and self-organizing maps. *Human Movement Science* **30**: 966–975, 2011.
4. Venugopal G, Navaneethakrishna M, Ramakrishnan S, Extraction and analysis of multiple time window features associated with muscle fatigue conditions using sEMG signals, *Expert Systems with Applications* **41**: 2652–2659, 2014.
5. Roshan JM, Rajendra AU, Jen HT, Andrea P, Ratna Y, Chua KC, Ng EYK, Louis T, Application of empirical mode decomposition (EMD) for automated detection of epilepsy using EEG signals, *International Journal of Neural Systems* **22**: 1250027-1250043, 2012.
6. Kang MC, Shing HL, Jia JW, Cheng DC, Exercise muscle fatigue detection system implementation via wireless surface EMG and empirical mode decomposition, In: *IEEE Proceedings of 35th Annual International Conference of the EMBS*, 1001- 1004, 2013

MUSCLE ACTIVATION DURING PUSH UP EXERCISE UNDER STABLE AND UNSTABLE CONDITIONS

BELLI GUIDO

School of Pharmacy, Biotechnology and Motor Sciences, University of Bologna, Italy

CIACCI SIMONE

*Department of Biomedical and Neuromotor Sciences,
University of Bologna, Italy*

RUDATIS ANDREA

Zenith Wellness Center, Bondeno (FE), Italy

PEGREFFI FRANCESCO

*Villa Laura Hospital, Bologna
University of Bologna, Italy*

FANTOZZI SILVIA

*Department of Electrical, Electronic, and Information Engineering,
University of Bologna, Italy*

BACKGROUND: Push up exercise is a popular and common way of strengthening the upper body in clinical, fitness and sport fields. Recently, trainers and researchers suggest to perform this exercises under unstable condition with specific tools, in order to increase muscle activation.

PURPOSE: The aim of this study is to investigate the electromyographic activity (EMG) of shoulder and trunk muscles during 4 different kind of isometric push up exercises performed with elbow flexed and extended.

METHODS: Ten healthy subjects volunteered for the study. Three unstable conditions (TRX, BALL, SKIMMY) and one stable condition (STEP) for two different elbow joint angles (90° flexion – FLEX ; full extension - EXT) were tested during 5 seconds isometric push ups. EMG was recorded for Anterior Deltoids (DA), Pectoralis Major (GP), Triceps Brachialis (TRI), Latissimus Dorsi (GD), Rectus Abdominis (RA), Obliquus Externus (OE). Data were processed in order to calculate EMG Root Mean Square (RMS) and normalize to stable condition (Step).

CONCLUSIONS: All unstable conditions show higher muscle activity in both joint angle positions compared to stable condition. In particular, TRX evidences the highest EMG data in FLEX and EXT condition: TRX is higher than BALL, STEP and SKIMMY in EXT condition ($p<0.01$) and higher than STEP and SKIMMY ($p<0.01$) in FLEX condition. TRB, RA and OE are the most activated muscles in all conditions for both FLEX and EXT with different values related to specific tools. GP, DA and GD are higher in FLEX than EXT ($p<0.01$) while RA is higher in EXT angle compared to FLEX ($p<0.05$).

These findings suggest that adding instability is a good way to improve trunk muscle activity in both joint angle positions, while shoulder muscle activity is more related to elbow condition.

Keywords: push up, electromyography (EMG), unstable surfaces

1. Introduction

Push up is a popular and common exercise that is normally performed in prone position by raising and lowering the whole body using the arms. The purpose of this exercise is to primarily target shoulder and

trunk muscles in order to improve both mobilizing and stabilizing functions around elbow, gleno-humeral and core area.^{1,2} The basic version is a closed kinetic chain movement that requires muscle co-contraction and dynamic joint stability and is quickly adaptable to people's fitness level using simple variations to increase or decrease the training load. Since the specific technique is easy to perform and no particular equipment is needed, ACSM highly recommends it for training and testing different kind of people in sport and rehabilitation.¹ In the last years, push up has been widely investigated using electromyography technique (EMG) in order to quantify muscle activity patterns during basic execution and his variations (hands position, feet position, hand-wrist rotation).^{2,3,4} Recently, the addition of unstable surfaces (like fitball, wobble board, bosu) while performing this exercise has been promoted by trainers and researchers to increase stabilizer function around shoulder and elbow joints,^{5,6,7,8,13,14} to improve muscle performance after training time,¹⁰ and to elicit higher core stability and strength level.^{9,11,12} The justification for the use of labile surface is based on its potential to maintain postural stability and neuromuscular control in the whole body, even if contradictory data exists about his effectiveness.^{5,6,10} Lastly, suspension training is a new kind of push up version performed with specific tools (TRX, sling surfaces) that improve stability and proprioception around shoulder girdle.^{15,16} Since science is actually poor about this and his comparison with other unstable surfaces, the goal of present work is to analyze the EMG activity while performing different kinds of push up using stable, unstable and sling surfaces. It is hypothesized that instability will elicit greater muscle activity in both shoulder and trunk region compared to stable condition.

2. Methodology

2.1 Experimental Approach

The current study aim to quantify muscular activity during 4 kinds of isometric push up (PU) performed with 2 different elbow joint's angles in healthy and physically active people. The 4 PU conditions were related to specific equipment used during our analysis: a stable condition using single step (STEP) and 3 unstable conditions using respectively 2 soccer balls (BALL), 2 inflated discs (SKIMMY), a sling tool (TRX). The 2 elbow joint's angles were defined at 90° flexion (FLEX) and full extension (EXT).

All data were collected in a single day session with repeated measure of PU in a random order using EMG. A pre-test familiarization session was performed 7 days before in order to improve specific technique for each condition.

2.2 Participants

Ten healthy and physically active male volunteered for the study (mean age $22,7 \pm 2,06$, weight $74,2 \pm 8,89$ Kg, height $1,75 \pm 0,5$ m).

Inclusion criteria were:^{10,12,15,16}

- Performing regular physical activity (at least two sessions per week);
- One year experience using instability training with same tools of current study;
- Absence of surgery and recent joint or muscle-tendon injuries to trunk and arm.

2.3 Warm-up and testing session

Before performing the test, people participated to a warm-up session composed of 5 minutes cardio training (using the bicycle ergometer or tapis roulant, Air Machine, Italy) followed by 10 minutes dynamic mobility training in the upper body.

After warm up, participants rested 5 minutes and started the testing session with PU executed in a random order.

They performed 3 PU for each surface condition (STEP, BALL, SKIMMY, TRX) in both FLEX and EXT joint angle. Each position was isometrically held for 5 seconds with 1minute rest between repetitions.

FLEX PU were performed with hands on specific tool slightly wider than shoulder-width apart, shoulders at 60° abduction and elbows at 90° flexion, feet together on the floor, trunk and lower limb aligned with neutral spine.

EXT PU were performed were performed with hands on specific tool slightly wider than shoulder-width apart, shoulders above the hands and elbow full extended, feet together on the floor, trunk and lower limb aligned and neutral spine.

2.4 Skin Preparation and Electrodes Placement

Before warm up session, the skin was prepared and the electrodes were placed. The skin surface was shaved, abraded with fine sandpaper and cleaned with alcohol wipes, in order to remove hair, dead cells and sweat, reducing skin impedance and ensuring good adhesion of the electrodes.

The following muscles on the right side of the body were investigated: pectoralis major (PM), anterior deltoid (DA), triceps brachialis (TRI), latissimus dorsi (GD), rectus abdominis (RA), obliquus externus (OE); ground electrode was fixed on the anterior superior iliac spine. All the electrodes were disposable with pre-applied conducting gel and were placed on each muscle with a preset inter-electrode distance of 20 mm.^{12,13,14,15,16}

2.5 EMG Data Collection

During the testing session the neuromuscular activity has been detected by using the BTS Pocket EMG device (BTS Bioengineering, Italy). The EMG signals of all muscles were collected during the whole 5 seconds period of isometric contraction with a sampling frequency of 1000 Hz, 16 bit A/D converted and analyzed with BTS Myolab software. Since the first and last second were discarded, a 3 seconds signal was obtained and then processed to a 20-400 Hz band pass filter, full wave rectified and finally root mean square amplitude algorithm (RMS) was calculated to assess the electrical activity of each muscle. All data were normalized to stable condition (STEP) at both FLEX and EXT angle in order to compare stable-unstable tools in 2 different joint angle.¹²

2.6 Statistical Analysis

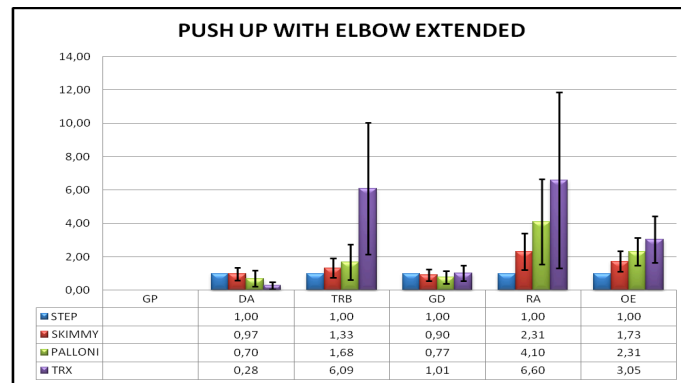
EMG normalized data resulting from 3 PU repetitions were averaged and the obtained values were defined as mean \pm standard deviation for each muscle in all conditions for both joint angles.^{15, 16} Averaged values were then processed for following statistical analysis:

- A 2 way repeated ANOVA (4 surfaces x 6 muscles) was used to investigate surface effect across all muscles separately for FLEX and EXT angle;

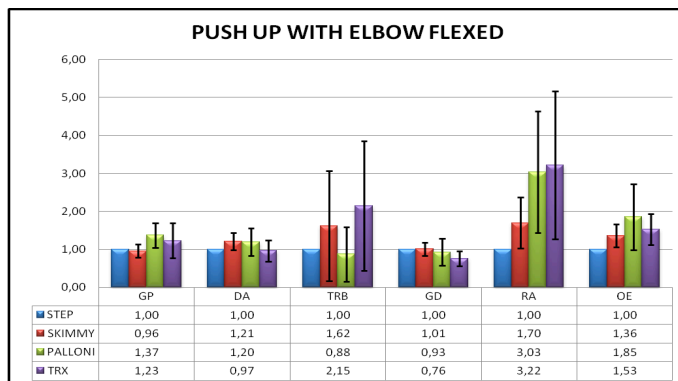
- A 2 way repeated ANOVA (4 surfaces x 6 muscles x 2 joint angle) was used to compare FLEX and EXT in different conditions for all muscles. Significance was set with $p < 0.05$.

3. Results

Graphic 1 and 2 show RMS mean values for each muscle in all conditions respectively in FLEX (graph 1) and EXT (graph 2) joint angles.



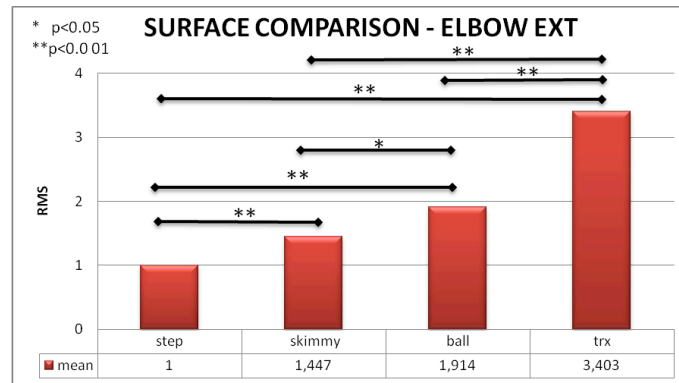
Graph 1: RMS values in elbow extended condition



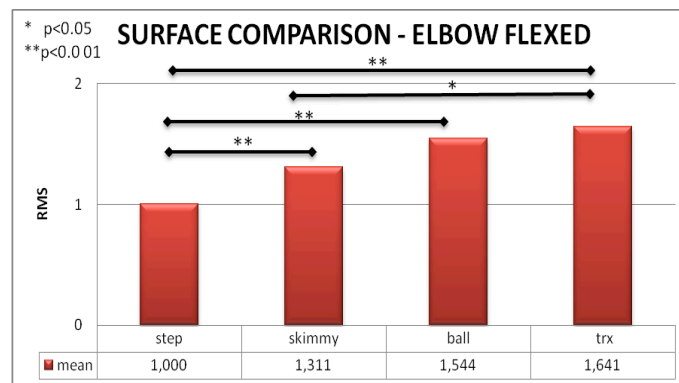
Graph 2: RMS values in elbow flexed condition

ANOVA evidences significance for surface, muscle and surface x muscle interaction in FLEX and EXT ($p=0.00$).

In EXT, TRX has significantly more global EMG activity compared to STEP (reference value : 1, $p=0.00$), SKIMMY (1,44, $p=0.00$) and BALL (1,91, $p=0.00$), BALL compared to STEP and SKIMMY ($p < 0.02$), SKIMMY compared to STEP ($p=0.00$) (graph 3). In FLEX, STEP (reference value: 1) has significantly less global EMG activity compared to SKIMMY, BALL and TRX (respectively 1.31, 1.54, 1.64, $p=0.00$) and SKIMMY compared to TRX ($p=0.03$) (graph 4).



Graph 3: Global RMS values for each surface in elbow flexed condition



Graph 4: Global RMS values for each surface in elbow flexed condition

In FLEX vs EXT comparison, FLEX shows higher global RMS activity compared to EXT, even if not significantly (2,18 vs 1,94, $p>0.05$): FLEX is higher than EXT in STEP (+39%, $p=0.00$), SKIMMY (+34%, $p=0.00$) and BALL (+17%, $p=0.03$). In muscle x angle interaction, ANOVA evidences higher values for DA and GD in FLEX compared to EXT (+71% and +34%, $p=0.00$) and for RA in EXT compared to FLEX (+40%, $p=0.04$).

4. Conclusions

The present work investigated EMG during different kind of isometric push up performed with specific tools. Previously, instability demonstrated to significantly improve shoulder and trunk muscular activity during PU and his variations using labile surfaces.^{7,8,12,13,14} In particular, gleno-humeral and core stabilizer increase their activity in relation to body position and surface:¹³ more body is parallel to the floor and instability under hands or feet is high, so training load and muscle activity are to the highest degree for both static and dynamic movements.^{9,11} Recently, Maeo¹⁵ and Snarr¹⁶ reported that TRX can be an efficient sling surface to improve shoulder and trunk activity in FLEX and EXT angle; present work confirms their hypothesis and suggests that FLEX position is more related to shoulder region (DA, GD, GP) while EXT position to core region (RA, OE).

References

1. ACSM. ACSM's Health-Related Physical Fitness Assessment Manual. Baltimore, Lippincott Williams & Wilkins (2nd edition), 2008
2. Cogley RM, Archambault TA, Fibeger JF, et al, Comparison of muscle activation using various hand positions during the push-up exercise, *J Strength Cond Res*, 19:628-633, 2005
3. Gouvali MK, Boudolos K, Dynamic and electromyographical analysis in variants of push-up exercise, *J Strength Cond Res*.19:146-151, 2005
4. Youdas JW, Budach BD, Ellerbusch JV, Stucky CM, Wait KR, Hollman JH, Comparison of muscle-activation patterns during the conventional push-up and Perfect push up exercises, *J Strength Cond Res*, 24:3352–3362, 2010
5. Lehman GJ, Gilas D, Patel U, An unstable support surface does not increase scapulothoracic stabilizing muscle activity during push up and push up plus exercises, *Man Ther* 13 (6): 500-506, 2008
6. Lehman, GJ, Gordon T, Langley J, Permrose P, Tregaskis S, Replacing a Swiss ball for an exercise bench causes variable in trunk muscle activity during upper limb strength exercises, *Dyn Med* 3 (4): 6, 2005
7. Lehman GJ, MacMillan B, MacIntyre I, Chivers M, Fluter M, Shoulder muscle EMG activity during push up variations on and off Swiss ball, *Dyn Med* 5:7, 2006.
8. Lee SY, Daehee L, Jungseo P, The Effect of hand position changes on electromyographic activity of shoulder stabilizers during Push-up Plus exercise on stable and unstable surfaces, *J Phys Ther Sci*, 25: 981–984, 2013
9. Marshall PW, Murphy PA, Core stability exercises on and off a Swiss ball, *Arch Phy Med Rehab* 86 (2): 242-249, 2005
10. Chulvi-Medrano I, Martínez-Ballester E, Masiá-Tortosa L, Comparison of the effects of an eight-week push-up program using stable versus unstable surfaces, 7(6):586-94, 2012
11. Behm DG, Drinkwater EJ, Willardson JM, et al, The use of instability to train the core musculature, *Appl Physiol Nutr Metab*, 35:91-108, 2010
12. Norwood, JT, Anderson GS, Gaetz, MB, Twist PW, Electromyographic activity of the trunk stabilizers during stable and unstable bench, *Journal of Strength and Conditioning Research*, 21: 343-347, 2007
13. Sandhu JS, Mahajan S, Shenoy S, An electromyographic analysis of shoulder muscle activation during push-up variations on stable and labile surfaces. *Int J Shoulder Surg*, 2(2):30-5, 2008
14. Holtzmann, M, Gaetz M, Anderson G, EMG activity of trunk stabilizers during stable and unstable push up, *Can J of Applied Physiol*, 29:55, 2004
15. Maeo S, Chou T, Yamamoto M, Kaneisha H, Muscular activities during sling- and ground-based push-up exercise, *BMC Research Notes*, 7:192, 2014
16. Snarr RE, Esco MR, Electromyographic Comparison of Traditional and Suspension Push-Ups, *J Hum Kin* 39:75-83, 2013

FUNCTIONAL EVALUATION OF A METHOD TO SPECIFY AN APPROPRIATE EXERCISE LOAD FOR WEIGHT LOSS IN OVERWEIGHT SUBJECTS

*LEYDI NATALIA VITTORI, ***DAVID NEIL MANNERS, **PASQUALINO MAIETTA LATESSA, ***CLAUDIO TENTONI

School of Pharmacy, Biotechnology and Sport Science; University of Bologna, Bologna, Italy ; Department for Life Quality, University of Bologna, Bologna, Italy; ***Department of Biomedical Sciences and Neuromotor, University of Bologna, Bologna, Italy*

Fat oxidation, physical exercise, overweight, heart rate, Fatmax

Introduction

There is a growing need to tailor programmes of physical activity to an increasingly numerous population of older adults with a variety of related health problems including weight control, hypertension, and diabetes. Among the potential benefits of regular aerobic exercise is the metabolic oxidation of lipidic substrates. Several previous studies have tried to determine the exercise intensity that maximises the rate of oxidation (FAT_{max}) using incremental or constant load exercise tests (1,2,3,4). The protocols were used to identify the heart rate and work rate for which RER was a minimum and hence fat oxidation was maximized, but typically in healthy, trained adults. The objective of the current study was to verify the reliability of a new test protocol $FAT_{max_{work}}$ designed for sedentary adults, analysed using the INCA software package (5).

Methods

Twenty-five overweight subjects, aged 50.9 ± 4.5 years, with BMI 27.5 ± 1.7 kg m⁻², were recruited. All subjects were monitored using a MedGraphics VO2000 metabolimeter during the $FAT_{max_{work}}$ treadmill test (briefly, initial speed 3 km h⁻¹, then increments of 1 km h⁻¹ every 5 minutes, for 20 minutes total), followed by a constant load test of 1 h duration at the chosen workrate: the FAT_{max} zone was estimated by INCA using a quadratic fit of lipidic power production against work rate.

Results

Testing was completed without cardiovascular or other acute health events in all subjects, but for 6 subjects data were not collected for technical reasons. For subjects who completed both tests (11 F), the average Fatzone was estimated by INCA at $54.2 \pm 4.9\%$ max HR, RER 0.86 ± 0.09 , 130 ± 64 W. The results from the constant load test differed by 0.01 ± 1.92 for RER and -0.22 ± 1.92 for %HR. The Fatzone differed by gender most notably in the work rate proposed: 158.3 ± 71.6 W for men and 115.2 ± 34.5 W for women at similar heart rates and RER.

Subjects were set to run at a constant rate corresponding to the heart rate indicated by INCA. They managed to maintain this target heart rate (mean difference \pm SD: -0.2 ± 1.9 b.p.m.), and in doing so lipid oxidation was very close to the expected value (difference in RER: -0.008 ± 0.022).

Discussion

Our results are comparable to those previously obtained using other test protocols, and demonstrate the reliability of our procedure, which was developed with a view to its capacity to be safely applied in a wide range of subjects. FATmax_{zone} testing with INCA software appear to meet the requirements for a safe, reliable and efficient method for calculating the FatMax.

References

- (1) J. Achten, M. Gleeson, A.E. Jeukendrup. *Med Sci Sports Exerc*, **2002**;34, 92-97.
- (2) J. Achten, M.C. Venables, A.E. Jeukendrup. *Metabolism* **2003**; 52, 747-52.
- (3) X. Chenevière, F. Borrani, et al. *Metabolism* **2009**; 58, 1778-86
- (4) E. Makni E, W. Moalla, et al. *Int J Obes (Lond)*. **2012**; 36, 908-13
- (5) L.N. Vittori, D.N. Manners, et al. *17th Annual Congress ECSS* **2012**; Abstract 1455

S7M: Medical physics - MRI imaging

Chairs: Paola Fantazzini, Nico Lanconelli

SEGMENTATION OF SUBCORTICAL REGIONS IN MR BRAIN IMAGES USING COMBINATION
OF FUZZY C-MEANS AND GAUSSIAN DISTRIBUTION MODEL BASED AUGMENTED
LAGRANGIAN MULTIPHASE LEVEL SETS

GANESAN KAVITHA

SHAPE ANALYSIS OF CORPUS CALLOSUM IN ALZHEIMER BRAIN MR IMAGES USING
COHERENCE ENHANCING DIFFUSION FILTERING AND IMPROVED VARIATIONAL LEVEL SET

K. R. ANANDH

MINKOWSKI FUNCTIONALS BASED ANALYSIS OF HIPPOCAMPUS IN ALZHEIMER'S BRAIN MR
IMAGES

GANESAN KAVITHA

PERFIDI FILTER SEQUENCES TO ACQUIRE MRI IMAGES WITH SPECIFIC RANGE OF T1 SIGNAL
COMPONENTS SUPPRESSED

ESTER MARIA VASINI

NMR RELAXOMETRY AND IMAGING TO QUANTIFY THE RATIO FAT-TO- WATER IN MUSCLE
TISSUE.

MANUEL MARIANI

DTI-BASED TRACTOGRAPHY IN NORMAL SUBJECTS AND BRAIN INJURY PATIENTS

GIULIA LUCCONI

SEGMENTATION OF SUBCORTICAL REGIONS IN MR BRAIN IMAGES USING COMBINATION OF FUZZY C-MEANS AND GAUSSIAN DISTRIBUTION MODEL BASED AUGMENTED LAGRANGIAN MULTIPHASE LEVEL SETS

A R JAC FREDO† G KAVITHA† and S RAMAKRISHNAN*

†Department of Electronics Engineering, MIT campus, Anna University, Chennai, India.

*Non-Invasive Imaging and Diagnostics Laboratory, Biomedical Engineering Group, Department of Applied Mechanics, Indian Institute of Technology Madras, India.

E-mail address: †jack247029@gmail.com, †kavithag_mit@annauniv.edu, *sramki@iitm.ac.in

In this work, combined fuzzy c-means and Gaussian distribution model based augmented Lagrangian multiphase level set method is used to segment the subcortical regions of control and autistic skull stripped MR brain images. The images are skull stripped using geodesic active contour method. The fuzzy c-means and Gaussian distribution model acts as the intensity discriminator for the level sets. The augmented Lagrangian function avoids the re-initialization procedure. The segmented images are validated with the ground truth. The results show that the multiphase level set method is able to segment the subcortical regions such as corpus callosum, brain stem and cerebellum. The correlation of segmented subcortical regions with the corresponding ground truth gives high values in control and autistic subjects. As the multiphase level set method is able to segment the subcortical regions of brain, this method seems to be clinically significant in the diagnosis of neurodevelopmental disorders.

Keywords: Autistic; subcortical regions; multiphase level sets; fuzzy c-means and Gaussian distribution model; correlation;

1. Introduction

Autism is a neurodevelopmental disorder characterized by social and communication defects.¹ Autism is characterized by accelerated growth of cortical regions and premature slow growth rate of subcortical regions such as corpus callosum, brain stem and cerebellum². Magnetic Resonance (MR) imaging is a non-invasive method to analyze the morphology of brain in children and adults.

Multi-region segmentation is challenging task due to noise, intensity inhomogeneity, poor contrast and weak boundaries in image. The region based contour models detects exterior and interior boundaries of multiple objects in images with noise, weak boundaries and are less sensitive to initial contour.³

In MR brain images, during the segmentation of corpus callosum, similar grey level regions such as brain stem and cerebellum are also extracted.⁴ Fuzzy c-mean clustering is used as the intensity discriminator for region based level set methods to segment the region of interest in medical images.⁵ Also, a fuzzy Gaussian distribution model which use statistical characteristics of local intensities is used for the accurate segmentation of MR brain images⁶. The combination of fuzzy c-mean and Gaussian distribution model is used to segment the regions in medical images.⁷

In this work, fuzzy c-means and Gaussian distribution model based augmented Lagrangian multiphase level set method is used to segment the subcortical regions of brain. The segmented images are validated with the ground truth.

2. Materials and Methods

The structural MR images considered for the analysis is obtained from the public database Autism Brain Image Data Exchange.⁸ Initially, the MR images are pre-processed to remove non-brain

tissues using geodesic active contour method.⁹ The skull stripped images are further processed to segment the brain subcortical regions.

Combined fuzzy c-mean and Gaussian distribution model based augmented Lagrangian multiphase level set segmentation

The multiphase level set method comprises of more than one level set function and is used to segment multiple regions of interest. In multiphase method, the level set functions ϕ_1, \dots, ϕ_k are denoted by a vector valued function $\Phi = (\phi_1, \dots, \phi_k)$ and the membership functions $M_i(\phi_1(y), \dots, \phi_k(\phi))$ is defined by $M_i(\Phi)$. The energy of a multiphase level set function with fuzzy as intensity descriptor⁷ is given by

$$\varepsilon(\Phi, c, b, \sigma) = \int \sum_{i=1}^N e_i(x) M_i(\Phi(x)) dx \quad (1)$$

where e_i is the fuzzy c-mean and Gaussian model based intensity descriptor given by

$$e_i = \left(|I - bc_i|^2 \right) + K \left(\log(\sqrt{2\pi}\sigma_i) + \frac{|I - bc_i|^2}{2\sigma_i^2} \right) \quad (2)$$

Here I is the original image, b is the bias field, c is the cluster centre, σ is the variance and K is the Gaussian kernel function.

The function F used in the formulation of multiphase level set is given by $F(\Phi, c, b)$. The minimization of energy with augmented Lagrangian regularized evolution¹⁰ is given by

$$\begin{aligned} \frac{\partial \phi_1}{\partial t} &= - \sum_{i=1}^N \frac{\partial M_i(\phi)}{\partial \phi_1} e_i + \nu \delta(\phi_1) \text{div} \left(\frac{\nabla \phi_1}{|\nabla \phi_1|} \right) + \left[(\alpha - \mu) \text{div} \left(\frac{\nabla \phi_1}{|\nabla \phi_1|} \right) \right] \\ &\vdots \\ \frac{\partial \phi_k}{\partial t} &= - \sum_{i=1}^N \frac{\partial M_i(\phi)}{\partial \phi_k} e_i + \nu \delta(\phi_k) \text{div} \left(\frac{\nabla \phi_k}{|\nabla \phi_k|} \right) + \left[(\alpha - \mu) \text{div} \left(\frac{\nabla \phi_k}{|\nabla \phi_k|} \right) \right] \end{aligned} \quad (3)$$

Where ∇ is the gradient operator, $\text{div}(\cdot)$ is the divergence operator and the function. ν , α and μ are constants which corresponds to the penalty and length terms in the regularization function. The multiphase level set method used in this work forms two contours. The values of parameters considered for the segmentation are $\nu = 0.001 \times 255^2$, $\alpha = 0.2$, $\mu = 0.1$, $\varepsilon = 4$ and the size of Gaussian window is 17×17 . The number of iterations used to segment the brain subcortical regions is 350.

The segmented regions are validated with the corresponding ground truths. The geometrical measure area¹¹ is measured from each subcortical region of segmented and ground truth images. Each subcortical region of ground truth images are correlated against the segmented region.

3. Results and discussion

Figure 1 (a) show the mid-slice of control and autistic MR brain images in sagittal view. The MR images are skull stripped using the geodesic active contour method. The final contours evolved over the skull stripped images using multiphase level set method are shown in figure 1 (b). One of the

contours in level set function extracts the high intensity pixels and the other extracts the low intensity pixels. The three intensity levels of pixels segmented using contours are shown in figure 1 (c). The high intensity pixel regions are extracted and are shown in figure 1 (d). From these images the desired subcortical regions are labelled and separated from the undesired regions. The extracted brain subcortical regions are shown in the figure 1 (e) and the corresponding ground truths are shown in figure 1 (f). The result shows that the energy minimization of multiphase level set method with three clusters based fuzzy c-means and Gaussian distribution model is optimal and able to segment the brain subcortical regions from the MR brain images.

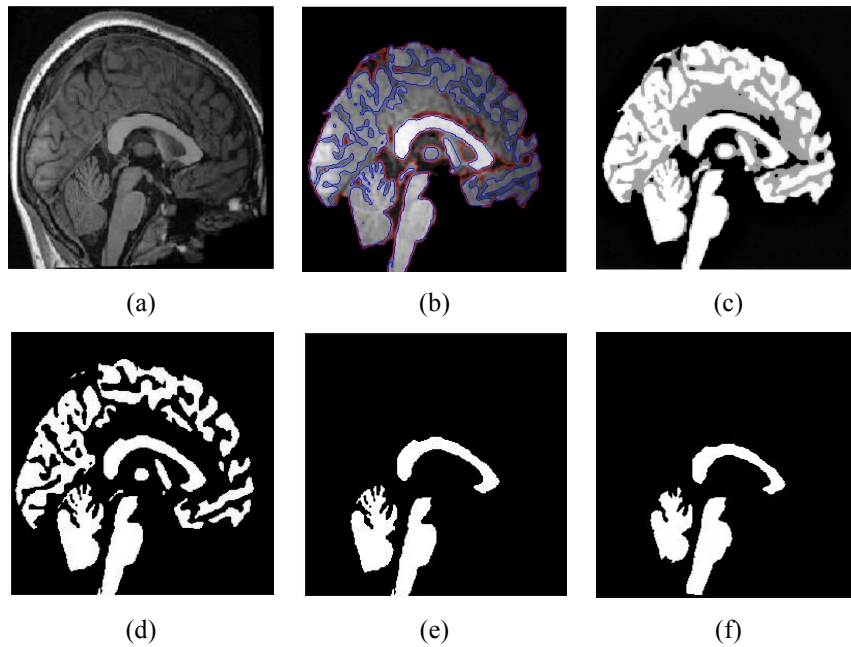


Figure 1 (a) T1 weighted mid-sagittal view image (b) Final contour evolved in skull stripped control image (c) Segmented regions (d) High intensity regions (e) Brain subcortical regions and (f) Ground truth

The segmented images are validated with expert's ground truth images. Table 1 presents the correlation values of corpus callosum, brain stem and cerebellum area of segmented images with ground truth. Corpus callosum gives a high correlation of 0.94 for controls and 0.93 in the case of autistic subjects. Brain stem gives a correlation of 0.92 in both control and autistic subjects. Cerebellum gives a correlation of 0.86 and 0.84 in control and autistic subjects respectively. This depicts that the combined fuzzy c-means and Gaussian distribution model based multiphase level set is able to extract the subcortical regions more accurately.

Table 1 Correlation values of segmented subcortical regions with ground truth

Subcortical regions	Correlation value (R)	
	Control	Autism
Corpus callosum	0.94	0.93

Brain stem	0.92	0.92
Cerebellum	0.86	0.84

4. Conclusion

In this work, the subcortical regions of control and autistic subjects are segmented from skull stripped MR brain images using combined fuzzy c-means and Gaussian distribution model based augmented Lagrangian multiphase level set method. The fuzzy c-means and Gaussian distribution model acts as the intensity discriminator for the level sets. The segmented subcortical regions are validated with the ground truth. The results show that the multiphase level set method is able to segment the subcortical regions such as corpus callosum, brain stem and cerebellum. The subcortical regions of controls give high values of correlation with ground truth compared to the autistic subjects. This frame work seems to be useful for diagnosis of autism like neurodevelopmental disorder.

References

1. American Psychiatric Association, Diagnostic and statistical manual of mental disorders, fifth edition, Washington, DC, 2001.
2. Fahim C, Meguid NA, Nashaat NH, Yoon U, Mancini-Marie A, Evans AC, The neuroanatomy of the autistic phenotype, *Res Autism Spect Dis* **6**:898-906, 2012.
3. Chan TF, Vese LA., Active contour without edges, *IEEE T Image Process* **10**:266-277, 2001.
4. Elsayed E, Coenen F, Jiang C, Garcia-Finana M, Sluming V, Corpus callosum MR image classification, *Knowl-Based Syst* **23**:330-336, 2010.
5. Li C, Huang R, Ding Z, Gatenby JC, Metaxas DN, Gore JC, A level set method for image segmentation in the presence of intensity inhomogeneities with application to MRI, *IEEE T Image Process* **20**:2007-2016, 2011.
6. Tianming Z, Jun Z, Liang X, Yunjie C, Zhihui W, An improved variational level set method for MR image segmentation and bias field correction, *Magn Reson Imaging* **31**:439-447, 2013.
7. Kuo-Kai S, Van-Truong P, Thi-Thao T, Po-Lei L, Global and local fuzzy energy-based active contours for image segmentation, *Nonlinear Dyn* **67**:1559-1578, 2012.
8. Di Martino A, Yan CG, Li Q, Denio E, Castellanos FX, Alaerts K, Anderson JS, Assaf M, Bookheimer SY, Dapretto M, Deen B, Delmonte S, Dinstein I, Ertl-Wagner B, Fair DA, Gallagher L, Kennedy DP, Keown CL, Keyser C, Lainhart JE, Lord C, Luna B, Menon V, Minshew NJ, Monk CS, Mueller S, Müller RA, Nebel MB, Nigg JT, O'Hearn K, Pelphrey KA, Peltier SJ, Rudie JD, Sunaert S, Thioux M, Tyszka JM, Uddin LQ, Verhoeven JS, Wenderoth N, Wiggins JL, Mostofsky SH, Milham, MP, The autism brain imaging data exchange: towards a large-scale evaluation of the intrinsic brain architecture in autism, *Mol Psychiatry*, 2013.
9. Caselles V, Kimmel R, Sapiro G, Geodesic active contours, *Int J Comput Vision* **22**:61-7, 1997.
10. Chunxiao L, Fangfang D, Shengfeng Z, Dexing K, Kefeng L, New variational formulations for level set evolution without reinitialization with applications to image segmentation, *J Math Imaging Vis* **41**:194-209, 2011.
11. Suganthi M, Madheswaran M, An improved medical decision support system to identify the breast cancer using mammogram, *J Med Syst* **36**:79-91, 2012.

SHAPE ANALYSIS OF CORPUS CALLOSUM IN ALZHEIMER BRAIN MR IMAGES USING COHERENCE ENHANCING DIFFUSION FILTERING AND IMPROVED VARIATIONAL LEVEL SET METHOD

K. R. ANANDH, C. M. SUJATHA

*Department of ECE, CEG Campus, Anna Univeersity
Chennai - 600025, India. Email: anandhmurali@gmail.com*

S. RAMAKRISHNAN

Non-Invasive Imaging and Diagnostics Laboratory
Biomedical Engineering Group, Department of Applied Mechanics
Indian Institute of Technology Madras, India
Email: sramki@iitm.ac.in

In this work, an attempt has been made to analyze the shape changes of Corpus Callosum (CC) in Alzheimer MR brain images using coherence enhancing diffusion filtering and an improved variational level set method. Coherence enhancing diffusion filtering has been used to obtain the edge map. Improved variational level set method is used to segment CC using edge map. Geometric features are obtained from extracted CC and are analyzed. Results show that coherence enhancing diffusion filtering is able to provide edges with distinct boundaries. Improved variational level set method could perform the segmentation of CC in both the normal and AD images. Geometric features such as area, minor axis, solidity and equivalent diameter are able to show distinct variations between the control normal and AD subjects. As shape changes of CC are prominent in the diagnosis of AD, this study seems to be clinically useful.

Key words: Alzheimer's Disease; Corpus Callosum; Level set; Coherence enhancing diffusion filtering

1. Introduction

Alzheimer's Disease (AD) is a complex neurodegenerative disorder that leads to memory impairment problems in patients. Manifestation of AD causes atrophy of gray matter and white matter structures and thus results in whole brain shrinkage. The etiology of the disease is still completely unknown. Hence, the early diagnosis of the disease is highly essential.^{1, 3} Corpus Callosum (CC) is the largest white matter structure in the brain which connects the left and right cerebral hemisphere. Atrophy of white matter results in the shape changes of CC and reflects the disease progression of AD.⁴ Since there exist a large overlap in the volume measurements of normal and AD subjects, shape based analysis is feasible to quantify the distinction.⁵ Magnetic Resonance (MR) imaging is a non-invasive method of brain imaging system which reflects the neuronal pathology due to AD.⁶ Deformable active Fourier contour model and rule based technique are used in the segmentation of CC.^{8, 9} Level Set (LS) methods are active contour models that are implicitly defined as dynamic curves or surfaces to undergo contour evolution to track complex topological changes. In any LS method, Gaussian filtering is conventionally used to generate the edge map. However this causes blurring and loses the edge information. Coherence enhancing diffusion filtering is a nonlinear diffusion process which is employed as the pre-processing step for segmentation to generate the edge map.^{12, 13} In this work, coherence enhancing diffusion filtering and improved

variational level set method are used to segment CC. Geometric features are extracted from the segmented CC.

2. Methods

Brain MRI images obtained from OASIS database are considered for this analysis.¹⁰

2.1 Level Set Method

The level set evolution equation of improved variational level set method is given by

$$\frac{\partial \varphi}{\partial t} = \tau \left\{ \mu g_{new} [\nabla^2 \varphi - \text{div} \left(\frac{\nabla \varphi}{|\nabla \varphi|} \right)] + v g_{new} \delta_\varepsilon(\varphi) \right\} \quad (1)$$

where, $\mu > 0$ and $\lambda > 0$ are constants, δ_γ is the dirac function, α is the variable that controls the speed of the contour and g_{new} is the edge map.

2.2 Coherence enhancing diffusion filtering

The tensor product of gradient of Gaussian smoothed version of an image $u(x, t)$ is used as the structure descriptor and is given as

$$J_0(\nabla u_\sigma) := \nabla u_\sigma \otimes \nabla u_\sigma := \nabla u_\sigma \nabla u_\sigma^T \quad (2)$$

where ∇u_σ is the gradient smoothed version of the image $u(x, t)$. The orientations are average by applying component wise convolution with a Gaussian K_ρ : as shown as

$$J_\rho : (\nabla u_\sigma) := K_\rho * \nabla u_\sigma \otimes \nabla u_\sigma \quad (\rho \geq 0) \quad (3)$$

By taking the gradient of Eq. (3), the edge stopping function g_{new} is obtained and integrated into Eq. (2) for the level set to correctly segment CC. Geometric features are extracted from the segmented CC and are normalized.

3. Results and Discussion

A representative set of normal and AD brain MR image sagittal view is shown in Fig. 1. It is seen that, the size and orientation of CC are found to be varying in both the normal and AD subjects. It is observed to have varying length in both the normal and AD conditions. These images are subjected to coherence enhancing diffusion filtering to obtain the edge map. The diffusion parameter sigma is fixed as 10 and is used in the diffusion process. Time parameter has been fixed as 3 and it decides the amount of diffusion. The total diffusion process took 100 iterations to complete the filtering process for every single image. By taking the gradient of the filtered image, the edge maps are obtained.

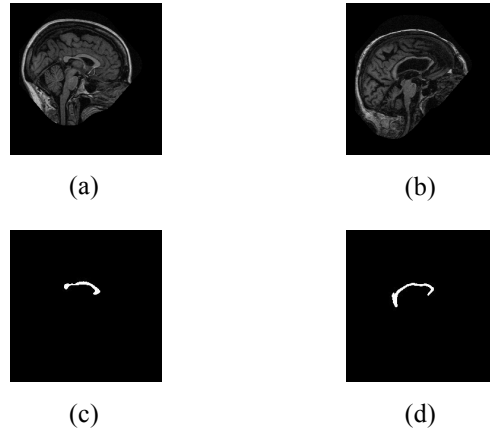


Fig. 1. Representative set of (a) normal, (b) AD MR images, (c) segmented normal and (d) AD CC images

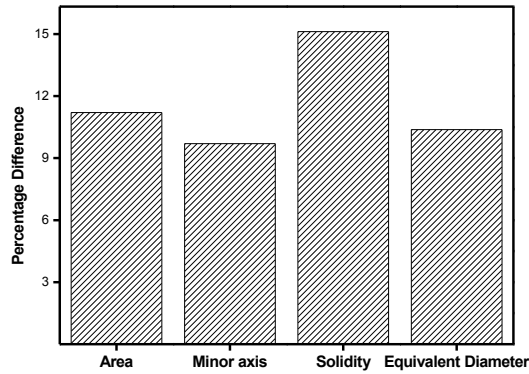


Fig. 2. Variations in the geometric features of segmented CC of normal and AD subjects

Further, the images are subjected to segmentation of CC using improved variational level set method by providing initial contour. The initial contour evolves continuously by shrinking towards the edge map of CC. During the LS evolution, the speed parameter α is set as 0.5 to control speed of the level set function towards the region of CC. The LS took 22 iterations to segment CC in all the images. The extracted geometric features such as area, minor axis, solidity and equivalent diameter shows variations in their mean and SD values as shown in Table. 1. Fig. 2. also reflects the variations in the pathology due to AD conditions.

Table 1- Variations of geometrical features

Geometric Features	Normal	AD
	Mean±SD	Mean±SD
Area	0.66±0.16	0.59±0.10
Minor axis	0.75±0.09	0.68±0.09
Solidity	0.64±0.13	0.55±0.10
Equivalent diameter	0.81±0.10	0.73±0.10
SD-Standard Deviation		

4. Conclusion

In this study, coherence enhancing diffusion filtering with improved variational level set method is used to segment CC in both normal and AD images. Geometric features are extracted from the segmented CC to quantify the variations. Results show that this method is able to segment CC in all the images. The extracted shape based features could reflect the pathology due to AD conditions. Thus this study seems to be clinically useful.

5. Reference

1. Weiner MW, Veitch DP, Aisen PS, Beckett LA, Cairns NJ, Green RC et al, The Alzheimer's Disease Neuroimaging Initiative: a review of papers published since its inception, *Alzheimer's & Dementia* **8**:1-68, 2012.
2. Kidd PM, Alzheimer's disease, amnesic mild cognitive impairment, and age-associated memory impairment: current understanding and progress toward integrative prevention, *Altern Med Rev* **2**:85, 2008.
3. Di Paola M, Spalletta G and Caltagirone C, In Vivo Structural Neuroanatomy of Corpus Callosum in Alzheimer's Disease and Mild Cognitive Impairment Using Different MRI Techniques: A Review, *J Alzh Dis* **20**:67-95, 2010.
4. Ferrarini L, Walter MP, Hans O, Mark AB et al, Shape differences of the brain ventricles in Alzheimer's disease, *NeuroImage*, **32**:1060-1069, 2006.
5. Mahanand BS, Suresh S, Sundararajan N and Kumar MA, Identification of brain regions responsible for Alzheimer's disease using a Self-adaptive Resource Allocation Network, *Neural Networks*, **32**:313-322, 2012.
6. Vachet C, Yvernault B, Bhatt K and Smith RG, Automatic corpus callosum segmentation using a deformable active Fourier contour model, *Proc. Soc Photo Opt Instrum Eng.* 2012.
7. Herron TJ, Kang X and Woods D, Automated measurement of the human corpus callosum using MRI, *Frontiers in neuroinformatics*, **6**:1-15, 2012.
8. Kuo, Hsien-Chi, et al. Level Set Segmentation of Breast Masses in Contrast-Enhanced Dedicated Breast CT and Evaluation of Stopping Criteria. *J Digit Imag* : 1-11, 2013.
9. Weickert J, Coherence-enhancing diffusion of colour images, *Image and Vision Comp* **17**:201-212, 1999.
10. Marcus DS, Wang TH, Parker J, Csernansky JG, Morris JC and Buckner RL, Open Access Series of Imaging Studies (OASIS): Cross-sectional MRI Data in Young, Middle Aged, Nondemented, and Demented Older Adults, *J. Cogn. Neuroscience*, **19**:1498-1507, 2007.

MINKOWSKI FUNCTIONALS BASED ANALYSIS OF HIPPOCAMPUS IN ALZHEIMER'S BRAIN MR IMAGES

KAYALVIZHI. M¹, KAVITHA. G¹, SUJATHA. C.M² and RAMAKRISHNAN. S³

¹Dept. of Electronics Eng., Madras Institute of Technology, Anna University, Chennai-600 044, India

²Dept. of ECE., College of Engg. Guindy, Anna University Chennai 600 025, India.

³Non-Invasive Imaging and Diagnostics Laboratory, Biomedical Engineering Group, Department of Applied Mechanics, Indian Institute of Technology Madras, Chennai-600 036, India.

kayalvizhi@gmail.com

In this work, an attempt is made for detection of Alzheimer's disease (AD) severity in MR images using Minkowski functionals (MFs). The normal and abnormal images considered in this work are obtained from MIRIAD database. Initially, the ROI is selected from original T1 sagittal image. The ROI of hippocampus are subjected to analysis using Minkowski functional. The prominent Minkowski feature is correlated with the Mini-Mental State Examination (MMSE) score. Results show that the Minkowski area and Euler number of hippocampus provide better discrimination of normal and abnormal subjects. Its correlation with MMSE is observed to be high for normal and abnormal Alzheimer subjects. This suggests that spatio temporal characterization improves the discrimination capability, while simultaneously eliminating the need for precise segmentation. Hence this index could be used for the study of progression in neurodegenerative disorder such as AD.

Keywords: Alzheimer's, Minkowski functional, hippocampus ROI

1. Introduction

Alzheimer's disease (AD) is an irreparable neurodegenerative disease. The senile plaques (SP), neurofibrillary tangles (NFT) and other pathological changes such as hippocampus atrophy, ventricle enlargement appear in the brain atleast 10 years before the onset of clinical symptoms of AD[1]. Early diagnosis and treatment can effectively prevent AD further deterioration; hence researchers have drawn more attention to the early diagnosis of AD.

Structural magnetic resonance imaging (MRI) techniques provide a tool for examining alterations of brain. In MR brain images, the hippocampus is a deep brain sub cortical small grey matter (GM) structure. It shows no clear boundaries along significant portions of its surface and appears with low contrast. In many studies, region of interest (ROI) analysis is carried out by computing bounding box of hippocampus [2] and further analysis is performed.

Among various image analysis techniques, texture analysis is proved to be useful in identifying tissue changes and has the potential to support early diagnosis of AD. Recently, a 2D method to quantify atrophy in temporal region for diagnosis of early AD and tracking the progression of AD is framed [3]. MFs are used in pathology detection of bone and breast images [4].

2. Methods

The images considered in this work are obtained from the MIRIAD (Minimal Interval Resonance Imaging in Alzheimer's Disease) database [5]. The pathology conditions are classified as mild, moderate and severe subjects based on mini-mental state examination (MMSE) score suggested by Petrella J.R et al [6]. The ROI is extracted by computing a bounding box [2]. Minkowski functionals are derived for the selected hippocampus ROI. They are computed by binarizing the segmented regions through the application of several threshold levels between minimum and maximum intensity limits [4]. Then an optimal choice of threshold level is selected. The three Minkowski functionals obtained are area, perimeter and Euler number are calculated as:

Area = Number of white pixels (1)

Perimeter = $4 \times \text{Area} + 2 \times \text{Number of open edges}$ (2)

Euler number = $\text{Area} - \text{Number of open edges} + \text{Number of open vertices}$ (3)

The optimal threshold is selected for computing the Minkowski feature. The selection is done by subjecting integral feature of each threshold value to t-test for normal and different abnormal images. The threshold value which gives significant p value is considered for analysis. The integral Minkowski feature are calculated at the significant threshold value for the hippocampus ROI.

The Mini-Mental State Exam (MMSE) score is used to detect and track the progression of cognitive impairment associated with Alzheimer's disease. The clinical relevance of the features is obtained by correlating the significant feature with the MMSE score. The obtained features are further subjected to t-test.

3. Results and discussion

The ROI is selected from the normal and abnormal AD sagittal MR Images.

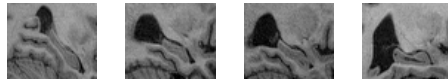


Fig 1 ROI of T1 sagittal MRI in (a) normal, (b) mild, (c) moderate and (d) severe AD subjects

1(a) 1(b) 1(c) 1(d)

Fig 1(a) shows the ROI of normal sagittal T1 MR image. The images of AD abnormalities for mild, moderate and severe subjects are shown in fig 1(b-d). The image shows that as disease progress the hippocampus which accounts for the atrophy decreases and the surrounding ventricles enlarge. The hippocampus ROI is subjected to spatial temporal characterization using Minkowski functionals. Figure 2(a)-(c) shows the integral mean of Minkowski feature area when different threshold levels are applied on the hippocampus ROI. This feature helps in discrimination of normal and pathology images. For first few threshold levels, the feature value increases and for higher order these value remains constant. The plot shows dependence of the features on the threshold levels. Fig 2 shows at threshold level six there is distinct variation of normal and abnormal subjects for all the three features. At this threshold value the features such as area ($p < 0.0001$), perimeter ($p < 0.01$) and Euler number ($p < 0.001$) have prominent p-value. Hence threshold level six is considered for analysis of hippocampus in MR sagittal images.

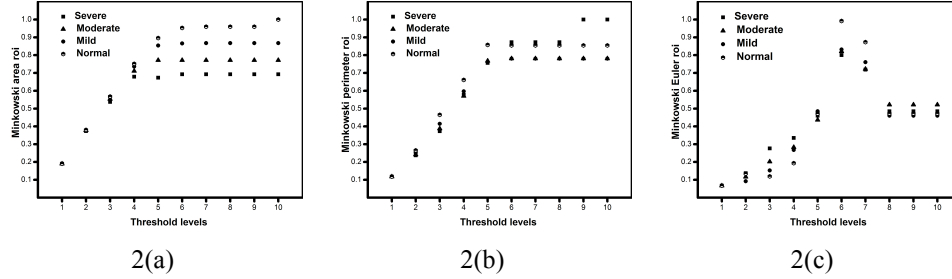


Fig 2 Comparison of integral mean of Minkowski functionals of hippocampus ROI for different threshold levels (a) area (b) perimeter and (c) Euler Number

The normalized average and standard deviation values of the Minkowski feature for hippocampus normal and abnormal subjects are shown in table 1. The mean value of Minkowski feature is high for normal subjects. Minkowski area of hippocampus ROI is found to be low for abnormal subjects which could be due to atrophy associated with pathological conditions and enlargement of the surrounding ventricles.

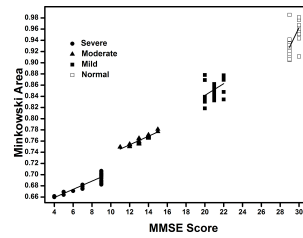


Figure 3 Correlation between Minkowski area and MMSE score for Hippocampus

Minkowski Features	Mean \pm Standard deviation of hippocampus ROI			
	Normal (N=30)	Abnormal (N=90)		
		Mild	Moderate	Severe
Area	0.95 ± 0.02	0.86 ± 0.016	0.77 ± 0.008	0.69 ± 0.015
Perimeter	0.87 ± 0.06	0.78 ± 0.10	0.78 ± 0.10	0.85 ± 0.07
Euler Number	0.99 ± 0.15	0.78 ± 0.25	0.72 ± 0.25	0.70 ± 0.22

Table 1. Normalized mean and standard deviation of the Minkowski feature for hippocampus ROI

The Euler number which accounts for the number of holes, increases in abnormal subjects. This is due to the enlargement of ventricle resulting in increased number of holes in pathology conditions. Hence the Euler number is less in AD subjects. The Minkowski perimeter is not much distinct for normal and abnormal conditions. Hence Minkowski area with significant p-value of hippocampus can be used for discrimination of normal and abnormal subjects.

The correlation of normalized Minkowski area with MMSE score is shown in fig 3. The MMSE score decreases as the disease progresses. The MMSE score highly correlates with the Minkowski area for both normal and abnormal conditions. Fig 3 shows the correlation coefficient (R) of Minkowski area of hippocampus ROI with respect to the cognitive index is 0.76 for normal subjects. In abnormal subjects, the value of R is found to be 0.86, 0.95 and 0.92 for mild, moderate and severe respectively. Thus Minkowski area of hippocampus could be used as a measure in differentiation of severity conditions in AD. Hence this Minkowski functional which considers structural changes of regional hippocampus can be used in study of progression of AD.

4. Conclusion

In this work, an analysis is carried on hippocampus ROI of MR brain images, to study the progression of AD. The ROI is subjected to Minkowski functional based analysis. Results show that the analysis on

hippocampus is able to discriminate normal and abnormal Alzheimer Disease (AD) conditions. It is observed that the Minkowski area provide better discrimination of normal and abnormal subjects. Its correlation with MMSE is observed to be high for normal and very high for moderate Alzheimer subjects. The Minkowski functional area, which considers the atrophy in hippocampus and the changes in the surrounding region can be used in detection of severity condition in AD.

References

1. Xia, Hong, Longzheng Tong, Xiaoxia Zhou, Jing Zhang, Zhen Zhou, and Weifang Liu, Texture Analysis and Volumetry of Hippocampus and Medial Temporal Lobe in Patients with Alzheimer's Disease, *Biomedical Engineering and Biotechnology (ICBEB), 2012 International Conference on*, **2012**: pp. 905-908, 2012
2. Chen, Wenyan, Shutao Li, Fucang Jia, and Xiaodong Zhang, Segmentation of hippocampus based on ROI atlas registration, *IT in Medicine and Education (ITME), 2011 International Symposium on*, vol. 1: pp. 226-230, 2011.
3. Menéndez-González, Manuel, Alfonso López-Muñiz, José A. Vega, José M. Salas-Pacheco, and Oscar Arias-Carrión, MTA index: a simple 2D-method for assessing atrophy of the medial temporal lobe using clinically available neuroimaging, *Frontiers in aging neuroscience*, vol. 6, 2014.
4. Huber Markus B., Mahesh B. Nagarajan, Gerda Leinsinger, Roger Eibel, Lawrence A. Ray and Axel Wismüller, Performance of topological texture features to classify fibrotic interstitial lung disease patterns, *Medical physics*, vol. 38, no. 4: pp. 2035-2044, 2011.
5. Malone Ian B., David Cash, Gerard R. Ridgway, David G. MacManus, Sebastien Ourselin, Nick C. Fox, and Jonathan M. Schott, MIRIAD—Public release of a multiple time point Alzheimer's MR imaging dataset, *NeuroImage*, vol. 70: pp. 33-36, 2013.
6. Petrella Jeffrey R, Edward Coleman R and Murali Doraiswamy P, Neuroimaging and early diagnosis of Alzheimer disease: a look to the future, *Radiology* vol. 226, no.2 : pp. 315-336, 2006.

PERFIDI FILTER SEQUENCES TO ACQUIRE MRI IMAGES WITH SPECIFIC RANGE OF T_1 SIGNAL COMPONENTS SUPPRESSED

V. BORTOLOTTI^{1,2}, L. BRIZI^{3,4}, P. FANTAZZINI^{3,4},
M. MARIANI^{3,4}, M. VANNINI^{1,2}, E.M. VASINI¹

¹*Department of Civil, Chemical, Environmental and Material Engineering (DICAM), University of Bologna, Via Terracini, 28, 40131, Bologna, Italy*

²*Interdepartmental Centre for Industrial Research in Energy and Environment, Via Angherà 22, 47900 Rimini, Italy
villiam.bortolotti@unibo.it
marianna.vannini2@unibo.it
estermaria.vasini2@unibo.it*

³*Department of Physics and Astronomy, DIFA, University of Bologna, Viale Berti Pichat 6/2, 40127 Bologna, Italy*

⁴*Centro Enrico Fermi, Piazza del Viminale 1, Roma, Italy
leonardo.brizi2@unibo.it
paola.fantazzini@unibo.it
manuel.mariani@unibo.it*

1

In order to well distinguish different tissues of the human body, it is of paramount importance to find procedures and sequences that improve the contrast of Magnetic Resonance Imaging (MRI) images. In particular, the possibility to image only specific parts of organs and/or tissues while ignoring all the others is a very valuable feature. A way to address this problem is to develop dedicated MRI sequences able to filter the ^1H nuclei signals on the basis of the different longitudinal relaxation times (T_1) of the tissues and to produce images where components are suppressed. Instead of using standard signal selection/attenuation sequences, such as the Short Time Inversion Recovery and Multiple Inversion Recovery, whose effects are to zero the signal for a discrete number of T_1 values, we developed the Parametrically Enabled Relaxation Filters with Double and multiple Inversion (PERFIDI) filter sequences. These sequences acting on a range of T_1 behave as electronic band-pass, high-pass and low-pass filters, primarily focused on the components which pass through, rather than on those blocked.

We tested PERFIDI filter sequences on a synthetic two-component test tube sample. Preliminary applications on biological tissues have shown that this technique can effectively work on a range of T_1 values.

Keywords: MRI images; PERFIDI filter; Image contrast.

1. Introduction

In medical practice, the diagnostic power of Magnetic Resonance Imaging (MRI) is related to its ability to well distinguish the different tissues of the human body. It is therefore of paramount importance to find experimental procedures and sequences that improve the contrast of MRI images. A way to address this problem is to develop dedicated MRI sequences able to image only specific parts or components of organs and/or tissues. In particular methods have been developed that, on the basis of the different longitudinal relaxation times (T_1) of the tissues, are able to selectively filter the images.

For this reason, we have developed and used the innovative Parametrically Enabled Relaxation Filters with Double and multiple Inversion (PERFIDI) sequences that implement T_1 filters^{1,2,3}.

Given a sample characterized by a distribution of T_1 , PERFIDI filter sequences using preambles of inversion pulses prepended to standard sequences, allow one to obtain an effective attenuation of the signal in a selected range of T_1 values, while the remaining signal undergoes a computable attenuation³. These features make PERFIDI filter sequences different from other techniques dedicated to the signal selection found in literature, such as Short Time Inversion Recovery and Multiple Inversion Recovery⁴, whose effects, in general, is to zero the signal for a discrete number of T_1 values³. In other words, the PERFIDI method has analogies with electronic band-pass, high-pass and low-pass filters, that are primarily focused on the components which pass through, rather than on those blocked³.

The essence of the PERFIDI method lies in the linear algebraic combination (with sign) of magnetization signals. Therefore, it can work only if memory is kept of the polarity of the nuclear magnetization vector. In Nuclear Magnetic Relaxometry this is not a problem, because the magnetization signal is always recorded with sign. On the contrary, in MRI usually a “magnitude” image is recorded and visualized. This image is formed from the real and imaginary images computed by means of a 2D Fourier transform of the raw data. Therefore, in order to perform the PERFIDI method it is necessary to process the real and imaginary images to restore the magnetization sign.

Because phase-sensitive inversion-recovery provides enhanced T_1 contrast, the restoration of the magnetization signal polarity has long been studied, especially in relation to the well known Inversion Recovery (IR) sequence⁵. In many medical applications there are potential benefits from signal polarity restoration⁶, for example for Imaging Pulmonary Blood Flow and Perfusion⁷, Black-Blood Coronary Vessel Wall Imaging⁸ and to improve tissue contrast in neuroimaging⁹. Some methods are based on the identification of zero-crossing time of the inversion recovery curve¹⁰, others provide the sign of the signal by using a phase-correction method¹¹. In our work, we used a reference image having a defined polarity of signal magnetization in every image pixel. Once the polarity of the magnetization was known, it has been possible to apply the image PERFIDI filters. In this work we tuned and tested the PERFIDI method on both a synthetic sample and on biological tissue samples, obtaining very good results.

2. Materials and Methods

As previously stated, the PERFIDI filtering is performed by means of a linear combination of images acquired with proper sequences called PERFIDI blocks, each characterized by specific delays. Each PERFIDI block, is made of two parts (see figure 1). The first one is a presaturation preamble, made in our application of two inversion pulses, whose timing is varied depending on the desired filter behavior, while the second one is a standard sequence. In figure 1 a PERFIDI block time diagram is shown in which the second part is a Spin-echo (SE) sequence.

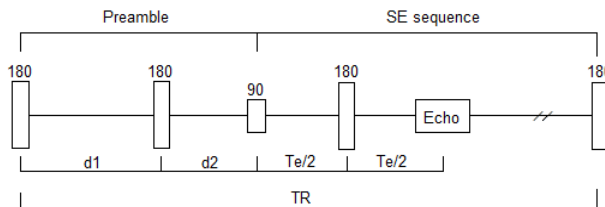


Fig.1. Time diagram of a PERFIDI block: presaturation preamble prepended to a SE sequence.

The simplest PERFIDI filter is obtained by subtracting images acquired by two elementary PERFIDI block sequences characterized by a suitable choice of two different delays. The first image is de facto a reference image (called OFFSET) which permits one to set the magnetization sign with respect to B_0 . In the OFFSET image d_1 , the elapsed time between the two inverse pulses of the preamble part (see figure 1), has been set to 5 times the repetition time (TR). d_2 , the delay between the preamble and the sequence, was equal to 5 ms (the shortest available). In practice, PERFIDI OFFSET block is an IR sequence with the inversion time as short as possible. Therefore, neglecting the relaxation occurring in the first 5 ms, the polarity of the magnetization of every pixel of the OFFSET image is opposite to that of B_0 . The second image (called PERFIDI SE) has been acquired setting d_1 equal to 200 ms, $d_2 = 5$ ms. For both the acquisitions TR = 3500 ms and, to enhance the signal to noise ratio, 4 scans were used. For further details about the PERFIDI block sequences, the reader is addressed to references 2 and 3.

The signal polarity of each pixel in the PERFIDI SE image is obtained by comparison with the known polarity of that pixel in the OFFSET image.

Once the polarity was restored, it has been possible to implement the imaging PERFIDI filters by means of the following linear combinations:

$$\text{PERFIDI high-pass} = \text{PERFIDI SE image} - \text{PERFIDI OFFSET image} \quad (1)$$

$$\text{PERFIDI low-pass} = -(\text{PERFIDI SE image} + \text{PERFIDI OFFSET image}) \quad (2)$$

PERFIDI block sequences have been implemented on an ARTOSCAN tomograph (ESAOTE, Genova, Italy).

2.1. The Sample

The sample used to test the PERFIDI method was composed of two concentric test tubes (10 mm and 25 mm in diameter) filled with two aqueous solutions of EDTA at different concentrations. The inner tube contained a solution characterized by $T_1 = 45$ ms and $T_2 = 43$ ms. The external tube contained a solution with $T_1 = 800$ ms and $T_2 = 755$ ms.

The sample has been positioned in the center of the receiver coil with the axis of the tubes parallel to the axis of the coil (see figure 2), in this way a transverse section image shows two concentric circles.



Fig.2. The concentric test tubes sample inside the ESAOTE transmitter/receiver coil.

3. Results and Discussion

Applying the linear combinations (1) and (2) it has been possible to obtain T_1 filtered images. In figure 3 the images obtained by high-pass and low-pass PERFIDI filters in the relaxation times domain are shown. In figure 3(a) the short relaxation time component, which is contained in the inner test tube, is completely filtered in favor of the long relaxation time component. In the low-pass image of figure 3(b)

the situation is reversed: in this case the signal of the inner test tube is not damped, while the rest of the sample signal is filtered.

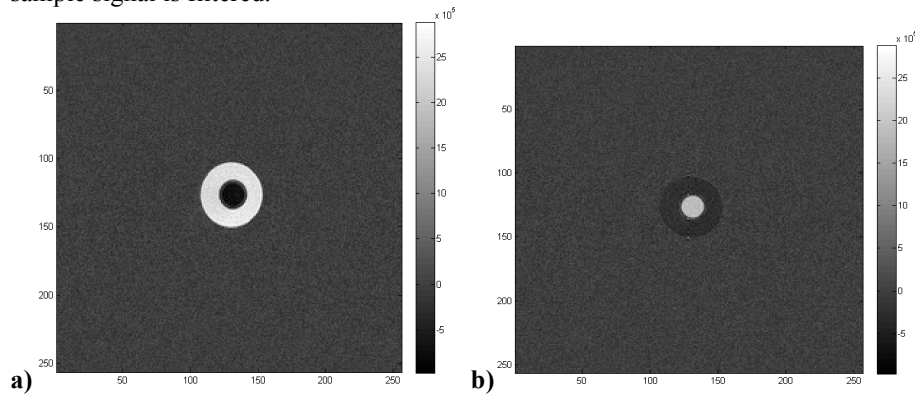


Fig.3. PERFIDI filter results in the relaxation times domain on a phantom made of two concentric test tubes filled with different EDTA solutions: high-pass (a) and low-pass (b).

4. Conclusion

The application of PERFIDI filter sequences on a synthetic two-component sample produced the expected results. The PERFIDI high-pass and the low-pass filters, acting on components with given T_1 relaxation time distributions, have produced high contrast images. Preliminary use of PERFIDI sequences on biological tissue has shown that T_1 filtering techniques can effectively be used on samples characterized by distributions of T_1 values.

References

1. Fantazzini P, Sykora S, Italian Patent BO2005A000445, 2005.
2. Sykora S, Bortolotti V, Fantazzini P, PERFIDI: Parametrically Enabled Relaxation Filters with Double and Multiple Inversion, *Magn Reson Imaging*, **25**: 529-532, 2007.
3. Bortolotti V, Fantazzini P, Gombia M, Greco D, Rinaldin G, Sykora S, PERFIDI filters to suppress and/or quantify relaxation time components in multi-component systems: An example for fat-water systems, *J Magn Reson*, **206**: 219-226, 2010.
4. Bernstein M.A., King K.F., Zhou X.J., Handbook of MRI, Pulse Sequence, Elsevier Academic Press, 2004.
5. Ma J, Multislice and multicoil Phase-sensitive Inversion-recovery Imaging, *Magn Reson Med*, **53**: 904-910, 2005.
6. Szumowski J, Durkan MG, Foss EW, Brown DS, Schwarz E and Crawford DC, Signal polarity restoration in a 3D inversion recovery sequence used with delayed gadolinium-enhanced magnetic resonance imaging of cartilage (dGEMRIC), *J Magn Reson Imaging*, **36**:1248-1255, 2012.
7. Mai VM, Chen Q, Bankier AA, Zhang M, Hagspiel KD, Berr SS and Edelman RR, Imaging pulmonary blood flow and perfusion using phase-sensitive selective Inversion Recovery, *Magn Reson Med*, **43**:793-795, 2000.
8. Abd-Elmoniem KZ, Weiss RG and Stuber M, Phase-sensitive black-blood coronary vessel wall imaging, *Magn Reson Med*, **63**: 1021-1030, 2010.
9. Hou P, Hasan KM, Sittin CW, Wolinsky JS and Narayana PA, Phase-sensitive T_1 inversion recovery imaging: a time-efficient interleaved technique for improved tissue contrast in neuroimaging, *Am J Neuroradiol*, **26**: 1432-1438, 2005.

10. Bakker CJG, De Graaf CN and Van Dijk P, Restoration of signal polarity in a set of inversion recovery NMR images, *IEEE T Med Imaging*, vol. MI-3, NO. 4:197-202, 1984.
11. Park HW, Cho MH and Cho ZH, Real value representation in inversion recovery NMR imaging by use of a phase-correction method, *Magn Reson Med*, 3: 15-23, 1986.

NMR RELAXOMETRY AND IMAGING TO QUANTIFY THE FAT-TO-WATER RATIO IN MUSCLE TISSUE

V. BORTOLOTTI^{1,2}, L. BRIZI^{3,4}, P. FANTAZZINI^{3,4}, M. MARIANI^{3,4}, M. VANNINI^{1,2}, E.M. VASINI¹

¹*Department of Civil, Chemical, Environmental and Material Engineering (DICAM), University of Bologna, Via Terracini, 28, 40131, Bologna, Italy*

²*Interdepartmental Centre for Industrial Research in Energy and Environment, Via Angherà 22, 47900 Rimini, Italy
villiam.bortolotti@unibo.it
marianna.vannini2@unibo.it
estermaria.vasini2@unibo.it*

³*Department of Physics and Astronomy, DIFA, University of Bologna, Viale Berti Pichat 6/2, 40127 Bologna, Italy*

⁴*Centro Enrico Fermi, Piazza del Viminale 1, Roma, Italy
leonardo.brizi2@unibo.it
paola.fantazzini@unibo.it
manuel.mariani@unibo.it*

Fat suppression in Magnetic Resonance Imaging (MRI) images is an important diagnostic topic. In this work, through NMR Relaxometry and Imaging of ¹H nuclei we estimated the Fat/Water (F/W) ratio on pig loins, assumed as model of human muscle tissue, by analyzing ¹H longitudinal relaxation times (T_1) distributions and quantitative MRI images. It is known that water and fat proton signals in tissues have different T_1 values. The innovative characteristic of our approach is to assume that T_1 values follow a quasi-continuous distribution, instead of a discrete distribution. F/W ratios of the samples were determined through NMR Relaxometry by distinguishing the signal of fat ¹H nuclei from that of the water through the choice of a proper cut-off on the T_1 distributions. F/W ratio was determined on MRI images acquired with the “classic” Short Time Inversion Recovery sequence. Innovative *Parametrically Enabled Relaxation Filters with Double and multiple Inversion* (PERFIDI) sequences, that implement band-pass filters, were also used. The correlation between NMR and an independent destructive chemical analysis performed on the same samples gave very good results for both Relaxometry and Imaging techniques.

Keywords: NMR Relaxometry, MRI images, Fat/Water ratio, Fat suppression

1. Introduction

In order to increase the diagnostic power of Magnetic Resonance Imaging (MRI) in Medicine it is important to find experimental procedures able to improve the contrast of images. To better distinguish the different tissues of the human body, often the differences of the Nuclear Magnetic Resonance (NMR) relaxation times of ¹H nuclei of the different organs and tissues are exploited. Among the others, one of the main problem is related to the fact that in specific examinations it is crucial to focus on the analysis of specific parts or components of organs and/or tissues disregarding the remaining parts or components. A way to solve this problem is to develop dedicated MRI sequences able to filter selectively part of the NMR signal, on the basis of the different relaxation times of the components. Starting from these issues, NMR Relaxometry and MRI sequences were developed and applied to the specific problem to distinguish fat and water signal of tissues, and in particular evaluate the fat-to-water ratio (F/W). The developed procedures were checked by assuming samples of animal meat (pork loins) as model systems of human muscle tissues.

2. Materials and Methods

2.1. Samples

19 pork loins, 24 hours after death, were frozen and stored. The samples were left at room temperature for 2 hours before NMR analyses to reach an appropriate experimental temperature. Smaller samples were removed for chemical analyses.

2.2. Chemical Analysis

Two specimens, taken from the same loin, were minced together for the chemical analyses. The sample was used for the estimation of fat and moisture content according to AOAC 950.46, and 960.39 official methods respectively¹. Results of both analyses were expressed as grams per 100 grams of wet sample.

2.3. NMR Relaxometry and MRI sequences

NMR Relaxometry measurements were performed by using the permanent magnet ($B_0 = 0.2$ T) of an ARTOSCAN tomograph (Esaote S.p.A., Genova, Italy) equipped with a portable NMR console (Stelar, s.r.l., Mede, Pavia, Italy). The Inversion Recovery (IR) sequence (recycle delay 2s, 64 inversion times selected in logarithmic scale, $\pi/2$ duration=60 μ s) was used to acquire the relaxation curve of the longitudinal nuclear magnetization component. Longitudinal relaxation times (T_1) quasi-continuous distributions were obtained by inversion of the experimental multi-exponential relaxation curves with UpenWin Software², which relies on the UPen algorithm^{3,4}. MRI images were acquired by the ARTOSCAN tomography (Esaote S.p.A., Genova, Italy). In the standard Short Inversion Recovery (STIR) sequence the parameters used were $T_R = 2$ s (repetition time), inversion time = 50 ms, $T_E = 18$ ms (echo time), slice thickness 3 mm, 4 scans. For the suppression of fat signal we also used PERFIDI filters^{5,6,7} sequences, which use the linear combination of two Spin Echo sequences preceded by a two inversion pulse preamble. The preamble is made of two inversion pulses with an inter-pulse delay d_1 . After a delay d_2 from the second inversion pulse, the standard sequence begins. In this case the measurement parameters were: first image: $d_1 = 5 T_R$, $d_2 = 5$ ms; second image: $d_1 = 150$ ms, $d_2 = 5$ ms; for both images: $T_E = 18$ ms, $T_R = 2000$ ms. To obtain the fat-to-water ratio (F/W) by the images, $(F/W)_{MRI}$, a proper image segmentation algorithm, averaging 3 sections for each sample, was used implemented in the home-made ARTS software, to count the pixels assigned to fat and to moisture respectively.

2.4. Correlation between NMR Relaxometry / MRI and chemical data

By definition the ratio F/W obtained by NMR, $(F/W)_{NMR}$ (here NMR stands for both Relaxometry and Imaging) should be proportional to the corresponding ratio by chemical analysis $(F/W)_{CH}$ through a proportionality constant k that should depend on the number of 1H nuclei per mole of water and fat, and that should vary with fat composition. A linear relationship is then expected between the two quantities and represented by the equation:

$$\left(\frac{F}{W}\right)_{CH} = k \cdot \left(\frac{F}{W}\right)_{NMR + off} \quad (1)$$

where *off* represents an offset.

3. Results and Discussion

3.1. 1H NMR Relaxometry

The T_1 distributions of ^1H obtained by IR measurements show the same features for all the 19 loins: a small peak or shoulder/tail in the range 10-150ms and a predominant peak centred at about 300ms, which can be assigned to fat and water protons respectively.

The method is based on the assumption that the tail or shoulder is due to fat, the large peak to water (Figure 1).

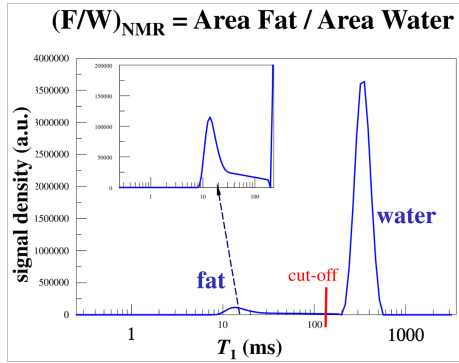


Fig. 1 - Example of T_1 distribution of the fresh loin samples with the indication of the cut-off which splits the fat and water components for the evaluation of the $(F/W)_{\text{IR-NMR}}$.

The F/W ratio obtained from T_1 distribution $(F/W)_{\text{IR-NMR}}$ should be done by the ratio of the two areas under the two features. The ratios were computed for different values of cut-offs and the results compared with the values from chemical analysis (Figure 2).

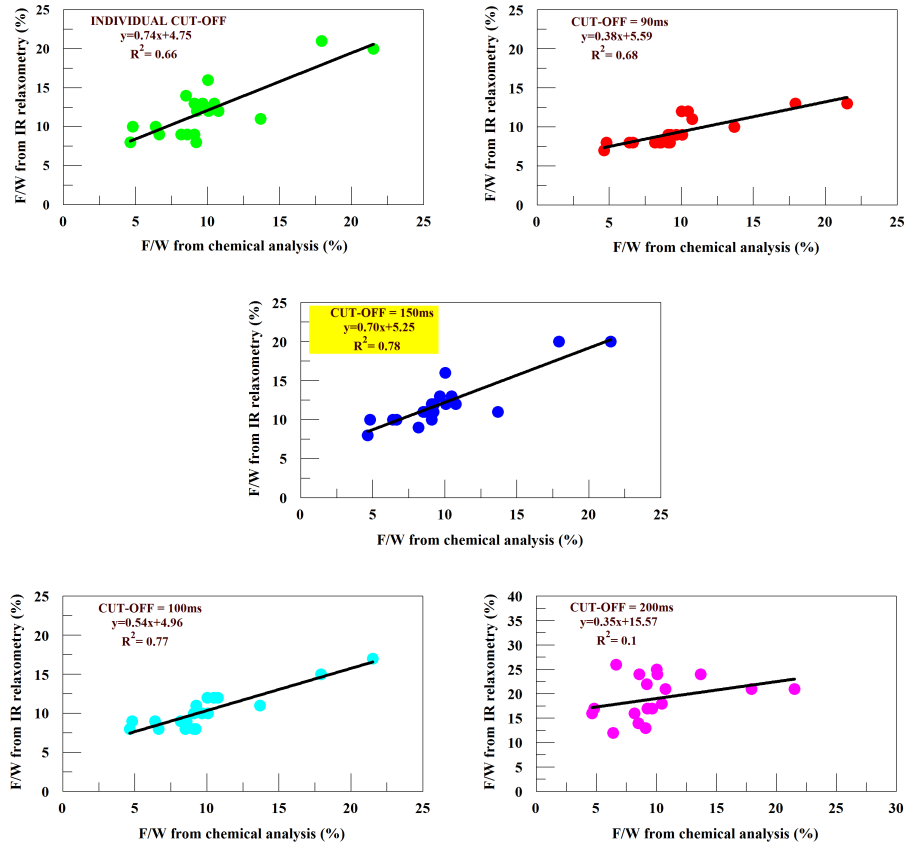


Fig. 2 - Plots of $(F/W)_{\text{IR-NMR}}$ versus chemical data for a set of pork loins. The plots refer to F/W computed for different cut-offs on the ^1H T_1 distributions.

A linear relationship was found between the $(F/W)_{\text{IR-NMR}}$ values and the $(F/W)_{\text{CH}}$ values. Among the values chosen (cut-off = 90ms, 100ms, 150ms, 200ms and an individual cut-off for each sample), the most promising one resulted to be the one at 150ms (see figure 2). Also, it is interesting to note that the best-fit straight lines do not go to zero for zero $(F/W)_{\text{CH}}$. This could be due to the fact that the chemical analysis does not give the membrane lipids which, however, are detected by NMR.

3.2. MRI

The linear relationship (1) can be fit to MRI data obtained with the standard STIR sequence, frequently used for fat suppression purpose. A wider scatter of $(F/W)_{\text{MRI}}$ data was obtained as compared with the $(F/W)_{\text{IR-NMR}}$ results. This is due to the fact that the fat pixels should be black (zero signal), but, as expected, the sequence does not suppress all fat signal equally. In fact the STIR sequence, by its nature, sets to zero the signal of the component with a specific T_1 , but, as we have shown with Relaxometry, fat is characterized by a distribution of T_1 values. Thus, the use of the more appropriate sequence based on a low-pass PERFID filter, which strongly attenuates the signal in selected range of T_1 values and affects the remaining signal with a computable attenuation, should give better results and lead to a better

determination of the F/W ratio. A preliminary attempt of application of this method is shown in Figure 3, where a STIR image of an internal slice of a loin sample is compared with the corresponding image obtained by a preliminary PERFIDI low-pass sequence method.

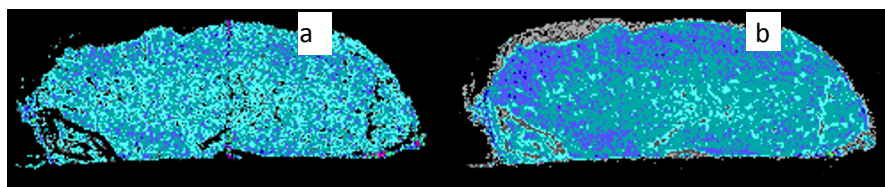


Fig. 3 – Comparison between images of a slice of loin taken with a preliminary PERFIDI sequence method (a) and a conventional STIR sequence (b). A better fat signal suppression is obtained with the PERFIDI filter sequence.

4. Conclusions

Through NMR Relaxometry and MRI images we evaluated the fat-to-water ratio content in pig loins considered as proper model of human muscle tissue. These two techniques revealed themselves to be suitable for this issue. Very good results were obtained by using IR Relaxometry data, with the assumption that ^1H nuclei of fat and water are separable on a quasi-continuous T_1 distribution. The comparison with chemical independent analysis validated this hypothesis. We also set dedicated procedures based on the application of PERFIDI filter sequences^{5,6,7} which are very promising as efficient tools for fat signal suppression.

References

1. AOAC. (2002) Official methods of analysis (17th ed.) Association of Official Analytical Chemists, Arlington, Virginia (USA). Official Method 950.46 for moisture in meat; Official Method 960.39 for ether extract in meat.
2. Bortolotti V, Brown RJS, Fantazzini P, UpenWin: a software to invert multi-exponential decay data, villiam.bortolotti@unibo.it, <http://www.unibo.it/PortaleEn/Research/Services+for+companies/UpenWin.htm>.
3. Borgia GC, Brown RJS, Fantazzini P, Examples of marginal resolution of NMR relaxation peaks using UPEN and diagnostics, *Magn Reson Imaging* **19**: 473-475, 2001.
4. Fantazzini P, Brown RJS, Units in distributions of relaxation times, *Concepts Magn Reson* **27 A**: 122-123, 2005.
5. Sykora S, Fantazzini P, Italian Patent BO2005A000445, 2005.
6. Bortolotti V, Fantazzini P, Gombia M, Greco D, Rinaldin G, Sykora S, PERFIDI filters to suppress and/or quantify relaxation time components in multi-component systems: an example for fat-water systems, *J Magn Reson*, **206**: 219-226, 2010.
7. Sykora S, Bortolotti V, Fantazzini P, PERFIDI: Parametrically Enabled Relaxation Filters with Double and Multiple Inversion, *Magn Reson Imaging*, **25**: 529-532, 2007.

DTI-BASED TRACTOGRAPHY IN NORMAL SUBJECTS AND BRAIN INJURY PATIENTS

G. LUCCONI¹, P. CENNI², C. ROMEO², N. SCRITTORI³

(1) Post-graduate School in Medical Physics, University of Bologna, Italy

(2) Neuroradiology Department, S.Maria delle Croci Hospital, Ravenna, Italy

(3) Medical Physics Department, S.Maria delle Croci Hospital, Ravenna, Italy

We investigated different DTI software and tumour effect on fibers.

DTI brain images of 25 healthy and 5 brain-injury patients were acquired with Philips Achieva 1.5T scanner using EPI-SE DTI sequence with 16 directions.

Images were analyzed with Philips FiberTrack module, DTI-Studio and FSL. We studied corticospinal tracts and corpus callosum, using different FAmin and max_angle values as termination criteria. Group studies were performed.

The number and volume of tracts are reduced when FAmin is increased and max_angle is decreased, with p-values <0.01 . According to the evaluation of experienced neuroradiologists, FAmin=0.15 and max_ang=27° were chosen to compare software. Results of FSL fibertracking with 1 or 2 fibers per voxel are no statistically different.

T-tests between Philips and DTI-Studio lead to p-values >0.05 for corticospinal tract and <0.05 for corpus callosum. FSL analysis leads to higher ADC and lower FA values, with significant differences with other software. In brain injury patients we measured different fibers orientation, reduced FA and increased ADC around the lesion.

Even if DTI fibertracking is a promising non-invasive preoperative imaging tool, the outcome is strongly influenced by the algorithm used and the parameters chosen for the seed generation and fiber propagation.

Keywords: DTI, fibertracking, preoperative imaging

Introduction:

Neuronal tissue consists of tightly packed and coherently aligned axons that are surrounded by glial cells and often organized in bundles. The movements of water molecules are therefore hindered to a greater extent in a direction perpendicular to the axonal orientation than parallel to it.

Diffusion tensor imaging (DTI) is a magnetic resonance technique that is sensitive to the diffusion of water in tissue and has become of great interest in the last years to reveal the anisotropy and orientation of white matter tracts of the brain in vivo. This information can then be used to delineate white matter pathways of the brain by employing fiber tracking algorithms. DTI has thus become an integral part of preoperative diagnostic imaging in many neurosurgical centers.

To-date there has been no general consensus on the optimal diffusion tensor acquisition protocol and different algorithms have been implemented, using either a deterministic or probabilistic approach. Besides, the outcome of a DTI study might be strongly influenced by the parameters chosen for the seed generation and fiber propagation (curvature change and anisotropy thresholds).

In this work we compared different DTI software and evaluated the tumour effect on fibers.

Materials and methods:

In this study, diffusion-tensor MR imaging was performed in 25 healthy and 5 brain injured patients; none of the healthy patients had a neurologic or psychiatric disease or brain injury in his or her previous medical history. We focused on corticospinal tracts and corpus callosum.

Patients were scanned in a supine position with a Philips Achieva 1.5 T scanner using a diffusion weighted echo-planar sequence with 16 directions, whose parameters are reported in Table 1.

A T1-weighted three-dimensional rapid gradient echo sequence was acquired for anatomic reference.

TR (ms)	9388	MX ACQ.	112×110
TE (ms)	70	VOX ACQ. (mm³)	2×2×2
EPI factor	59	FAT SAT.	SPIR
NSA	3	b value (s/mm²)	0-800
Slice thickness (mm)	2	No. of directions	16
Slice gap (mm)	0	No. of slices	60
FOV (mm³)	224×224×120	Scan %	98.3
FOLD.	A-P	Acquisition time (min)	7:49
SENSE	SI	SAR (W/Kg)	< 0,4

Table 1. Acquisition parameters of diffusion weighted echo-planar sequence used in this study

Images were analyzed with three different software packages: Philips FiberTrack module, DTI-Studio and FSL. In all cases data were subjected to image quality control before processing and corrected for eddy currents and motion artefacts; images were also registered to the reference volume at b=0.

The comparison was performed on a qualitative level through visual inspection of the fibers and quantitatively by a statistical analysis of apparent diffusion coefficient (ADC), fractional anisotropy (FA) and eigenvalues through ANOVA and t-test.

For Philips FiberTrack module different anisotropy thresholds (minimum FA between 0.15 and 0.5) and maximal angles (15 - 40 degrees) were tested. An automated 3D ROI was chosen for seed generation as to grant the reproducibility of the process. Data were interpolated with a third order polynomial fit.

Experienced neuroradiologists were asked to evaluate the outcome of the analysis and the thresholds values they indicated as optimal were chosen as standard settings in the software comparison.

The study of the corticospinal tract was performed choosing for seed generation either a single ROI in the internal capsule or two ROIs placed in the internal capsule and in the cortex.

FSL probabilistic fiber tracking algorithm was applied considering both one and two fibers per voxel. Group studies were also performed in order to obtain the tracts common to at least 80% of the subjects.

Results:

The study performed with Philips FiberTrack module showed how the number and volume of tracts are strongly dependent on the thresholds chosen in the algorithm: we observed an evident reduction when minimal FA was increased and maximal angle was decreased (Fig. 1 and Fig. 2); the visual inspection was confirmed by statistical tests leading to p-values < 0.01 .

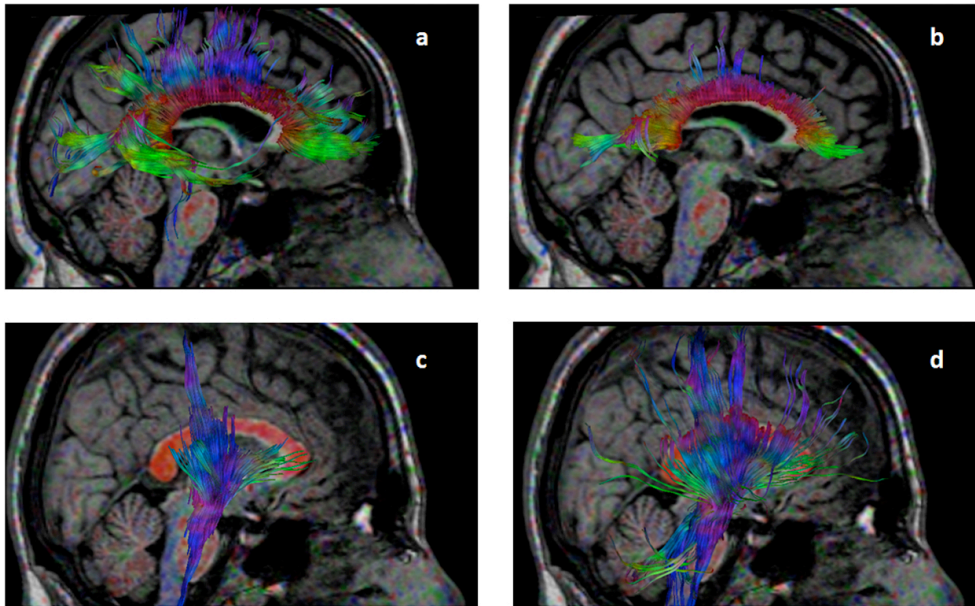


Fig. 1. Comparison of different threshold parameters: a) $FA_{\min} = 0.2$; $ang_{\max} = 27^\circ$; b) $FA_{\min} = 0.5$; $ang_{\max} = 27^\circ$; c) $FA_{\min} = 0.15$; $ang_{\max} = 15^\circ$; d) $FA_{\min} = 0.15$; $ang_{\max} = 40^\circ$

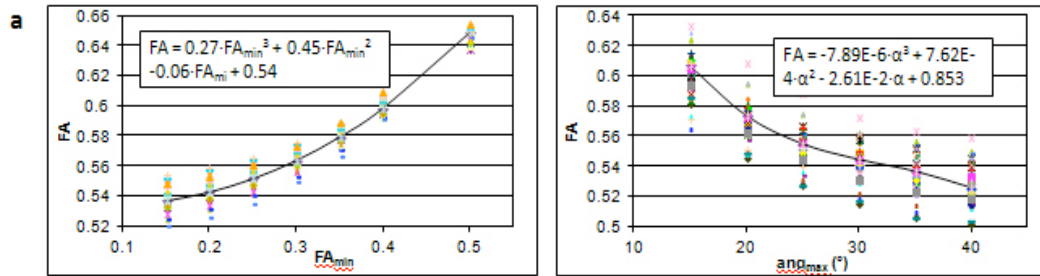


Fig. 2. Third order polynomial fit for corpus callosum (a) and corticospinal tracts (b)

According to the evaluation of experienced neuroradiologists, we chose 0.15 and 27° as the minimal FA and maximal angle for the comparison of the different software packages.

As for the corticospinal tract, fibers obtained considering a single seed ROI and two ROIs were visually quite different (Fig. 3), the last method being more accurate in selecting the proper fibers; statistical tests on FA, ADC and eigenvalues led to p-values between 0.01 and 0.05.

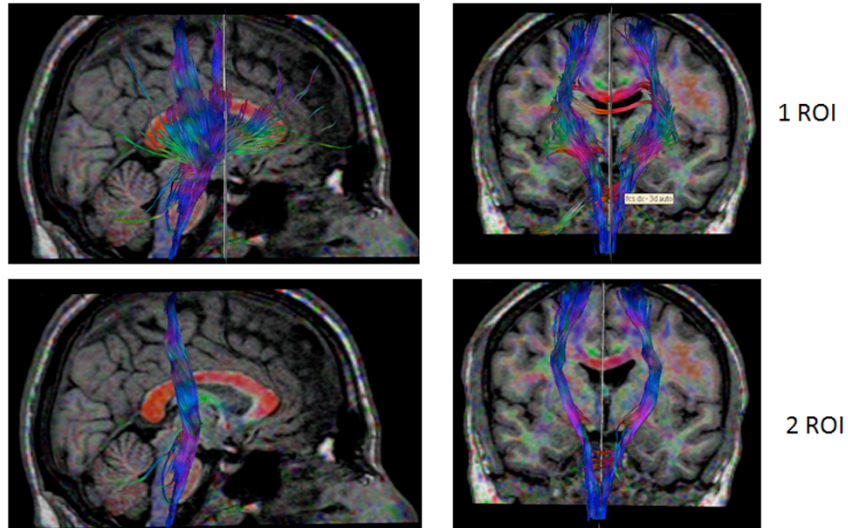


Fig. 3. Comparison of fibers obtained considering a single seed ROI in the internal capsule and two ROIs in the internal capsule and in the cortex

Results of FSL fibertracking with 1 or 2 fibers per voxel were no statistically different, with p-values > 0.05 for all parameters considered in this study. In Fig. 4 is reported the result of the group studies.

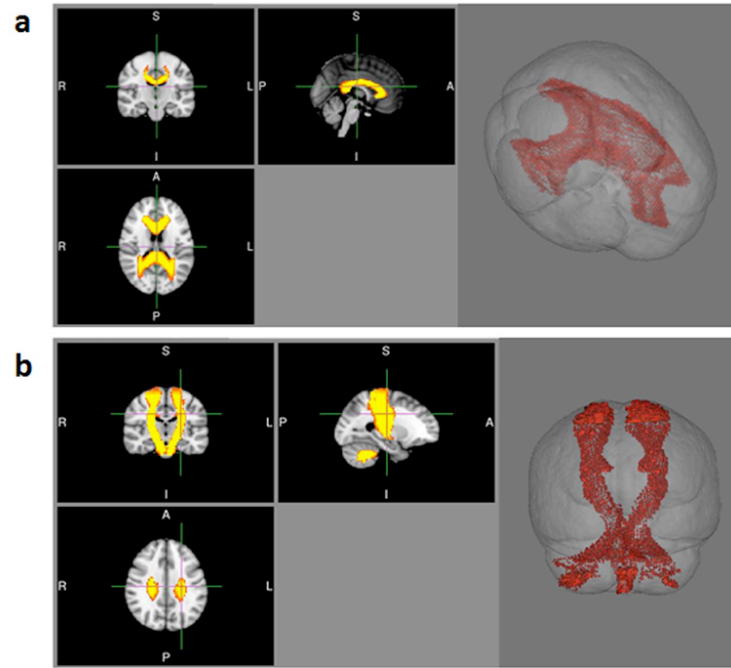


Fig. 4. Fibers common to at least 80% of the subjects for corpus callosum (a) and corticospinal tracts (b)

T-tests between Philips and DTI-Studio showed p-values > 0.05 for all parameters in corticospinal tract and < 0.05 for all parameters except λ_1 for corpus callosum. FSL analysis led to higher ADC and lower FA values, with significant differences with the other software (Fig. 5).

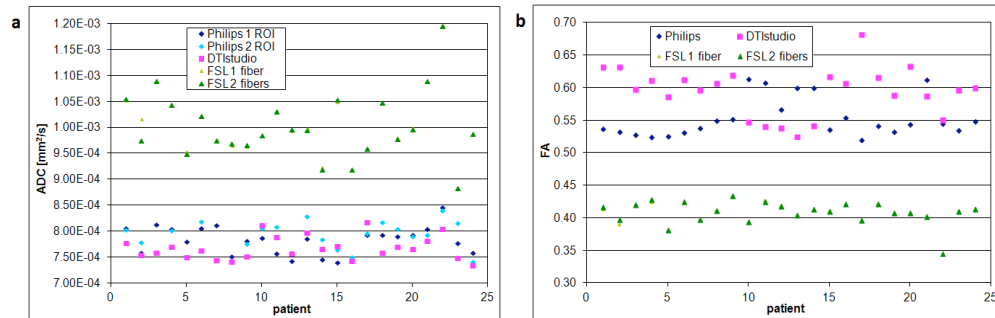


Fig. 5. Comparison of the results of different software packages. (a) ADC for right corticospinal tract; (b) FA for corpus callosum

In brain injury patients we measured reduced FA and increased ADC around the lesion; different fibers orientation was observed too. In Fig. 6 is reported an example of glioblastoma; the corticospinal tract is evidently interrupted.

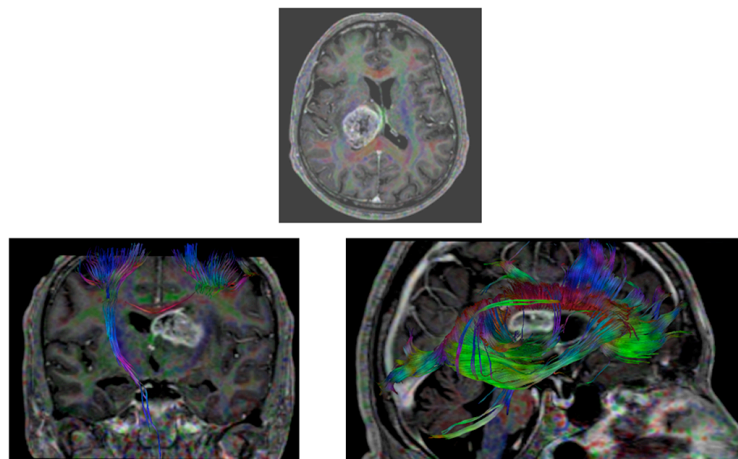


Fig. 6. Fibertracking on a patient affected by a glioblastoma

Conclusion:

This work has shown that the outcome of a DTI study is strongly influenced by the type of algorithm used for the fiber tracking, as well as the parameters chosen for the seed generation and fiber propagation.

The results of statistical tests between the DTI software considered in this study showed clearly that the differences in the displayed fiber bundles are relevant.

However, every software package adopts modified versions of available algorithms and the modifications are hardly ever fully disclosed; besides it is not always possible to export seed ROIs, thus creating an additional uncertainty in the comparison.

Visual inspection of the fibers remains therefore the best way to evaluate the outcome of the different tools and the opinion of experienced neuroradiologists is mandatory in the choice of the optimal parameters.

Considering these results, findings based on DTI tractography should be interpreted carefully, even if DTI fiber tracking presents a promising non-invasive preoperative imaging tool, which is still being developed and needs to be refined further.

References

- Assaf Y. and Pasternak O., Diffusion Tensor Imaging (DTI)-based White Matter Mapping in Brain Research: A Review. *J Mol Neurosci* 34, 2008
- Feigl G. C. et al, Magnetic Resonance Imaging Diffusion Tensor Tractography: Evaluation of Anatomic Accuracy of Different Fiber Tracking Software Packages. *World Neurosurgery*, article in press.
- Hagmann P. et al, Understanding Diffusion MR Imaging Techniques: From Scalar Diffusion-weighted Imaging to Diffusion Tensor Imaging and Beyond. *Radiographics* 26, 2006
- Hasan K.M. et al, A review of diffusion tensor magnetic resonance imaging computational methods and software tools. *Computers in Biology and Medicine* 41, 2011
- Lazar M. et al, White Matter Tractography Using Diffusion Tensor Deflection. *Human Brain Mapping* 18, 2003
- Soares J.M. et al, A hitchhiker's guide to diffusion tensor imaging. *Frontiers in Neuroscience* 7, 2013.

